

FINAL REPORT

FLUORINE-HYDROGEN PERFORMANCE EVALUATION
PHASE I, PART II: NOZZLE PERFORMANCE
ANALYSIS AND DEMONSTRATION

FACILITY FORM 802

N67-33148	
(ACCESSION NUMBER)	(THRU)
<u>368</u>	<u>1</u>
(PAGES)	(CODE)
(NASA CR OR TMX OR AD NUMBER)	<u>27</u>
	(CATEGORY)

By

B. J. Waldman
E. B. Shusterprepared for
NATIONAL AERONAUTICS AND SPACE ADMINISTRATION

Contract NASw-1229

ROCKETDYNE
North American Aviation, Inc.
6633 Canoga Avenue, Canoga Park, California



ROCKETDYNE • A DIVISION OF NORTH AMERICAN AVIATION, INC.

NASA CR-72038
Rocketdyne R-6636-2

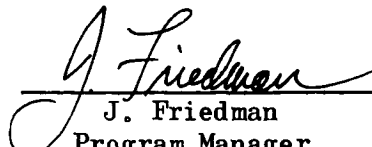
FINAL REPORT
FLUORINE-HYDROGEN PERFORMANCE EVALUATION
PHASE I, PART II: NOZZLE PERFORMANCE
ANALYSIS AND DEMONSTRATION

By

B. J. Waldman
Advanced Projects
Large Engines, Engineering

E. B. Shuster
Project Support
Small Engines, Engineering

Technically Reviewed and Approved By:


J. Friedman
Program Manager
Small Engine Division

April 1967

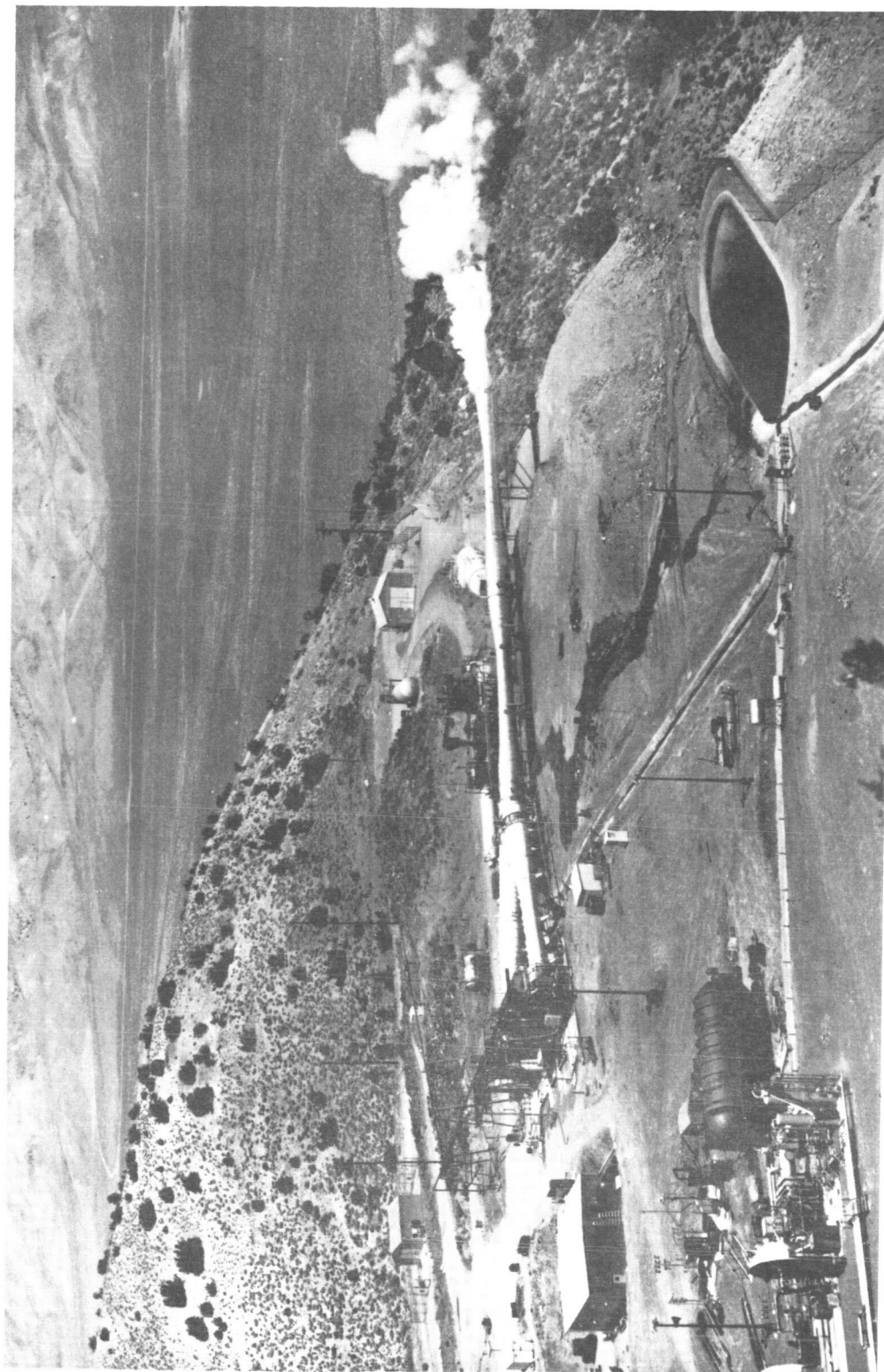


ACKNOWLEDGMENTS

The authors gratefully acknowledge the valuable contributions, both technical and literary, of the following people: M. Yost, R. Burry, S. Clapp, and H. Barber for their competent advice and direction; J. Shoji for his work on performance analysis and contour optimization; R. Fatyol for his conduct of the heat transfer studies; J. Weber and J. Steinberg for the chemical reaction kinetic studies; the Nevada Field Laboratory personnel and, in particular, T. Nielson, W. Smith, and R. Dentner for their support on the test program; R. Koerner, and A. Huebner for assistance in directing the test program; the staff of the Rocket Nozzle Test Facility and, in particular, C. Reyes for conducting the cold flow test program.



ROCKETDYNE • A DIVISION OF NORTH AMERICAN AVIATION, INC.



Frontispiece: Rocketdyne's Nevada Field Laboratory, Area B



FOREWORD

This report presents the theoretical and experimental results of a 2-year study titled Fluorine/Hydrogen Performance Evaluation Program. The Contract, NASw-1229, was conducted by Rocketdyne, a Division of North American Aviation, Inc., and was directed for the National Aeronautics and Space Administration by F. Stephenson (NASA Headquarters) and P. Herr (NASA-LeRC).

The report is submitted in two volumes:

Phase I, Part I. Analysis, Design, and Demonstration of High-Performance Injectors for the Liquid Fluorine-Gaseous Hydrogen Propellant Combination

Phase I, Part II. Nozzle Performance Analysis and Demonstration

ABSTRACT

This volume, Part II of the Fluorine/Hydrogen Performance Evaluation Program Report presents the results of a research program conducted under NASA Contract NASw-1229. Analytical and experimental studies were performed to establish the deliverable thrust chamber performance of the fluorine/hydrogen propellant combination. Six high area ratio nozzle contours were tested in an altitude simulation facility, and the results were compared to analytical predictions. A new type of nozzle contour, intended to improve delivered performance by encouraging chemical recombination, was designed and experimentally evaluated.



CONTENTS

Acknowledgments	i
Foreword	iii
Abstract	iii
Introduction	1
Summary	5
Conclusions	9
Data Correlation	11
Thrust Chamber Efficiency	11
Specific Impulse	37
Nozzle Pressure Correlation	37
Controlled Expansion Nozzle Design	49
Circular Throat Contour Study	54
Task III, Nozzle Design Selection	64
Task IV, Controlled Expansion Nozzle Analysis	70
Performance Analysis	81
Aerodynamic Analysis	81
Drag Analysis	85
Heat Loss Effect	89
Chemical Kinetic Analysis	95
Propellant Impurities	98
Performance Prediction	105
Nozzle Wall Pressure Prediction	114
Chemical Reaction Kinetics	115
Introduction	115
Reaction Rate Study	115
Comparison of Sudden Freezing and Full Kinetic Program	129
Test Hardware	137
Task III Nozzles	137



Task IV Nozzles	143
Combustion Chamber	148
Test Facility and Procedure	155
Altitude Test Capsule	155
Altitude-Simulation System	159
Propellant Systems	162
Control System	168
Instrumentation	168
Test Procedure	180
Performance Data Reduction and Evaluation	185
Data Reduction	185
Data Evaluation	195
Test Results	199
Data Summary	199
Discussion	218
Measurement System Analysis	226
Cold Flow Nozzle Test Program	227
Theoretical Analysis	227
Model Description	231
Facility Description	234
Performance Parameters	234
Test Results	239
Heat Transfer	247
Mathematical Model	247
Measurement Procedure	259
Data Reduction	259
Results	261
Theoretical Performance Maps	271
Nomenclature	291
Nozzle Performance Parameters	291



Nozzle Geometry Parameters	282
Instrumentation Parameters	294
Chemical Reaction Kinetic Parameters	295
Heat Transfer Parameters	296
References	298
<u>Appendix A</u>	
Effect of Throat Radius of Curvature on Bell Nozzle	
Characteristics	301
<u>Appendix B</u>	
Test Results	307
<u>Appendix C</u>	
Measurement System Analyses	327

ILLUSTRATIONS

1. Thrust Chamber Efficiency vs Mixture Ratio, Long Throat	
15-Degree Conical Nozzle, 50 psia	13
2. Thrust Chamber Efficiency vs Mixture Ratio, Long Throat	
15-Degree Conical Nozzle, 100 psia	14
3. Thrust Chamber Efficiency vs Mixture Ratio, Long Throat	
15-Degree Conical Nozzle, 175 psia	15
4. Thrust Chamber Efficiency vs Mixture Ratio, 70-Percent	
Bell Nozzle, 50 psia	17
5. Thrust Chamber Efficiency vs Mixture Ratio, 70-Percent	
Bell Nozzle, 100 psia	18
6. Thrust Chamber Efficiency vs Mixture Ratio, 70-Percent	
Bell Nozzle, 175 psia	19
7. Thrust Chamber Efficiency vs Mixture Ratio, Controlled	
Expansion Nozzle, 50 psia	20
8. Thrust Chamber Efficiency vs Mixture Ratio, Controlled	
Expansion Nozzle, 100 psia	21
9. Thrust Chamber Efficiency vs Mixture Ratio, Controlled	
Expansion Nozzle, 175 psia	22
10. Thrust Chamber Efficiency vs Mixture Ratio,	
10-Degree Conical Nozzle, 50 psia	23
11. Thrust Chamber Efficiency vs Mixture Ratio,	
Short Throat 15-Degree Conical Nozzle, 50 psia	24
12. Thrust Chamber Efficiency vs Mixture Ratio,	
20-Degree Conical Nozzle, 50 psia	25
13. Thrust Chamber Efficiency Comparison at a	
Chamber Pressure of 50 psia	27
14. Nozzle Performance Comparison at 50 psia	28



15.	Thrust Chamber Efficiency vs Chamber Pressure, 15-Degree Conical Nozzle, Mixture Ratio = 15:1	29
16.	Thrust Chamber Efficiency vs Chamber Pressure, 70-Percent Bell Nozzle, Mixture Ratio = 15:1	30
17.	Thrust Chamber Efficiency vs Chamber Pressure, Controlled Expansion Nozzle, Mixture Ratio = 15:1	31
18.	Thrust Chamber Efficiency Comparison at Mixture Ratio = 15:1 .	32
19.	Predicted Kinetic Efficiencies Over an Extended Chamber Pressure Range	34
20.	Difference Between Experimental and Predicted Nozzle Efficiencies for all Task III Test Data	35
21.	Difference Between Experimental and Predicted Thrust Chamber Efficiencies for all Task IV Test Data	36
22.	Specific Impulse Comparison at a Chamber Pressure of 50 psia	38
23.	Specific Impulse Comparison at a Chamber Pressure of 100 psia	39
24.	Specific Impulse Comparison at a Chamber Pressure of 175 psia	40
25.	Specific Impulse Comparison at a Chamber Pressure of 50 psia	41
26.	Specific Impulse Comparison for Long-Throat and Short- Throat 15-Degree Cones at 50-psia Chamber Pressure	42
27.	Wall Pressure Correlation for Long-Throat 15-Degree Conical Nozzle at 50-psia Chamber Pressure	43
28.	Wall Pressure Correlation for 70-Percent Bell Nozzle at 50-psia Chamber Pressure	44
29.	Wall Pressure Correlation for Controlled Expansion Nozzle at 50-psia Chamber Pressure	45
30.	Wall Pressure Correlation for 10-degree Conical Nozzle at 50-psia Chamber Pressure	46



31. Wall Pressure Correlation for Short-Throat 15-degree Conical Nozzle at 50-psia Chamber Pressure	47
32. Wall Pressure Correlation for 20-degree Conical Nozzle at 50-psia Chamber Pressure	48
33. Bell Nozzle Contour Parameters	50
34. Extreme Nozzle Contours Considered in the Circular Throat Contour Study	55
35. Sample Nozzle Optimization Map	57
36. Geometric Efficiency as a Function of Throat Radius of Curvature	59
37. Drag Efficiency as a Function of Throat Radius of Curvature	60
38. Kinetic Efficiency as a Function of Throat Radius of Curvature	62
39. Overall Efficiency as a Function of Throat Radius of Curvature	63
40. Types of Throat Contours	65
41. Performance Decrement Regions of the Circular Throat Contour $(\rho/R_t)_D$ of 5.0	66
42. Nomenclature for Controlled Expansion Nozzle	68
43. Controlled Expansion Nozzle Contour	71
44. Geometric Efficiency versus Axial Coordinate at End of Conical Section	74
45. Effect of α and $(X/R_t)_B$ on Geometric Efficiency	77
46. Effect of α and $(X/R_t)_B$ on Drag Loss	78
47. Effect of α and $(X/R_t)_B$ on Combined Geometric and Drag Efficiency	79
48. Concave-In Throat Contour Controlled Expansion Bell Nozzle	80



49. Effect of Area Ratio on Geometric Efficiency of a 15-Degree Conical Nozzle	84
50. Geometric Efficiency of Bell Nozzle	86
51. Geometric Efficiency of Controlled Expansion Nozzle	87
52. Drag Loss for 15-degree Conical Nozzle-Turbulent Boundary Layer	90
53. Drag Loss for 70-percent Bell Nozzle-Turbulent Boundary Layer	91
54. Drag Loss for Controlled Expansion Nozzle-Turbulent Boundary Layer	92
55. Drag Loss for 20-degree Conical Nozzle-Turbulent Boundary Layer	93
56. Drag Loss for 10-degree Conical Nozzle-Turbulent Boundary Layer	94
57. Heat Loss Correction Factor vs Chamber Pressure	96
58. 15-Degree Cone Streamlines--Throat Region	99
59. 70-Percent Bell Nozzle Streamlines--Throat Region	100
60. Effect of Mixture Ratio on Kinetic Efficiency at Stagnation Pressure of 50 psia	101
61. Effect of Mixture Ratio on Kinetic Efficiency at Stagnation Pressure of 100 psia	102
62. Effect of Mixture Ratio on Kinetic Efficiency at Stagnation Pressure of 175 psia	103
63. Theoretical Effect of Stagnation Pressure on Kinetic Efficiency at Mixture Ratio = 15:1	104
64. Theoretical Efficiency Accounting for Geometric, Drag and Heat Loss for 15-degree Conical Nozzle	106
65. Theoretical Efficiency Accounting for Geometric, Drag and Heat Loss for 70-percent Bell Nozzle	107
66. Theoretical Efficiency Accounting for Geometric, Drag, and Heat Loss for Controlled Expansion Nozzle	108



67.	Theoretical Efficiency Accounting for Geometric, Drag, and Heat Loss for 10-degree Conical Nozzle	109
68.	Theoretical Efficiency Accounting for Geometric, Drag, and Heat Loss for 20-degree Conical Nozzle	110
69.	Theoretical Efficiency Accounting for Geometric, Drag, and Heat Loss for the 15-degree Conical Nozzle	111
70.	Theoretical Efficiency Accounting for Geometric, Drag, and Heat Loss for the 70-Percent Bell Nozzle	112
71.	Theoretical Efficiency Accounting for Geometric, Drag, and Heat Loss for the Controlled-Expansion Nozzle	113
72.	H + H + Ar Recombination Rate Constant vs Temperature	117
73.	H + H + H ₂ O Recombination Rate Constant versus Temperature	118
74.	H + H + H ₂ Recombination Rate Constant versus Temperature	119
75.	H + H + H Recombination Rate Constant versus Temperature	120
76.	Fluorine/Hydrogen Theoretical and Experimental Vacuum Specific Impulse vs Mixture Ratio for NASA-Lewis 15-degree Conical Nozzle	125
77.	Fluorine-Hydrogen Composition and Temperature at the Bray Freezing Point Versus Mixture Ratio	127
78.	Liquid Fluorine-Gaseous Hydrogen Vacuum Specific Impulse vs Weight Mixture Ratio for NASA-LeRC Test Nozzles	128
79.	Bray Vacuum Specific Impulse vs Ratio of Required to Available Reaction Rate at the Freezing Point	132
80.	Long Throat 15-Degree Conical Nozzle Design	138
81.	70-Percent Bell Nozzle Design	139
82.	Long Throat 15-Degree Conical Nozzle Being Installed in the Test Facility	140



83.	Seventy-Percent Bell Nozzle	141
84.	Controlled Expansion Nozzle Design	144
85.	Controlled Expansion Nozzle	145
86.	Short Throat 15-Degree Conical Nozzle Design	146
87.	Short-Throat, 15-Degree Conical Nozzle	147
88.	10-Degree Conical Nozzle Design	149
89.	20-Degree Conical Nozzle Design	150
90.	10-Degree Conical Nozzle	151
91.	20-Degree Conical Nozzle	152
92.	Combustion Chamber Design	153
93.	Nevada Field Laboratory, Small Engine Division	
	Test Area B	156
94.	NFL 4B Altitude Simulation Capsule	157
95.	NFL 4B Altitude Simulation Capsule, Movable Forward Section	158
96.	NFL Altitude Simulation System	160
97.	NFL Hyperflow Engine	161
98.	Task III Schematic Flow Diagram of Nevada Field Laboratory Test Stand 4B, LF_2/GH_2 Performance Program	163
99.	Task IV Schematic Flow Diagram of Nevada Field Laboratory Test Stand 4B, LF_2/GH_2 Performance Program	164
100.	NFL 4B Fluorine Tank Installation	165
101.	NFL 4B Fluorine Tank Control System	166
102.	NFL 4B Test Stand Instrumentation Schematic	170
103.	Measurement Systems, Block Diagram	172
104.	Discharge Coefficient vs Reynolds Number for Hydrogen Sonic Venturi	175
105.	Flow Coefficient vs Nozzle Inlet Pressure (Hydrogen Gas Only)	177
106.	Typical Flowmeter Calibration	179



107.	Engine Start and Shutdown Sequence	182
108.	Sample Pressure Recordings	188
109.	Hydrogen Flowrate vs Venturi Upstream Pressure	191
110.	Variation of Liquid Fluorine Density with Temperature at Indicated Pressures	194
111.	Characteristic Velocity Efficiency vs Chamber Pressure Buzz Level	220
112.	Effect of Fluorine Temperature on Chamber Pressure Oscillation at $P_c = 50$ psia	222
113.	Effect of Fluorine Temperature on Injector Pressure Drop at 50-psia Chamber Pressure	223
114.	Liquid Fluorine/Gaseous Hydrogen Injector Completion of Task IV	225
115.	Theoretical Pressure Profile of Task IIII Controlled Expansion Nozzle Flowing Air	228
116.	Theoretical Drag Loss for Cold-Flow Model of the Task III Controlled Expansion Nozzle	229
117.	Effect of Stagnation Pressure on Vacuum C_F Efficiency of Cold-Flow Model of Task III Controlled Expansion Nozzle	230
118.	Cold-Flow Test Model ($\epsilon = 60:1$, 80 Percent Length)	233
119.	Photograph of Cold-Flow Nozzle of Controlled Expansion Nozzle	235
120.	Rocket Nozzle Test Facility	236
121.	Photographs of Cold-Flow Model Mounted on Single Component Force Balance	237
122.	Comparison Between Theoretical and Experimental Pressure Profile of Task III Controlled Expansion Nozzle Flowing Air	242
123.	Cold-Flow Vacuum Performance Results	243
124.	Cold-Flow Schlieren Photographs, Controlled Expansion Model	246



125.	Schematic Cross Sections of Heat Transfer	
	Isolation Segments	248
126.	Typical Computer Output	254
127.	Experimental Local Heat Flux vs Expansion Area Ratio, Long Throat 15-degree Conical Nozzle	264
128.	Experimental Local Heat Flux vs Expansion Area Ratio, 70-percent Bell Nozzle	265
129.	Experimental Local Heat Flux vs Expansion Area Ratio, Controlled Expansion Nozzle	266
130.	Experimental Local Heat Transfer Coefficient vs Expansion Area Ratio, Long Throat 15-degree Conical Nozzle	267
131.	Experimental Local Heat Transfer Coefficient vs Expansion Area Ratio, 70-percent Bell Nozzle	268
132.	Experimental Heat Transfer Coefficient vs Expansion Area Ratio, Controlled Expansion Nozzle	269
133.	Performance Model Comparison	272
134.	Characteristic Velocity vs Mixture Ratio-- Chemical Equilibrium	274
135.	Characteristic Velocity vs Mixture Ratio-- Frozen Composition	275
136.	Characteristic Velocity vs Chamber Pressure-- Chemical Equilibrium	276
137.	Characteristic Velocity vs Chamber Pressure-- Frozen Composition	277
138.	Vacuum Specific Impulse vs Mixture Ratio-- Chemical Equilibrium	278
139.	Vacuum Specific Impulse vs Mixture Ratio-- Frozen Composition	279



140.	Vacuum Specific Impulse vs Mixture Ratio--	
	Frozen at the Throat	280
141.	Vacuum Specific Impulse vs Expansion Area Ratio--	
	Chemical Equilibrium	281
142.	Vacuum Specific Impulse vs Expansion Area Ratio--	
	Frozen Composition	282
143.	Vacuum Specific Impulse vs Expansion Area Ratio--	
	Frozen at the Throat	283
144.	Vacuum Thrust Coefficient vs Mixture Ratio--	
	Chemical Equilibrium	284
145.	Vacuum Thrust Coefficient vs Mixture Ratio--	
	Frozen Composition	285
146.	Vacuum Thrust Coefficient vs Mixture Ratio--	
	Frozen at the Throat	286
147.	Vacuum Thrust Coefficient vs Expansion Area Ratio--	
	Chemical Equilibrium	287
148.	Vacuum Thrust Coefficient vs Expansion Area Ratio--	
	Frozen Composition	288
149.	Vacuum Thrust Coefficient vs Expansion Area Ratio--	
	Frozen at the Throat	289



TABLES

1. Overall Nozzle Efficiencies	53
2. Wall Coordinates Controlled Expansion Nozzle	72
3. Performance Efficiency Comparison for Final Selected Controlled Expansion Nozzle	75
4. Geometric Efficiency of Conical Nozzles Based on Aerodynamic Throat Area	83
5. Fluorine Impurities Corrections	105
6. Experimental Recombination Rate Constants and Selected Rate Expressions From Literature Survey	116
7. Literature Survey and Revised Rate Expressions	121
8. Recombination Rate Constants and Third-Body Efficiencies	123
9. Recommended B Values for Kinetic Analysis	133
10. Exit Composition for Various Kinetic Models	135
11. Instrumentation	169
12. Data Reduction Table for Test 013	186
13. NFL Data Summary	200
14. Nozzle Test Data	203
15. Nozzle Pressure Data for Long Throat 15-degree Conical Checkout Nozzle	209
16. Nozzle Pressure Data for 70-percent Bell Nozzle	210
17. Nozzle Pressure Data for Controlled Expansion Nozzle	212
18. Nozzle Pressure Data for Long Throat 15-degree Conical Nozzle	213
19. Nozzle Pressure Data for Short Throat 15-degree Conical Nozzle	215
20. Nozzle Pressure Data for 10-degree Conical Nozzle	216
21. Nozzle Pressure Data for 20-degree Conical Nozzle	217



22. Measurement Precision	226
23. Cold-Flow Model Geometric Parameters	232
24. Controlled Expansion Nozzle Cold-Flow Program	
Data Tabulation	240
25. Wall Pressure Tap Locations Measured From Throat Plane . .	241
26. Experimental h_g and q/A as a Function of Chamber	
Pressure and Mixture Ratio	262
27. Figure Numbers for Theoretical Performance Maps	273



INTRODUCTION

The fluorine/hydrogen propellant combination is, on a theoretical basis, one of the most promising of the advanced liquid bipropellant systems. Whether this high theoretical performance could be achieved in practice, however, has long been questioned. Limited previous experimental data exhibited interesting trends; significant performance losses were evident at low chamber pressures but the losses were more sensitive to nozzle contour than existing theory would have indicated. Consequently, a performance investigation program was undertaken to establish the true potential of this propellant combination while extending the pressure range of available test data, and to develop an improved theoretical performance model which would correlate the new and existing performance data.

This program had the following major objectives:

1. Demonstration of high combustion efficiencies over a range of chamber pressures and mixture ratios
2. Precise determination of deliverable performance in high-area-ratio nozzles for a range of chamber pressures and mixture ratios
3. Experimental evaluation of the controlled expansion nozzle concept as a means of improving nozzle efficiency
4. Determination of the effect of various nozzle configurations on performance
5. Establishment of a kinetic model and rate constants capable of accurate performance predictions
6. Evaluation of heat transfer characteristics of the fluorine/hydrogen propellant combination



The program was initially divided into three major tasks; subsequently a fourth task was added to clarify performance trends.

Task I: Hardware Design and Analysis

1. Analysis and design to establish injector, chamber, and nozzle configurations
2. Thrust chamber performance analysis and nozzle contour design, including the design of a controlled expansion nozzle contour

Task II: Injector Performance Demonstration

1. Experimental demonstration of an injector/chamber configuration(s) that provides minimum corrected c^* efficiency of 97 percent over a nine-point chamber pressure/mixture ratio matrix
2. Determination of thrust chamber longitudinal and circumferential heat transfer characteristics

Task III: Nozzle Performance Tests

Experimental evaluation of vacuum specific impulse efficiency attainable in heat sink hardware from 60:1 area ratio nozzles of 15-degree conical, 70-percent bell, and controlled expansion contours

Task IV: Investigation of Nozzle Geometry Effects on Performance

1. Analysis of three additional nozzles including a 10-degree conical, a 20-degree conical, and a 15-degree conical with a different throat radius of curvature ratio
2. Experimental evaluation of vacuum specific impulse efficiency attainable from the Task IV nozzles



This volume contains a description of the work performed under Part II of the program, containing Tasks III and IV and the portion of Task I devoted to nozzle design and analysis. The most significant achievements during this phase of the program were the experimental evaluation of the controlled expansion nozzle and the comparison of the analytically predicted and the delivered performance of the six nozzles tested.

The initial sections of this report present the correlation of the experimental data obtained for the various nozzles, and the optimization procedure for the controlled expansion nozzle design. Supporting details are provided in subsequent sections and include the methods and equipment used to conduct the test program and to evaluate the data, the experimental heat transfer results, and the results of a cold flow performance investigation of the controlled expansion nozzle. Theoretical performance maps are also presented.



SUMMARY

Thrust chamber performance characteristics of the fluorine/hydrogen propellant combination were investigated theoretically and experimentally. In four major tasks, performance analyses and nozzle design studies were conducted, high injector efficiency was demonstrated, and high area ratio nozzle performance was established. This volume of the project final report contains the results of the analytical and experimental studies related to the high area ratio nozzle performance investigation.

Using a triplet pattern injector developed earlier in the program and discussed in Volume 1, performance tests were made with six different nozzle contours. The contours were all area ratio 60:1 and included nozzles of 15-degree (2 throat configurations), 10-degree and 20-degree half angles, a 70-percent length aerodynamically optimized bell nozzle, and an 80-percent length controlled expansion nozzle. The controlled expansion nozzle was designed to minimize the combined kinetic, aerodynamic, and drag losses and thus achieve a maximum performance improvement over the aerodynamically optimized (conventional) bell nozzle.

The thrust chambers and the test stand were highly instrumented and produced high quality test results. The theoretical model produced satisfactory agreement with the experimental values of nozzle performance for all of the nozzles tested.

The thrust chambers were short-test-duration heat sink designs. The combustion chamber for all configurations utilized copper, and the nozzle extensions for all except the controlled expansion design utilized steel. The initial chambers used copper for the throat section while those in Task IV used low carbon steel. The controlled expansion nozzle was fabricated entirely of copper.



Nozzle performance tests were conducted at Rocketdyne's Nevada Field Laboratory (NFL) medium thrust altitude simulation facility. This facility consists of two horizontal firing altitude test capsules with a common two-stage, steam-powered, ejector-diffuser system capable of producing an altitude in excess of 100,000 feet for 150-seconds duration. Sixty-six hyperflow starts were made, producing 105 high quality data points. Several engine tests were conducted at ambient conditions during system calibration and checkout. Data were obtained for each of the Task III nozzles (15-degree long throat conical, 70-percent bell, and controlled expansion) at nominal chamber pressures of 50, 100, and 175 psia with mixture ratio varied over the nominal range of 9:1 to 15:1. In addition, some mixture ratios as low as 4:1 were obtained to provide better definition of the performance vs mixture ratio curves. Testing during Task IV was limited to a nominal chamber pressure of 50 psia; however, mixture ratio covered the same nominal range.

Theoretical nozzle performance analyses were performed for each of the nozzles over the complete test matrix of chamber pressures and mixture ratios. Performance loss modes considered were aerodynamic, viscous drag, chemical reaction kinetic, and heat loss. Additional calculations were made to assess the effect of propellant impurities on performance efficiency to facilitate comparisons between theory and experiment. A study of the reaction kinetic literature and the performance data obtained during this and other fluorine/hydrogen test programs led to a selection of a new set of rate constants and third body efficiencies. To aid in verification of the aerodynamic efficiency prediction of the controlled expansion nozzle, a 1/5-scale model was tested in the Rocketdyne cold flow facility.

The theoretical calculations predicted the mean of the experimental data within 0.5 percent. The data scatter was relatively small with Task III showing virtually all of the data within 2 percent and two-thirds within 1 percent. The Task IV data with instrumentation systems optimized for the single pressure range operation had approximately half the data scatter with



the major portion within 0.5 percent of the mean. Within this small disagreement, there was a general trend for the cones to perform slightly higher than theory and for the contoured nozzles to perform slightly lower than theory. The dependence of performance efficiency on chamber pressures was accurately predicted by the theoretical model. Results indicate that at moderate pump-fed chamber pressures, the delivered efficiency becomes very high.

The scatter of the test data was sufficiently small in comparison to the performance difference between the nozzles that a definite trend was established. As predicted, the controlled expansion nozzle performed approximately 1 percent higher than the bell at 50 psia. The 15-degree long throat cone performance, however, was approximately 1 percent higher than the controlled expansion nozzle, although there was some overlap. Performance was predicted to have been essentially the same.

The second 15-degree conical nozzle, which has a different throat radius of curvature ratio, ρ/R_T , performed essentially the same as the initial design indicating that this parameter has a minor effect on nozzle performance. This was as predicted. The other Task IV conical nozzles performed generally as predicted except, as was typical with all the conical types, the performance was approximately 0.25 percent higher than theory.

As part of the investigation program, several of the nozzles had wall pressure measurements along the length of the nozzle. The values from these measurements were compared to the kinetically predicted values and showed good agreement.

Nozzle wall temperature data were obtained for some nozzles to establish the axial and circumferential variations in heat transfer. (Heat transfer data for the combustion chamber were obtained in the injector test program and are discussed in Volume 1.)



CONCLUSIONS

As a result of investigations performed under this contract, the following items were demonstrated:

1. The deliverable performance of fluorine/hydrogen can now be predicted with confidence, and in the range tested to within approximately 0.5 percent.
2. The "controlled expansion" nozzle contour has successfully demonstrated that nozzles can be designed to encourage chemical recombination and deliver higher performance than standard aerodynamically designed contours of equal length.
3. High combustion efficiencies (greater than the contractually required value of 97 percent) can be obtained over a wide range of chamber pressures and mixture ratios using a single injector.
4. Experimental data have verified the sensitivity of kinetic efficiency to chamber pressure, mixture ratio, and nozzle contour.
 - a. The theoretical model accurately predicts the relationship between chamber pressure and thrust chamber efficiency. Over the pressure range tested (50 to 175 psia), the slope of efficiency vs pressure is steep, leading to high efficiencies at approximately 500 to 600 psia.
 - b. The experimental curves of efficiency vs mixture ratio agreed well with theory in the 9 to 15 mixture ratio range but the limited number of data points in the vicinity of 4 to 6 appeared to be 1 to 2 percent higher than theory.
 - c. The six nozzle contours tested were considerably different but the mean of the performance of each was predicted within 0.5



percent by the theory. However, the cones were consistently 0.25 to 0.5 percent above theory, while the controlled expansion and bell nozzles were 0.5 percent below theory; as a result the difference between the cones and the other two nozzles were approximately 1 percent greater than predicted.



DATA CORRELATION

In this section, the performance data generated in the Task III and IV test programs are compared to theoretical predictions. The comparisons are made both in terms of thrust chamber efficiency and delivered specific impulse. For the task III nozzles, each of the three nominal chamber pressures, 50, 100 and 175 psia, are shown over a mixture ratio range of 4 to 18 while the Task IV nozzles are shown at the nominal chamber pressure of 50 psia over the same mixture ratio range. Nominal mixture ratio range was 9 to 15; however, the extended range was used to obtain better curve definition due to the small performance variations in the 9 to 15 range.

THRUST CHAMBER EFFICIENCY

Thrust chamber efficiency, theoretically, is equal to one minus the sum of the divergence, drag, kinetic, and heat loss corrections where the corrections are expressed as the difference between one and the calculated efficiency.

Thus:

$$\eta_{TC_{theo}} = 1 - [(1 - \eta_G) + (1 - \eta_D) + (1 - \eta_k) + (\xi_{HL_{I_s}} - 1)]$$

This can be simplified to:

$$\eta_{TC} = \eta_G + \eta_D + \eta_k - \xi_{HL_{I_s}} - 1$$

Experimentally, the value is equal to the delivered vacuum specific impulse efficiency, corrected for the effects of combustion inefficiency and propellant impurities.



Thus:

$$\eta_{TC_{exp}} = \frac{\eta_{I_{vac}}}{\eta_{c*_{corr}}} + (\xi_{I_{I_s}} - 1)$$

Where $\eta_{c*_{corr}}$ represents combustion efficiency corrected by converting the measured efficiency to the aerodynamic throat, no heat loss and pure fluorine conditions.

Mixture Ratio Effects

The efficiency correlations vs mixture ratio for the various nozzles are shown in Fig. 1 through 14. In each case, the distance between 1.0 and line A is the heat loss. Line B represents the sum of the heat loss and divergence effects; line C the sum of heat loss, divergence, and drag effects. Line D in each figure represents the sum of heat loss, divergence, drag, and kinetic effects and is the theoretically predicted curve of thrust chamber efficiency vs mixture ratio for the indicated nozzle and chamber pressure.

The two 15-degree nozzles discussed and described as "long throat" (Task III) and "short throat" (Task IV) are identical except for the nozzle contour at the exit of the throat section. The radius of curvature ratios, ρ/R_T , are 3.635 and 0.392, respectively, thus the long and short designation.

From Fig. 1 through 3, for the 15-degree long throat conical nozzle, it is seen that there is a consistent trend for the mean of the data to be approximately 0.5 percent above the theoretical line. In Fig. 2, for 100 psia, one point is shown for the conical nozzle used early in the

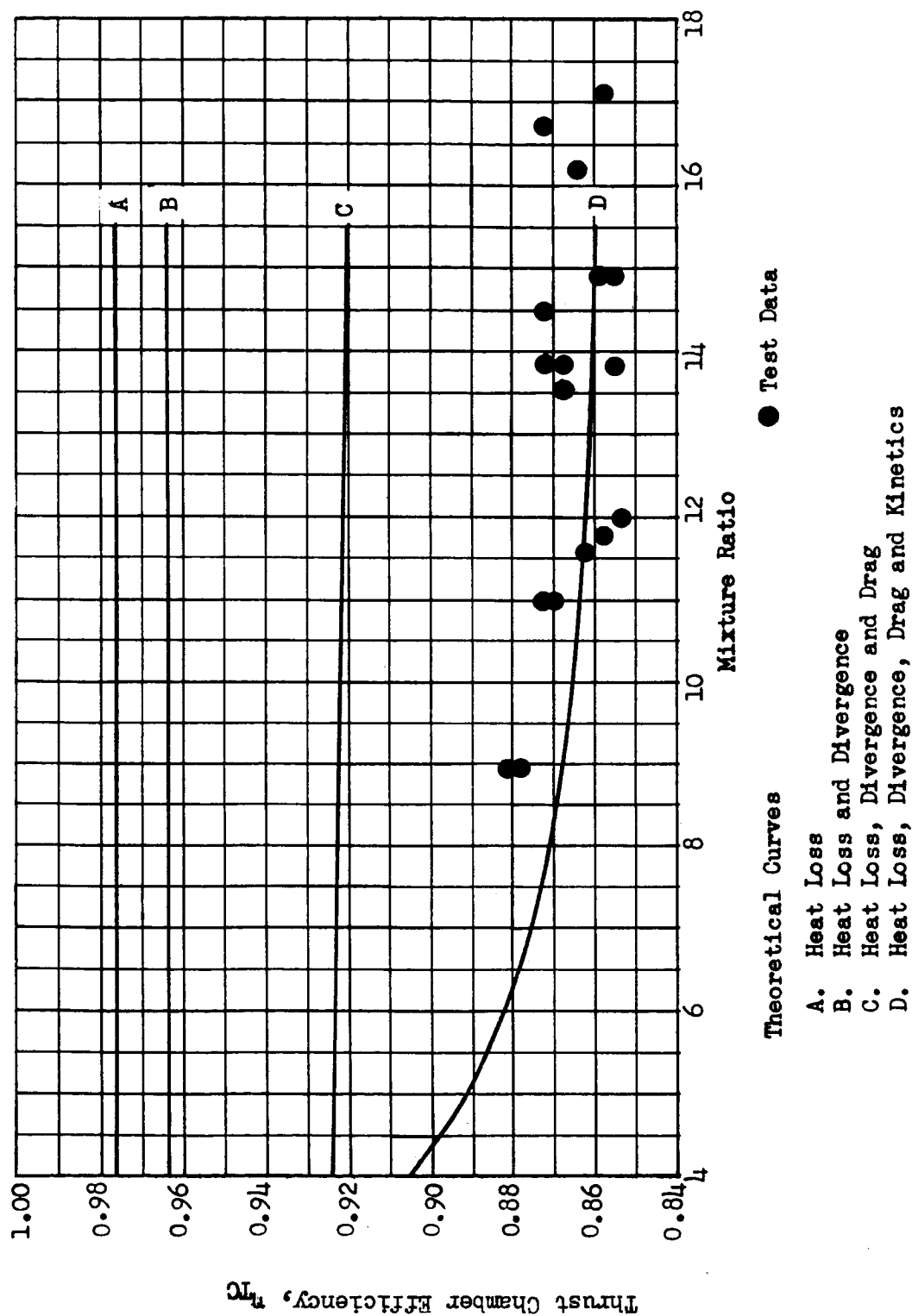


Figure 1. Thrust Chamber Efficiency vs Mixture Ratio, Long Throat 15-Degree Conical Nozzle, 50 psia

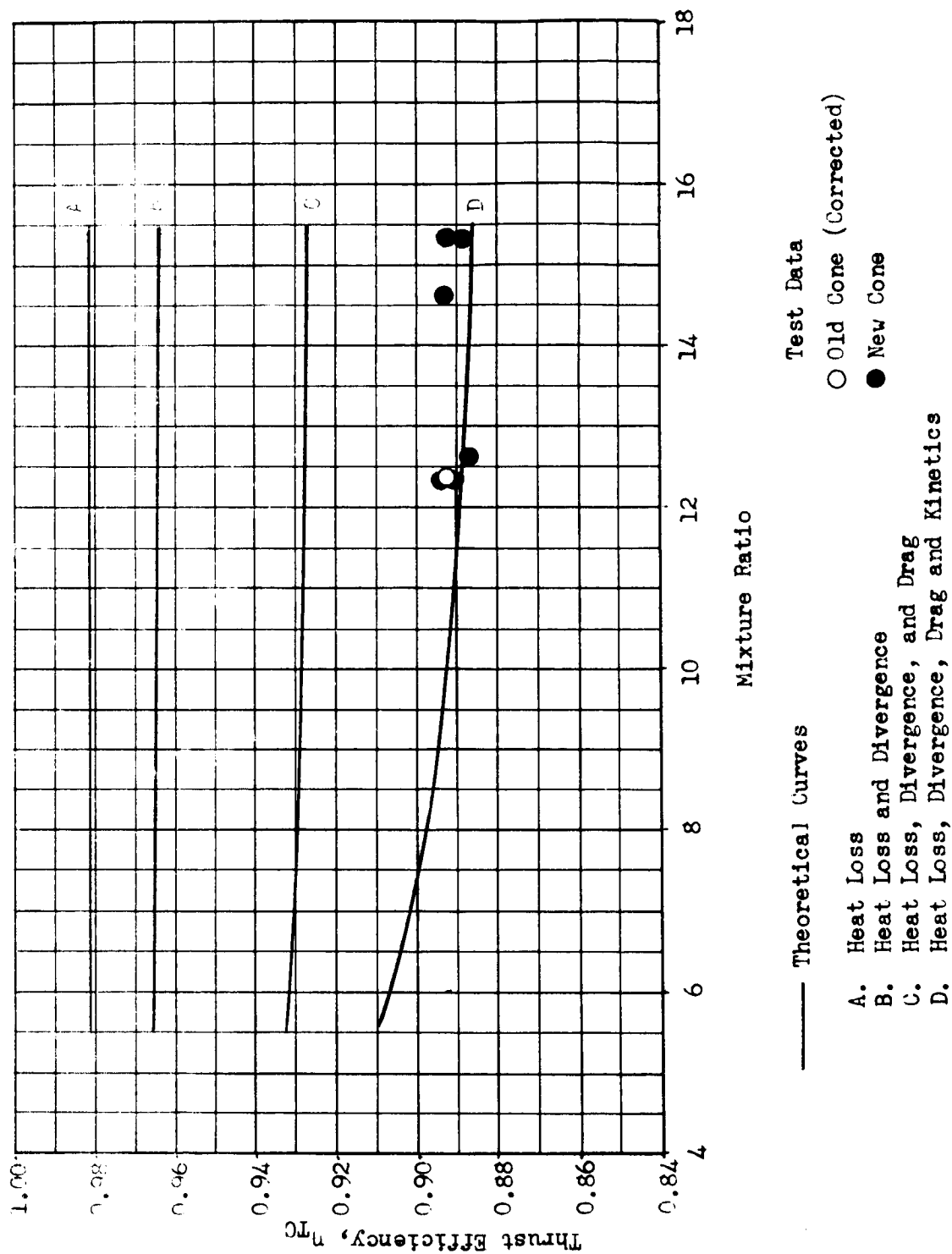


Figure 2. Thrust Chamber Efficiency vs Mixture Ratio, Long Throat 15-Degree Conical Nozzle, 100 psia

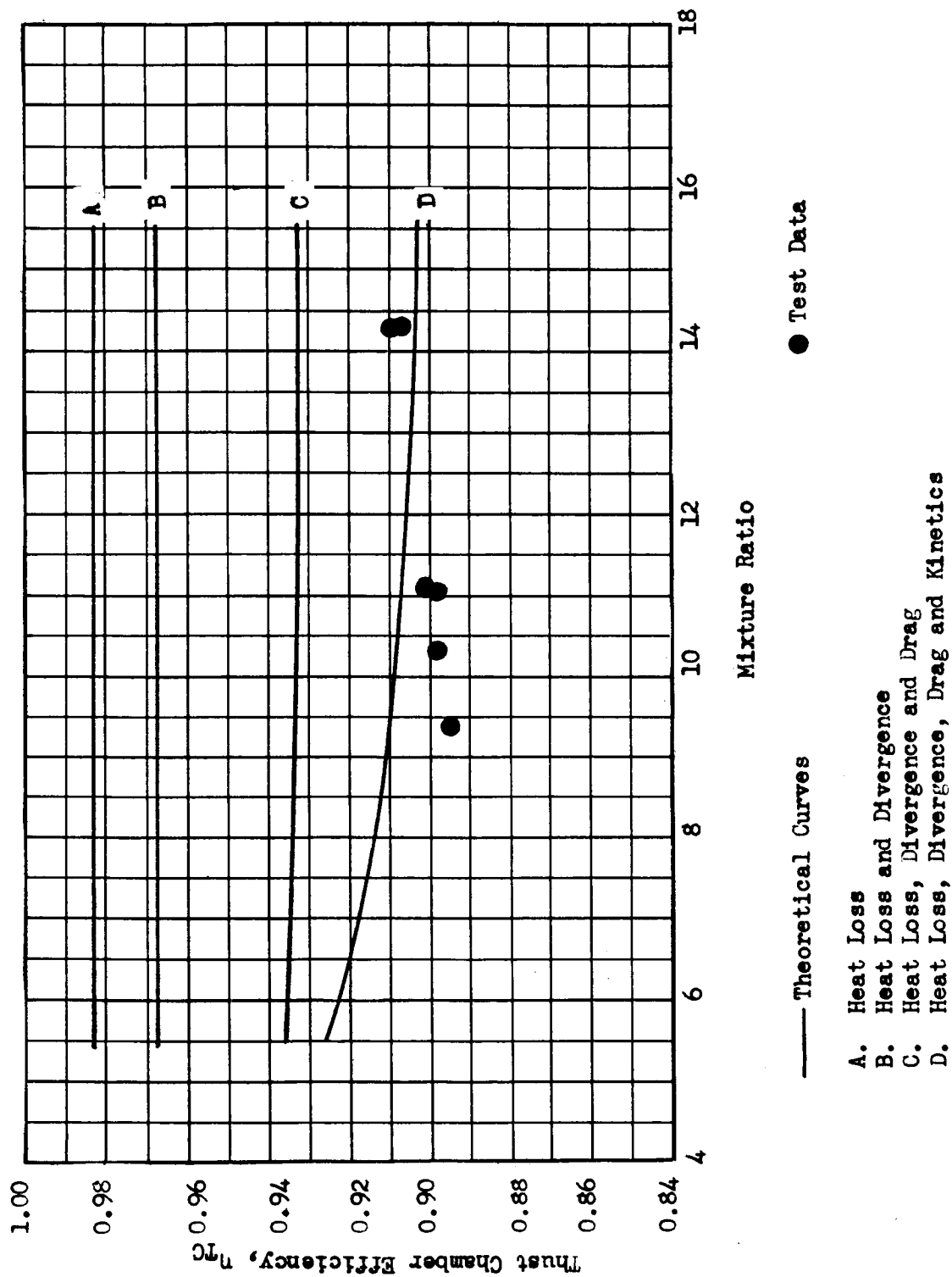


Figure 3. Thrust Chamber Efficiency vs Mixture Ratio, Long Throat 15-Degree Conical Nozzle, 175 psia



program for system checkout. This data point is shown 1 percent higher than observed because an imperfection in the contour produced approximately a 0.5-percent geometric efficiency loss relative to the perfect cone, and because the test was actually at 85 psia which caused an additional efficiency reduction of 0.5 percent on a theoretical basis.

Data and theory for the 70-percent bell nozzle are compared in Fig. 4 through 6. Here it is seen that in the 9 to 15 mixture ratio range the mean of the data are generally 0.5 percent below the theoretical line. At the very low mixture ratios, there is a tendency for the data to be 1 to 2 percent higher than theory (although this is somewhat obscured by the unexplainably low data between mixture ratios of 5 and 8 at 100 psia). This trend, if more thoroughly verified, would indicate that H_2 may be a more efficient third body (in recombination reactions) than has been assumed. This deduction is based on the greatly increased concentration of H_2 in the combustion products at low mixture ratios (Fig. 77).

The results for the controlled expansion nozzle are shown in Fig. 7 to 9. Here, in the 9 to 15 mixture ratio range, the data are about 0.5 percent below the theory at 50 psia, 1 to 1.5 percent low at 100 psia, and in virtually perfect agreement at 175 psia. In view of the excellent agreement at pressures of 50 and 175 psia, the data at 100 psia appear somewhat anomalous, although the tight scatter of the data tends to support the validity of these points. At very low mixture ratios for 50 psia the data, as was the case for the bell, are 1 to 2 percent above the theoretical line.

Task IV data are shown in Fig. 10 through 12 for the 10-degree, 15-degree short throat, and 20-degree conical nozzles, respectively. The mean of all of the test data is 0.24 percent higher than the theory. This is consistent with the previous results with the 15-degree long throat nozzle.

The 50-psia data and theory for the three Task III nozzles are summarized in Fig. 13. The 15-degree long throat cone and controlled expansion

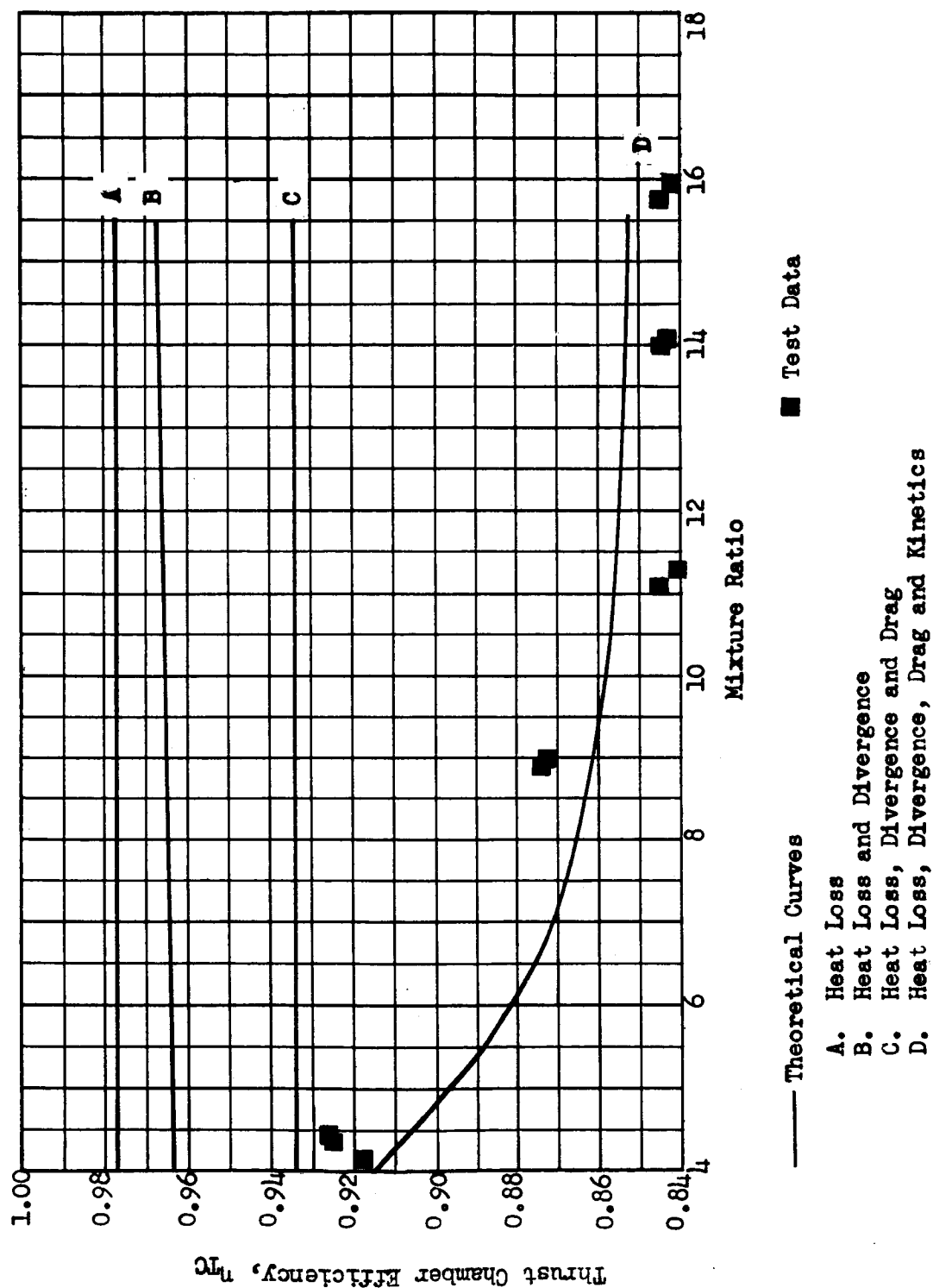


Figure 4. Thrust Chamber Efficiency vs Mixture Ratio, 70-Percent Bell Nozzle, 50 psia

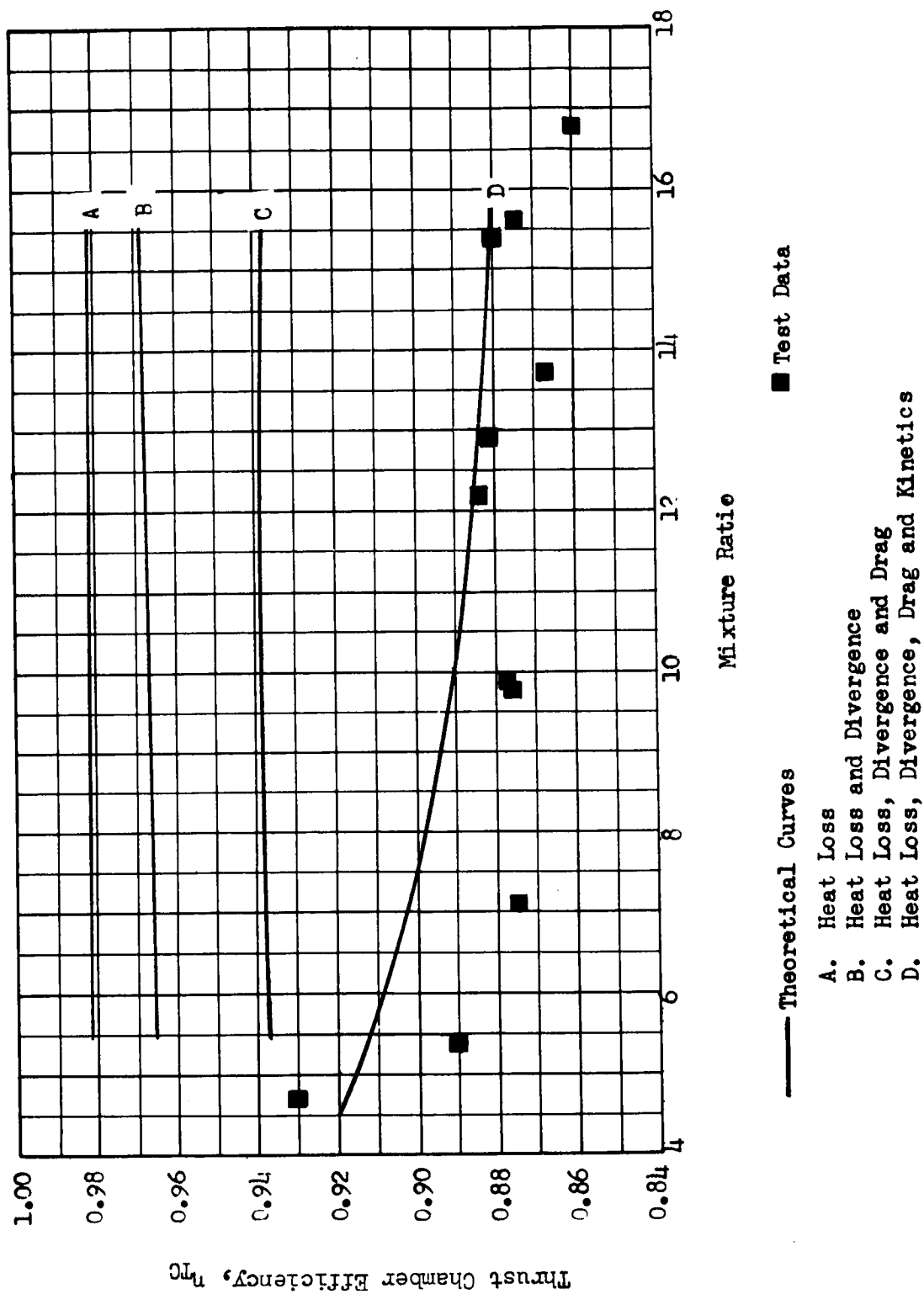


Figure 5. Thrust Chamber Efficiency vs Mixture Ratio, 70-Percent Bell Nozzle, 100 psia

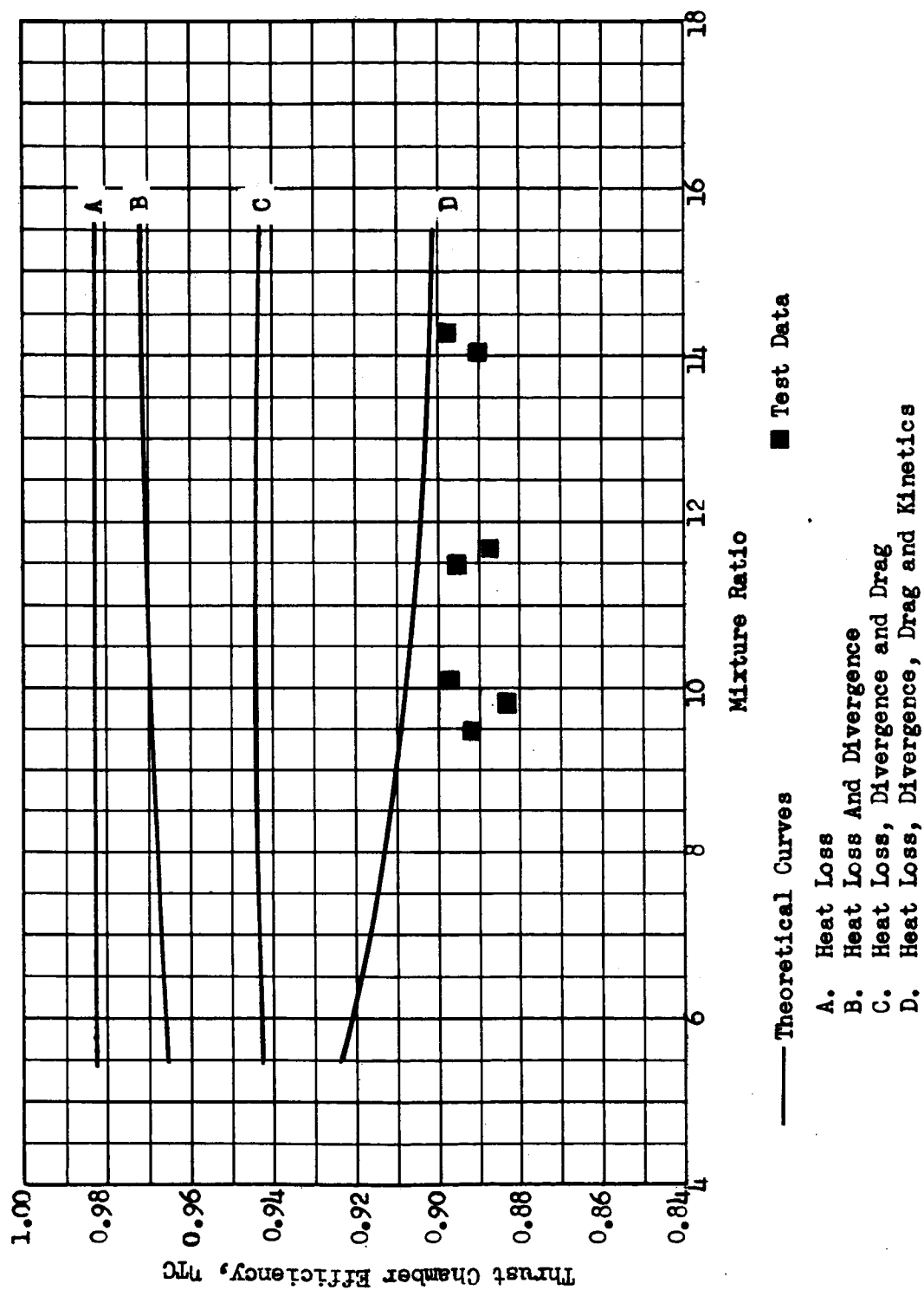


Figure 6. Thrust Chamber Efficiency vs Mixture Ratio, 70-Percent Bell Nozzle, 175 psia

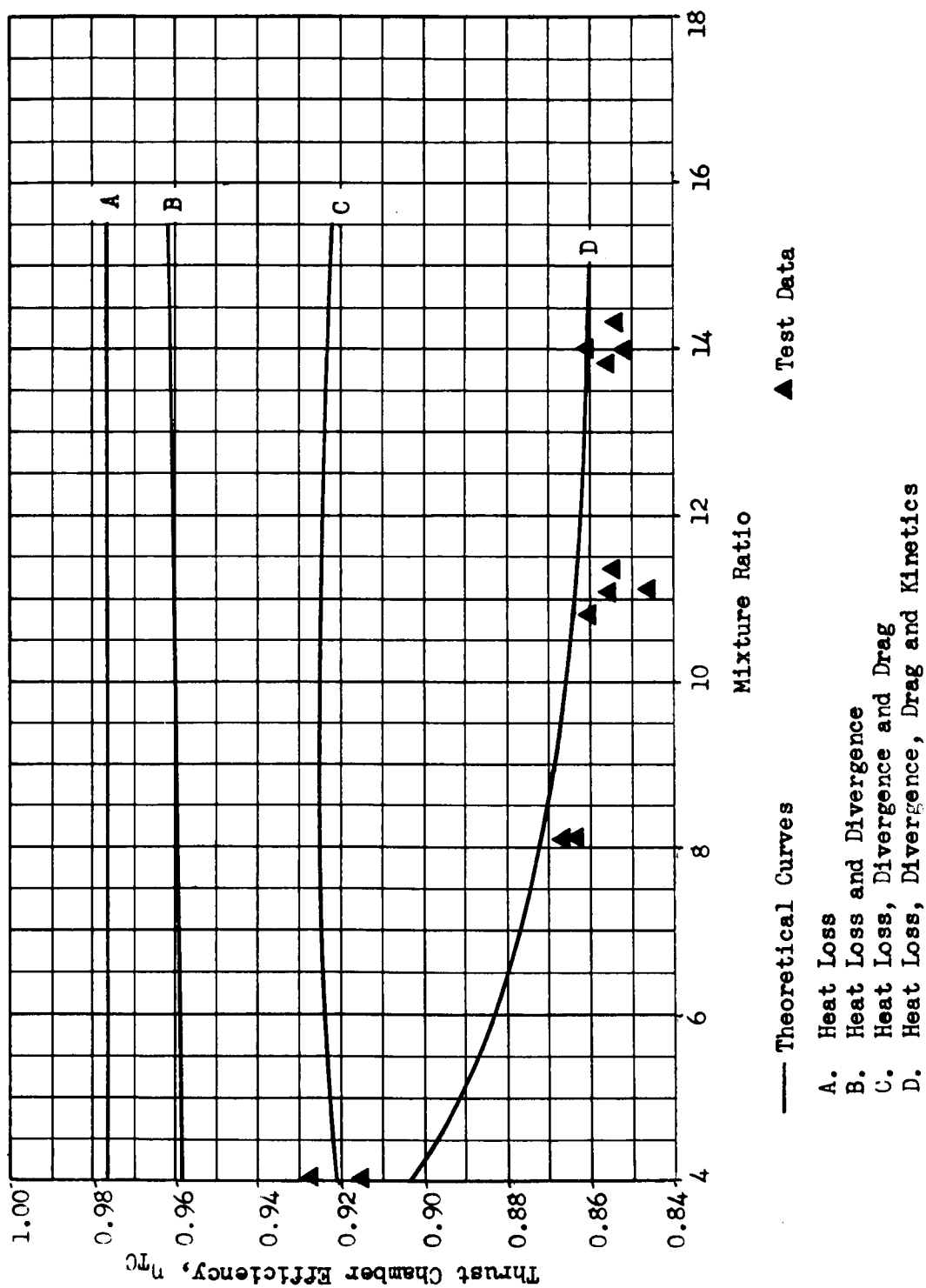


Figure 7. Thrust Chamber Efficiency vs Mixture Ratio, Controlled Expansion Nozzle, 50 psia

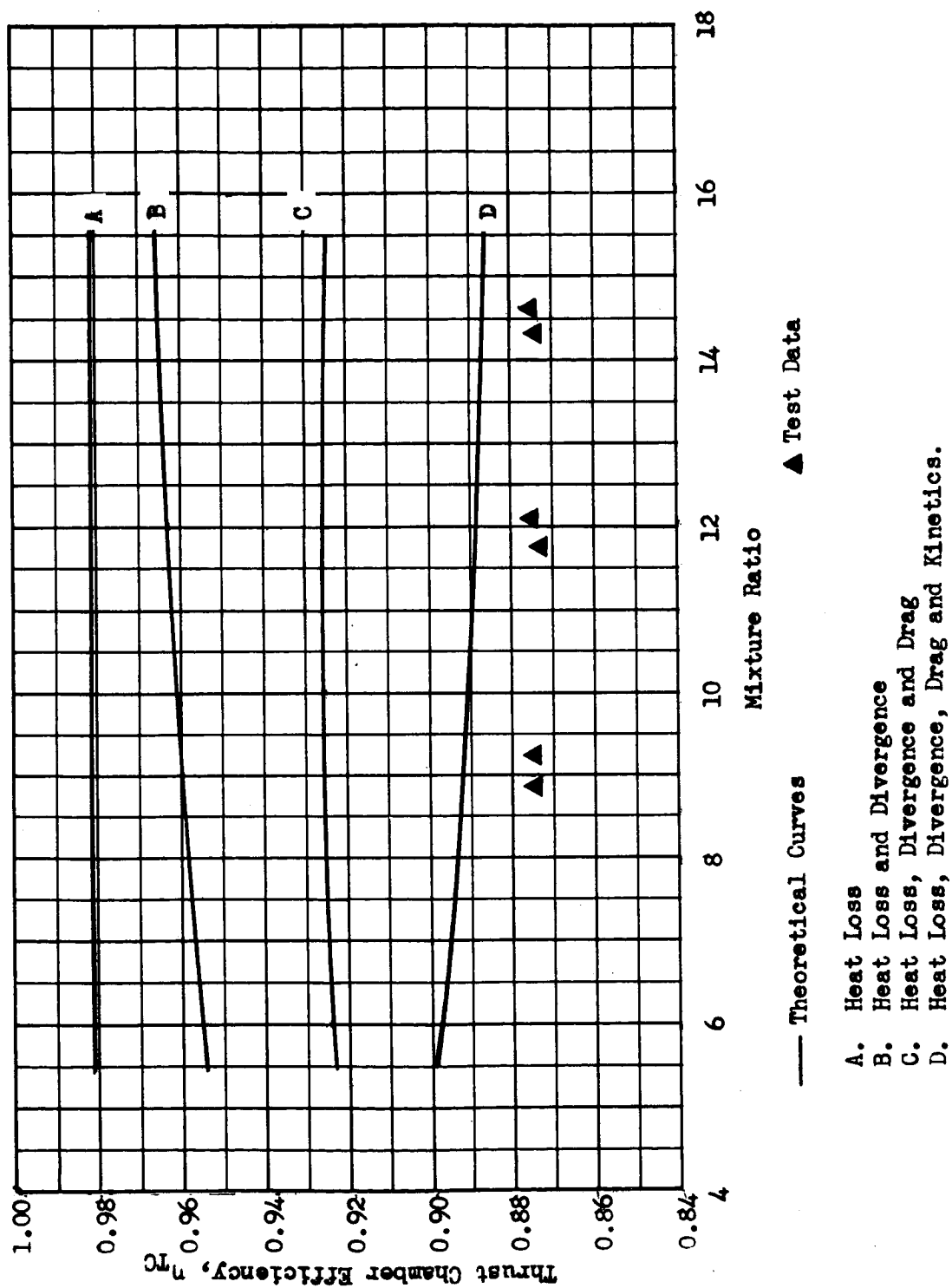


Figure 8. Thrust Chamber Efficiency vs Mixture Ratio, Controlled Expansion Nozzle, 100 psia

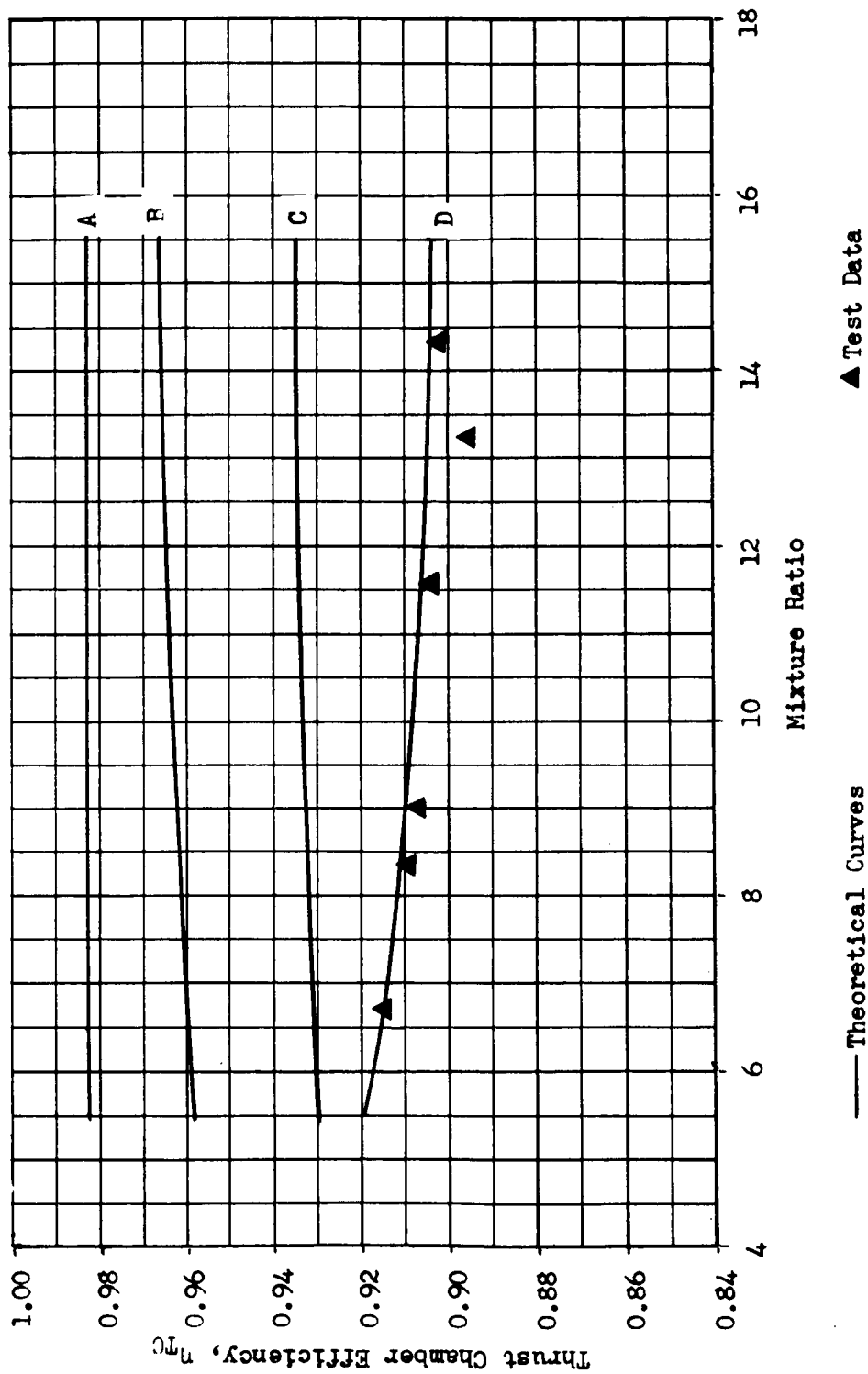


Figure 9. Thrust Chamber Efficiency vs Mixture Ratio, Controlled Expansion Nozzle, 175 psia

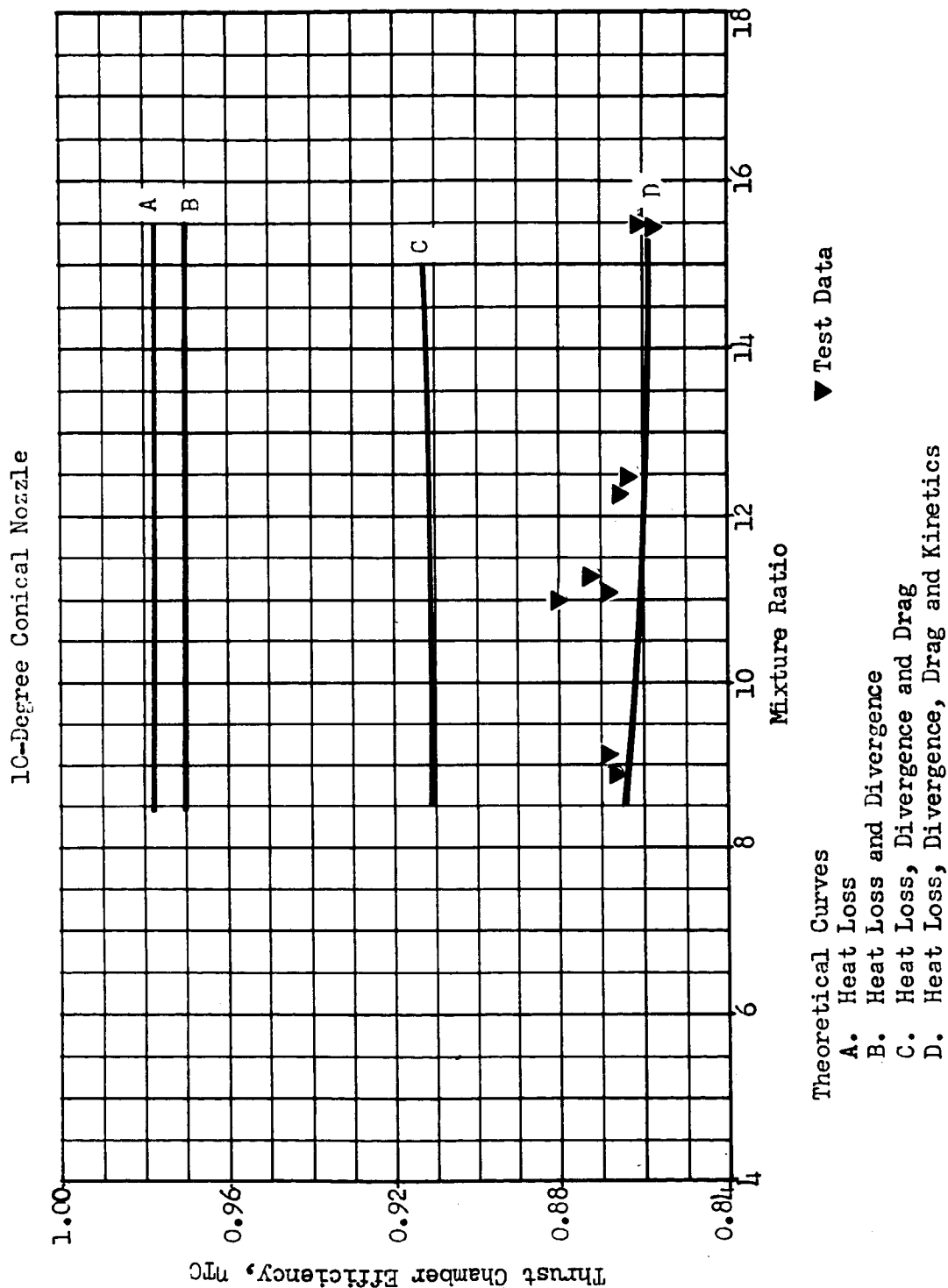
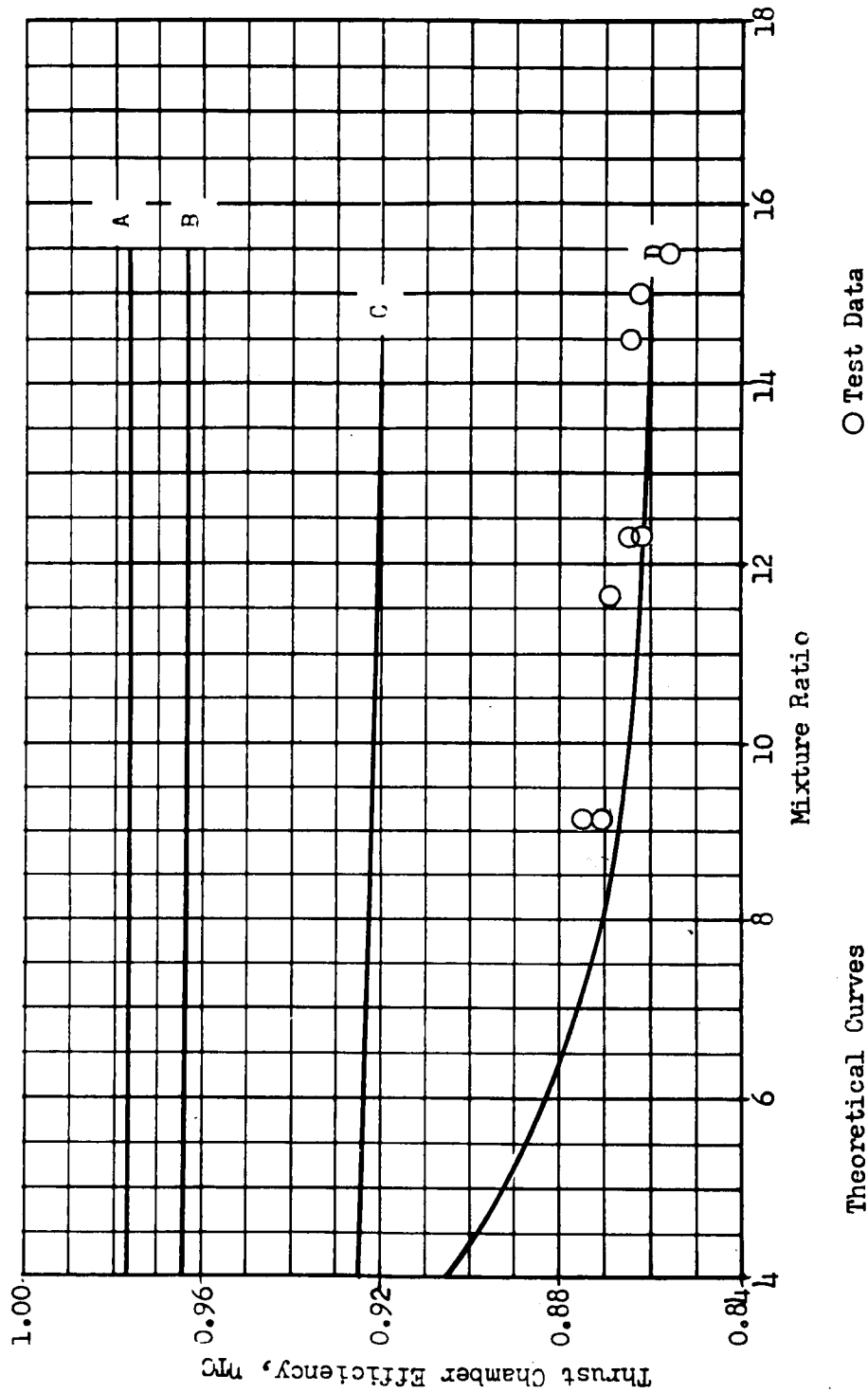


Figure 10. Thrust Chamber Efficiency vs Mixture Ratio, 10-Degree Conical Nozzle, 50 psia



15-Degree Conical Nozzle, $P/R_T = 0.392$



Theoretical Curves

- A. Heat Loss
- B. Heat Loss and Divergence
- C. Heat Loss, Divergence and Drag
- D. Heat Loss, Divergence, Drag and Kinetics

○ Test Data

Figure 11. Thrust Chamber Efficiency vs Mixture Ratio, Short Throat 15-Degree Conical Nozzle, 50 psia

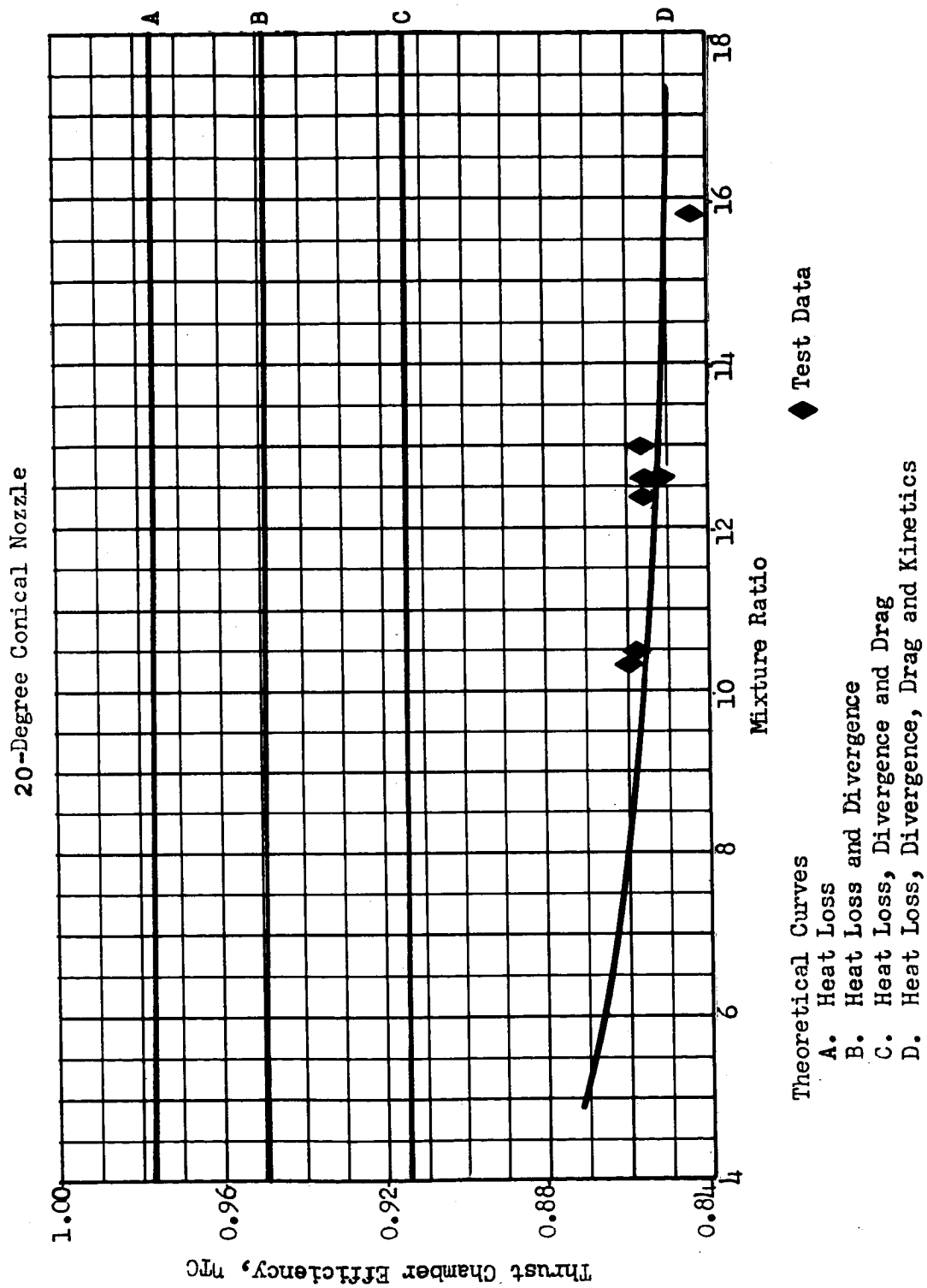


Figure 12. Thrust Chamber Efficiency vs Mixture Ratio, 20-Degree Conical Nozzle, 50 psia



nozzles were predicted to have equal performance, both about 1 percent higher than the 70-percent bell. From the figure it is clear that the controlled expansion nozzle performance is, indeed, 1 percent higher than the bell although both are about 0.5 percent below their theoretical lines. The controlled expansion data points overlap the lower portion of the cone data scatter, although the mean of the cone data is 0.5 percent above theoretical. Thus, in the 9 to 15 mixture ratio range, the 15-degree cone performed 1 percent higher in relation to the other two nozzles than was predicted, but all the nozzles performed within 0.5 percent of theory. At the very low mixture ratios, as predicted, the mean of the bell data becomes slightly higher than or equal to the mean of the controlled expansion data. However, all five data points are above the theoretical lines.

Figure 14 compares the performance of the Task IV conical nozzles and the Task III 15-degree conical nozzle. The 10- and 15-degree cones achieved nearly equal performance as a result of the increased kinetic efficiency and decreased drag efficiency of the 10-degree relative to the 15-degree cone. The 20-degree cone had lower performance than any of the others. The two 15-degree cones had essentially equal performance, verifying that in the range of conditions tested the divergence angle, and not the throat radius of curvature, dominates the performance.

Chamber Pressure Effects

To compare the experimental and theoretical trends with chamber pressure, Fig. 15 to 18 are presented. The theoretical lines on these figures are analogous to the similar lines on Fig. 1 to 14, but express the variation of performance with chamber pressure for a mixture ratio of 15:1. The bars indicate the location and width of the data band on the efficiency vs mixture ratio curves. It is seen that the bands for the 15 degree long throat cone and bell parallel the curves almost exactly, with the

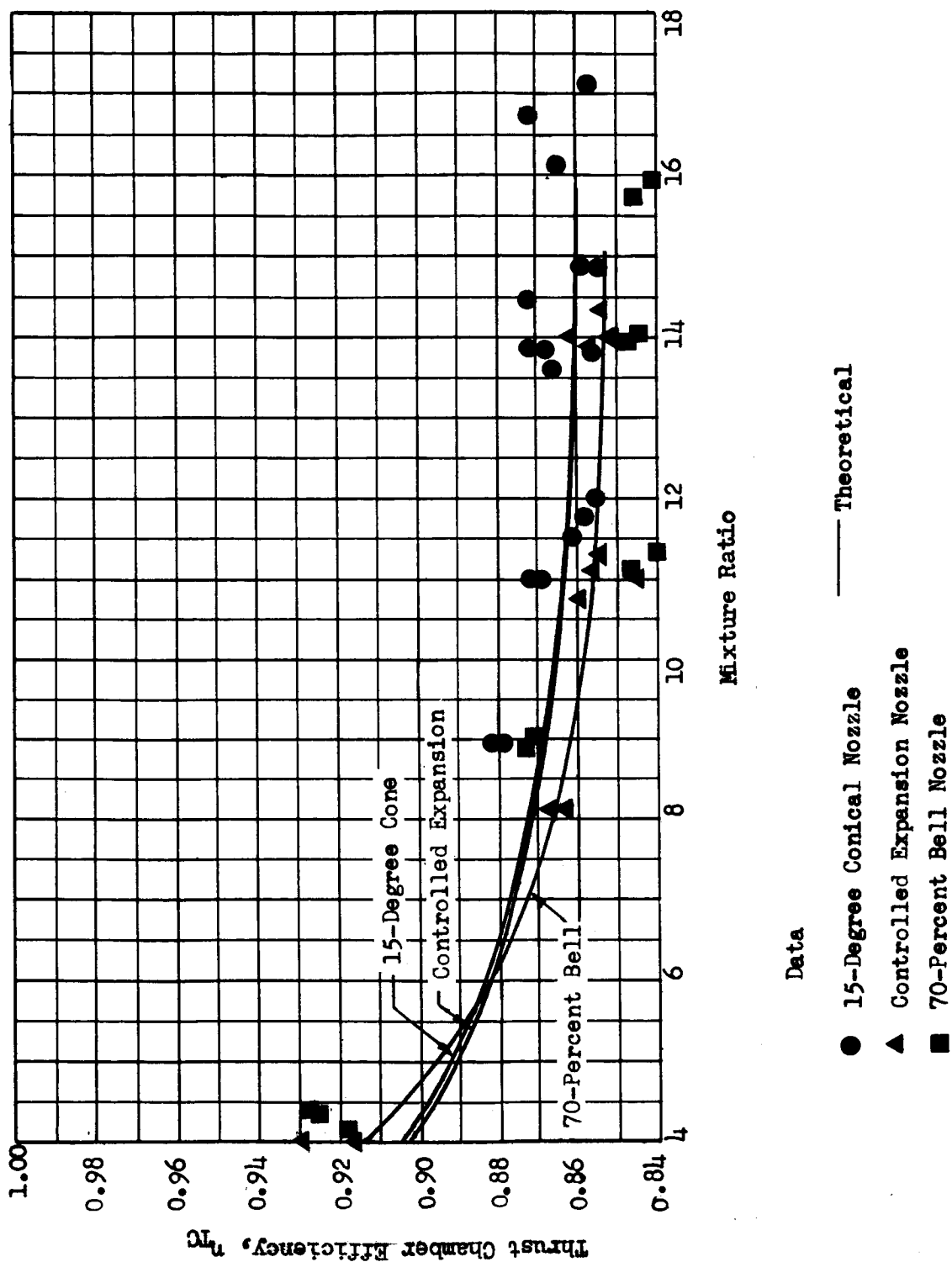


Figure 13. Thrust Chamber Efficiency Comparison at a Chamber Pressure of 50 psia

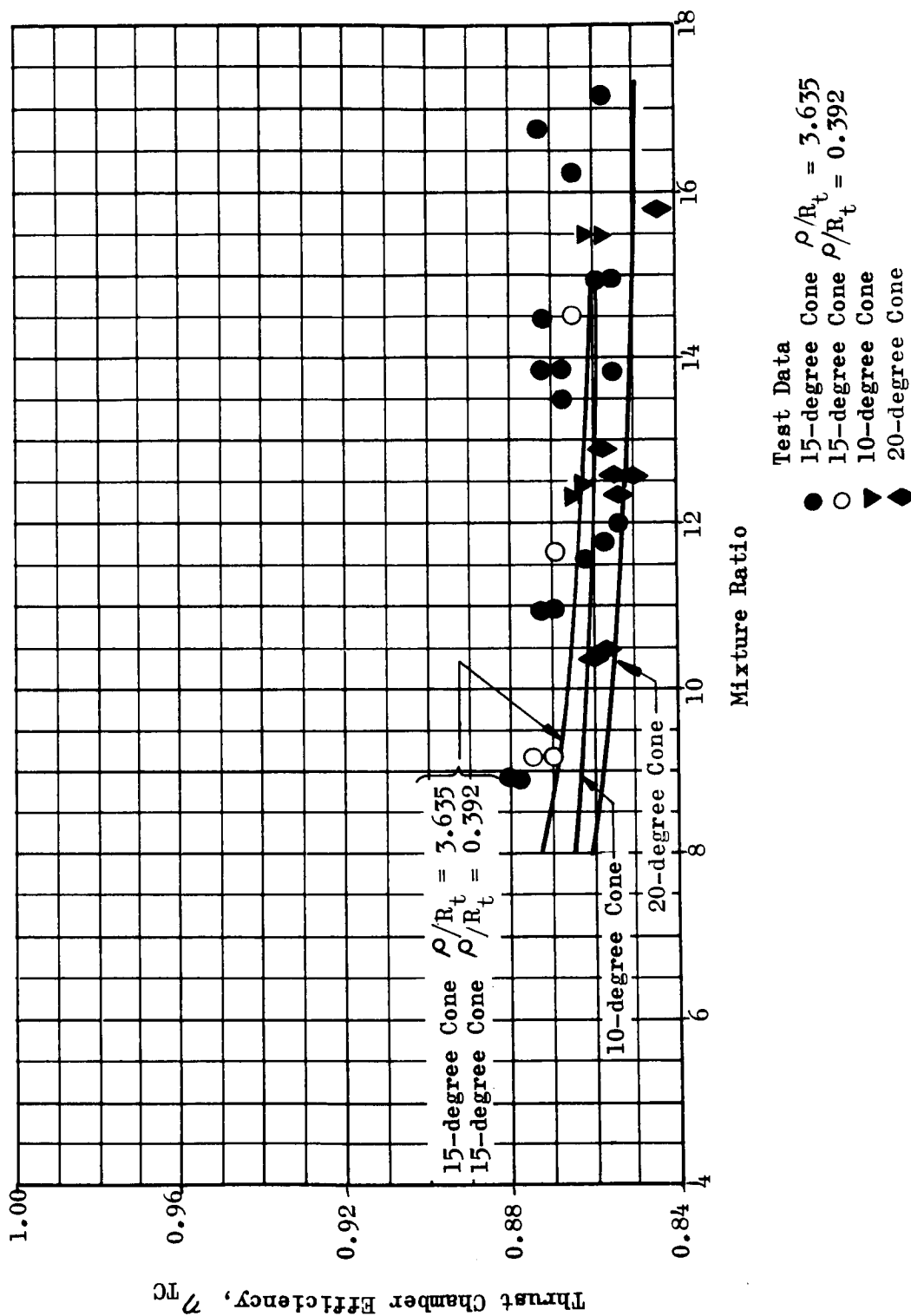
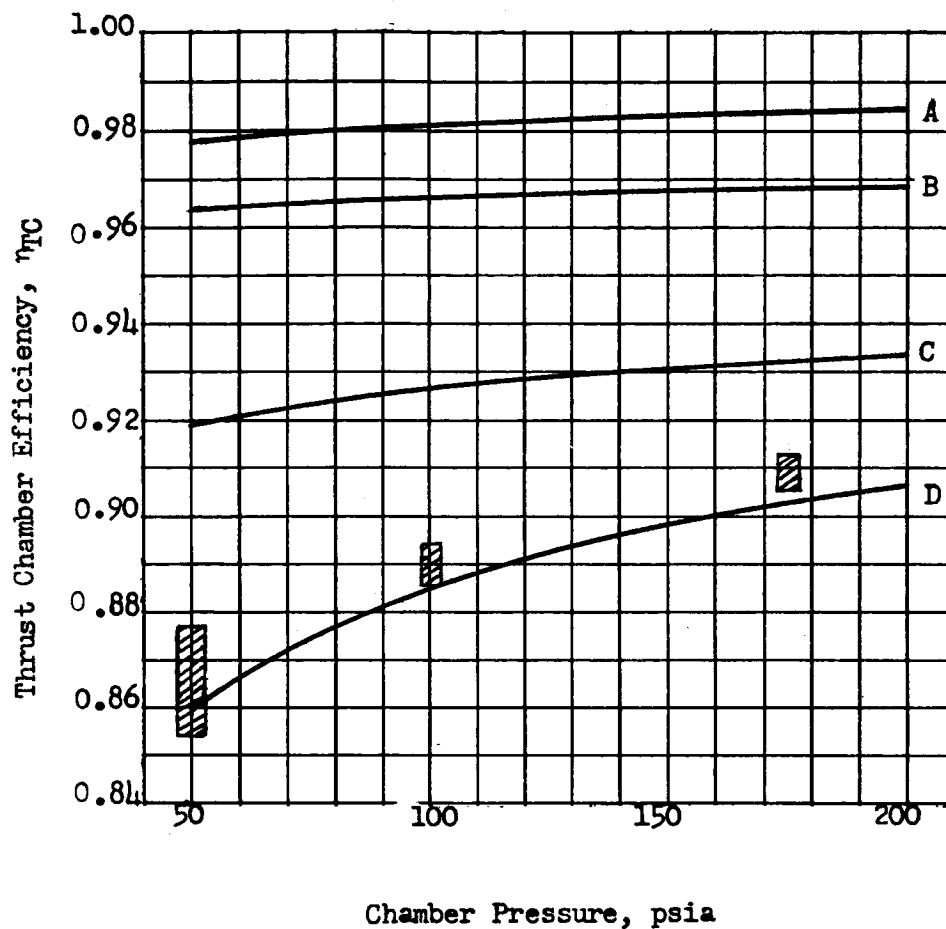


Figure 14. Nozzle Performance Comparison at 50 psia

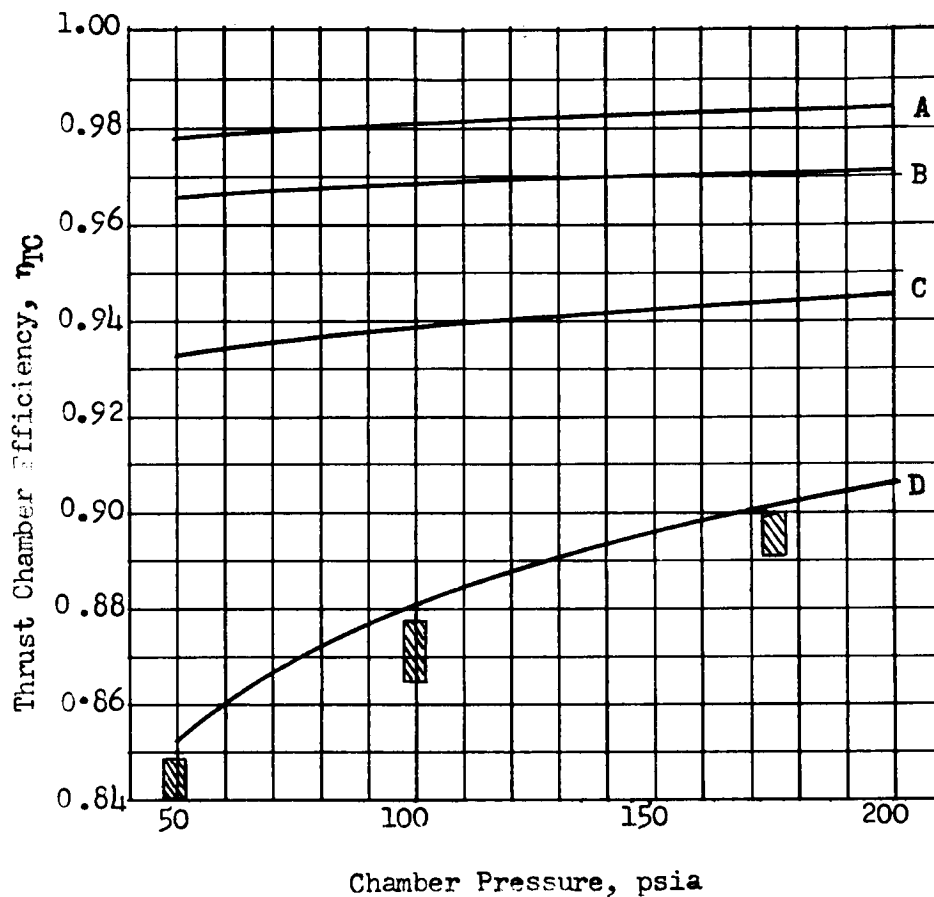


— Theoretical Curves

- A. Heat Loss
- B. Heat Loss and Divergence
- C. Heat Loss, Divergence and Drag
- D. Heat Loss, Divergence, Drag and Kinetics

 Test Data

Figure 15. Thrust Chamber Efficiency vs Chamber Pressure,
15-Degree Conical Nozzle, Mixture Ratio = 15:1



— Theoretical Curves

- A. Heat Loss
- B. Heat Loss and Divergence
- C. Heat Loss, Divergence and Drag
- D. Heat Loss, Divergence, Drag and Kinetics


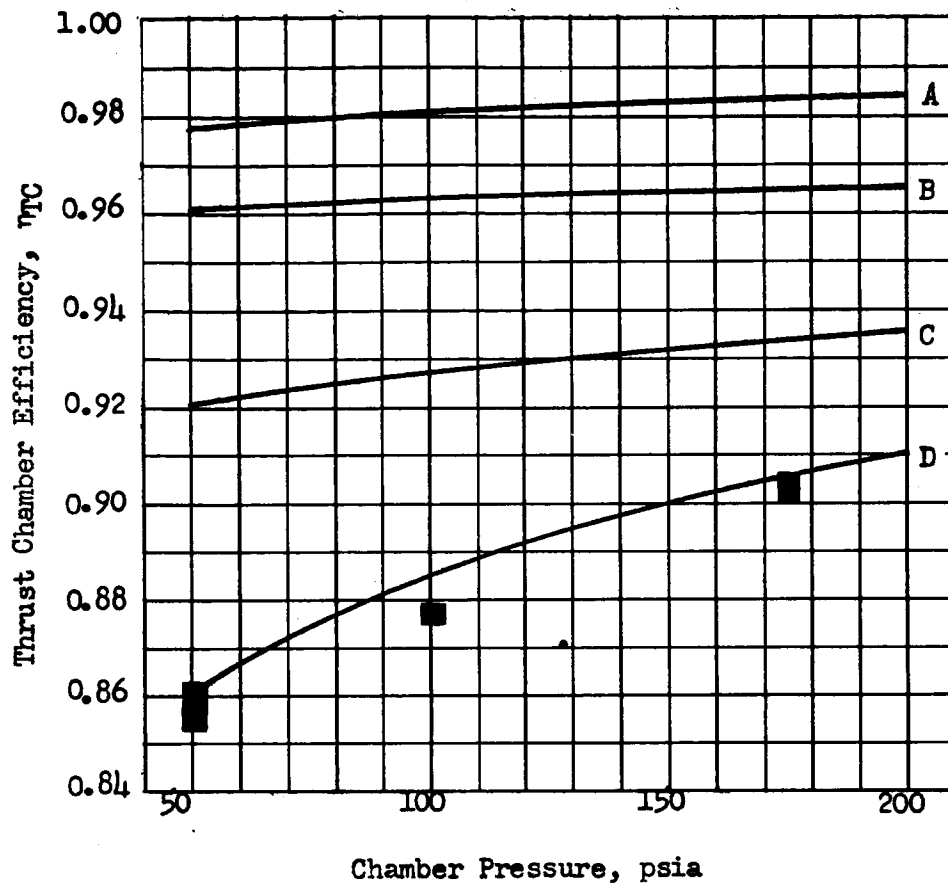
 Test Data

Figure 16. Thrust Chamber Efficiency vs Chamber Pressure, 70-Percent Bell Nozzle, Mixture Ratio = 15:1



— Theoretical Curves

- A. Heat Loss
- B. Heat Loss and Divergence
- C. Heat Loss, Divergence and Drag
- D. Heat Loss, Divergence, Drag and Kinetics

■ Test Data

Figure 17. Thrust Chamber Efficiency vs Chamber Pressure,
Controlled Expansion Nozzle, Mixture Ratio = 15:1

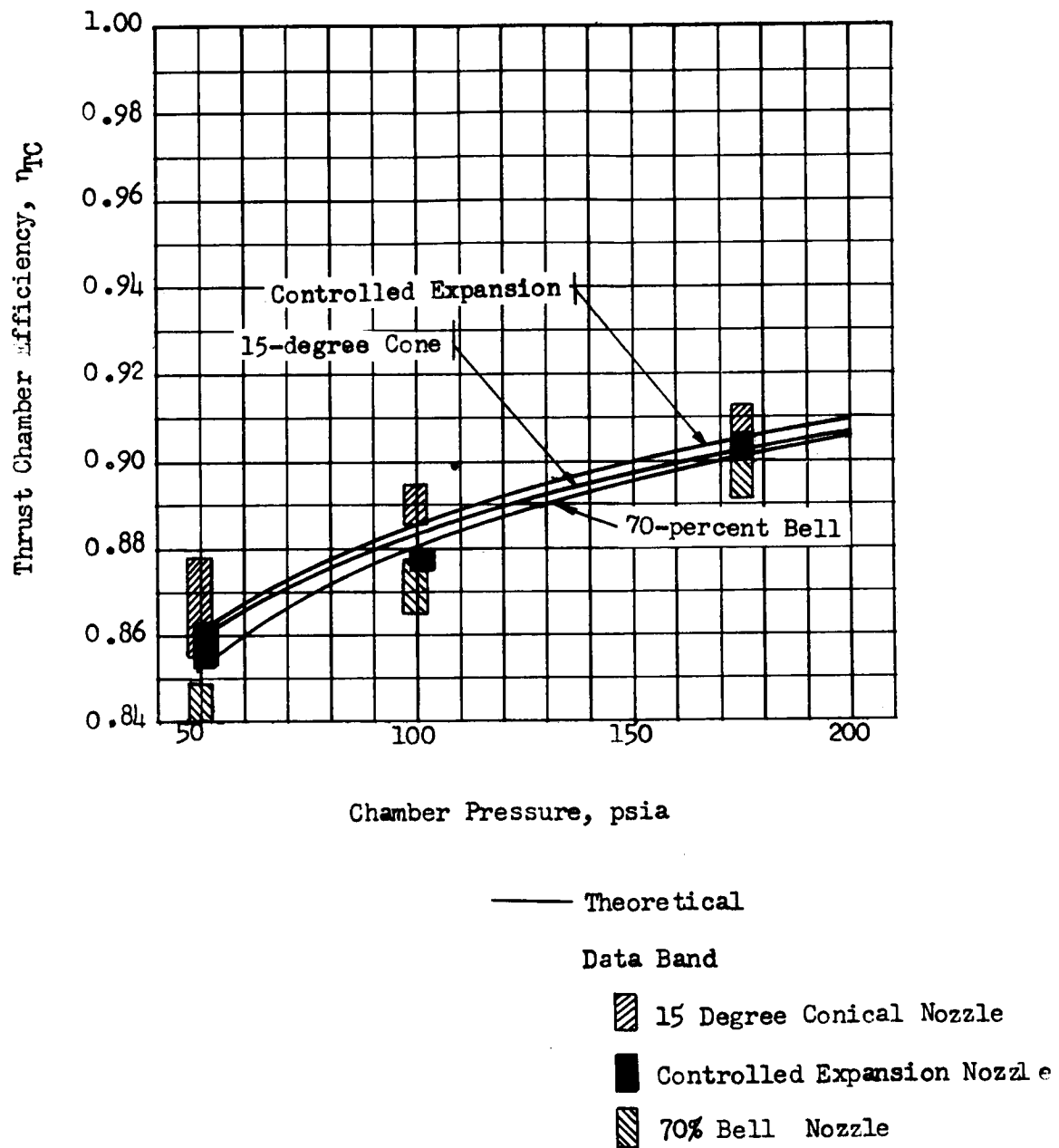


Figure 18. Thrust Chamber Efficiency Comparison at Mixture Ratio = 15:1



cone data 0.5 percent above its theoretical line and the bell 0.5 percent below. As was evident from the curves vs mixture ratio, the controlled expansion nozzle is in good agreement except at 100 psia where it seems low.

The data bands and theoretical lines are summarized in Fig. 18 . (The bands for the controlled expansion nozzle have been displaced slightly to the right for the sake of visibility.) The difference in performance for the three nozzles is evident. The controlled expansion nozzle maintains its advantage over the 70-percent bell for the entire range of pressures from 50 to 175 psia. The cone remains slightly higher than expected.

The theoretical analysis is seen to predict the dependence of thrust chamber efficiency on chamber pressure with a high degree of accuracy.

The efficiencies of all three nozzles improved by approximately 5 percent over the range from 50 to 175 psia. From Fig. 19 it is seen that the kinetic efficiency alone increases 5 percent for the cone and 6 percent for the bell when the pressure is increased from 50 to 600 psia. The heat loss and drag losses also decrease over this range, leading to high fluorine/hydrogen performance predictions at moderate pump-fed chamber pressures.

A brief statistical analysis was conducted to determine the accuracy of the analytical predictions. Figures 20 and 21 show the Task III and Task IV data, respectively, plotted as deviation from theory vs mixture ratio. For the Task III data, the mean value of the deviation was -0.2 percent, and the standard deviation was approximately 1 percent. Thus, the theory predicted two-thirds of the data points within 1 percent and virtually all of the data points within 2 percent. For the Task IV data, the mean value of the deviation was +0.23 percent and the standard deviation 0.5 percent. Thus, virtually all of the data were predicted within 1 percent.

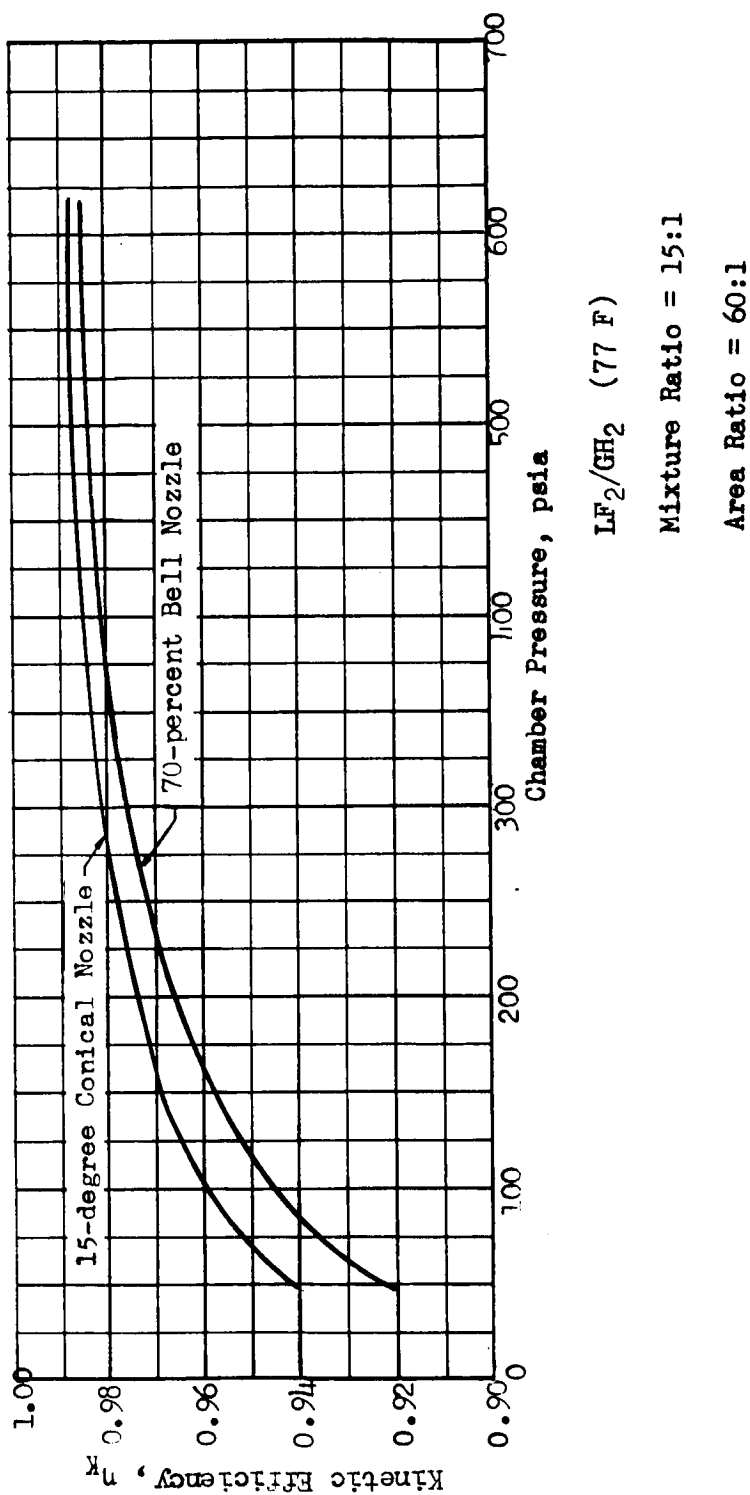


Figure 19. Predicted Kinetic Efficiencies Over an Extended Chamber Pressure Range

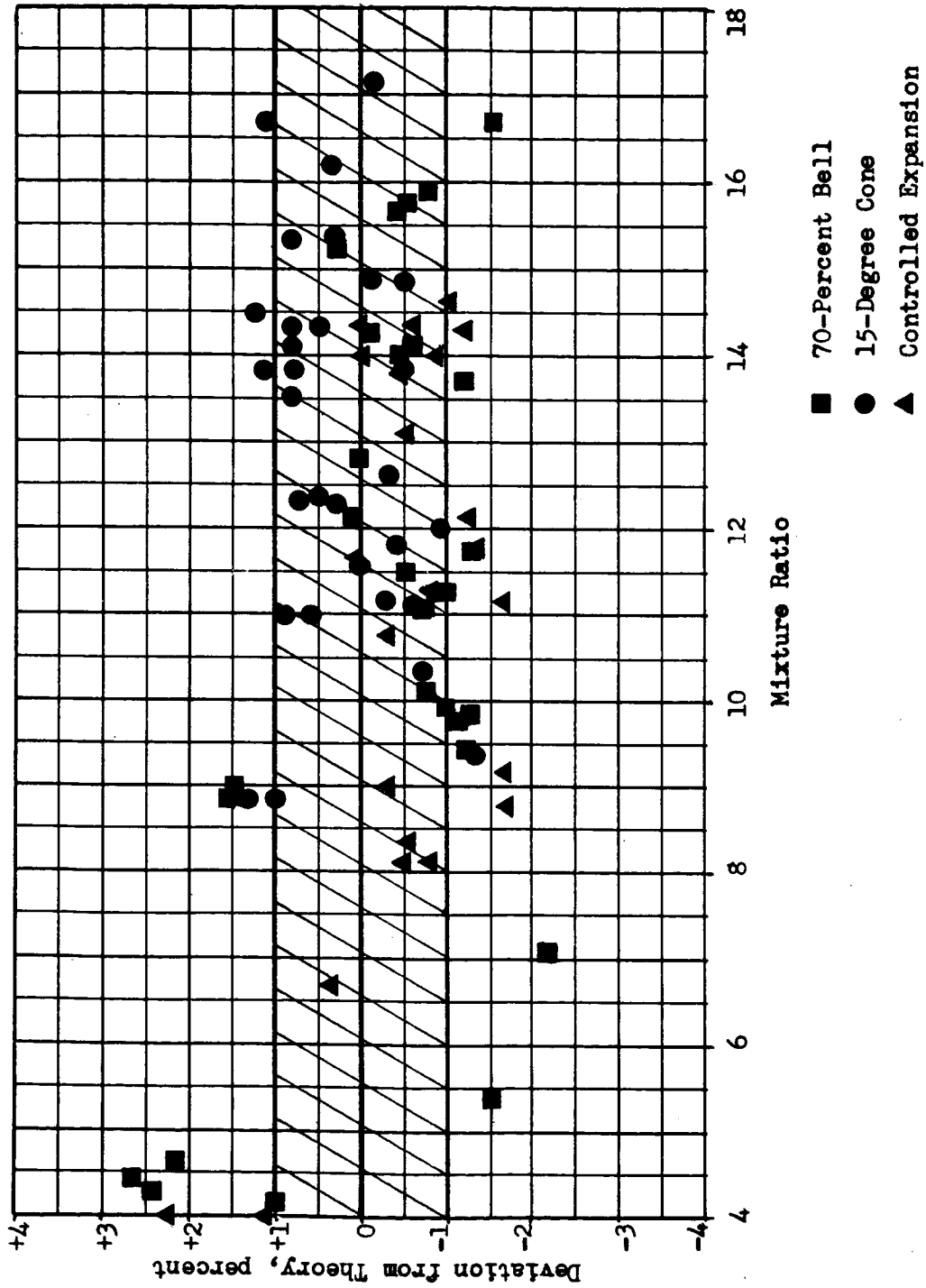


Figure 20. Difference Between Experimental and Predicted Nozzle Efficiencies for all Task III Test Data

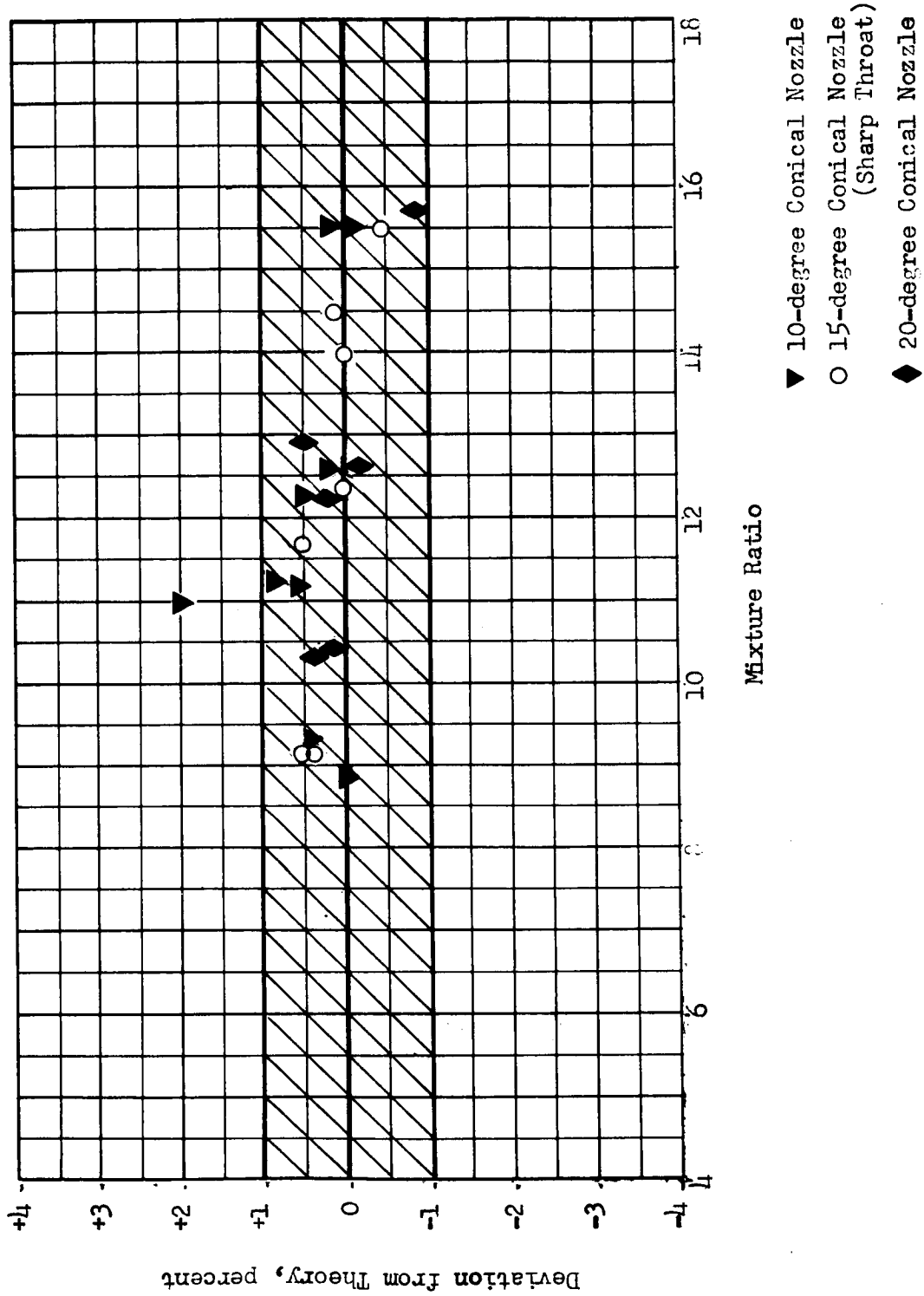


Figure 21. Difference Between Experimental and Predicted Thrust Chamber Efficiencies for All Task IV Test Data



The shift in the mean value is indicative of the type of nozzles tested in the two tasks. As was pointed out previously, the conical nozzles tended to perform slightly higher than theory while the contoured nozzles were somewhat lower. The tighter data band indicated in Task IV is a result of optimization of the instrumentation systems for the single chamber pressure level of operation.

SPECIFIC IMPULSE

Figures 22 through 26 show the delivered specific impulse and the theoretical predictions for the various nozzles. For comparative purposes, all data were corrected to a nominal combustion efficiency of 98 percent. This was done to reduce the data scatter caused by the flow measurements, which are not as precise as the thrust and chamber pressure measurements. The 98-percent value is an approximate mean of the combustion efficiencies. These data have the same characteristics as the nozzle efficiency, with the conical nozzles in general, slightly higher than the predicted values and the contoured nozzles slightly below, with the differences in the order of 0.5 percent or less. The two 15-degree conical nozzles are compared in Fig. 26.

NOZZLE PRESSURE CORRELATION

As part of the performance study, nozzle pressure profile measurements were made for the various nozzles. These are shown in Fig. 27 through 32, along with a theoretical predicted equilibrium profile, and a predicted actual profile accounting for kinetic effects. Again, good correlation between the predicted and actual values can be noted, further emphasizing the ability of the analytical technique to predict nozzle performance and flow characteristics.

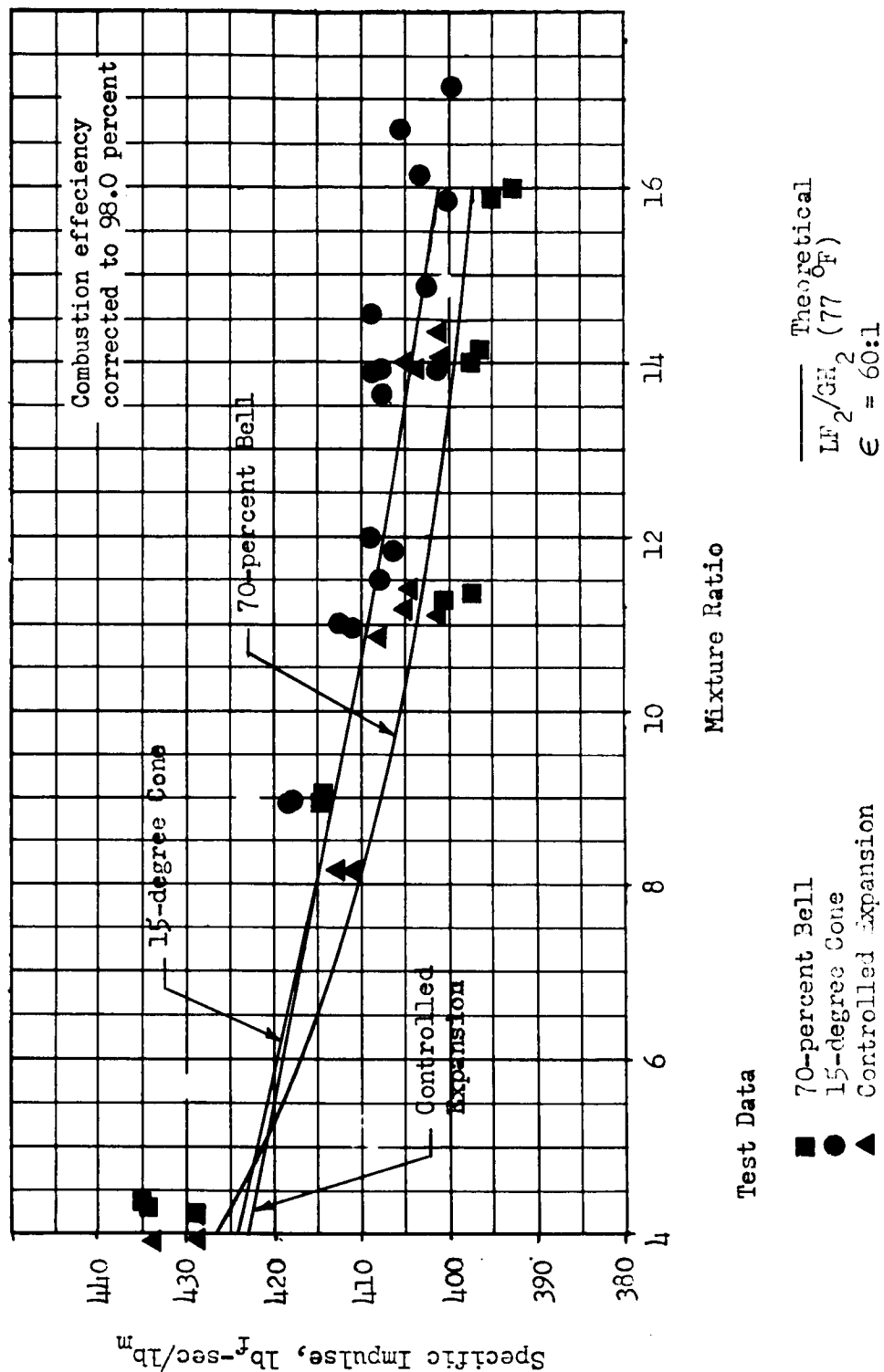


Figure 22. Specific Impulse Comparison at a Chamber Pressure of 50 psia

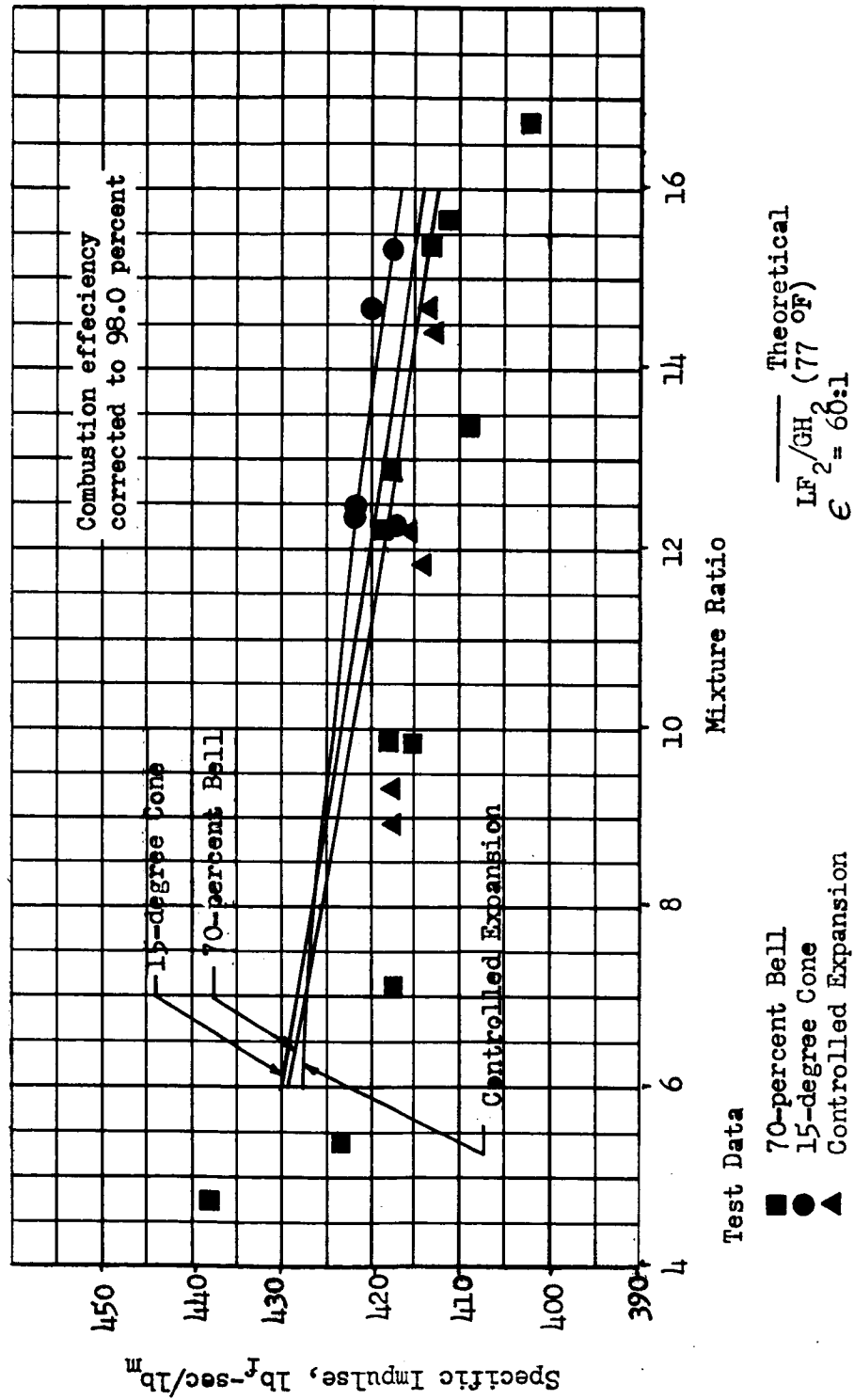


Figure 23. Specific Impulse Comparison at a Chamber Pressure of 100 psia

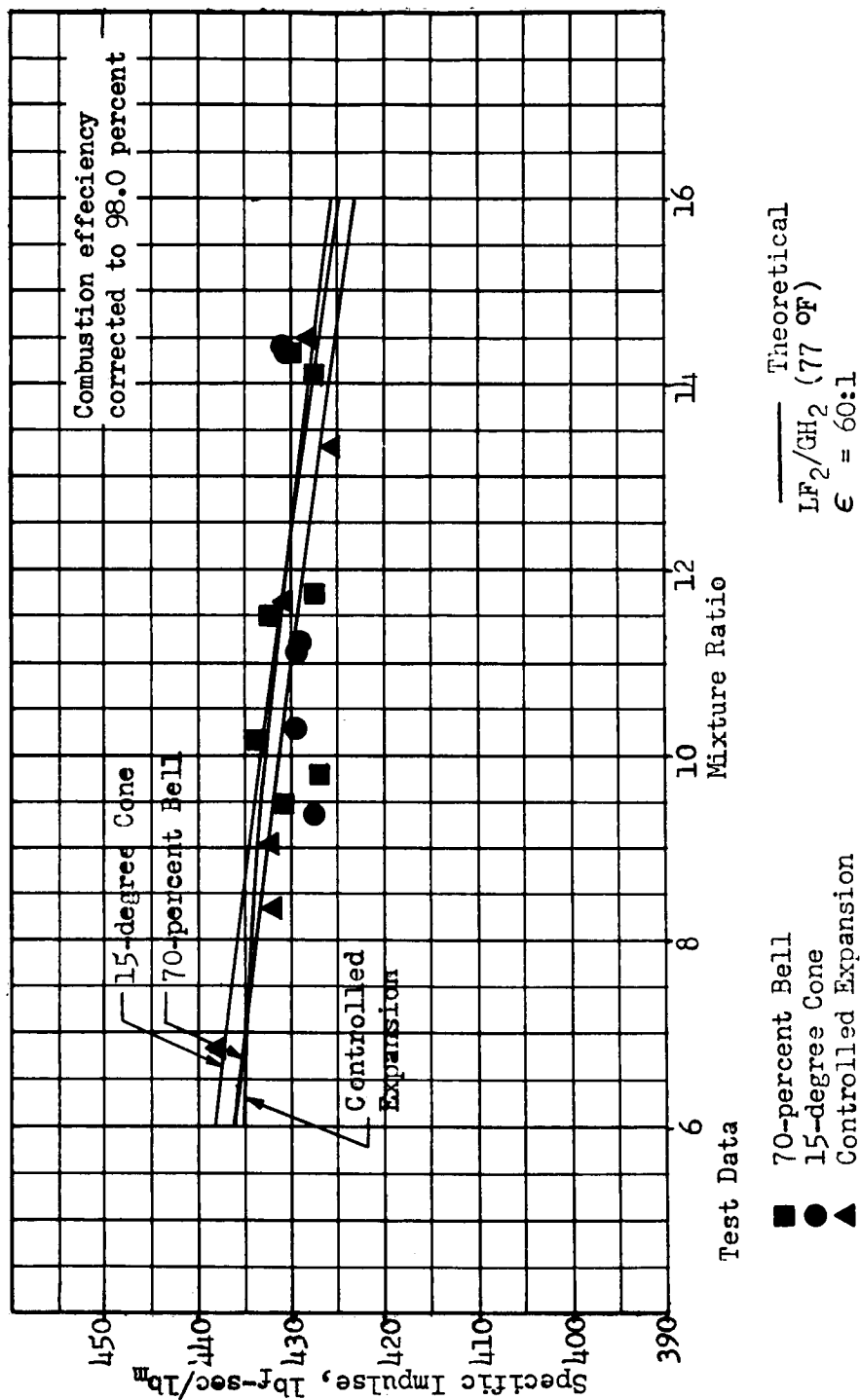


Figure 24. Specific Impulse Comparison at a Chamber Pressure of 175 psia

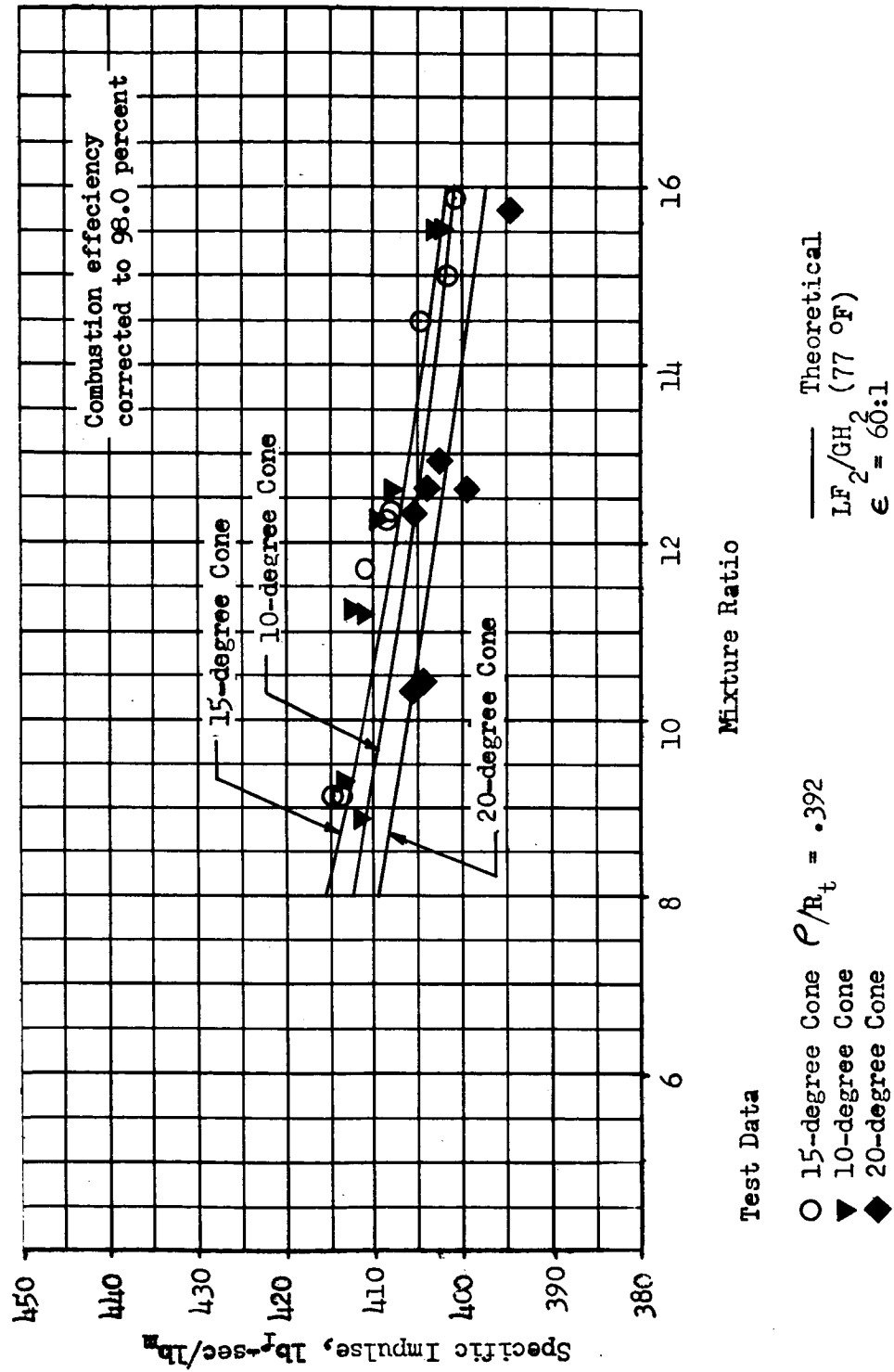


Figure 25. Specific Impulse Comparison at a Chamber Pressure of 50 psia

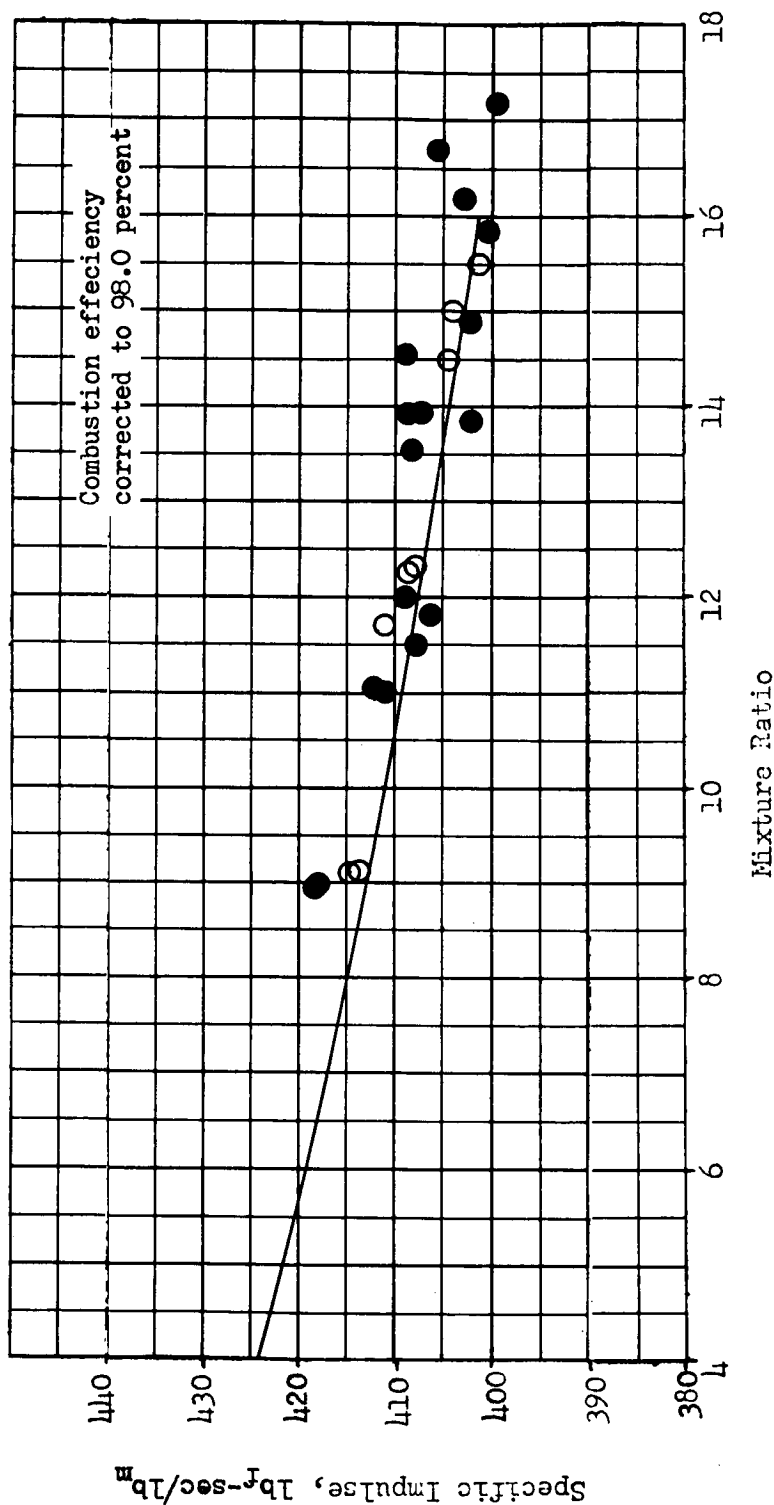


Figure 26. Specific Impulse Comparison for Long-Throat and Short-Throat 15-degree Cones at 50-psia Chamber Pressure

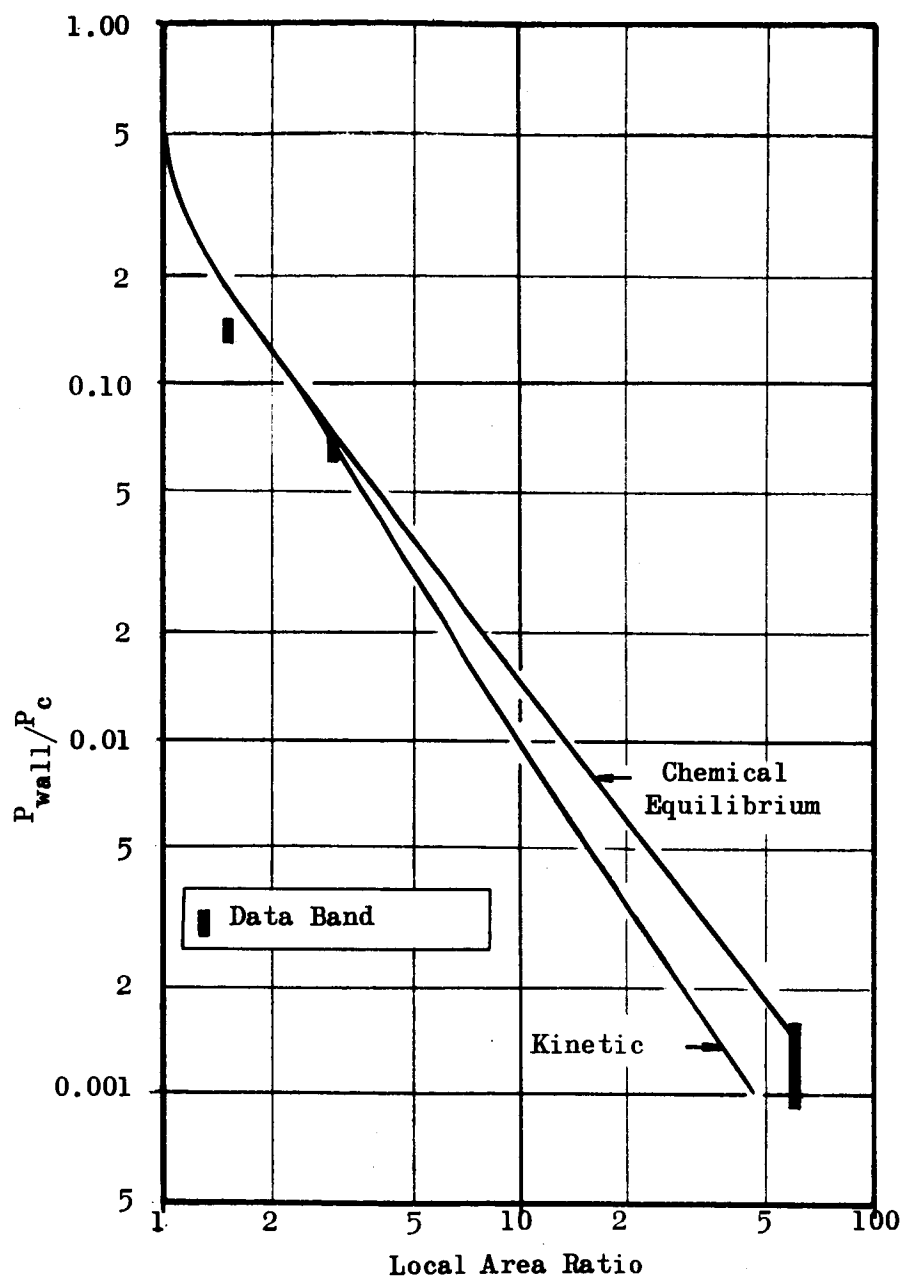


Figure 27. Wall Pressure Correlation for Long-Throat 15-degree Conical Nozzle at 50-psia Chamber Pressure

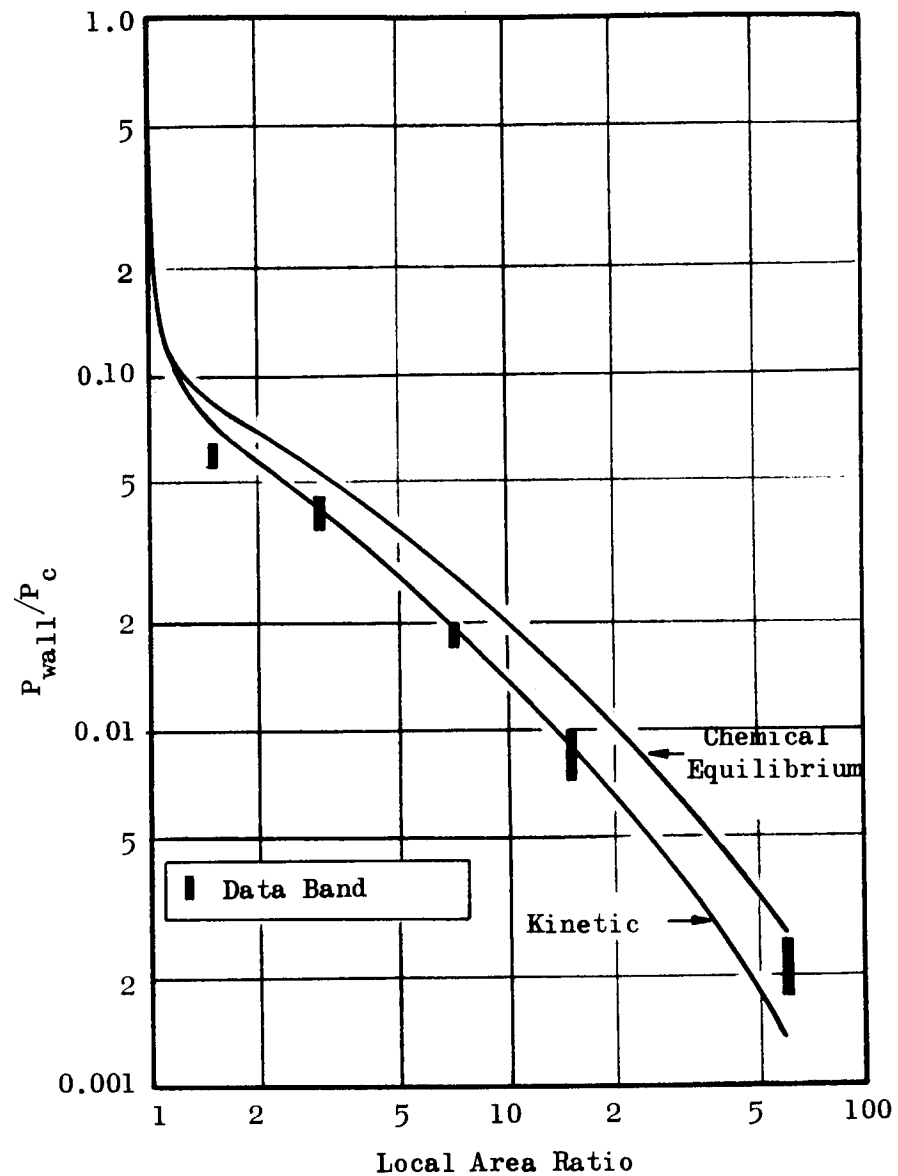


Figure 28. Wall Pressure Correlation for 70-percent Bell Nozzle at 50-psia Chamber Pressure

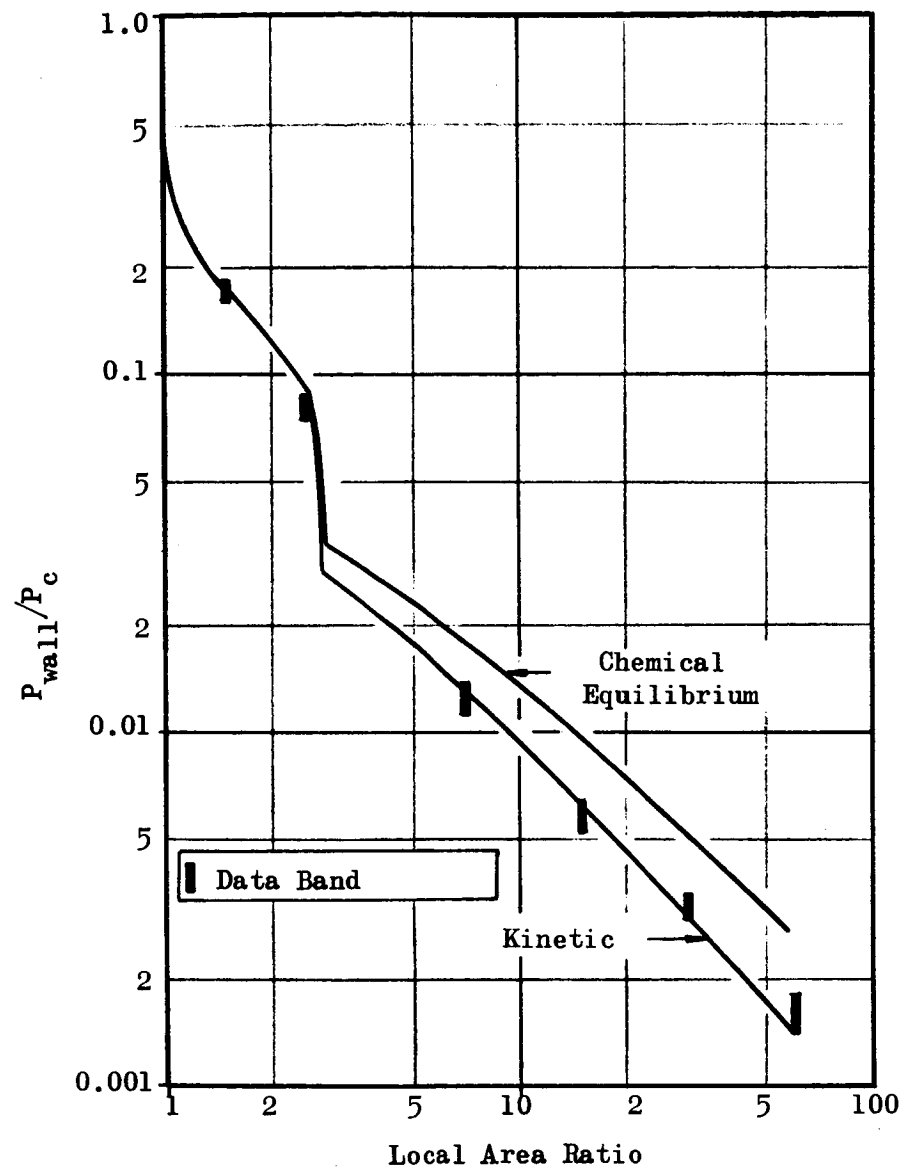


Figure 29. Wall Pressure Correlation for Controlled Expansion Nozzle at 50-psia Chamber Pressure

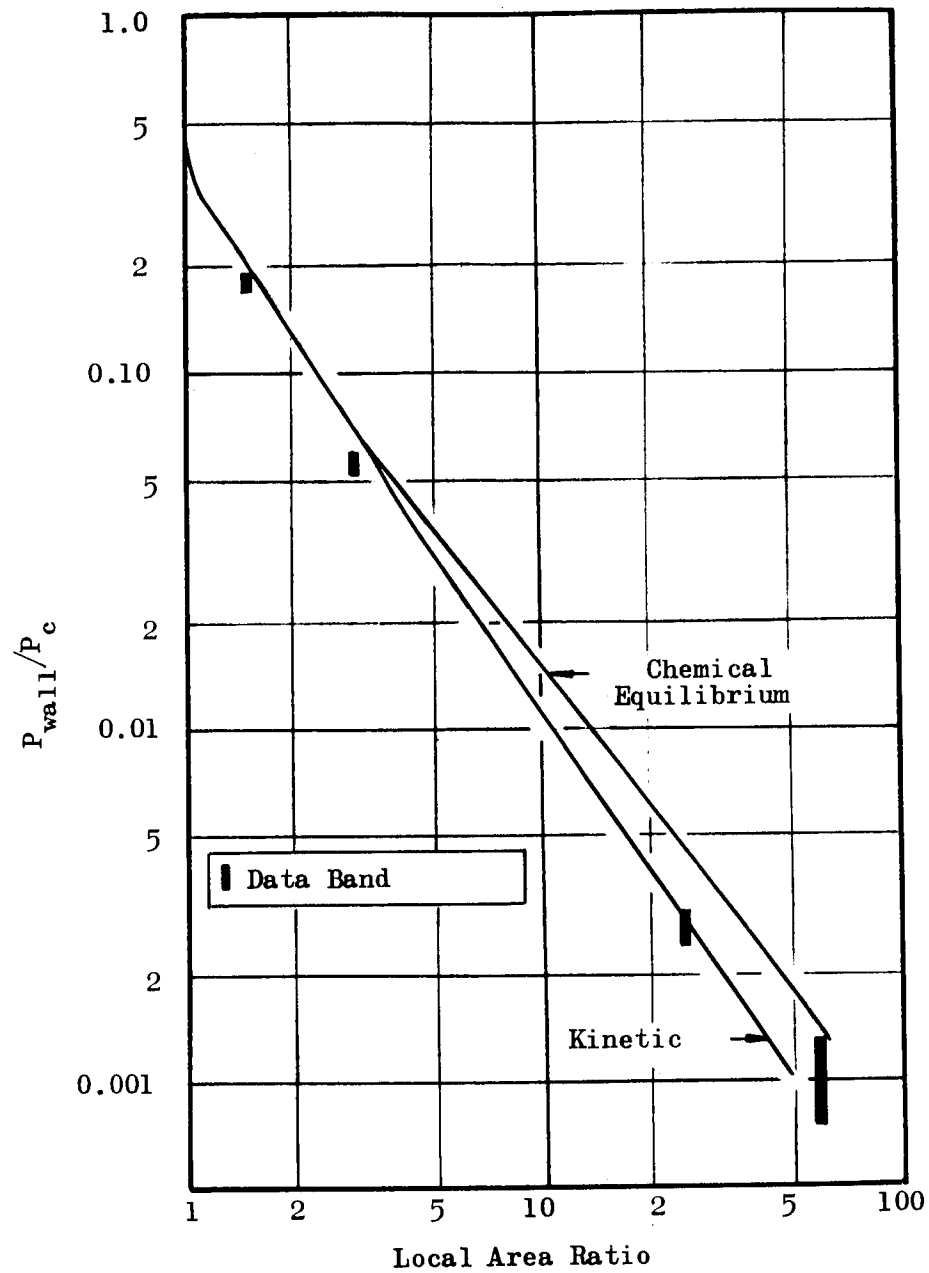


Figure 30. Wall Pressure Correlation for 10-degree Conical Nozzle at 50-psia Chamber Pressure

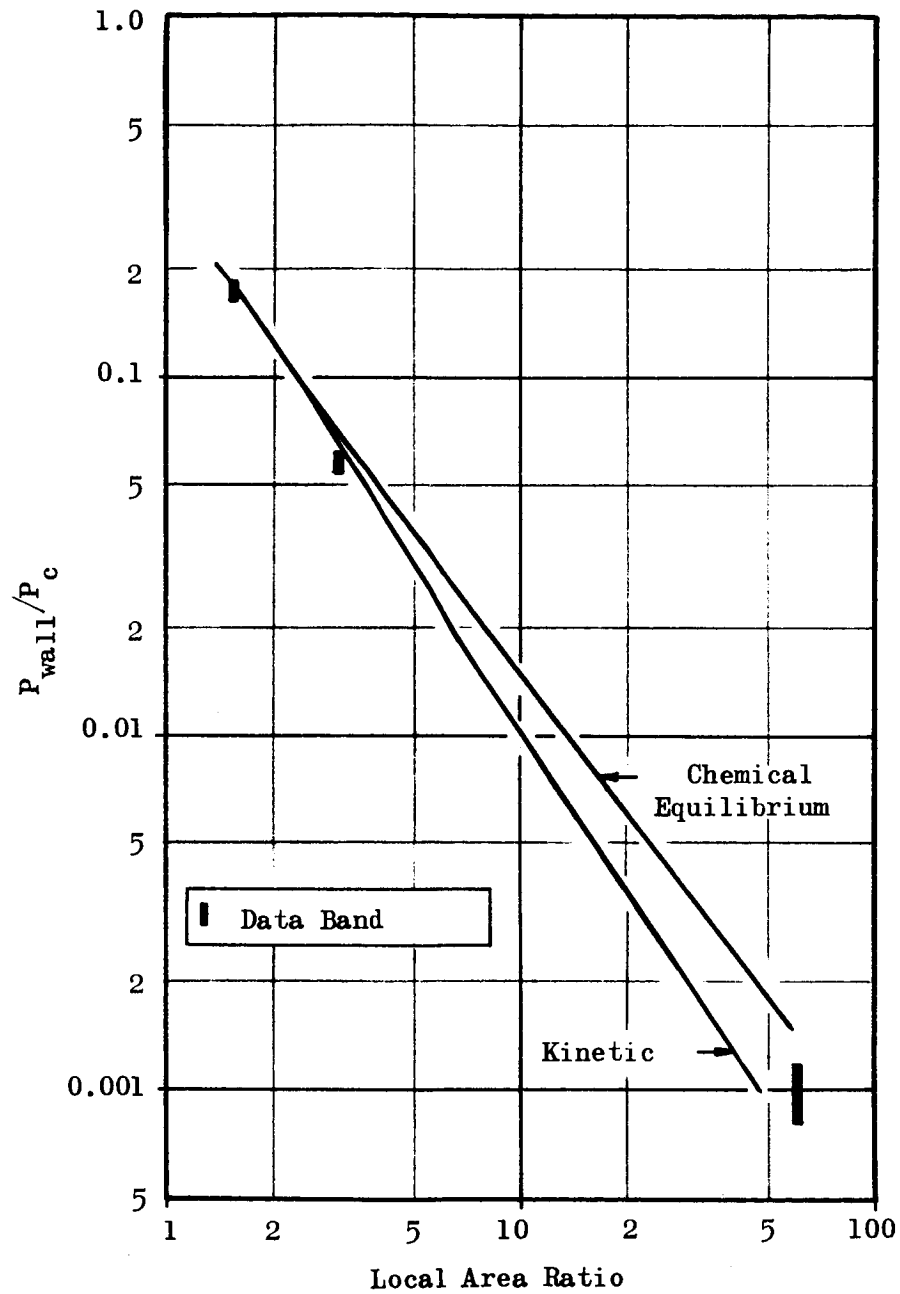


Figure 31. Wall Pressure Correlation for Short-Throat 15-degree Conical Nozzle at 50-psia Chamber Pressure

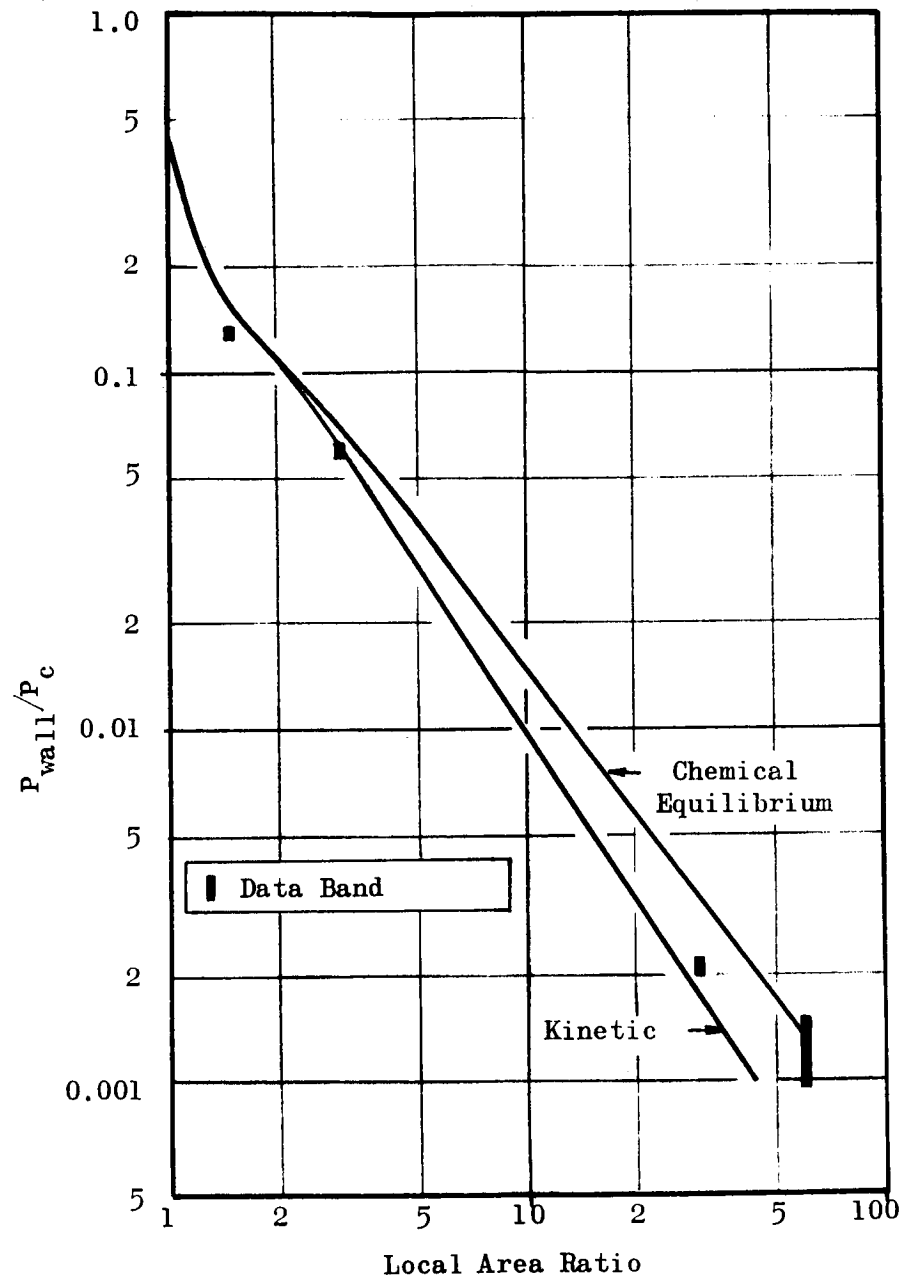


Figure 32. Wall Pressure Correlation for 20-degree Conical Nozzle at 50-psia Chamber Pressure



CONTROLLED EXPANSION NOZZLE DESIGN

One of the primary objectives of this program was the development of a controlled expansion nozzle contour which would provide increased performance when compared to conventional-type nozzles. Prior to this program, nozzles were generally designed to maximize aerodynamic (geometric) efficiency. This was satisfactory for most propellant combinations in that a minimum of dissociation occurs and consequently chemical kinetic effects on nozzle performance are small.

In this program, where the fluorine-hydrogen was tested at low chamber pressures, kinetic effects were large. Therefore, an optimization procedure considering aerodynamics, chemical kinetics, and viscous drag was utilized to develop a nozzle (controlled expansion) which would minimize the sum of these losses. It was found that significant overall performance gains could be achieved by proper contouring of the nozzle throat region. Because a study of this type and in this depth had not been attempted previously, the Task III study was broken into two phases: the first exploratory, and the second a design selection. In Task IV, further studies were conducted to improve the performance of the Task III controlled expansion contour. This section discusses in detail the studies conducted and the results.

The Task III exploratory phase was restricted to circular throat contours of varying throat circle radius, ρ/R_t , as shown in Fig. 33. The value of, ρ/R_t defines an entire nozzle, because a ground rule of the study was that the downstream section would always be the aerodynamic optimum associated with the upstream section defined by ρ/R_t . Nozzles of the type thus restricted were studied by varying the single parameter ρ/R_t .

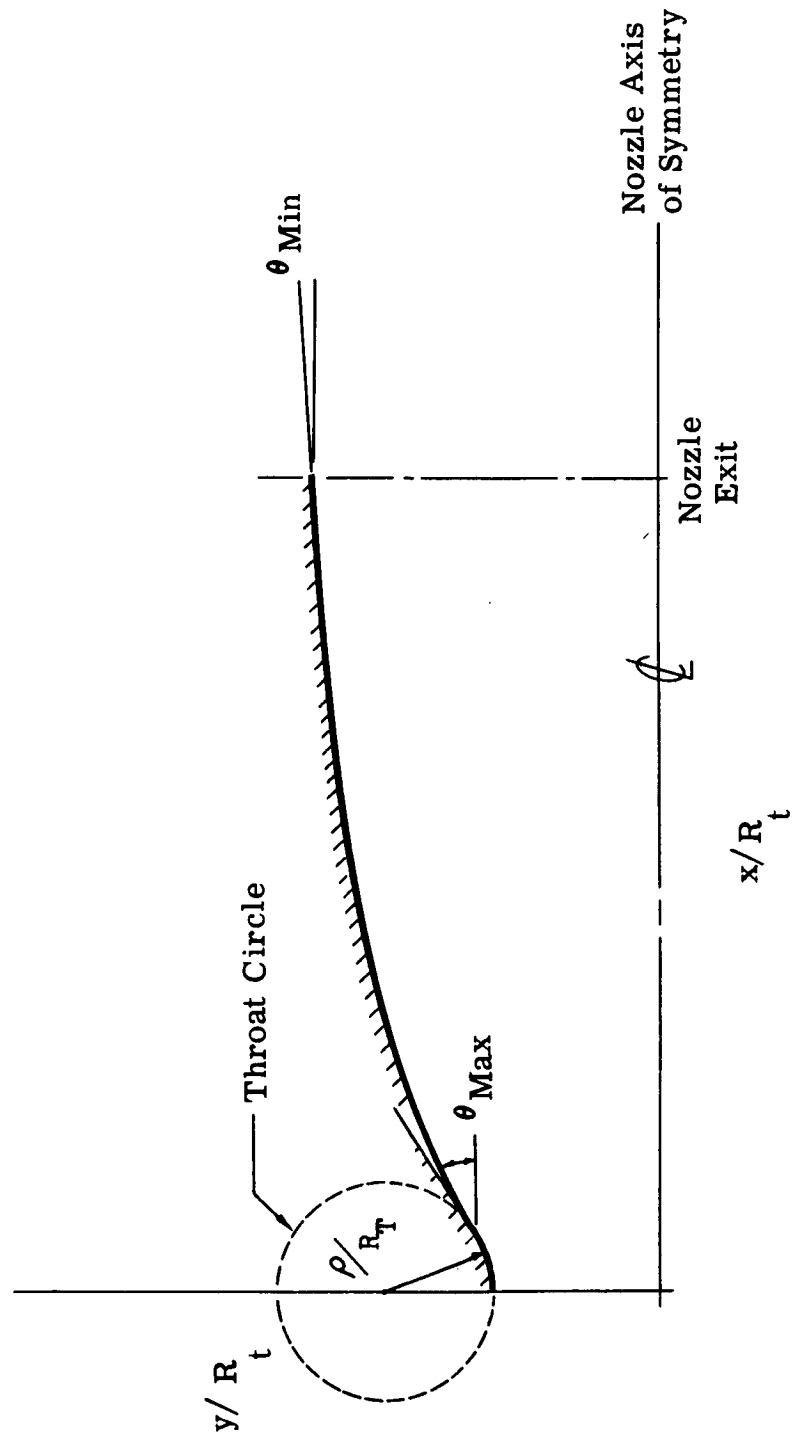


Figure 33. Bell Nozzle Contour Parameters



The circular throat-type bell nozzle contour was optimized for liquid fluorine/gaseous hydrogen (77 F) for the fixed nozzle parameters of 60:1 area ratio and 80 percent length (based on a sharp throat 15-degree cone) and a 2.1-inch throat radius. Chamber pressures of 50 and 100 psia at mixture ratios of 15:1 and 12:1, respectively, were analyzed.

Several bell nozzles, each having a different throat circle radius (varying from a ρ/R_t of 0.0001 to 10) were designed and analyzed. Based on the literature survey (Table 6) reaction rate constants, the optimum throat circle radius (ρ/R_t) for the 100-psia chamber pressure and 12:1 mixture ratio condition was approximately 5.0, and for 50 psia and 15:1 the optimum ρ/R_t had not yet been reached at the upper limit of 10. This result is particularly significant in light of the common practice of using fairly small values of the throat radius ratio.

The geometric, drag, and kinetic efficiencies of the nozzles analyzed are shown in Fig. 36, 37, and 38, respectively. Details of these analytical procedures are presented in the Performance Analysis section. As shown in Fig. 39, overall efficiency gains of approximately 0.3 and 1 percent were achieved by the optimum circular throat bell nozzle over the conventional 0.392 ρ/R_t bell nozzle at the 100-psia and 50-psia chamber pressure conditions, respectively.

The second phase of the Task III study used the knowledge gained in the exploratory phase and utilized a more sophisticated throat contour. This study indicated that the kinetic efficiency could be further improved by the use of contours of more advanced types.

An analysis was conducted on a nozzle formed by a 15-degree cone truncated at the experimentally indicated freezing point. A circle of 0.5 ρ/R_t was added at this point, the breakpoint, and an optimum aerodynamic section attached.



For this nozzle, gains of approximately 0.1 percent over the optimum circular throat bell nozzle and 0.3 to 0.5 percent over the Task III 15-degree cone were predicted. This represents gains of 0.5 to 1.1 percent over a conventional 70-percent bell nozzle (ρ/R_t) of 0.392. These results are shown in Table 1.

Because of the significant potential gains of this type of nozzle, a conical throat region followed by an aerodynamically optimized section was selected for use in the Task III test program. The breakpoint was selected as the point at which the experimental kinetic efficiency indicated that chemical freezing was occurring for a chamber pressure of 50 psia and a mixture ratio of 15:1. Thus, the breakpoint was chosen at a local area ratio of 2.63. The selected Task III controlled expansion nozzle is shown in Fig. 43. Resultant theoretical efficiency improvement was 1 percent over the 70-percent bell at 50 psia, 15 mixture ratio. However, based on the experimental efficiency of the 15-degree cone, an improvement for the controlled expansion nozzle over the 70-percent bell of 2 percent was predicted.

In the Task IV studies, the conical throat region was varied parametrically to determine the ultimate potential of this type of nozzle design. Contoured throat regions were also investigated. The largest performance gain relative to the Task III contour was predicted for a conical throat region of 12 degrees. This nozzle was predicted to achieve a 0.3-percent performance gain over the Task III contour. Continued effort on the controlled expansion nozzle was expected possibly to produce a 0.5-percent performance improvement. However because this additional potential improvement was small, this contour was not tested in Task IV.



TABLE 1

OVERALL NOZZLE EFFICIENCIES

(Propellant: LF_2/GH_2)

Overall Nozzle Efficiency, η Chamber Pressure and Mixture Ratio	15-Degree Cone Nozzle $(\rho/R_t)_D = 3.635$ $\epsilon = 60:1$	80-Percent Bell Nozzles, $\epsilon = 60:1$		
		Conventional Bell Nozzle $(\rho/R_t)_D = 0.392$	Optimum Circular Throat Bell Nozzle at $P_c = 100$, $MR = 12$ $(\rho/R_t) = 5.0$	Selected Nozzle (15-Degree Cone, Bell) $(\rho/R_t)_D = 3.635$
$P_c = 100$ psia $MR = 12:1$	0.8961	0.8940	0.898	0.899
$P_c = 50$ psia $MR = 15:1$	0.8596	0.8548	0.8656	0.8654



CIRCULAR THROAT CONTOUR STUDY

In optimizing the circular throat bell nozzle, a (ρ/R_t) range from 0.0001 to 10 was investigated. Several bell nozzles were designed and analyzed. Each nozzle was designed to achieve optimum geometric performance subject to the specified circular throat contour. The optimization was performed for the following conditions.

Propellant:	Liquid fluorine/gaseous hydrogen (77 F) at chemical equilibrium
Nozzle Area Ratio:	60:1
Nozzle Length:	80 percent of a sharp throat 15-degree cone
Throat Radius:	2.1 inches (approximately 2500 pounds of thrust at 100-psia chamber pressure).

A chamber pressure of 50 psia and a mixture ratio of 15:1 were also analyzed. The range of the contours included in this study is indicated by the comparison shown in Fig. 34.

The bell nozzles were designed and analyzed using variable property flow fields for the above propellant parameters. The nozzles were designed for optimum aerodynamic performance using the Rao aerodynamic optimization criterion.

The first step in the bell nozzle contour design was to construct a "map" to obtain the optimum aerodynamic control surface. In mapping, two parameters are used: θ_{\max} , the wall angle where the aerodynamic portion of contour attaches to the throat circle, and M_D^* , the Mach number at a point on the characteristic line (see page 56), having flow angle at the wall of θ_{\max} .

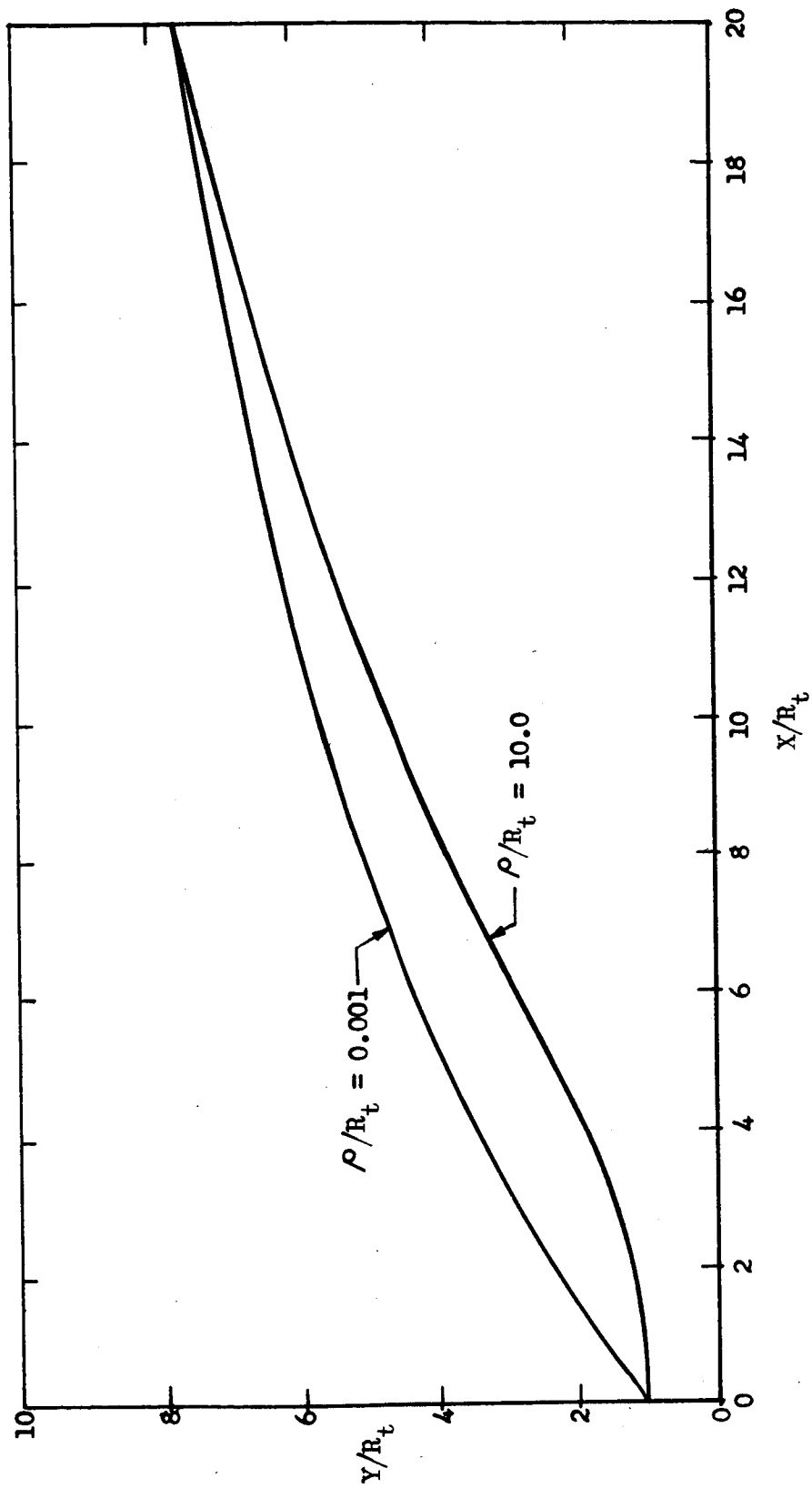
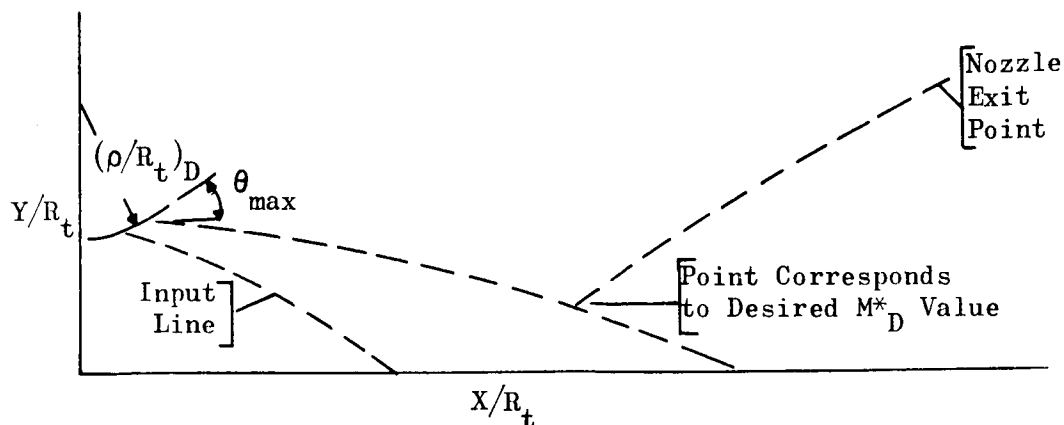


Figure 34. Extreme Nozzle Contours Considered in the Circular Throat Contour Study



Each combination θ_{\max} , M^*_D is associated, through the Rao criterion, with an aerodynamically optimum nozzle of some area ratio and some percent length. The problem in nozzle optimization is to find the point θ_{\max} , M^*_D associated with the desired area ratio and percent length.

As an example of this procedure, Fig. 35 contains the map used to optimize the contour with a throat radius ratio of 0.5. The values of θ_{\max} and M^*_D for the desired ϵ and δ were interpolated and found to be 33.8 degrees and 2.7361, respectively. Having determined these two values, the optimum contour was generated by using the method of characteristics "in reverse;" i.e., the procedure was used starting from the control surface and moving upstream.

For future bell nozzle designs with circular throat contours, variations of the nozzle contour parameters with throat circle radius are discussed and presented in Appendix A.

Once designed, the nozzles were analyzed for aerodynamic, drag, and kinetic efficiency by the procedures discussed in the Performance Analysis section, using the preliminary reaction rates shown in the first column of Table 6 for the chemical kinetic analysis. The stream-tube kinetic analysis procedure was used throughout the study.



LF_2/GH_2 (77 F)

Chamber Pressure = 100 psia

Mixture Ratio = 12:1

$(R/R_t)_D = 0.5$

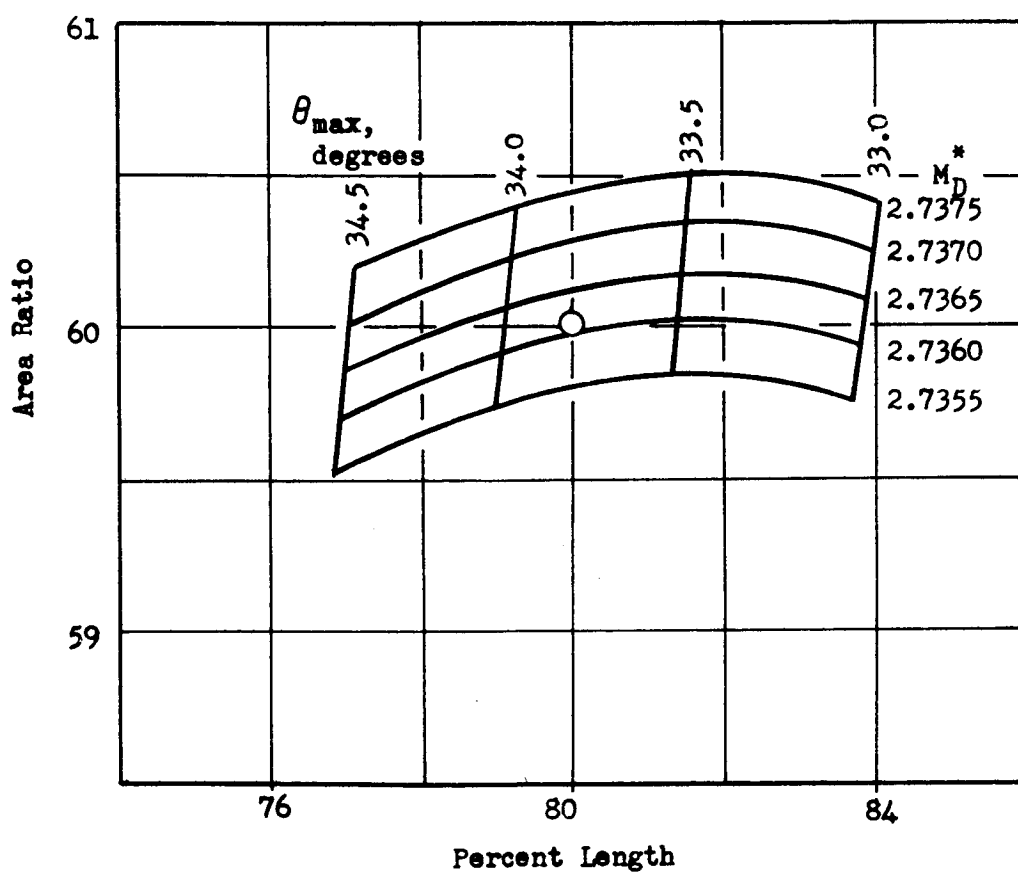


Figure 35 . Sample Nozzle Optimization Map



Nozzle Geometric Efficiency

The geometric efficiency analysis results indicated that because an increase in $(\rho/R_t)_D$ resulted in a decrease in available nozzle length for the optimum aerodynamic contour, a decrease in nozzle geometric efficiency occurred as shown in Fig. 36. Over the extreme variation of $(\rho/R_t)_D$ of 0.0001 to 10, the geometric efficiency decreased from 0.9942 to 0.9805 a decrease of 1.33 percent.

Drag Efficiency

The viscous drag efficiencies of the bell nozzles were determined for laminar and turbulent boundary layers at a chamber pressure of 100 psia and a mixture ratio of 12:1, as shown in Fig. 37. The shape of the drag efficiency curve is explained by a tradeoff between wall surface area in the high shear region near the throat, which increases with increasing throat radius, and the total surface area, which decreases. The heat transfer test results from the 15-degree cone (1.9:1 area ratio) Task II nozzle indicated that the boundary layer was turbulent; therefore, the drag efficiencies based on a turbulent boundary layer were used in computing overall nozzle efficiencies.

For a chamber pressure of 50 psia and mixture ratio of 15:1, the drag efficiencies were obtained by ratioing the drag efficiency of the 70-percent bell Task III nozzle at a chamber pressure of 100 psia and a mixture ratio of 12:1, and applying this correction to all the 100 psia and 12:1 mixture ratio drag results.

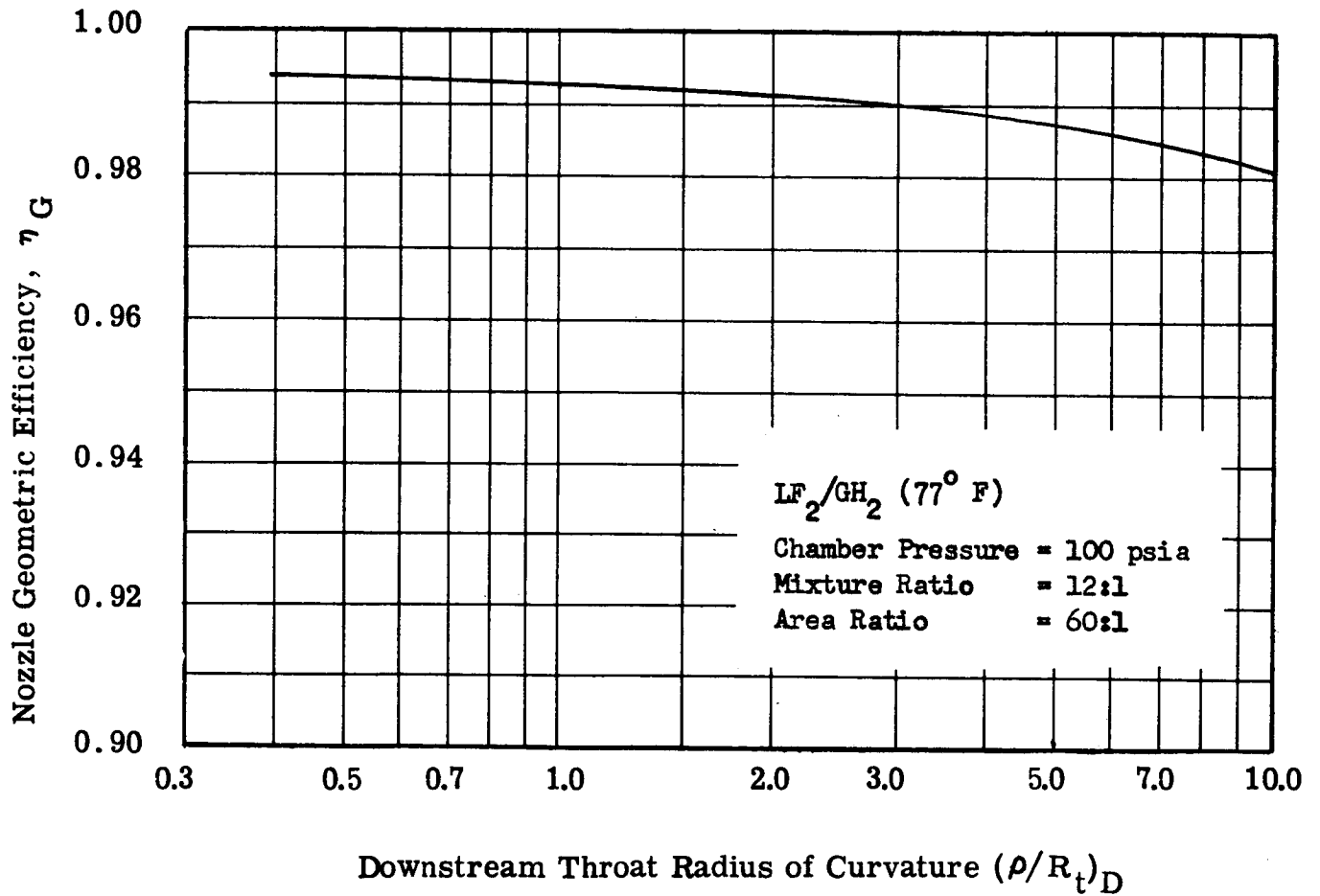


Figure 36. Geometric Efficiency as a Function of Throat Radius of Curvature

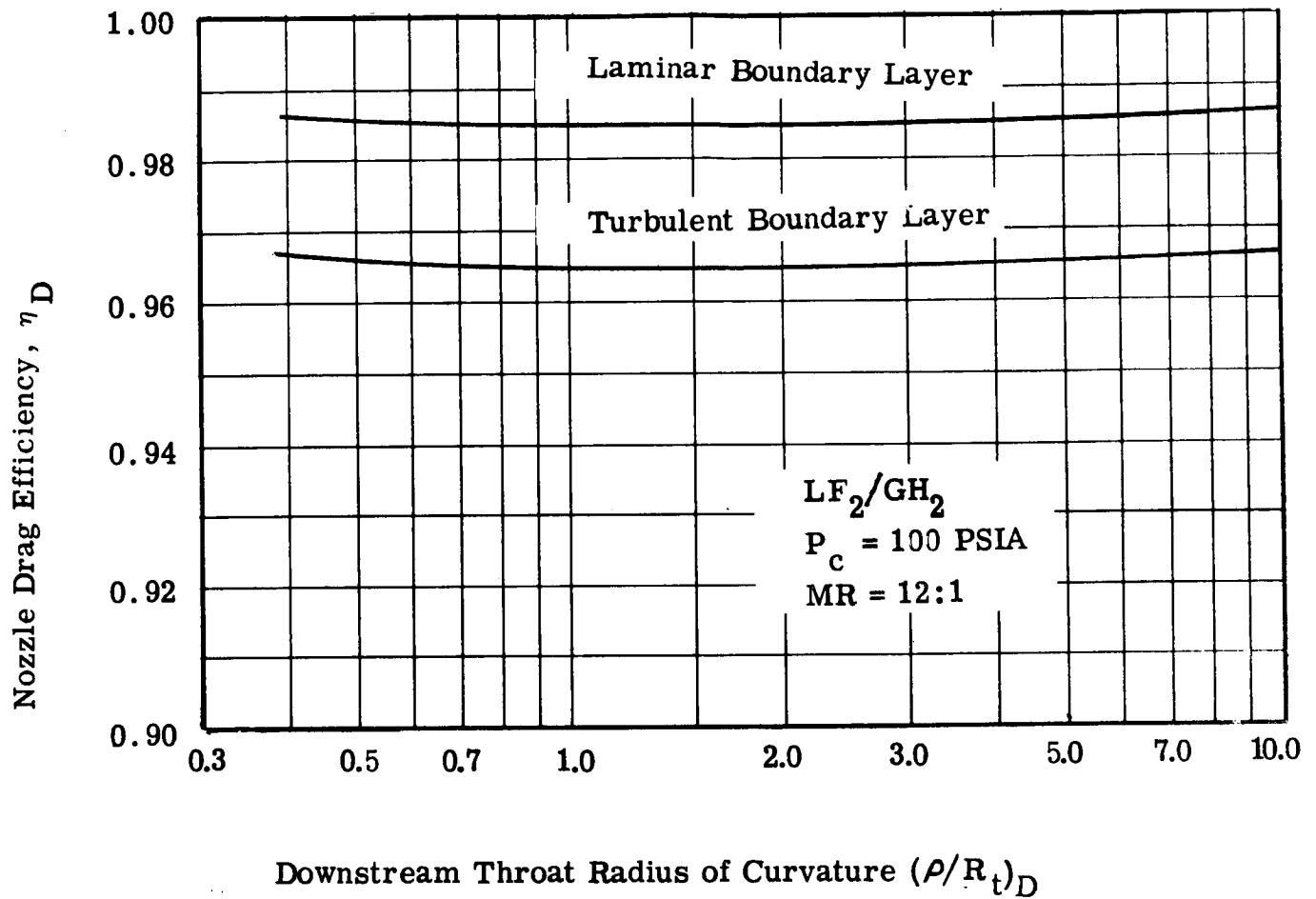


Figure 37. Drag Efficiency as a Function of Throat Radius of Curvature



Reaction Kinetic Efficiency

Streamtube kinetic performance analyses were performed for the bell nozzles having a $(\rho/R_t)_D$ of 0.392, 1, 2, 5, and 10 for chamber pressures of 50 and 100 psia at mixture ratios of 15:1 and 12:1, respectively.

As indicated in Fig. 38, the η_K increased with an increase in $(\rho/R_t)_D$. (Although the η_K vs $(\rho/R_t)_D$ curve on a semilog plot indicated an increasing slope in the curve, a linear plot of the same parameters would result in a decreasing slope.) A larger $(\rho/R_t)_D$ decreases the nozzle flow expansion rate which in turn increases η_K . An increase of 2.2 percent was achieved by increasing $(\rho/R_t)_D$ from 0.392 to 10 at a chamber pressure of 50 psia and a mixture ratio of 15:1. At 100-psia chamber pressure and 12:1 mixture ratio, the η_K increase was 0.8 percent.

Overall Nozzle Efficiency

The overall nozzle efficiency was defined as $\eta_G + \eta_D + \eta_K - 2$ and is shown in Fig. 39. The overall nozzle efficiency of the circular throat contour bell nozzles attained a maximum for a $(\rho/R_t)_D$ of approximately 5 for the 100-psia chamber pressure.

For 50 psia and mixture ratio of 15:1, the overall efficiency continued to increase over the entire range of $(\rho/R_t)_D$ analyzed. This indicates that for this condition the $(\rho/R_t)_D$ attaining the maximum overall efficiency was greater than 10.

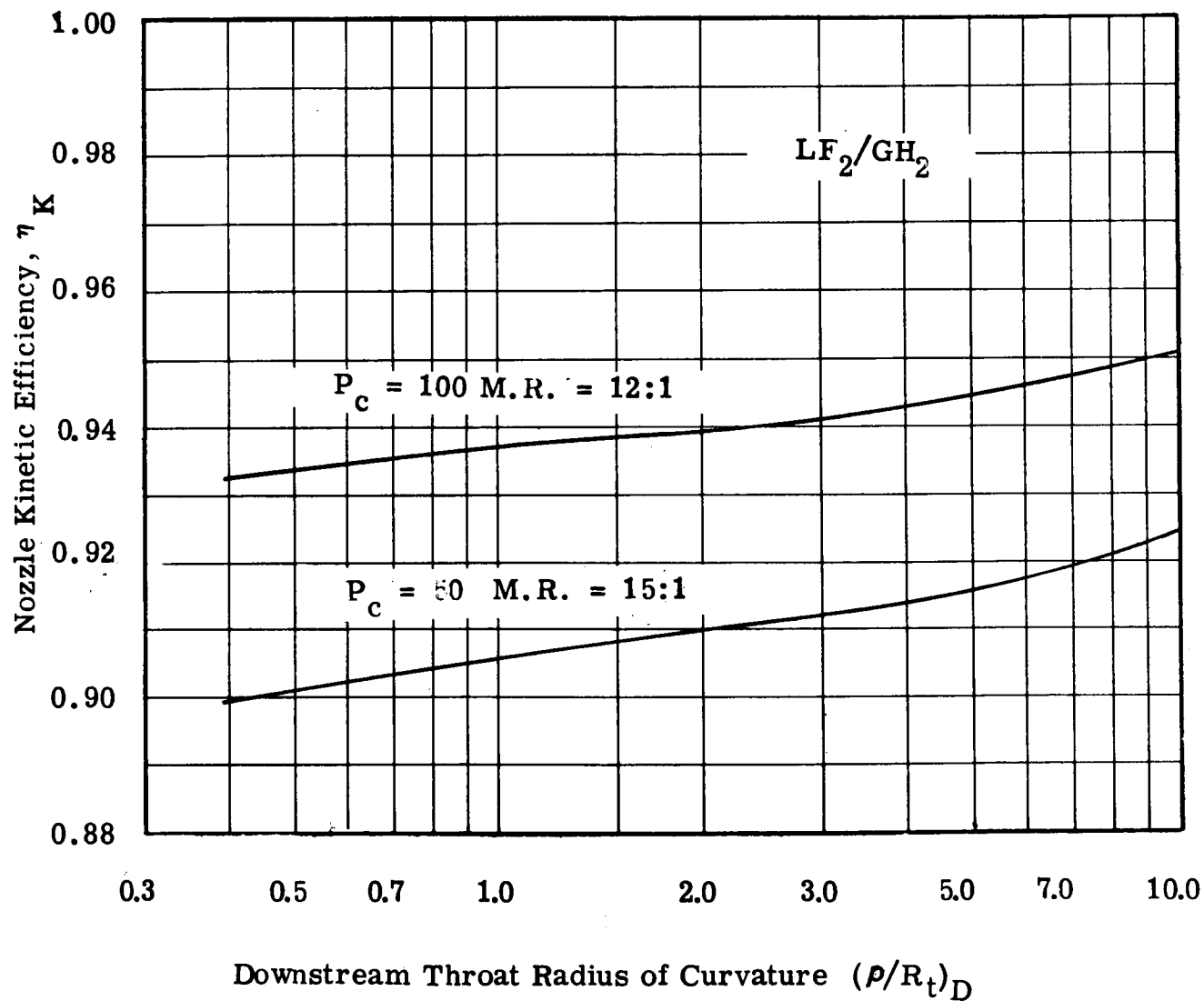


Figure 38. Kinetic Efficiency as a Function of Throat Radius of Curvature

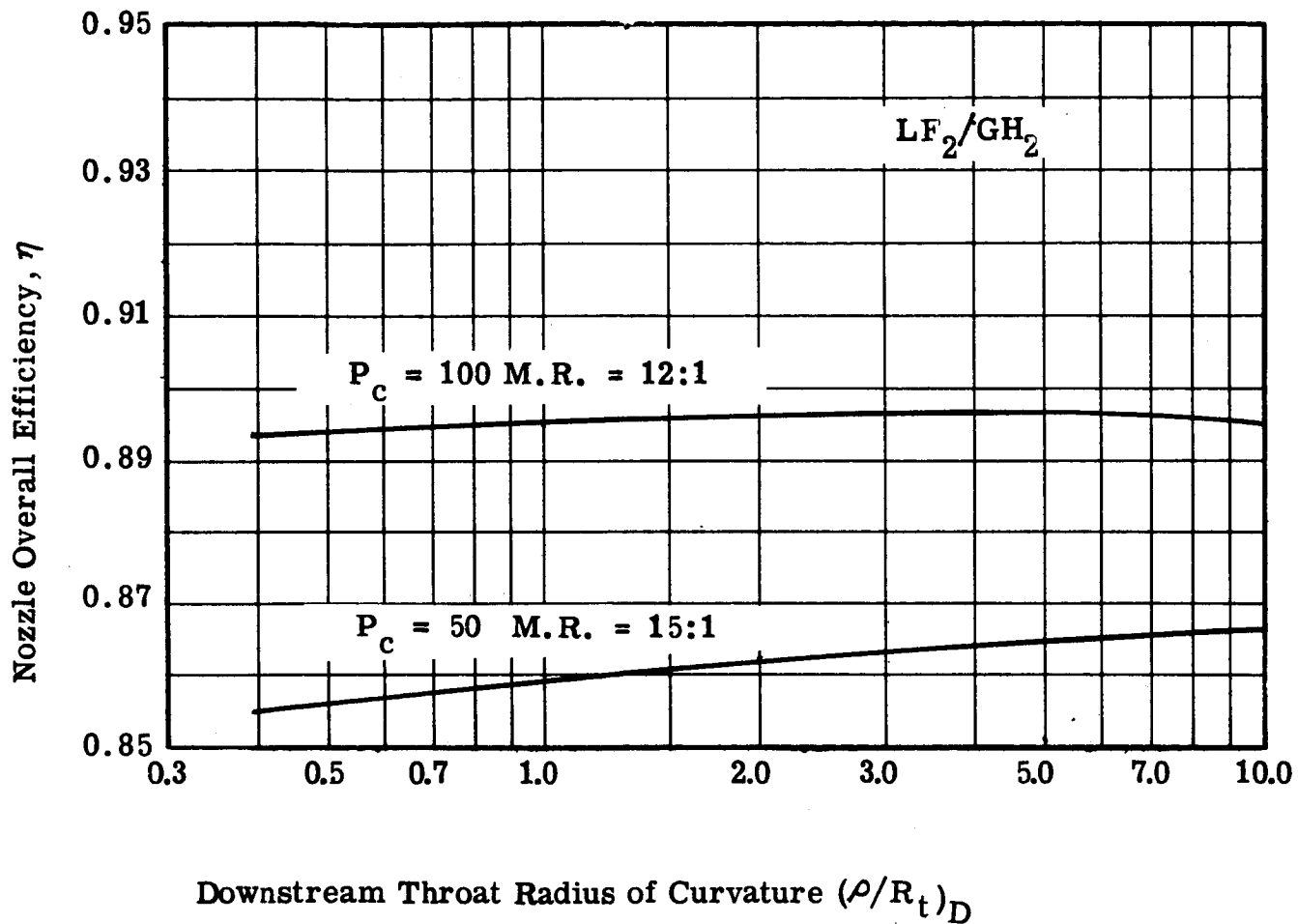


Figure 39. Overall Efficiency as a Function of Throat Radius of Curvature



TASK III, NOZZLE DESIGN SELECTION

The circular throat contour optimization study showed that significant overall performance gains can be achieved even by such a simplified version of the controlled expansion concept. The design selection study indicated that even larger performance gains can be achieved through a more sophisticated throat contour design, and provided some insight into what such a nozzle would look like. This insight resulted in some guidelines which were followed in selecting the contour to be fabricated and tested.

In discussing these guidelines, it is necessary to define the two general types of throat contours: (1) concave-out, and (2) concave-in. The concave-out throat contour (Fig. 40) has an increasing or constant slope. The slope of the concave-in throat contour (Fig. 40) increases and then later decreases.

Nozzle Geometric Efficiency Improvement

As indicated by Fig. A-1, an increase in $(\rho/R_t)_D$ results in a large increase in circular throat contour length to achieve the same wall angle, θ . An increase in throat contour length decreases the available aerodynamic length resulting in a decrease in η_g . Therefore, any method of decreasing the throat contour length without decreasing η_K would be beneficial. From the freezing surfaces shown in Fig. 41, it was noted that for the two conditions analyzed, (1) chamber pressure = 100 psia and mixture ratio = 12:1, and (2) chamber pressure = 50 psia and mixture ratio = 15:1, that portions of the circular throat contour (Regions 1 and 3) could be shortened with η_K remaining essentially constant, thus

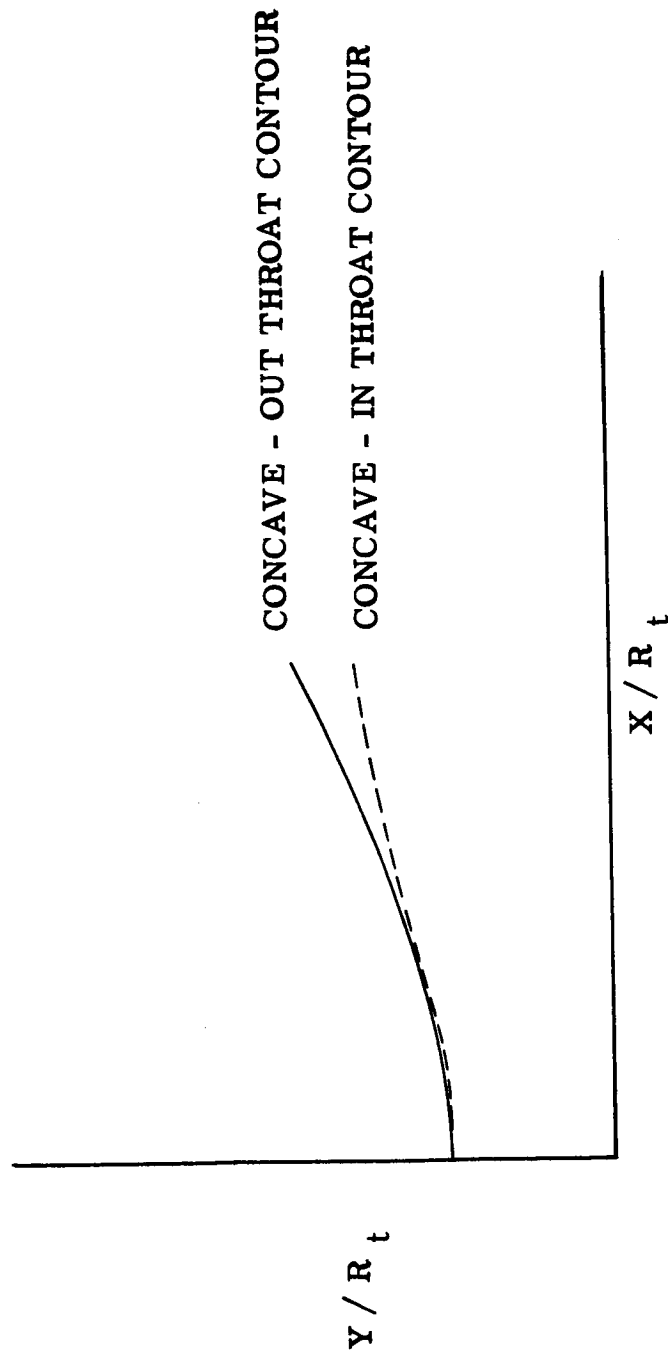


Figure 40. Types of Throat Contours

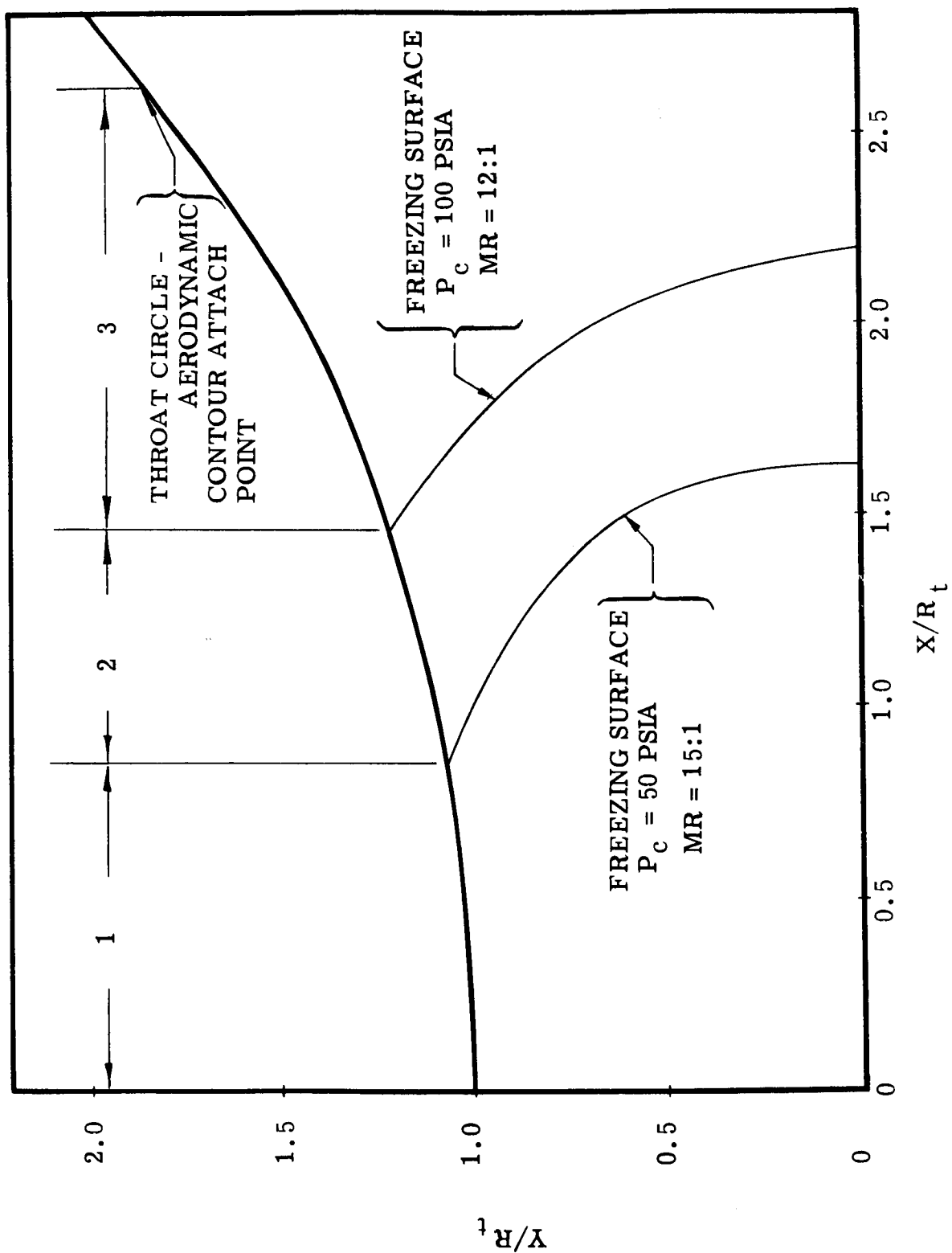


Figure 41. Performance Decrement Regions of the Circular Throat Contour (ρ/ρ_t)_D of 5.0



improving the overall performance. Ideally, this type of contour may be represented by a function which has a radius of curvature which is initially small, increases rapidly, and then decreases rapidly. However, more simply, it may be described by three tangentially-joined circles, a "triple-circle" throat contour, the first and last circles having a small radius of curvature and the second circle having a large radius of curvature.

Preliminary analysis performed on the ρ/R_t of 5.0 circular throat nozzle using two circles $(\rho/R_t)_1 = 5.0$ and $(\rho/R_t)_2 = 0.5$ indicated a net performance gain of approximately 0.1 percent over the $(\rho/R_t)_D$ of 5 circular throat bell nozzle.

Reaction Kinetic Efficiency Improvement

In the preceding discussion, the geometric efficiency was improved with η_K essentially fixed. An observation of η_G , η_K , and η_D (Fig. 36 through 38) indicated that η_K had the lowest value of any of the efficiencies (approximately 0.93) and therefore the greatest room for improvement. This observation, coupled with the fact that the 15-degree long throat cone had a higher kinetic efficiency than any of the circular throat nozzles studied, led to the investigation of a nozzle which was formed by a 15-degree cone truncated at the 100-psia chamber pressure, 12:1 mixture ratio freezing point. A ρ/R_t of 0.5 was added to the conical section and an optimum aerodynamic section attached as shown in Fig. 42.

This type of nozzle consists of an initial circle radius $(\rho/R_t)_1$, which becomes tangent at the angle, α , to a conical section extending to $(X/R_t)_B$. A circle of radius $(\rho/R_t)_3$ turns the wall from angle, α , to the angle indicated for an aerodynamically optimized contour from that point to the nozzle exit.

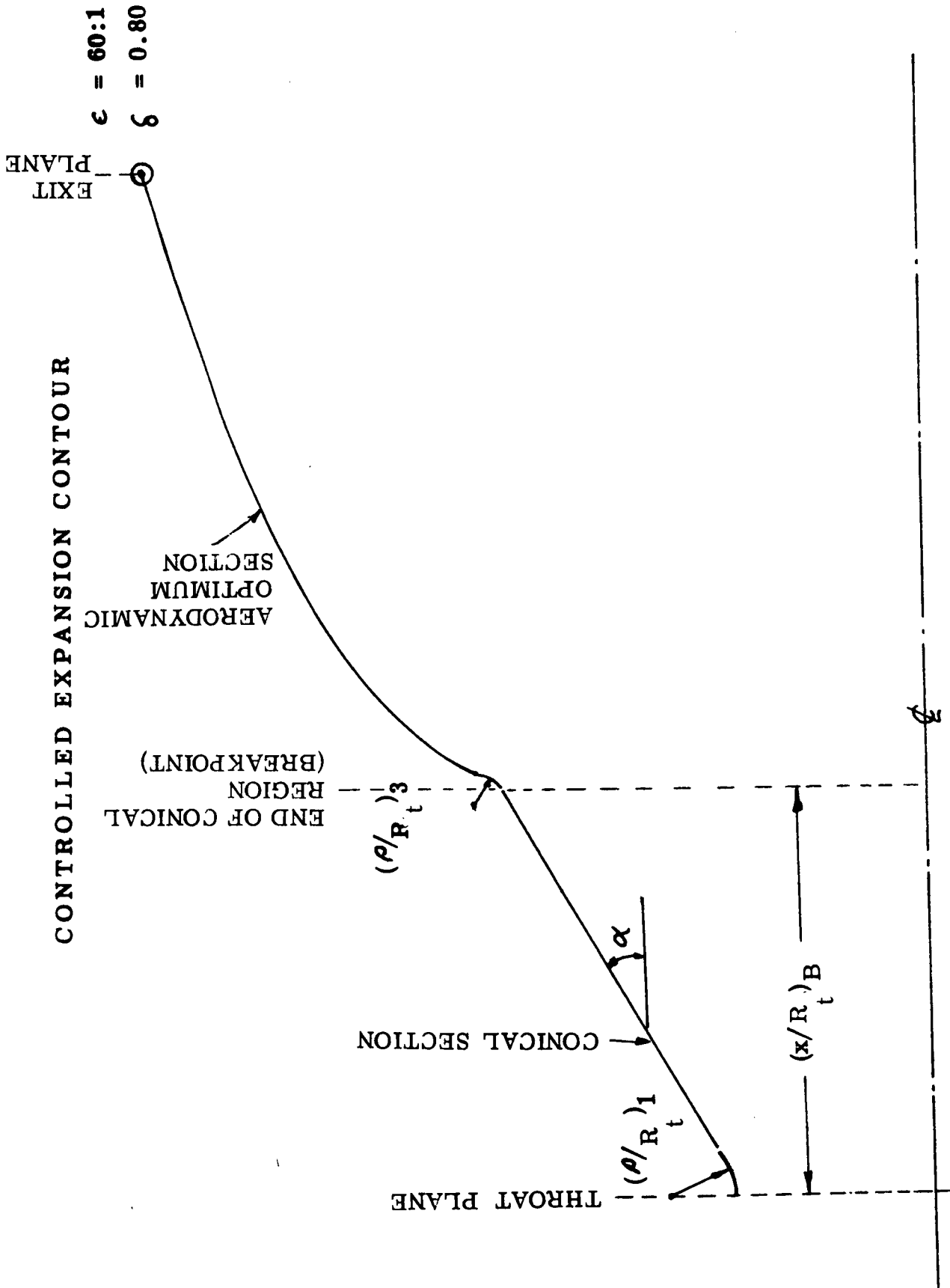


Figure 42. Nomenclature for Controlled Expansion Nozzle



The analyzed contour had $(\rho/R_t)_1$ of 3.635, α of 15 degrees, $(\rho/R_t)_3$ of 0.5, and a $(X/R_t)_B$ of 2.8. This type of throat contour is a simplified triple-circle throat contour

$$(\rho/R_t)_1 = 3.635, (\rho/R_t)_2 = \infty, (\rho/R_t)_3 = 0.5, \alpha = 15 \text{ degrees}$$

As shown in Table 1, this design showed gains of 0.5 to 1.1 percent over the conventional 70-percent bell nozzle, $(\rho/R_t)_D$ of 0.392. Gains of approximately 0.1 percent over the optimum circular throat bell nozzle and 0.3 to 0.5 percent over the 15-degree long throat cone were predicted.

Task III test data for the 15-degree long throat cone indicated experimental kinetic efficiencies approximately 1 percent higher than predicted, while data for the 70-percent bell indicated good agreement with theoretical predictions (although slightly lower than predicted).

Considering the possibility that the theoretical kinetic model was not sufficiently sensitive to nozzle contour, it was decided that the best chance of verifying the controlled expansion nozzle concept was to use a throat contour exactly duplicating that of the cone. In this way, the same kinetic efficiency should be achieved. In addition, a kinetic efficiency prediction for the new nozzle could be made independent of a kinetic theory.

At this time the decision was also made to select the contour with the greatest chance of verifying the controlled expansion concept. Because the greatest potential performance improvement is at a chamber pressure of 50 psia and a mixture ratio of 15:1, the breakpoint was selected at the indicated freezing point of the Task III 15-degree long throat at that pressure and mixture ratio.



This breakpoint occurred at a local area ratio of 2.63 and a normalized axial location of 2.8. The selected contour is shown in Fig. 43, and the coordinates are tabulated in Table 2. Figure 44 contains a graph of geometric efficiency vs the axial location of the breakpoint, from which it is seen that the efficiency is 0.9818. The drag efficiency was computed to be 0.961.

For this nozzle it was then possible to make two performance predictions, one based on theoretical kinetic efficiency and one based on the experimental kinetic efficiency of the 15-degree long throat cone (because the contour is identical to the cone out to the freezing point). Both performance predictions are shown in Table 3, and compared to the 70-percent bell and 15-degree long throat cone. When this nozzle was subsequently tested, the performance gain was correlated well by the theoretical kinetic efficiency value. The data correlation is discussed in more detail in the Data Correlation section.

TASK IV, CONTROLLED EXPANSION NOZZLE ANALYSIS

In Task IV, studies were conducted to increase further the performance advantage demonstrated for the controlled expansion nozzle. The contour was to be of the same general type used in Task III and is shown schematically in Fig. 41. Optimum values of $(\rho/R_t)_1$, α , $(\rho/R_t)_3$, and $(X/R_t)_B$ were to be determined to obtain the optimum contour.

The procedure selected for the study of these parameters was to begin by holding the two radii, $(\rho/R_t)_1$ and $(\rho/R_t)_3$, constant and varying α and $(X/R_t)_B$. This route was taken because the latter are considered to be the major parameters. Variations in the others should have only a minor influence on the result. A $(\rho/R_t)_1$ of 3.635 and a $(\rho/R_t)_3$ of 0.5 were selected.

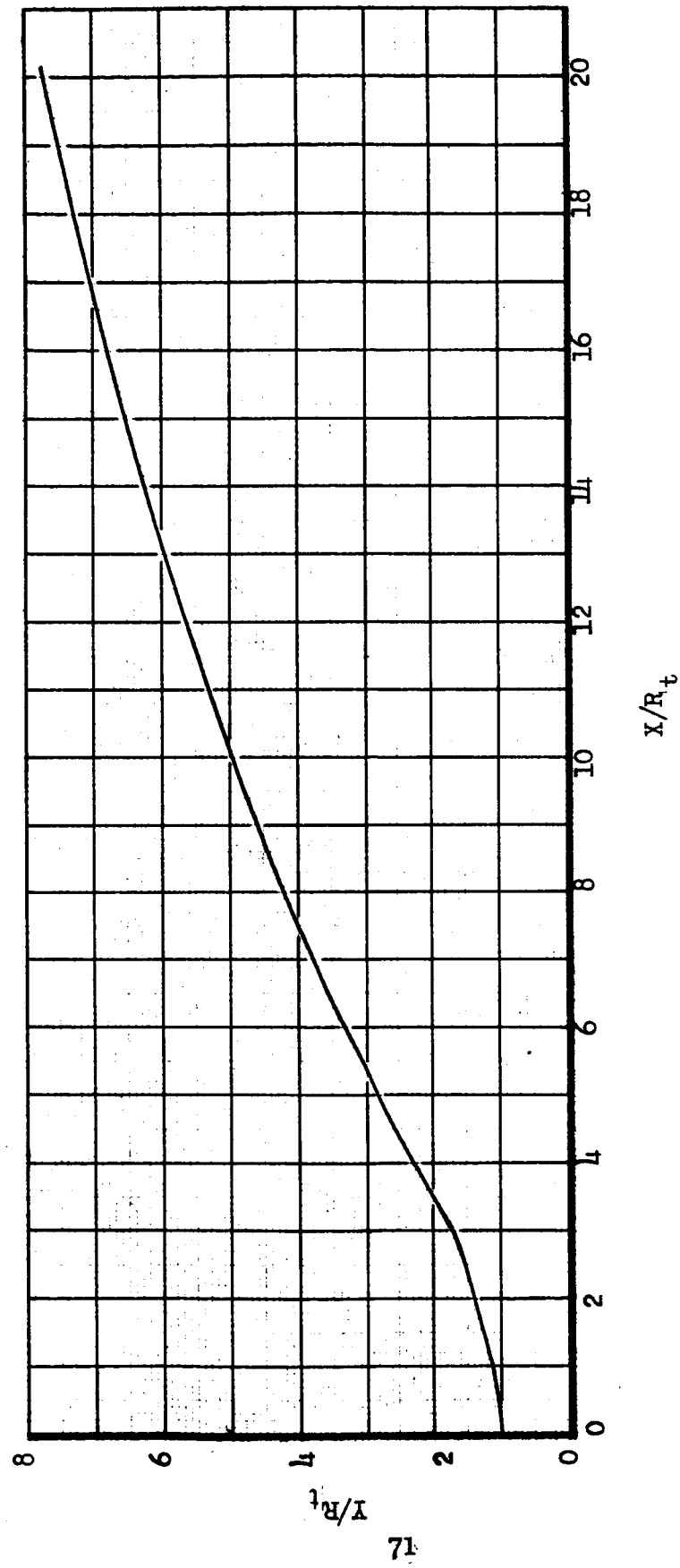


Figure 43. Controlled Expansion Nozzle Contour



TABLE 2

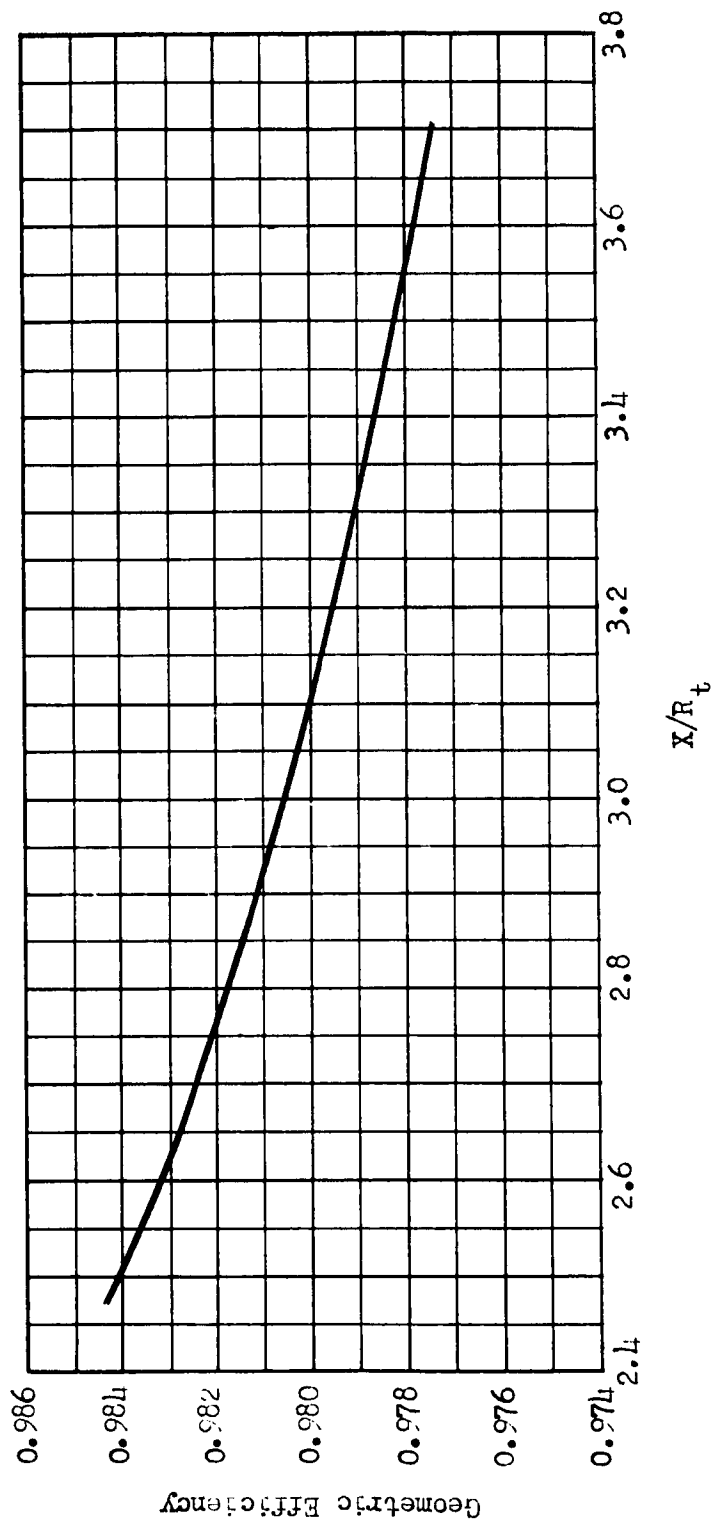
WALL COORDINATES CONTROLLED EXPANSION NOZZLE

 $(\epsilon = 60:1, 80 \text{ PERCENT LENGTH})$

$\underline{X/R_t}$	$\underline{Y/R_t}$	$\underline{\text{THETA}}$
0.932	1.121	14.872
1.015	1.143	15.000
1.078	1.160	15.000
1.245	1.205	15.000
1.381	1.236	15.000
1.501	1.274	15.000
1.638	1.310	15.000
1.826	1.361	15.000
2.109	1.437	15.000
2.382	1.510	15.000
2.659	1.587	15.000
2.804	1.623	15.010
2.804	1.623	15.010
2.808	1.624	15.510
2.812	1.625	16.010
2.816	1.627	16.510
2.821	1.628	17.010
2.825	1.629	17.510
2.829	1.630	18.010
2.833	1.632	18.510
2.837	1.633	19.010
2.841	1.635	19.510
2.845	1.636	20.010
2.849	1.638	20.510
2.854	1.639	21.010
2.858	1.641	21.510
2.862	1.642	22.010
2.866	1.644	22.510
2.870	1.646	23.010
2.874	1.647	23.510
2.882	1.651	24.510
2.886	1.653	25.010
2.890	1.655	25.510
2.894	1.657	26.010
2.897	1.659	26.510
2.901	1.660	27.010
2.905	1.662	27.510
2.909	1.665	28.010

TABLE 2
(Concluded)

<u>X/R_t</u>	<u>Y/R_t</u>	<u>THETA</u>
2.913	1.667	28.510
2.917	1.669	29.010
2.921	1.671	29.510
2.924	1.673	30.010
2.928	1.675	30.510
2.932	1.677	31.010
2.935	1.679	31.397
4.105	2.350	28.733
5.459	3.055	26.231
7.449	3.961	23.041
9.616	4.820	20.126
11.953	5.619	17.564
14.213	6.296	15.699
17.990	7.268	13.160
20.145	7.733	12.377



Compound Nozzle
80% Length
 $\epsilon = 60:1$

Figure 44. Geometric Efficiency versus Axial Coordinate at End of Conical Section.



TABLE 3

PERFORMANCE EFFICIENCY COMPARISON FOR FINAL SELECTED
CONTROLLED EXPANSION NOZZLE

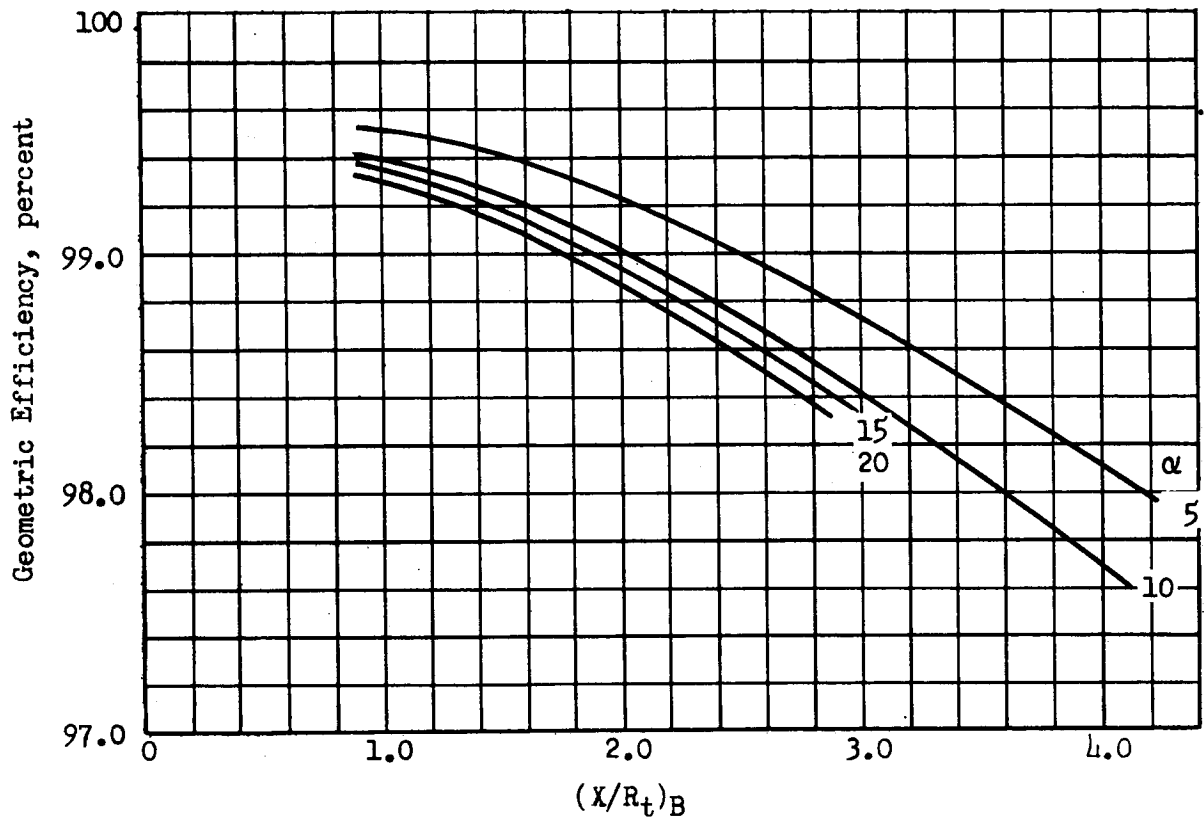
<div>Efficiency Nozzle</div>	Kinetic Efficiency, η_K	Geometric Efficiency, η_G	Drag Efficiency, η_D	Overall Efficiency, η
70-Percent Bell	0.917(theo)	0.988	0.968	0.873
15 Degree Long Throat Cone	0.950(theo)	0.985	0.956	0.891
Controlled Expansion {	0.945 (exp)	0.982	0.961	0.888
	0.940 (theo)	0.982	0.961	0.883



The geometric and drag efficiencies were computed for a range of α (5, 10, 15, and 20 degrees) and $(X/R_t)_B$ values. This was done by designing a Rao optimum contour for each throat region geometry defined by the parameters. Thus each value on the curve represents an aerodynamically optimized contour.

The geometric efficiency is plotted vs $(X/R_t)_B$ for four values of the half angle, α , in Fig. 45. The drag loss is plotted in the same way in Fig. 46. The sum of these two losses is shown in Fig. 47. It is seen that the result is far more dependent upon $(X/R_t)_B$ than upon α . The kinetic efficiencies were determined using the sudden freezing criterion using the selected reaction rate constants (Table 8). Combining the losses, the optimum half angle for the conical region was found to be 12 degrees with the conical breakpoint at a $(X/R_t)_B$ of 2.7. This nozzle was predicted to have an 0.3-percent performance advantage over the Task III nozzle which has a 15-degree half angle.

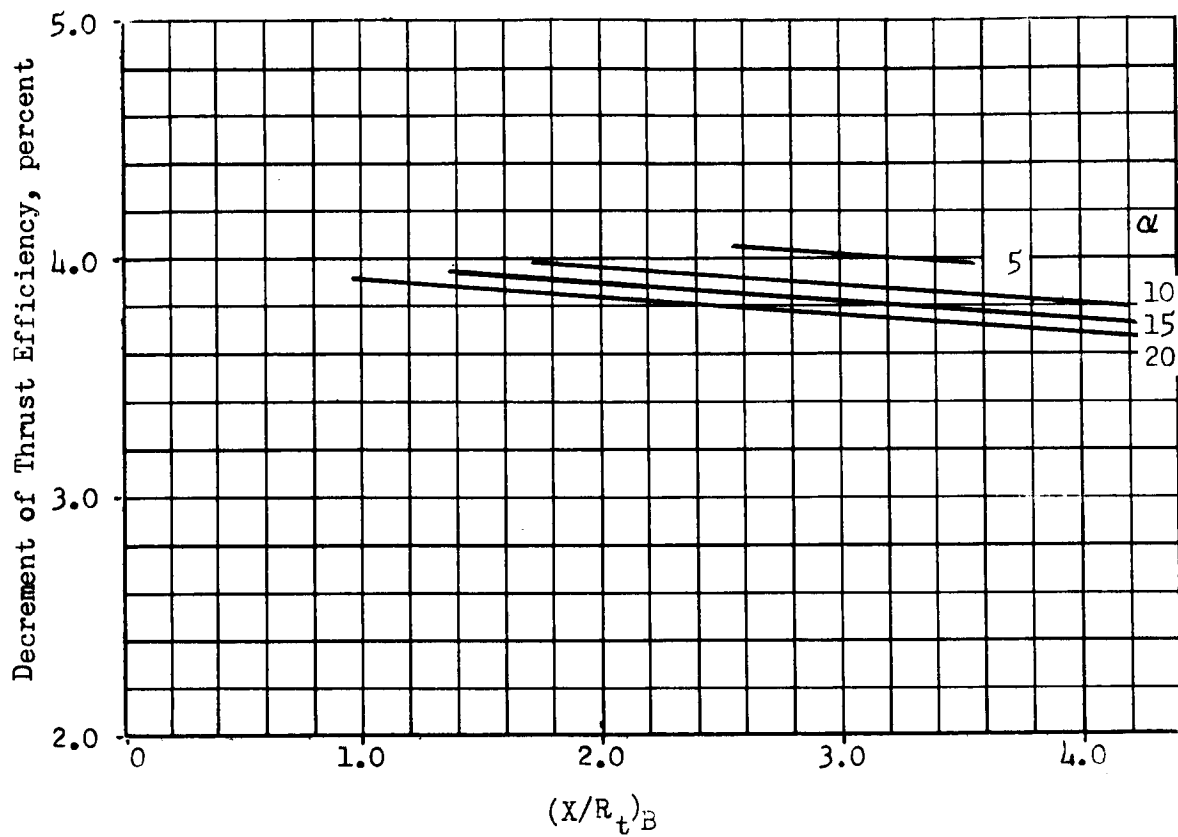
Since the gain achieved with the conical-type nozzle was small, attempts were made to obtain larger gains by contouring the wall in this area. Truncated segments of ideal nozzles were used. One such attempt is shown in Fig. 48. None of these has produced a larger gain than the 12-degree conical nozzle discussed above. Although a nozzle of this modified type should produce a larger gain than the more restricted conical type, it became clear that the gain would be small. Based on this information, it was anticipated that a continued effort on the controlled expansion nozzle might produce 1.5-percent better performance than an aerodynamically designed nozzle, where the first attempt produced 1 percent. Since this additional 0.5-percent would be difficult to verify experimentally, it was decided that a nozzle of this type would not be tested in Task IV.



$(\rho/R_t)_1 = 3.635$
 $(\rho/R_t)_3 = 0.5$
 $\delta = 80\%$

LF₂/GH₂ (77F)
 $P_c = 50$ psia
MR = 15:1
 $\epsilon = 60:1$

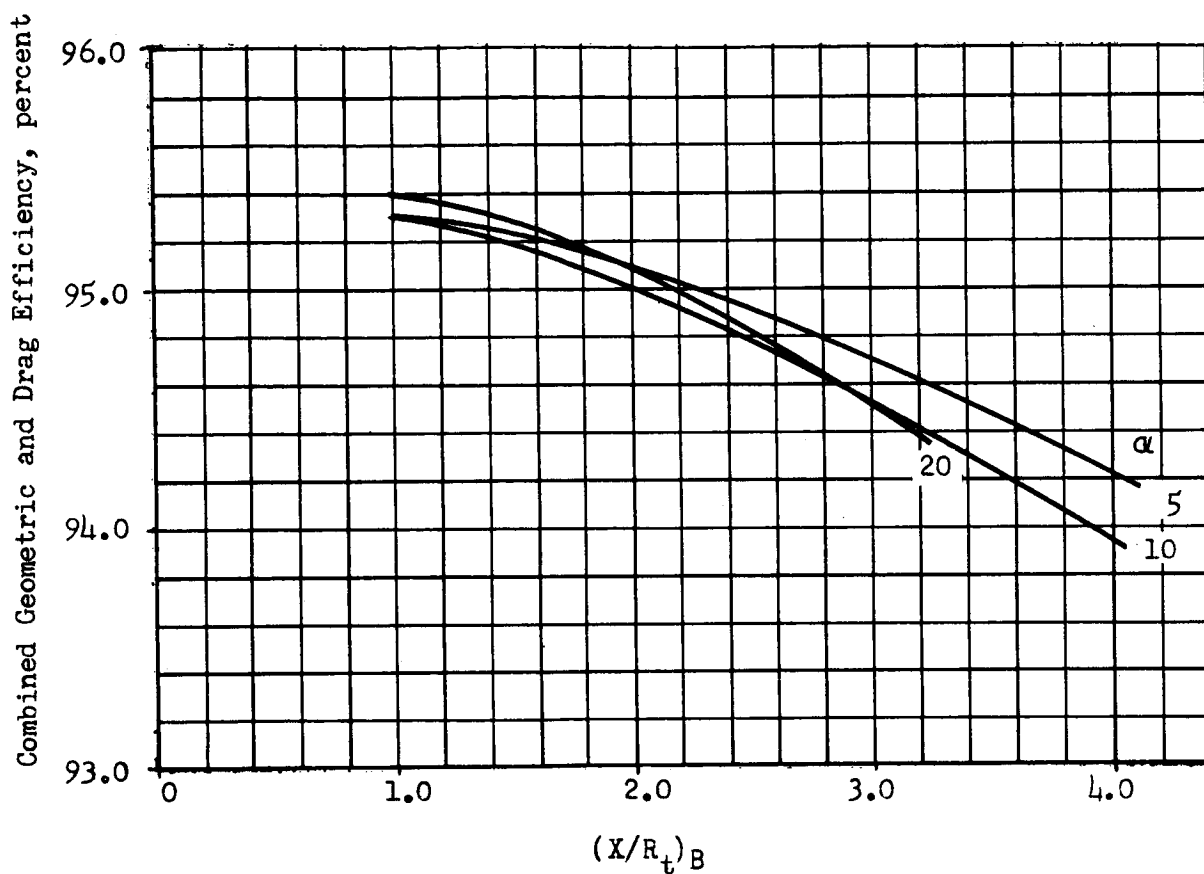
Figure 45. Effect of α and $(X/R_t)_B$ on Geometric Efficiency



$$\begin{aligned}(\rho/R_t)_1 &= 3.635 \\ (\rho/R_t)_3 &= 0.5 \\ \delta &= 80\%\end{aligned}$$

$$\begin{aligned}\text{LF}_2/\text{GH}_2 &(77\text{F}) \\ P_c &= 50 \text{ psia} \\ \text{MR} &= 15:1 \\ \epsilon &= 60:1\end{aligned}$$

Figure 46. Effect of α and $(X/R_t)_B$ on Drag Loss



$(\rho/R_t)_1 = 3.635$
 $(\rho/R_t)_3 = 0.5$
 $\delta = 80\%$

LF₂/GH₂ (77F)
 $P_c = 50$ psia
MR = 15:1
 $\epsilon = 60:1$

Figure 47. Effect of α and $(X/R_t)_B$ on Combined Geometric and Drag Efficiency

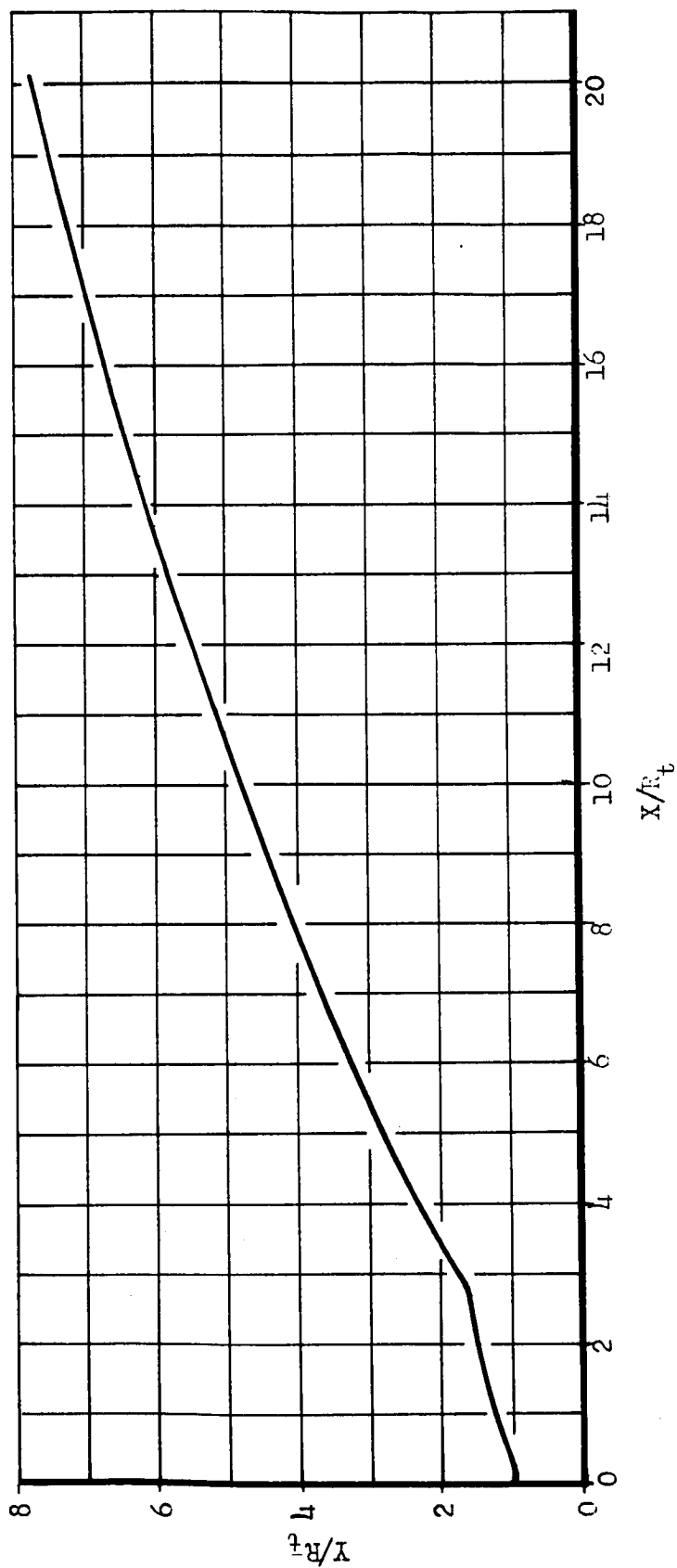


Figure 48. Concave-In Throat Contour Controlled Expansion Bell Nozzle



PERFORMANCE ANALYSIS

This section contains descriptions of the techniques used for and the results obtained from analyses of performance effects of inviscid aerodynamics, viscous drag, heat loss, chemical kinetics, and propellant impurities.

Since it was the purpose of the analytical portion of this program to predict performance with the greatest possible accuracy, the best available techniques were used throughout the analysis.

The performance losses computed in this section were considered as additive (rather than multiplicative) effects. The predicted loss is the sum of the individual losses.

AERODYNAMIC ANALYSIS

All aerodynamic analyses were performed using variable gas property techniques to provide the greatest accuracy. This approach required that, even for the same nozzle contour, separate analyses be performed for every change in chamber pressure or mixture ratio (since either affects the gas properties). Therefore, for each of the nozzles, analyses were performed at each pertinent chamber pressure and mixture ratio, consisting of a solution of the transonic flow field followed by a method-of-characteristics analysis of the supersonic nozzle.



Analysis

The first step in the aerodynamic analysis consists of solving the transonic potential flow field, which was the same for all nozzles, since the contour upstream of the throat was invariant throughout the program. The transonic analysis provides a starting line for the supersonic method-of-characteristics analysis used in the second step. The parabolic partial differential equations for irrotational compressible flow in the transonic regime have no known analytical solution. The well-known Sauer solution, which consists of using a second-order series expansion of the flow equations, is restricted to nozzles with gradual wall curvature ($\rho_i/R_t \approx 3$) in the throat inlet region.

For the nozzles used in this program, the inlet wall curvature ratio was smaller ($\rho_i/R_t = 1.5$) than can be analyzed using Sauer's method. Therefore, a much more accurate solution of the transonic flow problem, consisting of expanding the flow equations in a series retaining up to 33 terms, was used in the analysis. The complete transonic flow field was computed, specifying flow conditions at any point in the Mach number region from approximately 0.8 to 1.2. The solution provided a supersonic starting line for the nozzle analysis. In addition, the potential flow-field discharge coefficient was computed by comparing the flowrate obtained from this analysis with the flowrate associated with uniform parallel flow. The value thus obtained was 0.9945.

After the starting line was computed, the nozzle flow-field solution was obtained, using the method-of-characteristics for chemical equilibrium gas flow.



Results

For the 15-degree conical nozzle, the effects of changing chamber pressure and mixture ratio were found to be negligible, and the resulting efficiency, η_G , was 0.9854, based upon aerodynamic throat area. This value differs from the efficiency of the Task II 1.9 area ratio conical nozzle which had an efficiency of 0.9834. Except for the truncation to a low area ratio, the Task II and Task III nozzles were identical. This variation of efficiency with area ratio is typical for conical nozzles. An example is depicted in Fig. 49, which contains a graph of efficiency vs area ratio at a stagnation pressure of 100 psia and a mixture ratio of 12:1.

Because the efficiency of conical nozzles was found to be invariant with chamber pressure and mixture ratio, single values, listed in Table 4 were used for the 10-, 15-, and 20-degree cones.

TABLE 4

GEOMETRIC EFFICIENCY OF CONICAL NOZZLES
BASED ON AERODYNAMIC THROAT AREA
 $\epsilon = 60:1$

Nozzle Half-Angle, Degrees	η_G
10	0.9928
15	0.9854
20	0.9713

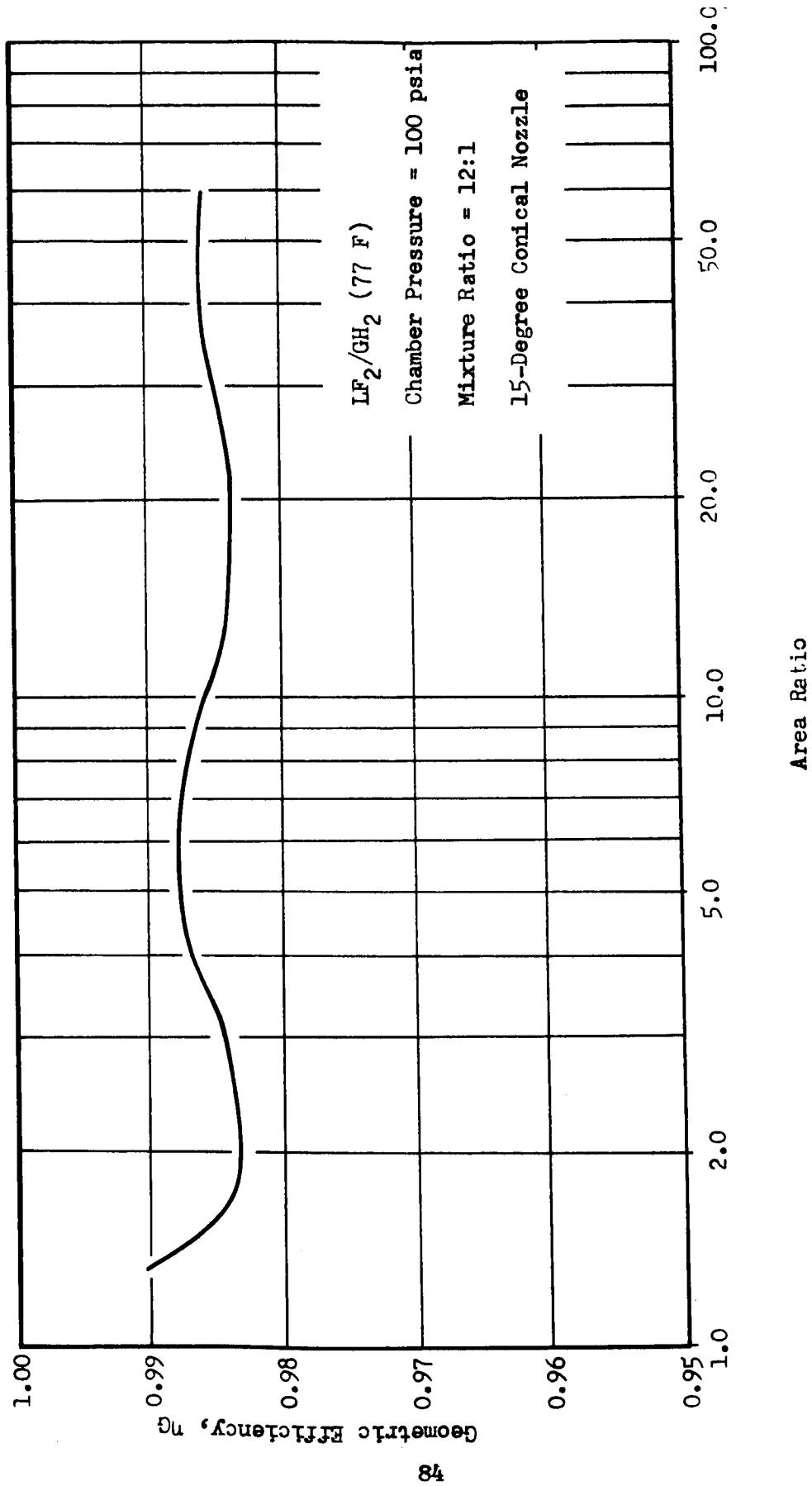


Figure 49. Effect of Area Ratio on Geometric Efficiency of a 15-Degree Conical Nozzle



For the bell nozzle, slight differences were noted between the efficiencies at different P_c - MR combinations, generally tending toward maximum efficiencies at high mixture ratios and low pressures. These differences are in the vicinity of 0.2 percent, and the results are shown in Fig. 50. The efficiency at a chamber pressure of 100 psia and 12:1 mixture ratio is slightly higher than would be expected, based upon the other points in the matrix. This is probably a result of the 70-percent bell nozzle contour being a precise optimum (aerodynamically) at that point.

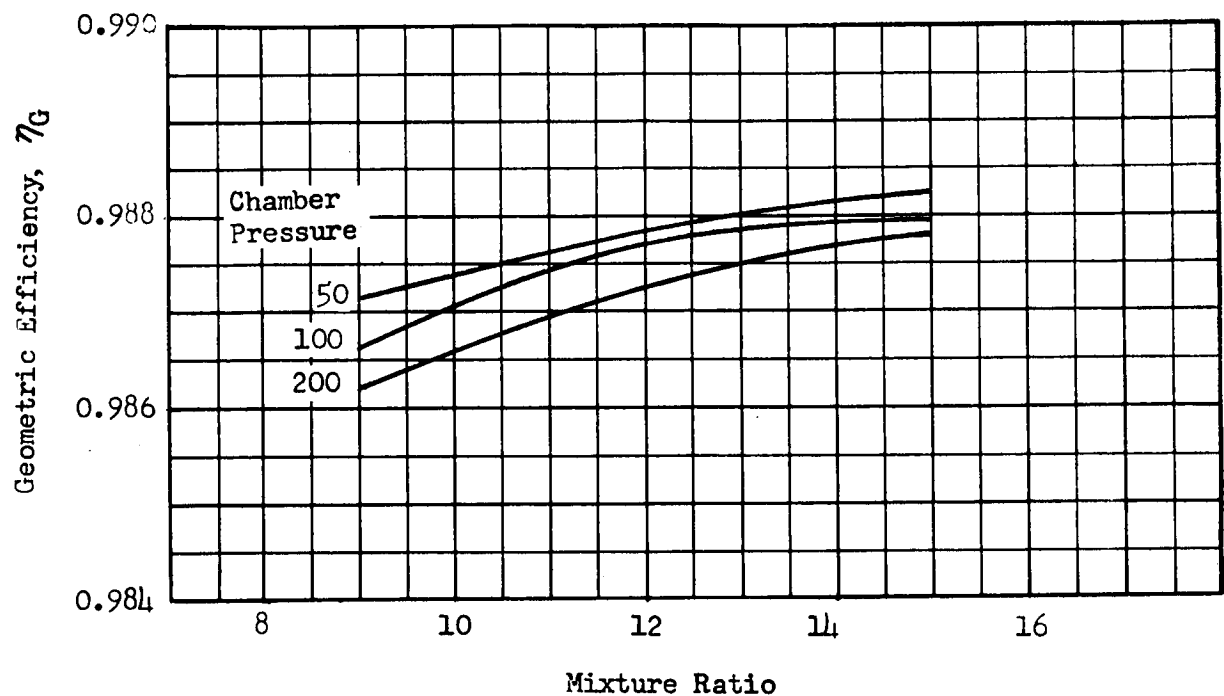
The efficiency curve for the controlled expansion nozzle is shown in Fig. 51. For this nozzle, the trend is steeper than that of the 70-percent bell; efficiency increases 0.5 percent from low to high mixture ratios.

DRAG ANALYSIS

A viscous drag analysis was conducted to determine the frictional losses associated with each of the nozzles at each nominal test point. Computations were based upon the turbulent boundary layer assumption, since heat flux data indicate a turbulent boundary layer.

Analysis

The method of analysis used for calculating the frictional drag losses for the nozzles is a boundary layer growth model which closely



Bell Nozzle
70 percent length
 $\epsilon = 60:1$

Efficiency Based Upon Aerodynamic Throat Area

Figure 50. Geometric Efficiency of Bell Nozzle

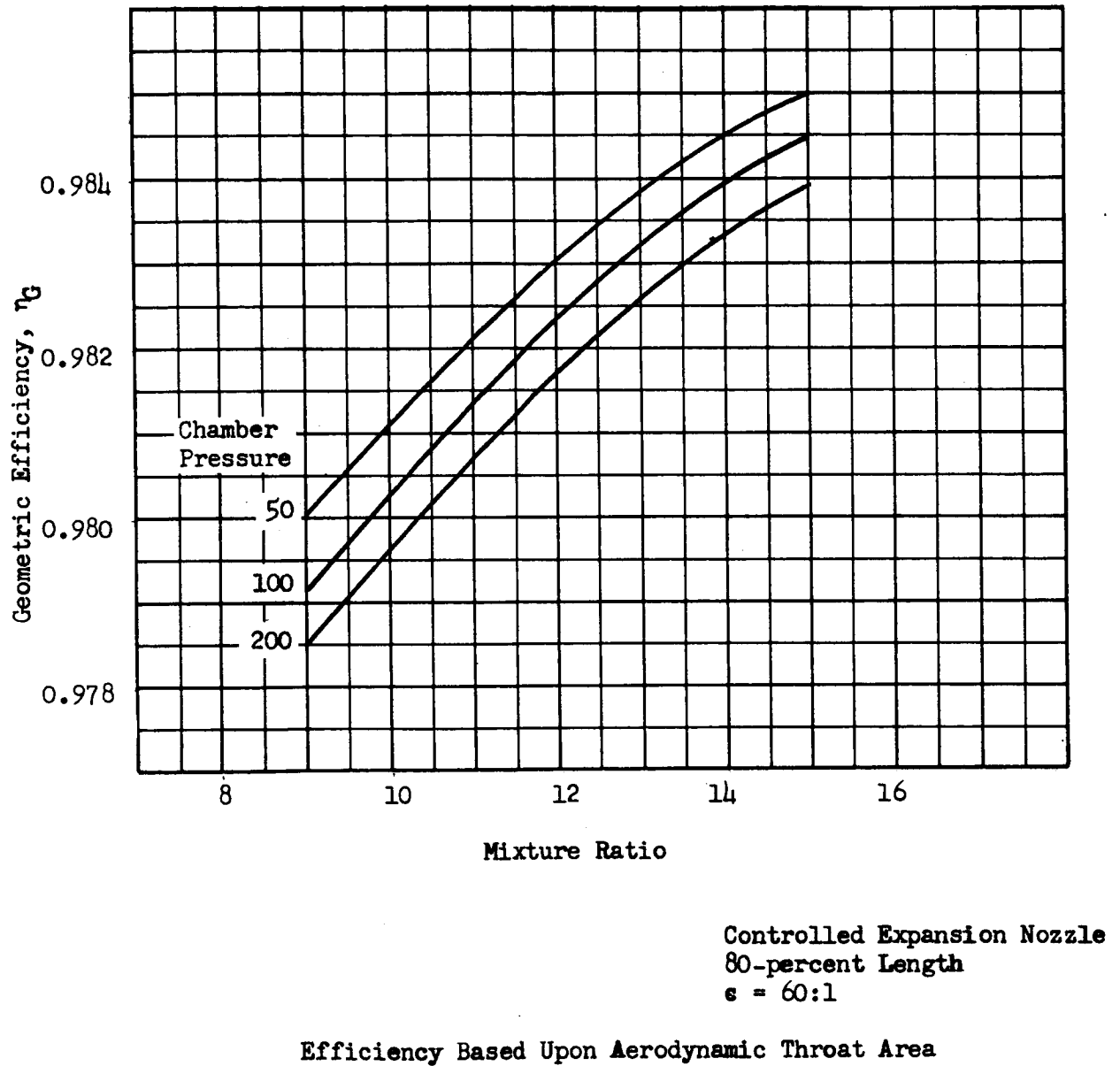


Figure 51. Geometric Efficiency of Controlled Expansion Nozzle



follows the approach documented in Ref. 24. The essential differences are:

1. The reference utilizes the one-seventh power law velocity profile, whereas the Rocketdyne program allows the exponent to vary from one-seventh to one-fifteenth to account for the high flow acceleration near the throat region. The variation of the exponent is based upon semi-empirical relations.
2. The skin friction coefficient correlation for the Rocketdyne method is based upon experimental data where the measured velocity profile exponent varied from one-seventh to one-fifteenth. Recent sources have indicated that the exponent has approached one-twentieth.
3. In Ref. 24 the integral momentum and energy equations for axisymmetric boundary layers are solved simultaneously. In the Rocketdyne method, the two equations are decoupled and solved separately. This is accomplished by assuming the energy thickness is equal to momentum thickness.

The standard procedure for gas viscosity computation is to compute viscosity for the combustion chamber gas composition by using the Wilke equation. The viscosity at any point during the expansion is then related to this value by the temperature ratio raised to a power (in this case the power was 0.65). However, for a gas in chemical equilibrium, the composition as well as the temperature changes during expansion. This effect was investigated and was found to be of second order.



Results

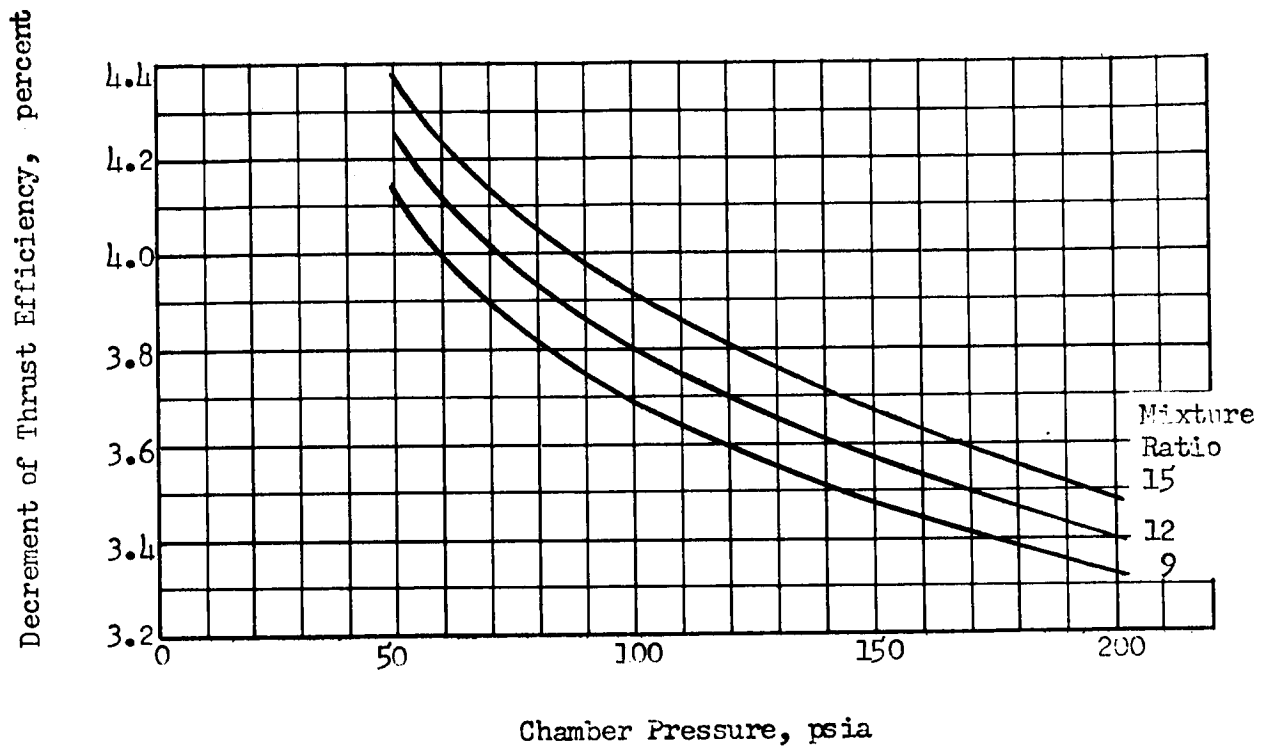
The analysis was employed for each nozzle at each of the nominal test points, and accounts for boundary layer effects from the injector to the nozzle exit. The results are shown in Fig. 52 to 58, and are presented as efficiency decrements defined as a percent of vacuum chemical equilibrium thrust coefficient.

The theoretical frictional losses for the 15-degree conical nozzles with an expansion area ratio of 60:1 are illustrated in Fig. 52. The loss is seen to increase with increasing mixture ratio, this is a result of the higher combustion temperature and combustion gas viscosity associated with increasing mixture ratio. Figures 53 to 58 are similar graphs for the other nozzles. The magnitude of the drag loss is seen to be related to the length of the nozzle, the 20-degree cone having the smallest surface area and therefore the smallest drag. The frictional losses shown in these figures include the loss in the combustion zone.

HEAT LOSS EFFECT

An analysis was performed to determine heat transfer correction coefficients for the purpose of correcting measured test data to a "no heat loss" condition.

The analysis was accomplished by use of heat transfer and performance computer programs. The first step was to determine the local heat transfer distribution for the defined nozzle contour. Chemical equilibrium performance computations were then made, subject to the distributed heat loss.



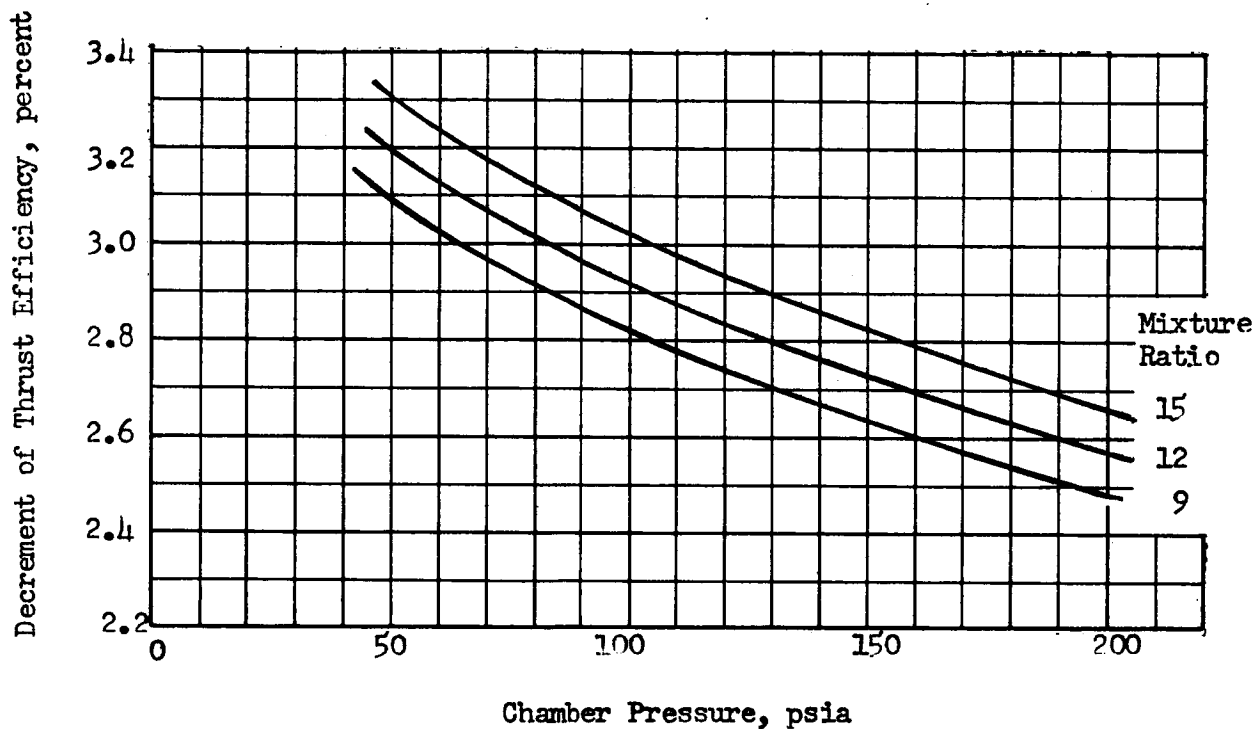
LF_2/GH_2 (77 F)

15-degree Cone

$\epsilon = 60:1$

$L^* = 30$ inches

Figure 52. Drag Loss for 15-degree Conical Nozzle-Turbulent Boundary Layer



LF_2/GH_2 (77 F)
70-percent Bell
 $\epsilon = 60:1$
 $L^* = 30$ inches

Figure 53. Drag Loss for 70-percent Bell Nozzle -
Turbulent Boundary Layer

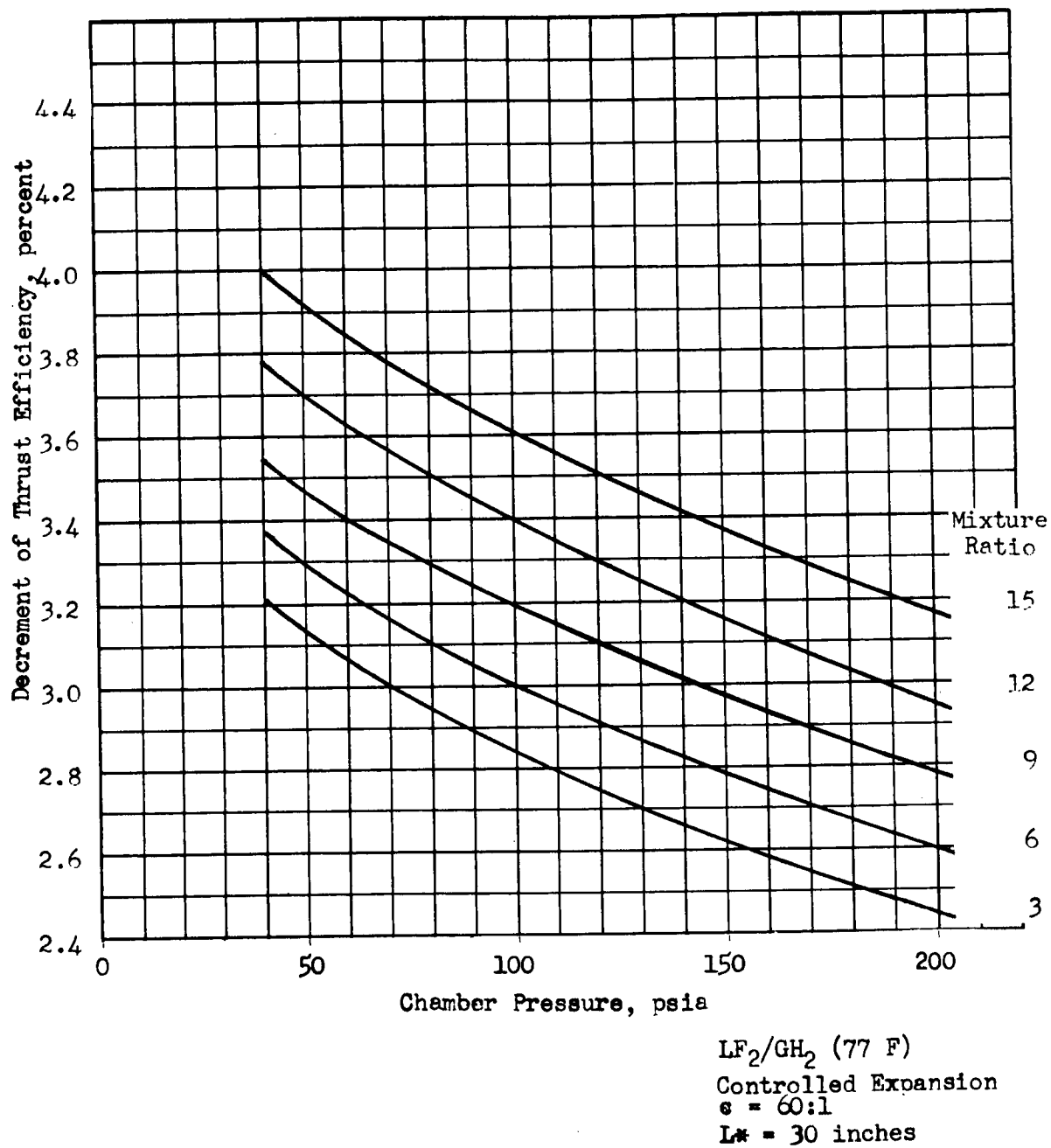
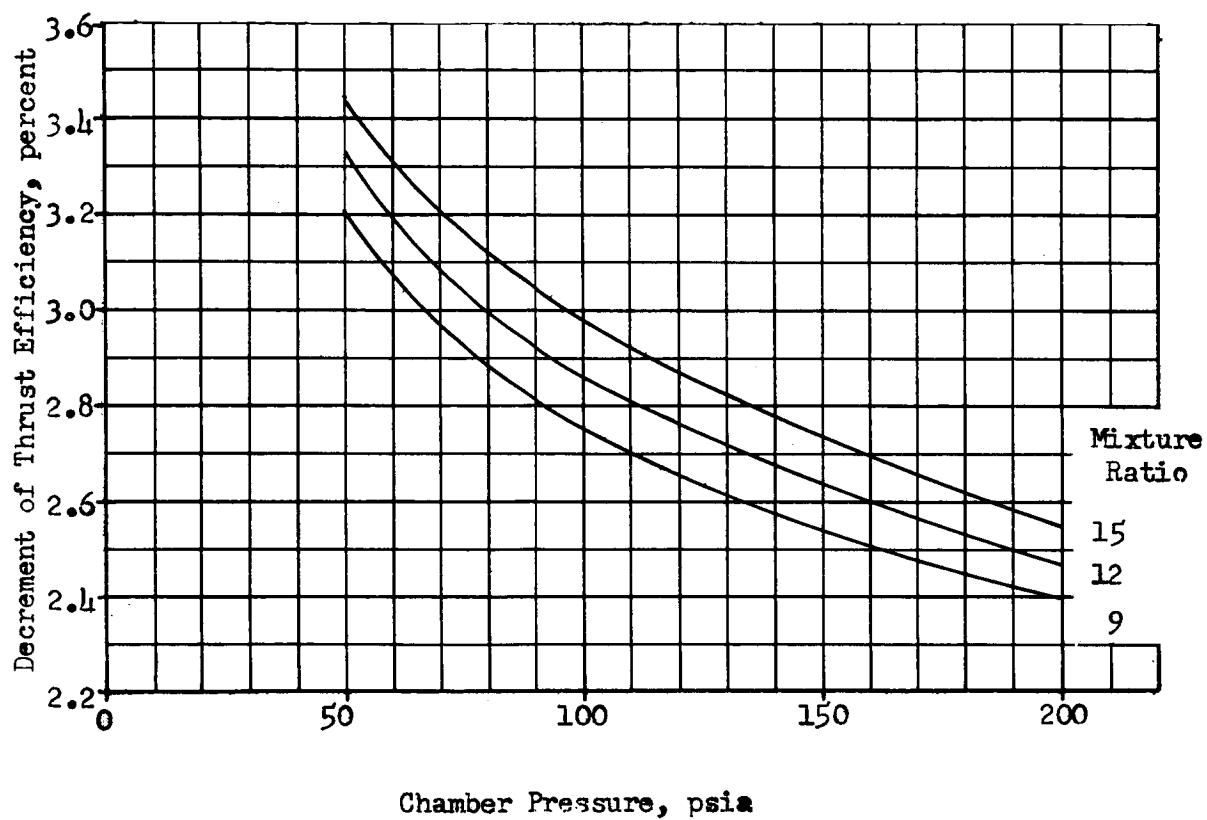
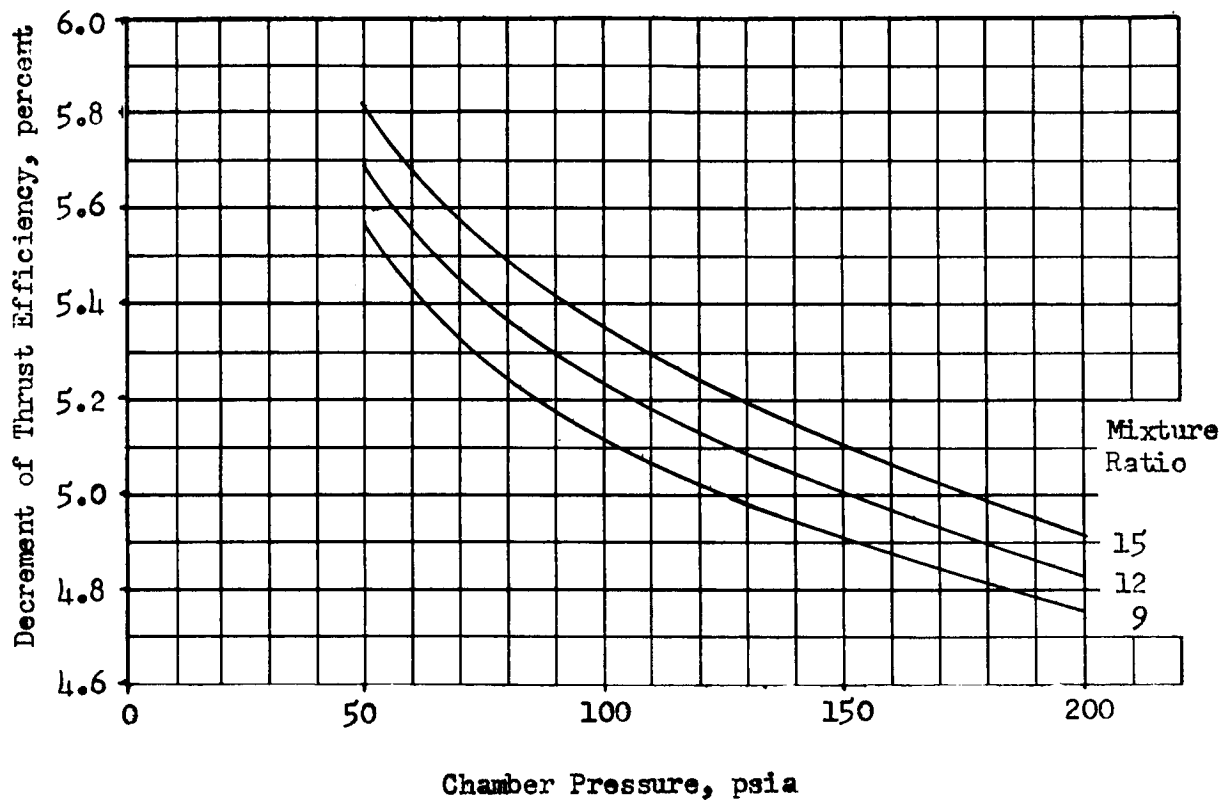


Figure 54. Drag Loss for Controlled Expansion Nozzle-Turbulent Boundary Layer



LF_2/GH_2 (°F)
20-degree Cone
 $\epsilon_* = 60:1$
 $L_* = 30\text{-inches}$

Figure 55. Drag Loss for 20-degree Conical Nozzle
Turbulent Boundary Layer



LF_2/GH_2 (°F)
10-degree Cone
 $\epsilon = 60:1$
 $L^* = 30$ inches

Figure 56. Drag Loss for 10-degree Conical Nozzle
Turbulent Boundary Layer



The c^* heat loss correction coefficient was determined by considering the effect of the heat loss in the combustion chamber only. The heat loss specific impulse correction coefficients were determined by considering the combined effect of heat loss in the combustion chamber and nozzle sections. The combustion chamber heat loss was considered to have been removed in a stagnation region. In the nozzle, heat was rejected along the full length according to the calculated distribution. As heat was removed at each station, the gas was allowed to reach chemical equilibrium at the reduced energy level. An isentropic expansion was then followed to the next station at which heat was removed and the process was then repeated.

The results of these calculations for the 15-degree, long-throat conical nozzle are shown in Fig. 57. The correction is shown in terms of reciprocal efficiency or correction factor as a function of chamber pressure. Because the heat lost in the chamber has the largest effect, and all the nozzles have the same chamber configuration, this figure was used for all the nozzles.

CHEMICAL KINETIC ANALYSIS

Reaction kinetic efficiencies of the nozzles were determined analytically by performing a stream tube performance analysis. This method divides the nozzle flow into a large number of stream tubes and applies the freezing point criterion to the essentially one-dimensional flow of each stream tube, providing a detailed kinetic evaluation of nonuniform flow fields.

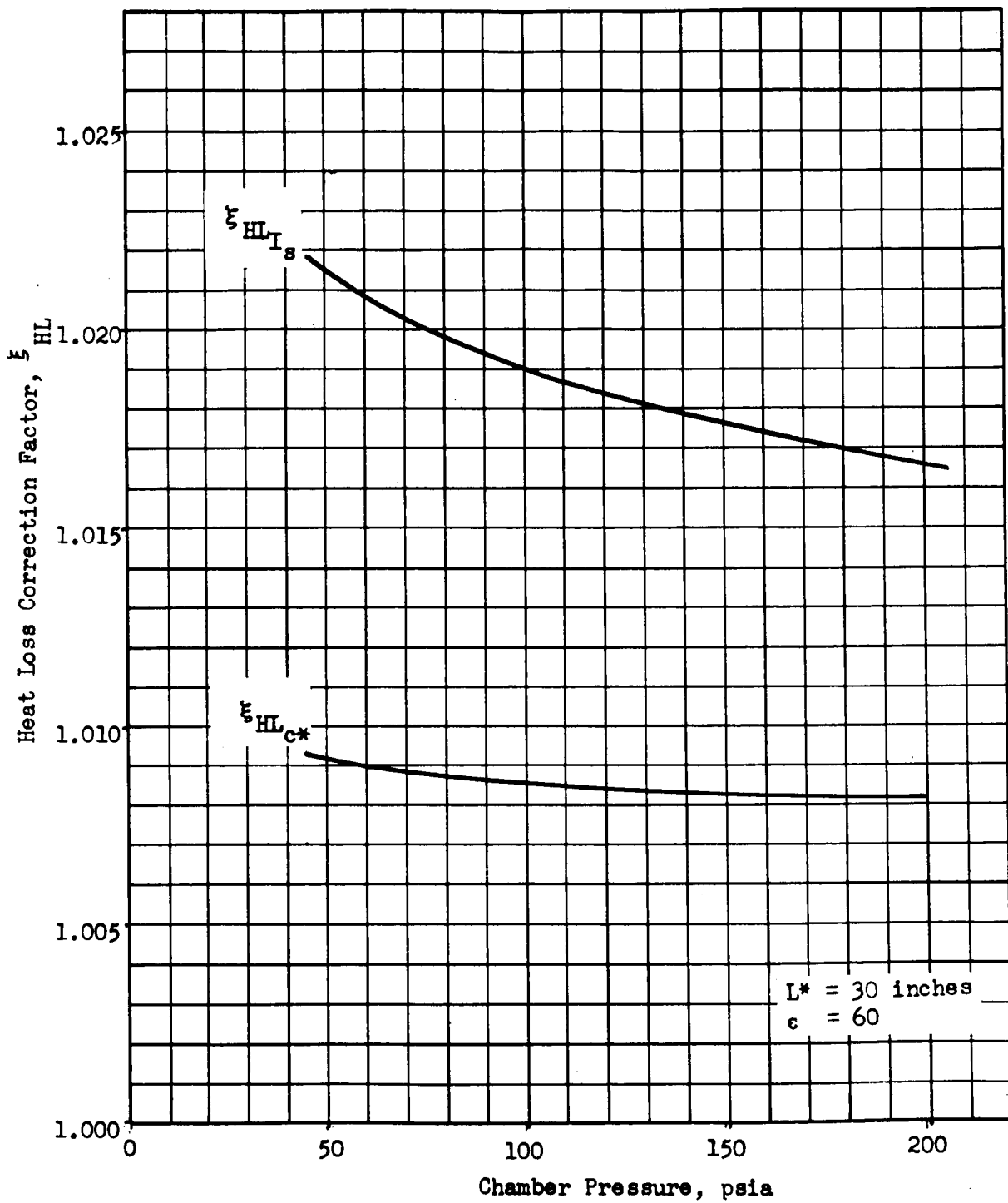


Figure 57. Heat Loss Correction Factor vs Chamber Pressure



Analysis of a large number of stream tubes accounts for three important effects which would not be accounted for in a one-dimensional analysis:

1. By assuming that the gas expands uniformly (one-dimensionally), the same chemical freezing point is applied to the entire flow field. Actually the flow expansion rates differ for different portions of the nozzle flow resulting in different freezing points.
2. Parts of the nozzle flow expand to different final area ratios at the nozzle exit.
3. An expanding gas must have velocity components normal to the thrust direction. Again, different portions of the flow may have different normal velocity components resulting in different final flow angles at the nozzle exit.

Once the flow field was divided into a large number of stream tubes, the stream tube kinetic analysis was performed after making the assumptions that the flow within each stream tube is uniform, and that the streamline pattern is not affected by the chemical freezing of the flow within the various stream tubes. Each stream tube has its own throat area, exit area, exit angle, and expansion rate. Since the number of stream tubes was large, flow conditions within each stream tube were approximated by uniform flow and defined by conditions at the center of the stream tube. The chemical freezing area ratio (freezing point) of each stream tube was then obtained by applying the freezing point criterion to a series of essentially one-dimensional flow systems. The total specific impulse (primary nozzle flow) was computed by integrating the impulse function across a selected control surface at the nozzle exit. This result accounts for both reaction kinetic and nozzle geometric losses. Using the nozzle geometric efficiency obtained from the nozzle flow field analysis, the reaction kinetic efficiency was determined.



Results

Expanded views of the streamline patterns for the throat regions of the 70-percent bell and 15-degree cone are shown in Fig. 58 and 59. Superimposed on these streamlines are the freezing surfaces for the midpoint of the test matrix, ($P_c = 100$, $O/F = 12:1$) demonstrating the nonuniformity of the flow field. Theoretical kinetic efficiency for the nozzles is shown as a function of mixture ratio in Fig. 60 to 62. Because the throat region of the 15-degree conical and the controlled expansion nozzles were identical, the theoretical kinetic efficiencies are identical. In Fig. 63 the kinetic efficiency is shown as a function of pressure for a mixture ratio of 15:1.

PROPELLANT IMPURITIES

The presence of impurities in the propellants necessitates two types of performance corrections. The first is a correction to account for the change in density caused by the different density of the impurities. The second is a correction to account for the lower theoretical performance with the impure propellant.

In the current program, the impurities were all in the oxidizer. Three batches of oxidizer were used. The oxidizer compositions and performance corrections are listed in Table 5. The effect of these small amounts of impurities on performance was found to be very insensitive to either chamber pressure or mixture ratio.



15-Degree Cone

Area Ratio = 60:1

LF_2/GH_2 (77 F)

Chamber Pressure = 100 psia

Mixture Ratio = 12:1

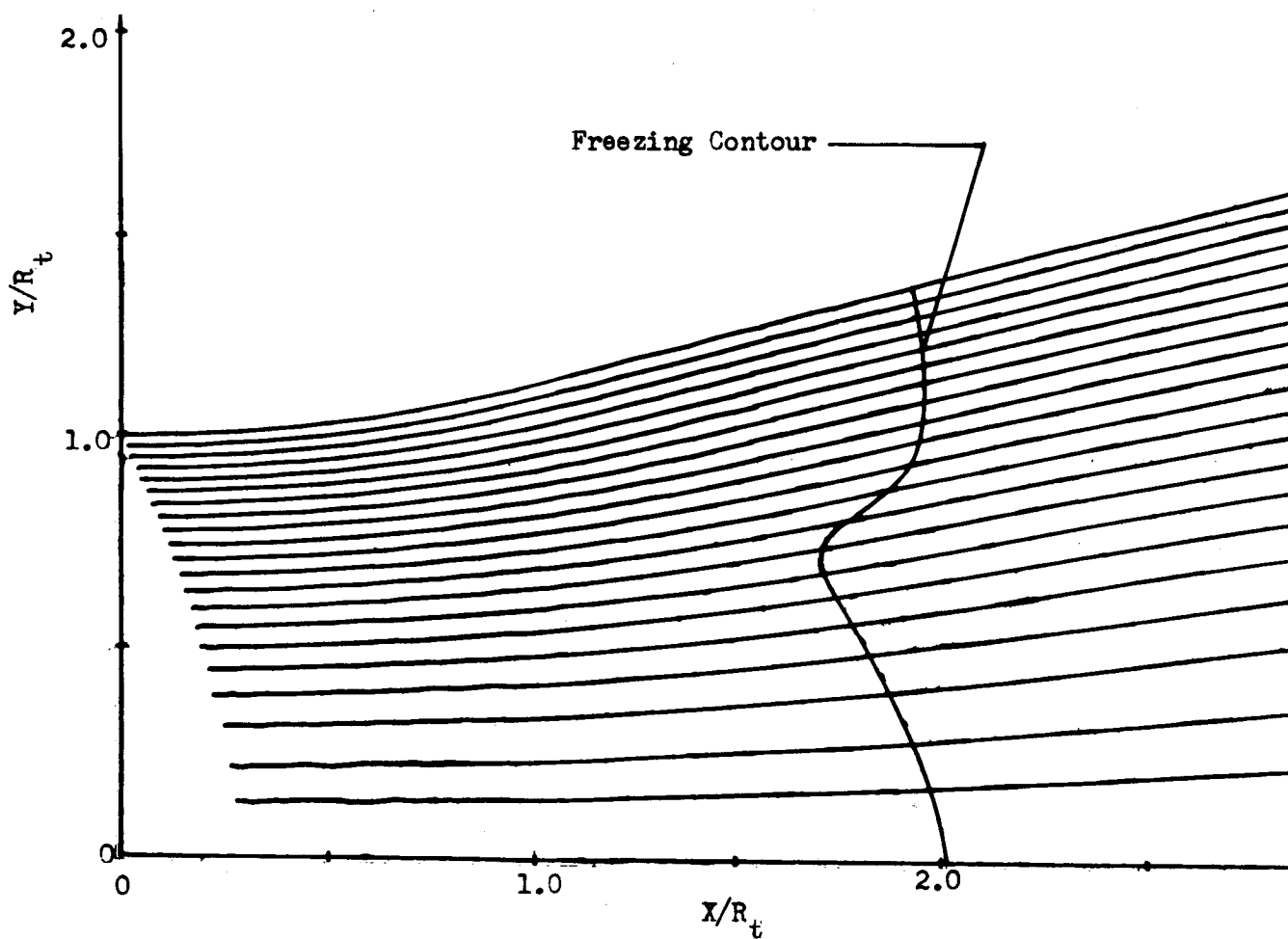


Figure 58. 15-Degree Cone Streamlines--Throat Region

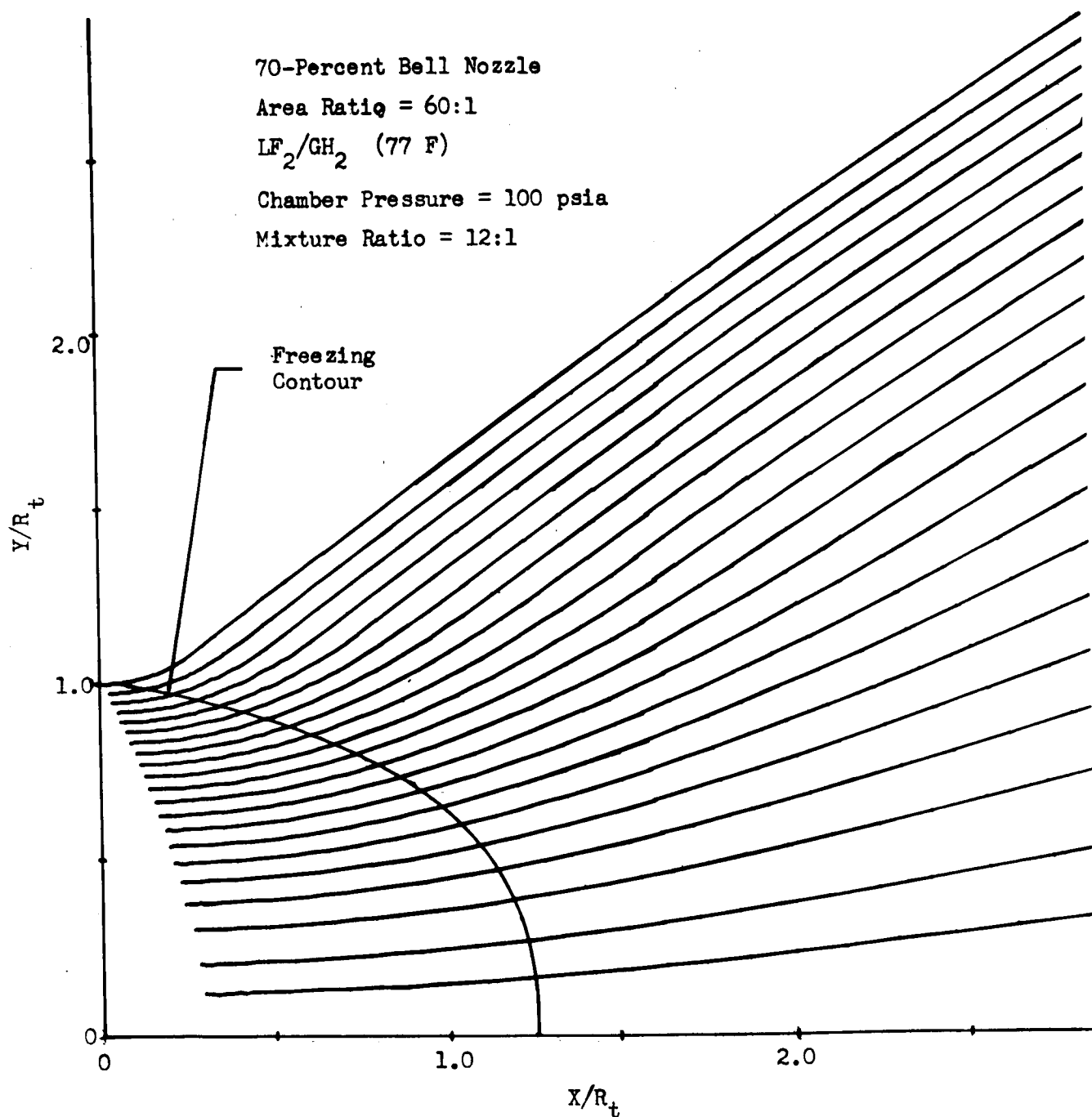
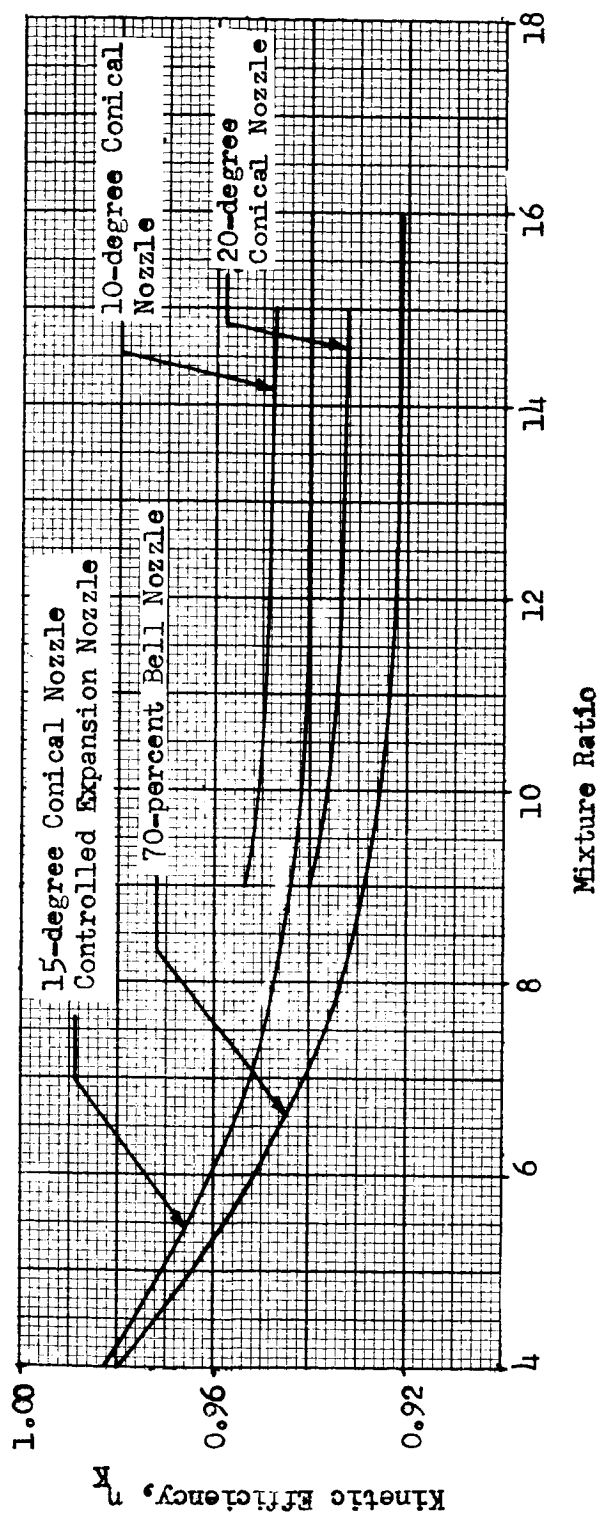


Figure 59. 70-Percent Bell Nozzle Streamlines - Throat Region



ROCKETDYNE • A DIVISION OF NORTH AMERICAN AVIATION, INC.

Stagnation Pressure = 50 psia



LF_2/GH_2 (77 °F)

Area Ratio = 60:1

Figure 60. Effect of Mixture Ratio on Kinetic Efficiency at Stagnation Pressure of 50 psia

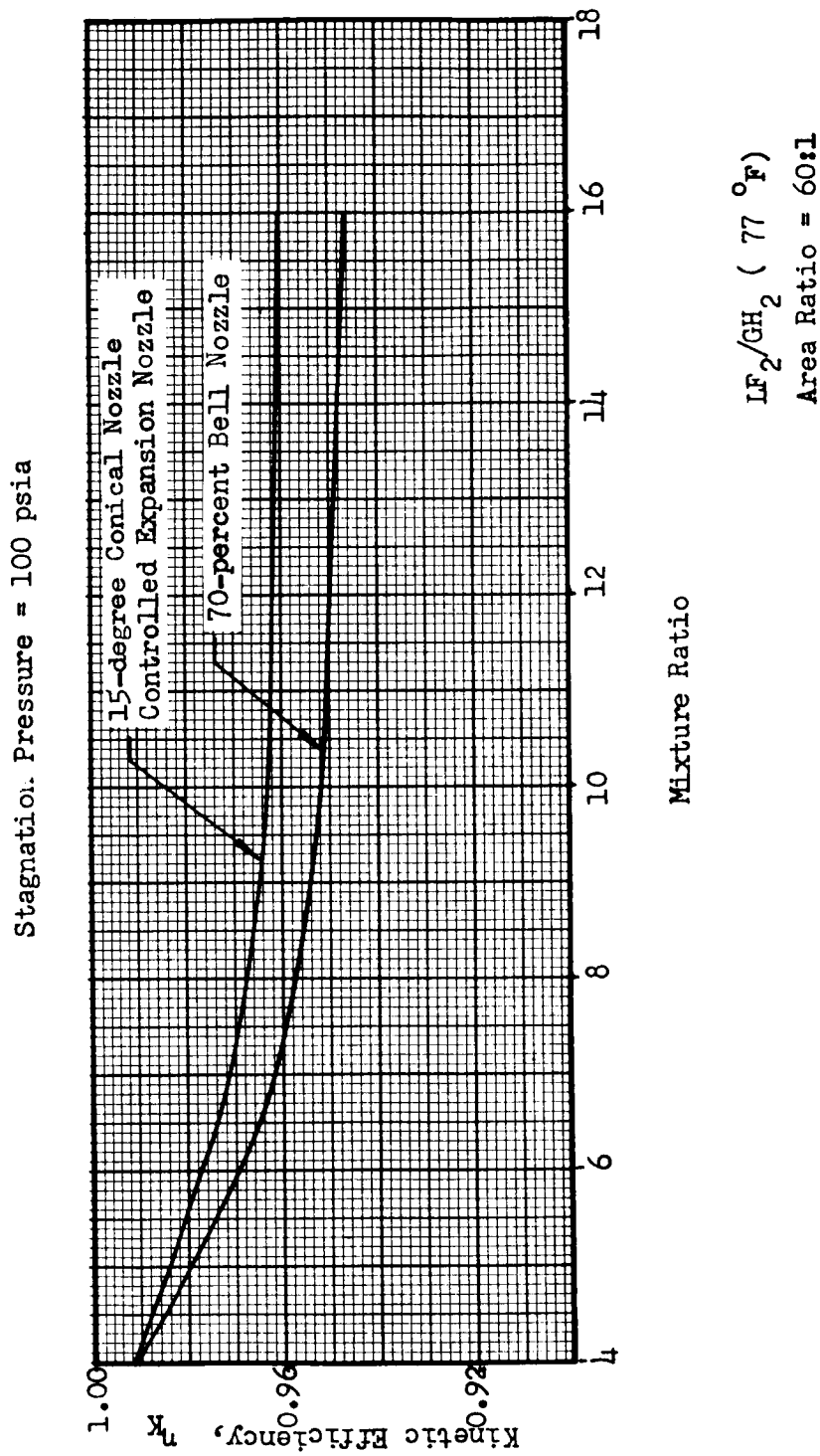
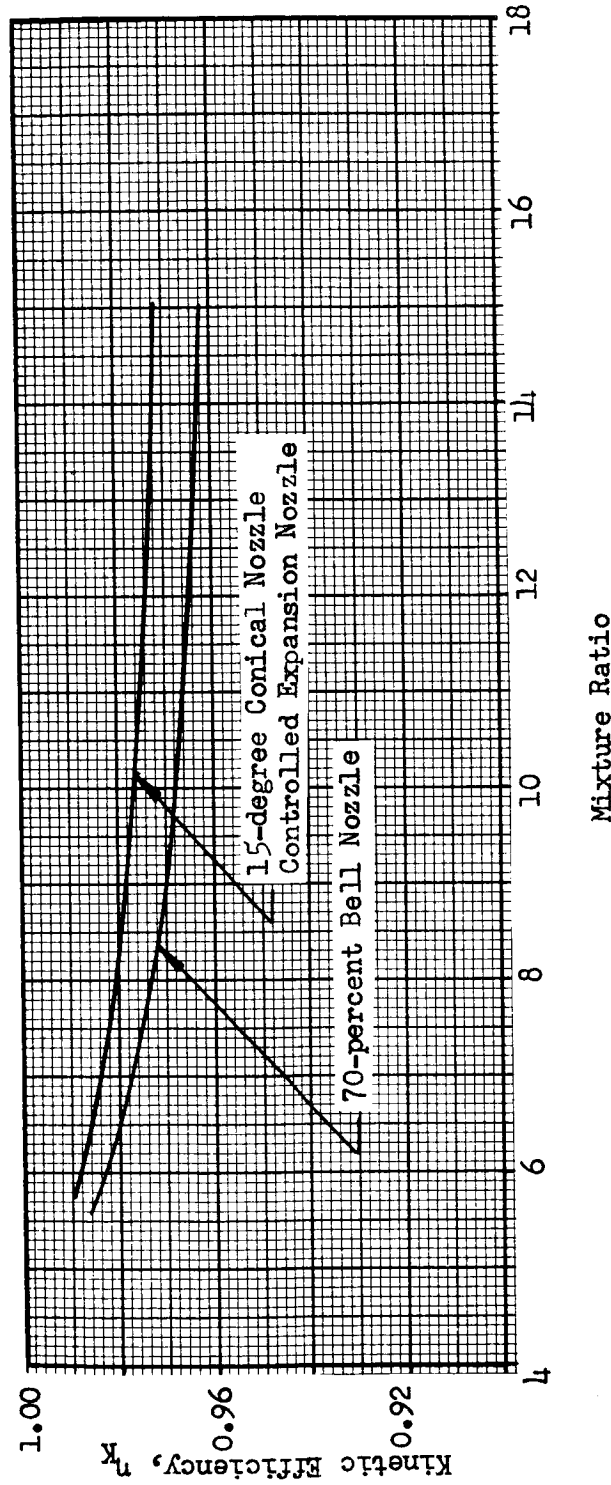


Figure 61. Effect of Mixture Ratio on Kinetic Efficiency at Stagnation Pressure of 100 psia



Stagnation Pressure = 175 psia



IF_2/GH_2 (77°F)
Area Ratio = 60:1

Figure 62. Effect of Mixture Ratio on Kinetic Efficiency at Stagnation Pressure of 175 psia

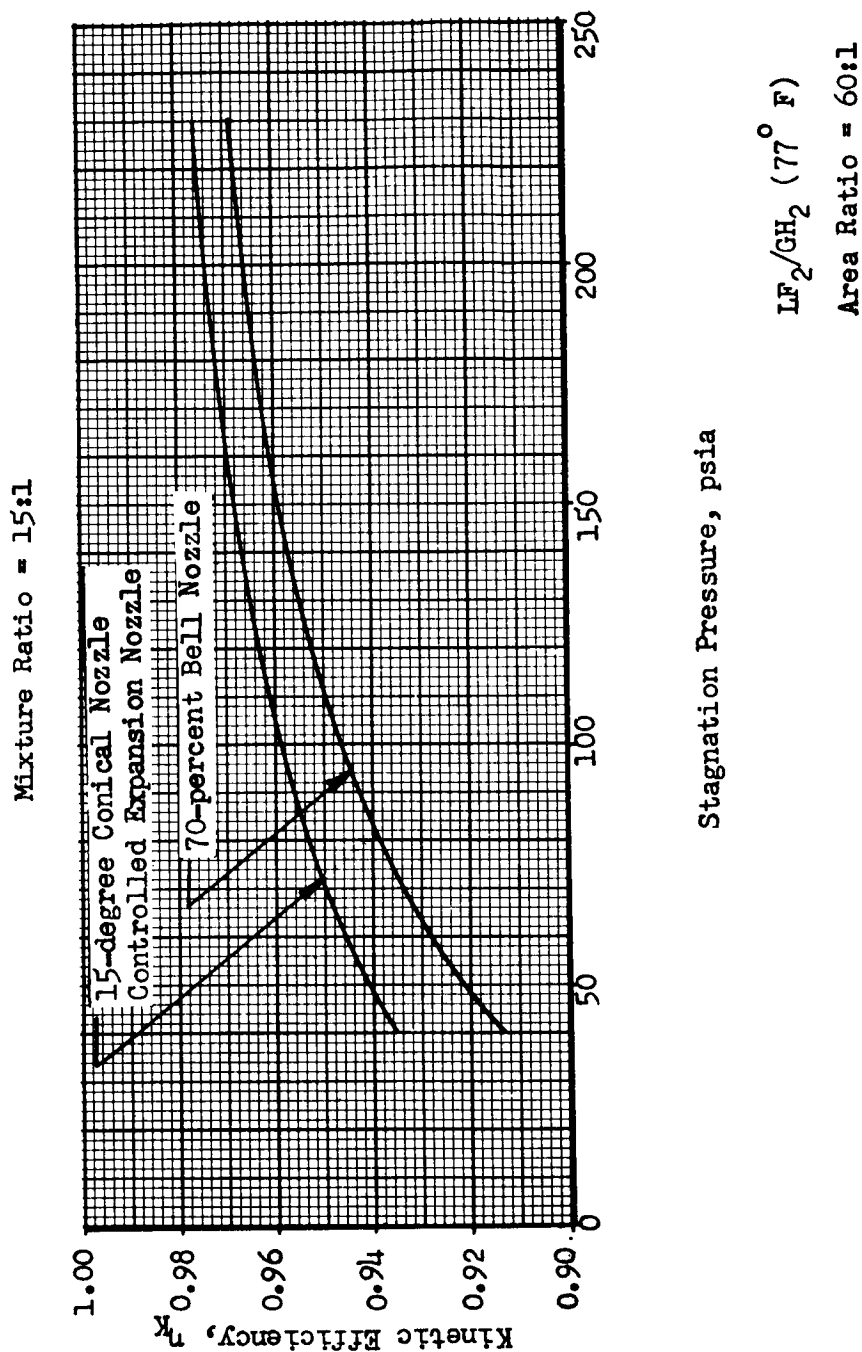


Figure 63. Theoretical Effect of Stagnation Pressure on Kinetic Efficiency at Mixture Ratio = 15:1



TABLE 5
FLUORINE IMPURITIES CORRECTIONS

Tests	Composition, percent weight			Density Correction	Characteristic Velocity Correction	Vacuum Specific Impulse Correction
	F ₂	Air	HF			
3 - 8	98.1	1.4	0.5	0.9881	1.0030	1.0040
9 - 39	98.5	1.1	0.4	0.9904	1.0024	1.0034
41 - 175 (1966)	99.3	0.5	0.2	0.9955	1.0011	1.0013
1 - 28 (1967)	99.3	0.5	0.2	0.9955	1.0011	1.0013

PERFORMANCE PREDICTION

To combine the individual losses discussed above into a thrust chamber performance prediction, the following equation is used

$$\eta_{TC} = 1 - (1 - \eta_G) - (1 - \eta_D) - (1 - \eta_K) - (\xi_{HL_{I_s}} - 1)$$

This equation results from subtracting the sum of the losses from one, and can be simplified to

$$\eta_{TC} = \eta_G + \eta_D + \eta_K - \xi_{HL_{I_s}} - 1.0$$

Since the kinetic efficiency was the quantity sought experimentally, and the impurity correction coefficient depends upon details of individual tests, it was found convenient for data interpretation to combine the geometry, drag, and heat loss terms into single curves. These are presented versus chamber pressure for the nozzles in Fig. 64 to 68 and versus mixture ratio in Fig. 69 through 71.

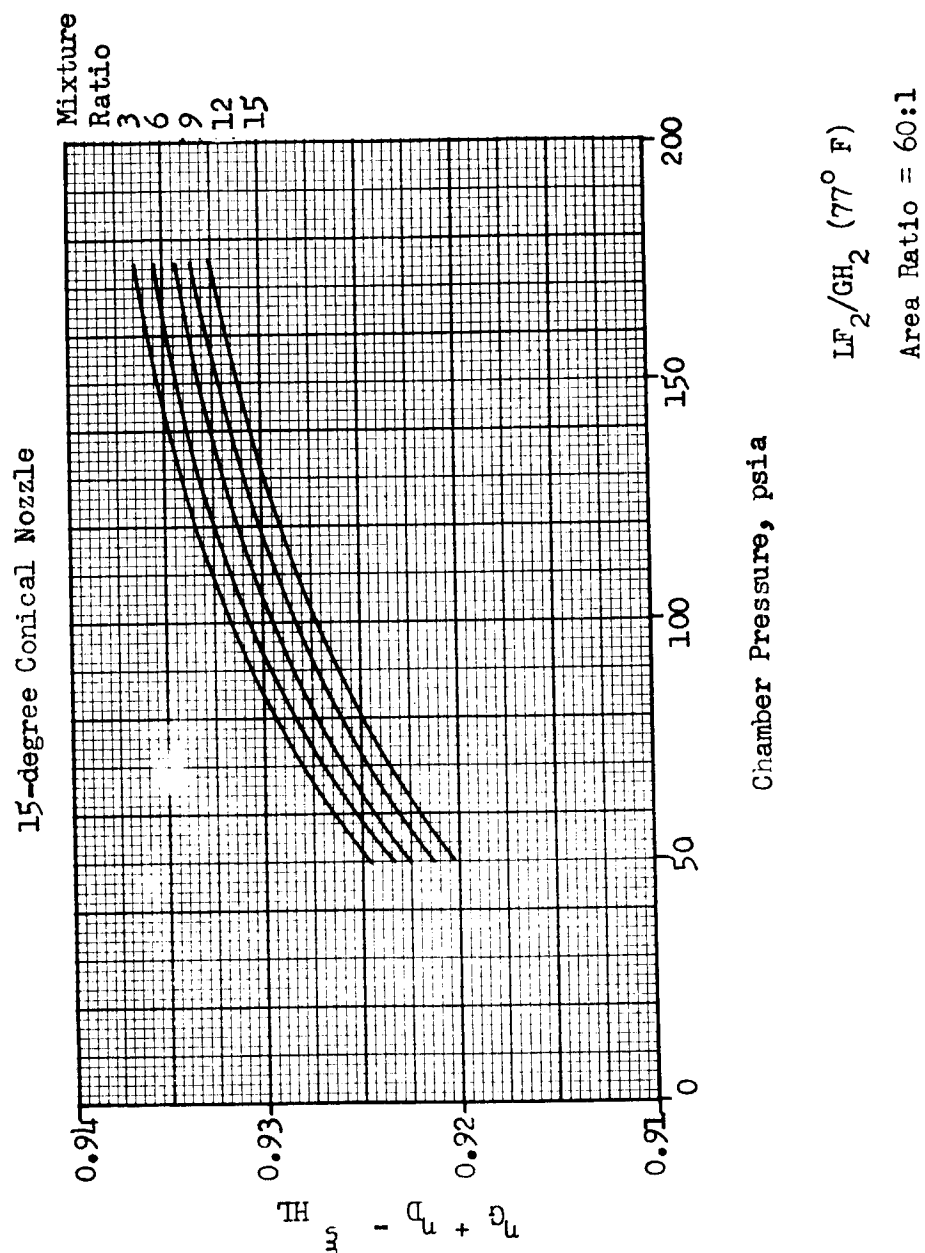


Figure 64. Theoretical Efficiency Accounting for Geometric, Drag and Heat Loss for 15-degree Conical Nozzles

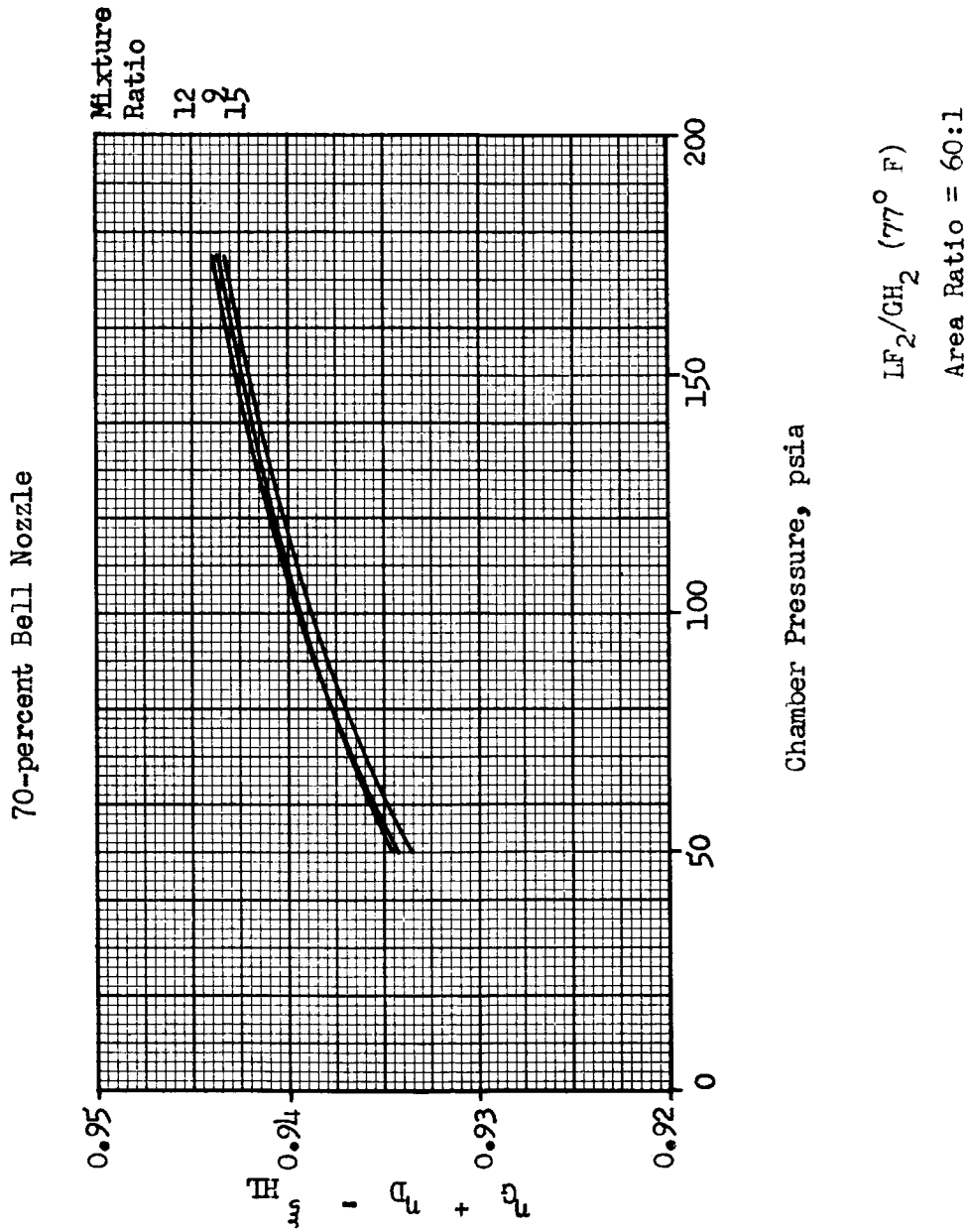


Figure 65. Theoretical Efficiency Accounting for Geometric, Drag and Heat Loss for 70-percent Bell Nozzle

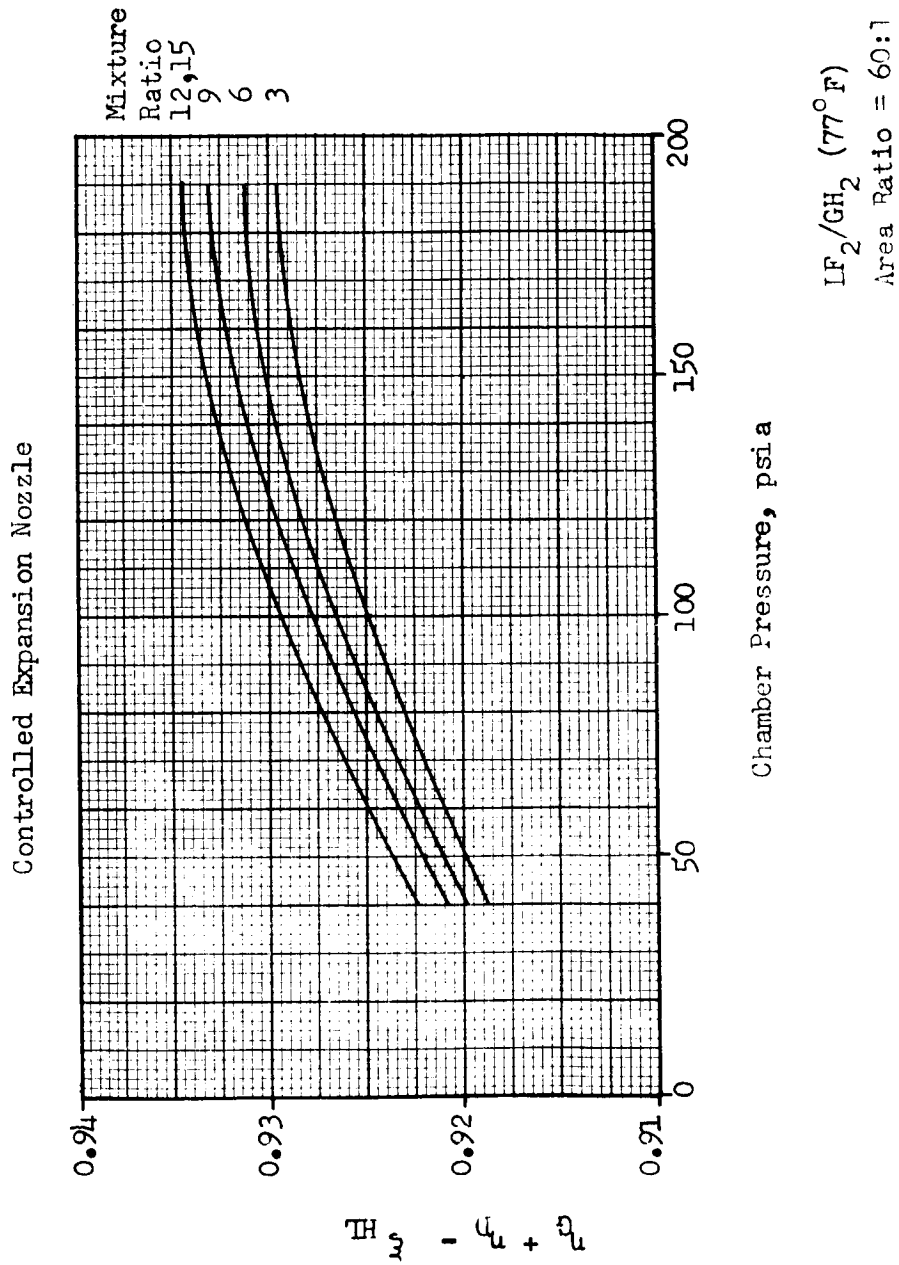


Figure 66. Theoretical Efficiency Accounting for Geometric Drag, and Heat Loss for Controlled Expansion Nozzle

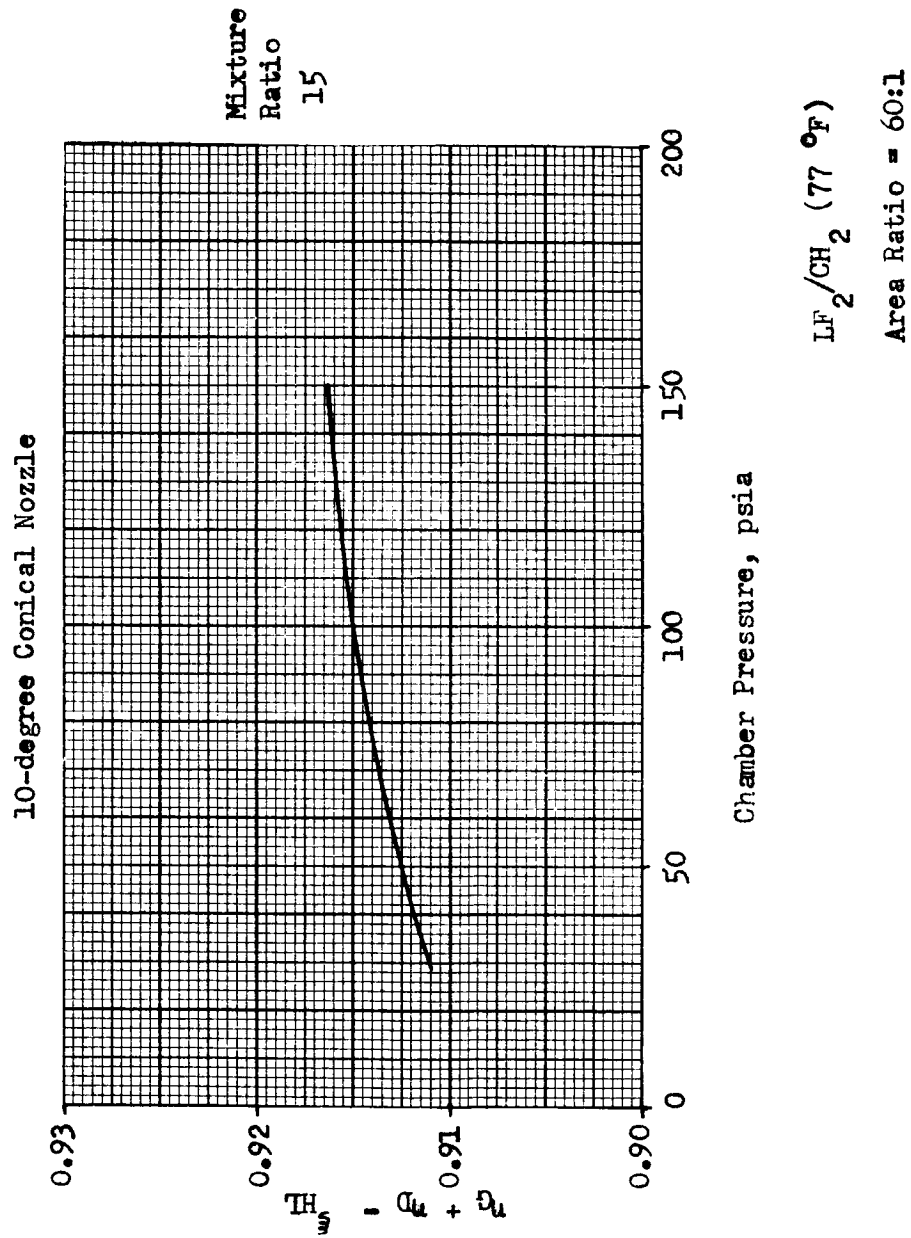


Figure 67. Theoretical Efficiency Accounting for Geometric, Drag, and Heat Loss for 10-degree Conical Nozzle

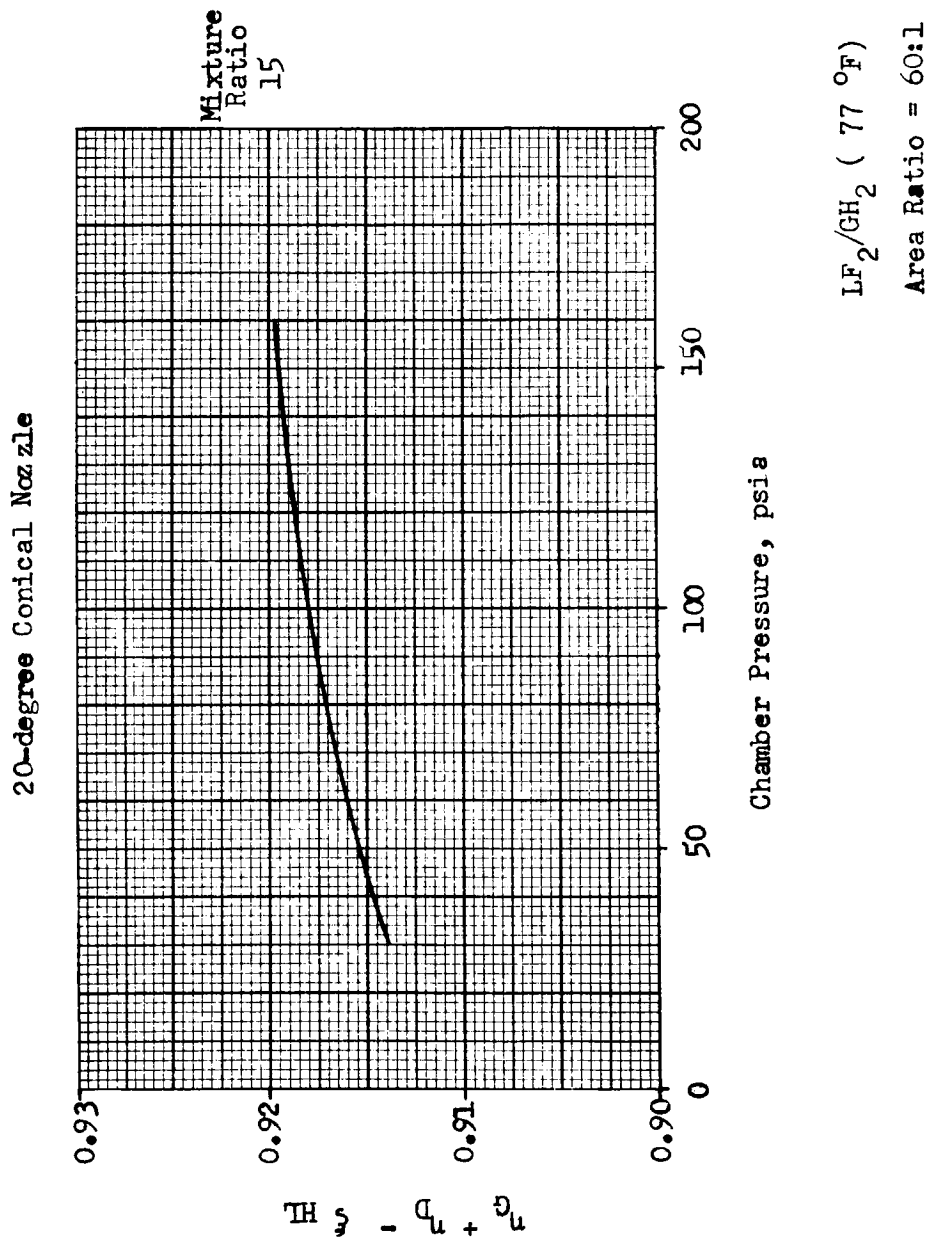
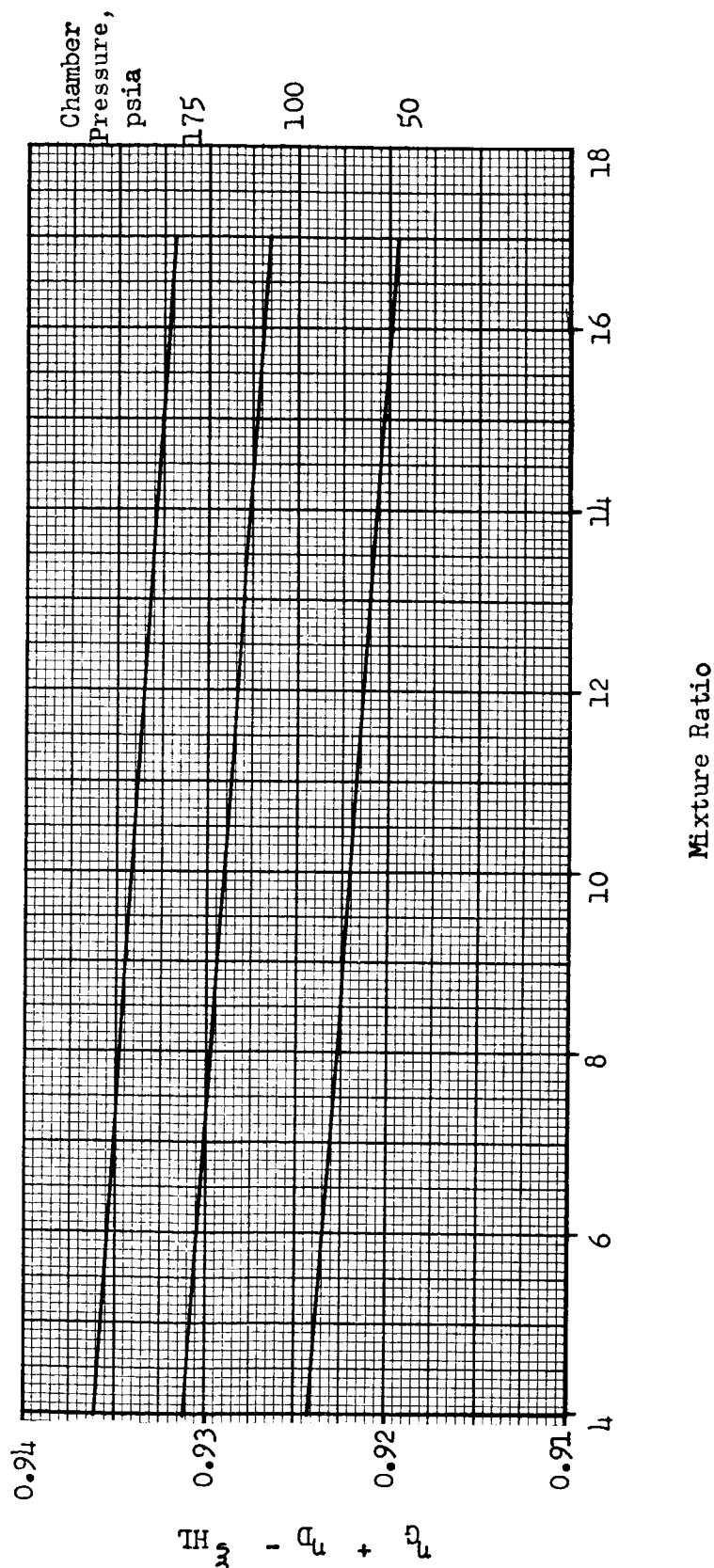


Figure 68. Theoretical Efficiency Accounting for Geometric, Drag, and Heat Loss for 20-degree Conical Nozzle



15-Degree Conical Nozzle



LF_2/GH_2 (77° F)

Area Ratio = 60:1

Figure 69. Theoretical Efficiency Accounting for Geometric, Drag, and Heat Loss for the 15-degree Conical Nozzle



70-Percent Bell Nozzle

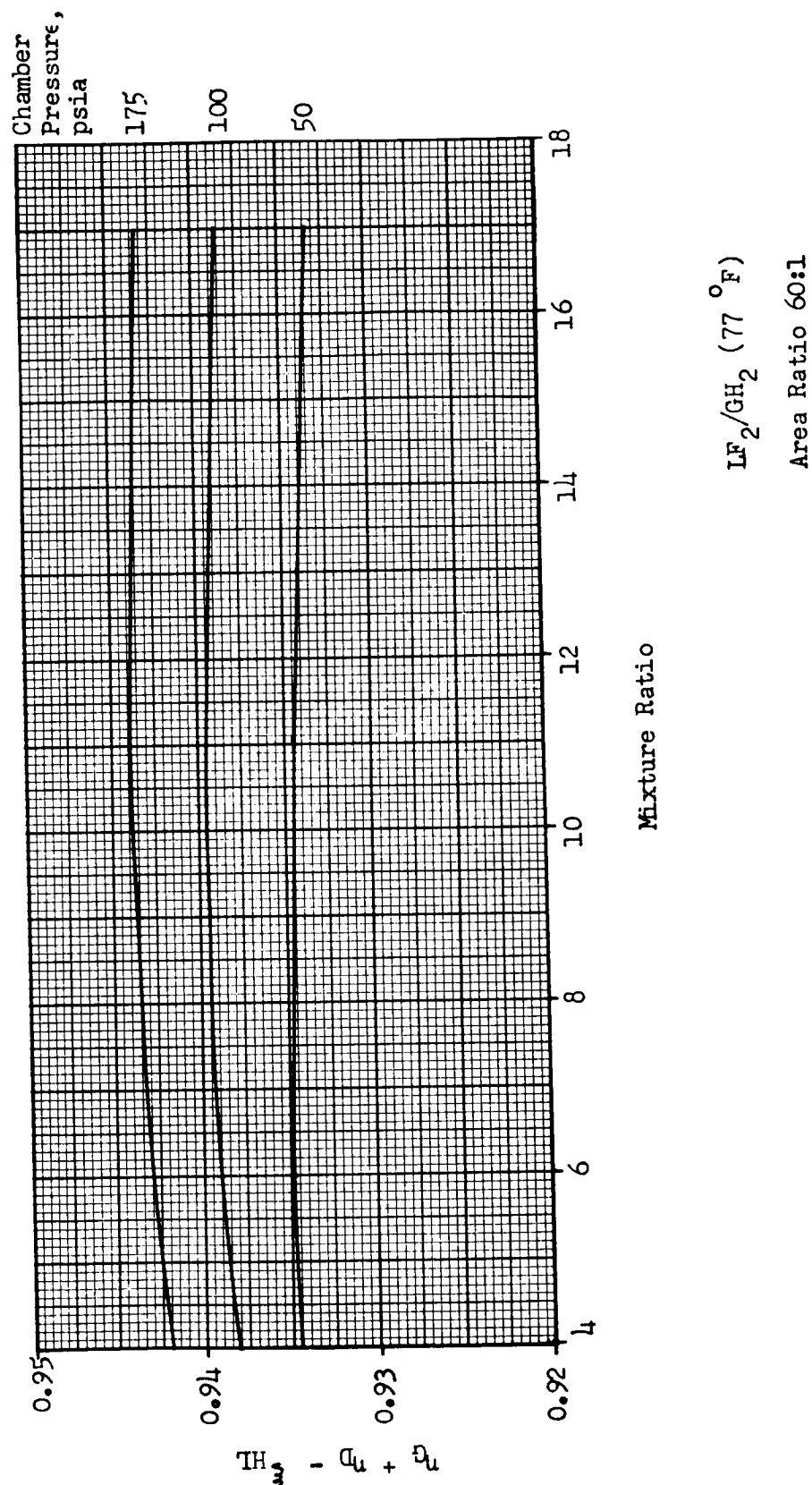
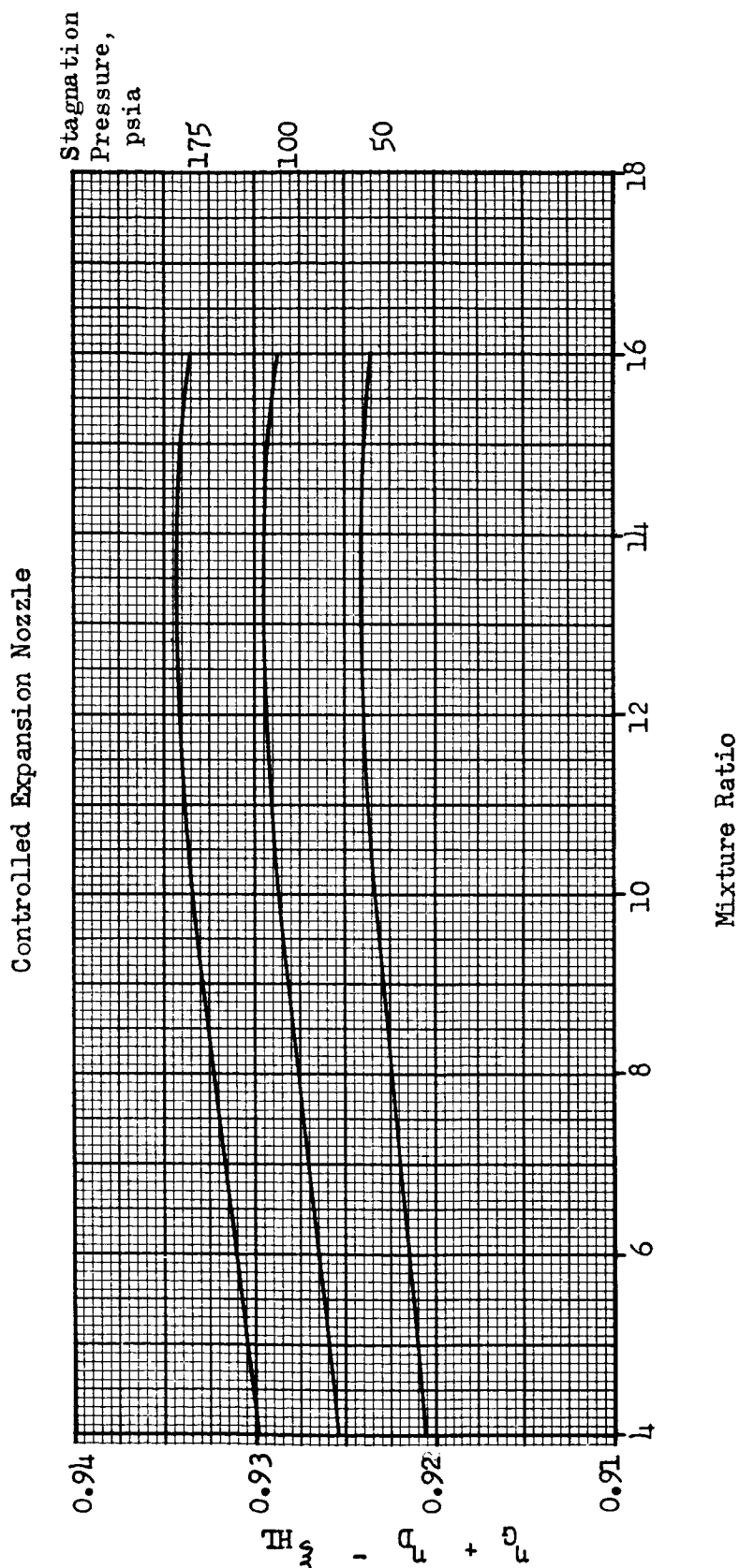


Figure 70. Theoretical Efficiency Accounting for Geometric, Drag, and Heat Loss for the 70-percent Bell Nozzle



LF_2/GH_2 (77 °F)

Area Ratio = 60:1

Figure 71. Theoretical Efficiency Accounting for Geometric, Drag, and Heat Loss for the Controlled-Expansion Nozzle



NOZZLE WALL PRESSURE PREDICTION

The method of predicting the nozzle wall pressure utilizes results from both the aerodynamic and stream tube kinetic analyses. The aerodynamic analysis defines the variation of local area ratio of the outer stream tube with position along the wall. From the stream tube kinetic analysis, the freezing area ratio of this stream tube is obtained. Nozzle wall pressures upstream of the freezing area ratio are obtained directly from the chemical equilibrium aerodynamic analysis, and downstream pressures are obtained from kinetic propellant data for the determined wall stream tube freezing area ratio. The predicted pressure profiles are shown in Fig. 27 to 32 of the Data Correlation Section.



CHEMICAL REACTION KINETICS

INTRODUCTION

A three-phase reaction kinetic study was performed to develop an accurate performance model for fluorine/hydrogen. Initially, a literature survey was conducted to select a preliminary set of rate constants and third-body efficiencies. Comparative computer runs were made between full kinetic and sudden freezing (Bray) performance programs to calibrate and improve the latter. After Task III test data became available, a second reaction rate study and a third-body efficiency study were conducted to select a revised set of values. These three studies are summarized in this section. The actual use of the kinetic model in conjunction with the streamline analysis procedure is discussed in the Performance Analysis section.

REACTION RATE STUDY

Literature Survey

The literature was reviewed for experimental recombination rates obtained in various environments and for a variety of third bodies. Most of the data are summarized in Table 6 with the more complex situations presented in Fig. 72 to 75. Selected rate expressions are shown in the first column of Table 7. Considerable data leading to relative third-body efficiencies were found for hydrogen recombination, the most important reaction in this system. However, such data are not available for the recombination of HF or F₂ whose rates were measured only with argon.



TABLE 6

EXPERIMENTAL RECOMBINATION RATE CONSTANTS AND
SELECTED RATE EXPRESSIONS FROM
LITERATURE SURVEY

Recombination	Rate Constant, cc ² /mole sec	Temperature, K	Experimental Temperature Dependence**	Ref.	Selected Rate Expression, cc ² /mole ² sec
H + H + Ar	See Fig. 3				$1.0 \times 10^{18} T^{-1}$
O + O + O ₂	4.6×10^{14}	3500	$T^{-0.5}$ to T^{-2}	14	$1.6 \times 10^{18} T^{-1}$
H + H + N ₂	7.2×10^{14} 1.7×10^{15}	1400 1072	-- --	21 20	$2.8 \times 10^{18} T^{-1}$
H + H + H ₂ O	See Fig. 4				$4.0 \times 10^{18} T^{-1}$
O + O + O	1.4×10^{15}	3500	$T^{-0.5}$ to T^{-2}	14	$5.0 \times 10^{18} T^{-1}$
H + H + H ₂	See Fig. 5				$8.0 \times 10^{18} T^{-1}$
H + H + H	See Fig. 6				$2.0 \times 10^{19} T^{-1}$
H + OH + N ₂	1.1×10^{17} 6.5×10^{16}	1072 1400	-- --	20 21	$8.7 \times 10^{19} T^{-1}$
H + OH + H ₂ O	5.4×10^{17} $1.1 \times 10^{17*}$ 1.0×10^{17}	1650 1072 1400	-- -- --	13 20 21	$1.1 \times 10^{20} T^{-1}$
H + OH + H ₂	1.6×10^{17}	1400	--	21	$2.3 \times 10^{20} T^{-1}$
H + F + Ar	5.5×10^{14}	4500	T^{-1} to T^{-2}	22	$2.5 \times 10^{18} T^{-1}$
F + F + Ar	4×10^{12}	1430	T^{-1}	23	$5.7 \times 10^{15} T^{-1}$

*Maximum Value

**Temperature term in rate expression: CT^n

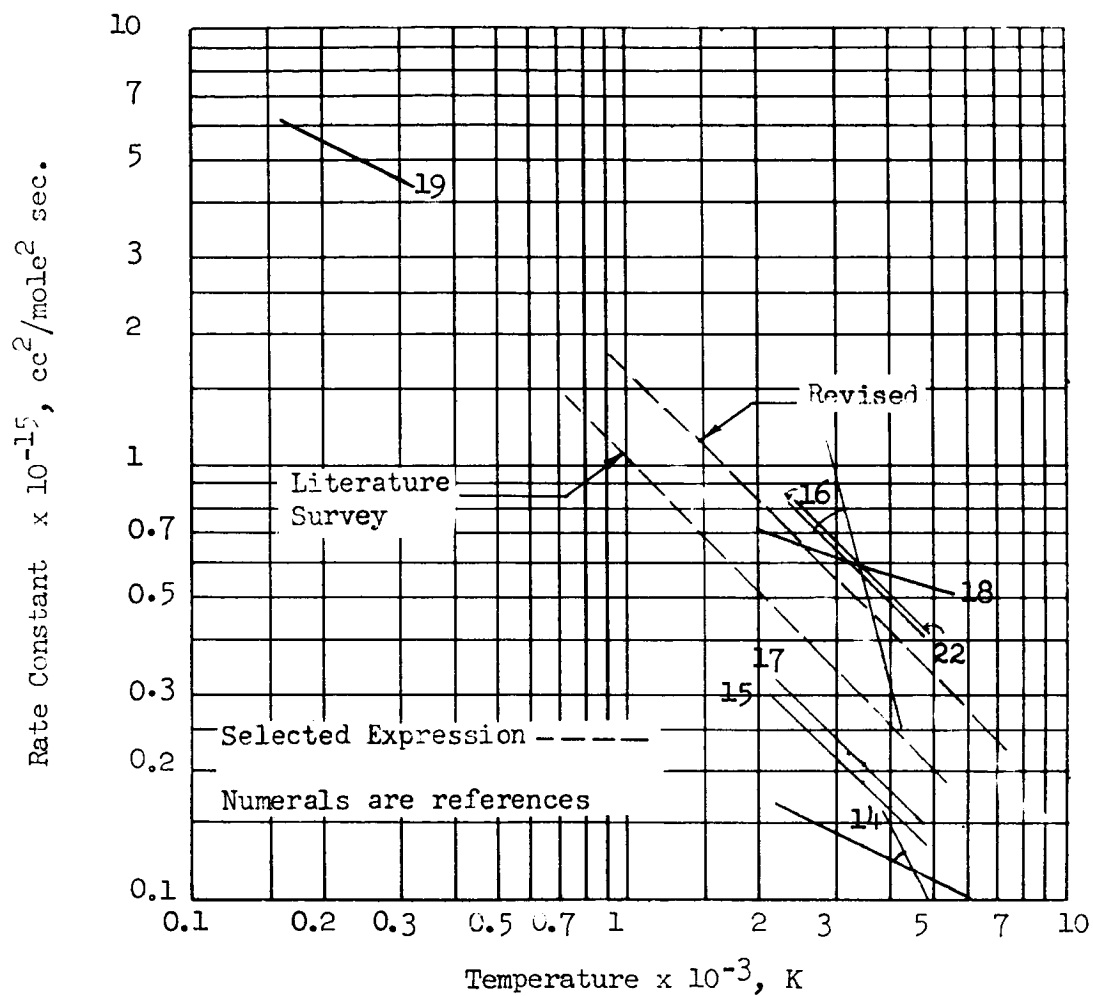


Figure 72. $\text{H} + \text{H} + \text{Ar}$ Recombination Rate Constant vs Temperature

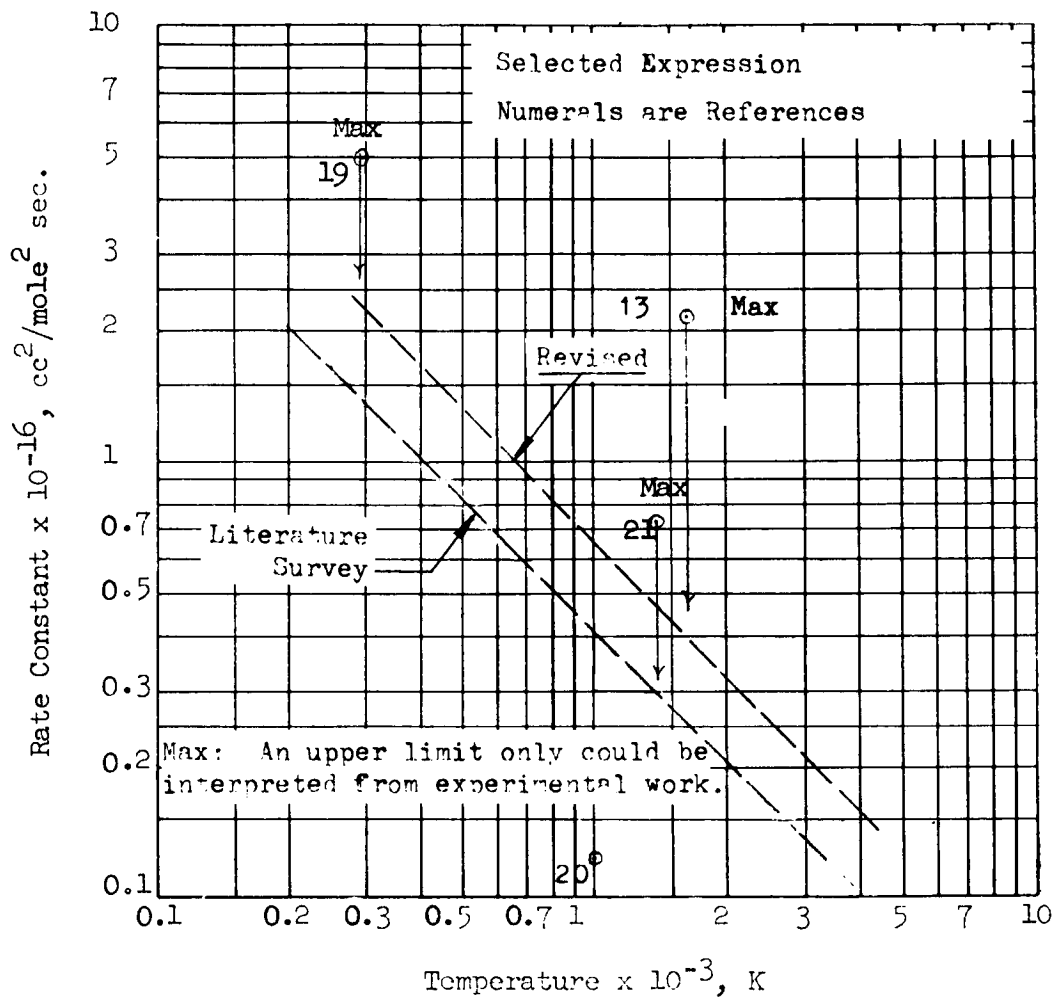


Figure 73. $\text{H} + \text{H} + \text{H}_2\text{O}$ Recombination Rate Constant
versus Temperature

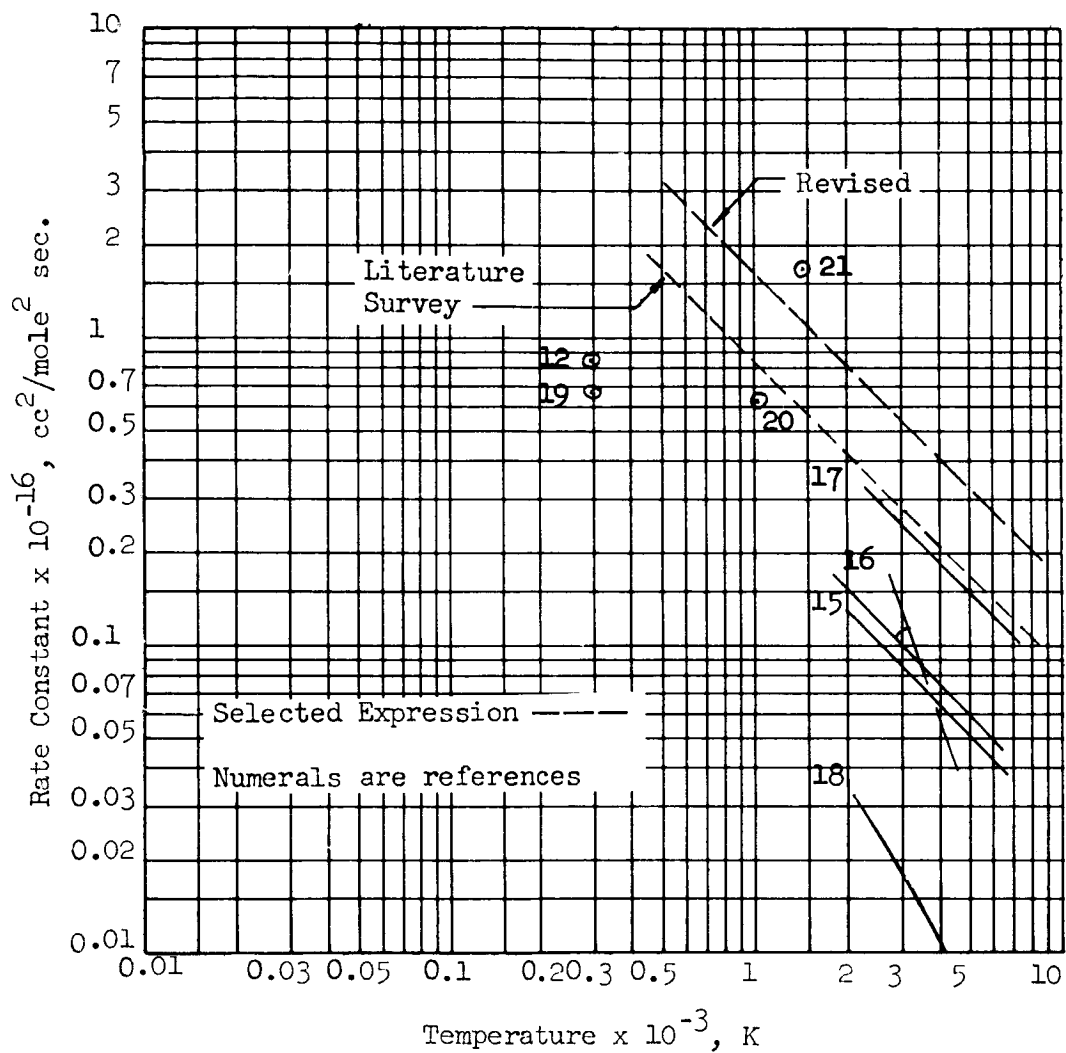


Figure 74. $\text{H} + \text{H} + \text{H}_2$ Recombination Rate Constant
versus Temperature

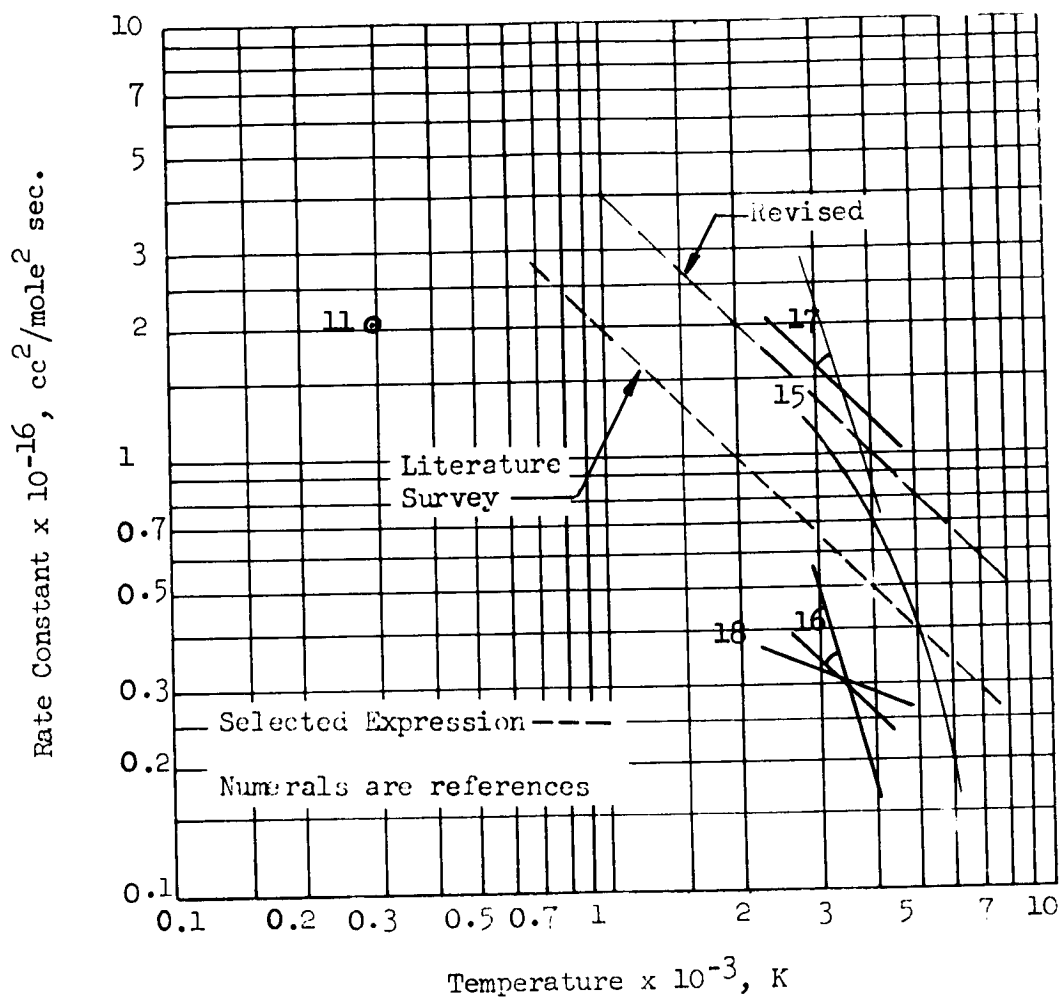


Figure 75. $\text{H} + \text{H} + \text{H}$ Recombination Rate Constant versus Temperature



TABLE 7

LITERATURE SURVEY AND REVISED RATE EXPRESSIONS

Recombination Reaction	Figure	Selected Rate Expression $\text{cc}^2/\text{mole}^2\text{sec}$	
		Literature Survey	Revised
$\text{H} + \text{H} + \text{Ar}$	72	$1.0 \times 10^{18} \text{ T}^{-1}$	$1.6 \times 10^{18} \text{ T}^{-1}$
$\text{O} + \text{O} + \text{O}_2$	-	$1.6 \times 10^{18} \text{ T}^{-1}$	$2.6 \times 10^{18} \text{ T}^{-1}$
$\text{H} + \text{H} + \text{N}_2$	73	$2.8 \times 10^{18} \text{ T}^{-1}$	$4.8 \times 10^{18} \text{ T}^{-1}$
$\text{H} + \text{H} + \text{H}_2\text{O}$		$4.0 \times 10^{18} \text{ T}^{-1}$	$6.4 \times 10^{18} \text{ T}^{-1}$
$\text{O} + \text{O} + \text{O}$	-	$5.0 \times 10^{18} \text{ T}^{-1}$	$8.0 \times 10^{18} \text{ T}^{-1}$
$\text{H} + \text{H} + \text{H}_2$	75	$8.0 \times 10^{18} \text{ T}^{-1}$	$1.6 \times 10^{19} \text{ T}^{-1}$
$\text{H} + \text{H} + \text{H}$		$2.0 \times 10^{19} \text{ T}^{-1}$	$4.0 \times 10^{19} \text{ T}^{-1}$
$\text{H} + \text{OH} + \text{N}_2$	-	$8.7 \times 10^{19} \text{ T}^{-1}$	$1.35 \times 10^{20} \text{ T}^{-1}$
$\text{H} + \text{OH} + \text{H}_2\text{O}$	-	$1.1 \times 10^{20} \text{ T}^{-1}$	$1.8 \times 10^{20} \text{ T}^{-1}$
$\text{H} + \text{OH} + \text{H}_2$	-	$2.3 \times 10^{20} \text{ T}^{-1}$	$4.5 \times 10^{20} \text{ T}^{-1}$
$\text{H} + \text{F} + \text{Ar}$	-	$2.5 \times 10^{18} \text{ T}^{-1}$	$4.0 \times 10^{18} \text{ T}^{-1}$
$\text{F} + \text{F} + \text{Ar}$	-	$5.7 \times 10^{15} \text{ T}^{-1}$	$8.0 \times 10^{15} \text{ T}^{-1}$



Third-body efficiency is defined as the ratio of the recombination rate constant with the particular third body to the rate constant with argon as the third body. The rate expressions and the third-body efficiencies for the HF system selected as a result of the literature survey are listed in the first column of Table 8. These efficiencies were derived for hydrogen recombination and were assumed for HF and F_2 recombination in lieu of experimental data. The data that are available for the $H + OH + M = H_2O + M$ reaction suggest that this is a reasonable assumption for HF recombination. The exact values used for F_2 recombination are unimportant, since this reaction is too slow to contribute significantly to the total recombination.

In selecting the efficiencies, a somewhat high value for H_2 was chosen so that there would be higher recombination efficiency at lower mixture ratios since such a trend was observed in a NASA-LeRC F_2/H_2 test program. Similarly, referring to Table 8, a value for H significantly higher than that of H_2 was avoided so that the effect of H_2 would not be overwhelmed. The efficiency of HF, because of its smaller capture cross-section, was chosen less than that of H_2O , which was given an efficiency of approximately 4 for both $H + H$ and $H + OH$.

The assignment of a very high efficiency for HF caused by formation of an activated intermediate, H_2F (Ref. 10) is at present unwarranted, since there is no evidence for the existence of such a specie. A similar intermediate, H_2O , could be postulated as a third body for H_2O recombination. In this case, a lack of evidence for the existence of the specie is corroborated by a modest efficiency for H_2O .

The temperature dependence was chosen as T^{-1} , since most investigators indicated a preference for this value. The others indicated ranges of temperature dependence which included T^{-1} , and only one indicated a slight preference for T^{-2} , (Ref. 22)



TABLE 8

RECOMBINATION RATE CONSTANTS AND THIRD-BODY EFFICIENCIES

(A) Recombination Rates		
Recombination Reaction	Rate Constant, $\text{cc}^2/\text{mole}^2\text{sec}$	
	Literature Survey	Revised
$\text{H} + \text{H} + \text{Ar} = \text{H}_2 + \text{Ar}$	$1.0 \times 10^{18} \text{ T}^{-1}$	$1.6 \times 10^{18} \text{ T}^{-1}$
$\text{H} + \text{F} + \text{Ar} = \text{HF} + \text{Ar}$	$2.5 \times 10^{18} \text{ T}^{-1}$	$4.0 \times 10^{18} \text{ T}^{-1}$
$\text{F} + \text{F} + \text{Ar} = \text{F}_2 + \text{Ar}$	$5.0 \times 10^{15} \text{ T}^{-1}$	$8.0 \times 10^{15} \text{ T}^{-1}$
(B) Third-Body Efficiencies		
Third Body	Efficiency Relative to Argon	
	Literature Survey	Revised
F_2	1	1
HF	2	4
F	4	5
H_2	8	10
H	20	25



The selected rate expressions and third-body efficiencies are believed to be good interpretations of the kinetic data; however, in certain cases it is easy to see that different interpretations could produce values differing by a factor of two to four from those adopted here. Furthermore, an across-the-board increase or decrease in rate constants by at least twofold should be permissible in view of the wide variations in experimental values.

Comparison of Theoretical Performance Calculations With Previous Experimental Data

An extensive and well-documented test program was conducted for this system by Auckerman and Church at NASA's Lewis Research Laboratories (Ref. 8). In that program, three nozzles were tested in a vacuum at pressures from 10 to 60 psia over a range of mixture ratios from 6 to 16. A curve of corrected experimental specific impulse for the 15-degree conical nozzle at 60 psia is shown together with theoretical equilibrium, frozen, and Bray program values in Fig. 76. The rate constants used for the lower Bray curve were recommended in Ref. 9, and involved estimates for the recombination rates of HF and F_2 .

It can be seen that this curve differs from the experimental curve in shape, slope, and particularly, height. It has been hypothesized (by Wilde) that the high delivered performance at low mixture ratios may result from an extremely high third-body efficiency for HF in the hydrogen recombination reaction (Ref. 10). To test this, Bray calculations were made with the hydrogen recombination rate increased one hundred-fold. The results are shown as the upper Bray curve in Fig. 76, where it can be seen that, while the impulse level of this curve is improved, there is still a discrepancy between its slope and that of the experimental curve. It has been suggested that the HF recombination reaction is the most important reaction in this system (Ref. 9): however, increasing the rate for this reaction made the slope agreement considerably worse.

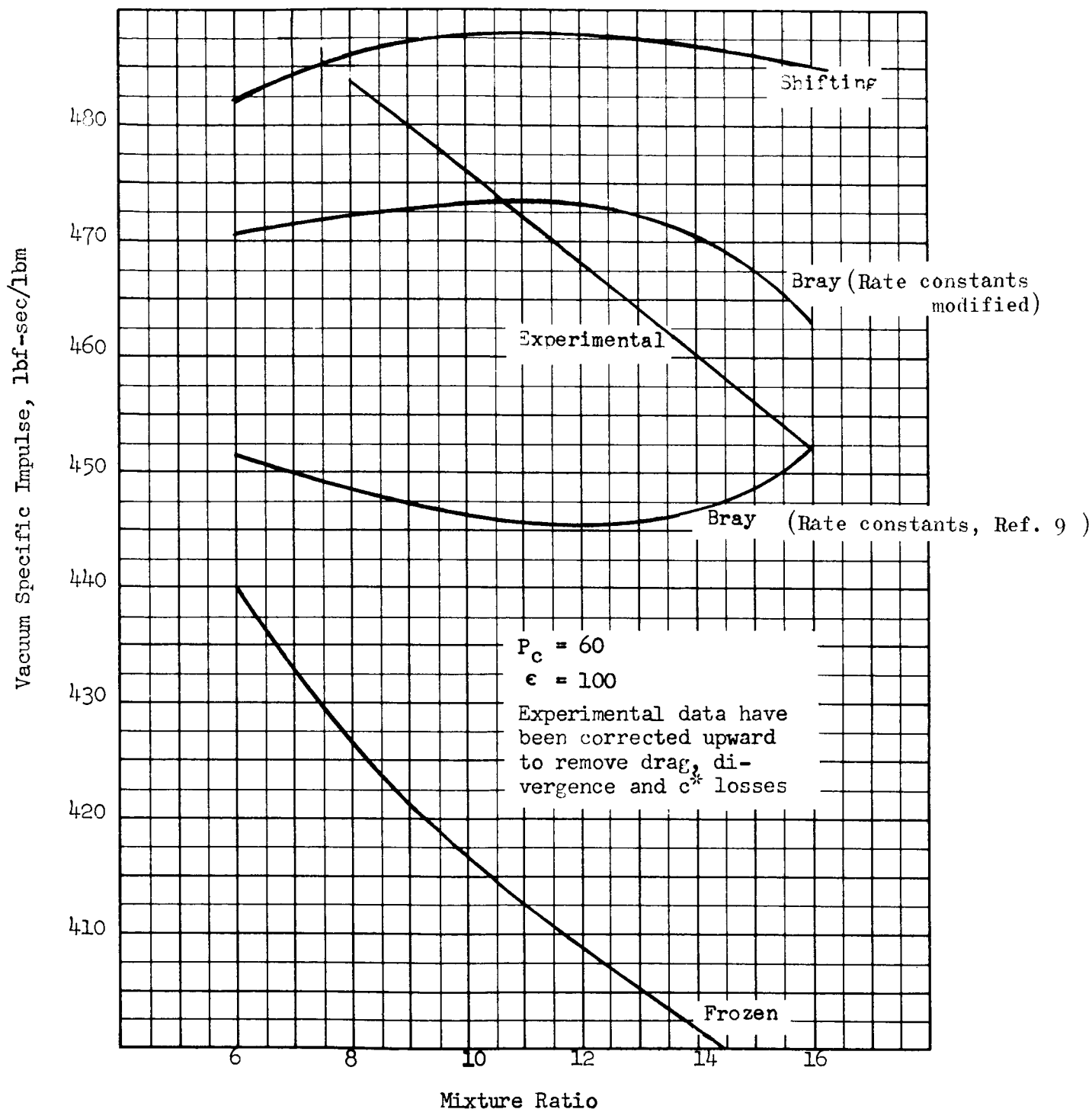


Figure 76. Fluorine/Hydrogen Theoretical and Experimental Vacuum Specific Impulse vs Mixture Ratio for NASA-LeRC 15-degree Conical Nozzle



An additional reason that the HF recombination is not the most important reaction in this system is that atomic fluorine concentration is much lower than atomic hydrogen concentration, except at extremely high mixture ratios. This can be seen in Fig. 77, which shows composition at the freezing point vs mixture ratio. It has been found that even simultaneously increasing the hydrogen recombination rate while decreasing the HF recombination rate results in nearly as great an increase in impulse at high mixture ratios as at low mixture ratios, and thus does not improve the correlation between the slopes of the experimental and Bray curves.

In conjunction with the literature survey, Bray program calculations were made for the three LeRC nozzles, using the rate constant expressions in the first column of Table 7 and B values of 3.1 for the 15-degree cone and 2.5 for the 70-percent bell and 25-degree cone. (The value B is a ratio used in conjunction with the Bray Criterion to determine the freezing point, and it is discussed in more detail on page 131.) The results are shown in Fig. 78 together with the corresponding test data corrected upward to remove drag and divergence losses. Only one theoretical curve is shown for the 70-percent bell and 25-degree cone, since the calculated values are within 1 second for these two nozzles. The Bray calculations for the 15-degree cone are still lower than the test results, down about 1.5 percent at high mixture ratios and 4 percent at low mixture ratios. This represents a considerable improvement from the previous analysis, Fig. 76, but further improvement was still necessary. Agreement for the bell and 25-degree cone is excellent, generally better than 1 percent across the full mixture ratio range.

Revision of Rate Expressions

Comparisons of the early Task III test data with theoretical kinetic efficiencies, based upon the rate expressions selected as a result of the

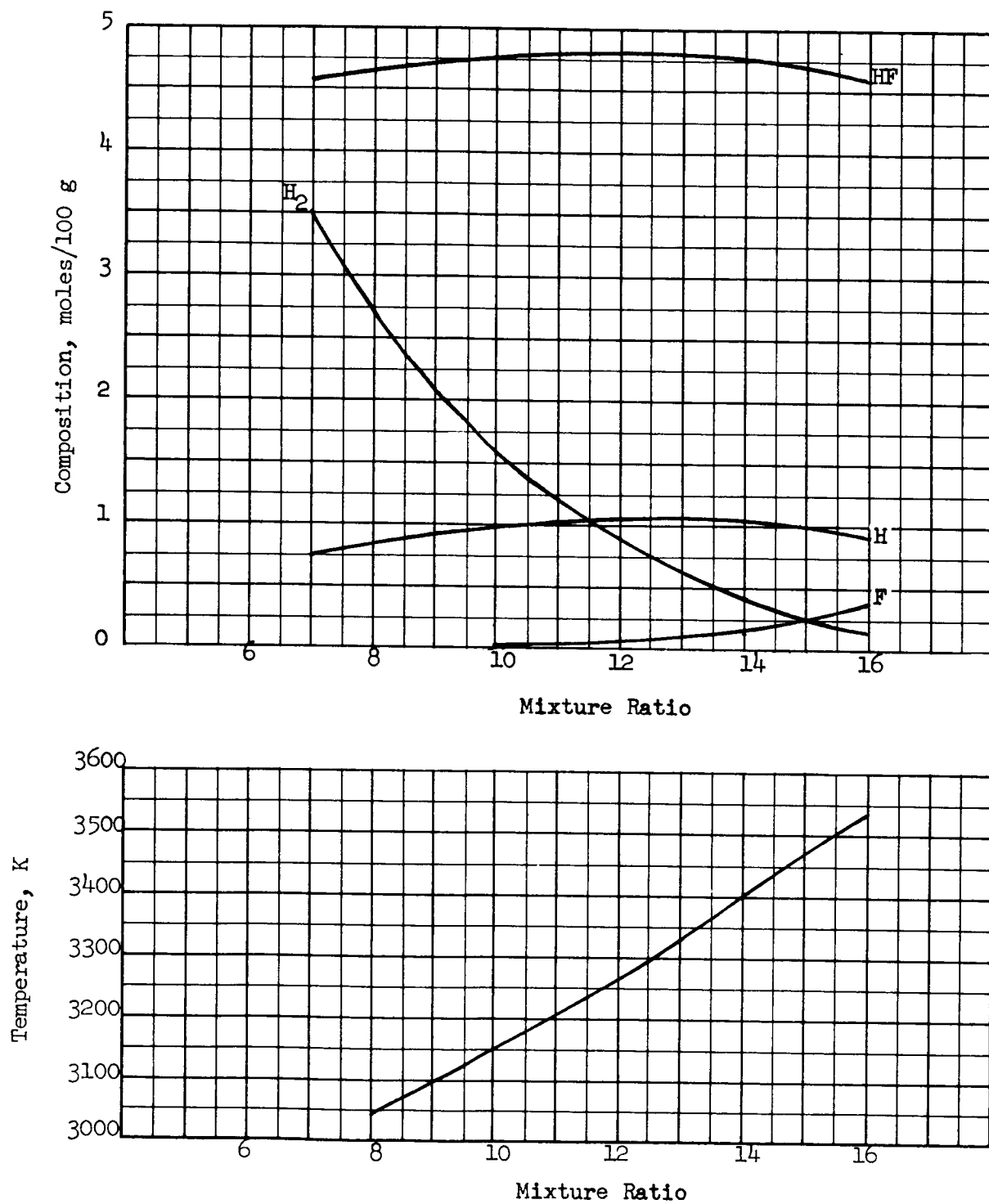


Figure 77. Fluorine-Hydrogen Composition and Temperature at the Bray Freezing Point Versus Mixture Ratio

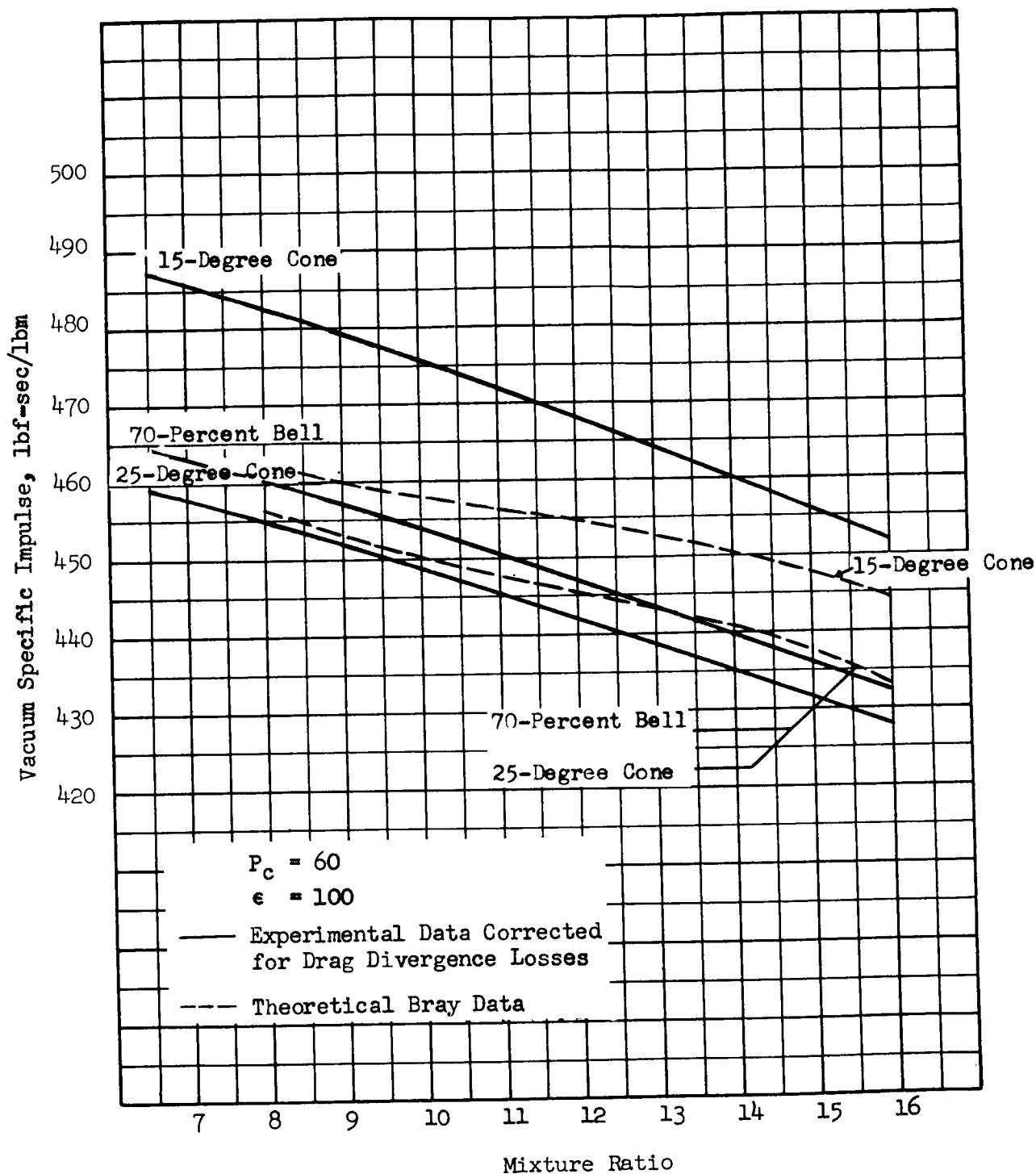


Figure 78. Liquid Fluorine-Gaseous Hydrogen Vacuum Specific Impulse vs Weight Mixture Ratio for NASA-LeRC Test Nozzles.



literature survey, showed that the experimental efficiencies are generally about 1 percent higher than the theoretical. This suggested that the rate expressions had been selected slightly low. Thus, a new set of rate constants was selected higher by factors generally in the vicinity of 2. The revised values are shown in the second columns of Tables 7 and 8, and in Fig. 72 through 75. It can be seen in these figures that the final selections are still within the experimental ranges, but are generally near the upper limit.

The revised rate constants are still in good agreement with the LeRC test data. For the 70-percent bell, theoretical values range from 0 to 1.5 percent high. Agreement for the 15-degree cone is slightly improved, however, it remains from 1 to 3.5 percent low.

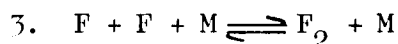
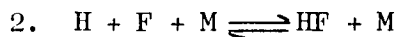
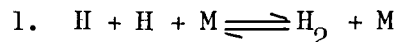
Correlation with all the data obtained in the current program is shown in detail in the Data Correlation section. In general, all of the nozzles gave excellent agreement; however, the 15-percent cone was consistently approximately 1 percent higher in relation to the other nozzles than was predicted. All the nozzles are approximately 1.5 percent high at very low mixture ratios.

COMPARISON OF SUDDEN FREEZING AND FULL KINETIC PROGRAM

To aid in the investigation of F_2/H_2 kinetics, a full kinetic performance calculation program was used. The machine procedure, developed by the United Aircraft Corporation under NASA Contract NAS3-2572, numerically integrates the system of reaction kinetics, one-dimensional gas dynamics, and state equations to calculate bulk thermodynamic properties and chemical composition in flow passages of varying cross-sectional area.



The reactions first considered were:



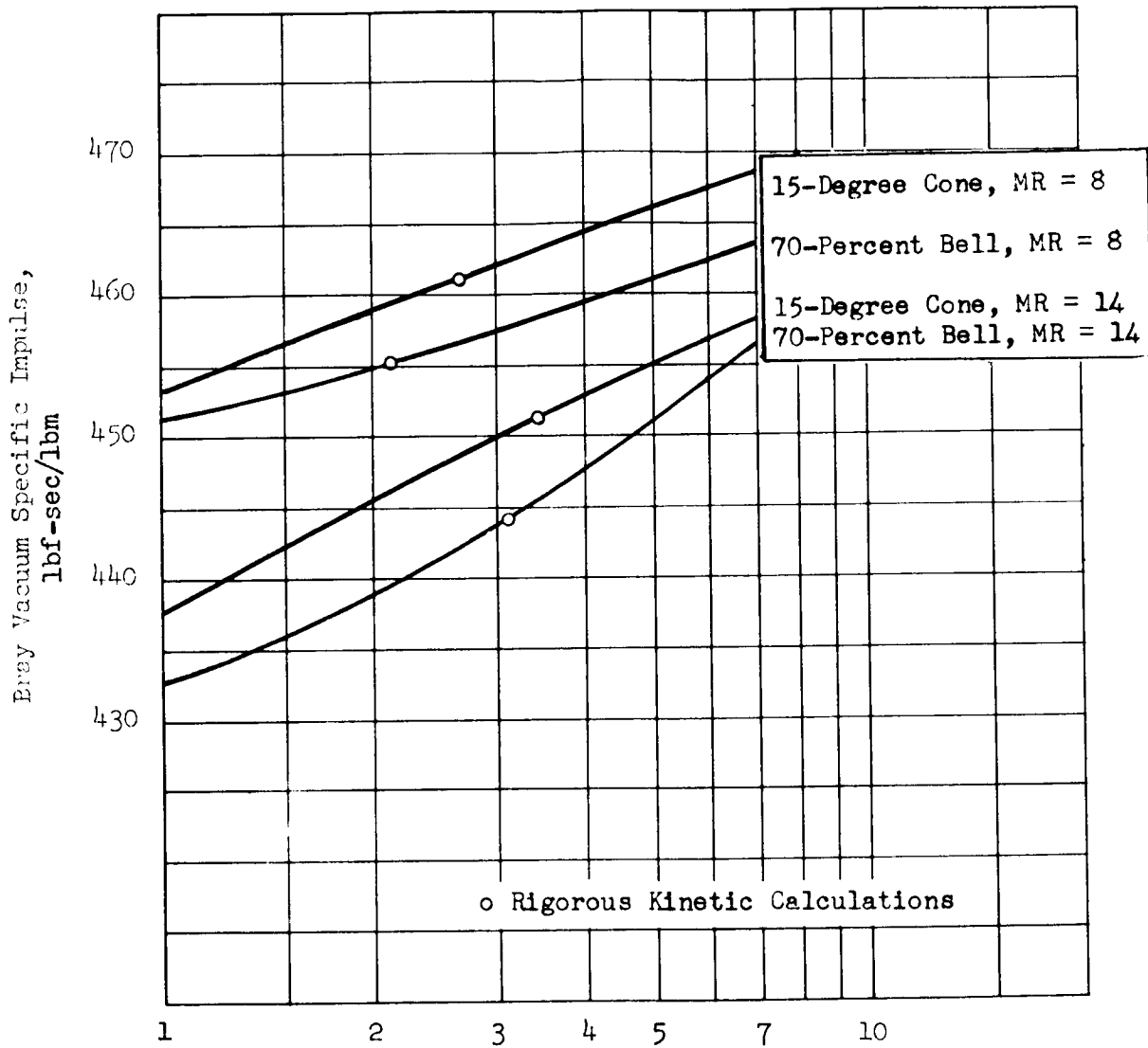
It was found that reaction (5) continued in equilibrium after the other reactions were no longer in equilibrium. This situation contributed to excessive machine computational times -- 35 to 45 minutes (of IBM 709 $\frac{1}{2}$ time) per calculation. It was decided to eliminate F_2 and the attendant reactions (3) and (5), since the concentration of F_2 is small, on the order of 10^{-8} moles/gram. Considering only reactions (1), (2), and (4), and species H, F, HF, and H_2 , computational times were reduced to 2-5 minutes per calculation with only a negligible loss in program accuracy. The program was then used for both the nozzles tested at Lewis Research Center and those used on this contract.

Bray calculations using the same rate expressions produced specific impulse values significantly lower than the kinetic calculations. This discrepancy was not attributed to the manner in which the reactions are handled by the program, since the sudden-freezing model used, similar to that used by Franciscus and Lezberg (Ref. 6), which accounts for the rate of change of molecular weight through all three-body reactions. This model simultaneously takes into account all recombination reactions together with the valid approximation that binary reactions are much faster than recombination reactions. There is, however, an arbitrary feature in all sudden-freezing models, and that is the manner in which the net equilibrium rate of recombination, r_{eq} , is compared with the kinetically possible rate of recombination, r_{kin} . It has been the convention to specify that the freezing point



occurs when $r_{eq} = r_{kin}$, presumably because Bray stated that r_{eq}/r_{kin} "is expected to be in the order of unity," Ref 2 and 3. Actually, the precise value, B, which should be used for the above ratio might be expected to depend upon the composition of the system, the kinetic data, and the nozzle geometry. The value of B was found to be slightly dependent upon mixture ratio, as shown in Fig. 79. Values of 2.7 and 3.4 for B correlate the 15-degree cone at mixture ratios of 8 and 14, respectively, while values of 2.1 and 3.1 correlate the bell for the same mixture ratios. Recommended B values for the LeRC nozzles were 3.1 for the cone and 2.5 for the bell. These produced agreement between the Bray and the kinetic calculations to better than 2 seconds across the full mixture ratio range. For this program, the recommended B values are shown in Table 9.

For high area ratio nozzles, the values of B required to produce agreement between the Bray and kinetic programs are those which cause the same degree of heat release in the nozzle. At low mixture ratios, these correspond to the same exit composition and degree of recombination. This can be seen for the 15-degree Lewis cone in Table 9, which shows exact agreement between molecular weights and specific impulse values at a mixture ratio of 8. The fact that the value of B is appreciably greater than 1 is attributed to a limited degree of recombination which is shown by the kinetic program to occur after r_{kin} equals r_{eq} ($B = 1$). The situation for the 70-percent bell is similar to the above except that a slightly lower B is required. This is because of the greater rate of expansion in the bell which causes recombination to decrease more rapidly after r_{kin} equals r_{eq} . As the rate of expansion becomes very great in the vicinity of the freezing point, B approaches 1.



B, Ratio of Required to Available Reaction Rate at the Freezing Point

Figure 79 . Bray Vacuum Specific Impulse vs Ratio of Required to Available Reaction Rate at the Freezing Point



TABLE 9

RECOMMENDED B VALUES FOR KINETIC ANALYSIS

Nozzle	B*
10-degree cone	4.0
15-degree cone	3.4
Controlled expansion	3.4
20-degree cone	3.0
70-Percent bell	2.4

*B = ratio of required to available
reaction rate at the freezing
point.



At high mixture ratios, where there is an appreciable amount of F at the freezing point, the kinetic program shows subsequent disappearance of the F because of the moderately exothermic reaction, $F + H_2 \rightleftharpoons HF + H$.

However, with the Bray model, the expanding gases do not have the advantages of this heat release, since all reactions cease at the freezing point. Thus, a slightly greater degree of recombination is required with the Bray model to obtain the necessary heat release, and this is effected by a slightly higher value for B. This can be seen in terms of molecular weights, for a mixture ratio of 14, Table 10. A similar situation is expected in systems containing oxygen and hydrogen when there are appreciable amounts of OH or O at high mixture ratios.



TABLE 10

EXIT COMPOSITION FOR VARIOUS KINETIC MODELS

		Mixture Ratio = 8			Mixture Ratio = 14		
		Kinetic	Bray B = 2.6	Bray B = 1.0	Kinetic	Bray B = 3.4	Bray B = 1.0
CONSTITUENT	H	0.94	0.94	1.10	1.34	1.08	1.24
	F	0.00	0.01	0.02	0.00	0.17	0.28
	H ₂	2.70	2.71	2.63	0.18	0.40	0.37
	HF	4.68	4.67	4.66	4.91	4.74	4.63
Molecular Weight		12.01	12.01	11.89	15.55	15.65	15.33
I _s , lbf-sec/lbm		461	461	453	452	452	438

Note: Composition is expressed in moles/100 g

LeRC 15-degree Cone, Stagnation Pressure = 60 psia,
Area Ratio = 100



TEST HARDWARE

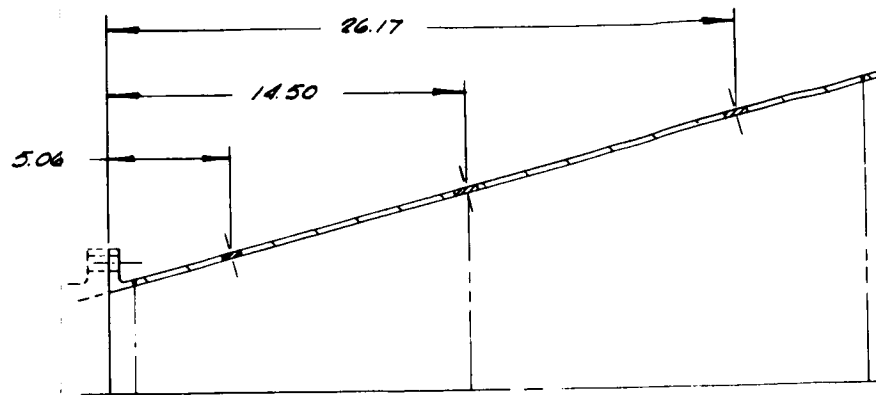
The experimental phase of the Task III and IV portions of the program required six nozzle configurations. These were two 15-degree conical designs (different throat radius of curvature ratios), a 70-percent bell design, a 10-degree conical design, a 20-degree conical design, and a controlled expansion design with an equivalent 80 percent length. The design and fabrication of these test assemblies are discussed in this section.

TASK III NOZZLES

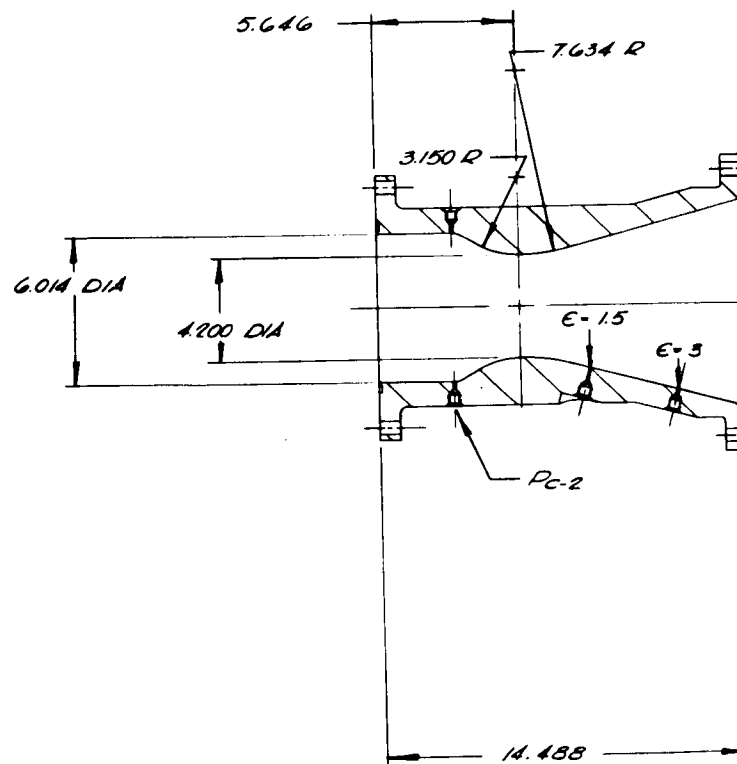
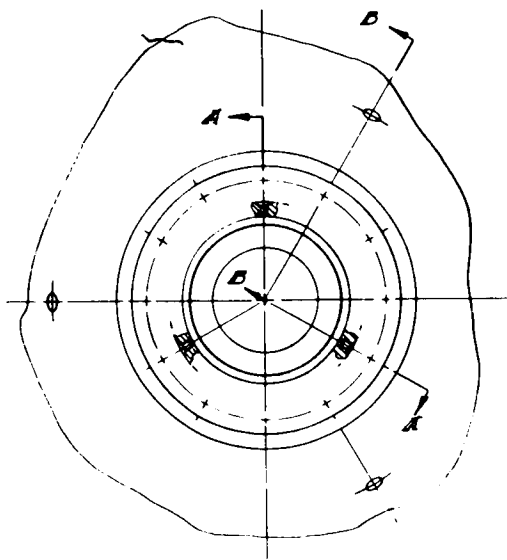
15-Degree Cone and 70-Percent Bell

Figures 80 and 81 show the final designs for the 15-degree long throat conical and the 70-percent bell nozzles, respectively. These are segmented assemblies consisting of copper throat sections and steel nozzle extensions. In each case, the throat section ends at an expansion area ratio of 4:1 with the overall assembly a 60:1 design. Originally, it was intended to fabricate the nozzles in an integral design entirely of copper; however, thermal studies indicated that copper was not required in the nozzle expansion region and subsequent discussions with fabricators indicated that significant schedule and cost advantages could be obtained with the segmented design. Figure 82 shows the conical nozzle extension, and Fig. 83 shows the 70-percent bell nozzle assembly.

Instrumentation for the nozzle assemblies included three nozzle inlet static pressure ports located 120 degrees apart, six nozzle static pressure profile measurements located at expansion area ratios of 1.5, 3, 7, 15, 30, and 60, and fifteen heat transfer measurement points, three each at area ratios



SECTION B-B
(TYP) 3 PLACES



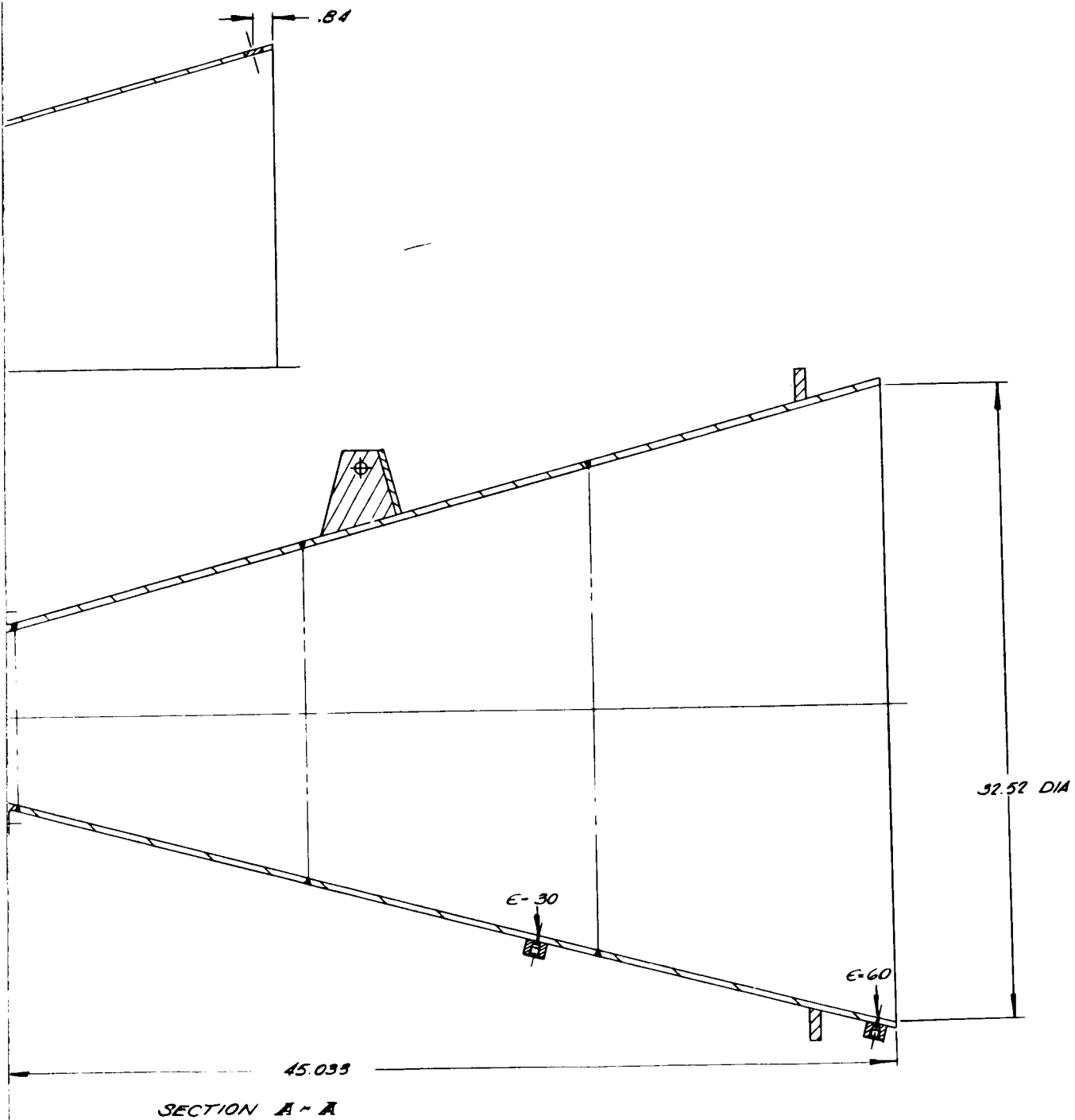
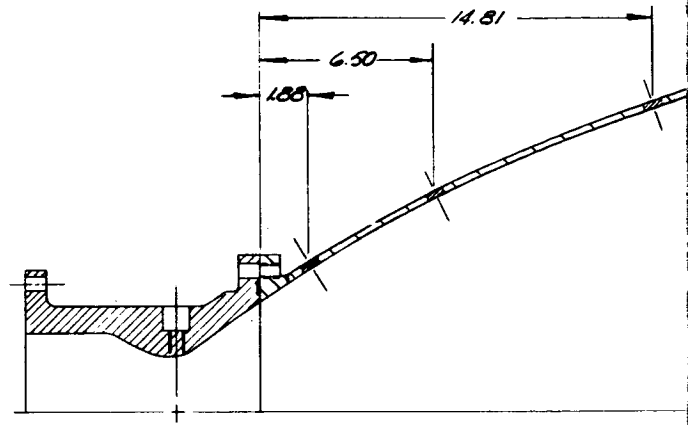
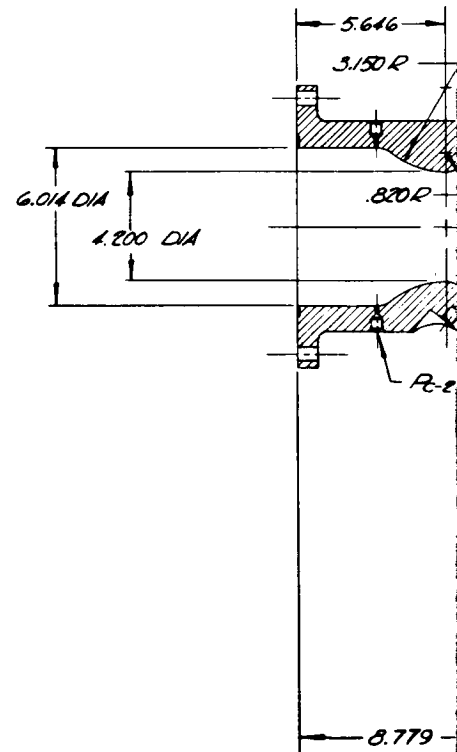
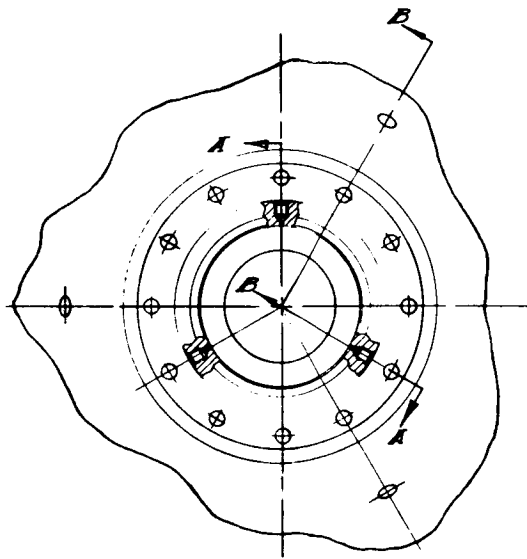


Figure 80. Long Throat 15-Degree Conical Nozzle Design



SECTION B-B
(TYR) 3 PLACES





ROCKETDYNE • A DIVISION OF NORTH AMERICAN AVIATION, INC.

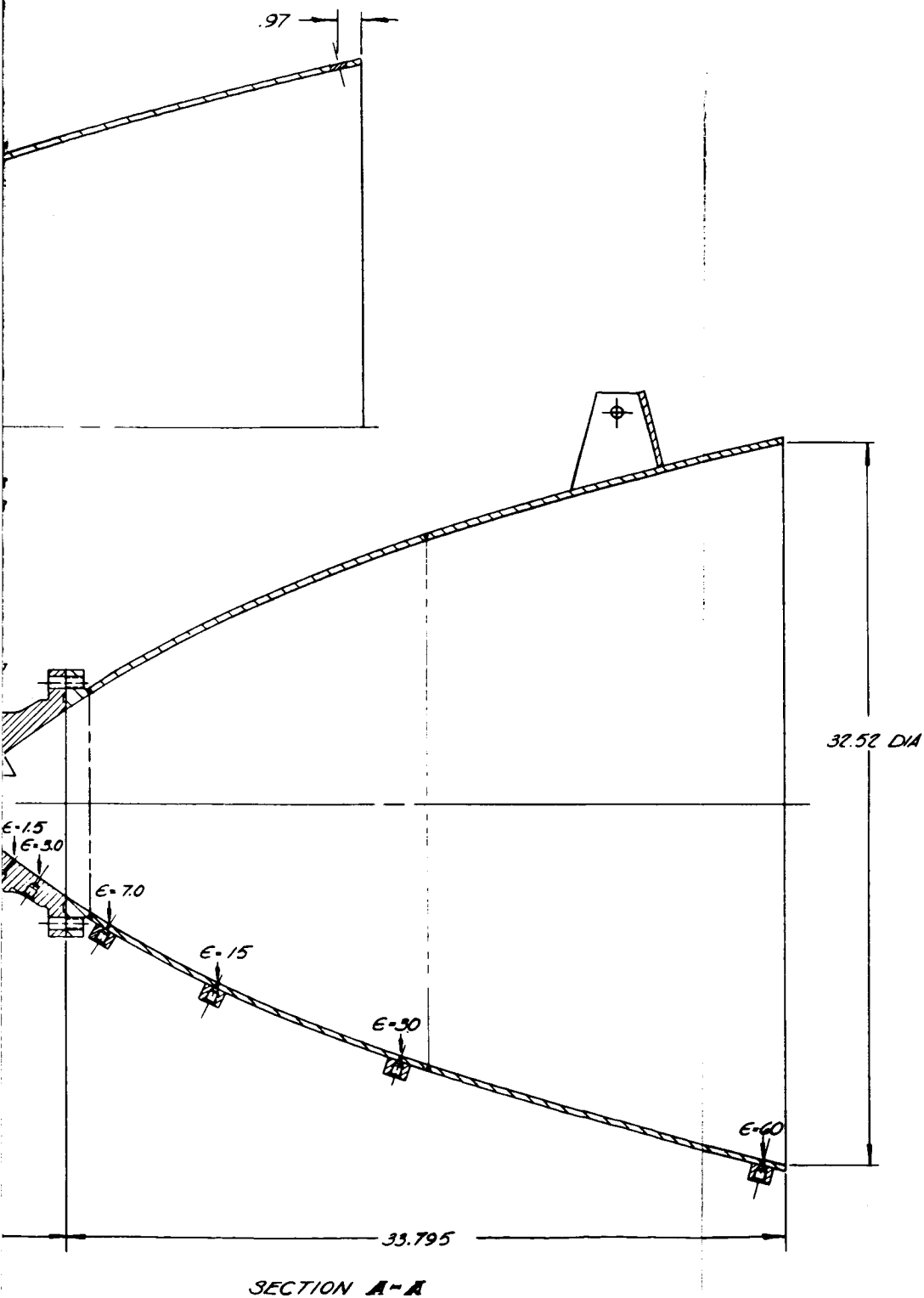


Figure 81. 70-Percent Bell Nozzle Design

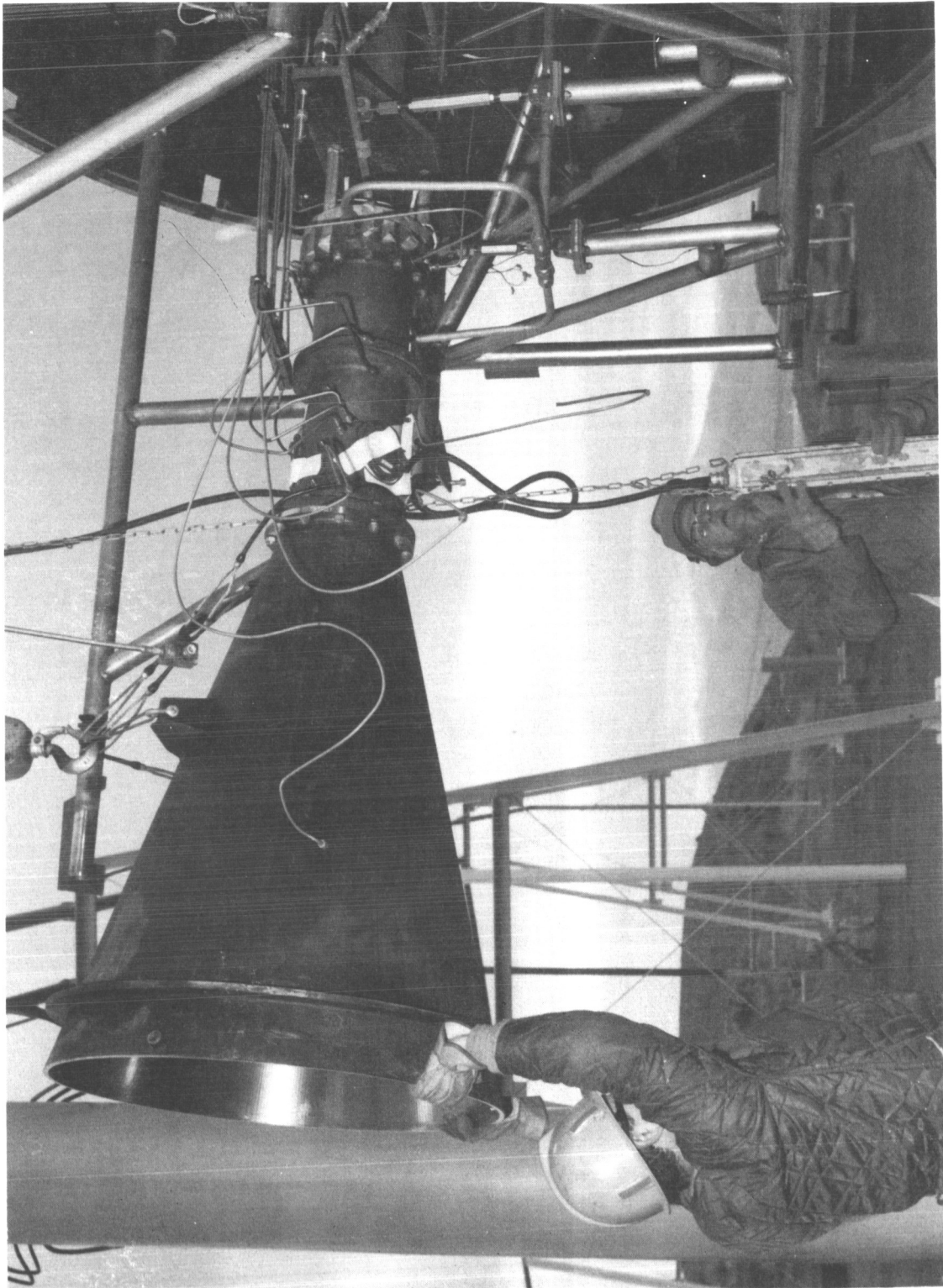


Figure 82. Long Throat 15-Degree Conical Nozzle Being Installed in the Test Facility

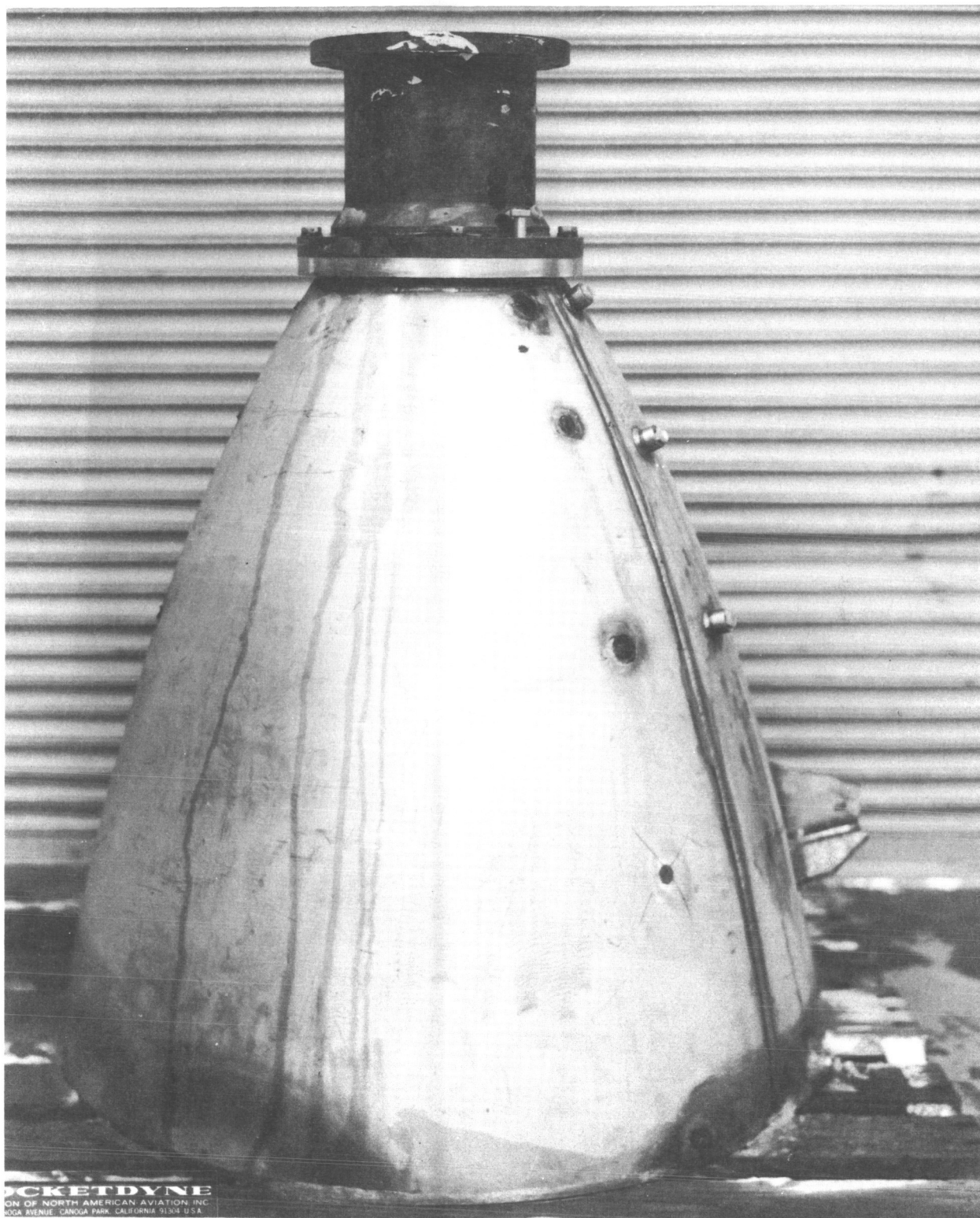


Figure 83. Seventy-Percent Bell Nozzle



of 1, 7, 15, 30, and 60. The latter, detailed in the heat transfer analysis section, consist of thermally isolated sections at the various nozzle stations. For the copper section, this thermal isolation is accomplished by machining an annular groove in the outer surface of the chamber wall with a minimum permissible supporting web left at the inner surface. This groove effectively limits conduction to a radial path through the chamber wall. For the nozzle extension, a copper plug was threaded into the wall and machined flush on both sides. The conductivity difference between the two materials plus the surface contact resistance of the joint results in the plug being essentially isolated from the surrounding wall for short-duration, high heat flux conditions.

Seals for the nozzle joint and for those upstream in the combustion zone were spiral-wound stainless steel and asbestos. These worked well throughout the program and no chamber leakage was noted at any time.

The throat sections for both the conical and bell nozzles were machined from solid-copper forged billets with the final machining on the nozzle portion after assembly to the nozzle extension to minimize the surface discontinuity at the joint.

The conical nozzle extension was fabricated from patterns cut from sheet stock. These were rolled to the proper configuration then welded together. This subassembly was trimmed and welded to a premachined flange section, and the whole assembly machined along the internal surface.



The bell nozzle extension was fabricated by the same processes, except that the shell sections, because of the multiple curvatures, were drop-hammer die forged. Only a minimum amount of machining cleanup was required after assembly to bring this nozzle to final contour.

Controlled Expansion Nozzle

The controlled expansion nozzle design is shown in Fig. 84 , while Fig. 85 shows the completed part. Selection of the internal contour for the nozzle is discussed in the Controlled Expansion Nozzle Design section.

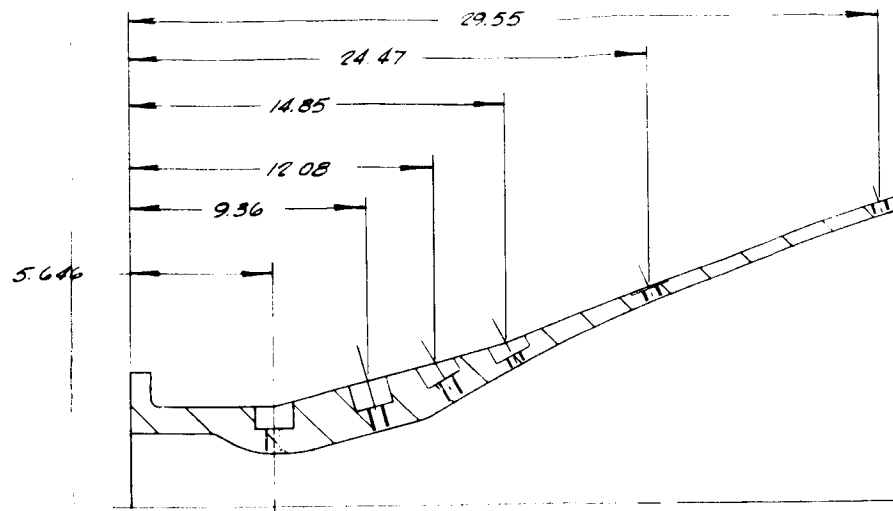
The nozzle is fabricated entirely of copper and is of single-piece construction with no separate nozzle extension.

Instrumentation for the nozzle was similar to the previous designs except that the thermal isolation grooves were employed throughout, and additional nozzle pressure measurements were made in the area where chemical freezing was expected to occur.

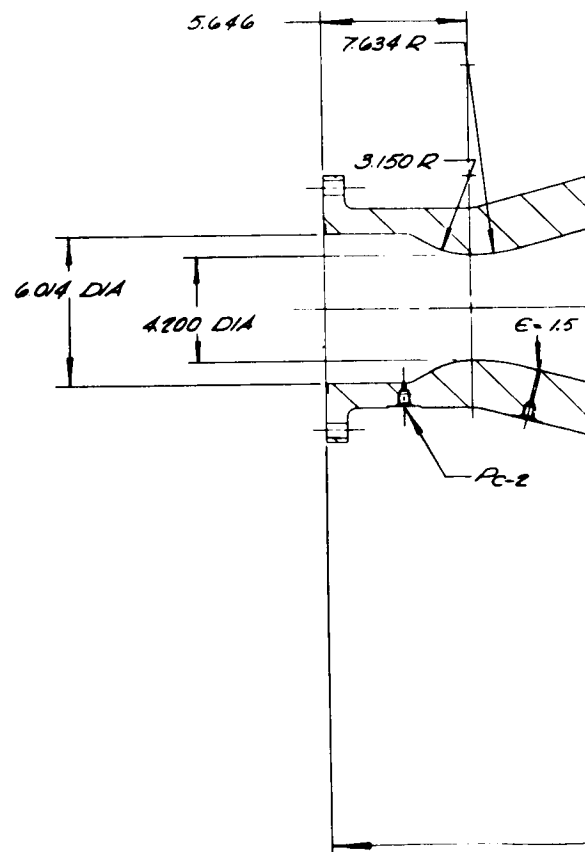
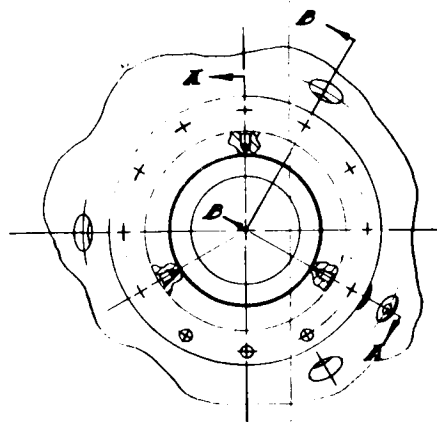
TASK IV NOZZLES

15-Degree Cone

Figure 86 shows the short throat 15-degree conical nozzle design used in Task IV, while Fig. 87 shows the completed assembly. This assembly utilized the nozzle extension from the previous task to which a new throat section was added. Because this portion of the program required operation at 50-psia chamber pressure only, low carbon steel was used throughout the chamber except for the combustion zone.



SECTION B-B
(TYP) 3 PLACES



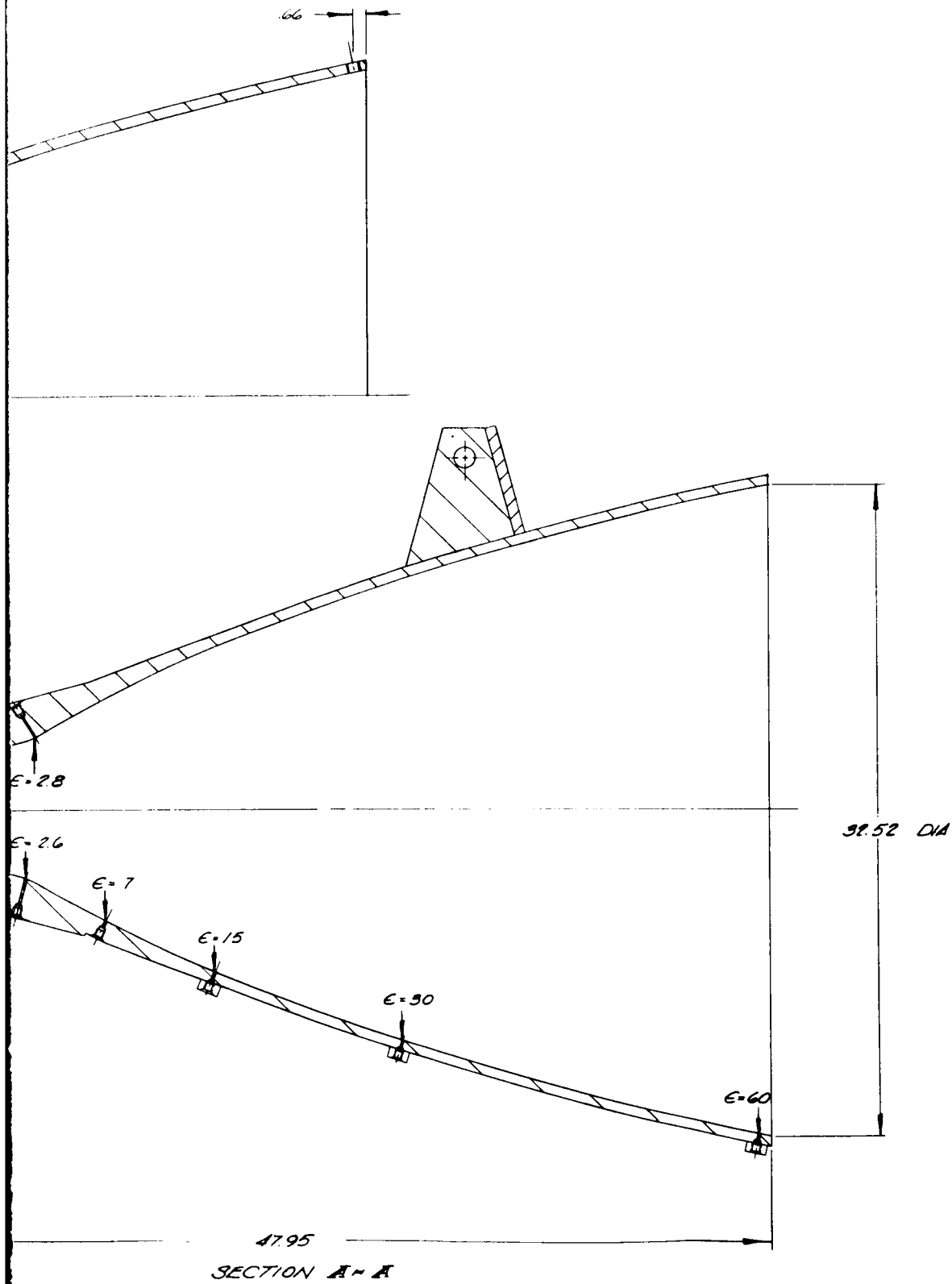


Figure 84. Controlled Expansion Nozzle Design

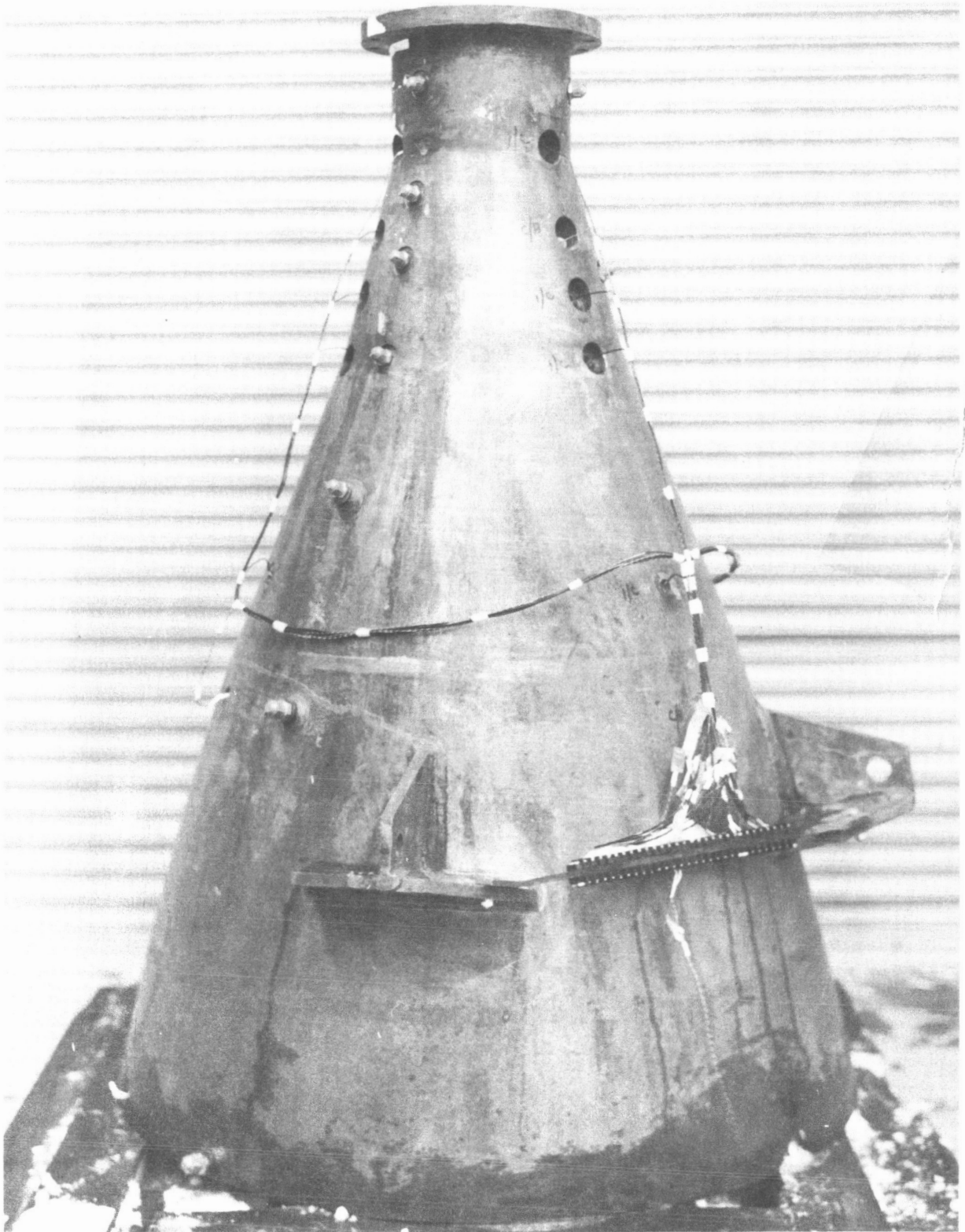
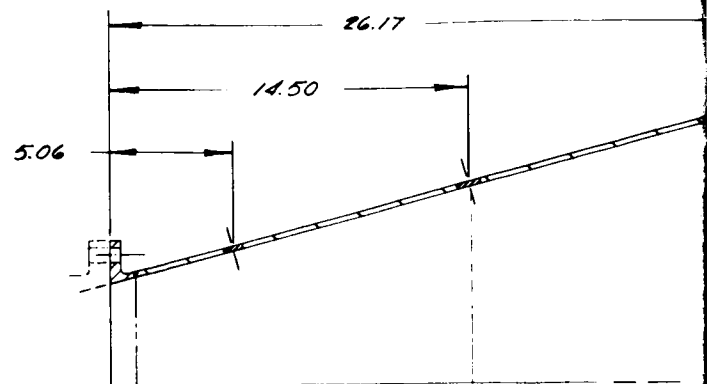
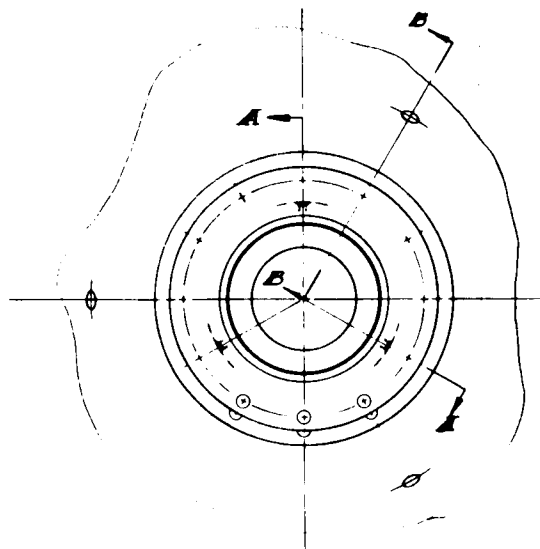
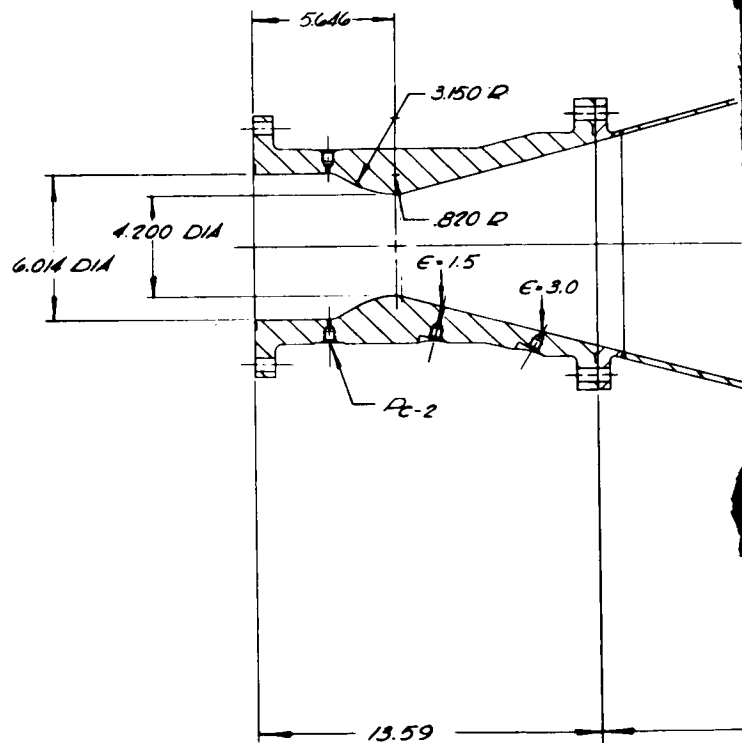


Figure 85. Controlled Expansion Nozzle



SECTION D-D
(TYP) 3 PLACES



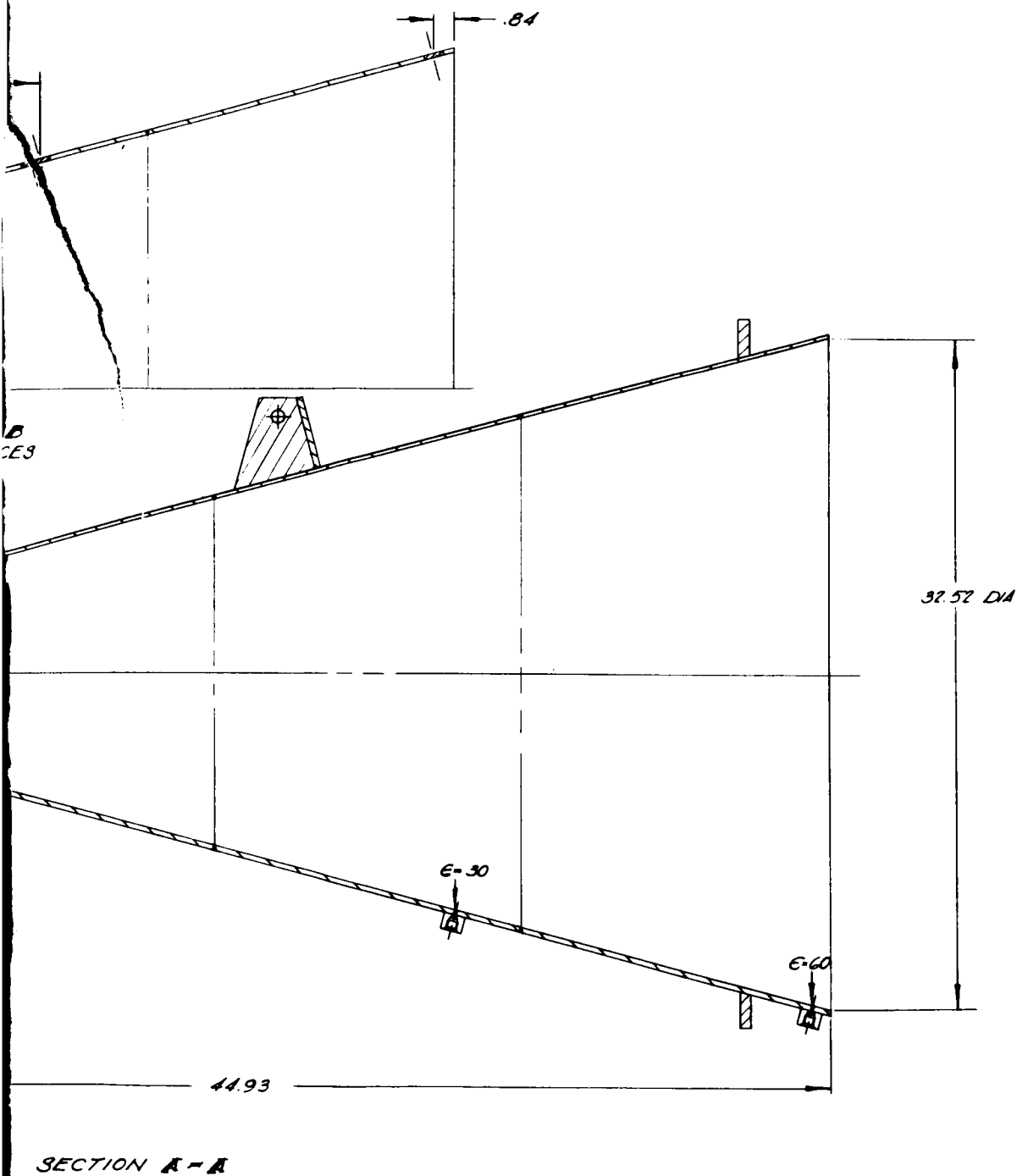


Figure 86. Short-Throat 15-Degree Conical Nozzle Design

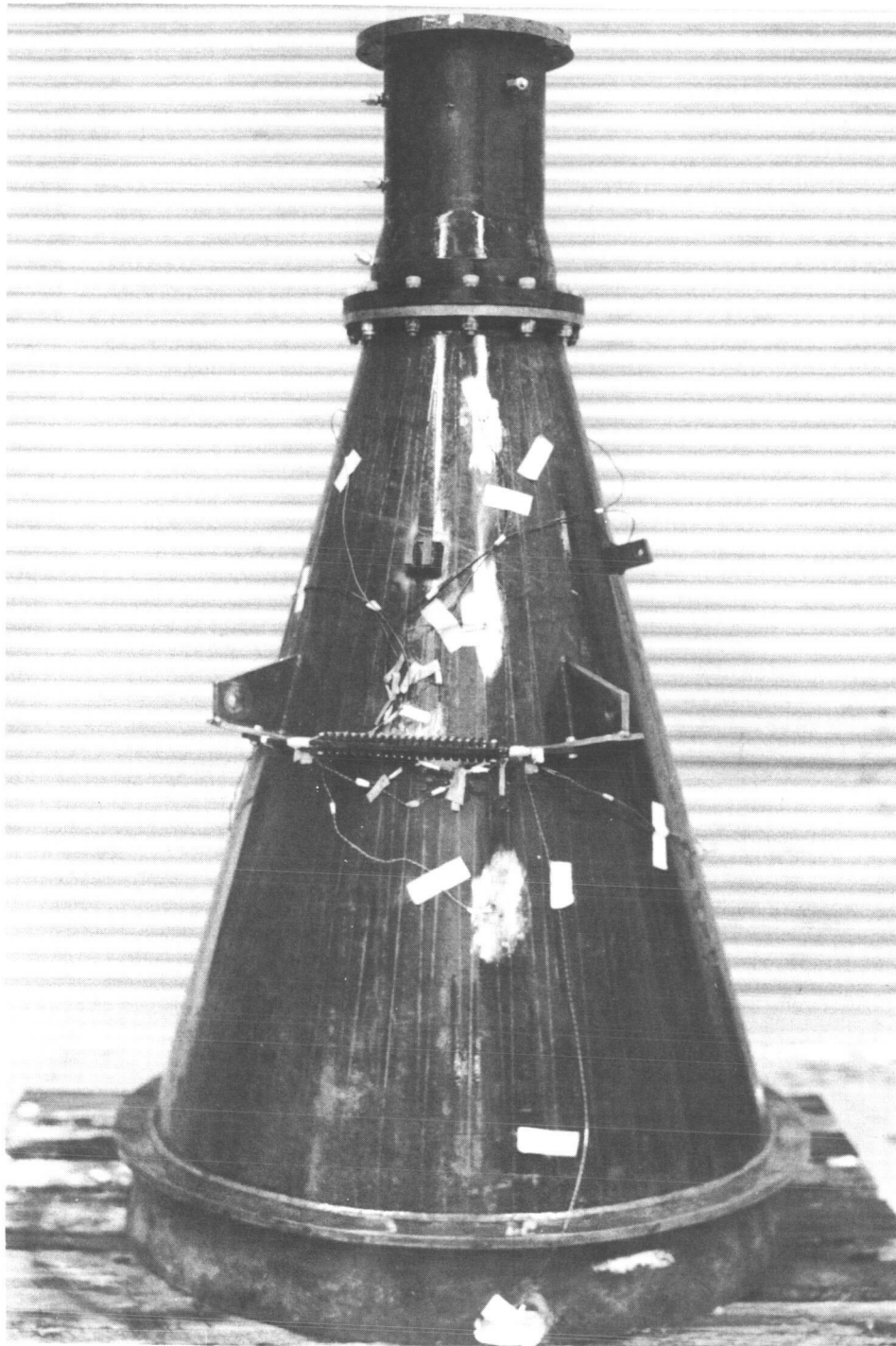


Figure 87. Short-Throat, 15-Degree Conical Nozzle



10-Degree and 20-Degree Cones

The designs for the 10-degree and 20-degree conical nozzles are shown in Fig. 88 and 89, while Fig. 90 and 91 show the completed assemblies. Again, these are similar to those discussed previously with the throat section and nozzle extension jointed at an area ratio of 4.1. These nozzles were fabricated in a manner similar to that discussed above for the initial 15-degree cone.

COMBUSTION CHAMBER

In addition to the nozzles, a copper combustion chamber section shown in Fig. 92 was designed and fabricated. This section in combination with the throat inlet section of the nozzles provided a characteristic length (L^*) of 30 inches. Instrumentation for this section was limited to injector-end chamber pressure taps because the heat transfer characteristics of the combustion chamber had been established in Task II.



1-641

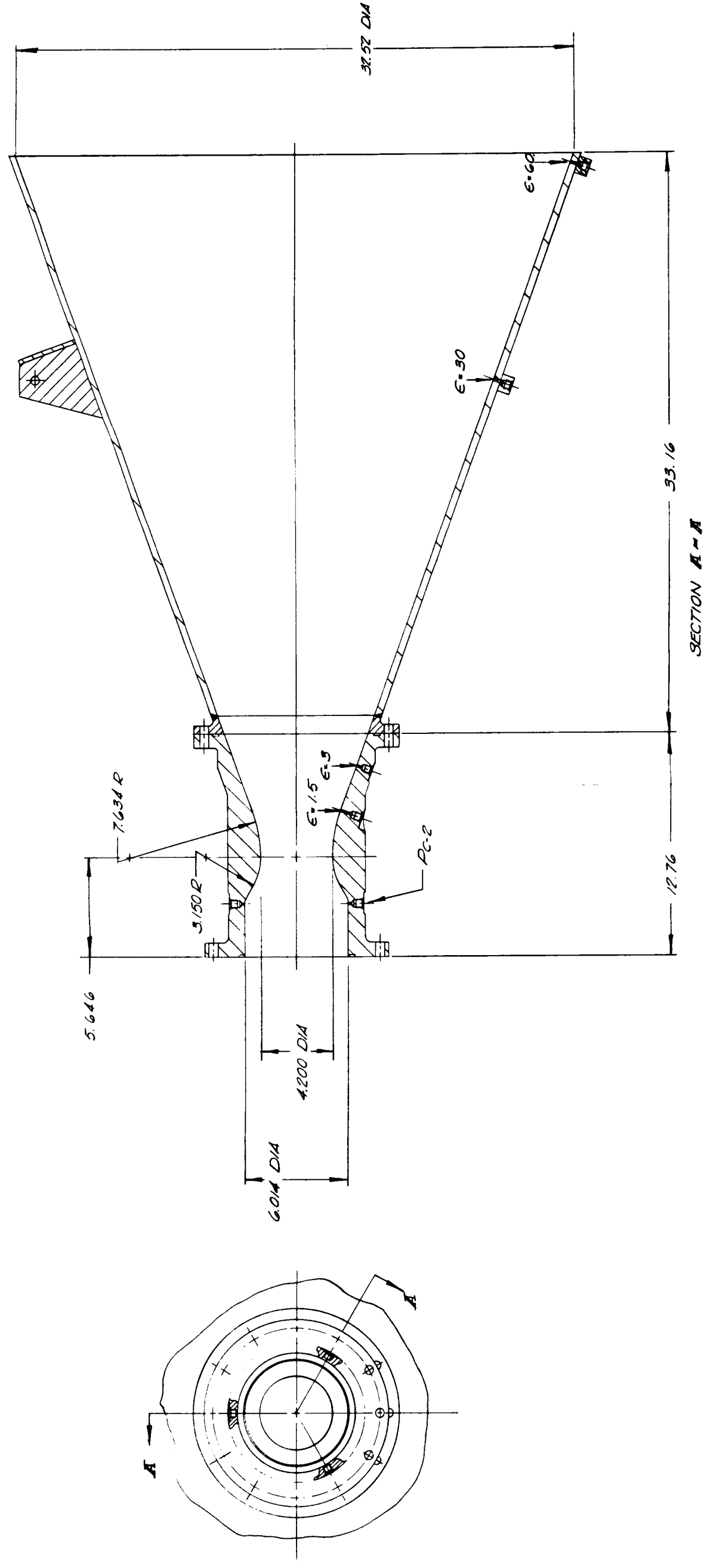


Figure 89. 20-Degree Conical Nozzle Design

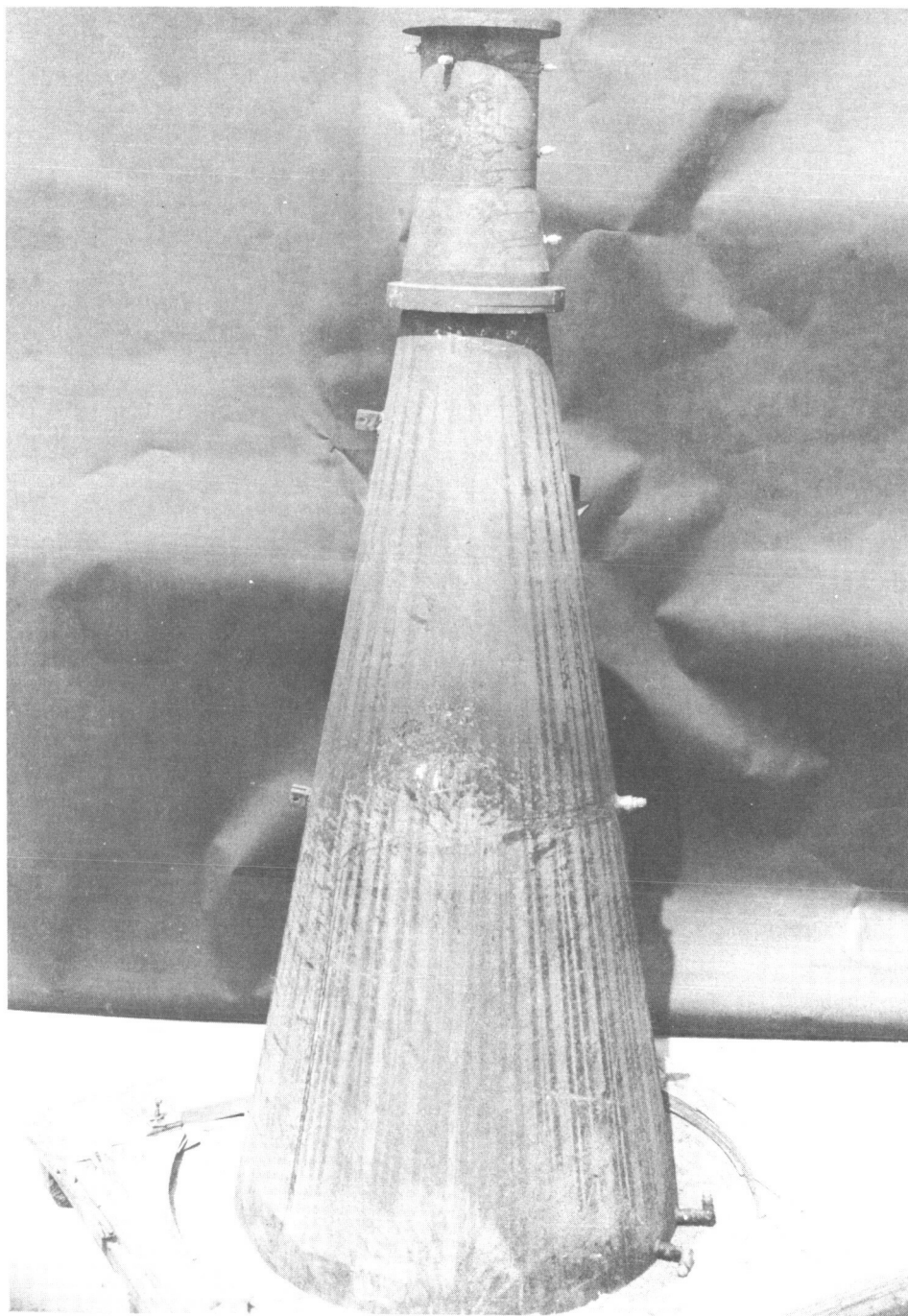


Figure 90. 10-Degree Conical Nozzle

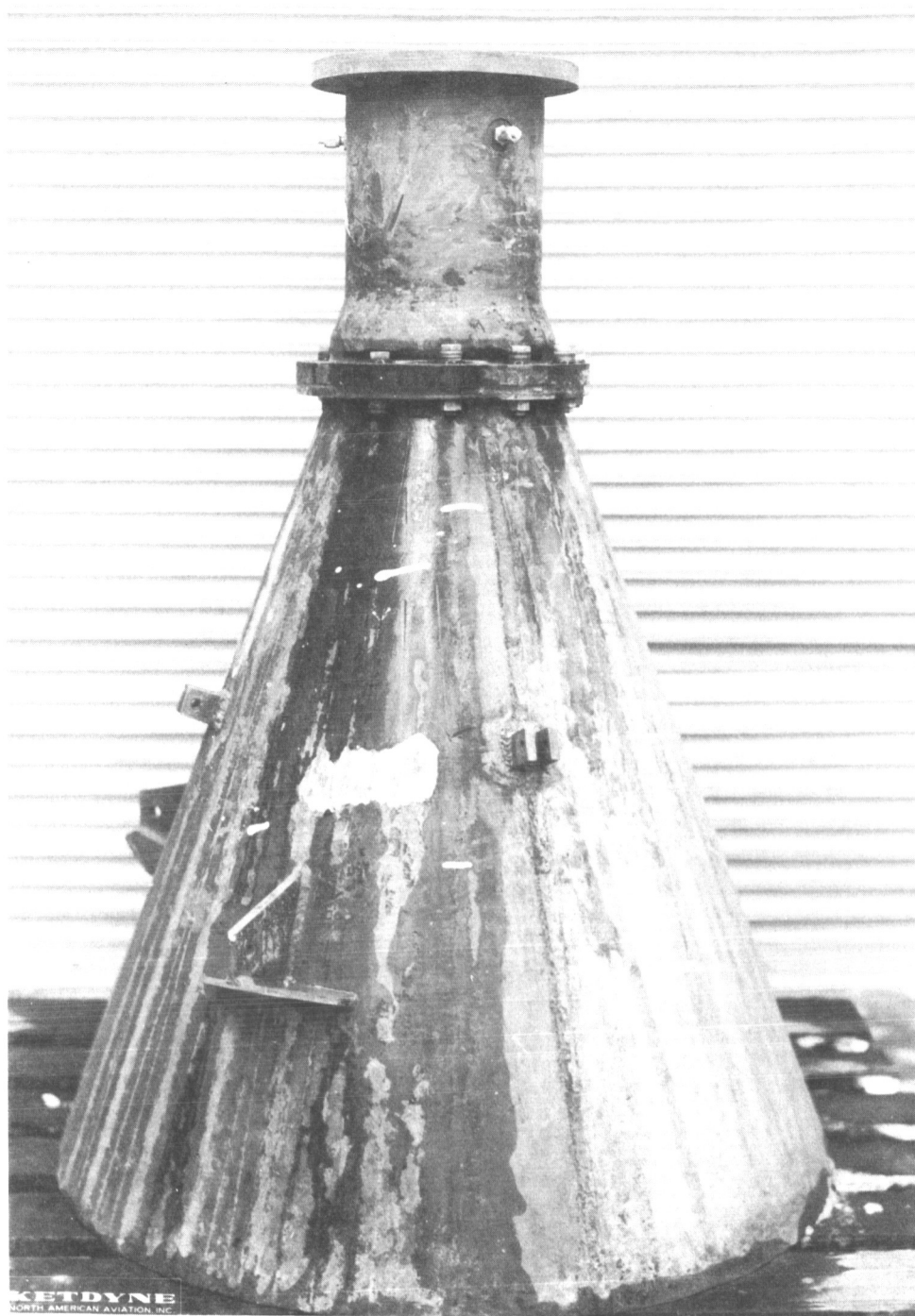
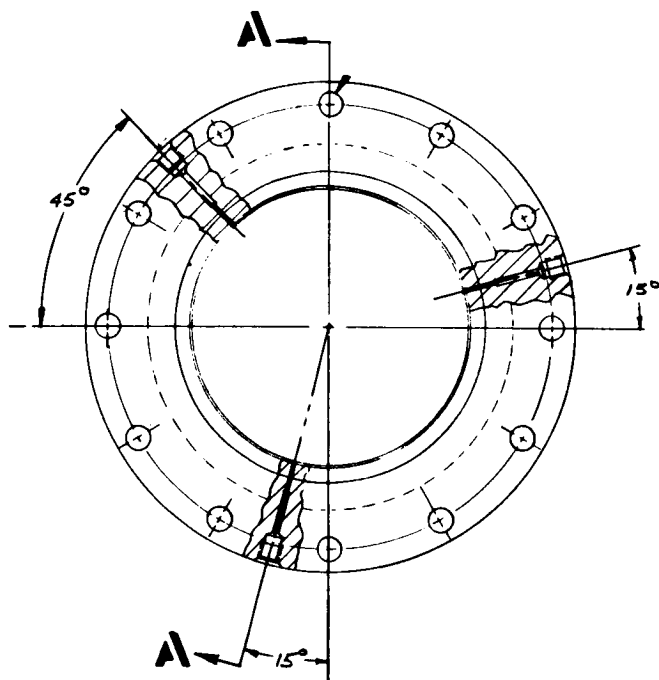


Figure 91. 20-Degree Conical Nozzle



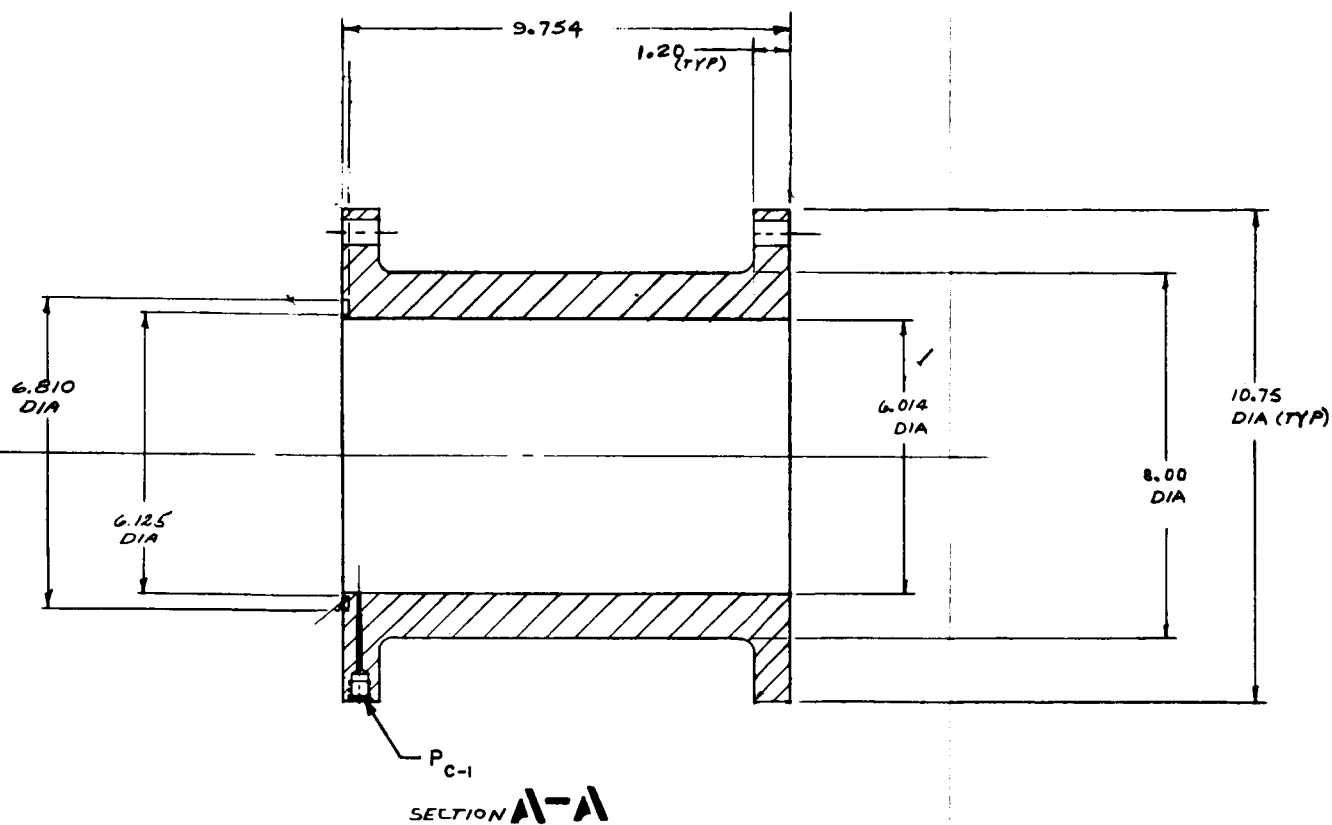


Figure 92. Combustion Chamber Design



TEST FACILITY AND PROCEDURE

The experimental portion for the Task III and IV portions of the program was conducted at the Nevada Field Laboratory. Firings were conducted in the Small Engine Division test area, Area B (Fig. 93), in the medium-thrust altitude facility. This facility consists of two horizontal-firing altitude test capsules (identified as 4A and 4B) with a common altitude-simulation system. The frontispiece shows the facility, of which only the 4B position was employed in this program. The facility was originally constructed in support of the LEM descent engine program and consequently it was necessary to add both liquid-fluorine and gaseous-hydrogen capability to the area, as discussed below.

The rigid data precision requirements of this program required that special attention be given to instrumentation and instrumentation systems. For this reason, all critical measurements were made redundant.

Test and fluorine passivation procedures are discussed at the end of this section.

ALTITUDE TEST CAPSULE

The altitude test capsule consists of a cylinder approximately 10 feet in diameter, with a hemispherical forward end. The aft end opens into the altitude-simulation system. The forward end of the capsule is mounted on a movable trolley for access and hardware installation. The capsule is shown in the open position in Fig. 94, with the 70-percent bell nozzle installed. Figure 95 is another view of the forward section with only



Figure 93. Nevada Field Laboratory, Small Engine Division Test Area B

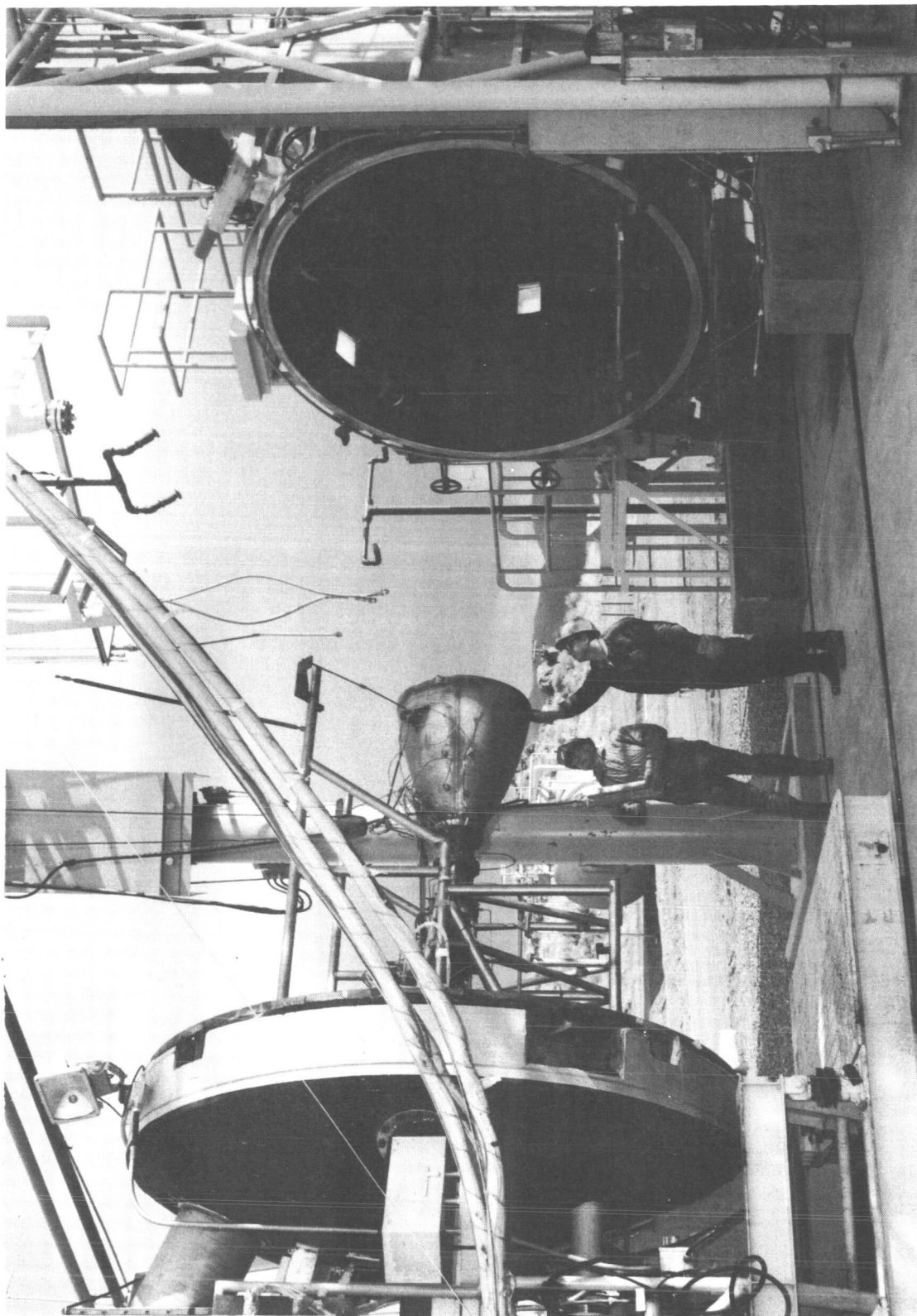


Figure 94. NFL 4B Altitude Simulation Capsule

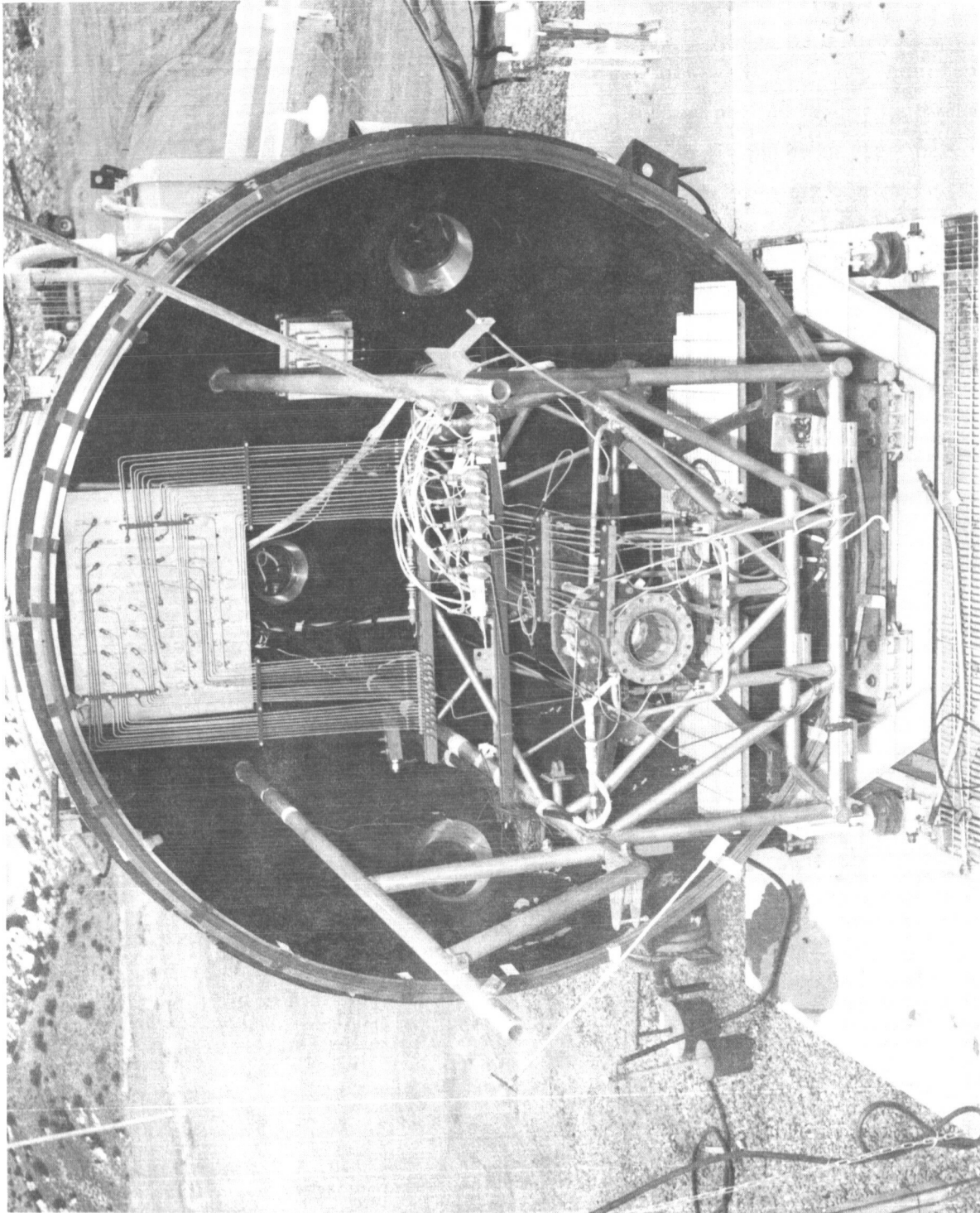


Figure 95. NFL 4B Altitude Simulation Capsule, Movable Forward Section



the injector and combustion chamber section installed. It shows the cantilevered supporting structure, transducer installation, and camera and viewing ports. Separate access doors are provided so that it is not necessary to remove the forward section for general work around the engine and hardware inspection after each test. The horizontally mounted engine fires directly into the initial diffuser stage.

ALTITUDE-SIMULATION SYSTEM

The altitude-simulation system used in this program is capable of maintaining an altitude in excess of 100,000 feet for 150 seconds and consists of three diffuser stages. The first stage is driven by the engine, while the other two stages are powered by supersonic steam ejectors. Figure 96 is a schematic drawing of the system. The steam is supplied by a hyperflow engine shown in Fig. 97. This hyperflow engine consists of an Atlas sustainer-type injector, modified to operate on liquid oxygen and alcohol, and a special water-film-cooled thrust chamber, with additional water injection at the lower portion of the primary combustion zone. The total flowrate is approximately 550 lb/sec, with inlet steam conditions of 300 to 315 psia and 420 to 480 F. The flow is divided between the two ejector-diffuser sections in approximately a 1:5 ratio with the first stage at 90 lb/sec.

The two altitude capsules are each isolated from the ejector-diffuser sections by 10-foot butterfly-type isolation valves. This valve is closed until after the hyperflow has reached altitude in the first diffuser inlet section, opened during the test, and then closed prior to hyperflow shutdown at the end of the test. This prevents the hyperflow transients from affecting the engine hardware, particularly at shutdown when a high-pressure wave travels up the diffuser sections.

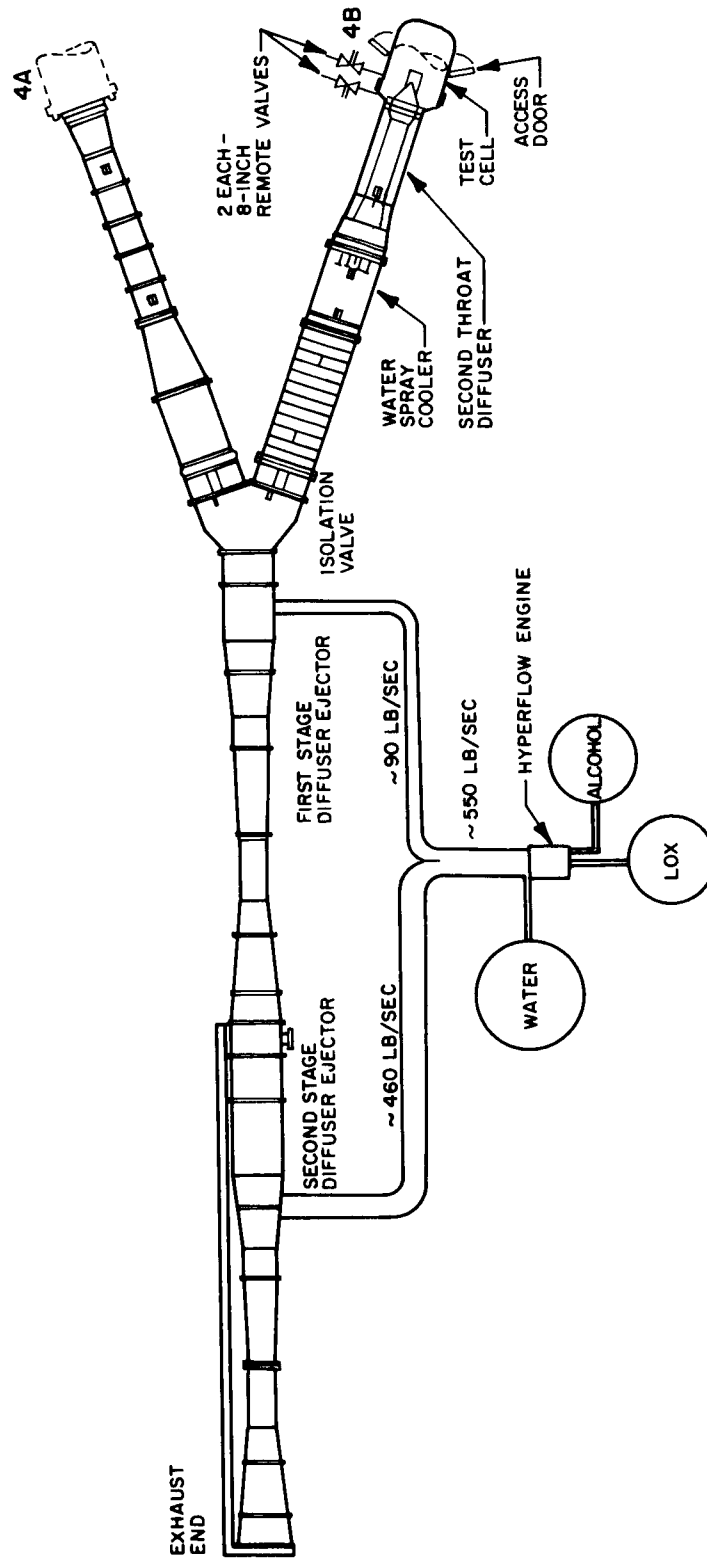


Figure 96. NFL Altitude Simulation System

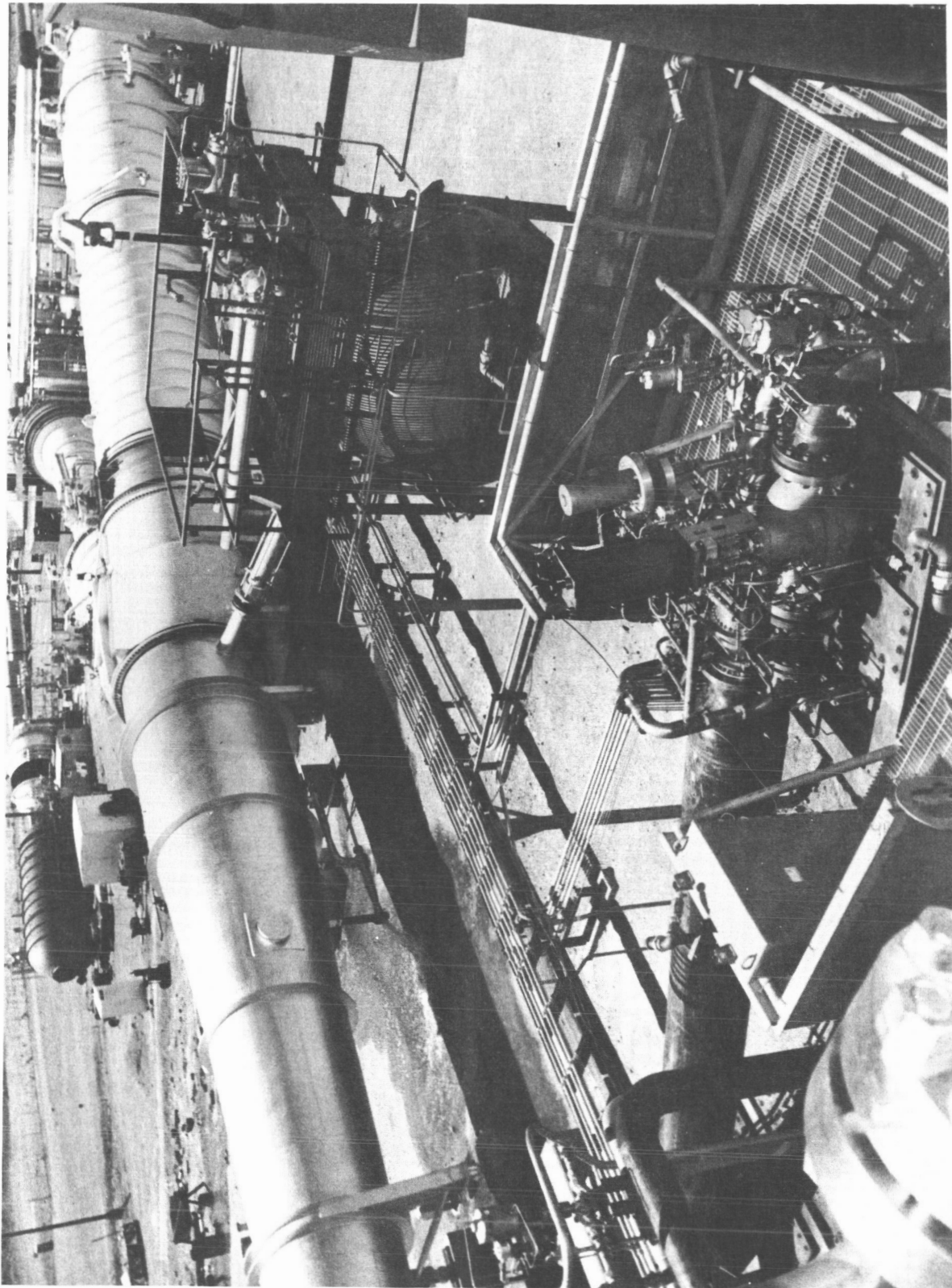


Figure 97. NFL Hyperflow Engine



Ejector-diffuser system performance was satisfactory throughout the program; approximately 7000 seconds of operation were accumulated.

PROPELLANT SYSTEMS

Schematic flow diagrams for the test facility are shown in Fig. 98 and 99 for Tasks III and IV, respectively.

Fluorine System

For this program, a liquid fluorine tank was permanently installed adjacent to the 4B altitude capsule. This tank installation is shown in Fig. 100, and is shown with the control system and various propellant lines in Fig. 101. The tank is a triple-wall assembly consisting of a 500-gallon, 475-psi stainless steel tank submerged in a liquid nitrogen jacket with both in an insulation-filled vacuum jacket. This tank thus serves not only as the engine run tank but provides on-stand storage of liquid fluorine.

The liquid fluorine flow system is liquid nitrogen jacketed from the run tank to the main valve, with the main valve mounted inside the altitude capsule as close as feasible to the engine.

Flow measurements were made in the horizontal section just prior to the entry to the capsule and just upstream of the main valve.

The initial system did not have the accumulator shown just upstream of the flowmeters in the schematic. Early in the program, however, it was noted that temperature spikes were occurring in the liquid fluorine.

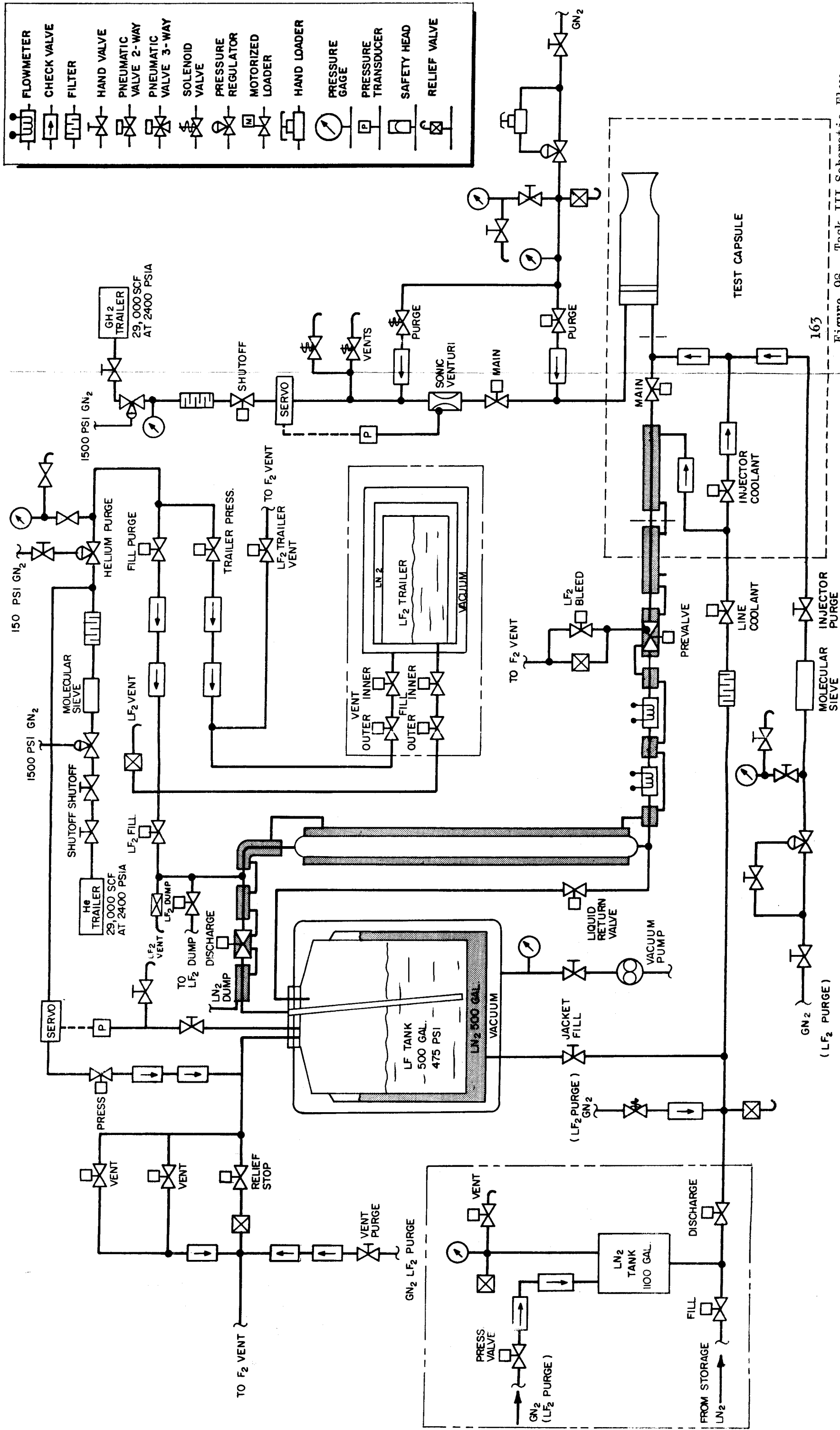


Figure 98. Task III Schematic Flow Diagram of Nevada Field Laboratory Test Stand 4B, LF₂/GH₂ Performance Program

163-2

163-1

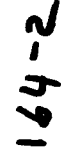


Figure 99. Task IV Schematic Flow Diagram of Nevada Field Laboratory Test Stand 4B, LF_2/GH_2 Performance Program

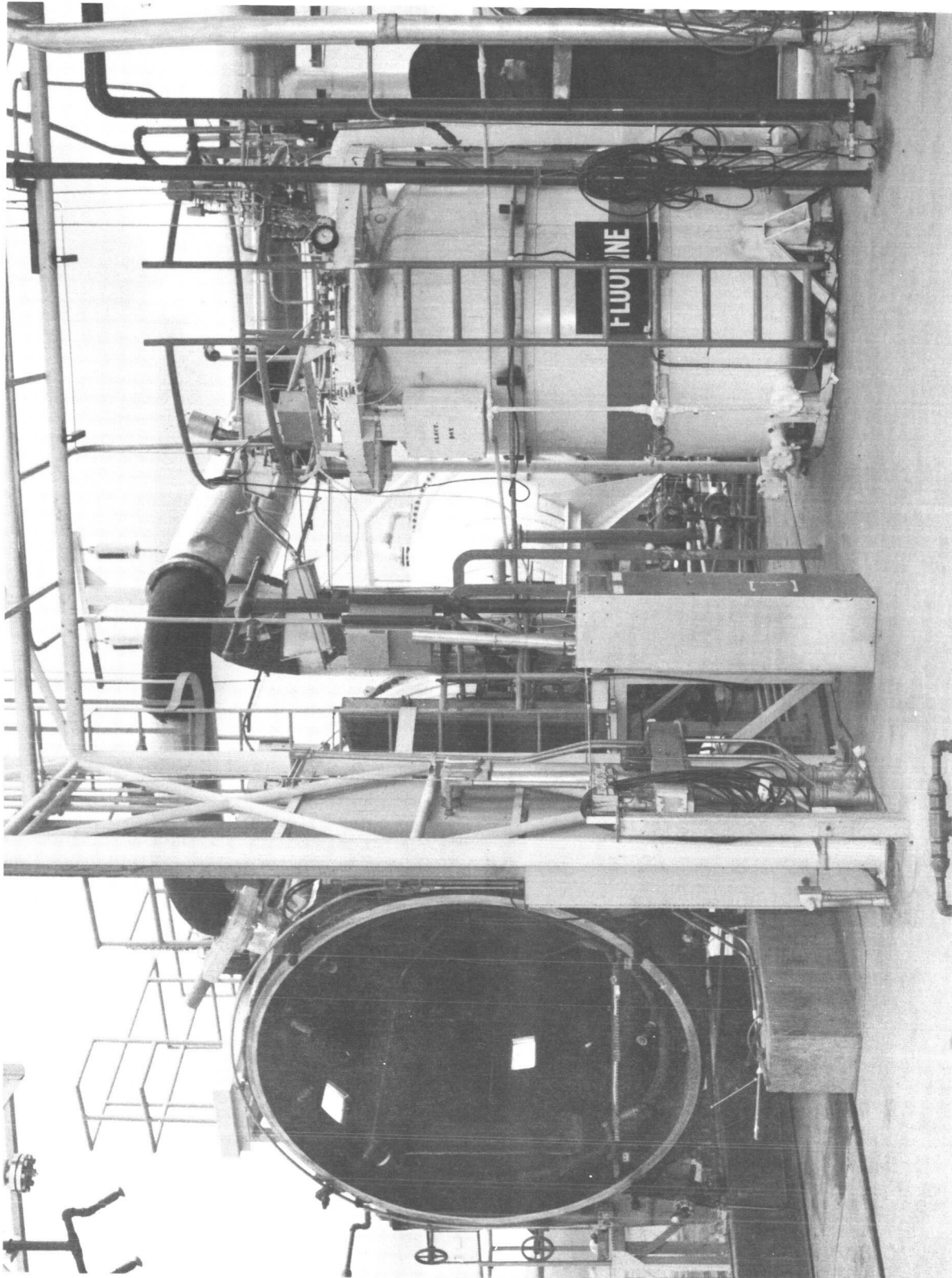


Figure 100. NFL 4B Fluorine Tank Installation

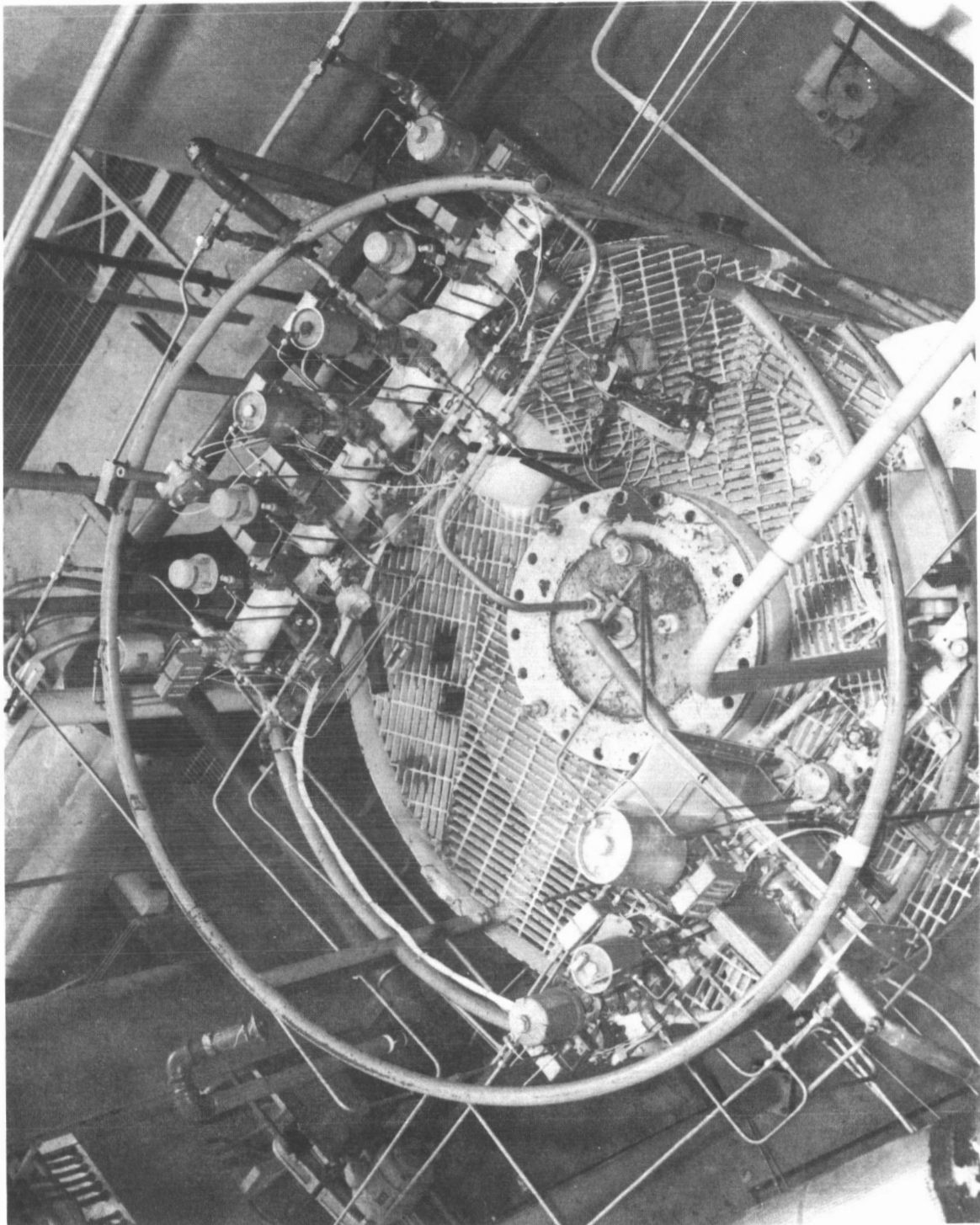


Figure 101. NFL 4B Fluorine Tank Control System



This phenomenon was isolated to the tank discharge (vertical from the top of the tank) or dip tube portion of the system, and was related to a non-jacketed section of line from the liquid surface to the vacuum tank flange. The accumulator, which is liquid nitrogen jacketed and has sufficient volume for a complete series of engine tests, resolved the problem. Downstream of the liquid fluorine main valve, a T-section was installed as shown to allow a liquid nitrogen bleed through the main propellant feed line to the engine and through the injector. This chills the injector assembly and minimizes fluorine flashing at engine start, and consequently minimizes start transient variations.

Hydrogen System

Hydrogen was stored in, and used directly from a high-pressure mobile trailer. This hydrogen was supplied by the high-pressure pumping system in Area D at NFL. The overall system is shown in the schematic.

Chamber Pressure Operating Range

As noted in the Test Results section, the maximum chamber pressure obtained during Task III was approximately 180 psia. It was originally intended to operate over a range of 50 to 200 psia as had been demonstrated in the Task II portion of the program. However, the completed propellant system could not, within the tank pressure limitations of 475 psi on fluorine and 2400 psi on hydrogen, reach this design objective. It was decided that this pressure value was sufficiently high to establish the relationship between performance and pressure. Therefore, all high-pressure tests were scheduled for 175 psia.



CONTROL SYSTEM

Variation in propellant flowrates, and consequently either chamber pressure or mixture ratio, is accomplished by a servocontrolled pressurizing system for the fluorine tank and by a servocontrolled regulator for the hydrogen sonic venturi upstream pressure. The system was designed such that several mixture ratios could be selected by setting a series of potentiometers which are wired to a selector switch. Changing the selector switch automatically readjusts the pressures to the required levels.

The only problem experienced in connection with system operation was in the response and damping ratio of the hydrogen system. The system is very susceptible to the ratio of manifold (storage bottle) pressure to regulated pressure. If this ratio is high, the system tends to oscillate at approximately 1 cps. Depending upon the amplitude, this oscillation may or may not be reflected in chamber pressure. Several times during the program, changes were made in the gain and damping ratio of the servoamplifier to adjust for this problem, and several test data points were lost because of high hydrogen flowrate variations during single tests. This condition was alleviated by the system adjustments and by changing the start sequence to give a long fuel lead, approximately 1 second, as compared to the initial tests, which used simultaneous flow start.

INSTRUMENTATION

The necessity of determining small differences in performance among various nozzle designs dictated that special emphasis be placed upon instrumentation and instrumentation systems. Initial evaluation of the requirements revealed that certain parameters were critical for determining performance; i.e., flowrates, thrust, and chamber pressure. For this reason, the critical items in these measurements were made redundant. Table 11 is a listing of the various measurements made, and their respective locations are shown in Fig. 102.



TABLE 11

INSTRUMENTATION

Hydrogen System

Supply Manifold Pressure	DIGR*
Venturi Upstream Pressure Redundant (2)	DIGR
Venturi Upstream Temperature-Redundant (2)	DIGR
Venturi Downstream Pressure	DIGR

Fluorine System

Tank Pressure	DIGR
Flowmeter Pressure-Redundant (2)	DIGR
Flowmeter Temperature-Redundant (2)	DIGR
Flowrate-Redundant (2)	DIGR and Oscillograph

Engine

Chamber Pressure, Injector End-Redundant (2)	DIGR and Oscillograph
Chamber Pressure, Nozzle Inlet-Redundant (3)	DIGR and Oscillograph
Hydrogen Injector Pressure	DIGR and Oscillograph
Hydrogen Injection Temperature	DIGR
Fluorine Injection Pressure	DIGR and Oscillograph
Fluorine Injection Temperature	DIGR
Nozzle Pressure - ϵ = 1.5, 3, 7, 15, 30, 60	DIGR
Nozzle Temperature - ϵ = 1, 7, 15, 30, 60	Oscillograph
Thrust-Redundant (2) (4 for Task IV)	DIGR and Oscillograph
Accelerometer	Oscillograph
Altitude Capsule Pressure	DIGR

*Direct-Inking
Graphic Recorder

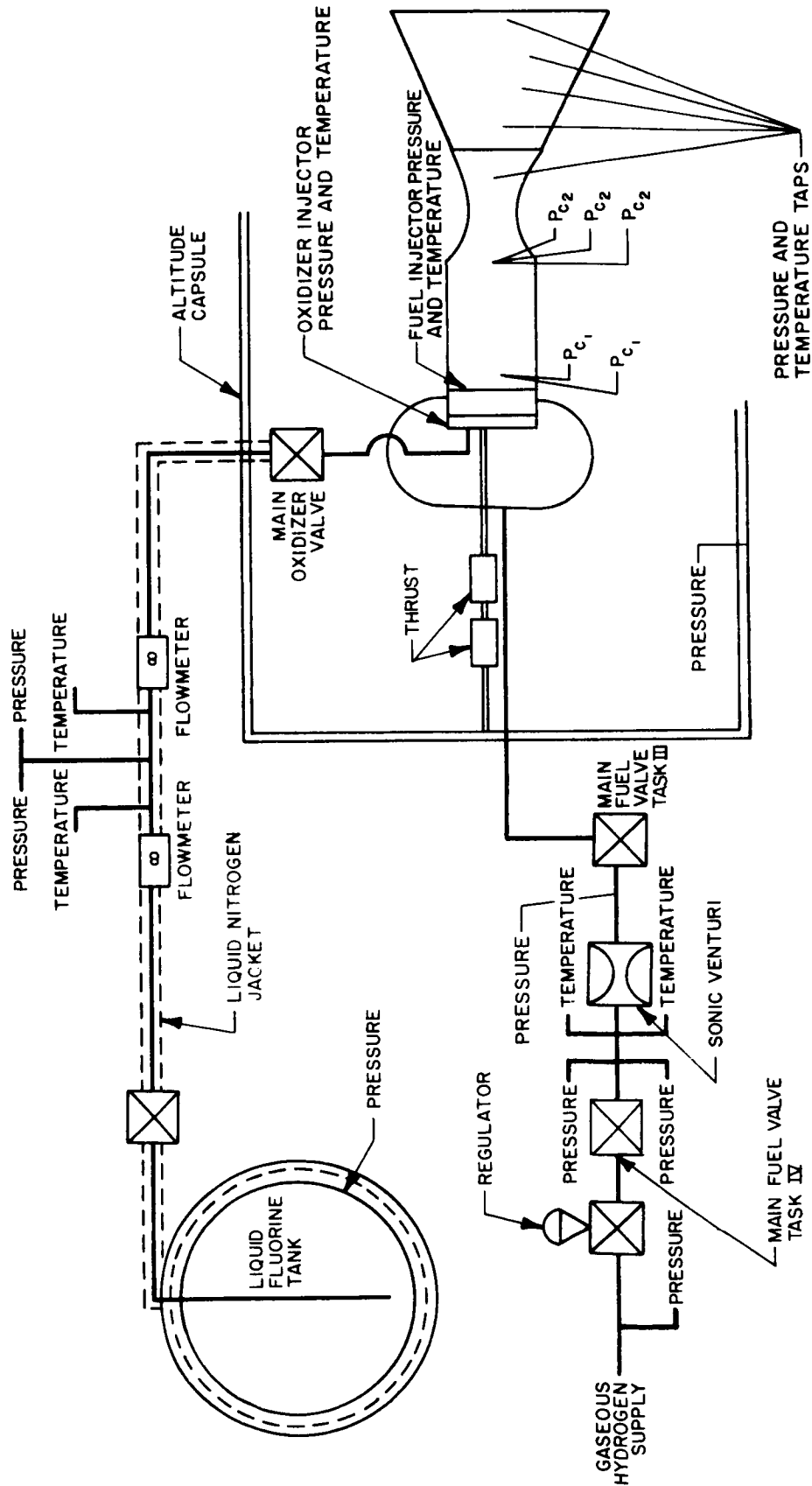


Figure 102. NFL 4B Test Stand Instrumentation Schematic



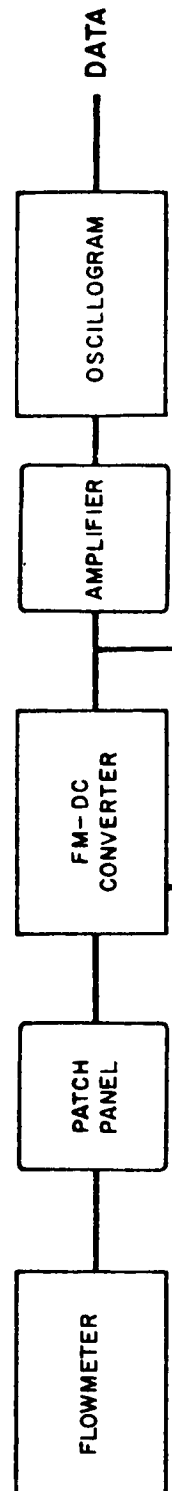
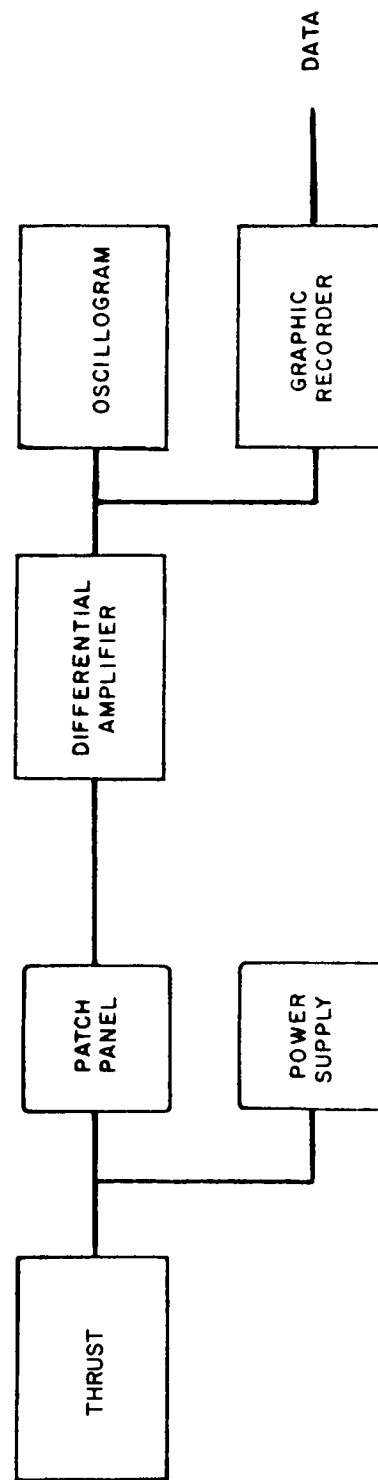
Instrumentation capabilities at the NFL facility include conventional direct-inking graphic recorders (DIGR), oscillograph, and tape and sequence recorders. There are 64 Foxboro circular-type recorders, which provide high accuracy at minimum response for precise steady-state performance characterization, 3 oscillographs with 36 channels each, and 2 tape recorders with 7 channels each for high-frequency measurements. In addition, there are 3 Esterline Augus sequence recorders with 40 channels each. Figure 103 is a block-diagram representation of the various instrumentation systems.

For this program, primary performance calculations were all based upon the DIGR measurements except for the liquid fluorine flowmeter outputs, which were recorded directly on an oscillograph. The other oscillograph measurements were used to monitor engine performance with respect to combustion oscillations.

Thrust

The thrust chamber assembly was supported by pinned members in the radial direction, which allowed free movement parallel to the engine axis. Measurement was made by series Baldwin-Lima-Hamilton double-bridge load cells. These cells, one for high-thrust-range operation (5000 pounds) and one for the lower ranges, provide a redundant measurement by the double-bridge network. For Task IV, two low-range load cells provided four thrust measurements for each test.

Calibration of the load cells was conducted before and after each hyperflow test by means of a separate calibration load cell and a manually operated hydraulic loader. This load cell was previously calibrated against a proving ring traceable to the National Bureau of Standards.



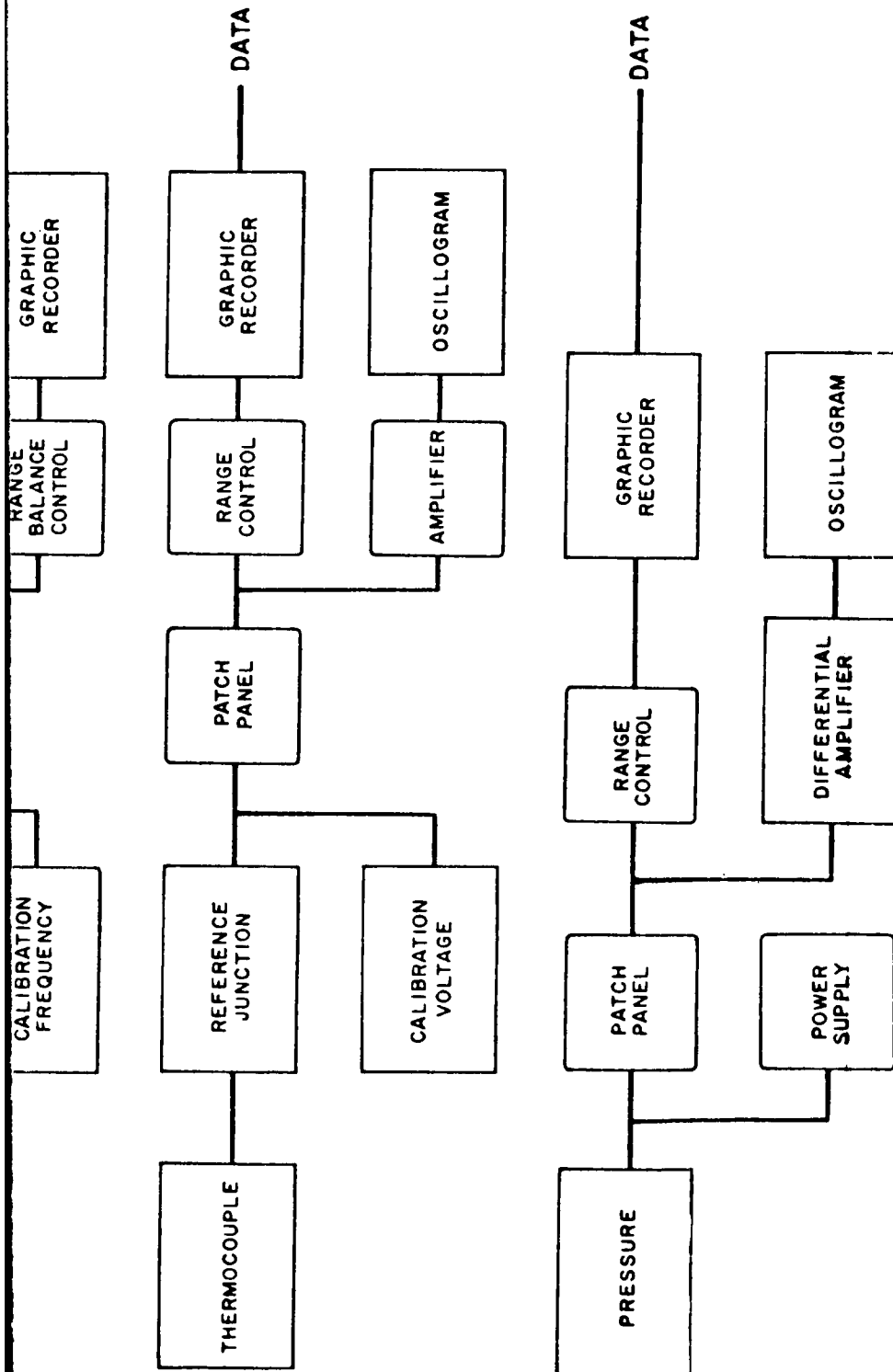


Figure 103. Measurement Systems, Block Diagram



The system loads the run transducers in the same manner as the engine, through a yoke-tension rod assembly. The procedure includes an upscale and downscale calibration in six to eight equal increments. Thus, a check of both system linearity and hysteresis is made prior to each test. From the calibration, a key number at the expected run value was calculated. To minimize test stand effects, propellant plumbing was mounted radially to the engine with long, straight sections to allow free movement of the chamber assembly; in addition, all instrumentation lines had S-shaped sections and, as stated previously, all support mountings were radial with pinned joints at either end. A constant surveillance of calibration and installations was maintained to ensure that no binding or drag was occurring.

Pressure

Pressure measurements were made throughout the system as indicated in the table and figure with multiple measurements for those parameters critical to performance calculations, such as chamber pressure and sonic venturi inlet pressure.

Transducers were of the bonded strain gage, d-c type. These were calibrated on receipt to determine that they satisfied the specifications as to linearity, hysteresis, zero balance, and sensitivity. When these tests were passed, repeated verifications of the transducer sensitivity were made, and a calibration precision of the transducer was established. The calibration and verifications were accomplished with a dead weight tester or similarly precise calibration device traceable to the National Bureau of Standards. The transducer outputs for given pressure inputs were measured and recorded. The transducer output, with zero pressure applied



and the calibration resistor shunted across one leg of the bridge, was recorded. From these two measurements, the transducer key number or pressure equivalent to the unbalance output was determined. This key number was redetermined in subsequent verifications and its repeatability is the transducer precision.

Calibration of the recording system and establishment of the scale factor for each pressure measurement was accomplished by inputting a standard voltage. This generally is 80-percent transducer output and corresponds to the key number determined previously.

Flow Measurement

Fuel. Hydrogen flowrate was measured by a specially fabricated flow section containing a sonic venturi. This section, which contained upstream pressure and temperature and downstream pressure measurement provisions, was calibrated by the manufacturer (Ref. 25) and was similar to that used in Task II. The calibration for this nozzle is shown in Fig. 105 was calculated by standard procedures (Ref. 26).

Flowrate then is

$$\dot{w} = \frac{KP}{\sqrt{T_1}}$$

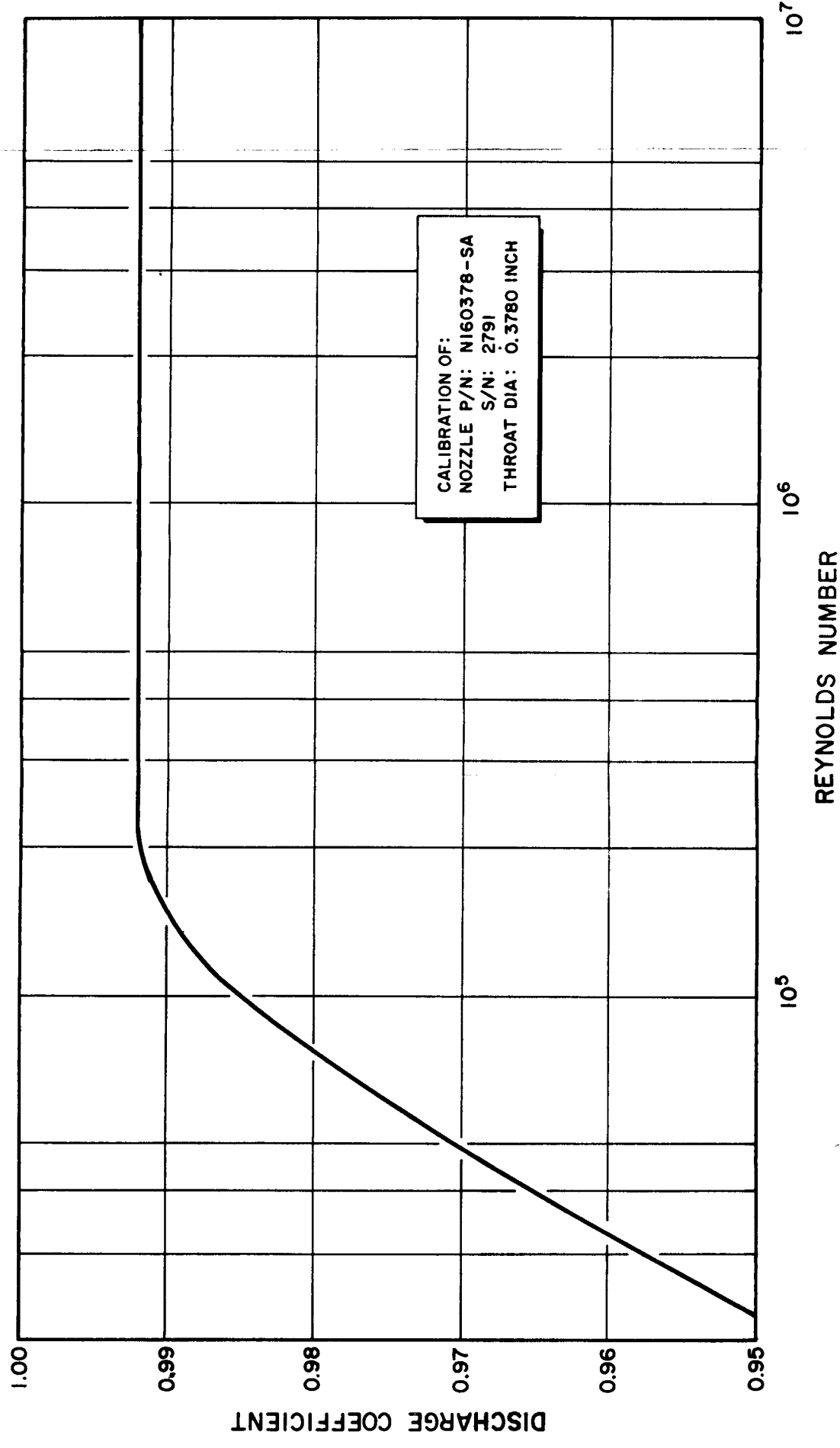


Figure 104. Discharge Coefficient vs Reynolds Number for Hydrogen Sonic Venturi

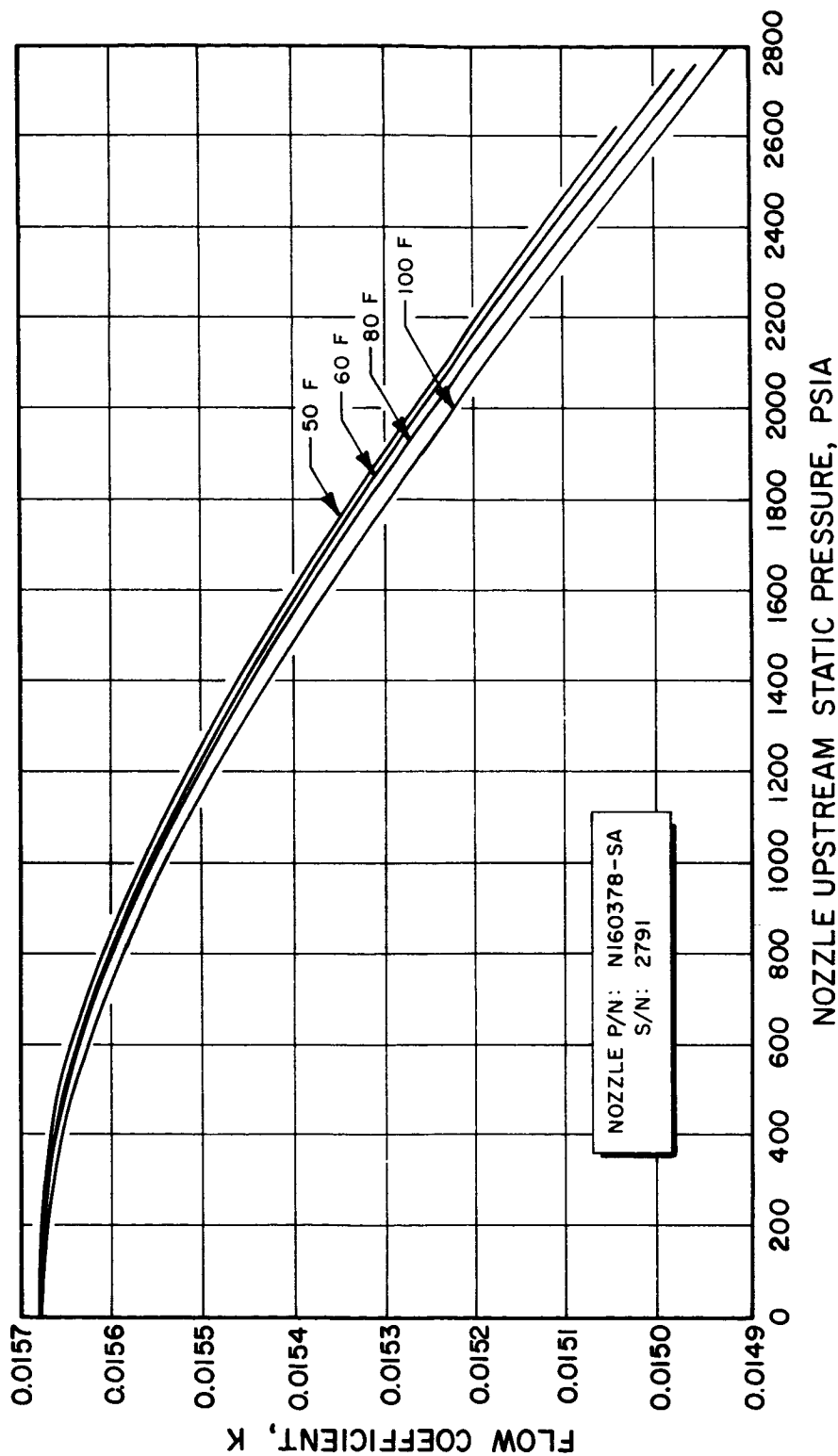


Figure 105. Flow Coefficient vs Nozzle Inlet Pressure (Hydrogen Gas Only)



where

K = flow coefficient

P = upstream pressure, psia

T_1 = upstream temperature, R

Oxidizer. Fluorine flowrate was measured using Fisher-Porter turbine-type volumetric flowmeters. These meters were calibrated at the SSFL flowmeter calibration bench prior to installation at NFL. This calibration, carried out over the range of interest for the flowmeter, was repeated several times. Figure 106 is plot of a typical flowmeter calibration. The points indicated are the test data, while the curve is an exponential fit to the data. This fit is calculated by a standard computer program which allows up to a fifth-order equation. The precision indicated is the precision of the curve fit to the test data. The plot is cycles per gallon vs cycles per second divided by viscosity.

Reduction of the flowmeter output to actual flow is discussed in the data reduction section.

Temperature

Fluorine temperature was measured using shielded platinum resistance bulbs, manufactured by Rosemount Engineering, immersed in the liquid stream. These transducers are calibrated by the vendor and are checked on receipt by immersion in liquid nitrogen.

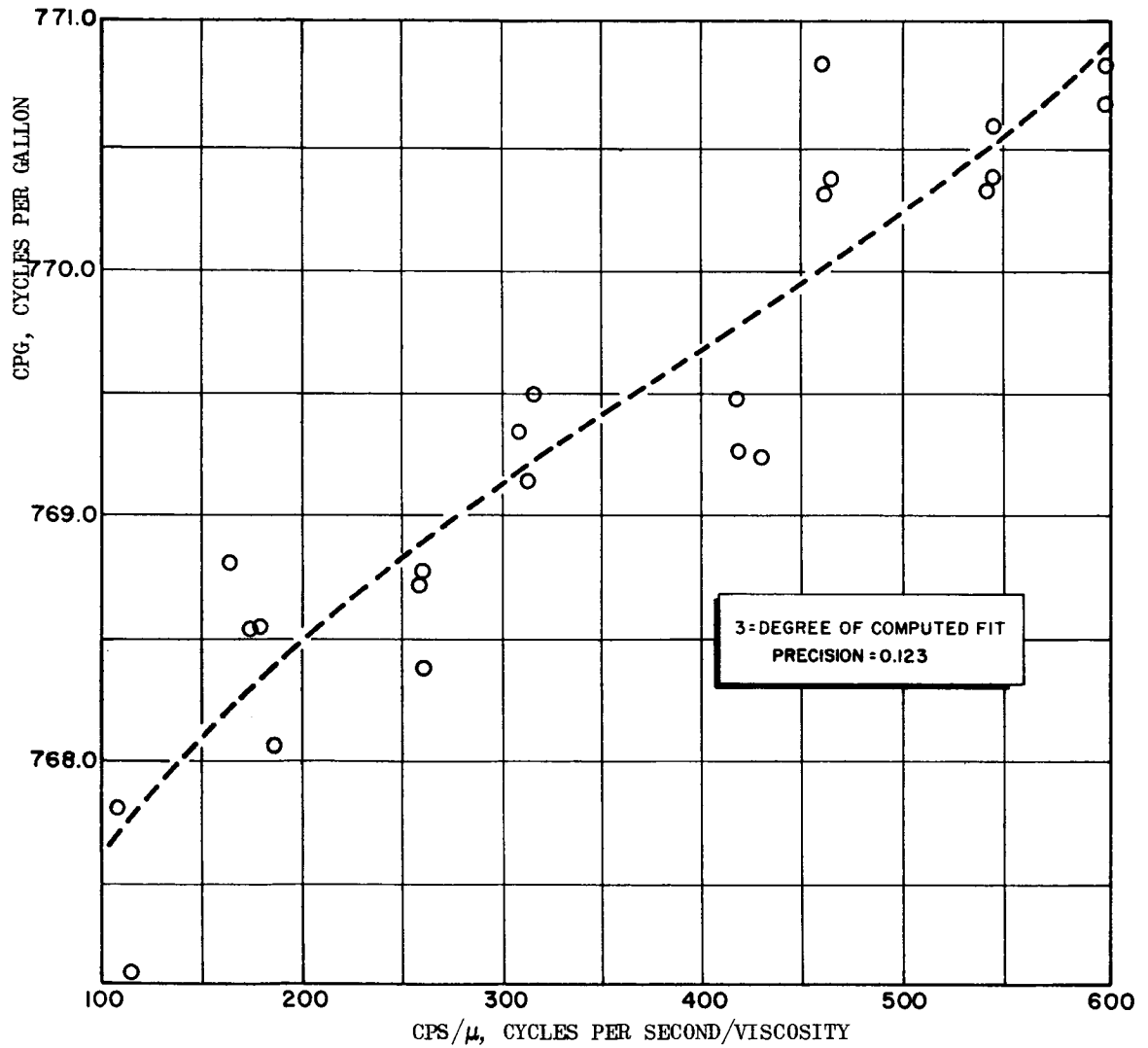


Figure 106. Typical Flowmeter Calibration



Thermocouples were assumed to follow standard National Bureau of Standards millivolt/temperature tables. Recorders were scaled according to expected values and calibrated electrically. Iron-constantan thermocouples were used for the hydrogen temperature measurements and for the major portion of the thrust chamber temperatures used in the heat transfer calculations.

TEST PROCEDURE

Fluorine Analysis

Periodic samples of the liquid fluorine were taken and analyzed to ensure that propellant quality satisfied the specification requirements. The propellant composition is shown in the Performance Analysis section.

Fluorine System Passivation

Prior to assembly, the fluorine system components were thoroughly cleaned and passivated by etching in nitric acid. The system up to the main valve was assembled and leak checked with helium at full working pressure. The system was then passivated with gaseous fluorine starting at low pressure and building up to 50 psi. The system was allowed to stand overnight.

The oxidizer feed line downstream of the main valve was passivated immediately prior to each test series by flowing fluorine through the system.



Test Sequence

Each hyperflow test consisted of several engine tests at a constant chamber pressure but at varying mixture ratios. Firings were sequenced through an automatic timer which controls operation of all system valves; however, the engine sequence start was initiated manually. This was to ensure that propellant tank pressures which were varied to control mixture ratio had reached proper values prior to test start. The facility operating sequence is described below:

1. Hyperflow start: hyperflow ignition established by an automatic sequence but verified visually prior to opening the main propellant valves. After main stage is established, the isolation valve is opened and the test capsule reaches altitude.
2. Engine test: initiated manually with start and shutdown sequences and duration controlled automatically (repeated as required).
3. Hyperflow shutdown: initiated manually with the isolation valve closed prior to sequenced shutdown procedure; capsule vented to atmospheric pressure with the isolation valve closed.

Engine test durations were varied as a function of the nominal chamber pressure with 4 seconds for 50 psia, 3 seconds for 100 psia, and 2 seconds for 175 psia. These durations were selected to minimize chamber wall temperature but still provide sufficient stabilized engine operation for performance evaluation.

The engine operating sequences for both start and shutdown are shown in Fig. 107.

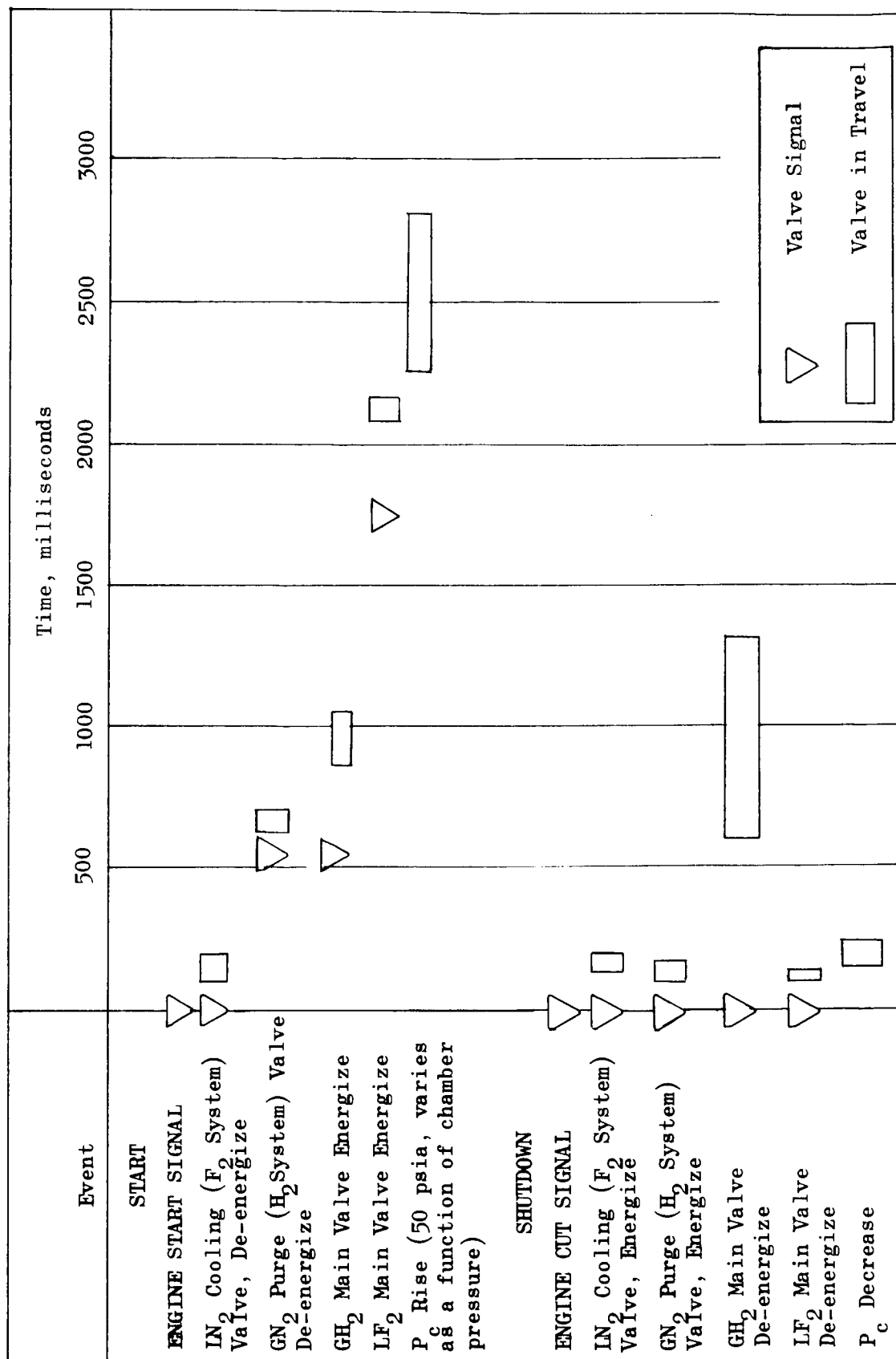


Figure 107. Engine Start and Shutdown Sequence



During the test setup, the fluorine system from the main valve to the engine was purged with gaseous nitrogen to ensure that all water vapor and contaminants were removed. Following this, liquid nitrogen was bled through this line and the injector to chill the system and minimize start transient variations caused by propellant flashing in the injector. As the sequence shows, the liquid nitrogen was shut off at the sequence start and was started again right at engine shutdown. This assured that the system was always primed and consequently prevented contamination from entering during the start or shutdown sequence. All purges were closed for approximately 6 seconds at 3 seconds after engine shutdown to allow a "zero" to be obtained on the thrust system. The purges were then reactivated until the next engine sequence start. A minimum of about 15 seconds was required between engine tests to accomplish the thrust zero and to readjust the tank pressures for the subsequent test.

A hydrogen lead of approximately 1 second was utilized to ensure stabilization of servocontrol systems. During the shutdown, the fuel system gaseous nitrogen purge was initiated prior to the main valve reaching a closed position. This again assured that no contaminants entered the system. Fuel leads from zero to 1.5 seconds were tried during the program with no adverse ignition effects.



PERFORMANCE DATA REDUCTION AND EVALUATION

To facilitate a thorough understanding of the performance test results, this section contains a detailed description of the procedures used to reduce and evaluate the Task III and IV performance test data. The computations are divided essentially into two categories: (1) data reduction to convert the test readings to pressures, thrust, temperatures and flow-rates, and (2) data evaluation to determine the performance parameters of interest. A sample case is followed through each step. The example selected is bell test 013, at the midpoint of the nominal test matrix, chamber pressure = 100 psia, mixture ratio = 12:1.

DATA REDUCTION

Reduction of basic test readings to performance data suitable for use in the nozzle analysis study was accomplished using standard procedures developed by the instrumentation and measurement analysis subsections of the Rocketdyne test organization. In addition, specific procedures were established at the program level to handle redundant measurements made during this phase of the test program.

Table 12 is a typical data reduction form used for this program. It shows the test deflections as read from the appropriate recorder, the recorder-transducer electrical zero, the "R-Cal" or electrical unbalance, and the transducer key number and precision where applicable. The final column shows the reduced value for the various parameters.



TABLE 12

DATA REDUCTION TABLE FOR TEST 013

Parameters	Zero	R-Cal	Test Deflection	KN	Precision	Reduced Value
Trailer Manifold Pressure	-0.2	79.7	65.5	2399.74	0.093	1973.3
GH ₂ Venturi Upstream Pressure No. 1, psig	-0.5	79.3	19.3	3494.82	0.050	594.6
GH ₂ Venturi Upstream Temperature No. 1, F	--		41	--	--	41
GH ₂ Venturi Upstream Pressure No. 2, psig	+0.1	79.2	20.2	2397.47	0.093	609.0
GH ₂ Venturi Upstream Temperature No. 2, F	--		42	--	--	42
GH ₂ Venturi Downstream Pressure, psig	-0.2	78.9	31.7	798.036	0.095	321.8
GH ₂ Venturi Downstream Temperature, F	-1.3	78.1	40.1	280.329	0.078	146.3
GH ₂ Injection Pressure, psig	+2.5	81.1	37.7	397.983	0.105	178.3
LF ₂ Tank Pressure, psig	+0.2	78.7	30.2	397.885	0.130	153.4
LF ₂ Flowmeter No. 1 Pressure, psig	--		20.0	--	--	-315.0
LF ₂ Flowmeter No. 1 Temperature, F	+0.2	78.7	30.1	402.648	0.540	153.6
LF ₂ Flowmeter No. 2 Pressure, psig	--		20.0	--	--	-315.0
LF ₂ Flowmeter No. 2 Temperature, F	+0.2	78.8	25.4	400.962	0.132	128.6
LF ₂ Injection Pressure, psig	--		25.0	--	--	-312.3
LF ₂ Injection Temperature, F	+0.3/+1.1	96.5	76.2	2904.75	--	2267.6
Thrust No. 1, pounds	-0.3/+1.2	96.0	76.2	2910.65	--	2266.7
Thrust No. 2, pounds	-0.4	78.9	87.0	80.147	0.113	88.39
Injector-End Pressure No. 1, psig	-1.2	77.4	86.0	79.887	0.119	88.68
Injector-End Pressure No. 2, psig	-3.0	76.3	78.4	79.942	0.109	82.11
Start of Contraction Pressure No. 1, psig	-1.9	77.2	79.2	80.008	0.589	82.08
Start of Contraction Pressure No. 2, psig	-4.3	74.8	77.5	79.705	0.130	82.43
Start of Contraction Pressure No. 3, psig	10.8	78.5	43.2	-10.550	0.539	6.54
Pressure at $\epsilon = 1.5$, psia	13.7	81.6	31.7	-10.470	0.132	4.35
Pressure at $\epsilon = 3$, psia	11.2	85.5	41.7	3.6042	0.074	1.98
Pressure at $\epsilon = 7$, psia	11.2	86.0	16.6	--	--	0.82
Pressure at $\epsilon = 15$, psia	13.5	82.5	73.4	--	--	0.64
Pressure at $\epsilon = 30$, psia	10.3	81.9	77.5	--	--	0.15
Pressure at $\epsilon = 6$, psia	10.8	82.9	67.9	--	--	0.135
Altitude Pressure, psia	--		188/0.6	--	--	313.33
LF ₂ Flowrate No. 1, cps	--		194/0.6	--	--	323.33
LF ₂ Flowrate No. 2, cps	--		24.512	--	--	12.04
Ambient Pressure, psia						



Pressure Measurements

The method for reduction of pressure transducer data is dependent on the type of the transducer. For a psig transducer, the measured pressure is determined by the use of the KN concept as follows:

$$P_m = \left(\frac{KN}{D_R - D_A} \right) (D_X - D_A)$$

where

P_m = measured pressure, psig

KN = key number, psig, physical input to a transducer corresponding to a specified electrical unbalance

D_A = system zero, when transducer is vented to atmospheric pressure

D_R = R-Cal deflection, recorder deflection for a specified electrical unbalance

D_X = test deflection

Figure 108a is an example of how the chart is read. As an example:

P_{c2} No. 1 for test 013

$$P_{c2} = \left(\frac{79.942}{76.3 - (-3.0)} \right) (78.4 - (-3.0)) = 82.11 \text{ psig}$$

For psia measurements, two methods are used which are dependent on the range of the transducer. For 0 to 15 psia, the measured pressure is calculated by means of KN concept, as follows:

$$P_m = \left[\left(\frac{KN}{D_R - D_A} \right) (D_X - D_A) \right] + P_a$$

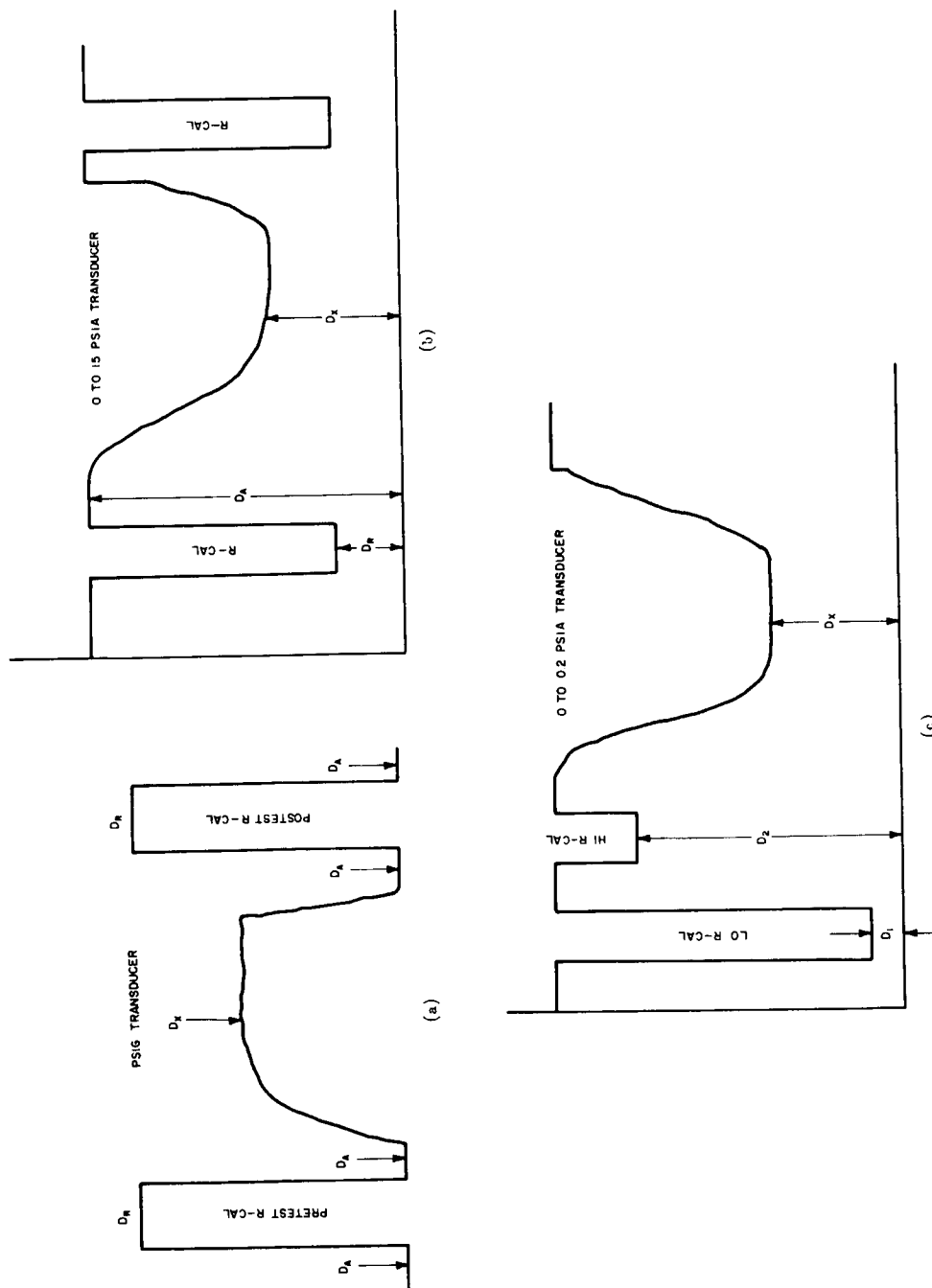


Figure 108. Sample Pressure Recordings



where

P_m = measured pressure, psia

P_a = ambient pressure, psia, at the time of the test

Figure 108b is an example of the chart while as an example:

$$P_e = 1.5 \text{ for test 013}$$

$$P_e = 1.5 = \frac{-10.550}{10.8 - 78.5} (43.2 - 78.5) + 12.04 = 6.54 \text{ psia}$$

For a psia transducer with a high-low R-Cal, which is typical of the low-range transducer such as 0 to 0.2 psia, used for nozzle pressure and altitude capsule measurements, the procedures are:

$$P_m = \left[\left(\frac{KN}{D_2 - D_1} \right) (D_X - D_1) \right] + P_3$$

where

P_m = measured pressure, psia

D_1 = chart zero to low R-Cal

D_2 = chart zero to high R-Cal

P_3 = intercept of the transducer which is the pressure equivalent to the low R-Cal electrical unbalance as established during calibration, psia

Figure 108c is an example of this type of chart.

This procedure was not followed directly for the test data reduction in that a plot of transducer reading vs voltage output was made, and the R-Cal read in terms of voltages. This simplifies the reduction in that the



intercept value can be the base point for the plot, and consequently, the chart can be read essentially directly.

Multiple Measurements. For averaging of the various parameters when multiple measurements were made, in particular the nozzle inlet pressure P_{c2} , it was decided that the precision of the various transducers should be taken into account. A weighted average based on this precision was selected as the most satisfactory method. Typically for reduction then:

$$P_{c2} \text{ for test 013} = \left[P_{c2} \text{ No. 1} \left(\frac{1.0}{0.109} \right) + P_{c2} \text{ No. 2} \left(\frac{1.0}{0.589} \right) + P_{c2} \text{ No. 3} \left(\frac{1.0}{0.130} \right) \right] / \left(\frac{1.0}{0.109} \right) + \left(\frac{1.0}{0.589} \right) + \left(\frac{1.0}{0.138} \right) = 82.24 \text{ psig}$$
$$P_{c2} = (82.24 + 12.04) \text{ psia}$$
$$= 94.28 \text{ psia}$$

Flowrates

Hydrogen. Hydrogen flowrates were read directly from the curves shown in Fig. 109. These were generated from the calibration data of the sonic venturi and show flowrate as a function of venturi upstream pressure and temperature.

As an example for \dot{w}_f for test 013:

$$\text{Average Upstream Venturi Pressure} = 599.6 + 12.04 = 611.64$$

$$\text{Upstream Venturi Temperature} = 41.5 \text{ F}$$

$$\dot{w}_f = 0.427 \text{ lb m/sec}$$

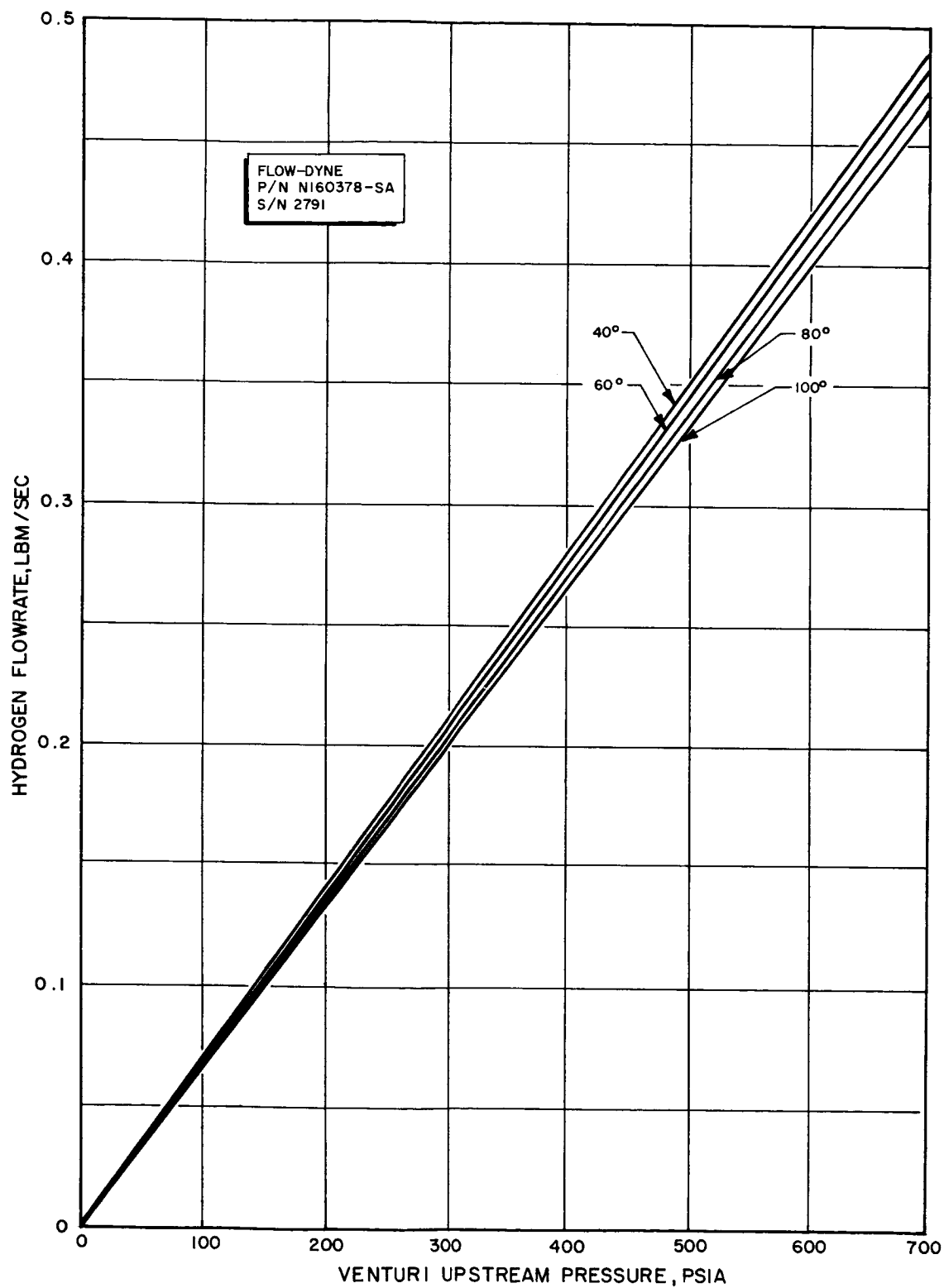


Figure 109. Hydrogen Flowrate vs Venturi Upstream Pressure



Fluorine. Fluorine flowrates were computed using the water calibration data from a calibration curve as shown in the facility section.

$$\dot{w}_0 = \frac{K \text{ (CPS)} (\text{SpG})_{\text{LF}_2}}{(\text{CPG})}$$

where

K = conversion constant for gal/sec to lb/sec

CPS = test run reading of cycles per second determined from oscillograph

$(\text{SpG})_{\text{LF}_2}$ = fluorine specific gravity at test conditions

(CPG) = cycles per gallon corrected for H_2O viscosity from the calibration curve

Specific gravity for fluorine is determined from the density vs temperature and pressure curves shown in Fig. 110. As an example of a fluorine flowrate calculation:

$$\dot{w}_0 \text{ No. 1} = \frac{0.13372 (313.33) (96.52)}{(772.79)} = 5.233 \text{ lb m/sec}$$

A later correction was made to account for impurities which are present because the density curve assumes pure fluorine. This is discussed in the data evaluation section of this sample data analysis.

Thrust

Vacuum thrust was computed in a two-step operation. Site thrust is determined by the KN method as:

$$F_M = \left[\frac{KN}{(D_R - D_A)} (D_X - D_B) \right]$$



where

F_M = measured thrust, pounds

D_A = system zero at the time the R-Cal is taken

D_R = R-Cal deflection

D_B = system zero at each engine test

D_X = test deflection

The system zero at each test is utilized to account for any zero shift caused by temperature or by the unbalanced forces that exist when the altitude system is started.

Site thrust for the two measurements was computed as above using the average key number from the pretest and post test calibrations. The two thrust measurements were then averaged and vacuum thrust computed by adding a correction for the altitude capsule pressure.

$$F_M \text{ No. 1} = \frac{2904.75}{(96.5 - 0.3)} (76.2 - 1.1) = 2267.6 \text{ lbf}$$

$$F_M \text{ No. 2} = 2266.7 \text{ lbf}$$

$$F_M \text{ average} = 2267.2 \text{ lbf}$$

$$P_A = \text{altitude capsule pressure} = 0.135 \text{ psia}$$

$$A_e = \text{nozzle exit area} = 827.18 \text{ sq in.}$$

$$F_{\text{vac}} = F_M \text{ average} + P_A A_e = 2267.2 + 111.7 = 2378.9 \text{ lbf}$$

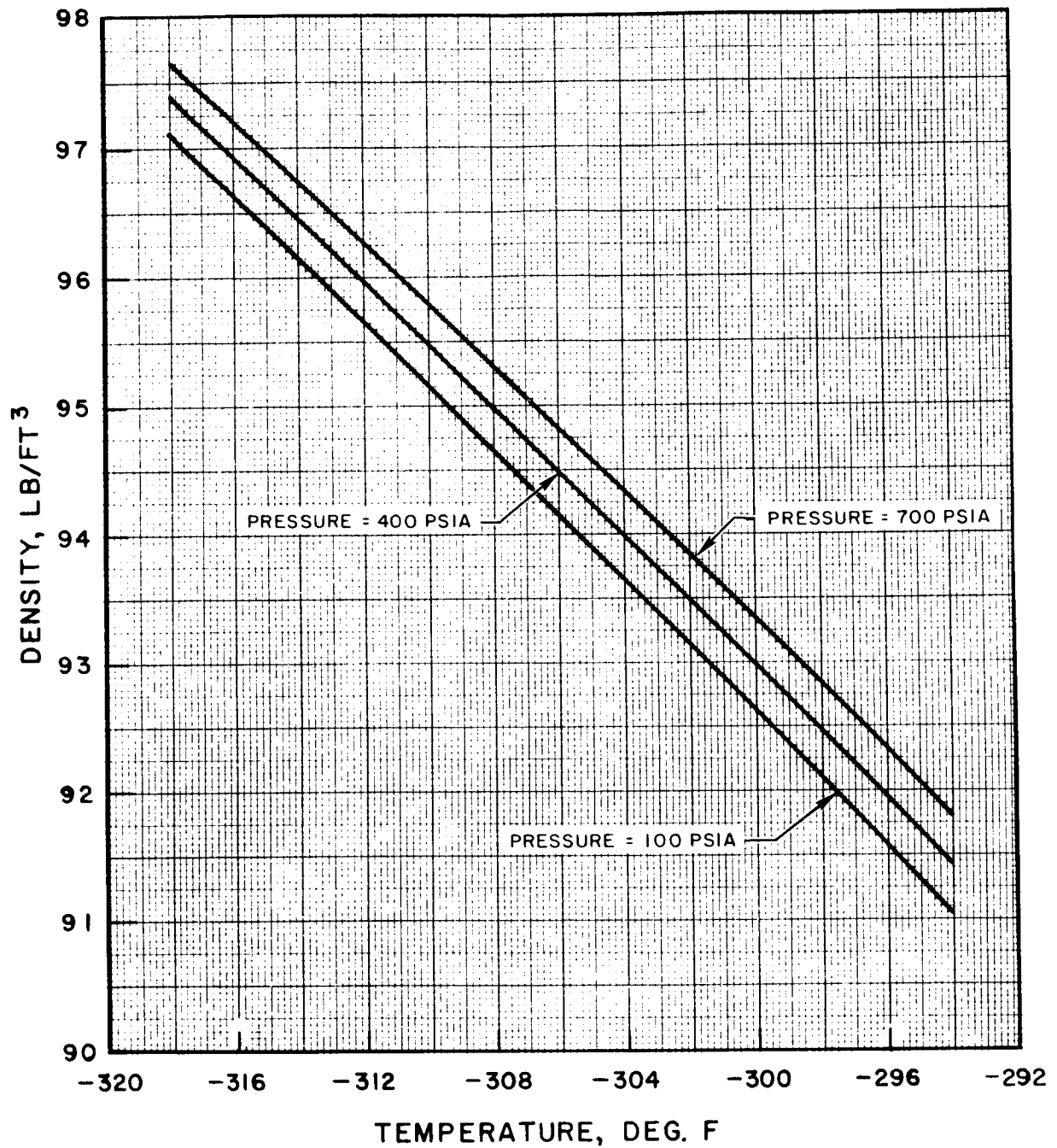


Figure 110. Variation of Liquid Fluorine Density with Temperature at Indicated Pressures.



DATA EVALUATION

The previous data reduction has produced the thrust, pressure, and flowrate data necessary to generate the desired performance parameters. The following calculations will convert these quantities to the kinetic and thrust chamber efficiencies.

Test Conditions

To obtain the stagnation pressure from the start-of-contraction static pressure P_{c2} , the assumption is made that the flow in this region is uniform and parallel and possesses the same stagnation-to-static pressure ratio as it would if it were in perfect chemical equilibrium. For fluorine/hydrogen at a contraction ratio of 2.05:1, this value is 1.054. Thus, the stagnation pressure is

$$P_c = (1.054) \times (94.28) = 99.37 \text{ psia}$$

The flowrate computed previously was based on the assumption of pure fluorine. For test No. 13 it is seen from Table 5 in the Performance Analysis section that the oxidizer was actually 98.5-percent fluorine and is only 99.04 percent as dense. Therefore the corrected oxidizer flowrate is

$$\begin{aligned}\dot{w}_{\text{oxid}_{\text{corr}}} &= (\dot{w}_{\text{oxid}})_{\text{ave}} \times (\rho_{\text{corr}_{\text{oxid}}}) = (5.270) \times (0.9904) \\ &= 5.219 \text{ lbm/sec}\end{aligned}$$

where

$$(\dot{w}_{\text{oxid}})_{\text{ave}} = \text{average apparent flowrate for pure fluorine}$$

$$\rho_{\text{corr}_{\text{oxid}}} = \text{density correction caused by impurities}$$



The correct mixture ratio is then

$$MR_{\text{corr}} = \frac{\dot{w}_{\text{oxid corr}}}{\dot{w}_{\text{H}_2}} = \frac{5.219}{0.427} = 12.21$$

The total flowrate is

$$\dot{w}_{\text{total corr}} = \dot{w}_{\text{oxid corr}} + \dot{w}_{\text{H}_2} = 5.219 + 0.427 = 5.646 \text{ lbm/sec}$$

For test 13, the geometric throat area was 13.84 sq in.

Characteristic Velocity (c^*)

The uncorrected c^* can be computed as

$$c^*_{\text{unc}} = \frac{P_c A_t g_c}{\dot{w}_{\text{total corr}}} = \frac{(99.37) \times (13.84) \times (32.174)}{5.646} = 7837.1 \text{ ft/sec}$$

The uncorrected c^* value is easily determined but is neither compatible with the definition of the theoretical thermochemical c^* , nor ~~is it~~ a measure of injector efficiency. To correct the c^* value, the throat area must be converted to aerodynamic throat area, and the c^* value must be converted to the conditions of no heat loss and pure fluorine. The ratio of aerodynamic to geometric throat area is the discharge coefficient C_D with a numerical value of 0.9945. The c^* correction caused by heat loss $\xi_{\text{HL } c^*}$ is seen from Fig. 57 to be 1.0084. The presence of impurities in the fluorine reduces the maximum attainable c^* , giving a correction factor, $\xi_{\text{I } c^*}$ from Table 5, of 1.0024.



The corrected c^* can then be computed as

$$c^*_{\text{corr}} = c^*_{\text{unc}} \times C_D \times (\xi_{HL_{c^*}} + \xi_{I_{c^*}} - 1.0) = (7837.1) \times (0.9945) + (1.0084 + 1.0024 - 1.0) = 7878.3 \text{ ft/sec}$$

For the test 13 parameters, the theoretical c^* value is found from Fig. 135 in the Performance Map section to be 8000 ft/sec. Thus, the corrected c^* efficiency ($\eta_{c^*_{\text{corr}}}$) is

$$\eta_{c^*_{\text{corr}}} = \frac{c^*_{\text{corr}}}{c^*_{\text{theo}}} = \frac{7878.3}{8000} = 0.9848$$

This efficiency is a direct measure of injector excellence. The loss modes which have been corrected for are properly attributable to the thrust chamber (discharge coefficient and heat loss) or the propellant (impurities), and will be accounted for in the following steps.

Vacuum Specific Impulse (I_{vac})

The delivered vacuum specific impulse is computed to be

$$I_{\text{vac}_{\text{test}}} = \frac{F_{\text{vac}}}{\dot{w}_{\text{total}_{\text{corr}}}} = \frac{2378}{5.646} = 421.2 \frac{\text{lbf-sec}}{\text{lbm}}$$

The theoretical chemical equilibrium value is found from Fig. 138 of the Performance Map section to be 485 lbf-sec/lbm. The delivered efficiency is thus

$$\eta_{I_{\text{vac}_{\text{test}}}} = \frac{I_{\text{vac}_{\text{test}}}}{I_{\text{vac}_{\text{theo}}}} = \frac{421.2}{485.0} = 0.8684$$



Thrust Chamber Efficiency (η_{TC}) and
Kinetic Efficiency (η_K)

$$\eta_{TC} = \frac{\eta_{I_{vac}}}{\eta_{c^*_{corr}}} + (\xi_{I_{I_s}} - 1) = \frac{0.8684}{0.9848} + (0.0034) = 0.8851$$

The losses included in the thrust chamber efficiency are kinetic, geometry, drag, and heat loss. Theoretical values of the last three of these have been combined in Fig. 65 of the Performance Analysis section. Thus, the experimental kinetic efficiency is

$$\eta_K = \eta_{TC} + 1 - (\eta_G + \eta_D - \xi_{HL}) = 0.8851 + 1.0 - 0.9383 = 0.9468$$

For this case, the theoretically predicted kinetic efficiency is found from Fig. 61 of the Performance Analysis section to be 0.950.



TEST RESULTS

During the Tasks III and IV portion of the program, 105 high quality data points were obtained. This section presents a summary of the data including hardware configuration, measured engine parameters, combustion stability characteristics, and performance values used for data evaluation. In addition, problems encountered during test operations and posttest hardware condition are discussed, and an analysis of the precision of the data measurement systems is presented.

DATA SUMMARY

A total of 186 engine tests were conducted in 66 hyperflow operations; in addition, several engine tests were conducted at ambient conditions for system and/or engine calibration. Appendix B presents a tabulation of the objectives and results of each test.

Table 13, a summary of the test data, shows measured engine parameters and combustion stability information. All terms are defined and calculated for a sample case in the preceding section.

Table 14 summarizes the data corrected to performance evaluation terms as described in the second part of the preceding section. The various corrections, and resultant nozzle efficiencies are shown in this table.

Nozzle wall pressures data are shown in Table 15 through 21. These data are shown as wall pressure normalized to nozzle stagnation pressure to eliminate the effects of slight chamber pressure variation from test to test.

Task III Test Number	Oxidizer Orifice Size	P _T psig	P _o F/M 1, psig	T _o F/M 1, F	P _o F/M 2, psig	T _o F/M 2, F	P _o F/M, lb/cu ft	P _o Inj, psig	T _o Inj, F	F/M 1, cps	F/M 2, cps	Ẇ _o 1, lb/sec	Ẇ _o 2, lb/sec	Ẇ _o Avg, lb/sec	P _f Vent U/S 1, psig	T _f Vent U/S 1, F	P _f Vent U/S 1, psig	T _f Vent U/S 1, F
003	--	191.3	173.3	-291	175.3	-292	90.6	109.6	-289.4	247.30	257.50	3.872	3.974	3.923	771.7	54	771.7	54
005*	--	197.3	177.4	-295	178.4	-293	91.3	105.6	-298	262.50	271.88	4.155	4.209	4.182	628.0	56	628.0	56
006*	--	201.3	183.5	-312	183.5	-315	96.26	106.2	-308	257.14	266.67	4.266	4.379	4.322	979.6	51	979.6	51
007*	--	201.3	174.3	-317	172.8	-319	97.25	101.6	-316	245.00	253.00	4.110	4.194	4.152	949.5	52	949.5	52
008	--	222.5	189.0	-318	189.1	-319	97.37	105.7	-317	267.50	275.75	4.501	4.567	4.534	504.8	53	504.8	53
009-1	--	179.3	155.6	-302.5	154.4	-303.5	93.53	138.7	-285	319.17	328.81	5.158	5.231	5.195	737.1	42	737.1	42
009-2	--	179.3	155.6	-314.5	155.5	-312.5	96.13	139.2	-306.7	308.75	315.79	5.137	5.165	5.151	743.1	42	743.1	42
010-1	--	193.9	169.3	-306.5	168.7	-309	94.78	146.8	-303.9	334.69	345.54	5.477	5.592	5.534	571.6	42	571.6	42
010-2	--	193.9	166.7	-317	167.2	-315	96.78	146.3	-312.5	327.03	336.59	5.499	5.541	5.520	580.7	43	580.7	43
011-1	--	205.6	176.9	-307.5	177.4	-309	94.93	151.3	-307.1	351.75	363.83	5.767	5.883	5.825	478.4	43	478.4	43
011-2	--	205.6	176.9	-317	173.3	-317.5	97.06	150.3	-313.0	338.75	351.02	5.684	5.788	5.736	481.4	44	481.4	44
012	--	150.4	127.7	-302.5	132.7	-300	93.13	114.3	-299.8	--	285.60	4.462	4.509	4.485	1336.0	40	1336.0	40
013	--	178.3	153.4	-315.0	153.6	-315.0	96.52	128.6	-312.3	--	323.33	5.233	5.307	5.270	594.6	41	594.6	41
014	--	186.4	161.5	-316.8	161.8	-316.0	96.87	135.3	-312.7	--	340.00	5.566	5.595	5.550	492.5	43	492.5	43
015*	--	52.56	47.90	-312.5	47.60	-311.5	95.73	42.4	-305.5	129.41	131.37	2.145	2.144	2.144	735.6	28	735.6	28
016*	--	58.75	52.44	-306.5	53.07	-308.5	94.60	46.5	-307.2	142.42	145.45	2.324	2.324	2.324	737.3	30	737.3	30
017*	--	62.09	55.97	-311.0	56.14	-311.5	95.55	48.5	-307.5	154.59	157.69	2.554	2.573	2.564	289.0	32	289.0	32
018*	--	62.56	56.48	-314.5	56.65	-314.0	96.25	48.5	-307.8	155.00	158.46	2.583	2.601	2.592	235.8	33	235.8	33
019*	--	62.56	56.48	-315.0	56.65	-315.0	96.42	49.0	-312	155.00	158.21	2.588	2.602	2.595	235.8	34	235.8	34
020*	0.210	220.1	213.6	-308.5	214.6	-308.0	94.8	48.3	-297.2	134.3	135.3	2.206	2.191	2.199	724.3	39	724.3	39
021	↓	220.1	214.1	-313.0	214.6	-312.5	95.9	49.4	-296.0	132.7	134.5	2.203	2.202	2.203	726.4	42	726.4	42
022*	↓	285.9	277.7	-315	276.9	-315	96.4	50.4	-306.7	153.9	155.8	2.567	2.560	2.564	363.2	42	363.2	42
023*	↓	307.3	297.9	-316	297.9	-316	96.6	50.9	-309.5	159.9	161.0	2.673	2.651	2.662	282.7	42	282.7	42
024	↓	320.5	311.0	-316	311.2	-315.8	96.6	52.9	-308.8	162.7	163.9	2.720	2.698	2.709	228.4	43	228.4	43
025	↓	320.5	310.5	-316	310.7	-315.8	96.6	53.4	-309.5	161.5	163.5	2.700	2.691	2.695	229.4	44	229.4	44
026*	↓	365.5	346.3	-312	347.9	-312	96.0	112.2	-307.0	275.0	284.37	4.567	4.640	4.603	819.9	--	819.9	--
027-1*	↓	401.5	379.7	-315.6	381.2	-315.2	96.8	117.8	-311.4	303.57	312.50	5.085	5.141	5.113	656.3	--	656.3	--
027-2*	↓	401.5	379.7	-316.0	381.2	-316.0	96.9	116.8	-312.0	290.57	298.25	4.872	4.912	4.892	518.8	--	518.8	--
028-1*	↓	429.9	404.5	-315.5	406.2	-315.2	96.8	122.4	-312.2	289.80	300.96	4.854	4.951	4.902	561.0	51	561.0	51
028-2*	↓	429.9	404.5	-315.9	406.2	-315.5	96.8	117.3	-312.6	301.47	310.91	5.050	5.115	5.082	410.4	40	410.4	40
029-1*	↓	363.4	344.1	-306.5	343.7	-306.5	94.65	111.4	-278.0	284.15	294.05	4.653	4.735	4.696	708.5	28	708.5	28
029-2*	↓	363.4	343.6	-312.5	343.1	-312.0	96.02	113.9	-305.5	272.92	282.29	4.537	4.608	4.572	703.5	28	703.5	28
030-1	↓	454.0	427.4	-313.6	428.3	-313.5	96.44	125.7	-310.3	310.58	321.43	5.183	5.268	5.225	592.1	29	592.1	29
030-2	↓	454.0	427.4	-316.3	428.3	-316.8	97.13	128.2	-313.1	311.70	322.62	5.238	5.328	5.283	593.1	29	593.1	29
031-1	↓	461.1	434.6	-316.8	435.0	-316.7	97.17	126.7	-313.6	315.38	326.25	5.305	5.388	5.346	491.7	30	491.7	30
031-2	↓	461.1	434.6	-317.2	435.0	-317.2	97.25	129.7	-313.8	318.75	329.85	5.364	5.441	5.402	491.7	30	491.7	30
032-1*	↓	746.3	327.6	-296.8	325.5	-299.4	91.90	112.0	-282.8	286.67	296.67	4.569	4.622	4.595	638.4	30	638.4	30
032-2*	↓	746.3	327.6	-310.5	326.5	-308.5	95.32	126.3	-296.3	268.29	277.78	4.434	4.494	4.464	634.4	30	634.4	30
033-1	↓	438.0	415.1	-316	415.5	-316.0	97.00	126.3	-312.5	310.71	321.15	5.223	5.311	5.267	588.3	30	588.3	30
033-2	↓	435.5	413.1	-316.6	412.9	-316.5	97.07	127.3	-312.5	310.00	320.00	5.211	5.284	5.247	588.3	30	588.3	30
034-1	↓	446.7	419.2	-317.3	419.1	-316.8	97.24	126.3	-314.0	312.50	323.44	5.261	5.344	5.302	495.1	29	495.1	29
034-2	↓	446.7	419.7	-317.8	419.1	-317.6	97.40	126.8	-315.0	311.11	321.21	5.240	5.313	5.276	497.1	29	497.1	29
035*	↓	285.5	279.8	-305.7	280.6	-305.8	94.43	52.1	-299.2	138.89	141.07	2.270	2.277	2.273	591.8	32	591.8	32
036*	↓	285.0	279.3	-306.8	280.0	-306.0	94.59	51.1	-298.8	140.35	143.40	2.297	2.320	2.308	560.7	32	560.7	32
037*	↓	376.6	368.9	-309.2	369.3	-309.7	95.39	57.2	-307.0	160.87	164.62	2.654	2.681	2.668	402.9	31	402.9	31
038*	↓	401.0	392.8	-310.1	392.9	-310.1	95.59	61.3	-307.5	165.67	169.67	2.739	2.765	2.752	309.5	31	309.5	31
039	↓	429.5	415.7	-312.7	416.0	-312.5	96.18	63.8	-309.7	170.00	174.49	2.829	2.861	2.845	263.2	32	263.2	32
041	0.223	407.1	398.4	-304.7	398.6	-304.8	94.20	61.8	-302.5	174.510	168.750	2.783	2.768	2.775	275.6	--	275.6	--
042	↓	407.1	398.9	-304.9	399.1	-305.0	94.25	62.3	-303.0	173.684	168.085	2.771	2.766	2.768	276.6	--	276.6	--
043	↓	439.0	429.3	-298.0	429.2	-298.0	92.54	69.5	-300.2	180.357	174.576	2.825	2.812	2.818	241.5	57.5	241.5	57.5
044	↓	438.5	429.3	-299.5	429.7	-299.5	92.92	78.1	-298.4	179.310	173.171	2.820	2.807	2.813	226.5	57.0	226.5	57.0
045	↓	438.0	428.8	-302.2	429.2	-302.2	93.60	78.1	-300.5	177.679	171.552	2.814	2.794	2.804	231.5	57.5	231.5	57.5
047-1*	↓	391.4	381.3	-308.0	384.0	--	94.97	--	-300.3	167.500	168.056	2.687	2.702	2.695	385.3	61	385.3	61
047-2*	↓	391.4	381.3	-308.1	384.0	--	95.00	64.3	-299.4	167.188	167.188	2.682	2.689	2.686	381.2	60	381.2	60
048*	↓	407.1	397.5	-307.7	399.2	--	94.92	64.8	-308.0	170.833	171.429	2.738	2.754	2.746	288.5	61	288.5	61
049*	↓	408.1	398.0	-294.6	399.7	--	91.63	67.3	-300.2	173.958	173.171	2.691	2.686	2.689	291.5	63	291.5	63
050*	↓	421.8	410.2	-296.2	412.9	--	92.07	80.0	-298.0	174.647	174.242	2.715	2.715	2.715	247.1	64	247.1	64
051*	↓	409.1	385.3	-304.5	387.5	--	94.15	61.8	-298.0	169.57	169.22	2.696	2.696	2.696	397.9	--	397.9	--
052*	↓	424.9	400.6	-304.6	403.8	--	94.16	62.8	-300.0	171.88	171.27	2.731	2.731	2.731	290.8	--	290.8	--
053*	↓	455.8	431.0	-298.4	433.6	--	92.65	68.9	-300.2	181.25	181.05	2.836	2.836	2.836	246.4	62	246.4	62
054*	↓	454.8	431.0	-298.0	433.1	--	92.55	76.0	-296.5	177.59	177.65	2.765	2.765	2.765	247.4	62	247.4	62
055*	↓	342.1	316.3	-311.7	316.9	--	95.82	123.3	-307.7	297.435	297.674	4.811	4.811	4.811	1022.0	60	1022.0	60
056*	↓	344.2	316.8	-311.9	317.9	--	95.87	123.8	-309.3	296.66	297.78	4.807	4.807	4.807	991.8	62	991.8	62
057*	↓	386.8	358.4	-304.5	361.1	--	94.09	135.0	-303.2	323.00	321.43	5.114	5.114	5.114	949.4	64	949.4	64
058	↓	409.7	349.2	-301.0	351.1	-300.6	93.15	281.3	-299.2	551.282	548.438	8.650	8.606	8.628	1342.2	72	1342.2	72
059																		

MARY

Alt 2, g	T _f Vent U/S 2, F	P _f Inj, psig	P _{alt} psia	W _f lb/sec	P _{c1} 1, psig	P _{c1} 2, psig	P _{c2} 1, psig	P _{c2} 2, psig	P _{c2} 3, psig	P _{c2} Avg, psig	P _{c2} psia	F ₁ lb	F ₂ lb	F _{avg} lb	F _{vac} lb	Percent Buzz, $\frac{P_{max} - P_{min}}{P_{c2}} \times 100$
2	55	117.5	0.116	0.540	68.31	67.89	65.81	63.62	64.17	63.94	76.18	1770.0	1754.2	1762.1	1858.2	4.1
5	58	144.2	0.116	0.443	71.24	72.26	66.03	65.85	66.49	66.20	78.44	1845.4	1831.6	1838.5	1934.6	5.2
4	52	240.7	0.124	0.687	77.82	78.06	73.39	73.32	73.47	73.42	85.57	2009.1	2001.8	2005.5	2108.3	11.8
4	53	216.3	0.119	0.667	74.79	75.62	70.06	70.08	70.25	70.14	82.30	1963.6	1959.8	1961.7	2060.3	15.6
7	53	122.8	0.121	0.361	73.68	74.30	68.05	67.55	67.84	67.92	80.07	1918.2	1917.8	1918.0	2018.3	4.5
	43	169.9	0.153	0.520	88.96	88.62	--	82.95	83.03	83.02	95.21	2214.9	2222.9	2218.9	2348.8	3.8
	44	171.7	0.147	0.523	89.47	89.12	--	83.45	83.73	83.68	95.87	2223.9	2241.0	2232.5	2352.3	5.0
	44	144.4	0.145	0.405	92.71	91.76	--	85.78	85.54	85.58	97.77	2301.8	2310.3	2306.1	2426.0	1.9
	45	135.9	0.139	0.412	92.20	91.66	85.89	85.78	85.94	85.91	98.10	2316.8	2322.3	2319.1	2434.1	1.5
	45	130.3	0.143	0.341	93.52	91.76	85.69	85.98	85.98	85.87	98.06	2322.8	2337.4	2330.1	2448.4	1.0
	46	132.4	0.137	0.343	91.50	91.36	85.18	85.07	85.34	85.24	97.43	2319.8	2325.3	2322.1	2435.4	0.9
0	41	--	0.131	0.939	86.37	86.24	82.01	81.78	82.12	82.03	94.07	2207.2	2209.3	2208.3	2316.7	4.6
0	42	146.3	0.155	0.427	88.39	88.68	82.11	82.08	82.43	82.24	94.28	2267.6	2266.7	2267.2	2378.9	2.8
0	43	132.5	0.133	0.357	90.11	88.99	82.82	82.89	83.03	82.91	94.95	2303.9	2296.9	2300.4	2410.4	1.6
1	28	163.2	0.080	0.527	35.40	35.67	33.36	33.49	33.55	33.45	45.56	1047.8	1048.6	1048.2	1113.3	17.0
7	30	81.4	0.075	0.273	30.54	30.80	27.84	27.95	28.21	28.00	40.11	950.5	949.4	949.9	1011.5	18.1
4	32	64.1	0.076	0.213	33.07	33.13	29.95	29.86	30.23	30.06	42.17	995.4	997.5	996.5	1058.4	14.9
6	34	54.9	0.076	0.174	34.38	34.45	31.05	31.07	31.24	31.13	43.24	1002.9	1005.0	1004.0	1066.9	9.5
6	35	55.6	0.076	0.175	34.99	34.45	31.15	31.28	31.44	31.28	43.39	1014.9	1015.5	1015.2	1078.1	11.2
	40	158.4	0.062	0.511	35.11	35.28	34.03	34.19	34.16	34.10	46.24	1078.4	1067.1	1072.7	1124.0	17.8
5	43	161.6	0.059	0.513	35.01	34.87	33.83	33.48	33.66	33.73	45.87	1064.7	1055.0	1059.9	1108.7	4.2
2	42	77.8	0.058	0.261	34.80	34.47	31.11	31.46	31.94	31.48	43.62	1048.0	1043.0	1045.5	1093.5	17.8
1	43	62.2	0.056	0.206	36.40	36.39	33.12	32.67	33.35	33.26	45.40	1069.3	1065.5	1067.4	1113.7	5.2
3	44	53.4	0.057	0.168	37.04	36.39	33.33	33.38	33.96	33.99	45.73	1075.4	1065.5	1070.5	1117.7	1.6
3	44	56.9	0.057	0.168	36.83	36.29	33.12	33.28	33.45	33.27	45.41	1072.3	1065.5	1068.9	1116.0	1.6
0	43	189.0	0.088	0.582	81.17	81.09	76.82	75.71	75.79	75.80	87.91	2086.0	2084.0	2085.0	2157.8	3.7
3	49	154.4	0.084	0.462	83.60	83.17	77.53	77.69	77.78	77.64	89.75	2158.2	2153.2	2155.7	2225.2	2.7
1	40	126.9	0.083	0.369	80.66	80.93	74.41	74.74	74.86	74.62	86.73	2098.0	2093.0	2095.5	2164.2	2.7
0	51	139.3	0.083	0.402	84.50	84.13	78.84	78.54	78.55	78.70	90.81	2203.4	2198.6	2201.0	2269.7	2.6
3	40	112.1	0.082	0.292	79.95	80.16	73.80	73.73	73.92	73.85	85.96	2079.9	2078.0	2078.9	2146.7	2.8
6	28	157.9	0.076	0.507	78.52	78.46	72.59	72.62	73.06	72.79	84.98	2019.6	2045.8	2032.8	2095.8	5.6
5	28	159.4	0.090	0.502	77.50	76.93	71.59	71.31	72.06	71.76	83.95	2001.4	2015.5	2008.5	2082.2	4.0
3	29	141.8	0.081	0.423	87.16	86.61	80.24	80.11	80.61	80.38	92.57	2280.3	2276.1	2278.3	2345.5	2.8
3	29	143.6	0.084	0.424	88.49	88.04	81.65	81.32	81.92	81.73	93.92	2301.6	2312.5	2307.1	2366.8	2.8
2	29	126.0	0.082	0.352	87.57	85.79	79.54	79.30	79.81	79.63	91.82	2271.2	2279.2	2275.2	2343.2	1.3
2	29	126.7	0.085	0.352	88.28	86.92	80.14	79.91	80.51	80.27	92.46	2295.5	2300.4	2298.0	2368.5	1.5
4	30	145.8	0.101	0.457	79.74	79.68	73.69	73.32	73.85	73.72	85.83	2068.1	2080.5	2074.3	2158.1	5.6
3	30	144.4	0.110	0.454	70.29	70.41	64.92	64.72	65.26	65.04	77.15	1840.6	1832.5	1836.6	1927.9	3.1
8	30	141.9	0.100	0.420	87.97	88.14	81.25	81.02	81.42	81.30	93.41	--	2280.1	2280.1	2363.1	3.1
8	29	144.4	0.101	0.420	88.06	88.75	81.45	81.02	81.62	81.48	93.59	--	2283.5	2283.1	2366.9	2.3
5	29	126.7	0.095	0.357	85.73	86.10	79.24	79.00	79.50	79.33	91.44	2262.2	2255.9	2259.0	2337.8	1.8
6	29	128.8	0.095	0.359	86.34	87.02	79.64	79.20	79.91	79.71	91.82	2271.3	2265.0	2268.1	2348.6	2.1
4	30	129.0	0.064	0.423	34.54	34.93	32.40	32.41	32.77	32.55	44.66	1045.6	1046.7	1046.1	1099.2	31.5
9	31	124.4	0.056	0.401	35.45	35.66	32.91	33.02	33.08	32.99	45.10	1063.7	1061.7	1062.7	1109.2	18.8
8	31	89.3	0.058	0.293	38.09	38.72	34.82	34.54	35.40	35.03	47.14	1142.1	1135.6	1138.9	1187.0	28.8
0	31	70.9	0.058	0.227	39.62	39.13	35.83	35.95	36.31	36.04	48.15	1158.6	1150.7	1154.7	1192.4	8.8
1	31	63.8	0.060	0.194	39.62	39.33	36.03	36.05	36.41	36.19	48.30	1166.2	1161.3	1163.8	1213.2	2.5
7	59	62.5	0.069	0.198	38.91	39.18	35.07	35.91	35.84	35.47	47.57	1130.4	1131.9	1131.2	1188.4	1.9
7	60.2	63.9	0.066	0.198	38.50	38.68	34.56	35.50	35.44	35.01	47.11	1122.4	1123.8	1123.1	1177.9	1.9
1	61	59.0	0.065	0.173	39.42	39.18	35.37	36.21	36.24	35.81	47.91	1148.1	1148.0	1148.1	1202.0	1.2
8	61	56.1	0.063	0.163	37.39	37.46	33.76	34.49	34.33	34.06	46.16	1104.8	1104.4	1104.6	1156.9	1.6
9	62	57.2	0.064	0.167	38.00	38.17	34.26	35.10	35.03	34.67	46.77	1135.2	1130.2	1132.7	1185.8	1.5
6	64	--	0.101	0.272	39.79	40.44	36.38	36.32	36.22	36.29	48.37	1158.4	1150.4	1154.4	1238.2	4.8
6	63	83.0	0.099	0.270	40.90	41.05	37.29	37.23	37.23	37.25	49.33	1171.3	1167.8	1169.6	1251.7	4.8
4	64	67.4	0.082	0.206	40.19	40.54	36.28	36.21	36.22	36.24	48.32	1156.8	1159.9	1158.4	1226.4	2.9
5	65	68.8	0.073	0.207	40.19	40.54	36.58	36.42	36.42	36.47	48.55	1163.3	1167.8	1165.6	1226.2	2.9
0	67	58.6	0.083	0.178	37.26	37.50	33.65	33.87	33.78	33.75	45.83	1095.8	1096.6	1096.2	1165.1	2.6
2	--	--	0.095	0.278	40.86	41.05	--	37.59	37.65	37.64	49.75	1181.5	1173.7	1177.1	1265.4	4.7
1	--	--	0.089	0.207	39.64	39.83	35.64	36.17	36.03	35.93	48.04	1154.0	1153.1	1153.6	1227.4	2.1
4	64	--	0.097	0.177	40.35	40.44	36.14	36.27	36.23	36.21	48.32	1165.4	1164.2	1164.8	1245.3	2.1
9	64	--	0.096	0.177	38.92	38.92	35.04	35.25	35.42	35.27	47.38	1141.1	1140.4	1140.8	1220.5	1.4
5	--	233.5	0.094	0.720	89.01	87.78	83.17	82.70	83.09	83.05	95.16	2294.0	2277.9	2286.0	2364.0	9.5
2	--	227.1	0.087	0.689	88.91	88.19	82.96	82.70	83.09	82.98	95.09	2311.8	2295.5	2303.7	2375.9	10.8
9	--	219.3	0.091	0.657	92.66	93.46	86.90	86.53	86.84	86.81	98.92	2427.4	2395.6	2411.5	2487.0	5.3
9	70	317.4	0.060	0.914	162.45	162.86	151.79	151.26	151.58	151.54	163.72	4044.0	4036.1	4040.1	4089.9	1.7
3	71	310.3	0.054	0.880	166.43	167.53	156.26	155.51	155.82	155.86	168.04	4205.5	4191.9	4198.7	4243.5	1.2

End chamber pressure

Jet chamber pressure

TABLE 13

(Continued)

[illegible]

*Indicates invalid test.



TABLE 13
(Concluded)

Task IV Test Number	Thrust Chamber Type	Oxidizer Orifice Size	P ₀ , F/M 1, psia	P ₀ , F/M 2, psia	T ₀ F/M 1, F	T ₀ F/M 2, F	ρ ₀ F/M, lb/cu ft	P ₀ Inj, psia	T ₀ Inj, F	V/M l, cps	V/M l, cps	W ₀ lb/sec	W ₀ lb/sec	W ₀ lb/sec	P _f Vent U/S 1, psia	P _f Vent U/S 2, psia	T _f Vent U/S 1, F	T _f Vent U/S 2, F	W _f lb/sec	P _f Inj, psia	P _{cl} l, psia	P _{cl} 2, psia	P _{c2} l, psia	P _{c2} 2, psia	P _{c2} 3 Avg, psia	P _{c2} psia	F ₁ l, lb	F ₁ 2, lb	F ₂ l, lb	F ₂ 2, lb	F ₂ Avg, lb	P _{alt} , psia	F _{vac} , lb	Percent Buzz, P _{max} - P _{min} 2P _{c2} x 10 ⁻²
159	15 CST	0.228 0.185	476.5	462.8	-300.4	-300.4	93.00	59.2	-295.0	292.929	295.832	2.445	2.467	2.456	376.4	377.8	60	--	0.267	83.6	37.28	37.83	34.57	34.48	34.31	34.46	46.56	1092.0	1098.6	1101.0	1097.2	0.055	1160.9	5.0
160		0.228 0.185	476.5	463.4	-300.2	-300.2	92.95	60.2	-295.3	293.016	295.576	2.445	2.464	2.454	376.4	377.8	58.4	--	0.267	84.6	37.08	37.47	34.47	34.43	34.26	34.40	46.50	1092.0	1100.2	1102.6	1098.3	0.055	1142.0	3.5
164*		0.228 0.207	476.5	463.4	-300.5	-300.5	94.35	60.4	-303.5	330.66	334.90	2.800	2.835	2.817	266.9	265.9	58.5	58.5	0.190	62.9	40.60	40.52	37.28	37.29	36.93	37.20	49.27	1175.9	1174.9	1170.2	1173.7	0.053	1217.2	11.8
165*		0.228 0.207	476.5	463.4	-300.5	-300.5	93.57	65.4	-303.0	320.09	322.60	2.688	2.708	2.698	450.5	451.4	59.5	60.0	0.318	103.1	40.70	40.52	38.65	38.54	37.91	38.41	50.49	1227.2	1224.2	1221.5	1224.3	0.048	1264.1	36.4
166		0.228 0.207	476.5	463.4	-300.5	-300.5	91.87	83.9	-296.0	330.29	333.08	2.723	2.746	2.734	262.9	263.9	60.5	61.0	0.188	65.6	39.14	39.31	36.03	36.19	36.09	36.12	48.19	1151.8	1152.0	1149.4	1151.1	0.056	1197.4	2.5
167		0.228 0.207	476.5	463.4	-300.5	-300.5	92.51	66.9	-298.0	316.92	320.49	2.635	2.660	2.647	315.5	315.5	61.5	62.0	0.225	74.8	38.59	38.81	36.28	36.24	36.04	36.11	48.18	1151.8	1150.3	1146.2	1149.5	0.056	1194.0	3.5
168*		0.228 0.207	476.5	463.4	-300.5	-300.5	93.08	64.5	-298.0	303.00	306.18	2.534	2.554	2.544	265.9	265.9	62.5	60.8	0.192	64.3	36.16	36.16	32.28	32.48	32.19	32.36	44.34	1151.8	1150.3	1146.2	1149.5	0.056	1194.0	3.5
169*		0.228 0.207	476.5	463.4	-300.5	-300.5	93.10	64.3	-298.3	293.51	296.07	2.455	2.469	2.462	293.5	295.4	64.5	62.0	0.231	64.3	36.41	36.41	32.53	32.78	32.54	32.65	44.83	1221.2	1206.8	1204.2	1217.4	0.0435	1253.4	4.6
171*		0.228 0.207	476.5	463.4	-300.5	-300.5	91.87	85.3	-292.7	301.77	305.77	2.493	2.516	2.505	267.9	266.9	63.5	62.5	0.213	85.3	35.34	35.34	31.63	31.84	31.65	31.74	43.91	1221.2	1206.8	1204.2	1217.4	0.0435	1253.4	4.6
172		0.228 0.207	476.5	463.4	-300.5	-300.5	94.40	66.6	-302.1	339.69	343.05	2.877	2.906	2.891	256.4	257.3	60.0	60.0	0.185	63.1	34.27	34.27	37.42	37.64	37.41	37.52	49.69	1224.4	1211.5	1205.8	1220.6	0.0485	1260.7	2.5
173		0.228 0.207	476.5	463.4	-300.5	-300.5	94.40	65.1	-302.2	328.48	331.50	2.782	2.808	2.795	311.8	312.7	67.0	68.0	0.221	73.5	37.47	37.47	37.69	37.41	37.56	37.56	49.73	1221.2	1206.8	1204.2	1217.4	0.0435	1253.4	3.0
174		0.228 0.207	476.5	463.4	-300.5	-300.5	91.42	84.0	-293.7	343.65	345.95	2.819	2.848	2.828	252.4	253.4	66.0	66.5	0.181	63.8	35.34	35.34	36.42	36.74	36.48	36.59	48.76	1200.7	1189.5	1203.4	1197.9	0.0405	1251.4	2.0
175		0.228 0.207	476.5	463.4	-300.5	-300.5	92.10	84.0	-293.7	328.86	332.56	2.717	2.735	2.736	310.8	310.7	64.0	65.0	0.222	74.2	37.47	37.47	37.69	37.41	37.56	37.56	49.73	1200.7	1189.5	1203.4	1197.9	0.0405	1251.4	2.0
1	10°C	0.228 0.207	476.5	463.4	-300.5	-300.5	95.09	62.4	-295.9	270.27	270.24	2.308	2.304	2.306	302.9	304.4	42.0*	42.0*	0.221	65.8	33.11	32.44	29.92	30.03	29.81	29.96	42.14	989.63	981.54	984.91	984.9	0.057	1030.7	3.7
2	20°C	0.228 0.207	476.5	463.4	-300.5	-300.5	95.01	65.4	-296.8	279.36	279.62	2.383	2.382	2.383	292.5	294.9	42.0*	42.0*	0.188	55.5	33.11	33.16	30.13	30.46	30.19	30.30	42.48	1003.62	997.16	999.06	999.9	0.048	1038.5	2.3
3	20°C	0.228 0.207	476.5	463.4	-300.5	-300.5	94.92	59.8	-290.6	270.83	271.15	2.408	2.408	2.408	302.9	303.4	42.0*	42.0*	0.220	66.5	33.97	33.97	30.84	31.37	31.04	31.15	43.33	1021.32	1021.31	1021.70	1021.9	0.046	1058.9	2.3
4	20°C	0.228 0.207	476.5	463.4	-300.5	-300.5	94.63	65.9	-290.0	287.77	287.88	2.444	2.443	2.444	294.9	294.9	42.0*	42.0*	0.188	59.4	34.08	33.01	30.94	31.07	30.88	30.99	43.17	1027.89	1024.15	1027.36	1027.6	0.063	1063.8	2.3
8*	20°C	0.228 0.207	476.5	463.4	-300.5	-300.5	92.48	84.3	-292.0	375.31	378.39	3.116	3.143	3.129	308.4	307.1	31	32	0.225	74.3	34.08	33.01	43.03	42.96	41.98	42.74	54.61	1309.2	1320.8	1320.6	1315.9	0.073	1374.6	1.9
9*	15°C	0.228 0.207	476.5	463.4	-300.5	-300.5	92.38	83.8	-294.0	391.49	392.96	3.247	3.261	3.254	250.8	250.5	32	33	0.185	67.1	41.66	41.66	43.03	43.01	41.98	42.76	54.63	1303.6	1315.1	1316.4	1311.0	0.067	1364.9	0.7
10	15°C	0.228 0.207	476.5	463.4	-300.5	-300.5	93.37	89.1	-291.2	331.43	334.21	2.778	2.801	2.789	308.1	312.9	42	42	0.225	73.1	38.49	38.27	38.49	38.27	38.37	38.37	50.52	1198.4	1189.3	1192.4	1193.4	0.067	1247.3	2.0
11	15°C	0.228 0.207	476.5	463.4	-300.5	-300.5	93.42	89.1	-294.2	346.92	350.95	2.909	2.943	2.926	252.4	253.2	43	43	0.185	63.8	42.06	42.06	38.54	38.60	38.43	38.54	50.69	1202.7	1197.8	1198.1	1199.5	0.060	1247.7	1.5
12	15°C	0.228 0.207	476.5	463.4	-300.5	-300.5	93.24	91.1	-293.8	335.72	338.62	2.810	2.834	2.822	308.0	310.9	44	44	0.223	74.2	42.17	42.17	38.69	38.95	38.58	38.79	50.94	1212.5	1211.9	1214.9	1213.1	0.053	1255.7	1.5
13	15°C	0.228 0.207	476.5	463.4	-300.5	-300.5	94.20	71.3	-295.5	327.03	328.21	2.766	2.775	2.775	308.0	309.5	35	36	0.225	71.9	41.21	41.21	38.69	38.14	37.77	38.02	50.12	1187.4	1189.7	1183.7	1186.9	0.061	1237.4	1.3
14	15°C	0.228 0.207	476.5	463.4	-300.5	-300.5	94.02	72.9	-296.4	335.00	341.03	2.827*	2.878	2.878	252.4	252.9	38	39	0.185	62.6	41.72	41.72	38.29	38.29	38.02	38.20	50.30	1207.0	1211.0	1204.8	1207.6	0.049	1248.1	0.6
15	15°C	0.228 0.207	476.5	463.4	-300.5	-300.5	93.82	71.3	-297.8	324.30	328.26	2.738*	2.764	2.764	306.0	308.5	40	40	0.223	73.3	40.04	40.04	38.55	38.69	38.69	38.60	50.70	1211.2	1213.3	1207.6	1211.4	0.048	1251.1	1.0
16	15°C	0.228 0.207	476.5	463.4	-300.5	-300.5	91.40	80.2	-292.4	335.85	339.38	2.736*	2.786	2.786	252.4	253.9	38	38	0.185	62.9	40.04	40.04	38.55	38.69	38.69	38.60	50.70	1174.0	1174.0	1169.6	1171.4	0.048	1211.1	0.6
17*	15°C	0.228 0.207	476.5	463.4	-300.5	-300.5	93.98	80.7	-293.4	344.47	348.97	2.741	2.741	2.741	309.0	309.5	44	44	0.223	71.3	39.69	40.06	36.35	36.71	36.23	36.50	48.73	1174.0	1174.0	1169.6	1171.4	0.063	1251.1	1.7
18*	15°C	0.228 0.207	476.5	463.4	-300.5	-300.5	94.05	75.7	-295.8	361.96	359.07	2.917*	2.862	2.862	254.5	255.9	47	47	0.186	62.3	40.47	40.82	36.76	37.01	36.79	36.89	49.12	1174.0	1174.0	1169.6	1171.4	0.051	1251.1	1.7
19*	15°C	0.228 0.207	476.5	463.4	-300.5	-300.5	93.97	74.0	-297.3	348.24	325.92	2.748	2.748	2.748	308.0	309.5	40	40	0.222	72.7	40.22	40.62	36.86	37.22	36.79	37.03	49.26	1174.0	1174.0	1169.6	1171.4	0.045	1251.1	1.7
20*	15°C	0.228 0.207	476.5	463.4	-300.5	-300.5	91.55	91.8	-291.3	361.16	339.03	2.833*	2.786	2.786	254.5	256.9	48	48	0.186	63.7	38.42	39.04	35.43	35.69	35.37	35.55	47.78	1174.0	1174.0	1169.6	1171.4	0.045	1251.1	1.7
21*	15°C	0.228 0.207	476.5	463.4	-300.5	-300.5	92.38	83.8	-294.0	391.49	392.96	3.247	3.261	3.254	250.8	250.5	32	33	0.185	67.1	41.66	41.66	43.03	43.01	41.98	42.76	54.63	1303.6	1315.1	1316.4	1311.0	0.067	1364.9	0.7
22*	15°C	0.228 0.207	476.5	463.4	-300.5	-300.5	93.37	89.1	-291.2	331.43	334.21	2.778	2.801	2.789	308.1	312.9	42	42	0.225	73.1	38.49	38.27	38.49	38.27	38.37	38.37	50.52	1198.4	1189.3	1192.4	1193.4	0.067	1247.3	2.0
23*	15°C	0.228 0.207	476.5	463.4	-300.5	-300.5	93.42	89.1	-294.2	346.92	350.95	2.909	2.943	2.926	252.4	253.2	43	43																



TABLE 14

NOZZLE TEST DATA

Task III Test Number	Nozzle Type	Data Slice	Oxidizer Flowrate, lbm/sec	Fuel Flowrate, lbm/sec	Vacuum Thrust, pounds	Oxidizer Density Correction	Corrected Oxidizer Flowrate, lbm/sec	Corrected Total Flowrate, lbm/sec	Chamber Pressure, psia	Mixture Ratio, o/f	Throat Area sq in	Discharge Coefficient	Heat Loss Correction to c*	Impurity Correction to c	Throat Shrinkage	U-corrected Characteristic Velocity, ft/sec	Corrected Characteristic Velocity, ft/sec	Theoretical Shifting Characteristic Velocity, ft/sec	Characteristic Velocity Efficiency	Delivered Vacuum Specific Impulse	Theoretical Shifting Vacuum Specific Impulse	Delivered Specific Impulse Efficiency	$\eta_G + \eta_D$ - ξ_{III}	Impurity Correction to Vac	Thrust Chamber Efficiency	Kinetic Efficiency
003	15 CLT		3.923	0.340	1858	0.9881	3.876	4.416	80.3	7.17	445.16	0.9945	1.00863	1.003	1.00	8094.7	8144.1	8301	0.9811	420.7	487.26	0.8634	0.9231	1.0040	0.8840	0.9609
005 *			4.182	0.443	1934		4.132	4.575	82.6	9.33			1.00864			8037.2	8086.2	8127	0.9950	422.7	486.95	0.8681	0.9225		0.8765	0.9540
006 *			4.322	0.687	2107.5		4.271	4.964	90.2	6.17			1.00855			8088.9	8138.2	8417	0.9669	424.5	486.6	0.8724	0.9246		0.9065	0.9817
007 *			4.132	0.667	2060.5		4.103	4.776	86.7	6.10			1.00859			8081.1	8130.4	8420	0.9656	431.4	486.45	0.8868	0.9243		0.9224	0.9981
008			4.534	0.361	2018.3		4.480	4.845	84.4	12.24			1.00861			7754.7	7802.0	7980	0.9777	416.6	484.44	0.8600	0.9215		0.8836	0.9621
009	70% B	1	5.195	0.520	2348.8		5.145	5.665	100.35	9.904	445.29		1.00847	1.0024		7888.0	7930.6	8117	0.9770	414.6	487.0	0.8513	0.9395	1.0034	0.8747	0.9352
009		2	5.151	0.523	2352.3	0.9904	5.102	5.627	101.05	9.76			1.00846			7996.5	8039.7	8125	0.9895	418.0	487.1	0.8581	0.9396		0.8706	0.9310
010		1	5.534	0.405	2426.0		5.481	5.886	103.05	13.53			1.00845			7800	7842.1	7937	0.9880	412.2	483.6	0.8524	0.9394		0.8662	0.9268
010		2	5.520	0.412	2434.1		5.467	5.879	103.48	13.27			1.00845			7837.8	7880.1	7930	0.9912	414.0	483.8	0.8557	0.9394		0.8667	0.9273
011		1	5.825	0.341	2448.4		5.769	6.111	103.36	16.92			1.00845			7531.5	7572.2	7735	0.9790	400.6	479.0	0.8363	0.9389		0.8576	0.9189
011		2	5.736	0.343	2435.4		5.681	6.024	102.69	16.56			1.00846			7590.8	7631.8	7759	0.9836	404.3	479.6	0.8430	0.9389		0.8605	0.9216
012			4.485	0.979	2316.7		4.442	5.377	99.15	4.73			1.00848			8211.0	8255.3	8578	0.9624	430.85	482.85	0.8923	0.9384		0.9306	0.992
013			5.270	0.427	2377.9		5.219	5.646	99.37	12.22			1.00847			7837.1	7879.4	8000	0.9849	421.2	485.0	0.8684	0.9385		0.8851	0.9468
014			5.550	0.357	2410.4		5.497	5.853	100.08	15.40			1.00847			7614.0	7655.1	7832	0.9774	411.8	481.15	0.8559	0.9389		0.8791	0.9402
015 *			2.144	0.527	1113.5		2.1234	2.6504	48.02	4.03			1.00923			8067.8	8116.7	8610	0.9427	420.0	479.1	0.8766	0.9343		0.9333	0.9990
016 *			2.339	0.273	1011.5		2.3165	2.5895	42.28	8.48			1.00935			7270.5	7314.6	8115	0.9013	390.6	486.3	0.8032	0.9338		0.8946	0.9608
017 *			2.564	0.213	1058.4		2.5394	2.7524	44.45	11.92			1.00931			7191.2	7234.8	7920	0.9135	384.5	482.8	0.7964	0.9340		0.8752	0.9412
018 *			2.592	0.174	1066.9		2.5671	2.7411	45.57	14.75			1.00928			7402.9	7447.8	7772	0.9583	389.2	478.7	0.8130	0.9335		0.8518	0.9183
019 *			2.395	0.173	1078.1		2.3701	2.7451	45.73	14.69			1.00928			7418.0	7462.9	7775	0.9598	392.7	478.8	0.8202	0.9336		0.8580	0.9244
020 *			2.199	0.511	1124.0		2.1779	2.6889	48.74	4.26			1.00922			8071.5	8120.6	8580	0.9465	418.0	480.5	0.8699	0.9344		0.9225	0.9881
021			2.203	0.513	1109.0		2.1819	2.6949	48.35	4.25			1.00923			7989.1	8037.7	8580	0.9368	411.5	480.5	0.8564	0.9344		0.9176	0.9832
022 *			2.365	0.261	1093.0		2.3384	2.7994	45.98	9.73			1.00923			7313.9	7358.8	8030	0.9164	390.4	485.5	0.8041	0.9394		0.8809	0.9415
023 *			2.562	0.206	1113.7		2.5364	2.8424	47.85	12.80			1.00927			7496.2	7541.8	7885	0.9565	391.8	485.0	0.8129	0.9341		0.8533	0.9192
024			2.799	0.168	1117.7		2.6830	2.851	48.20	15.97			1.00923			7528.2	7574.0	7740	0.9786	392.0	478.0	0.8201	0.9335		0.8414	0.9079
025			2.095	0.168	1116.0		2.6691	2.871	47.86	15.89			1.00924			7511.8	7557.5	7742	0.9762	393.4	478.1	0.8228	0.9335		0.8463	0.9128
026 *			4.616	0.582	2158.0		2.5717	5.1557	92.66	7.85			1.00852			8006.0	8049.2	8255	0.9751	418.7	487.55	0.8588	0.9390		0.8841	0.9451
027 *			4.898	0.462	2225		4.8510	5.3130	94.6	10.50			1.00851			7928.6	7971.2	8080	0.9865	418.8	486.3	0.8612	0.9392		0.8764	0.9372
027 *			4.891	0.369	2164		4.8441	5.2131	91.4	13.13			1.00853			7807.2	7849.4	7953	0.9870	415.1	483.6	0.8584	0.9363		0.8731	0.9368
028 *			5.138	0.402	2270		5.0887	5.4907	95.7	12.67			1.00850			7761.2	7802.8	7972	0.9788	413.4	484.4	0.8534	0.9389		0.8733	0.9364

*Indicates invalid test



TABLE 14
(Continued)

Task Test Number	Nozzle Type	Data Slice	Oxidizer Flowrate, lbm/sec	Fuel Flowrate, lbm/sec	Vacuum Thrust, pounds	Oxidizer Density Correction	Corrected Oxidizer Flowrate, lbm/sec	Corrected Total Flowrate, lbm/sec	Chamber Pressure, psia	Mixture Ratio, o/f	Throat Area, sq in	Discharge Coefficient	Heat Loss Correction to c	Impurity Correction to c*	Throat Shrinkage	Uncorrected Characteristic Velocity, ft/sec	Corrected Characteristic Velocity, ft/sec	Theoretical Characteristic Velocity, ft/sec	Characteristic Velocity Efficiency	Delivered Vacuum Specific Impulse	Theoretical Shifting Vacuum Specific Impulse	Delivered Specific Impulse Efficiency	$\eta_G + \eta_D$ - ξ_{HL}	Impurity Correction to I _{vac}	Thrust Chamber Efficiency	Kinetic Efficiency
028*	70% B	2	5.117	0.294	2147	0.9904	5.0679	5.3619	90.6	17.24	445.29	0.9945	1.00854	1.0024	1.00	7524.1	7564.7	7702	0.9822	400.4	478.0	0.8377	0.9376	1.0034	0.8563	0.9187
029*	15 CHT	1	4.631	0.500	2095.8		4.586	5.086	89.57	9.17	443.42		1.00856			7809.1	7851.7	8138	0.9648	412.1	487.1	0.8460	0.9285		0.8803	0.9518
029*		2	4.548	0.496	2082.2		4.504	5.000	88.48	9.08			1.00857			7846.8	7889.6	8142	0.9690	416.4	487.15	0.8548	0.9265		0.8855	0.9590
030		1	5.192	0.414	2345.5		5.142	5.556	97.57	12.42			1.00849			7787.0	7828.7	7990	0.9798	422.2	484.7	0.8711	0.9282		0.8925	0.9643
030		2	5.256	0.415	2366.8		5.206	5.621	98.99	12.54			1.00848			7808.9	7850.8	7992	0.9823	421.1	484.6	0.8690	0.9282		0.8881	0.9599
031		1	5.309	0.345	2343.2		5.258	5.603	96.78	15.24			1.00849			7659.1	7700.2	7837	0.9825	418.2	481.2	0.8691	0.9269		0.8880	0.9611
031		2	5.361	0.345	2368.5		5.310	5.655	97.45	15.39			1.00849			7641.2	7682.2	7829	0.9812	418.8	481.05	0.8706	0.9269		0.8907	0.9638
032*		1	4.528	0.547	2158.1		4.484	4.941	90.46	9.81			1.00854			8118.2	8161.7	8105	1.0070	436.8	486.7	0.8975	0.9281		0.8947	0.9666
032*		2	4.484	0.454	1927.9		4.441	4.895	81.32	9.78			1.00865			7366.5	7406.0	8095	0.9149	395.8	486.5	0.8094	0.9272		0.8881	0.9609
033		1	5.256	0.420	2363.1		5.206	5.626	98.45	12.39			1.00848			7759.4	7801.0	7988	0.9766	420.0	484.5	0.8669	0.9281		0.8911	0.9630
033		2	5.239	0.420	2366.9		5.189	5.609	98.64	12.34			1.00848			7798.0	7840.0	7988	0.9815	422.0	484.5	0.8710	0.9282		0.8908	0.9626
034		1	5.289	0.357	2337.8		5.238	5.595	96.38	14.67			1.00849			7638.4	7679.3	7875	0.9751	417.8	481.7	0.8673	0.9268		0.8928	0.9660
034		2	5.293	0.359	2348.6		5.242	5.601	96.79	14.60			1.00849			7662.7	7703.8	7875	0.9783	419.3	481.7	0.8704	0.9269		0.8931	0.9662
035*			2.273	0.423	1099.2		2.251	2.674	47.07	5.32			1.00925			7805.5	7853.2	8460	0.9383	411.1	484.4	0.8487	0.9283		0.9177	0.9894
036*			2.308	0.401	1109.2		2.286	2.687	47.54	5.7			1.00925			7845.3	7893.1	8412	0.9383	412.8	485.25	0.8507	0.9279		0.9100	0.9821
037*			2.668	0.293	1187.0		2.642	2.955	49.69	9.02			1.00920			7507.2	7552.7	8087	0.9339	404.4	486.07	0.8320	0.9226		0.8943	0.9717
038*			2.752	0.227	1192.4		2.726	2.953	50.75	12.01			1.00917			7620.6	7666.6	7928	0.9670	403.8	483.0	0.8360	0.9215		0.8679	0.9464
039			2.845	0.194	1213.2		2.818	3.012	50.91	14.53			1.00917	1.0011		7495.0	7540.7	7796	0.9672	403.8	479.55	0.8400	0.9208	1.0012	0.8719	0.9511
041			2.775	0.198	1188.4		2.763	2.961	50.14	13.95	443.55		1.0093			7511.0	7547.0	7832	0.9636	401.4	480.45	0.8355	0.9205		0.8681	0.9476
042			2.768	0.198	1177.9		2.756	2.954	49.65	13.92			1.0092			7455.0	7490.8	7837	0.9558	398.7	480.50	0.8298	0.9210		0.8692	0.9482
043			2.818	0.173	1202.0		2.805	2.978	50.50	16.21						7521.5	7557.6	7702	0.9813	403.6	477.20	0.8458	0.9205		0.8659	0.9424
044			2.813	0.163	1156.9		2.800	2.963	48.65	17.18						7282.8	7317.8	7640	0.9578	390.4	475.40	0.8212	0.9203		0.8584	0.9381
045			2.804	0.167	1185.8		2.791	2.958	49.30	16.71						7392.5	7428.0	7670	0.9684	400.9	476.25	0.8418	0.9175		0.8703	0.9528
047*		1	2.695	0.272	1238.2		2.683	2.955	50.98	9.86	443.78					7655.8	7692.5	8037	0.9571	419.0	485.45	0.8631	0.9224		0.9028	0.9804
047*		2	2.686	0.270	1251.7		2.674	2.944	51.99	9.90						7837.0	7874.6	8035	0.9800	425.2	485.40	0.8760	0.9225		0.8949	0.9724
048*			2.746	0.206	1226.4		2.734	2.940	50.93	13.27						7687.8	7724.7	7870	0.9815	417.1	481.40	0.8664	0.9212		0.8837	0.9625
049*			2.689	0.207	1226.2		2.677	2.884	51.17	12.93						7873.8	7911.6	7887	1.0031	425.2	481.80	0.8825	0.9212		0.8808	0.9596
050*			2.715	0.178	1165.1		2.703	2.881	48.30	15.19						7440.1	7475.8	7765	0.9628	404.4	477.20	0.8474	0.9198		0.8811	0.9613
051*			2.606	0.278	1256.4		2.684	2.962	52.44	9.65						7856.9	7894.6	8052	0.9805	424.2	485.65	0.8735	0.9225		0.8919	0.9694

*Indicates Invalid test



TABLE 14
(Continued)

Task III Test Number	Nozzle Type	Data Slice	Oxidizer Flowrate, lbm/sec	Fuel Flowrate, lbm/sec	Vacuum Thrust, pounds	Oxidizer Density Correction	Corrected Oxidizer Flowrate, lbm/sec	Corrected Total Flowrate, lbm/sec	Chamber Pressure, psia	Mixture Ratio, o/f	Throat Area sq in	Discharge Coefficient	Heat Loss Correction to c	Impurity Correction to c	Throat Shrinkage	Uncorrected Characteristic Velocity, ft/sec	Corrected Characteristic Velocity, ft/sec	Theoretical Shifting Characteristic Velocity, ft/sec	Characteristic Velocity Efficiency	Delivered Vacuum Specific Impulse	Theoretical Shifting Vacuum Specific Impulse	Delivered Specific Impulse Efficiency	$\eta_g + \eta_p$ $-\xi_{HL}$	Impurity Correction to I vac	Thrust Chamber Efficiency	Kinetic Efficiency
052 *	15	CLT	2.731	0.207	1227.4	0.9955	2.719	2.926	50.63	13.14	443.78	0.9945	1.0092	1.0011	1.00	7679.1	7716.0	7878	0.9794	419.5	481.55	0.8711	0.9212	1.0012	0.8904	0.9692
053 *			2.856	0.177	1245.3		2.823	3.000	50.93	15.95			1.0092			7534.0	7570.2	7718	0.9808	415.1	477.53	0.8692	0.9200		0.8872	0.9672
054 *			2.777	0.177	1220.5		2.765	2.942	49.49	15.62						7465.3	7501.1	7740	0.9691	414.9	478.15	0.8677	0.9202		0.8964	0.9762
055 *			4.811	0.720	2286.0		4.789	5.509	100.30	6.65			1.0085			8079.7	8112.8	8355	0.9710	415.0	478.15	0.8679	0.9307		0.8948	0.9641
056 *			4.807	0.689	2303.7		4.785	5.474	100.22	6.94			1.0085			8125.0	8158.3	8300	0.9829	420.8	487.40	0.8634	0.9307		0.8794	0.9487
057 *			5.114	0.657	2487.0		5.091	5.748	104.26	7.75			1.0085			8049.5	8082.5	8275	0.9767	432.7	487.75	0.8871	0.9302		0.9093	0.9791
058			8.628	0.914	4089.9		8.589	9.503	172.56	9.40	444.48		1.0083			8071.0	8104.1	8215	0.9865	430.4	488.50	0.8811	0.9343		0.8942	0.9599
059			9.084	0.880	4243.5		9.043	9.923	177.11	10.28						7933.3	7964.2	8163	0.9734	427.6	488.05	0.8761	0.9342		0.8992	0.9630
060			9.148	0.820	4238.5		9.107	9.927	176.05	11.11						7882.6	7913.3	8120	0.9745	427.0	487.55	0.8758	0.9337		0.8997	0.9660
061			9.220	0.824	4341.4		9.179	10.003	180.16	11.14						8005.4	8036.6	8117	0.9901	434.0	487.50	0.8903	0.9339		0.9002	0.9665
062			9.323	0.646	4240.2		9.281	9.927	172.82	14.37						7738.0	7768.2	7986	0.9727	427.1	484.55	0.8814	0.9327		0.9071	0.9744
063			9.323	0.643	4256.6		9.281	9.927	172.76	14.43					1.000	7755.3	7765.5	7965	0.9730	428.8	484.50	0.8850	0.9327		0.9087	0.9760
064		70% B	8.918	0.870	4224.6		8.878	9.794	176.68	10.20	444.68					8030.0	8061.3	8170	0.9867	431.8	488.1	0.8847	0.9341		0.8976	0.9635
065			8.886	0.927	4210.7		8.846	9.773	178.01	9.52						8099.6	8131.2	8210	0.9904	430.8	488.5	0.8819	0.9345		0.8914	0.9569
066			8.825	0.762	4175.5		8.785	9.517	173.72	11.53						8091.5	8123.1	8104	1.0023	437.4	487.2	0.8978	0.9332		0.8967	0.9633
067			9.077	0.630	4119.2		9.036	9.666	169.29	14.34						7788.1	7818.5	7965	0.9816	426.2	484.4	0.8799	0.9326		0.8973	0.9647
068			8.800	0.894	4142.0		8.760	9.634	176.38	9.80						8124.4	8156.1	8195	0.9953	429.0	488.3	0.8786	0.9341		0.8837	0.9496
069			8.945	0.759	4150.0		8.905	9.664	174.23	11.73						8017.1	8048.4	8092	0.9946	429.4	487.1	0.8815	0.9333		0.8873	0.9538
070			9.084	0.641	4109.0		9.043	9.684	170.16	14.04						7813.6	7844.1	7982	0.9827	424.3	484.8	0.8752	0.9326		0.8916	0.9590
078			2.655	0.232	1138.4		2.643	2.875	50.05	11.40			1.0092			7741.2	7778.4	7960	0.9772	396.0	483.8	0.8185	0.9344		0.8386	0.9042
079			2.653	0.234	1158.8		2.641	2.875	50.54	11.29			1.0092			7817.0	7854.5	7962	0.9865	403.1	483.9	0.8330	0.9344		0.8454	0.9120
080			2.761	0.194	1165.8		2.749	2.943	50.52	14.16			1.0092			7633.3	7669.9	7825	0.9802	396.1	480.2	0.8249	0.9388		0.8426	0.9038
081			2.733	0.194	1156.9		2.721	2.915	50.16	14.02			1.0093			7651.8	7689.3	7832	0.9818	397.9	480.3	0.8284	0.9333		0.8448	0.9113
082			2.528	0.582	1333.7		2.517	3.099	57.83	4.32			1.0090			8298.2	8336.4	8585	0.9710	430.4	481.1	0.8946	0.9352		0.9233	0.9881
083 *			2.541	0.582	1350.5		2.530	3.112	58.31	4.34			1.0090			8331.9	8370.2	8585	0.9750	434.0	481.1	0.9021	0.9355		0.9262	0.9907
084			2.684	0.294	1236.9		2.672	2.966	52.97	9.09			1.0092			7941.7	7979.8	8092	0.9861	417.0	486.1	0.8578	0.9350		0.8706	0.9336
085			2.652	0.294	1213.7		2.640	2.934	52.03	8.99			1.0092			7885.8	7923.7	8100	0.9782	413.7	486.2	0.8509	0.9350		0.8709	0.9339
086			5.561	0.536	2556.4		5.536	6.094	109.15	9.92			1.0084			7964.7	7996.6	8128	0.9838	419.5	487.2	0.8610	0.9402		0.8762	0.9360
087			5.753	0.443	2599.9		5.727	6.170	109.08	12.93			1.0084			7861.6	7893.0	7982	0.9888	421.4	484.4	0.8699	0.9406		0.8808	0.9402

*Indicates invalid test



TABLE 14
(Continued)

Task Test Number	Nozzle Type	Data Slice	Oxidizer Flowrate, lbm/sec	Fuel Flowrate, lbm/sec	Vacuum Thrust, pounds	Oxidizer Density Correction	Corrected Oxidizer Flowrate, lbm/sec	Corrected Total Flowrate, lbm/sec	Chamber Pressure, psia	Mixture Ratio, o/f	Throat Area, sq in	Discharge Coefficient	Heat Loss Correction to c*	Impurity Correction to c*	Throat Shrinkage	Uncorrected Characteristic Velocity, ft/sec	Corrected Characteristic Velocity, ft/sec	Theoretical Shifting Characteristic Velocity ft/sec	Characteristic Velocity Efficiency	Delivered Vacuum Specific Impulse	Theoretical Shifting Specific Impulse	Delivered Specific Impulse Efficiency	$\eta_G + \eta_D$ - ξ_{HL}	Impurity Correction to γ_{vac}	Thrust Chamber Efficiency	Kinetic Efficiency
088	70% B		5.773	0.367	2511.6	0.9955	5.747	6.114	105.01	15.66	444.68	0.9945	1.0084	1.0011	1.000	7637.6	7668.2	7832	0.9791	410.8	481.2	0.8537	0.9392	1.0012	0.8729	0.9337
089*			5.191	0.953	2558.0		5.168	6.121	114.24	5.42						8299.3	8332.5	8528	0.9771	417.9	485.2	0.8613	0.9403		0.8825	0.9422
090			5.056	0.932	2582.4		5.033	5.965	114.20	5.40						8513.3	8547.4	8530	1.0020	432.9	485.1	0.8924	0.9403		0.8916	0.9513
091			5.541	0.775	2624.5		5.516	6.291	115.05	7.12						8132.3	8164.8	8340	0.9790	417.2	487.7	0.8554	0.9403		0.8747	0.9344
092	Cont. Exp.		2.620	0.233	1118.8		2.608	2.841	48.22	11.20			1.0092			7547.3	7583.5	7970	0.9515	393.8	484.0	0.8136	0.9230		0.8561	0.9331
093			2.600	0.237	1135.8		2.588	2.825	48.72	10.92						7669.0	7705.8	7985	0.9650	402.1	484.4	0.8501	0.9230		0.8612	0.9382
094			2.722	0.194	1171.5		2.710	2.904	49.55	13.97	447.25					7631.2	7667.8	7835	0.9787	403.4	480.5	0.8595	0.9235		0.8587	0.9352
095			2.756	0.196	1175.4		2.744	2.940	49.59	14.00						7543.8	7580.0	7835	0.9675	399.8	480.5	0.8520	0.9237		0.8609	0.9372
096			2.630	0.235	1147.2		2.618	2.853	49.77	11.14						7802.3	7839.8	7975	0.9830	402.1	484.0	0.8308	0.9233		0.8462	0.9229
097			2.691	0.234	1180.2		2.679	2.913	50.63	11.45						7773.4	7810.7	7955	0.9819	405.1	483.7	0.8375	0.9233		0.8539	0.9306
098			2.718	0.192	1184.9		2.706	2.898	50.49	14.09						7792.3	7829.7	7830	0.9999	408.9	480.3	0.8513	0.9237		0.8524	0.9287
099			2.732	0.189	1160.0		2.720	2.909	49.29	14.39						7587.2	7623.6	7815	0.9755	398.8	479.9	0.8510	0.9230		0.8529	0.9299
100			2.266	0.586	1199.0		2.255	2.841	52.56	3.85			1.0091			8274.2	8313.1	8620	0.9644	422.0	478.2	0.8825	0.9205		0.9161	0.9956
101			2.277	0.586	1218.7		2.267	2.853	52.97	3.87			1.0091			8275.5	8314.3	8620	0.9645	427.2	478.2	0.8934	0.9205		0.9273	1.0068
102			2.452	0.299	1136.2		2.441	2.740	49.02	8.16			1.0092			8001.5	8039.9	8165	0.9847	414.7	486.6	0.8522	0.9216		0.8664	0.9448
103			2.446	0.298	1106.1		2.435	2.733	47.94	8.17			1.0092			7845.2	7882.9	8165	0.9655	404.7	486.6	0.8317	0.9216		0.8624	0.9408
104		a	5.075	0.541	234.97		5.052	5.539	100.19	9.34			1.0085			8089.9	8121.5	8150	0.9965	424.2	487.4	0.8703	0.9277		0.8744	0.9467
104		b	5.081	0.541	235.56		5.058	5.599	100.29	9.35			1.0085			8011.3	804.25	8150	0.9868	420.7	487.4	0.8632	0.9277		0.8737	0.9480
105		a	5.286	0.429	2366.9		5.262	5.691	99.52	12.26						7821.1	7853.2	8000	0.9816	415.9	484.9	0.8577	0.9388		0.8748	0.9360
105		b	5.226	0.430	2374.6		5.202	5.632	99.78	12.10						7923.7	7956.2	8010	0.9932	421.6	484.9	0.8695	0.9388		0.8765	0.9377
106			5.227		2307.9		5.203	5.558	96.01	14.66						7725.8	7757.5	7880	0.9845	415.2	482.1	0.8612	0.9290		0.8738	0.9468
107		a	4.869	0.544	2236.9		4.874	5.418	95.78	8.96						7906.5	7938.9	8185	0.9699	412.9	487.6	0.8468	0.9273		0.8741	0.9468
107		b	4.885	0.545	2252.6		4.863	5.408	96.38	8.92						7970.7	8003.4	8185	0.9772	416.5	487.6	0.8542	0.9273		0.8751	0.9478
108		a	5.124	0.429	2267.7		5.101	5.530	95.86	11.89						7792.8	7784.6	8020	0.9706	410.1	485.3	0.8450	0.9290		0.8716	0.9426
108		b	5.076	0.429	2278.6		5.053	5.482	96.41	11.78						7865.6	7897.8	8020	0.9848	415.7	485.3	0.8566	0.9290		0.8708	0.9481
109		a	5.168	0.358	2256.8		5.145	5.495	94.29	14.70						7674.4	7705.9	7880	0.9779	410.7	482.1	0.8519	0.9288		0.8722	0.9434
109		b	5.100	0.358	2257.0		5.077	5.435	94.08	14.18						7741.9	7773.6	7905	0.9834	415.3	482.7	0.8604	0.9288		0.8759	0.9471
110			8.615	0.948	4107.1		8.574	9.552	170.75	9.04			1.0083			7995.0	8026.2	8230	0.9752	430.0	488.4	0.8804	0.9327		0.9038	0.9711
111			8.741	0.748	4093.3		8.702	9.450	167.89	11.63			1.0083			7945.9	7976.9	8090	0.9860	433.2	487.0	0.8895	0.9316		0.9031	0.9715

*Indicates invalid test



TABLE 14
(Continued)

Task Test Number	Nozzle Type	Data Slice	Oxidizer Flowrate, lbm/sec	Fuel Flowrate, lbm/sec	Vacuum Thrust, pounds	Oxidizer Density Correction	Corrected Oxidizer Flowrate, lbm/sec	Corrected Total Flowrate, lbm/sec	Chamber Pressure, psia	Mixture Ratio, o/f	Throat Area sq in	Discharge Coefficient	Heat Loss Correction to c	Impurity Correction to c	Throat Shrinkage	Uncorrected Characteristic Velocity, ft/sec	Corrected Characteristic Velocity, ft/sec	Theoretical Shifting Characteristic Velocity, ft/sec	Characteristic Velocity Efficiency	Delivered Vacuum Specific Impulse	Theoretical Shifting Vacuum Specific Impulse	Delivered Specific Impulse Efficiency	$\eta_G + \eta_D$ Correction to η_{vac}	Impurity Correction to η_{vac}	Thrust Chamber Efficiency	Kinetic Efficiency
112	Cont.		8.923	0.613	4048.7	0.9955	8.883	9.496	164.21	14.49	447.25	0.9945	1.0083	1.0011	1.000	7734.1	7764.3	7955	0.9760	426.4	484.2	0.8806	0.9339	1.0012	0.9033	0.9694
114	Exp.		8.458	0.632	3823.0		8.420	9.052	156.67	13.32						7740.9	7771.1	7990	0.9726	422.3	484.9	0.8709	0.9336		0.8964	0.9628
115			7.974	0.953	3863.9		7.938	8.891	161.38	8.33						8118.0	8149.7	8265	0.9860	434.6	488.3	0.8900	0.9318		0.9036	0.9718
116			7.354	1.078	3689.2		7.321	8.399	154.35	6.79						8219.2	8251.3	8390	0.9835	439.2	487.7	0.9006	0.9309		0.9167	0.9864
117	15 CLT		2.715	0.225	1191.7		2.703	2.928	51.10	12.01			1.0092			7805.5	7843.0	7930	0.9890	407.0	482.9	0.8428	0.9230		0.8532	0.9302
118			2.696	0.227	1185.9		2.684	2.911	51.05	11.82	442.91					7767.2	7804.5	7940	0.9829	407.4	483.2	0.8431	0.9230		0.8588	0.9358
119			2.842	0.190	1199.8		2.829	3.019	49.01	14.89						7493.8	7529.8	7780	0.9678	397.4	479.2	0.8293	0.9204		0.8579	0.9375
120			2.736	0.183	1146.3		2.724	2.907	49.01	15.89						7467.1	7502.9	7780	0.9644	394.3	479.2	0.8228	0.9198		0.8542	0.9344
121			2.626	0.227	1151.8		2.614	2.841	49.46	11.52						7710.7	7747.7	7955	0.9739	405.4	487.7	0.8331	0.9212		0.8616	0.9404
122		a	2.667	0.184	1148.5		2.655	2.879	49.54	14.43						7728.6	7760.3	7810	0.9936	404.5	479.9	0.8430	0.9203		0.8494	0.9291
123 *		b	2.589	0.193	1117.2		2.577	2.770	47.90	13.35						7658.9	7695.7	7865	0.9785	403.3	481.2	0.8381	0.9207		0.8573	0.9368
124 *			2.564	0.583	1321.8		2.552	3.135	57.18	4.38			1.0091			8078.3	8116.3	8575	0.9465	423.6	481.3	0.8801	0.9261		0.9380	1.0119
125			2.568	0.586	1321.8		2.556	3.142	57.40	4.36			1.0091			8091.3	8129.3	8575	0.9480	420.7	481.3	0.8741	0.9261		0.9230	0.9969
126			2.702	0.299	1247.2		2.690	2.989	53.22	9.00			1.0092			7886.1	7924.0	8095	0.9789	417.3	486.2	0.8583	0.9231		0.8778	0.9547
127			2.704	0.300	1236.8		2.692	2.992	52.71	8.97						7802.7	7840.1	8095	0.9685	413.4	486.2	0.8503	0.9231		0.8810	0.9579
128			2.624	0.191	1132.6		2.612	2.803	48.04	13.68						7590.9	7627.3	7850	0.9716	404.1	480.8	0.8405	0.9202		0.8661	0.9459
129			2.630	0.191	1136.7		2.618	2.809	48.26	13.71						7609.4	7645.9	7850	0.9740	404.7	480.8	0.8417	0.9202		0.8652	0.9450
130			2.518	0.227	1122.8		2.507	2.734	47.87	11.04						7754.9	7792.1	7975	0.9771	410.7	484.1	0.8484	0.9207		0.8693	0.9486
130			2.510	0.227	1104.0		2.499	2.726	47.08	11.01						7649.3	7686.0	7975	0.9638	405.0	484.1	0.8366	0.9207		0.8690	0.9483

*Indicates invalid test

207-1



TABLE 14
(Concluded)

Task No. Test Number	Nozzle Type	Data Slice	Oxidizer Flowrate, lbm/sec	Fuel Flowrate, lbm/sec	Vacuum Thrust, Pounds	Oxidizer Density Correction	Corrected Oxidizer Flowrate, lbm/sec	Corrected Total Flowrate, lbm/sec	Chamber Pressure, psia	Mixture Ratio, o/f	Throat Area	Discharge Coefficient	Heat Loss Correction to c^*	Impurity Correction to c^*	Throat Shrinkage	Uncorrected Characteristic Velocity, ft/sec	Corrected Characteristic Velocity, ft/sec	Theoretical Shifting Characteristic Velocity, ft/sec	Characteristic Velocity Efficiency	Delivered Vacuum Specific Impulse	Theoretical Shifting Vacuum Specific Impulse	Delivered Specific Impulse Efficiency	$\eta_G + \eta_p$ $-\xi_{HL}$	Impurity Correction to I_{vac}	Thrust Chamber Efficiency	Kinetic Efficiency
159	15	GST	2.4560	0.2670	1140.90	0.9955	2.4660	2.7119	49.07	9.16	13.75	0.9945	1.0092	1.0011	1.0000	8004.65	8012.86	8072.04	0.9964	420.69	485.98	0.8657	0.9225	1.0012	0.8700	0.9475
160			2.4560	0.2670	1142.00		2.4630	2.7100	49.01	9.15	13.75		1.0092			8000.73	8038.94	8072.42	0.9959	421.41	485.41	0.8671	0.9225		0.8719	0.9494
164*			2.8170	0.1900	1217.20		2.8045	2.9945	51.95	14.76	13.77		1.0092			7682.95	7719.13	7784.18	0.9916	406.50	479.37	0.8480	0.9207		0.8765	0.9556
165*			2.6980	0.3180	1294.10		2.6859	3.0039	53.21	8.45	13.77		1.0091			7847.51	7884.10	8133.17	0.9694	420.85	486.55	0.8650	0.9233		0.8835	0.9702
166			2.7360	0.1880	1197.40		2.7217	2.9097	50.80	14.48	13.77		1.0092			7734.54	7770.95	7797.77	0.9666	411.52	479.70	0.8579	0.9206		0.8620	0.9414
167			2.6470	0.2250	1194.00		2.6351	2.8601	50.78	11.71	13.77		1.0092			7865.40	7902.62	7935.98	0.9958	417.47	485.51	0.8638	0.9216		0.8686	0.9470
172	10	C	2.8010	0.1850	1260.70		2.8751	3.0601	52.57	15.54	14.04		1.0092			7729.60	7766.11	7738.49	1.0036	411.98	478.98	0.8615	0.9116		0.8596	0.9179
173			2.7960	0.2210	1253.40		2.7796	3.0006	52.62	12.58	14.04		1.0092			7890.55	7927.55	7900.12	1.0035	417.71	482.29	0.8661	0.9116		0.8643	0.9527
174			2.8280	0.1810	1239.60		2.8124	2.9954	51.59	15.54	14.04		1.0092			7755.85	7790.55	7736.48	1.0070	414.10	478.17	0.8660	0.9116		0.8612	0.9496
175			2.7360	0.2220	1231.40		2.7210	2.9429	51.40	12.26	14.04		1.0092			7888.45	7925.74	7912.89	1.0016	418.42	482.66	0.8669	0.9116		0.8667	0.9551
1	20	C	2.2820	0.2210	1020.00		2.2717	2.4927	45.95	10.28	13.87		1.0094			7866.87	7905.48	7995.29	0.9890	409.19	484.92	0.8438	0.9149	1.0013	0.8565	0.9596
2		b	2.3060	0.2210	1050.70		2.2956	2.5166	44.42	10.59	13.87		1.0095			7875.52	7914.08	7988.40	0.9907	409.56	484.80	0.8448	0.9150		0.8560	0.9590
3			2.3850	0.1880	1038.50		2.3725	2.5605	44.77	12.62	13.87		1.0095			7802.25	7840.36	7882.20	0.9947	405.62	482.10	0.8414	0.9151		0.8471	0.9521
4			2.5080	0.2200	1058.90		2.4976	2.5176	45.67	10.44	13.87		1.0095			8093.95	8133.31	7988.05	0.9892	405.88	484.75	0.8677	0.9151		0.8552	0.9381
5			2.4440	0.1880	1065.80		2.4330	2.6210	45.50	12.94	13.87		1.0095			7745.74	7783.44	7868.70	1.0182	420.60	484.75	0.8426	0.9151		0.8535	0.9384
10			2.7490	0.2250	1247.30		2.7764	3.0014	53.25	12.45	13.87		1.0091			7916.05	7953.15	7912.15	1.0051	415.57	482.64	0.8610	0.9156		0.8580	0.9424
11			2.9260	0.1850	1247.70		2.9128	3.0978	53.45	15.75	13.87		1.0091			7695.66	7731.71	7728.08	1.0005	402.77	477.98	0.8426	0.9156		0.8455	0.9297
12			2.8920	0.2250	1255.70		2.8955	3.0525	53.60	12.60	13.87		1.0091			7900.25	7939.19	7901.78	1.0045	414.11	482.55	0.8586	0.9156		0.8560	0.9404
13	15	GST	2.7750	0.2250	1257.40		2.7625	2.9875	52.82	12.28	13.76		1.0091			7828.44	7865.19	7914.84	0.9957	409.21	478.56	0.8581	0.9218	1.0012	0.8647	0.9429
14			2.8780	0.1850	1298.10		2.8650	3.0500	53.02	15.49	13.76		1.0091			7696.96	7733.07	7743.28	0.9987	420.60	482.65	0.8554	0.9206		0.8578	0.9571
15			2.7640	0.2230	1251.10		2.7516	2.9746	53.44	12.54	13.76		1.0091			7954.81	7992.06	7913.29	1.0100	409.57	479.00	0.8546	0.9205		0.8615	0.9409
16			2.7860	0.1850	1211.10		2.7735	2.9585	51.55	16.99	13.76		1.0092			7682.50	7718.58	7769.44	0.9935	424.16	484.11	0.8562	0.9116		0.8581	0.9464
21	10	C	2.6290	0.257	1209.50		2.6145	2.8515	50.29	11.05	13.96		1.0092			7925.24	7960.82	7967.15	0.9992	420.72	486.17	0.8544	0.9116		0.8654	0.9538
23			2.4850	0.2780	1156.70		2.4715	2.7495	49.35	8.89	13.96		1.0092			8065.87	8102.26	8091.57	1.0015	424.25	485.90	0.8670	0.9116		0.8681	0.9565
25			2.6380	0.2540	1198.90		2.6255	2.8575	50.59	11.21	13.96		1.0092			7922.15	7959.73	7958.47	1.0002	419.90	485.90	0.8670	0.9116		0.8698	0.9581
26			2.5560	0.2740	1195.10		2.5419	2.8169	50.62	9.24	13.96		1.0092			8027.87	8111.15	8069.57	1.0051	424.25	485.95	0.8751	0.9116		0.8709	0.9595
27			2.6380	0.2530	1194.50		2.6255	2.8565	50.05	11.26	13.96		1.0092			7868.50	7905.66	7955.41	0.9957	418.17	485.85	0.8645	0.9116			0.9595



TABLE 15

NOZZLE PRESSURE DATA FOR LONG THROAT
15-DEGREE CONICAL CHECKOUT NOZZLE

Test No.	Nozzle Static Pressure Ratio, P_N/P_{C2-NS}						Nominal Chamber Pressure, psia
	$\epsilon = 1.5$	$\epsilon = 3$	$\epsilon = 7$	$\epsilon = 15$	$\epsilon = 30$	$\epsilon = 60$	
006	0.135	0.064	0.014	0.004	0.0012	0.00112	100
007	0.140	0.065	0.014	0.004	0.0010	0.00106	100
008	0.144	0.069	0.015	0.004	0.0009	0.00117	100



TABLE 16

NOZZLE PRESSURE DATA FOR 70-PERCENT BELL NOZZLE

Test No.	Nozzle Static Pressure Ratio, P_N/P_{C2-NS}						Nominal Chamber Pressure, psia
	$\epsilon = 1.5$	$\epsilon = 3$	$\epsilon = 7$	$\epsilon = 15$	$\epsilon = 30$	$\epsilon = 60$	
009	0.063	0.043	0.019	0.008	0.0067	0.00176	100 ↓
010	0.067	0.045	0.020	0.009	0.0060	0.00173	
011	0.067	0.044	0.020	0.009	0.0061	0.00171	
012	0.057	0.039	0.018	0.008	0.0065	0.00168	
013	0.066	0.044	0.020	0.008	0.0065	0.00155	100 ↓ 50
014	0.065	0.040	0.020	0.008	0.0064	0.00153	
015	0.056	0.038	0.016	0.007	0.0032	0.00208	
016	0.055	0.029	0.015	0.008	0.0008	0.00217	
017	0.057	0.027	0.015	0.007	0.0005	0.00200	50 ↓
018	0.059	0.030	0.016	0.008	0.0016	0.00197	
019	0.059	0.032	0.017	0.008	0.0018	0.00195	
020	0.055	0.038	0.017	0.007	0.0026	0.00209	
021	0.056	0.038	0.017	0.007	0.0027	0.00184	
022	0.059	0.040	0.017	0.007	0.0012	0.00189	
023	0.061	0.042	0.017	0.008	0.0018	0.00180	
024	0.062	0.043	0.017	0.008	0.0018	0.00176	
025	0.063	0.044	0.017	0.008	0.0017	0.00177	
026	0.063	0.043	0.018	0.013	0.0071	0.00192	
027-1	0.066	0.045	0.017	0.012	0.0069	0.00183	100 ↓ 100
027-2	0.068	0.046	0.018	0.013	0.0073	-	
028-1	0.067	0.046	0.020	0.015	0.0068	0.00176	
028-2	0.068	0.047	0.021	0.015	0.0077	-	

TABLE 16
(Concluded)

Test No.	Nozzle Static Pressure Ratio, P_N/P_{C2-NS}						Nominal Chamber Pressure, psia
	$\epsilon = 1.5$	$\epsilon = 3$	$\epsilon = 7$	$\epsilon = 15$	$\epsilon = 30$	$\epsilon = 60$	
064	0.065	0.0450	0.0211	0.00851	0.00500	0.00373	175 ↓
065	0.0644	0.0432	0.0203	0.0083	0.0048	0.0033	
066	0.0652	0.0475	0.0207	0.0083	0.0048	0.0034	
067	0.0645	0.0487	0.0204	0.0084	0.0049	0.0034	
068	0.0642	0.0428	0.0203	0.0083	0.0048	-	
069	0.0628	0.0462	0.0199	0.0085	0.0048	0.0034	175 ↓ 50
070	0.0603	0.0482	0.0193	0.0084	0.0049	0.0034	
078	0.0606	0.0399	0.0210	0.0113	0.0046	0.002	
079	0.0633	0.0424	0.0199	0.0113	0.0046	0.0019	
080	0.0642	0.0432	0.0201	0.0114	0.0046	0.0019	
081	0.064	0.0432	0.0200	0.0115	0.0046	0.0019	50 ↓ 100
082	0.0576	0.0379	0.0190	0.0080	0.0046	0.0024	
083	0.0577	0.0381	0.0190	0.0078	0.0046	0.0025	
084	0.0627	0.0416	0.0200	0.0080	0.0046	0.0018	
085	0.0618	0.0416	0.0196	0.0080	0.0046	0.0018	
086	-	0.0448	0.0210	0.0078	0.0046	0.0019	100 ↓ 100
087	-	0.0477	0.0212	0.0080	0.0046	0.0019	
088	-	0.0481	0.0213	0.0080	0.0047	0.0019	
089	0.0607	0.0411	0.0193	0.0078	0.0045	0.0019	
090	0.0618	0.0419	0.0192	0.0078	0.0044	0.0019	
091	0.0620	0.0435	0.0196	0.0078	0.0045	0.0019	100



TABLE 17

NOZZLE PRESSURE DATA FOR CONTROLLED EXPANSION NOZZLE

Test No.	Nozzle Static Pressure Ratio, P_N/P_{C2-NS}						Nominal Chamber Pressure, psia
	$\epsilon = 1.5$	$\epsilon = 2.6$	$\epsilon = 7$	$\epsilon = 15$	$\epsilon = 30$	$\epsilon = 60$	
092	0.174	0.0803	0.0128	0.00523	0.00315	0.00160	50 ↓
093	0.176	0.0826	0.0132	0.00569	0.00331	0.00160	
094	0.178	0.0839	0.0135	0.00591	0.00335	0.00152	
095	0.179	0.0845	0.0135	0.00591	0.00337	0.00151	
096	0.175	0.0821	0.0132	0.00598	0.00335	0.00149	
097	0.176	0.0823	0.0130	0.00579	0.00328	0.00163	
098	0.178	0.0842	0.0133	0.00600	0.00345	0.00148	
099	0.177	0.0838	0.0133	0.00594	0.00343	0.00184	
100	0.163	0.0751	0.0114	0.00460	0.00319	0.00178	
101	0.162	0.0751	0.0115	0.00466	0.00317	0.00162	
102	0.170	0.0785	0.0125	0.00504	0.00327	0.00151	50 ↓ 100 ↓
103	0.168	0.0774	0.0124	0.00557	0.00326	0.00159	
104	-	0.0832	0.0124	0.00580	0.00339	-	
105	-	0.0851	0.0131	0.00603	0.00352	0.00157	
106	-	0.0851	0.0136	0.00622	0.00359	0.00142	
107	-	0.0825	0.0124	0.00588	0.00333	0.00166	
108	-	0.0852	0.0130	0.00609	0.00344	0.00163	
109	-	0.0861	0.0135	0.00634	0.00356	0.00149	
110	0.183	0.0864	0.0126	0.00535	0.00159	0.000737	
111	0.187	0.0846	0.0132	0.00616	0.00138	0.000756	
112	0.188	0.0185	0.0137	0.00633	0.00120	0.000785	175 ↓ 175
114	0.186	0.0836	0.0134	0.00623	0.00385	0.00120	
115	0.181	0.0837	0.0123	0.00568	0.00362	0.00129	
116	0.178	0.0819	0.0118	0.00536	0.00334	0.00135	



TABLE 18

NOZZLE PRESSURE DATA FOR LONG THROAT 15-DEGREE CONICAL NOZZLE

Test No.	Nozzle Static Pressure Ratio, P_N/P_{C2-NS}			Nominal Chamber Pressure, psia
	$\epsilon = 1.5$	$\epsilon = 3$	$\epsilon = 60$	
029-1	0.139	0.066	0.00103	100 ↓
029-2	0.141	0.067	0.00095	
030-1	0.146	0.070	0.00071	
030-2	0.146	0.071	0.00078	
031-1	0.150	0.071	0.00078	
031-2	0.150	0.072	0.00080	
032-1	0.140	0.067	0.00104	
032-2	0.140	0.066	0.00098	
033-1	0.145	0.070	0.00083	
033-2	0.146	0.070	0.00087	
034-1	0.149	0.071	0.00085	100 ↓
034-2	0.150	0.070	0.00088	
035	0.130	0.059	-	50
036	0.133	0.061	0.00131	50 ↓
037	0.139	0.064	0.00113	
038	0.144	0.066	0.00112	
039	0.148	0.067	0.00108	
041	0.143	0.0672	0.00160	
042	0.148	0.0663	0.00141	
043	0.149	0.0655	0.00135	
044	0.149	0.0667	0.00140	
045	0.146	0.0655	0.00136	50

TABLE 18
(Concluded)

Test No.	Nozzle Static Pressure Ratio, P_N/P_{C2-NS}			Nominal Chamber Pressure, psia
	$\epsilon = 1.5$	$\epsilon = 3$	$\epsilon = 60$	
047	0.142	0.0654	0.00115	50 ↓
048	0.146	0.0669	0.00098	
049	0.147	0.0669	0.00096	
050	0.149	0.0673	0.00103	
051	0.138	0.0640	0.00145	
052	0.149	0.0670	0.00119	50 ↓
053	0.149	0.0663	0.00112	
054	0.149	0.0675	0.00110	100 ↓
055	-	-	0.00081	
056	0.135	-	0.00070	100 ↓
057	-	-	0.00069	
058	0.137	0.0712	0.00081	200 ↓
059	0.144	0.0688	0.00060	
060	0.144	0.0684	0.00065	
061	0.141	0.0712	0.00056	
062	-	0.0655	0.00032	
063	0.146	0.0662	0.00028	200



TABLE 19

NOZZLE PRESSURE DATA FOR SHORT THROAT 15-DEGREE CONICAL NOZZLE

Test No.	Nozzle Static Pressure Ratio, P_N/P_{C2-NS}			Nominal Chamber Pressure, psia
	$\epsilon = 1.5$	$\epsilon = 3$	$\epsilon = 60$	
159	0.172	—	0.00084	50 ↓ 50
160	0.174	—	0.00082	
161	0.168	0.0584	0.00088	
162	0.171	0.0589	0.00087	
163	0.174	0.0592	0.00084	
164	0.1724	0.0574	0.000963	
165	0.1686	0.0552	0.001029	
166	0.1763	0.0589	0.000984	
167	0.1754	0.0581	0.000961	
013	0.1753	0.0566	0.00112	
014	0.1763	0.0571	0.00102	
015	0.1753	0.0567	0.00097	
016	0.1771	0.0577	0.00105	



TABLE 20

NOZZLE PRESSURE DATA FOR 10-DEGREE CONICAL NOZZLE

Test No.	Nozzle Static Pressure Ratio, P_N/P_{C2-NS}				Nominal Chamber Pressure, psia
	$\epsilon = 1.5$	$\epsilon = 3$	$\epsilon = 25$	$\epsilon = 60$	
017	0.1766	0.0540	0.00249	0.00097	50
018	0.1802	0.0556	0.00251	0.00102	↓
019	0.1787	0.0543	0.00247	0.00100	
020	0.1801	0.0554	0.00250	0.00102	50
024	0.1756	0.0530	0.0024	0.00099	100
025	0.1718	0.0513	-	0.00099	50
026	0.1762	0.0534	0.00244	0.00100	↓
027	0.1730	0.0521	0.00229	0.00097	
028	0.1757	0.0532	0.00246	0.00099	
172	0.1818	0.0579	0.00284	0.00095	
173	0.1811	0.0568	0.002785	0.00091	↓
174	0.1830	0.0576	0.002822	0.00093	
175	0.1806	0.0567	0.002784	0.00091	



TABLE 21

NOZZLE PRESSURE DATA FOR 20-DEGREE CONICAL NOZZLE

Test No.	Nozzle Static Pressure Ratio, P_N/P_{C2-NS}				Nominal Chamber Pressure, psia
	$\epsilon = 1.5$	$\epsilon = 3$	$\epsilon = 30$	$\epsilon = 60$	
001-1	0.1297	0.0596	0.0021	0.00170	<div>50</div> <div>↓</div> <div>50</div>
001-2	0.1301	0.0594	0.0021	0.00166	
002	0.1311	0.0600	0.0022	0.00136	
003	0.1292	0.0589	0.0021	0.00120	
004	0.1314	0.0604	0.00215	0.00190	
010	0.1318	0.0606	-	0.00126	
011	0.1323	0.0608	-	0.00101	
012	0.1311	0.0609	-	0.00091	



DISCUSSION

Examination of the test data shows that correlation of data throughout the testing was excellent, and in general, all instrumentation performed very well. Transducers, including flowmeters, thrust cells, and pressures were changed several times during the program, sometimes in pairs, and sometimes in individual units, and yet the data were always consistent and repeatable.

Several anomalies were encountered during the testing; these were resolved and are discussed below.

Hydrogen Flow Measurement

The initial facility checkout tests resulted in excessively low combustion performance when compared to that previously demonstrated in the injector evaluation portion of the program. Because the previous data were well documented, it appeared that some discrepancy in the facility measurement system was responsible. Resolution of the problem occurred when analysis of the various system measurements indicated that the pressure ratio across the hydrogen sonic venturi was below that required to choke the meter. This condition results in actual flowrate possibly 30 to 40 percent below that indicated by the upstream pressures.

Because the injector inlet pressure was of the right magnitude, it was apparent that choking was occurring some place in the main propellant line. The yoke that forms the double inlet to the injector was replaced by larger diameter tubing, and subsequent testing indicated a venturi pressure ratio of approximately 1.8, well above that required for sonic flow.



Chamber Pressure Oscillations

A second irregularity, but one which was not isolated as a problem until somewhat later, was noted during the early testing. This was the occurrence of chamber pressure oscillations in the mid-frequency or "buzz" regime (250 to 500 cps). It was shown that a significant lowering of performance occurred when the amplitude of this buzzing exceeded a minimum value. Thrust chamber characteristic velocity efficiency as a function of chamber pressure buzz amplitude, defined as half the peak-to-peak pressure variation divided by the chamber pressure and expressed as a percentage, is shown in Fig. 110. As can be seen, at amplitudes greater than about 7 percent, a significant decrease in performance occurs; this results in questionable thrust coefficient values. It was therefore decided that any tests in which the buzz amplitude was greater than 5 percent would be invalidated.

The significant characteristic of the buzz was the operating range in which it occurred. It was almost entirely limited to the low chamber pressure (50 psia) and low mixture ratio (12:1 and less) regime. Since no similar problem had been encountered during the Task II testing, except during the characteristic length evaluation test series, and then only at very low values of characteristic length, it was apparent the problem was associated with operation of the engine-facility combination, and was probably the result of a coupling between the combustion process and the feed system.

Comparison of the flow systems for the Research Facility, where the Task II testing was done, and the NFL facility indicated that a "stiffer" liquid fluorine system had been utilized at the Research Facility. This is a result of shorter propellant lines and the use of a high-pressure-drop orifice at the engine inlet that essentially isolated the engine from the feed system. Orificing of the system was evaluated during subsequent low-pressure testing, and the problem was ultimately resolved by this method in combination with temperature control of the liquid fluorine.

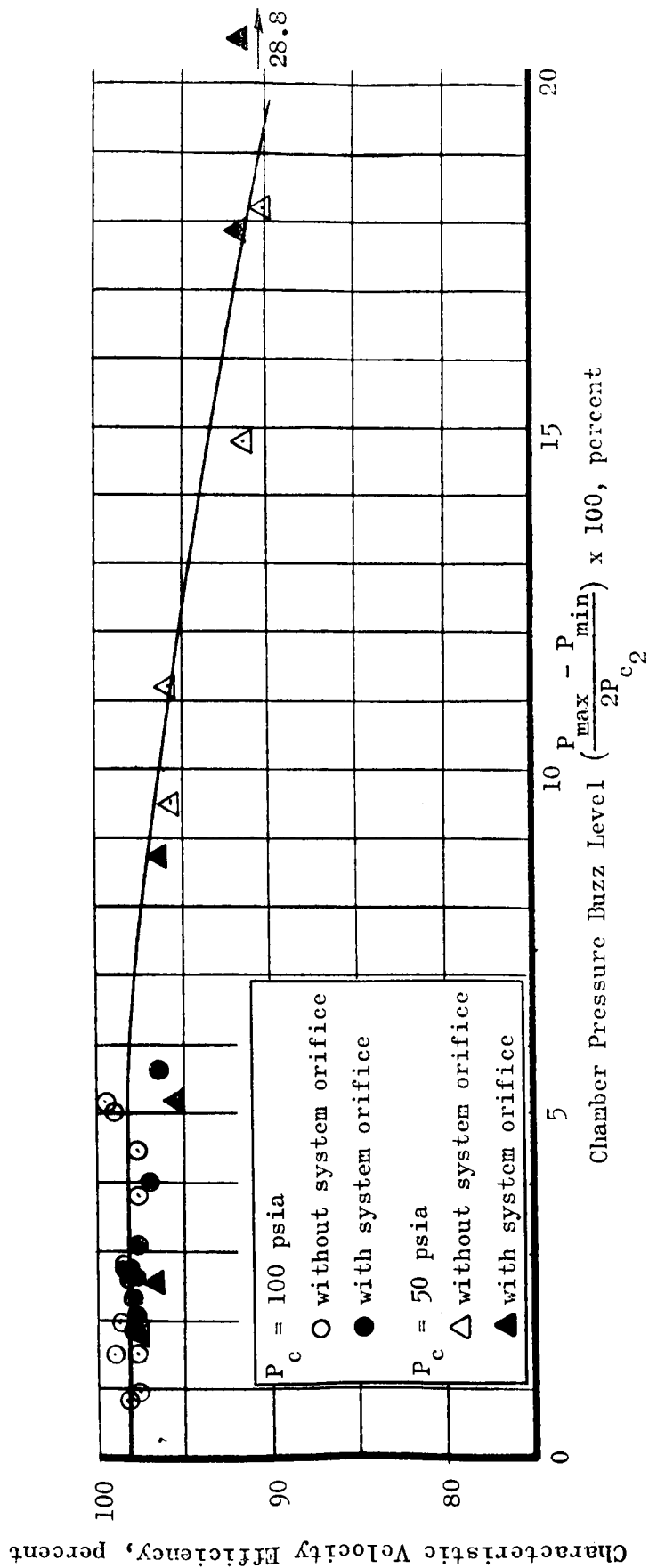


Figure 111. Characteristic Velocity Efficiency vs Chamber Pressure Buzz Level



As the data summary indicates, various orifices and orifice combinations were evaluated with the intended purpose of operating the system at maximum tank pressure for a specific mixture ratio-chamber pressure combination. The initial change was to install an orifice at the dome inlet, similar to what had been done in Task II. This alleviated the problem; however, it was not satisfactory for all operating modes. The ultimate result was the "distributed ΔP " system, in which an orifice was used at the oxidizer inlet and a second orifice at the main oxidizer valve.

Figure 112 shows the chamber pressure oscillation level as a function of fluorine temperature at the flowmeter. All testing at 50-psia chamber pressure is included. It is evident that this temperature has a significant affect on the oscillation level, with essentially no tests exceeding the allowable limit at temperatures above -300F. The hypothesis is that the higher temperatures result in increased boiling of the propellant as it passes through the injector and, in particular, the orifices. This is supported by Fig. 113 which shows the injector pressure drop as a function of propellant temperature. The shift in pressure drop is higher than can be accounted for, by the variation in propellant temperature, indicating a shift in effective orifice area (i.e., in discharge coefficient). This change in discharge coefficient would occur if the propellant were boiling in the orifice. The net result is not only increased pressure drop for an equivalent flow, but also additional system decoupling because of the damping provided by the gas in the orifice.

Fluorine temperature was controlled by adjusting the temperature of the liquid nitrogen in the line cooling jacket. This is accomplished by varying the pressure in the LN_2 storage vessel prior to the test.

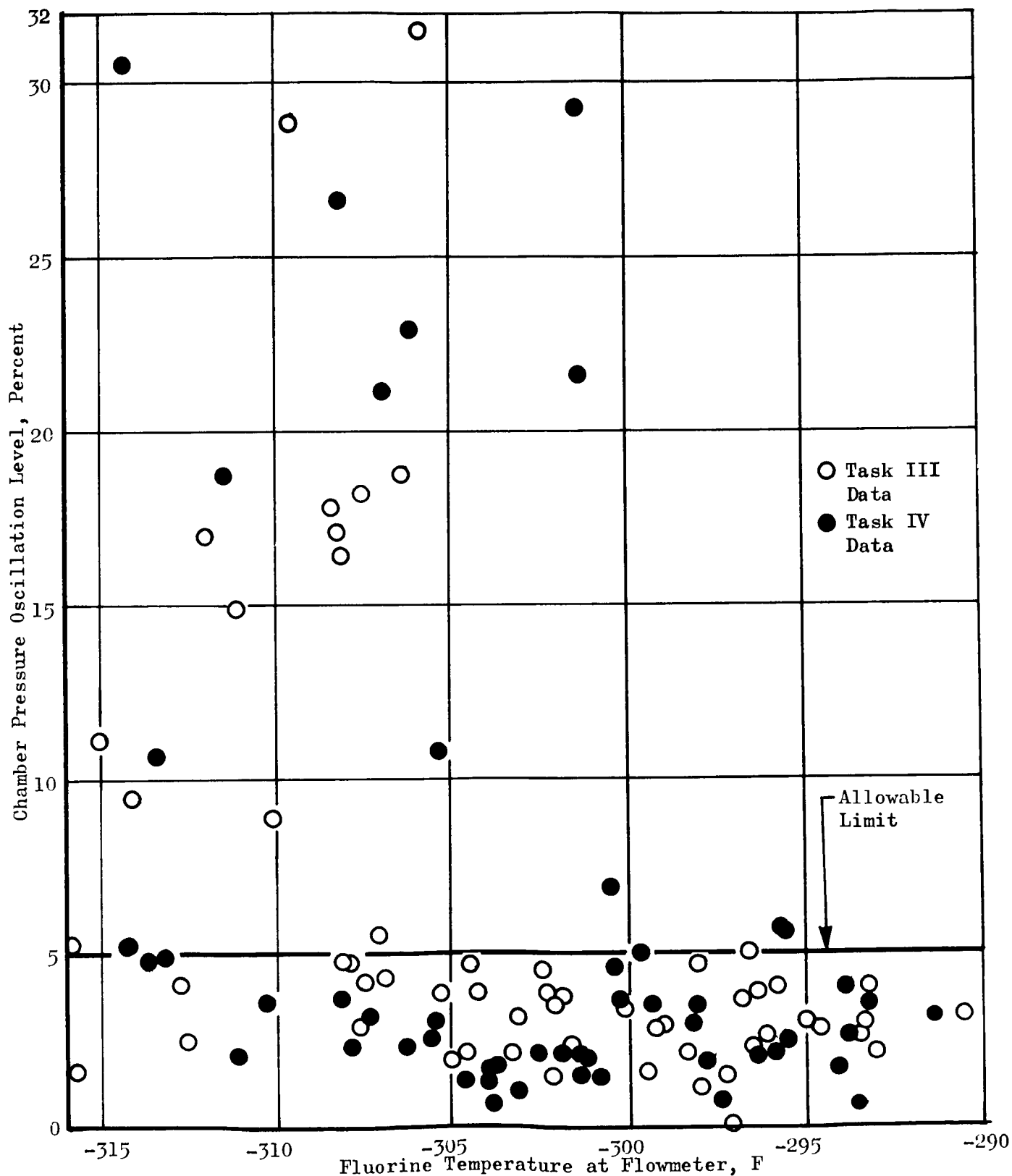


Figure 112. Effect of Fluorine Temperature on Chamber Pressure Oscillation at $P_c = 50$ psia

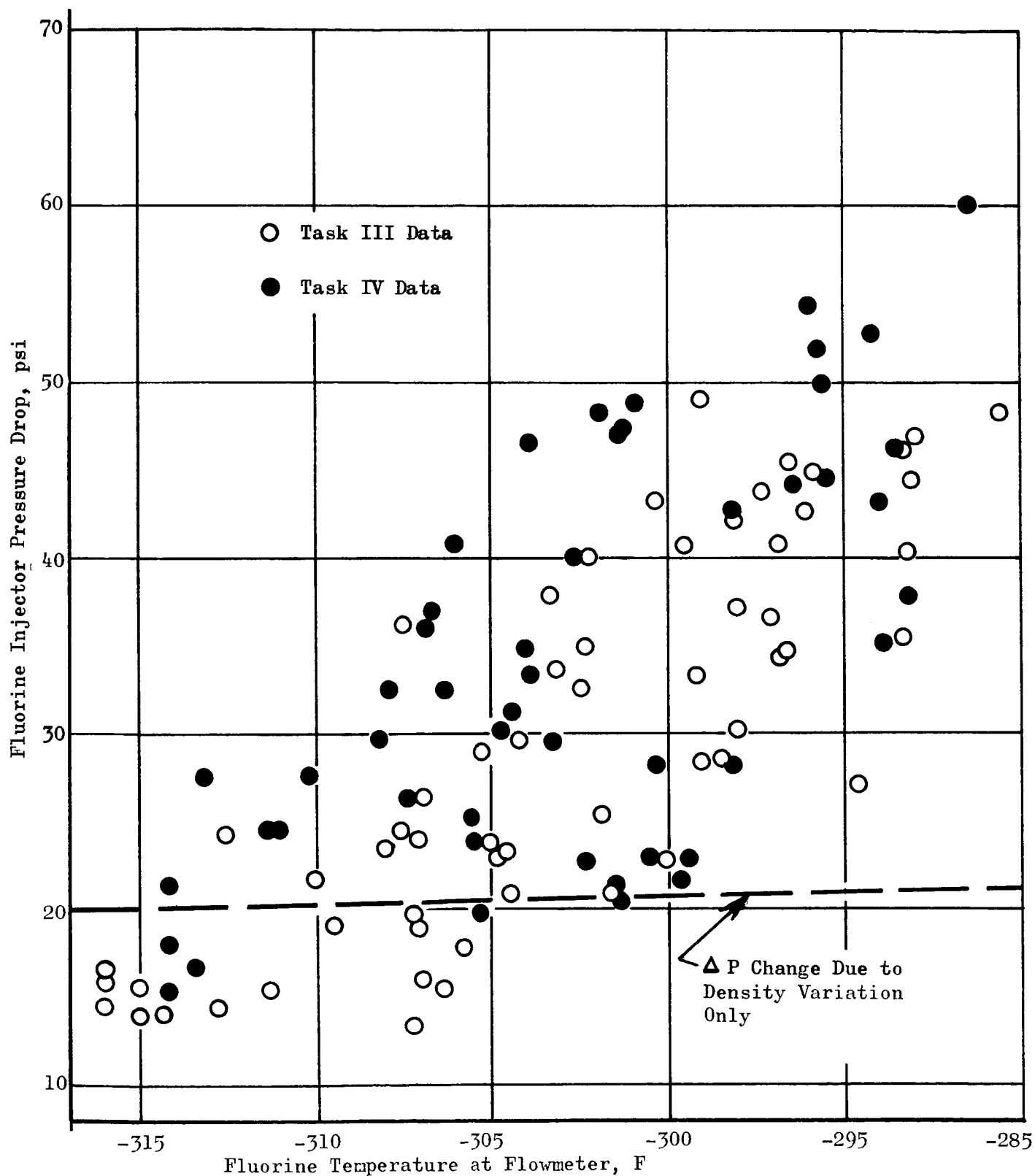


Figure 113. Effect of Fluorine Temperature on Injector Pressure Drop at 50 psia Chamber Pressure



This problem could undoubtedly be solved in other ways, such as changes to the flow system or changes to the injector, in particular the impingement distance or injection velocities. However, since it was not the major intent of the program to investigate injector combustion design techniques, the relatively simple and expedient system orificing and temperature control solution was taken.

Fluorine Temperature

As discussed in the flow system description, some problems with fluorine temperature occurred. These were resolved by the addition of the accumulator to the system.

Hardware Condition

Posttest hardware condition was excellent. Figure 114 shows the injector face at the conclusion of the Task III effort. Throughout the program the only engine hardware which was significantly damaged was the injector dome on test 046.

During the latter portion of the Task III effort, the combustion chamber showed signs of deterioration with minor erosion in the area from approximately 2 inches to 10 inches below the injector face with some flange warping and bulging. This section was replaced early in Task IV and, with all low chamber pressure operation in this phase, no problems were experienced.

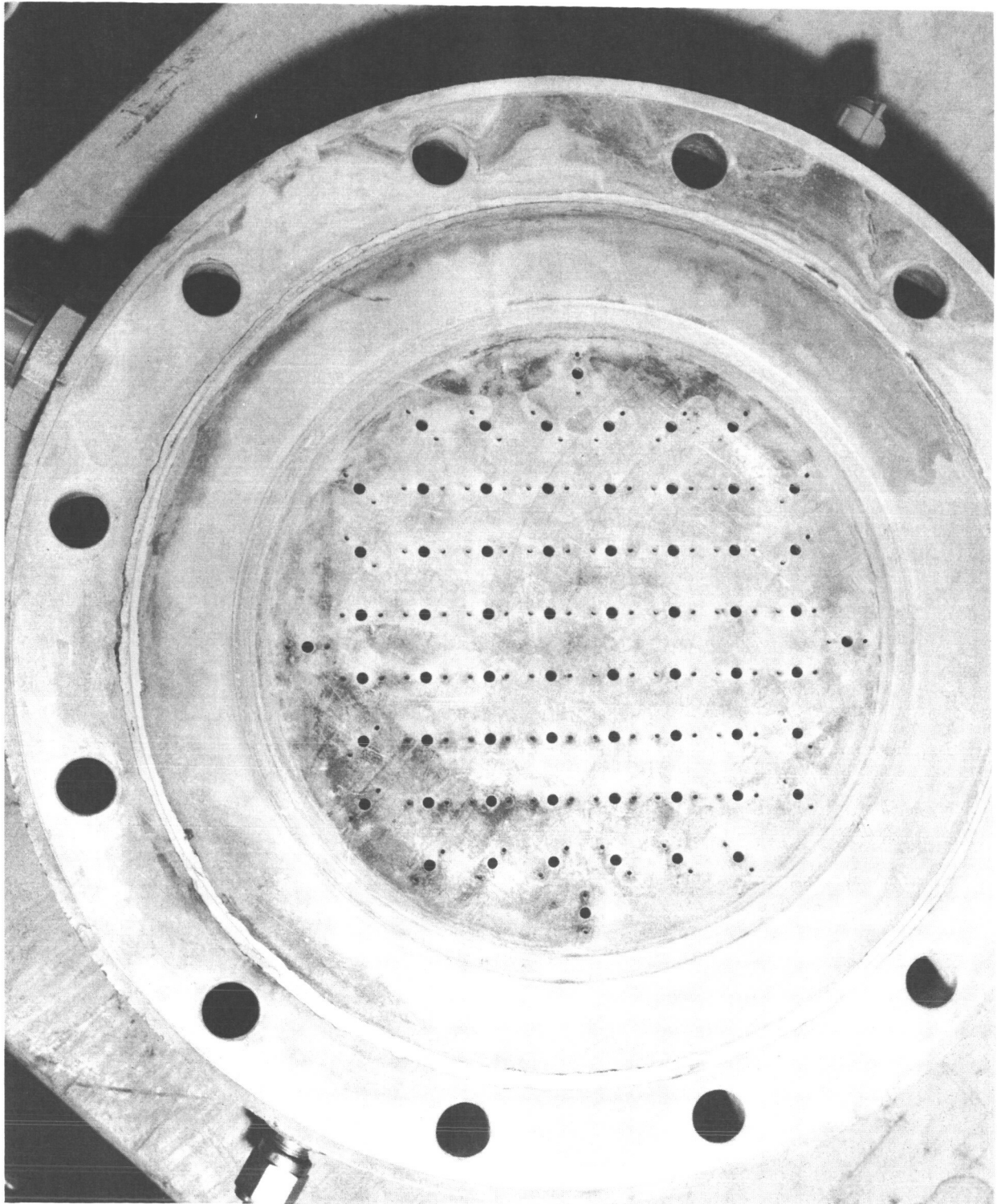


Figure 114. Liquid Fluorine/Gaseous Hydrogen Injector Completion of Task IV.



MEASUREMENT SYSTEM ANALYSIS

Analysis of the precision of the measurement systems was conducted as described in Appendix C. Because the primary performance parameter studied in this program was the thrust coefficient, detailed precision calculations are presented for thrust, chamber pressure, altitude pressure, throat area, and exit area. The individual imprecisions are listed in Table 22. The resultant thrust coefficient precision at a 95- percent confidence level is ± 0.403 percent. The quality of the Task IV data, as indicated in Fig. 21, substantiates this analysis.

TABLE 22

MEASUREMENT PRECISION

Parameter	Precision, percent
Measured Thrust	± 0.2015
Environmental Pressure	± 0.175
Exit Area	± 1.79
Vacuum Thrust	± 0.202
Chamber Pressure	± 0.097
Throat Area	± 0.32



COLD FLOW NOZZLE TEST PROGRAM

A series of cold flow tests was conducted at the Rocket Nozzle Test Facility on a 1/5 scale model, $\epsilon = 60:1$, of the controlled expansion nozzle. Thirty-eight tests were conducted with high pressure air as the test medium. Performance efficiency was measured as a function of simulated altitude conditions and varying chamber pressure (17 to 175 psia). Wall pressure profile data were also obtained during the test sequence.

Vacuum thrust efficiency increased by 1.2 percent as chamber pressure was varied from 17 to 175 psia. Under full-flow conditions wall pressures near the end of the nozzle were higher than predicted. Therefore, at the termination of the test program, photographs were taken to detect the presence of condensation of the exhaust jet.

THEORETICAL ANALYSIS

An analysis of the cold flow model was made in conjunction with the cold flow test program. Although the contour was the same as was analyzed for fluorine/hydrogen, the results are different because in this case the working fluid was dry air. The analytical procedures used were the same as those described in the Performance Analysis section.

An aerodynamic analysis using the method of characteristics resulted in an inviscid geometric efficiency of 0.9748 based on aerodynamic throat area. The resulting pressure profile is shown in Fig. 115. The predicted drag loss is shown in Fig. 116. A laminar boundary layer was expected for the cold flow tests. Vacuum efficiency is plotted vs chamber pressure in Fig. 117.

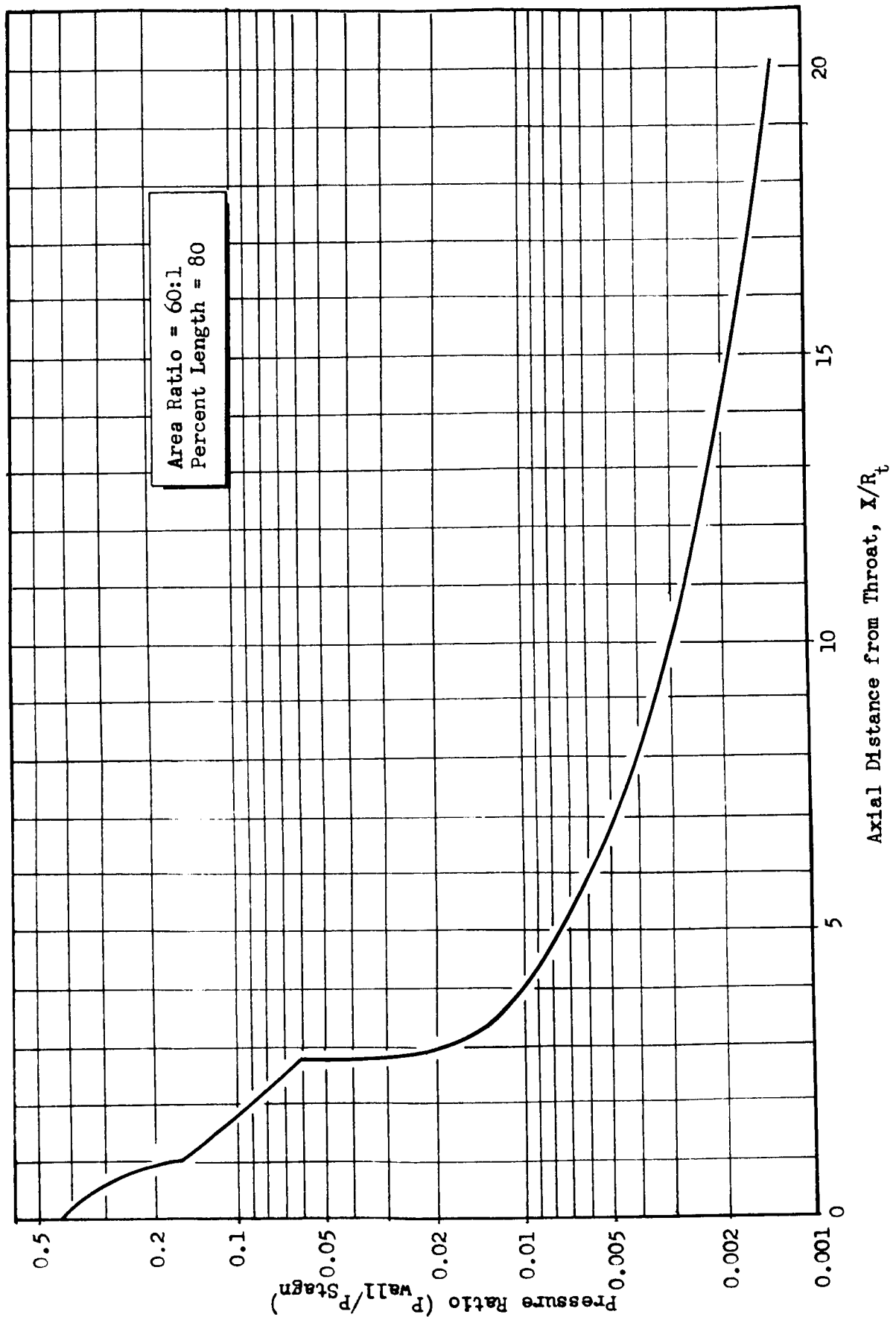
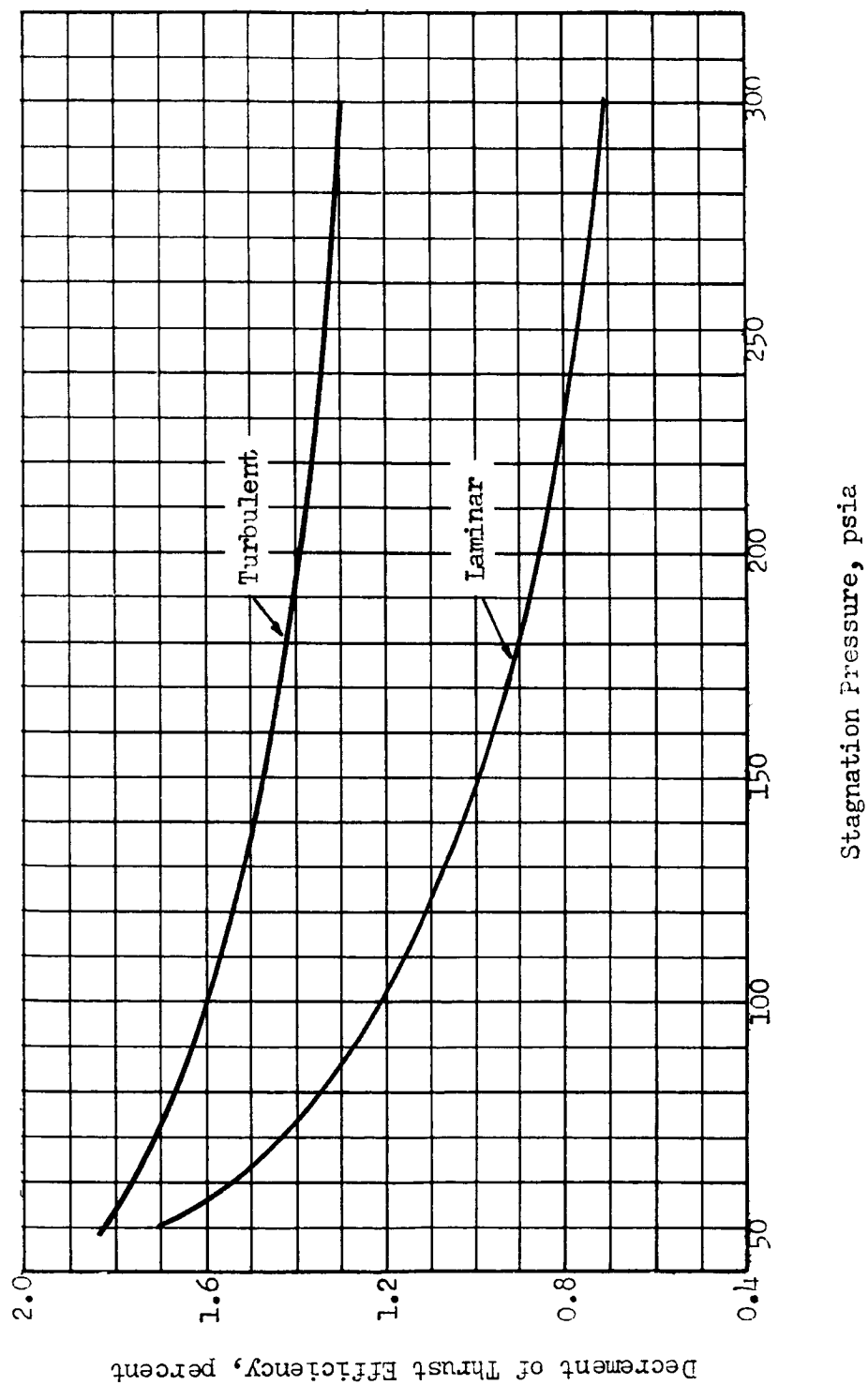
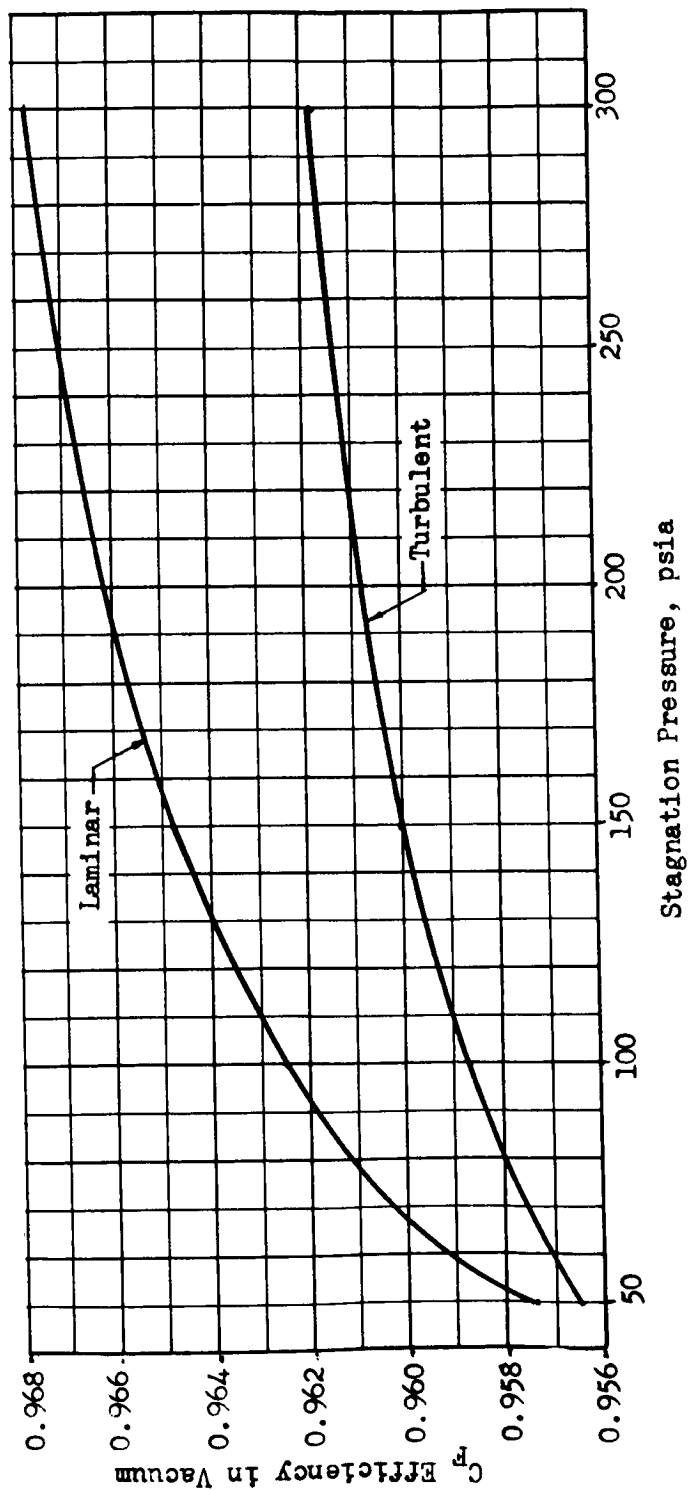


Figure 115. Theoretical Pressure Profile of Task III Controlled Expansion Nozzle Flowing Air



Area Ratio = 60
Percent Length = 80%

Figure 116. Theoretical Drag Loss for Cold Flow Model of the Task III Controlled Expansion Nozzle



Note: C_F is based upon Aerodynamic Throat Area (A^*)

Throat Radius = 0.4196 inches
Area Ratio = 60:1
Percent Length = 80

Figure 117. Effect of Stagnation Pressure on Vacuum C_F Efficiency of Cold Flow Model of Task III Controlled Expansion Nozzle



MODEL DESCRIPTION

The nozzle contour used was a precise subscale duplicate of the hot-firing controlled expansion nozzle. Normalized coordinates are listed in Table 23.

Flowrate maximum/minimum requirements of the test facility supply pressure system, operating range limits of the force measuring system, and the data tolerance limits of the test program were primary considerations in the selection of a model scale of 1/5 full size.

Primary model design considerations were based on the program objectives of obtaining thrust performance and pressure profile information. These objectives required a contour tolerance limit of 0.2 percent. A drawing of the model is shown in Fig. 118, and significant geometric parameters are presented in Table 23.

The model has a throat area of 0.5529 sq in., is 80 percent in length of a 15-degree cone of equivalent area ratio, and has an expansion area ratio of 60:1.

Material selection becomes critical when narrow tolerance limits on the inside contour are required, especially if the model scale results in large diameters and a decreasing wall thickness as the exit is approached. The high area ratio and high percentage nozzle length requiring an 85- to 95-percent material removal from the rough billet causes geometric instabilities that are not desirable in obtaining accurate models. For this reason, precipitation hardened stainless steel was chosen as the fabrication material for the model. Tempering of the material stabilized the billet for contouring and provided a hardened material suitable for final contour polishing.



TABLE 23

COLD-FLOW MODEL GEOMETRIC PARAMETERS

Geometrical Throat Diameter as Measured at the Model Research Shop, inches	0.8390
Geometrical Throat Area, sq in.	0.5529
Model Exit Diameter as Measured, inches	6.5014
Model Exit Area, sq in.	33.1973
Area Ratio	60.046
Nozzle Length From Throat, inches	8.4532
Overall Model Length, inches	10.203
Percent Length of an Equivalent 15-Degree Cone of the Same Area Ratio	80.000
Contraction Ratio at Plane of P_{c3} , P_{c2} , and P_{c1}	3.1948
Contraction Ratio at Plane of P_{c4}	2.0515
Approximate Thrust Level With Air at $P_c = 175$ psia, lbf	160
Approximate Mass Flowrate at $P_c = 175$ psia, lbm/sec	2.3
Approximate Reynolds Number at $P_c = 175$ psia	4.2×10^6

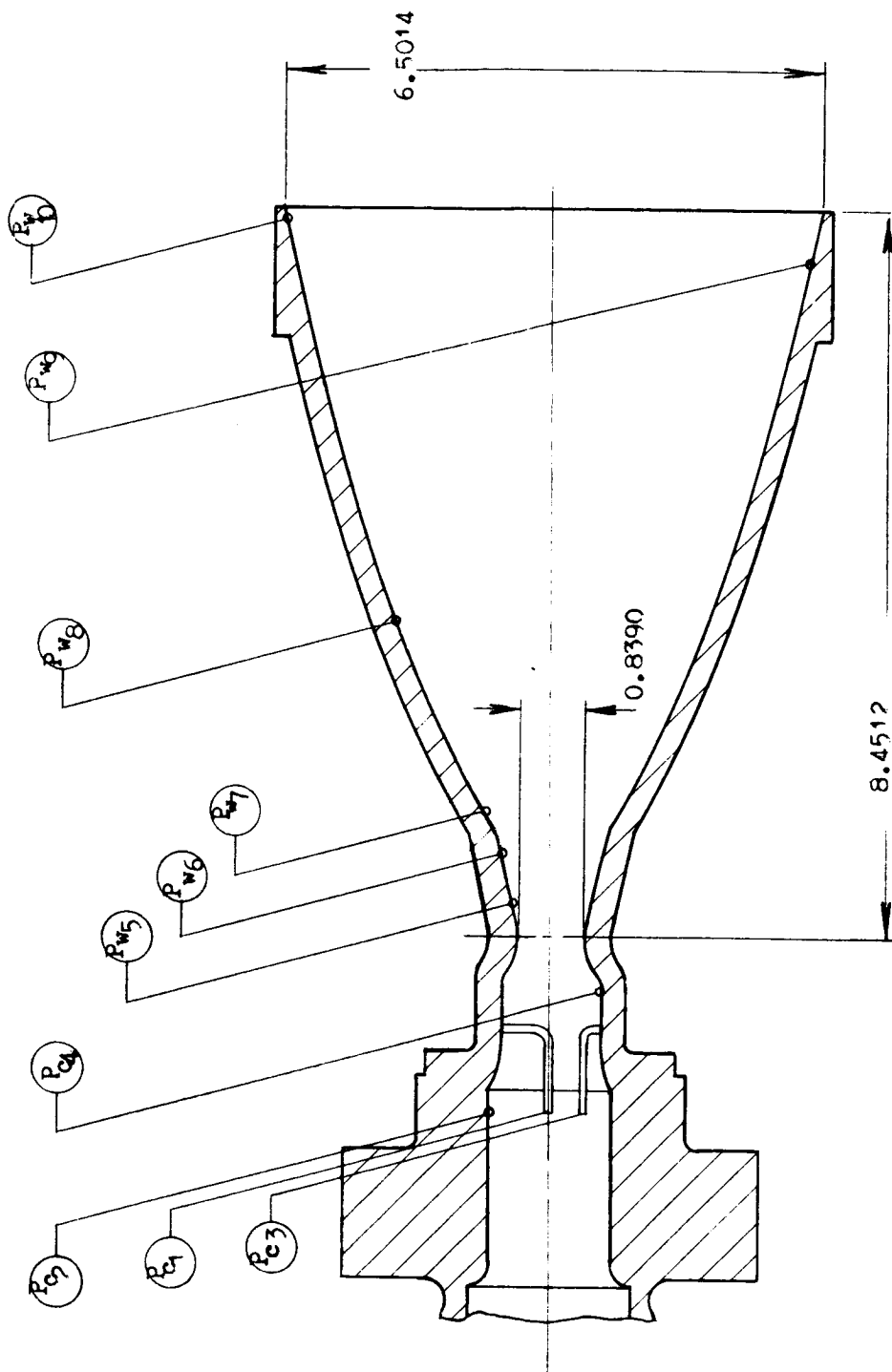


Figure 118. Cold Flow Test Model ($\epsilon = 60:1$, 80 Percent Length)



Final inspection of the model showed the throat diameter within 0.03 percent; the exit diameter within 0.01 percent; the throat area within 0.05 percent; the exit area within 0.02 percent and a maximum area deviation over the length of the nozzle not exceeding 0.4 percent.

The model is shown in Fig. 119.

FACILITY DESCRIPTION

The Rocket Nozzle Test Facility (RNTF) is an intermittent blowdown test section located at the Los Angeles Division of North American Aviation, Inc., but owned and operated by the Rocketdyne Division. The facility is primarily used to determine the performance characteristics of various nozzle configurations under cold flow conditions as a function of mass flow and altitude pressure ratio, (P_c/P_a) . The Rocket Nozzle Test Facility is shown in Fig. 120 and the model is shown mounted on the force balance in Fig. 121.

PERFORMANCE PARAMETERS

Having determined the mass flowrate and the model force, all the other necessary aerodynamic parameters may be readily computed.

1. Aerodynamic Throat Area, A^*

The effective throat area may be computed from

$$A^* = \frac{\dot{w} \sqrt{T_c}}{P_c K_c}$$

where the pressure, P_c , temperature, T_c , and critical flow function, K_c , are at chamber conditions and \dot{w} is the mass flowrate.

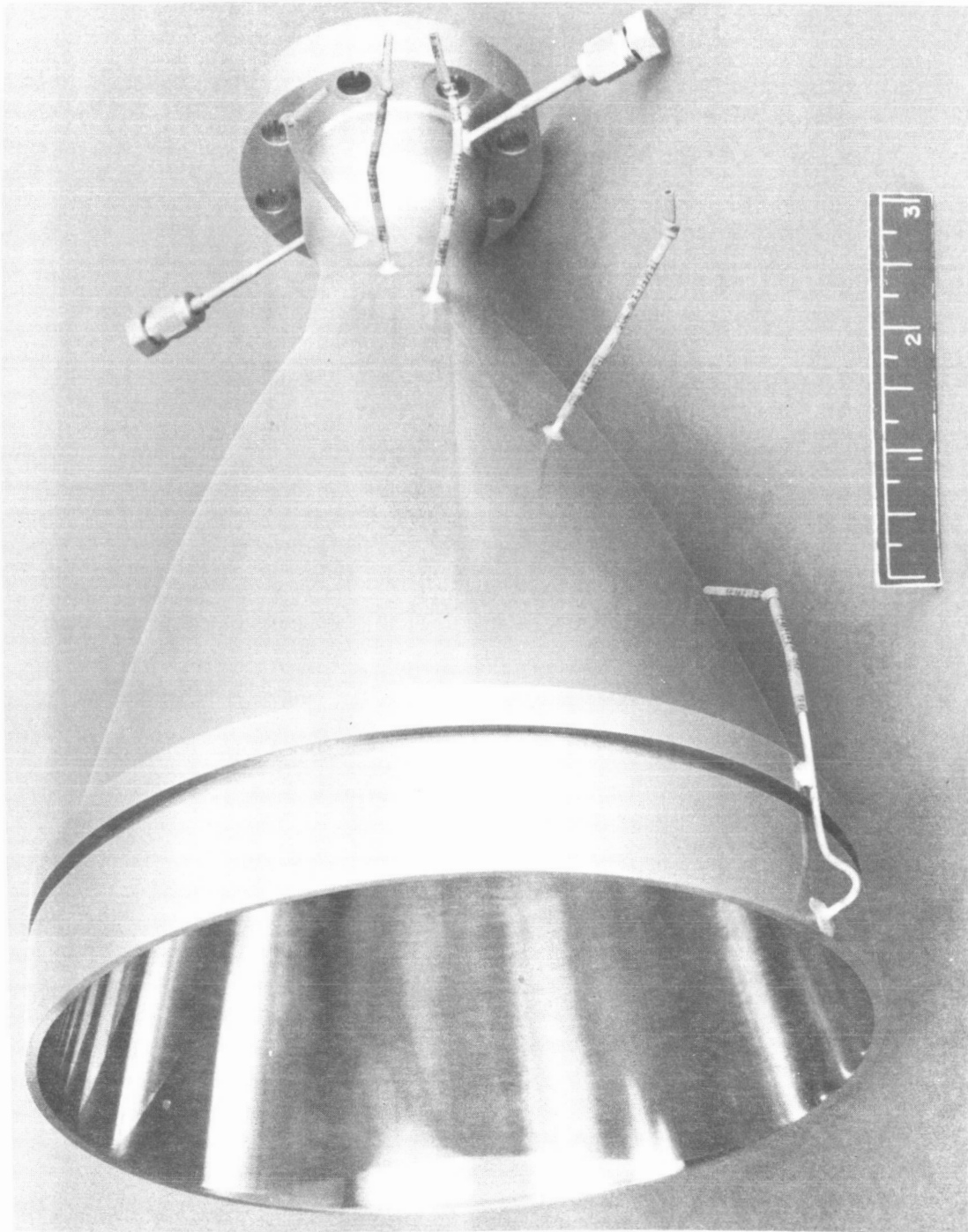
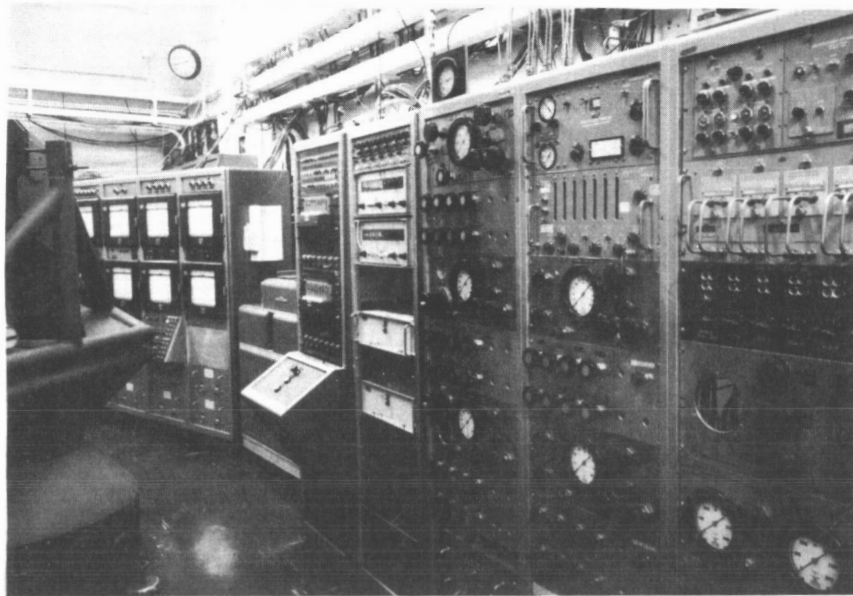
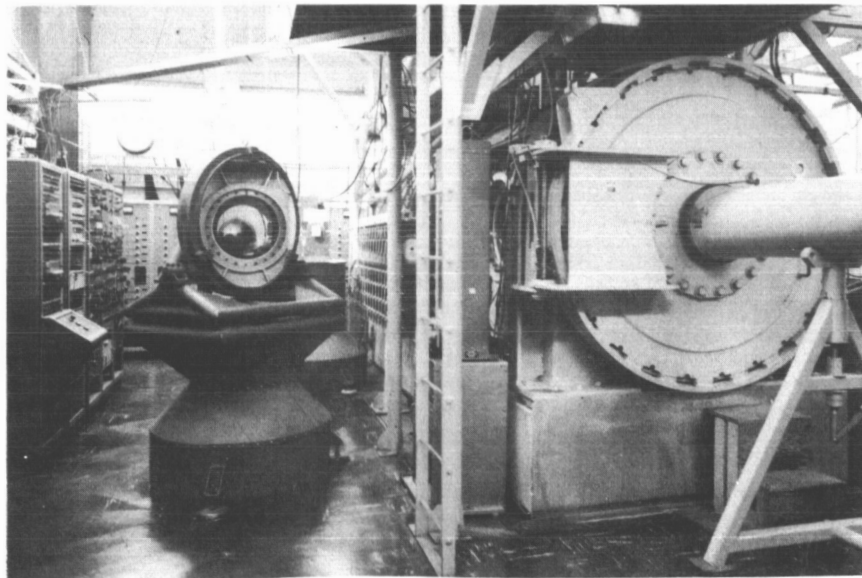


Figure 119. Photograph of Cold-Flow Nozzle of Controlled Expansion Nozzle



Instrumentation and Control Panels



Test Chamber

Figure 120. Rocket Nozzle Test Facility

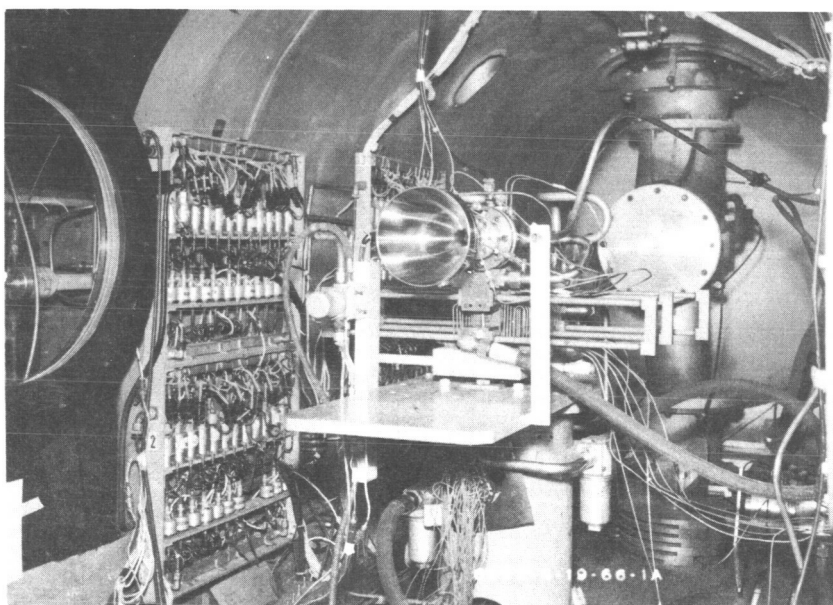
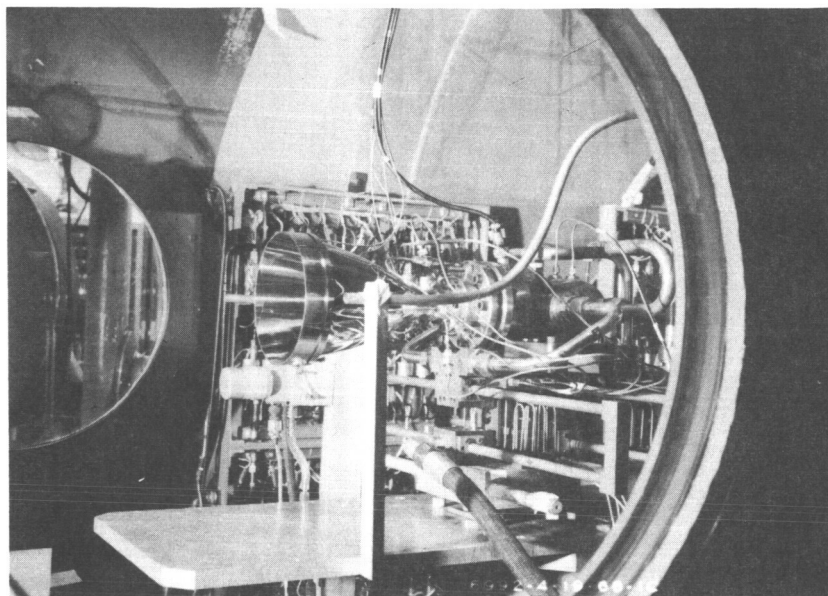


Figure 121. Photographs of Cold Flow Model Mounted on Single Component Force Balance



2. Model discharge coefficient, C_D

The discharge coefficient is defined as the ratio of actual to ideal weight flow

$$C_D = \frac{\dot{w}_a}{\dot{w}_i} = \frac{\dot{w} \sqrt{T_c}}{P_c A_t K_c}$$

3. Nozzle thrust coefficient, C_F

$$C_F = \frac{F K}{\dot{w} \sqrt{T_c}} + \frac{\epsilon^*}{PR}$$

where

F = force measured in pounds

\dot{w} = mass flowrate in lb/sec

$PR = P_c/P_a$

ϵ^* = ratio of exit area to the aerodynamic throat area.

4. Nozzle efficiency, η

$$\eta = \frac{C_{F_{vac}}}{C_{F_{vac \text{ ideal}}}}$$

where C_F is the thrust coefficient and C_{F_i} is the one-dimensional thrust coefficient.



TEST RESULTS

Model Discharge Coefficient

The effective throat area, A^* , of the model was computed for each test and is listed in the data tabulation Table 24. The model discharge coefficient A^*/A_t was nominally 0.989 at a stagnation pressure of 175 psia.

Nozzle Wall Pressures

Wall pressures along the contour were recorded at six locations. The model pressure tap designation and their respective locations are tabulated in Table 25. Experimental wall pressure results are presented vs nozzle axial length X/R_t in Fig. 122. Excellent agreement between theoretical and experimental results is evident along the initial portion downstream of the nozzle throat to an approximate axial location $X/R_t = 8.8$. The pressures recorded downstream of this portion were slightly above theoretical.

Nozzle Efficiency

The test model was tested over pressure ratios of 167 to 3844. The nozzle thrust efficiency test results are presented in Fig. 123 as a function of varying chamber pressure. Vacuum performance at $P_c = 175$ psia was 97.4 percent.



TABLE 24

CONTROLLED EXPANSION NOZZLE COLD-FLOW PROGRAM DATA TABULATION

Test No.	Chamber Pressure, psia	(P_{c4}/P_{cl})	Chamber Temperature, R	Axial Force, pounds	Mass Flowrate, lb/sec	Aerodynamic Throat Area, sq in.	Discharge Coefficient	Thrust Coefficient, F	Pressure Ratio, P_c/P_a	Vacuum Thrust Coefficient	Vacuum Thrust Efficiency
01	176.2	Off scale, no data	499.8	144.15	2.3081	0.5473	0.9898	1.4948	304.3	1.6907	97.41
03	176.6	0.953	499.5	156.98	2.3143	0.5474	0.9899	1.6240	913.7	1.6905	97.40
04	176.5	0.954	500.1	158.94	2.3102	0.5470	0.9893	1.6462	1359	1.6909	97.43
05	176.6	0.953	496.9	159.73	2.3194	0.5471	0.9896	1.6531	1695	1.6889	97.31
06	176.8	0.952	502.8	161.83	2.3073	0.5469	0.9891	1.6737	3844	1.6895	97.34
07	177.0	0.953	488.1	154.93	2.3446	0.5467	0.9888	1.6011	676	1.6909	97.42
08	50.2	0.951	518.5	45.27	0.6395	0.5446	0.9851	1.6558	2390	1.6813	96.86
09	50.3	0.949	521.5	45.36	0.6381	0.5445	0.9848	1.6578	2956	1.6785	96.70
13	175.8	0.952	485.9	129.75	2.3367	0.5474	0.9900	1.3487	167.2	Separated flow	
14	19.0	0.950	532.8	16.86	0.2380	0.5453	0.9862	1.6330	1456	1.6748	96.49
15	16.7	0.954	532.8	14.34	0.2907	0.5463	0.9881	1.5771	641	1.6719	96.33
16	40.9	0.944	528.5	36.23	0.5190	0.5479	0.9909	1.6166	974	1.6788	96.73
17	29.7	0.953	528.9	26.21	0.3771	0.5467	0.9888	1.6088	958	1.6719	96.34
18	51.6	0.952	523.9	45.69	0.6569	0.5468	0.9890	1.6187	956	1.6793	96.92
19	74.5	0.949	518.2	65.82	0.9512	0.5452	0.9861	1.6203	955	1.6824	96.93
20	100.3	0.953	510.8	89.00	1.2942	0.5466	0.9886	1.6234	983	1.6852	97.09
21	130.9	0.952	502.4	116.40	1.7077	0.5474	0.9901	1.6234	984	1.6886	97.15
22	171.2	0.956	491.5	152.84	2.2623	0.5476	0.9903	1.6304	995	1.6914	97.46
23	171.9	0.952	492.5	153.40	2.2682	0.5473	0.9899	1.6304	1005	1.6908	97.42



TABLE 25

WALL PRESSURE TAP LOCATIONS
MEASURED FROM THROAT PLANE
($R_t = 0.4195$ INCH)

Tap Designation	Axial Location, inches	Axial Location, (X/R_t)	Area Ratio
P_{w5}	0.4032	0.9609	1.309
P_{w6}	0.9532	2.2717	2.114
P_{w7}	1.4032	3.3441	8.317
P_{w8}	3.6332	8.6587	19.990
P_{w10}	7.828	18.6603	54.954
P_{w9}	8.3332	19.8599	59.074
Exit Plane	8.4532	20.14585	60.046

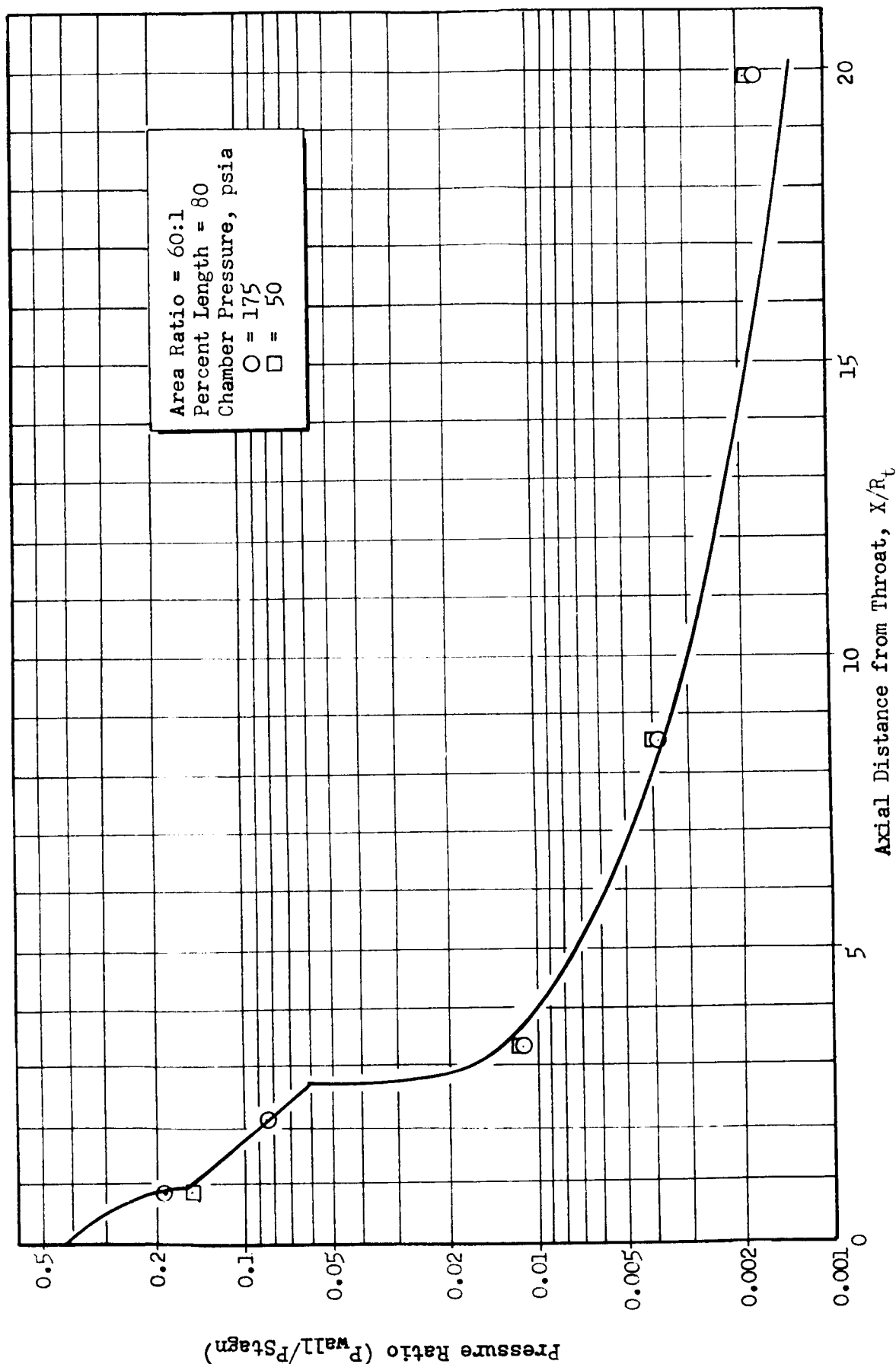


Figure 122. Comparison Between Theoretical and Experimental Pressure Profile of Task III Controlled Expansion Nozzle Flowing Air

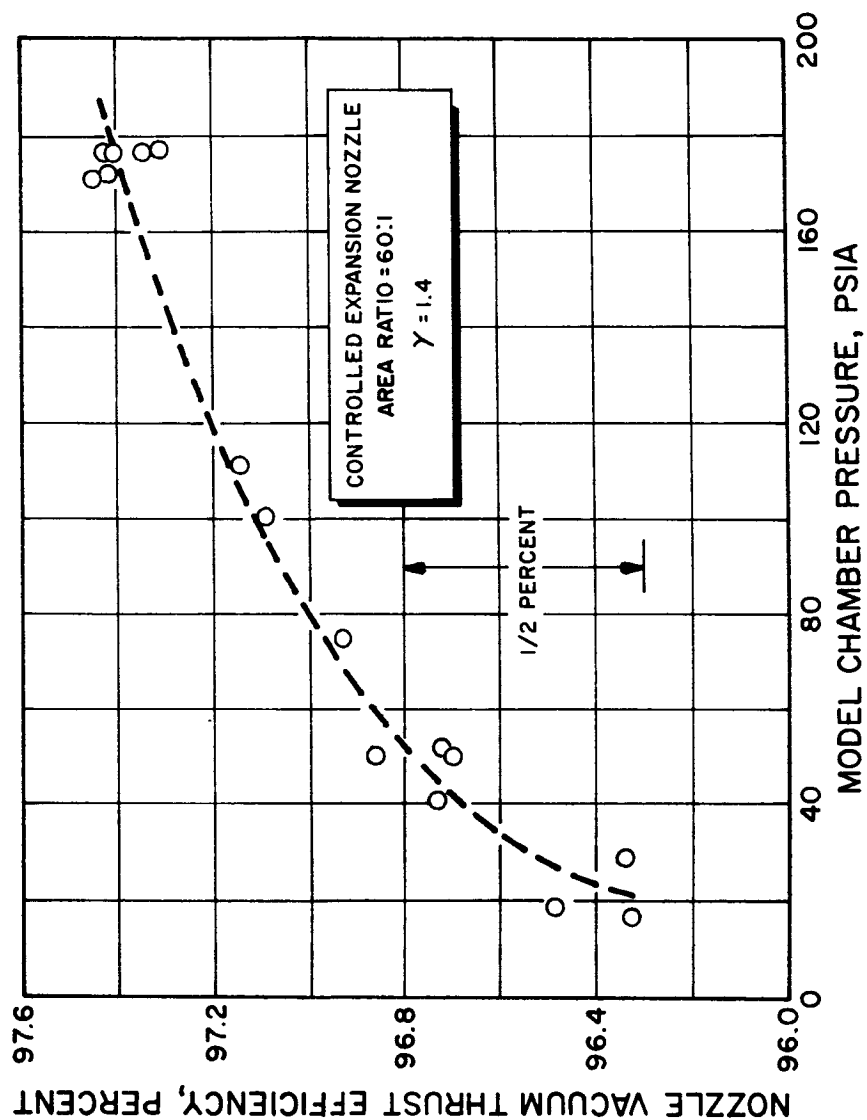


Figure 123. Cold-Flow Vacuum Performance Results



Under full flow conditions, the change in altitude performance is caused entirely by the variation in ambient conditions. Consequently, the determination of vacuum thrust performance for any test, where the nozzle exhaust is flowing full, may be based on the equation

$$C_{F_{vac}} = C_F + \frac{\epsilon^*}{(P_c/P_a)}$$

Vacuum performance, η_{vac} , was obtained as a function of chamber pressure. The model chamber pressure was varied from 17 to 175 psia.

Vacuum efficiency varied 1.2 percent, from 96.2 to 97.4 percent, as the chamber pressure was increased from 17 to 175 psia.

Experimental performance results were 0.9 percent above theoretical. Several tests were repeated using different instrumentation with identical performance results. All performance data taken were within a 0.15 percent scatter band.

A numerical integration of the experimental wall pressures also resulted in a 1.0 percent increase over the theoretical C_F prediction. It is possible that the increase in performance over theoretical is a result of condensation phenomena. The brevity of this cold flow program did not permit further investigation of this question.

Gas flow separation from the nozzle walls was detected at pressure ratios below 200. The overexpanded nozzle attempts to adjust itself by separating upstream of the nozzle exit to a lower area ratio. The resultant nozzle condition subsequently yields a higher performance efficiency (below $P_c/P_a = 200$) than would normally be computed from an ambient variation alone.



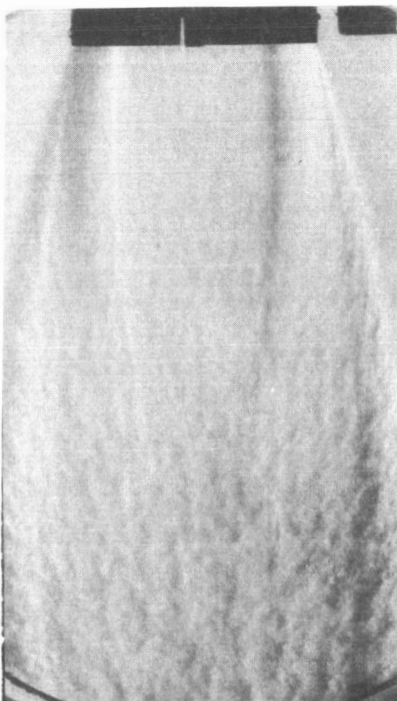
Schlieren Photographs

Schlieren photographs were taken of the jet exhaust with two light sources; a Mole-Richardson continuous light source and a newly installed high-intensity microflash unit. Definition of the shock patterns was more pronounced (higher contrast) with the continuous light source, but not as sharp as the intermittent flash unit. Turbulence was more readily viewable with the microflash light source. A comparison of two tests at approximately the same test conditions is shown in Fig. 124.

The variation of the exhaust pattern with increases in pressure ratio is also shown in Fig. 124. An oblique shock is clearly visible at the higher pressure ratios. At lower altitudes the nozzle is severely overexpanded and a normal shock (Mach disc) forms. The outline of the shock is clearly shown.



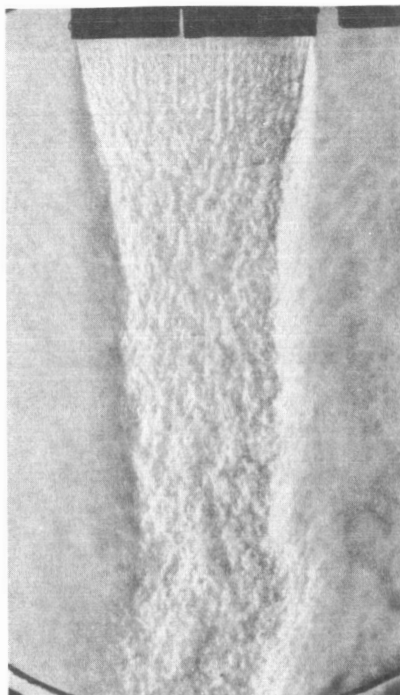
Test No. 10 (P_c/P_a) = 3660
Mole-Richardson Continuous Light Source



Test No. 5 (P_c/P_a) = 1605
Intermittent High-Intensity Light Source



Test No. 11 (P_c/P_a) = 189
Mole-Richardson Continuous Light Source



Test No. 2 (P_c/P_a) = 193
Intermittent High-Intensity Light Source

Figure 124. Cold-Flow Schlieren Photographs, Controlled Expansion Model



HEAT TRANSFER

Wall temperature measurements were taken to define the nozzle heat transfer characteristics for the Fluorine-Hydrogen propellant combination. The combustion chamber heat transfer characteristics are discussed in detail in Volume 1. The purpose of this section is to define the heat transfer characteristics of the three nozzle configurations which were investigated in Task III. These are the long throat 15-degree conical nozzle, the 70-percent bell nozzle, and the controlled expansion nozzle. The mathematical model, measurement procedure, and results are presented.

MATHEMATICAL MODEL

Nozzle local heat transfer coefficient and heat flux values were determined from temperature-time data measured on the cold side of the heat transfer isolation segments. The isolation segments which were described in the Hardware Description section are depicted in Fig. 125.

The rate of wall-temperature rise can be equated to the rate of convective heat transfer into the wall by the energy balance shown in Eq. 1, if the following assumptions are made:

1. The heat transfer isolation segments are thermally thin; i.e., no temperature gradient exists through the segment.
2. The axial conduction to or from the isolation segments is negligible.
3. Radiation losses are negligible.
4. The cold side of the isolation segments are perfectly insulated.

$$q/A = \rho C b \frac{dT_w}{d\theta} = h (T_r - T_w) \quad (1)$$

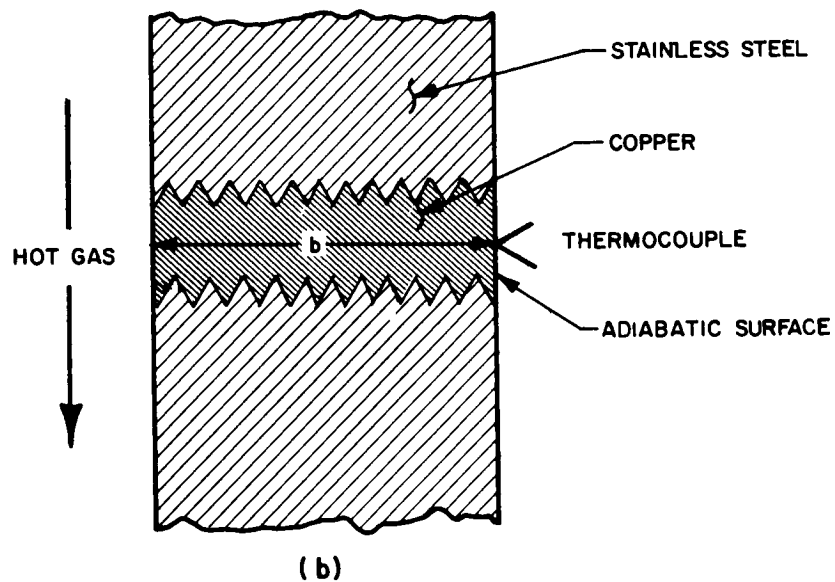
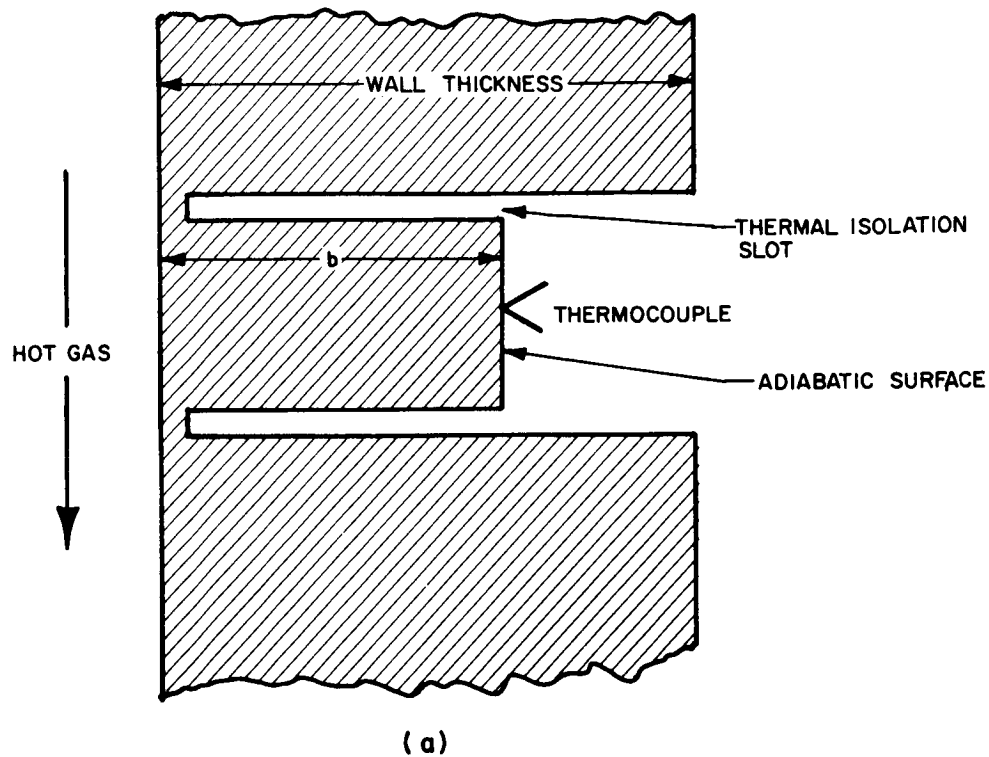


Figure 125. Schematic Cross Sections of Heat Transfer Isolation Segments



where

q/A = heat flux to segment, Btu/sq in.-sec

ρ = isolation segment density, lbm/cu in.

C = specific heat of segment material, Btu/lbm - R

b = isolation segment thickness, inches

T_w = wall temperature, R

θ = time, seconds

h = heat transfer coefficient, Btu/sq in.-sec-R

T_r = recovery temperature, R

Assuming the specific heat and heat-transfer coefficient are constant, the solution to Eq. 1 becomes:

$$\frac{T_r - T_w}{T_r - T_i} = e^{\beta\theta} \quad (2)$$

where

T_i = initial wall temperature at $\theta = \text{zero}$

$$\beta = \frac{h}{\rho C b}, \text{ sec}^{-1} \quad (3)$$

The parameter β has the dimension of time and is called the time constant. This simplified solution and definition of the time constant is presented for later reference.



Equation 1 can be used to relate the wall temperatures to actual heat transfer conditions in a variety of ways. An integral method was adopted for comparing the test results with the mathematical model to minimize the experimental errors. Equation 1 was solved for the case where the specific heat of the isolation segment and the heat transfer coefficients were linear functions of the wall temperature. In addition, the recovery temperature was assumed to be a step function of time. Equation 1 then becomes:

$$\rho C_o (1 + BT_w) \frac{dT_w}{d\theta} = h_o (1 + AT_w) (T_r - T_w) \quad (4)$$

where

C_o = specific heat of the isolation segment material extrapolated to zero degree R, Btu/lbm-R

B = coefficient of specific heat variation with temperature

h_o = heat transfer coefficient extrapolated to zero

A = coefficient of heat transfer coefficient variation with temperature

Solving Eq. 4, the result is

$$\ln \left(\frac{T_r - T_w}{T_r - T_i} \right) + \frac{1 - (B/A)}{1 + B T_r} \ln \frac{1 + A T_i}{1 + A T_w} = \frac{h_o (1 + A T_r) \theta}{\rho C_o b (1 + B T_r)} \quad (5)$$

From Eq. 5, it is shown that the wall temperature on the left side of the equation is linearly related to time, which allows the use of statistical methods for interpretation of the test data in terms of the isolation segment heat-transfer conditions. The temperature-time test data for each isolation segment were utilized to obtain a linear least squares regression curve of the following form:

$$y = A_o + A_1 \theta$$



where

$$y = \ln\left(\frac{T_r - T_w}{T_r - T_i}\right) + \frac{1 - (B/A)}{1 + B T_r} \ln\left(\frac{1 + A T_i}{1 + A T_r}\right) \quad (6)$$

The slope of the regression curve, A_1 , was then related to the slope in the mathematical model, Eq. 5.

$$A_1 = \frac{h_o (1 + A T_r)}{\rho C_o b (1 + B T_r)} \quad (7)$$

The slope derived from the test data is related to the heat transfer coefficient intercept by Eq. 7. A time constant for the above solution can then be defined analogous to the one shown in Eq. 3.

$$\beta_1 = \frac{h_o}{\rho C_o b} = \left(\frac{1 + B T_r}{1 + A T_r} \right) A_1 \quad (8)$$

Since temperature gradients occur through the isolation segments, a correction is made to the results derived above. A solution for the case where the heat transfer coefficient and material thermal properties are constant and the temperature gradient in the wall was approximated by a cubic polynomial is presented in Appendix II of Ref. 27. The solutions for the inside wall temperature, T_s , are:

$$T_s = (T_r - T_i) \left[1 - e^{-\beta_2 \theta} \right] \quad (9)$$

$$T_s = \frac{Bi T_r + 3 T_w}{3 + Bi} \quad (10)$$



where

$$\beta_2 = \frac{h/\rho \text{ cb}}{(1 + \frac{Bi}{h})} \cdot \text{sec}^{-1}$$

Bi = Biot number

T_w = outside wall temperature at time θ , R

Of particular interest in this solution is the time constant, β_2 . As the Biot number becomes small (i.e., the internal thermal resistance is small compared to the external film resistance), β_2 approaches the previously defined β_1 (Eq. 8). The ratio of the two time constants can then be formed.

$$\frac{\beta_2}{\beta_1} = \frac{1}{(1 + \frac{Bi}{h})} \quad (11)$$

Since the time constants are directly related to the slope of the computed regression curve, the further assumption is made that the computed slopes are similarly related.

$$\frac{A_2}{A_1} = \frac{1}{(1 + \frac{Bi}{h})} \quad (12)$$

Therefore, a new slope A_2 can be computed which will correct for temperature gradients in the isolation segment.

Equation 7, the relationship between the heat transfer coefficient intercept and the computed slope, now becomes

$$\frac{h_o (1 + A \text{ Tr})}{\rho C_o b (1 + B \text{ Tr})} = \frac{A_1}{(1 + \frac{Bi}{h})} \quad (13)$$



From Eq. 13, a value for the heat-transfer coefficient intercept can be computed. The local heat-transfer coefficient is then obtained from

$$h = h_0 (1 + A T_s) \quad (14)$$

where T_s is defined by Eq. 10.

Based upon results from Eq. 14, the local heat flux is calculated from

$$q/A = h (T_r - T_s) \quad (15)$$

A sample output for the computer program utilized in the computation of the heat transfer coefficients is shown in Fig. 126. The first-approximation values correspond to the case without the temperature gradient correction. In all cases, the values with the temperature gradient correction were utilized for data presentation.

The modification of the solution for temperature gradients imposes an additional restriction. The Biot number must be small for the correction to be valid. The maximum Biot number encountered in the test data was approximately 0.20. This number corresponds to a correction of approximately 5.0 percent to the heat transfer coefficient.

The assumption of negligible axial conduction is equally valid for the test data. Both isolation segment configurations (Fig. 125) utilized for temperature-time measurements should result in negligible axial conduction. Configuration (a) is essentially isolated because of the small thickness connecting the isolation segment to the remainder of the nozzle. Configuration (b) is also isolated because of the contact resistance between the copper plug and nozzle wall as well as the relatively low thermal conductivity of the stainless steel nozzle.



ROCKETDYNE

A DIVISION OF NORTH AMERICAN AVIATION, INC.

----- THRUST CHAMBER HEAT FLUX ANALYSIS -----

F2-H2 PROGRAM RENO TEST NO. 013 DATE 18 JAN. 66 T/C NO 4

NOZZLE CCDE	=	1	PC	=	99.3700
X	=	5.0130	MR	=	12.2200
254			CSEFF	=	0.9720
RADIUS	=	0.0000			
THICKNESS	=	0.3125			
WT/IN2	=	0.1009	CP INTERCEPT	=	8.58000000E-02
			CP SLOPE	=	1.38800000E-04
FG SLOPE	=	-5.00000000E-06	THER. COND.	=	5.05000000E-03
TR	=	6.7462328CE C3			

Figure 126. Typical Computer Output



ROCKETDYNE • A DIVISION OF NORTH AMERICAN AVIATION, INC.

----- THRUST CHAMBER HEAT FLUX ANALYSIS -----

F2-H2 PROGRAM RENO TEST NO. 013 DATE 18 JAN. 66 T/C NO 4

TIME (SEC)	TEMP (O R)	YTEMP
1.0000	607.080	-0.25882637E-03
1.5000	624.620	-0.18132966E-02
2.0000	642.160	-0.33760700E-02
2.5000	662.630	-0.52100152E-02
3.0000	680.180	-0.67912236E-02
3.5000	697.720	-0.83801304E-02
3.5700	700.640	-0.86453338E-02
4.0000	712.340	-0.97105162E-02

YTEMP(I) = C.29663020E-02 + (-0.32233473E-02) * TIME

S2YX = 0.16247365E-07
SE = 0.12746515E-03
SB = 0.17031344E-04
A1/SB= -0.18925971E 03
RCCEF= -0.99941423E 00

TIME AT WHICH OUTSIDE SURFACE TEMPERATURE BEGINS TO RISE ----- 0.92

Figure 126 (Continued)



THRUST CHAMBER HEAT FLUX ANALYSIS

F2-H2 PROGRAM RENO TEST NO. 013 DATE 18 JAN. 66 T/C NO 4

THE RIGT NUMBER, HEAT TRANSFER COEFFICIENT AND HEAT FLUX VALUES LISTED BELOW ARE FOR THE TIME
AT WHICH THE WALL TEMPERATURE WAS 680.2

HG INTERCEPT = 5.59213340E-05

..... FIRST APPROXIMATION

RIGT NUMBER = 3.44870980E-03
HG (BTU/IN2-SEC-F) = 5.57311520E-05
HEAT FLUX (BTU/SEC-IN2) = 3.38068380E-01

HG INTERCEPT = 5.59697550E-05

..... SECCND APPROXIMATION

RIGT NUMBER = 3.45169600E-03
HG (BTU/IN2-SEC-F) = 5.57794090E-05
HEAT FLUX (BTU/SEC-IN2) = 3.38361110E-01

Figure 126 (Concluded)



The thermal properties of copper were obtained from Ref. 27.

The values utilized in the heat transfer coefficient computations are listed below:

density $\rho = 0.323 \text{ lbm/cu in.}$

thermal conductivity, $k = 0.505 \times 10^{-2} \text{ Btu/in. sec F}$

specific heat, C (assumed to a function of temperature)

$$C = C_0 [1 + B T]$$

where

$$C_0 = 0.0858 \text{ Btu/lbm R}$$

$$B = 1.338 \times 10^{-4}$$

T = copper temperature, R

The recovery temperatures in the nozzle were calculated from the following relationship:

$$T_r = \left[\frac{1 + \frac{\gamma - 1}{2} R_T M^2}{1 + \frac{\gamma - 1}{2} M^2} \right] T_{c_a}$$

where

R_T = recovery factor

γ = ratio of specific heats

M = Mach number

T_{c_a} = actual combustion temperature, R



The recovery factor was assumed for a turbulent boundary layer,

$$R_T = (Pr)^{1/3}$$

where

Pr = Prandtl number

The actual combustion temperature is obtained from the theoretical combustion temperature, T_c , by appropriate reduction for combustion efficiency, η_{c*} :

$$T_{ca} = T_c (\eta_{c*})^2$$

Rocketdyne's theoretical performance evaluation computer model was utilized to obtain the theoretical combustion temperature as a function of chamber pressure and propellant mixture ratio. Typical Mach number distributions for each nozzle were obtained from an analysis of the nozzle flow by the method of characteristics. The Mach number distributions were assumed to vary negligibly with chamber pressure and mixture ratio in the region of interest.

The numerical value of the constant A was determined from correlation with test data. Data from Reno tests 007 and 008 were utilized to evaluate the actual variation of the heat transfer coefficient with wall temperature. Since the slope of the regression curve obtained for the time-temperature data is directly related to the heat transfer coefficient, the error estimate for the computed slope was chosen as the criterion for evaluation.



A wide range of values for A were assumed for each axial station in the nozzle. These values were then utilized to obtain the least squares regression curve for the temperature-time data. The value of -0.000005 for A minimized the error estimate for the computed slope at all axial positions. Therefore, the above value is utilized in the computation of all experimental heat transfer coefficients.

MEASUREMENT PROCEDURE

Local heat transfer coefficients and heat fluxes were determined by a transient temperature technique using isolation segments placed at various stations along the nozzle wall. Isolation segments were provided at five axial position for the conical and bell nozzles at expansion area ratios of 1, 7, 15, 30, and 59. The controlled expansion nozzle was instrumented at seven axial locations; expansion area ratios of 1, 2, 4, 7, 21, 30, and 59. Each axial station was provided with three isolation segments located 120 degrees apart, circumferentially. Transient temperature-time data were obtained from the thermocouples located on the cold side of the isolation segments. These data were then utilized to determine the local heat transfer coefficients and heat fluxes by the computational procedures described in the following section.

DATA REDUCTION

Representative tests were chosen for each nozzle configuration at the three chamber pressure levels investigated (50, 100, and 150 to 175 psia). To ensure that a valid linear slope was obtained, a least squares regression analysis was made of each temperature history; a correlation coefficient was utilized as the criteria for rejecting data. A minimum value of



0.9900 was chosen. Any temperature history which resulted in a correlation coefficient less than 0.9900 was discarded. The acceptable circumferential data points were averaged to obtain a mean heat transfer coefficient and heat flux at each axial station.

To provide a compatible basis for data presentation, standard conditions (chamber pressure and combustion efficiency) were utilized and all test data were corrected to these conditions on the basis of the turbulent-pipe-flow equation (Ref. 27). The following equation was used:

$$\eta(\text{sc}) = \left[\frac{P_c(\text{sc})}{P_c(\text{test})} \right]^{0.8} \left[\frac{\eta_{c*}(\text{test})}{\eta_{c*}(\text{sc})} \right]^{0.8} \eta(\text{test})$$

where

$\eta(\text{sc})$ = experimental heat-transfer coefficient at standard conditions, Btu/in.²-sec-R

$P_c(\text{sc})$ = chamber pressure at standard conditions, lb_f/in.² abs

$P_c(\text{test})$ = chamber pressure at test conditions, lb_f/in.² abs

$\eta_{c*}(\text{sc})$ = combustion efficiency at standard conditions (0.980)

$\eta_{c*}(\text{test})$ = uncorrected combustion efficiency at test conditions

$\eta(\text{test})$ = experimental heat-transfer coefficient at test conditions, Btu/in.²-sec-R

In all cases, the standard combustion efficiency was assumed to be 98.0 percent. The standard chamber pressures for each nozzle were chosen to minimize the data correction at any given chamber pressure level; the values assumed are tabulated below.

<u>Nozzle Configuration</u>	<u>Standard Chamber Pressure, lb_f/in.² abs</u>
Long Throat 15-degree Cone	50, 100, 175
Bell	50, 100, 160
Controlled Expansion	50, 100, 150

RESULTS

A typical computer output is shown in Fig. 126. Table 26 is a summary of the normalized local film coefficients and heat fluxes as a function of nozzle expansion area ratio, ϵ , for each test. The same data are shown graphically for the different nozzles in Fig. 127 to 132.



TABLE 26

EXPERIMENTAL h_g AND q/A AS A FUNCTION OF CHAMBER PRESSURE AND MIXTURE RATIO

Nozzle Type	Test No.	Chamber Pressure	Mixture Ratio	Film Coefficient, h_g						Heat Flux, q/A									
				$\epsilon=1$	$\epsilon=2$	$\epsilon=4$	$\epsilon=7$	$\epsilon=15$	$\epsilon=21$	$\epsilon=30$	$\epsilon=60$	$\epsilon=1$	$\epsilon=2$	$\epsilon=4$	$\epsilon=7$	$\epsilon=15$	$\epsilon=21$	$\epsilon=30$	$\epsilon=60$
Long Throat 15-Degree Conical Nozzle	029	100	9.1	5.553								3.084							
	030	100	12.5	5.361								3.222							
	031	100	15.4	5.721								3.387							
	032	100	9.8	6.974								3.512							
	033	100	12.3	5.733								3.472							
	034	100	14.6	5.656								3.390							
	035	50	5.3	3.961								1.782							
	036	50	5.7	3.484								1.550							
	037	50	9.0	3.860								1.833							
	038	50	12.0	3.363								1.859							
	039	50	14.5	3.578								2.003							
	048	50	13.2	2.406				0.137	0.068			0.020			0.086	0.042			0.013
	049	50	12.9	2.830				0.120	0.045			0.021			0.077	0.030		0.017	0.013
	050	50	15.1	2.711				0.128							0.076				
	051	50	9.6	2.584															
	052	50	13.1	2.857				0.116	0.069						0.072	0.041			
	053	50	15.9	3.010				0.116	0.053						0.075	0.035			
	054	50	15.5	3.108				0.131							0.083				
	055	100	6.6	4.910				0.373	0.137						0.197	0.070		0.038	0.019
	056	100	6.9	5.576				0.300	0.105						0.161	0.056		0.037	0.016
	057	100	7.7	5.346				0.363	0.096						0.196	0.052			
	058	175	9.4	9.336				0.448	0.173						0.279	0.113		0.052	0.037
	059	175	10.2	7.052				0.500	0.204						0.306	0.125		0.066	0.050
	060	175	11.1					0.497	0.164						0.303	0.101			
	061	175	11.1	8.048				0.462	0.181						0.304	0.117		0.066	0.051
	062	175	14.3	6.524				0.518	0.191						0.341	0.161			
	063	175	14.4	6.552				0.501							0.338				
Bell Nozzle	009	100	9.8				0.460	0.290						0.269	0.170		0.148	0.090	
	010	100	13.3				0.560	0.391						0.350	0.246		0.196	0.134	
	011	100	16.6				0.542	0.337						0.341	0.216		0.148	0.107	
	012	100	4.7				0.754	0.572						0.340	0.253		0.151	0.083	
	013	100	12.2				0.546	0.352						0.331	0.214		0.155	0.140	
	014	100	15.4				0.546	0.339						0.337	0.211		0.137	0.130	
	065	160	9.6	5.655			1.437	0.888						0.874	0.537		0.276		
	066	160	11.6	5.683															
	067	160	14.4	4.943															
	068	160	9.8	5.984				0.976	0.750					0.622	0.482		0.260		
	069	160	11.8	5.390				1.367	0.796					0.822	0.476		0.293		
	070	160	14.1	5.370				1.542	0.927					0.986	0.594		0.324		
	082	50	4.3	2.313				1.054	0.835					0.679	0.542		0.343		
	083	50	4.4	2.535				0.282	0.244					0.127	0.108		0.075	0.036	
							0.303	0.215					0.136	0.096		0.073	0.035		



TABLE 26
(Concluded)

Nozzle Type	Test No.	Chamber Pressure	Mixture Ratio	Film Coefficient, h_g							Heat Flux, q/A								
				$\epsilon=1$	$\epsilon=2$	$\epsilon=4$	$\epsilon=7$	$\epsilon=15$	$\epsilon=21$	$\epsilon=30$	$\epsilon=60$	$\epsilon=1$	$\epsilon=2$	$\epsilon=4$	$\epsilon=7$	$\epsilon=15$	$\epsilon=21$	$\epsilon=30$	$\epsilon=60$
Bell Nozzle	084	50	9.1	2.237			0.314	0.191		0.122	0.075	1.242			0.173	0.105		0.066	0.042
	085	50	9.0	3.038			0.317	0.196		0.131	0.085	1.581			0.166	0.103		0.070	0.045
	086	100	10.0	4.177			0.792	0.465		0.301		2.586			0.470	0.276		0.178	
	087	100	13.0	4.358			0.536	0.324		0.246		2.840			0.339	0.206		0.157	
	088	100	15.7	4.428			0.609	0.350		0.222		2.865			0.387	0.225		0.143	
	089	100	5.5	4.807			0.887	0.557		0.305		2.488			0.438	0.274		0.147	
	090	100	5.4	4.654			0.640	0.499		0.326		2.455			0.325	0.254		0.167	
	091	100	7.2	4.489			0.561	0.436		0.337		2.357			0.286	0.224		0.175	
	092	50	11.2	3.673					0.165	0.128	0.068	2.109					0.091	0.071	0.036
	093	50	11.0	3.320	0.904		0.154		0.151	0.133	0.060	1.879	0.520		0.088		0.085	0.075	0.034
	094	50	14.0	3.997	0.896		0.142		0.148	0.123	0.070	2.405	0.490		0.088		0.085	0.075	0.042
Controlled Expansion Nozzle	095	50	14.0	3.985	0.813		0.158		0.167	0.125	0.065	2.291	0.486		0.094		0.099	0.074	0.038
	102	50	8.2	3.861	0.928		0.159		0.182		0.093	2.029	0.498		0.084		0.096		0.049
	103	50	8.2	3.883	0.869		0.194		0.200	0.157	0.083	1.905	0.441		0.098		0.099	0.079	0.042
	104	100	9.4	5.059	2.446	0.397	0.312		0.309	0.199	0.128	3.012	1.453	0.234	0.181		0.180	0.117	0.074
	105	100	12.2	4.978	1.769	0.365	0.246		0.300	0.173	0.116	3.250	1.169	0.240	0.161		0.195	0.113	0.076
	106	100	14.7	5.332	1.455	0.375	0.234		0.327	0.164	0.139	3.369	0.949	0.244	0.152		0.211	0.106	0.089
	107	100	9.0	4.961	2.551	0.428	0.352		0.419		0.162	2.836	1.450	0.241	0.197		0.234		0.091
	108	100	11.8	4.794	1.959	0.478	0.346		0.358	0.245	0.157	2.978	1.219	0.296	0.213		0.218	0.150	0.111
	109	100	14.3	5.667	1.244	0.332	0.325		0.370	0.239	0.178	3.518	0.799	0.213	0.208		0.234	0.152	0.113
	114	150	13.4	5.705	3.500		0.564		0.567	0.360	0.180	3.669	2.228		0.356		0.355	0.225	0.112
	115	150	8.4	7.325	3.385	0.829	0.692		0.474		0.204	4.132	1.935	0.470	0.392		0.266		0.114
	116	150	6.8	6.828	3.306	0.609	0.582		0.450	0.324	0.210	3.487	1.727	0.318	0.305		0.234	0.169	0.109

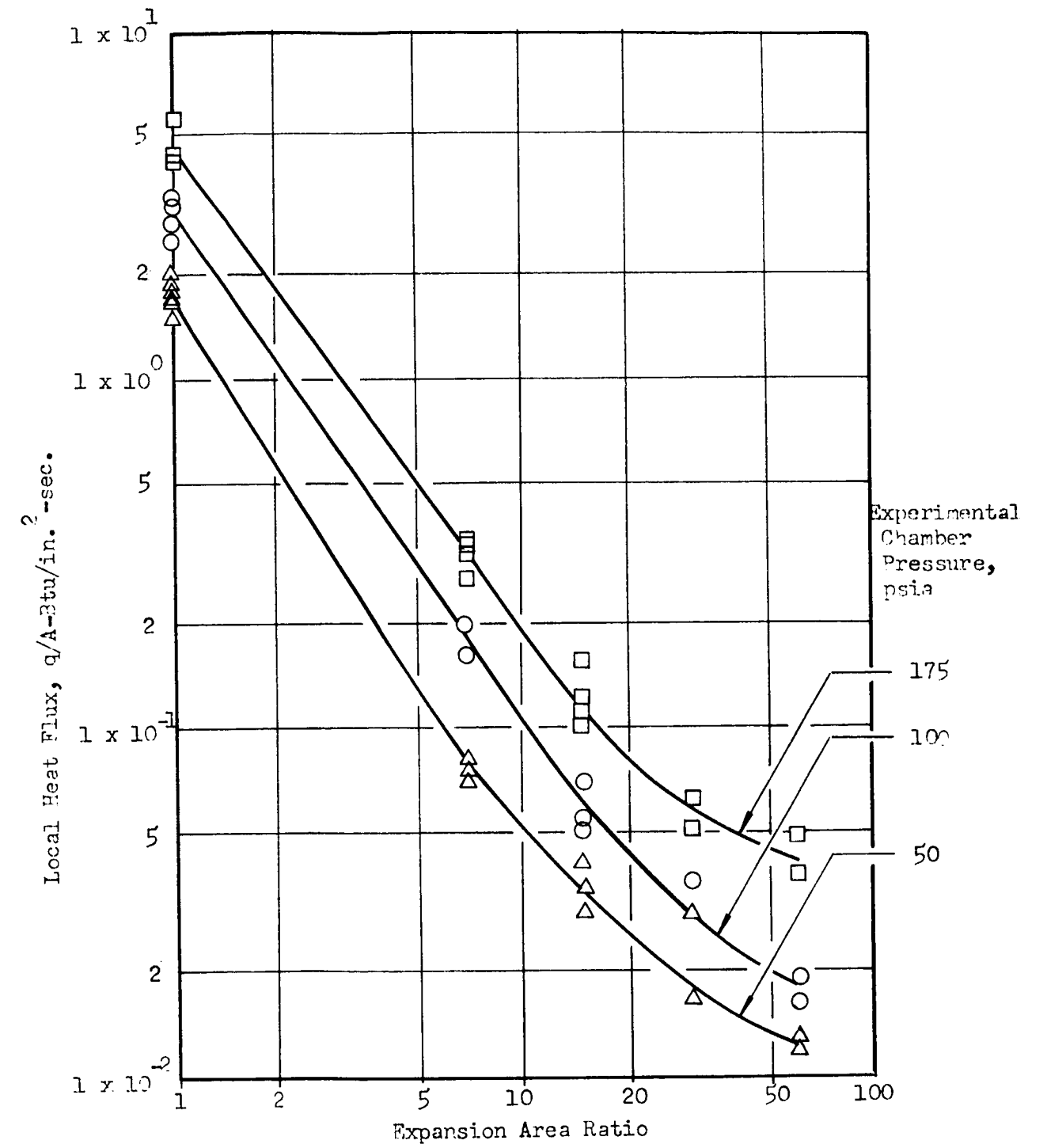


Figure 127. Experimental Local Heat Flux vs Expansion Area Ratio, Long Throat 15-degree Conical Nozzle

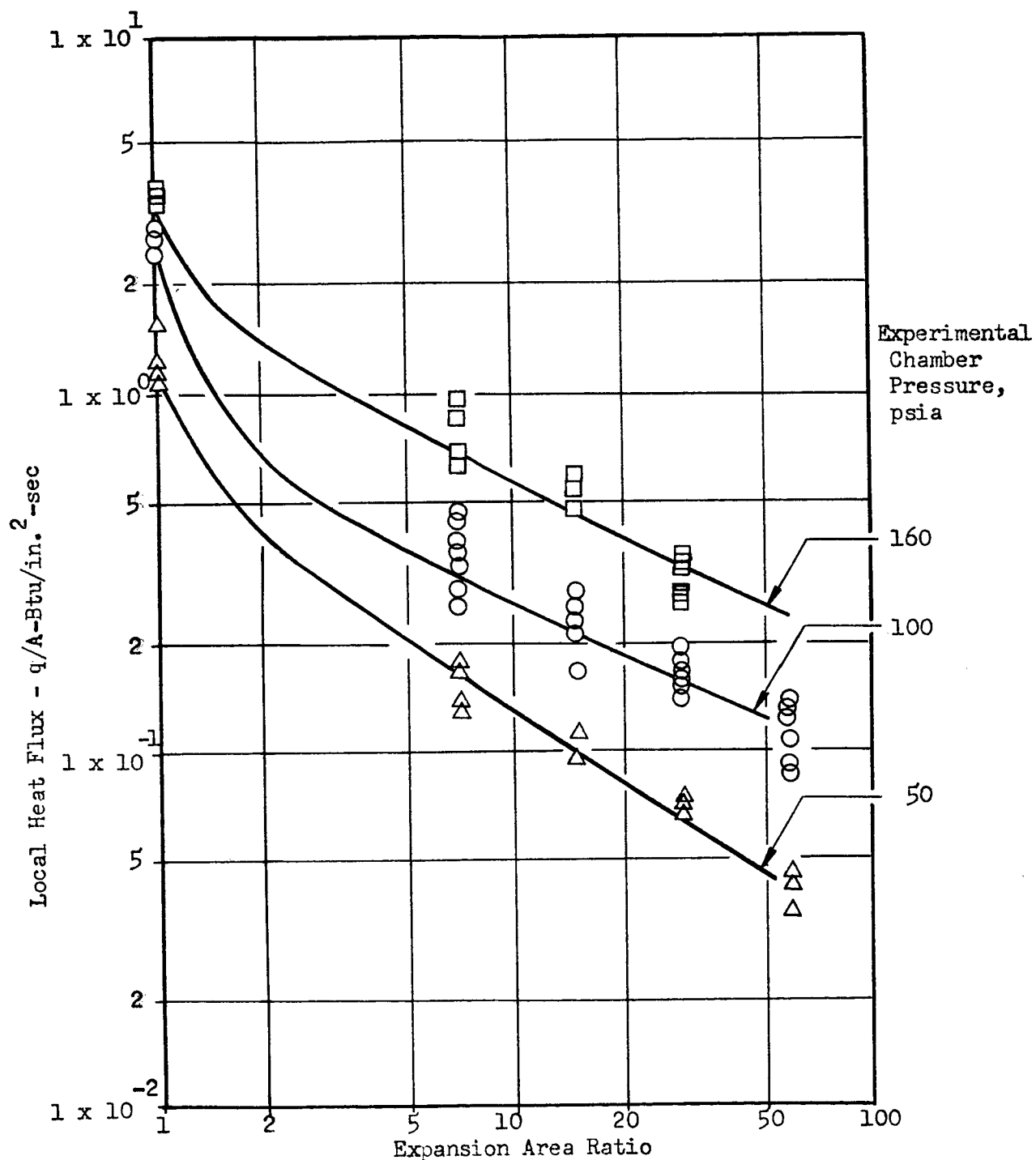


Figure 128. Experimental Local Heat Flux vs Expansion Area Ratio, 70-percent Bell Nozzle

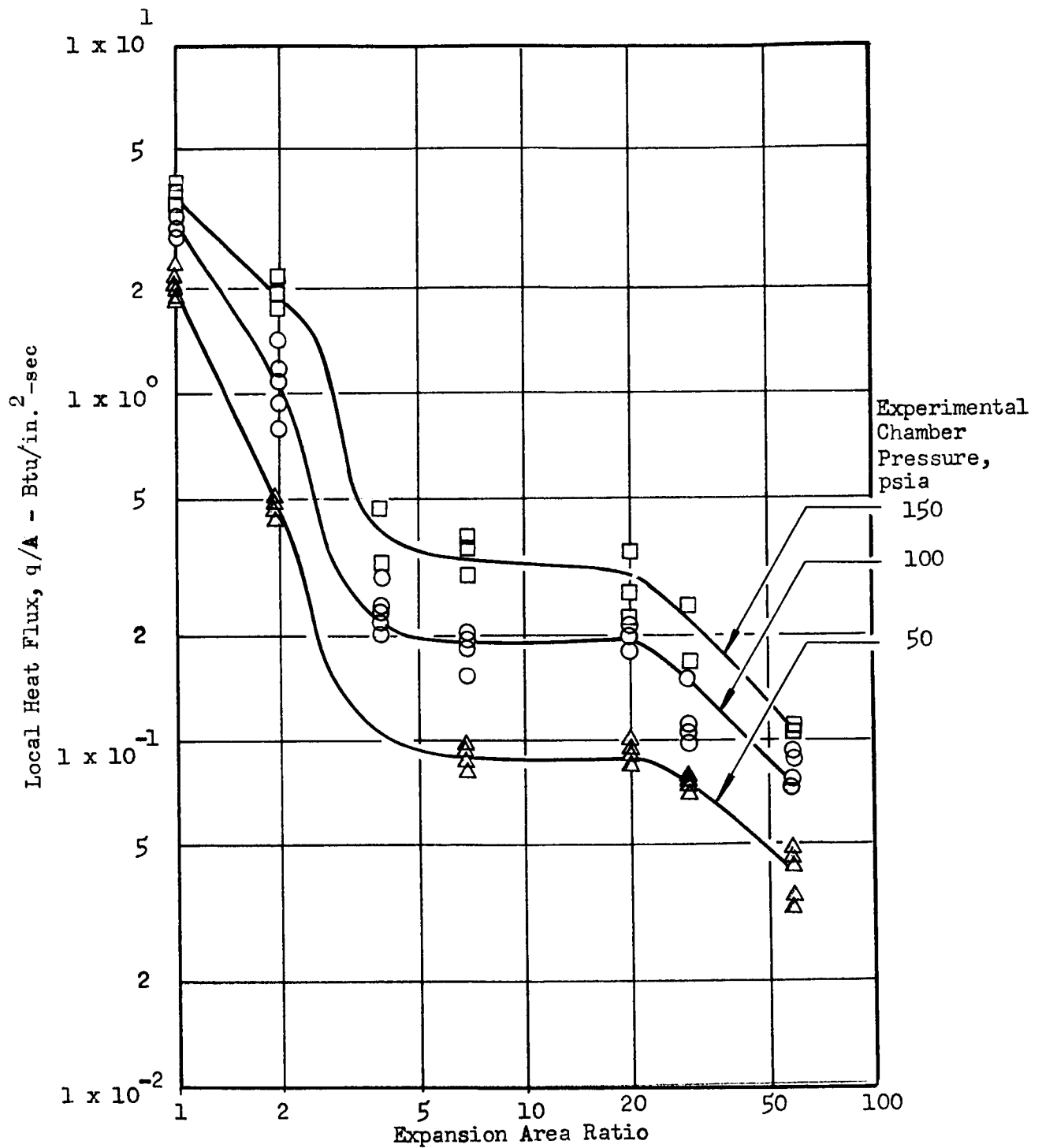


Figure 129. Experimental Local Heat Flux vs Expansion Area Ratio, Controlled Expansion Nozzle

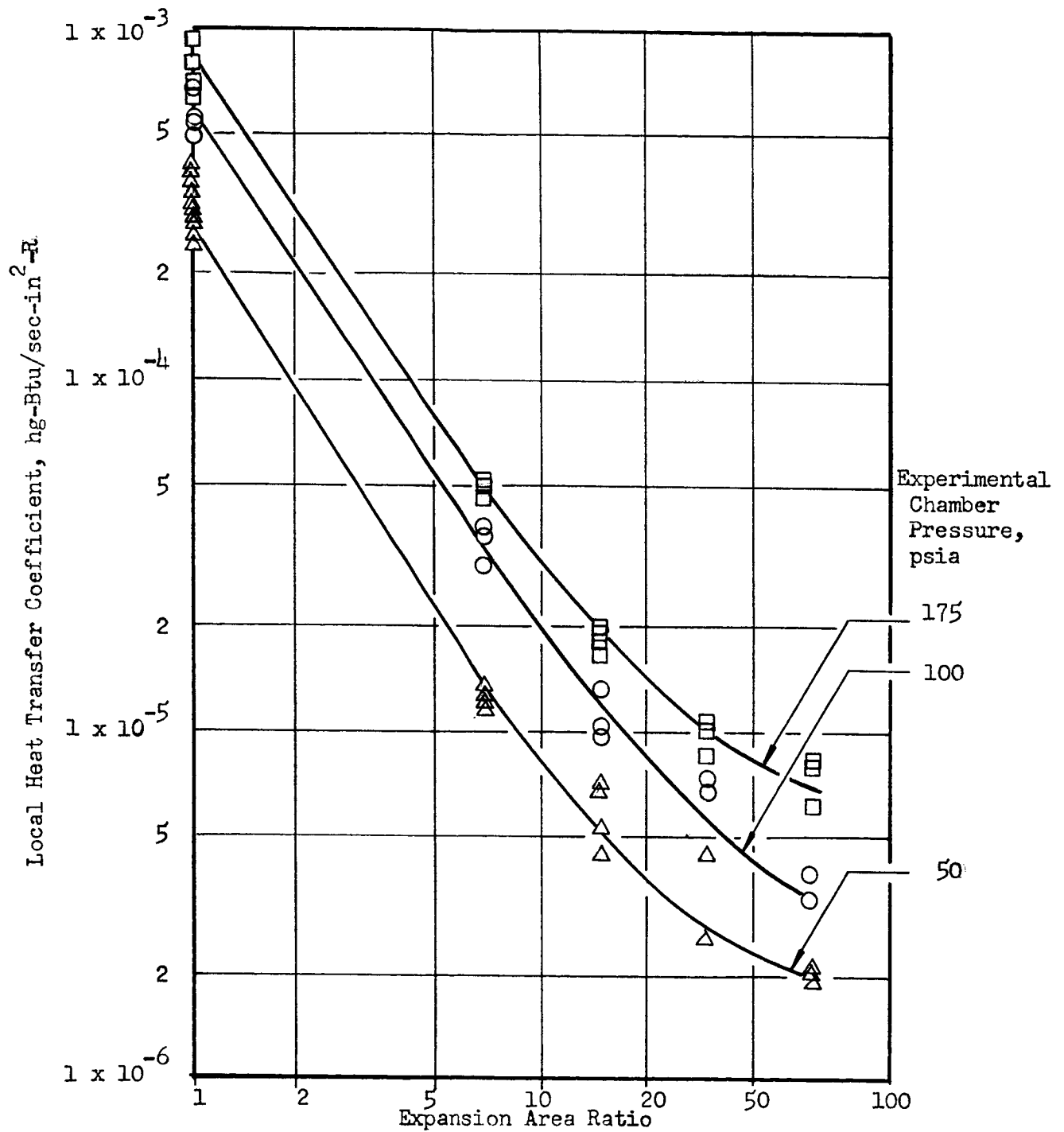


Figure 130. Experimental Local Heat Transfer Coefficient vs Expansion Area Ratio, Long Throat 15-degree Conical Nozzle

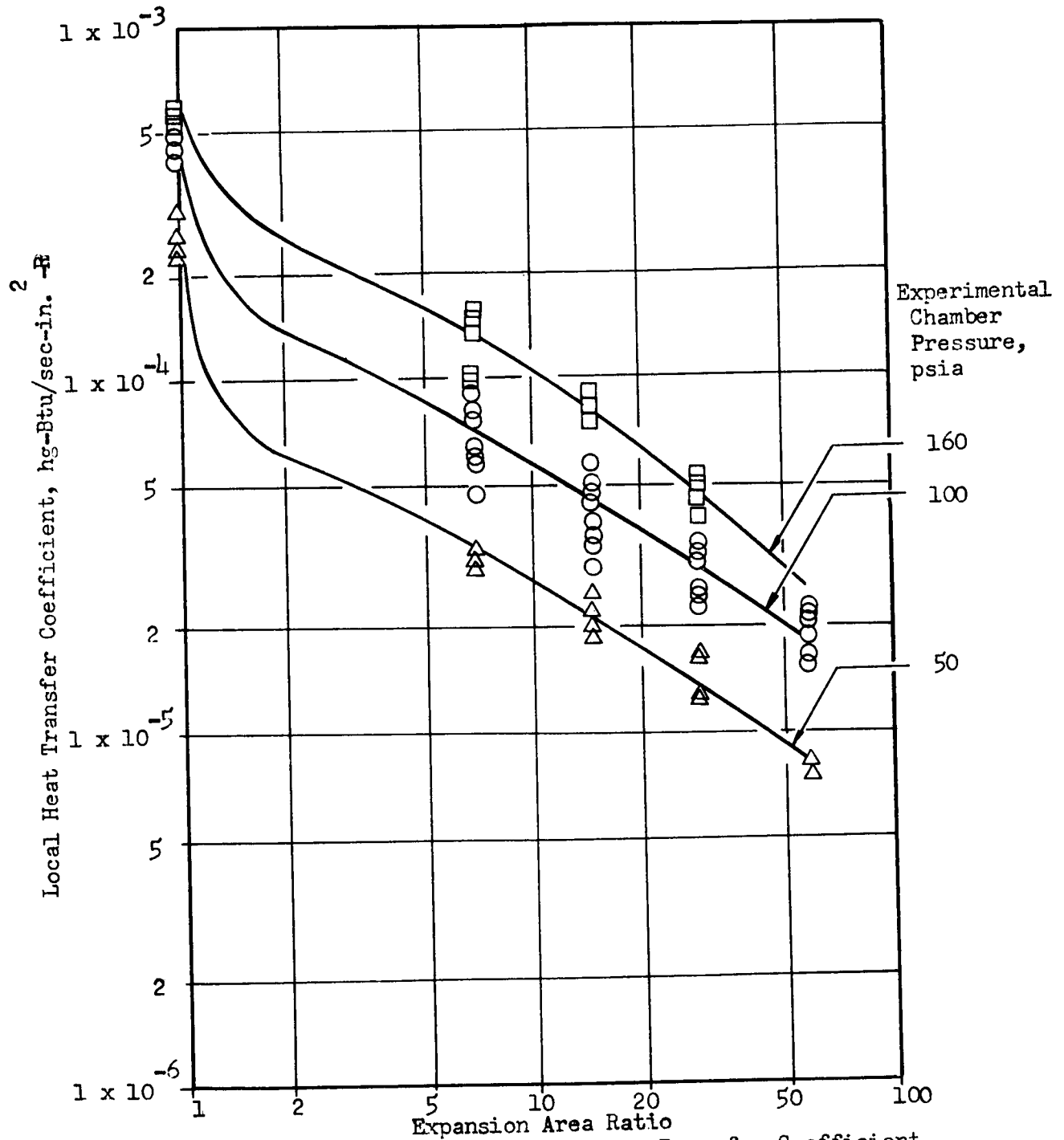


Figure 131. Experimental Local Heat Transfer Coefficient vs Expansion Area Ratio, 70-percent Bell Nozzle

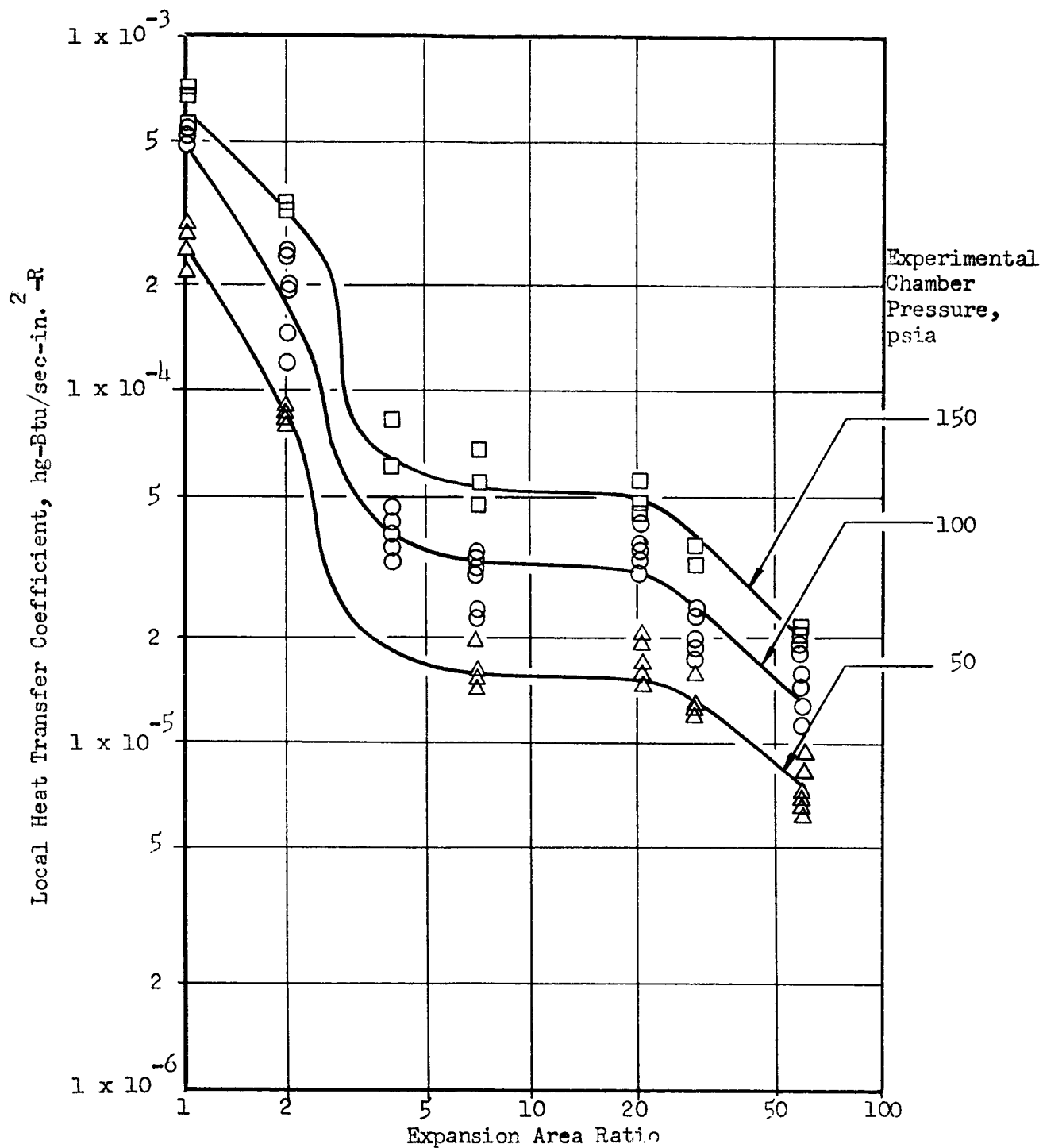


Figure 132. Experimental Heat Transfer Coefficient vs Expansion Area Ratio, Controlled Expansion Nozzle



THEORETICAL PERFORMANCE MAPS

A set of theoretical propellant performance maps for LF_2/GH_2 (at a temperature of 77 F) has been generated. These maps consist of graphs of characteristic velocity (c^*), vacuum specific impulse (I_{vac}), and vacuum thrust coefficient ($C_{F_{\text{vac}}}$) vs mixture ratio (MR), chamber pressure (P_c) and nozzle area ratio (ϵ). The maps are for the three propellant performance models: chemical equilibrium, frozen composition, and frozen at the throat.

The two common performance models, chemical equilibrium and frozen composition, are usually assumed to be, respectively, the upper and lower limits of expected performance. However, it was demonstrated in the injector optimization program, Task II, that near chemical equilibrium c^* values can be obtained. Therefore, a more realistic lower performance limit for the hardware size tested in Task III is the frozen-at-the-throat model. However, from Fig. 133 it is seen that the difference between the equilibrium and frozen performance values is caused more by nozzle effects than by combustor effects.

The performance curves were generated for liquid fluorine at its normal boiling point and gaseous hydrogen at 77 F. Although both the Task II (injector tests) and Task III (nozzle tests) test programs actually used fluorine at the normal boiling point temperature of nitrogen (because of the nitrogen jacket on the fluorine tanks), the effects on performance of the small difference in enthalpy are negligible. The heats of formation used were 0 for 77 F hydrogen and -3.01 kcal/gm-mole for liquid F_2 . The performance curves (figures) are arranged as shown in Table 27.

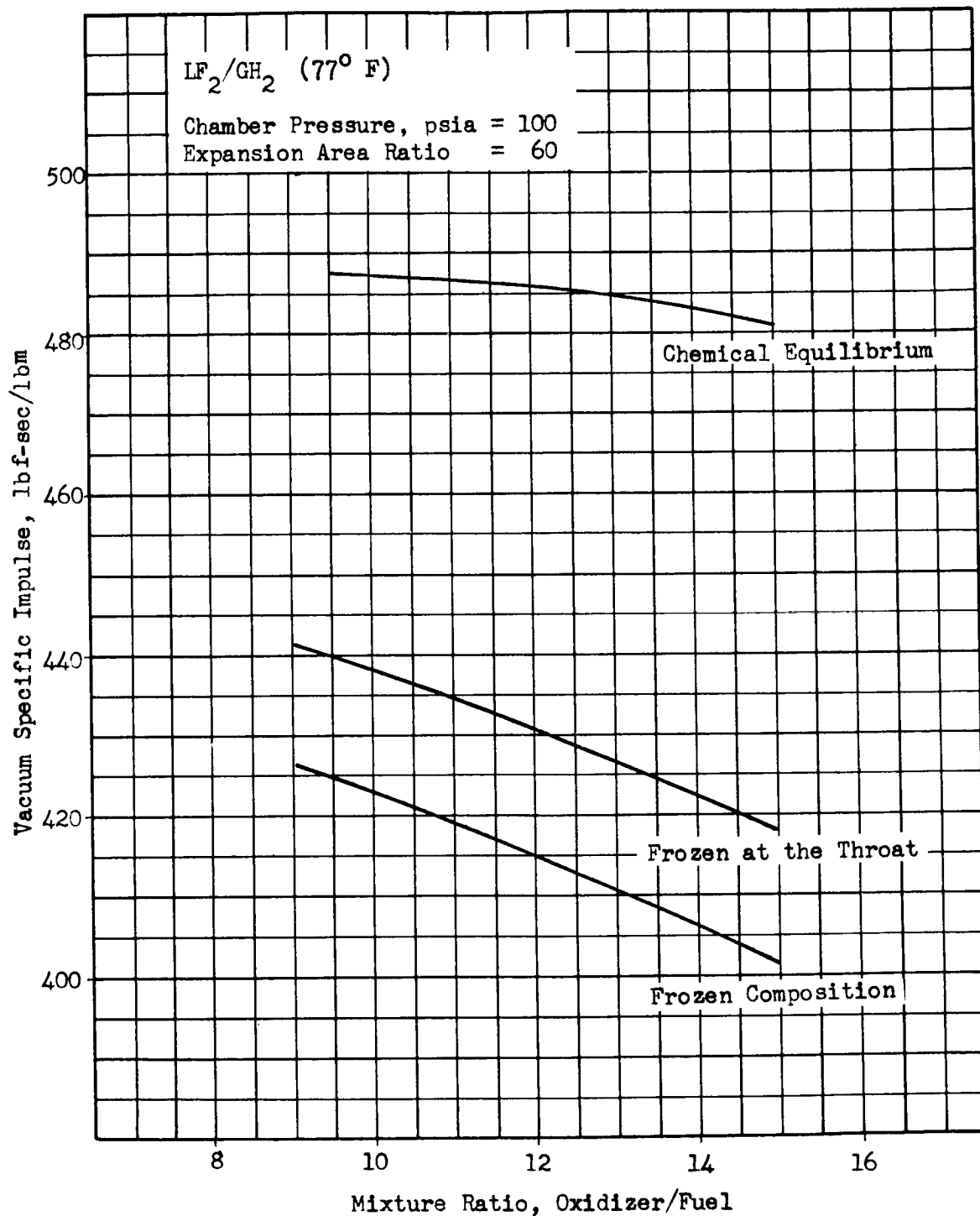


Figure 133. Performance Model Comparison



TABLE 27
FIGURE NUMBERS FOR THEORETICAL PERFORMANCE MAPS

Figure	Performance Model		
	Chemical Equilibrium	Frozen Composition	Frozen at the Throat
Characteristic Velocity vs Mixture Ratio	134	135	---
Characteristic Velocity vs Stagnation Pressure	136	137	---
Vacuum Specific Impulse vs Mixture Ratio	138	139	140
Vacuum Specific Impulse vs Area Ratio	141	142	143
Vacuum Thrust Coefficient vs Mixture Ratio	144	145	146
Vacuum Thrust Coefficient vs Area Ratio	147	148	149

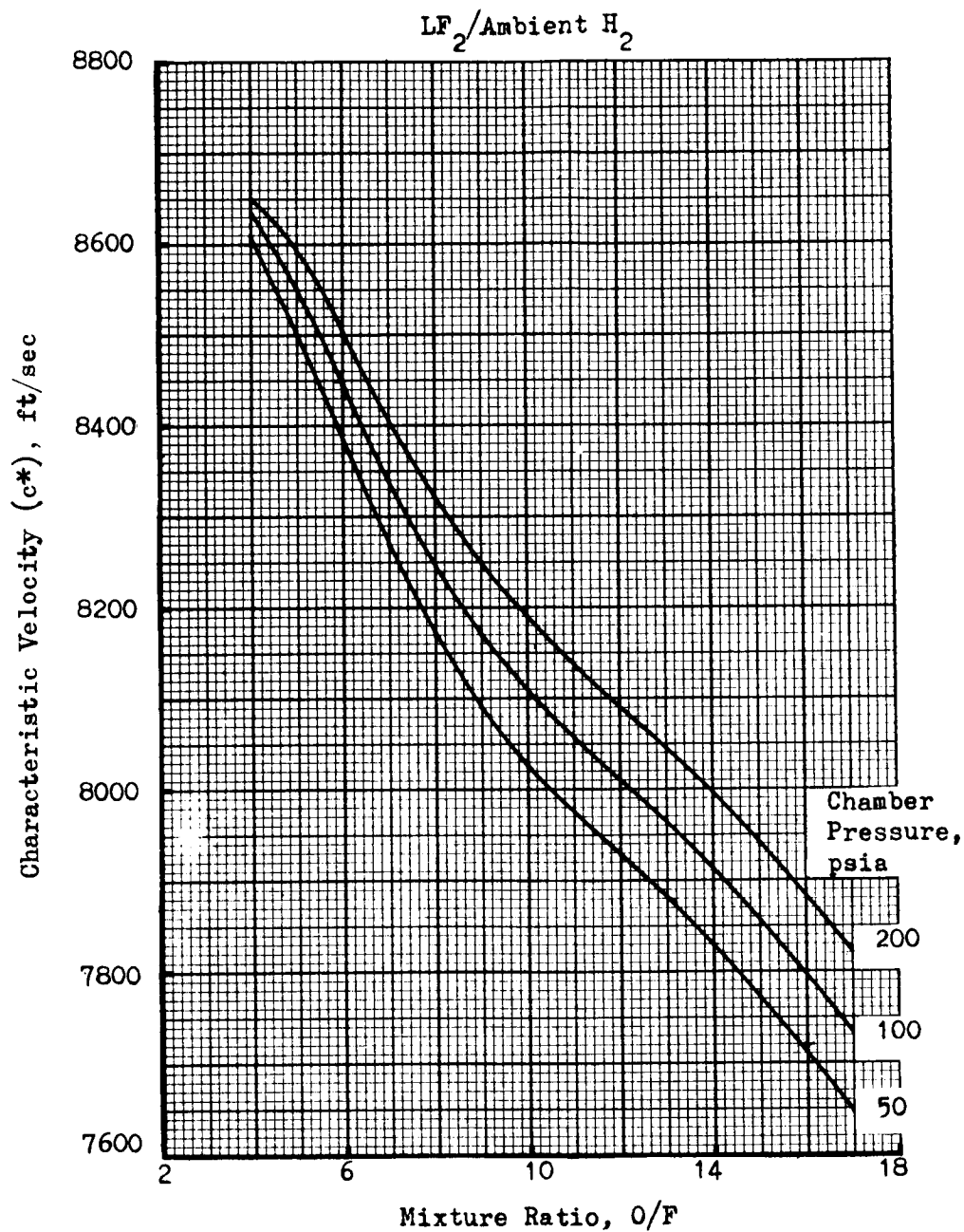


Figure 134. Characteristic Velocity vs Mixture Ratio—Chemical Equilibrium

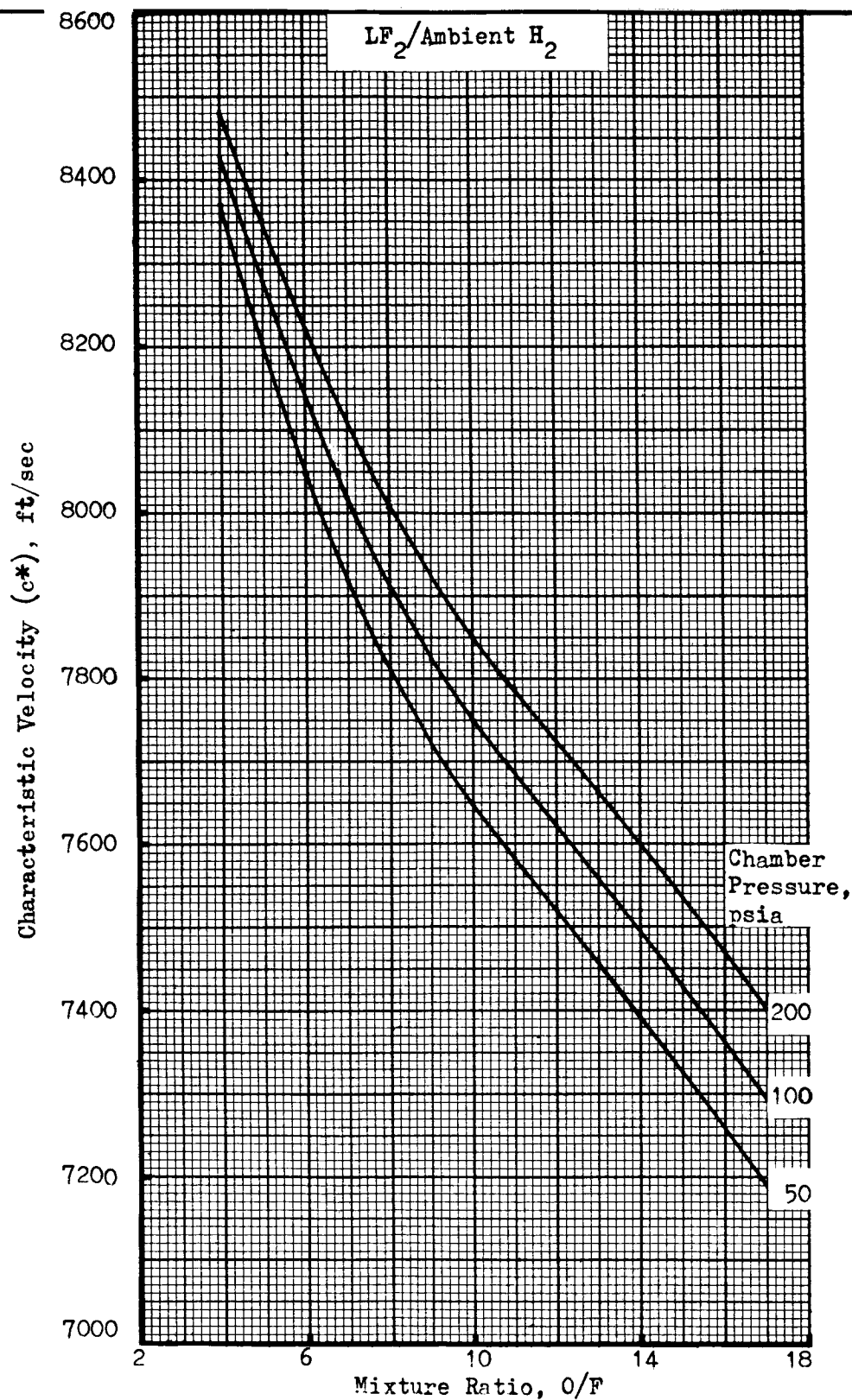


Figure 135. Characteristic Velocity vs Mixture Ratio—Frozen Composition

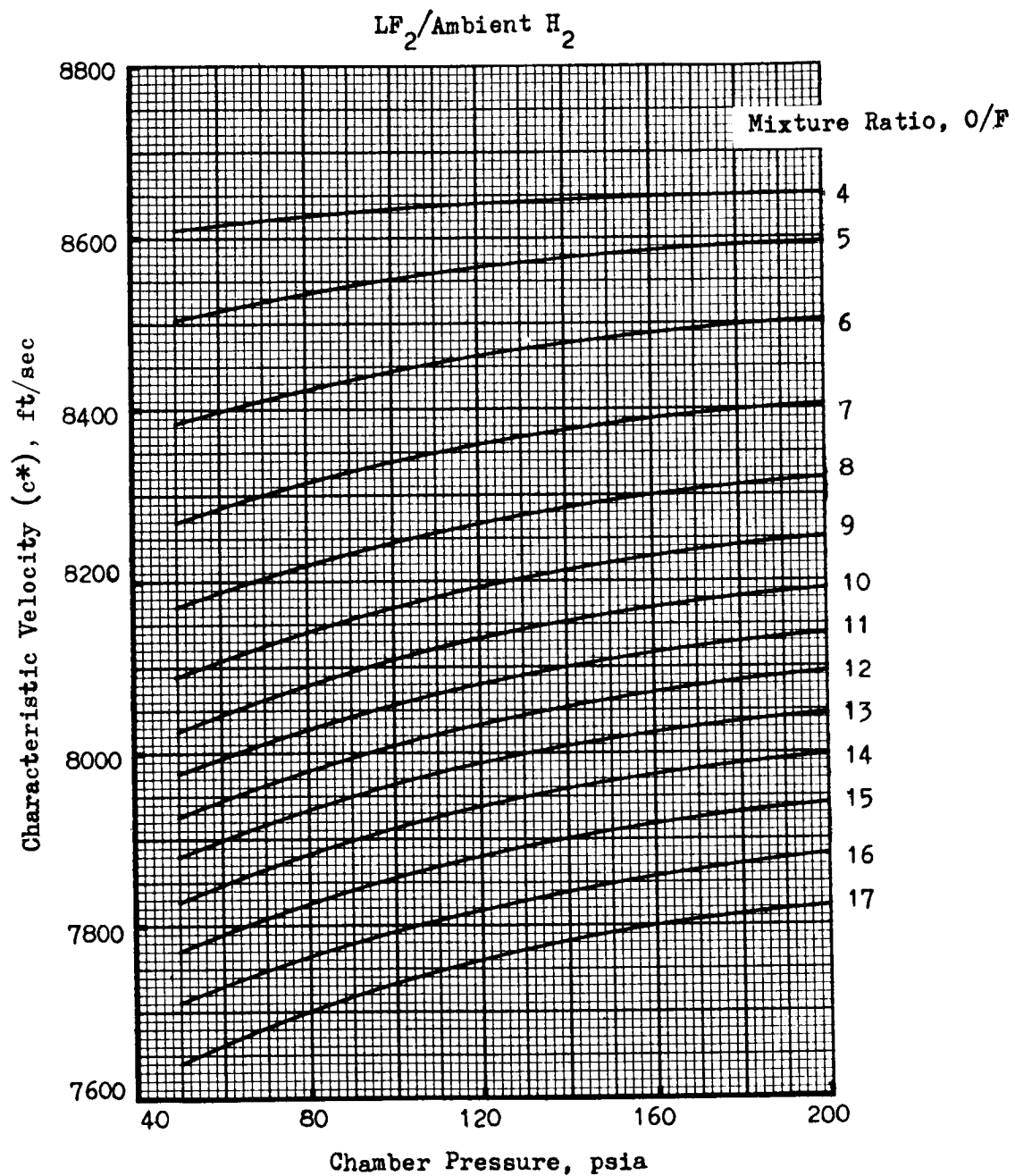


Figure 136. Characteristic Velocity vs Chamber Pressure
—Chemical Equilibrium

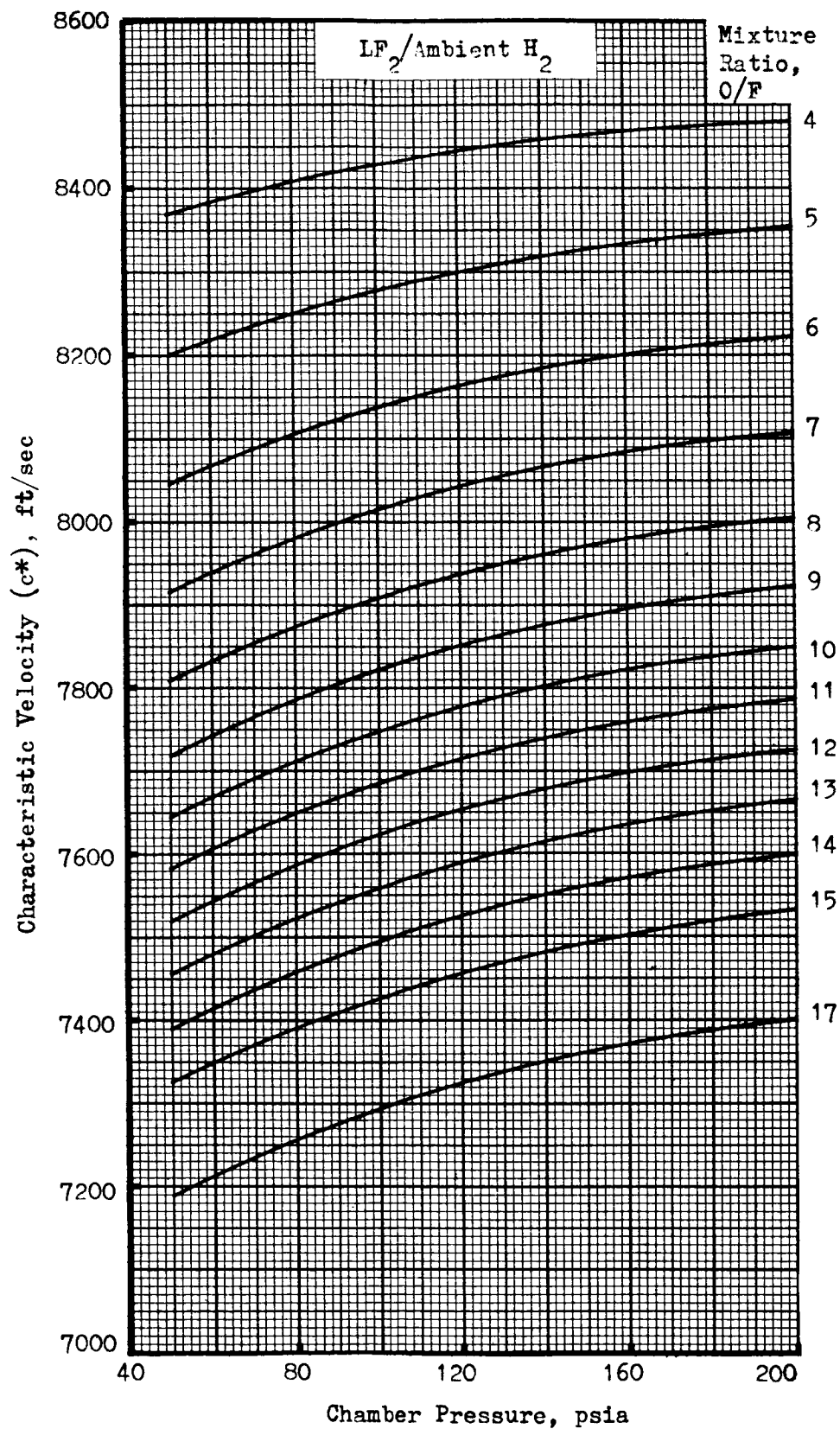


Figure 137. Characteristic Velocity vs Chamber Pressure
—Frozen Composition

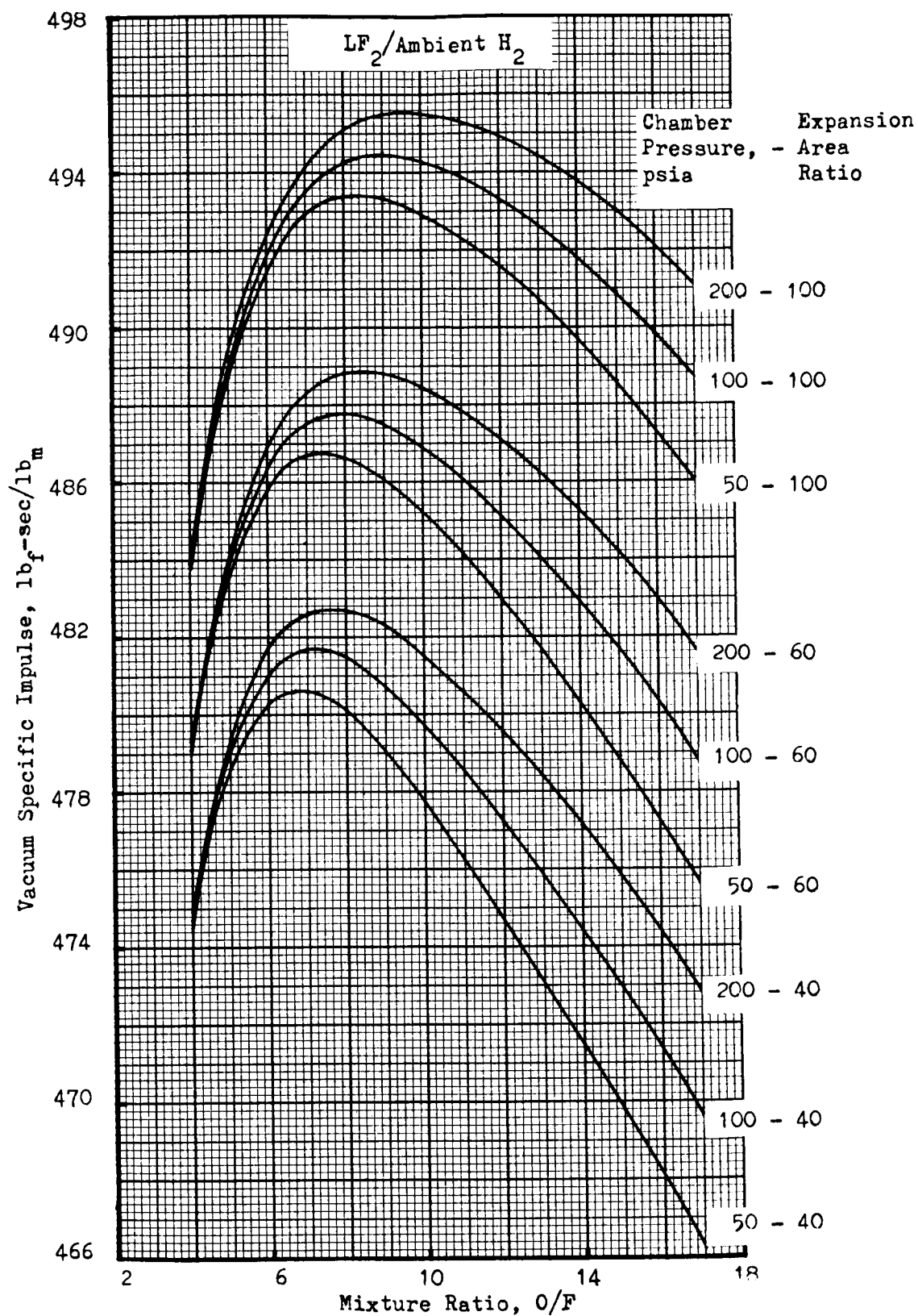


Figure 138. Vacuum Specific Impulse vs Mixture Ratio—Chemical Equilibrium

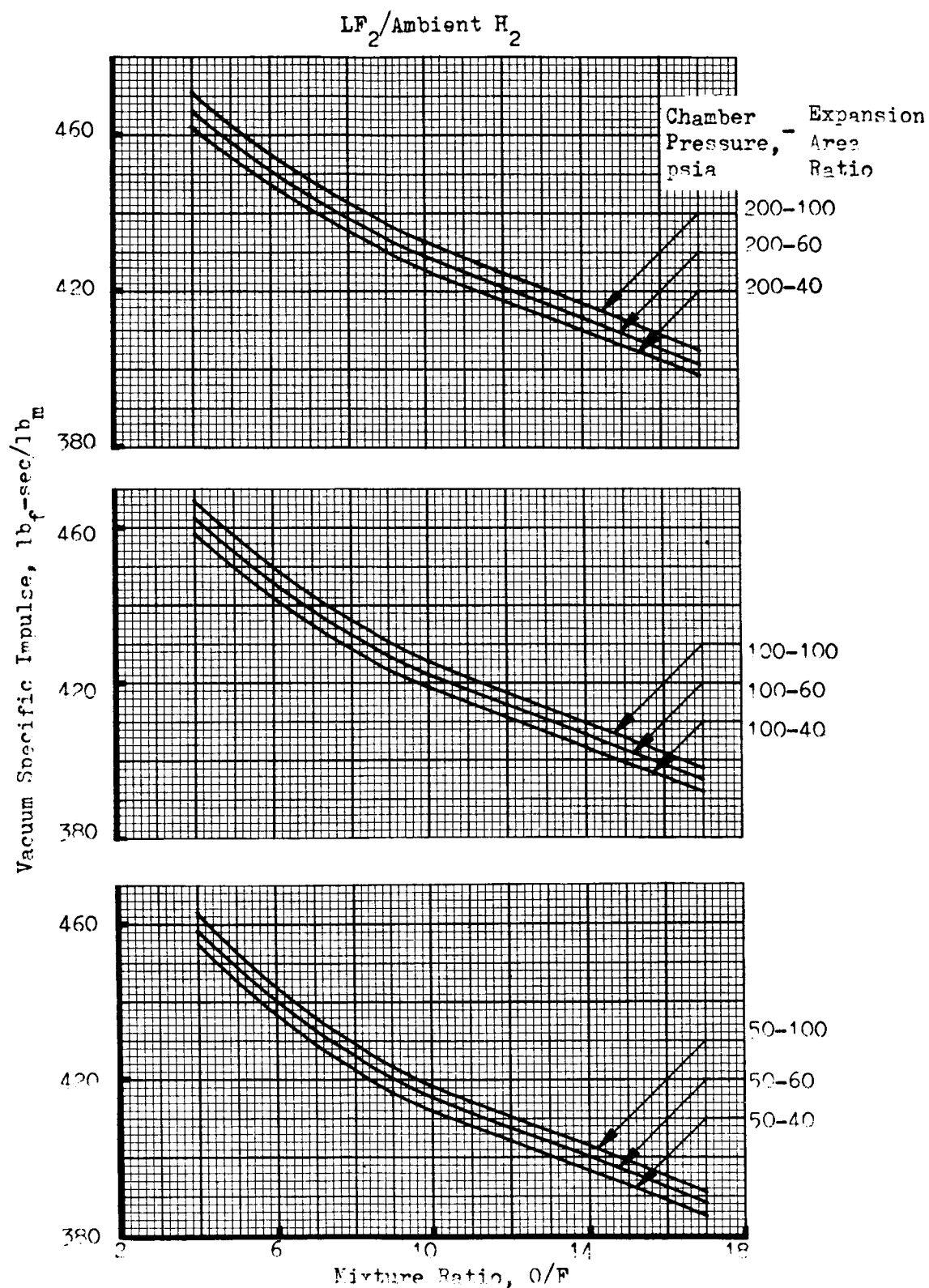


Figure 139. Vacuum Specific Impulse vs Mixture Ratio
—Frozen Composition

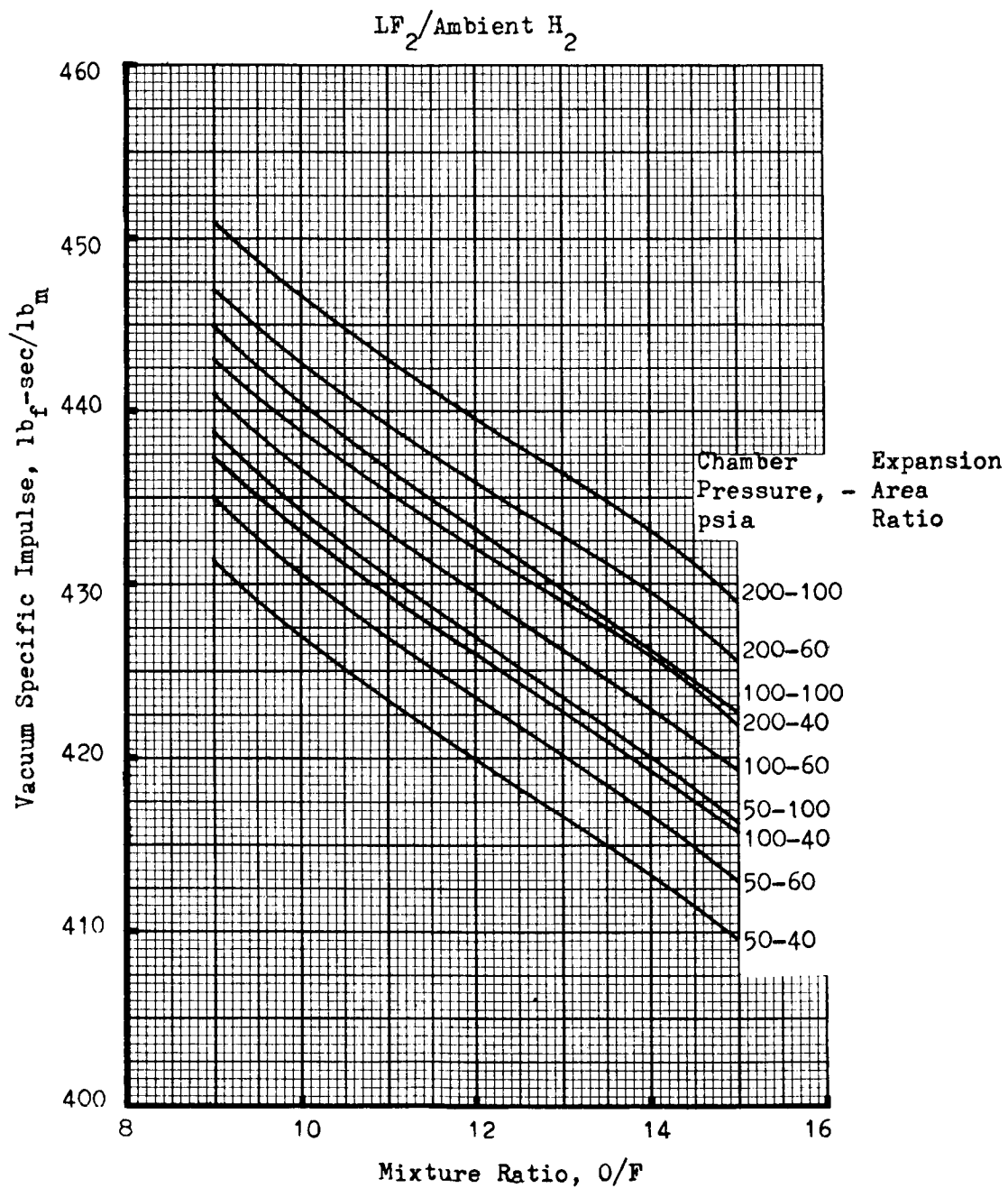


Figure 140. Vacuum Specific Impulse vs Mixture Ratio - Frozen at the Throat

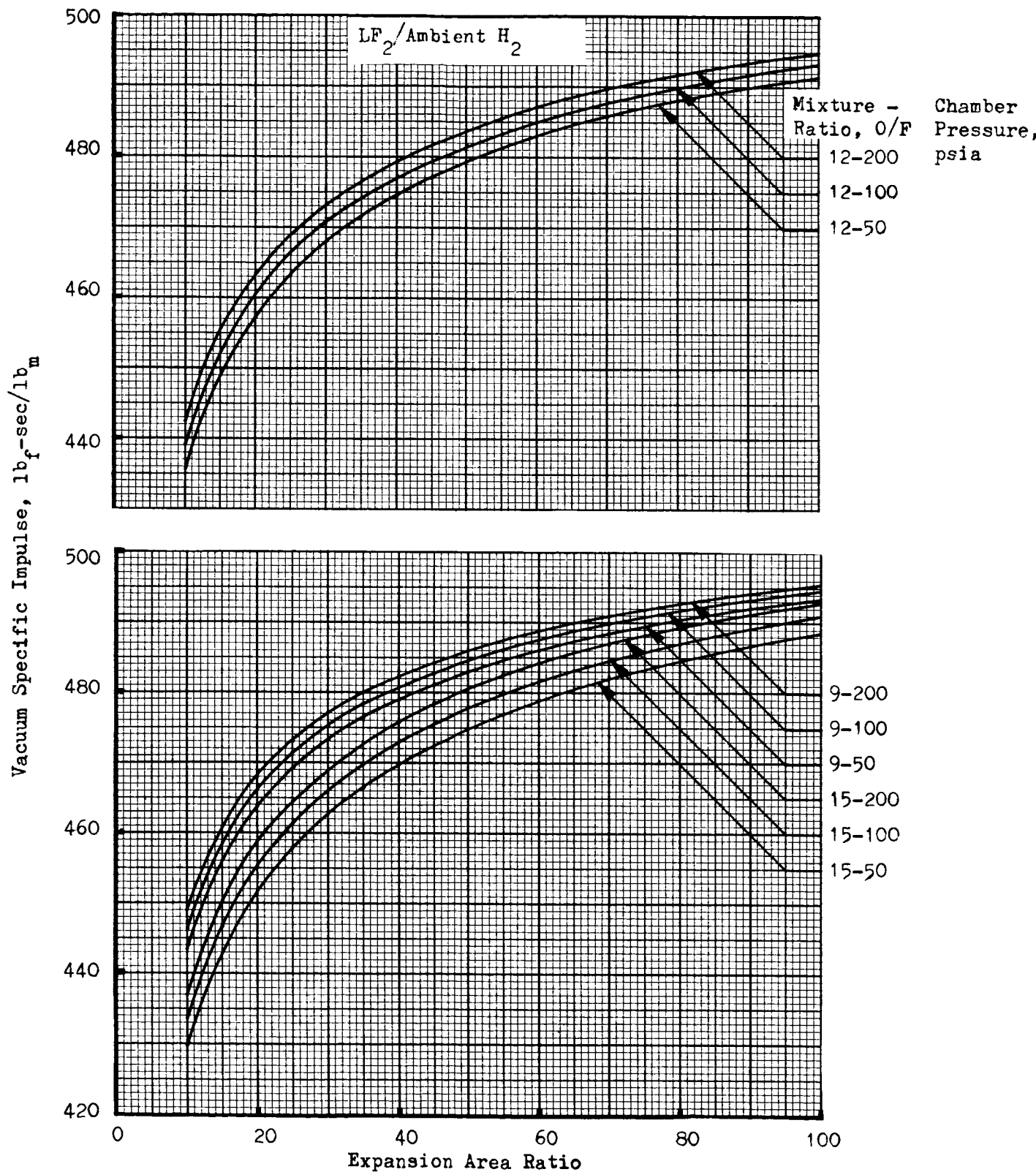


Figure 141. Vacuum Specific Impulse vs Expansion Area Ratio - Chemical Equilibrium

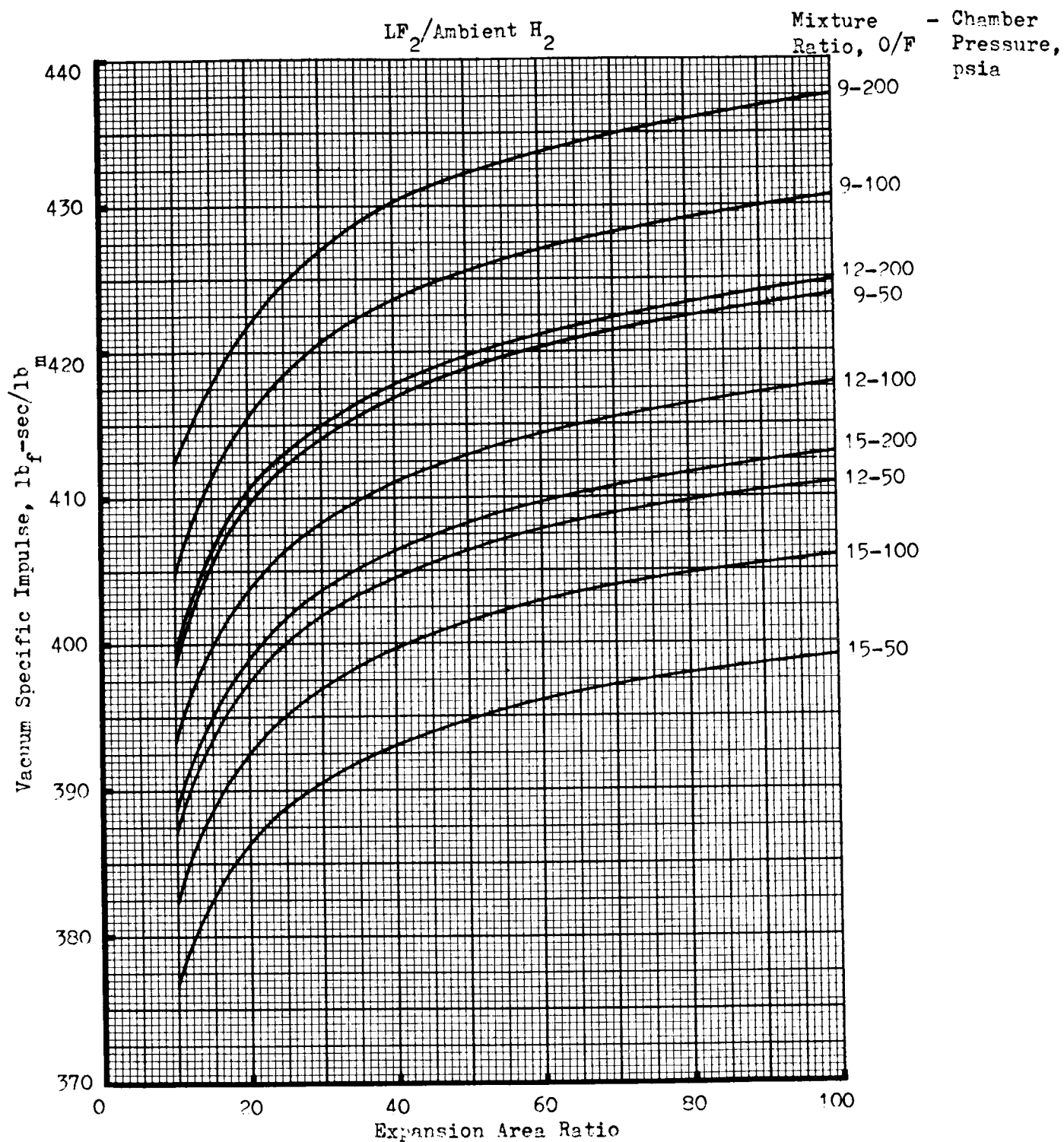


Figure 142. Vacuum Specific Impulse vs Expansion Area Ratio--Frozen Composition

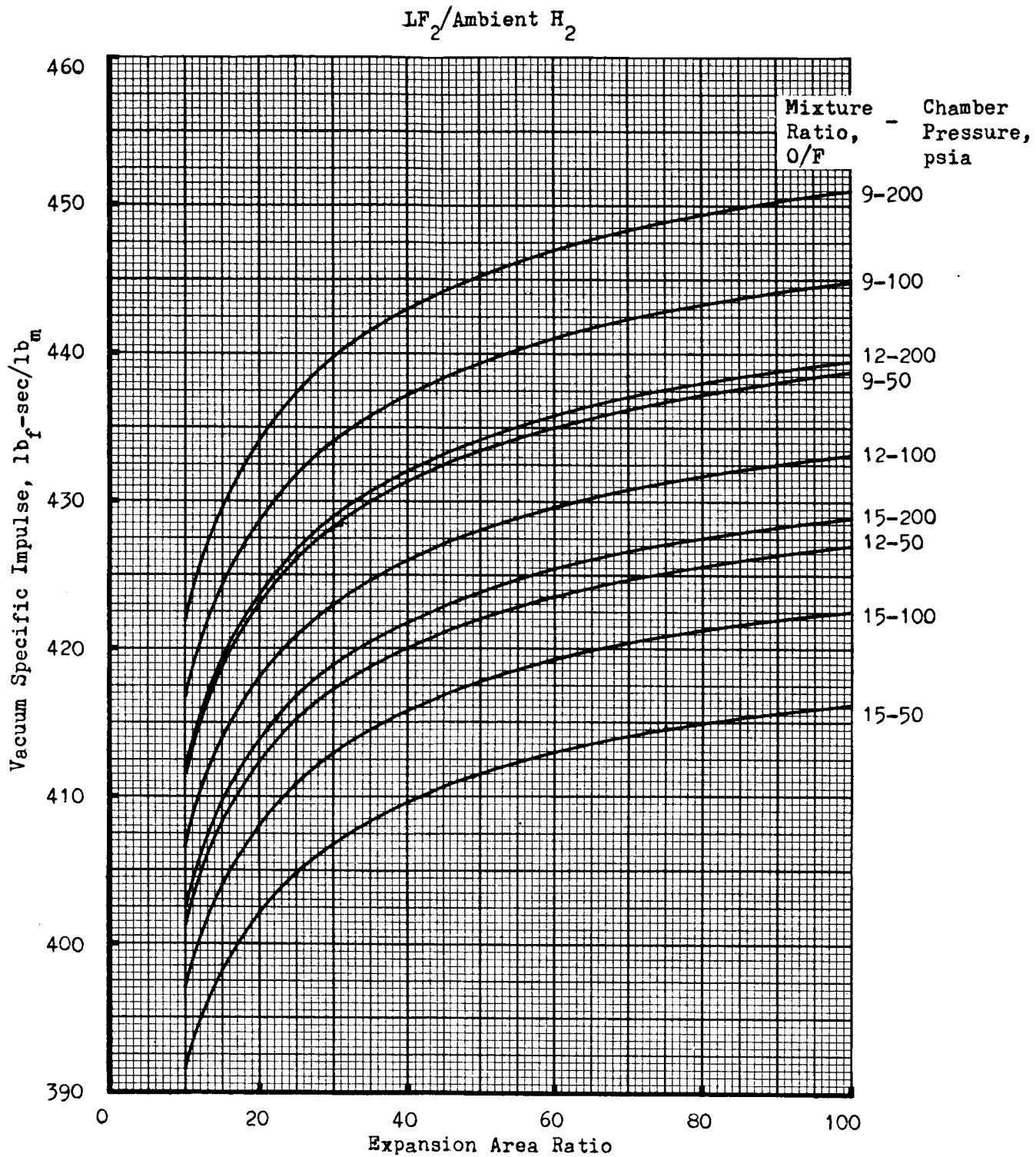


Figure 143. Vacuum Specific Impulse vs Expansion Area Ratio--
Frozen at the Throat

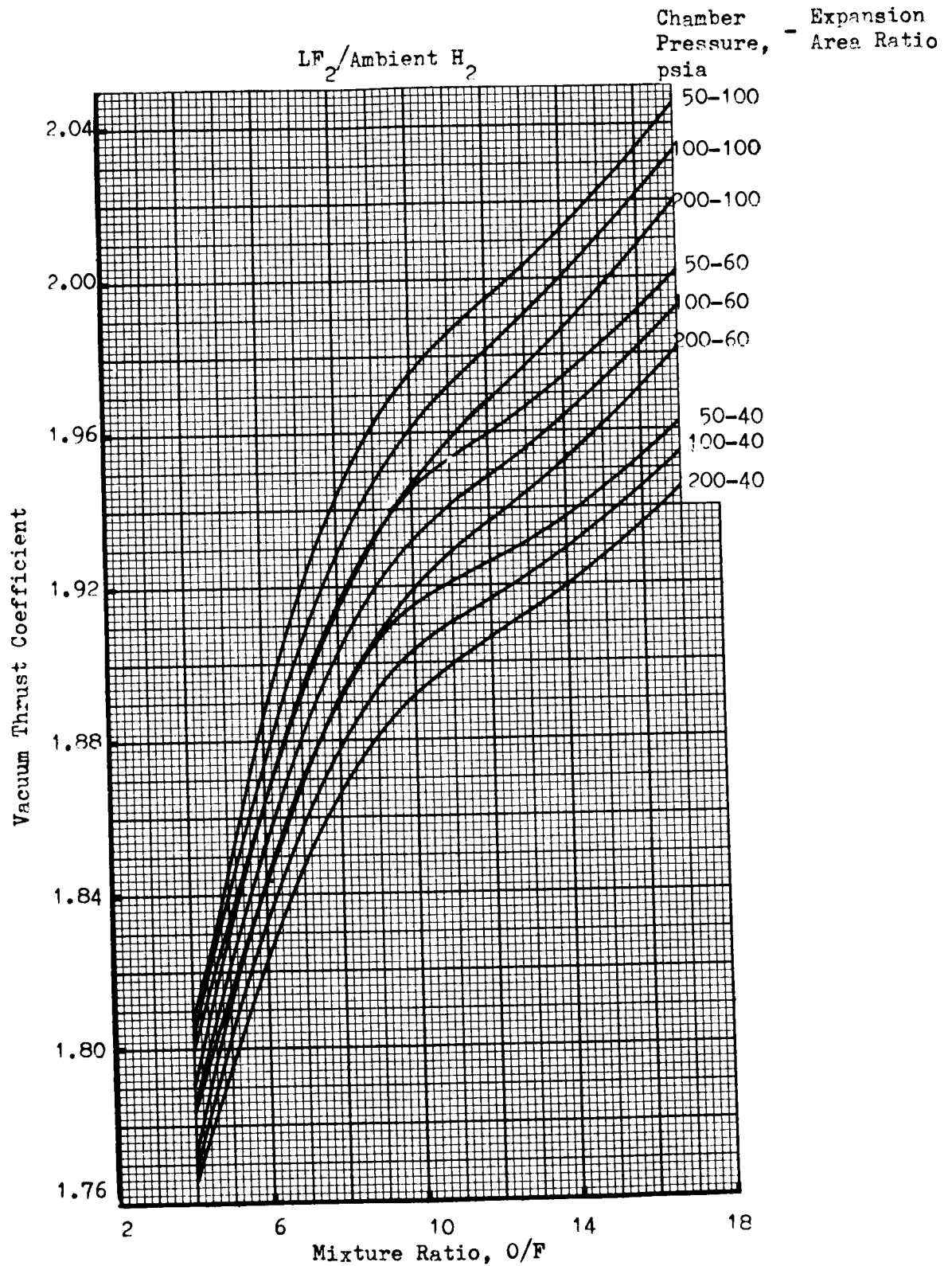


Figure 144. Vacuum Thrust Coefficient vs Mixture Ratio - Chemical Equilibrium

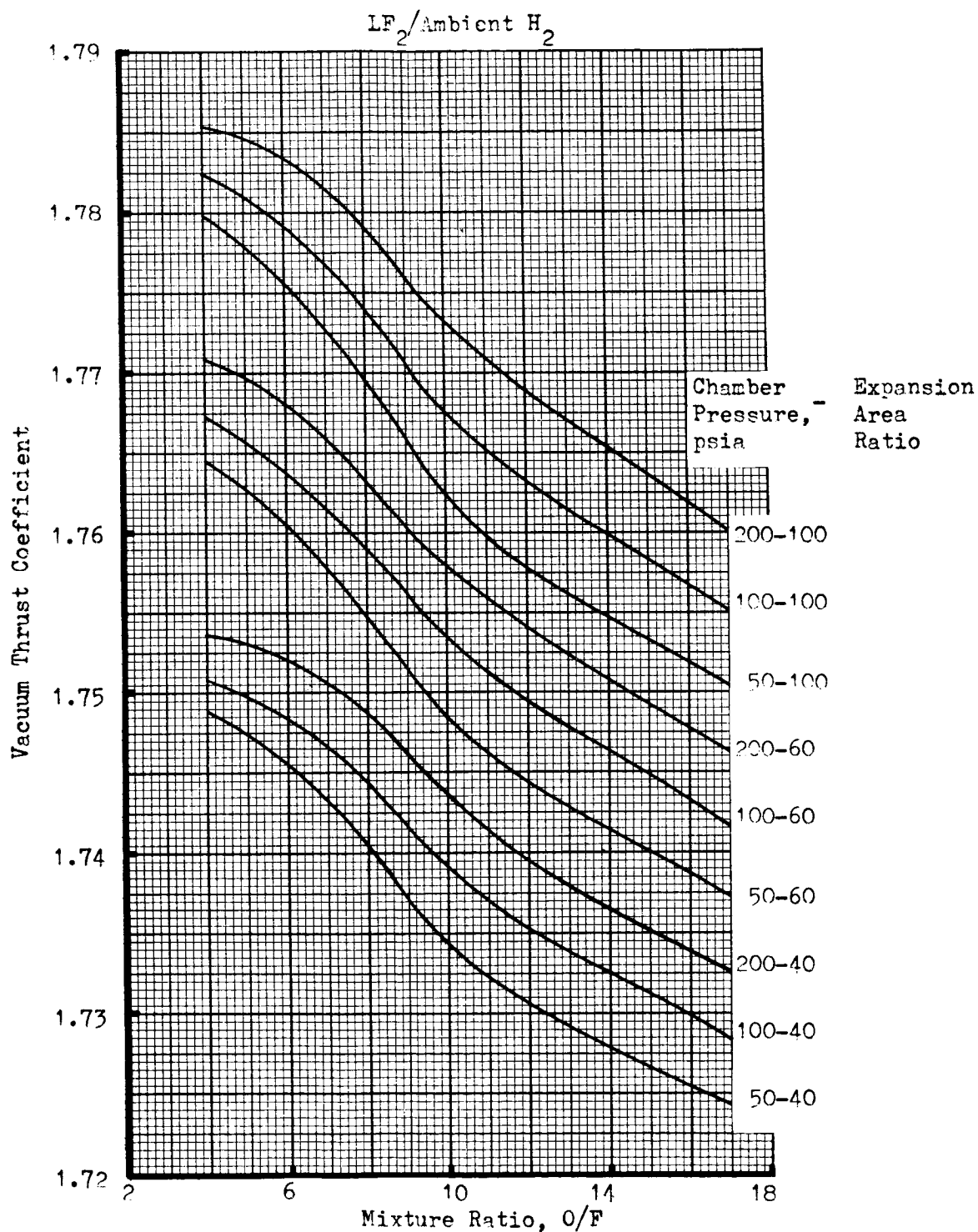


Figure 145. Vacuum Thrust Coefficient vs Mixture Ratio - Frozen Composition

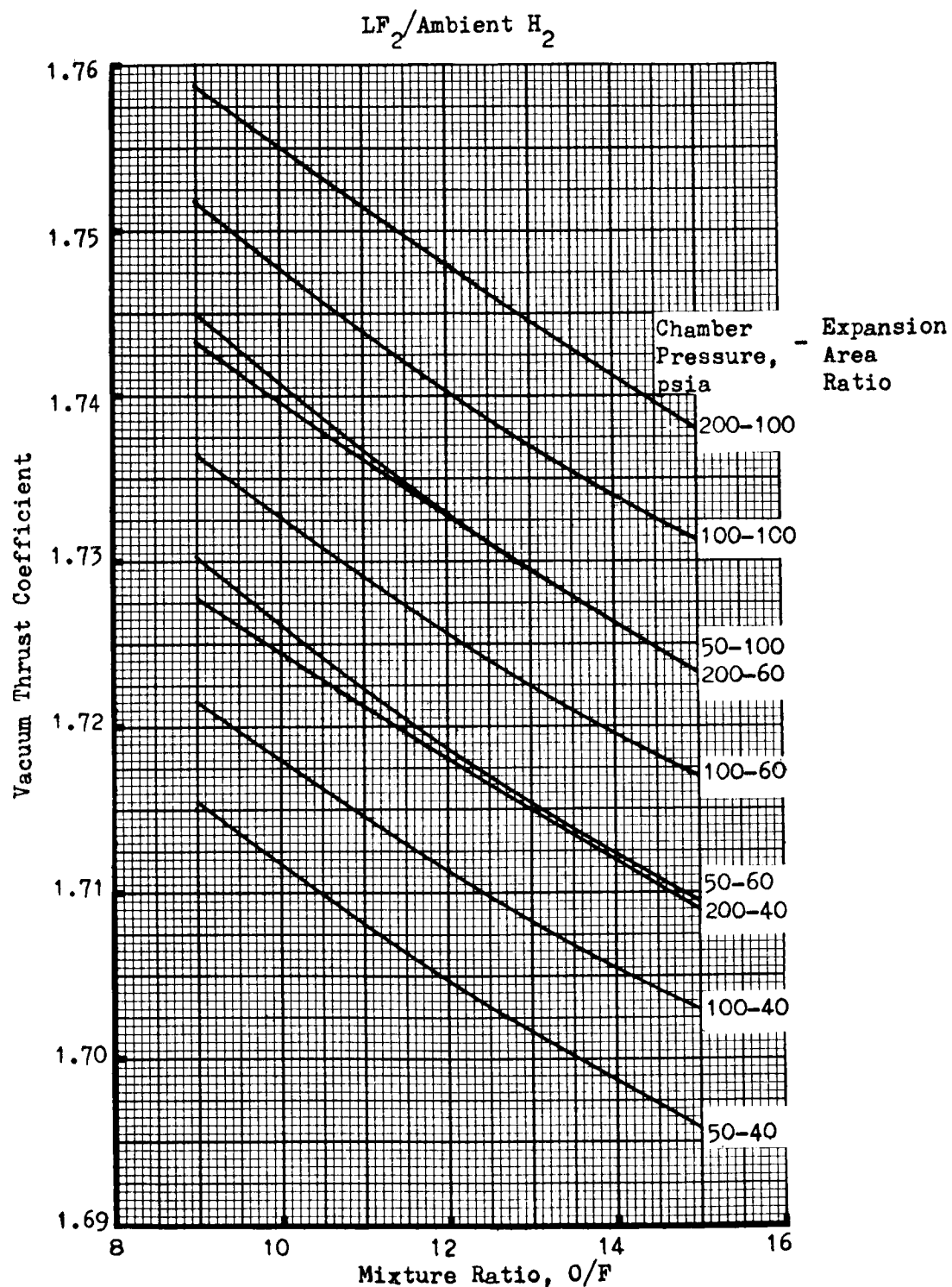


Figure 146. Vacuum Thrust Coefficient vs Mixture Ratio - Frozen at the Throat

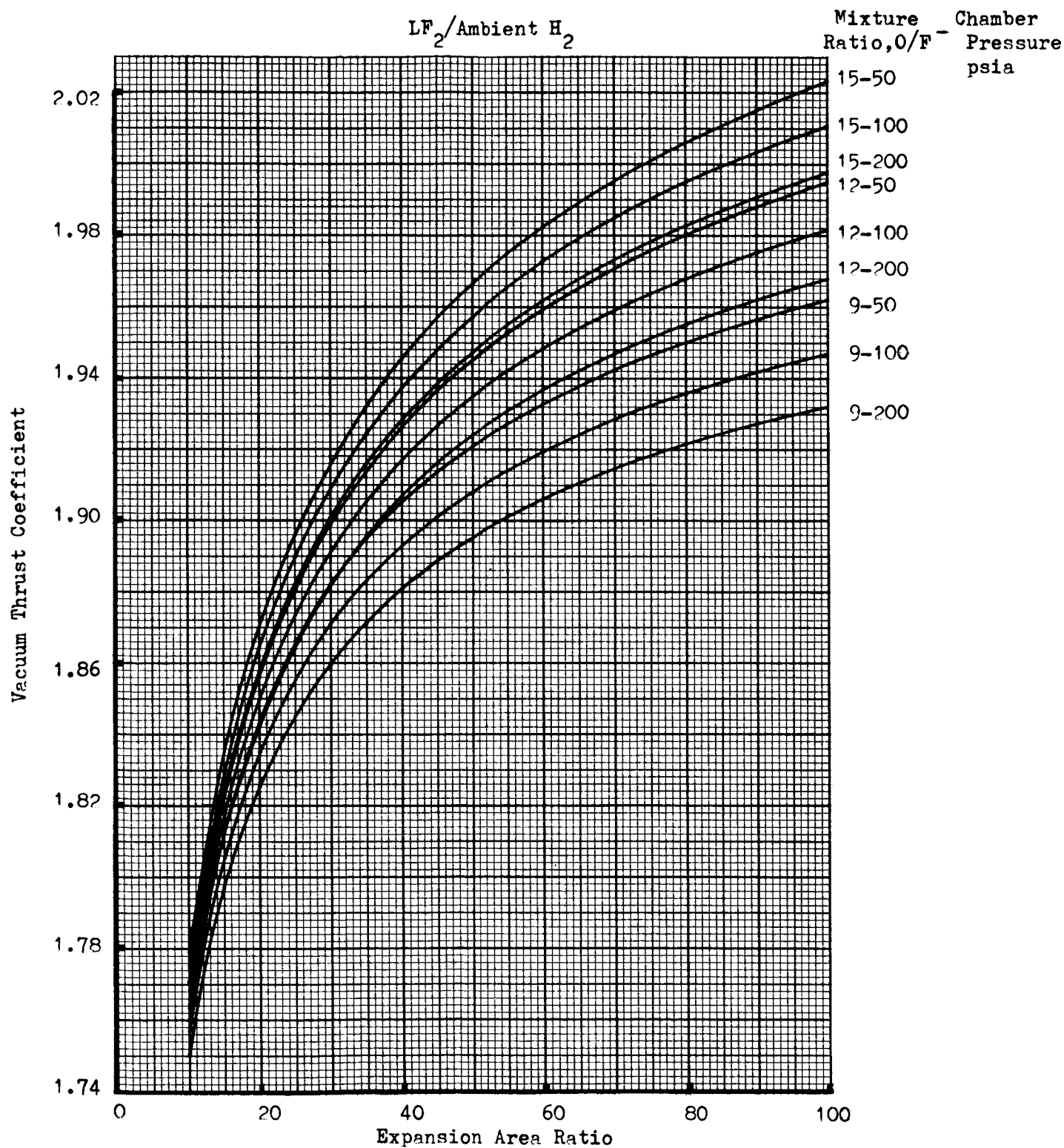


Figure 147. Vacuum Thrust Coefficient vs Expansion Area Ratio - Chemical Equilibrium

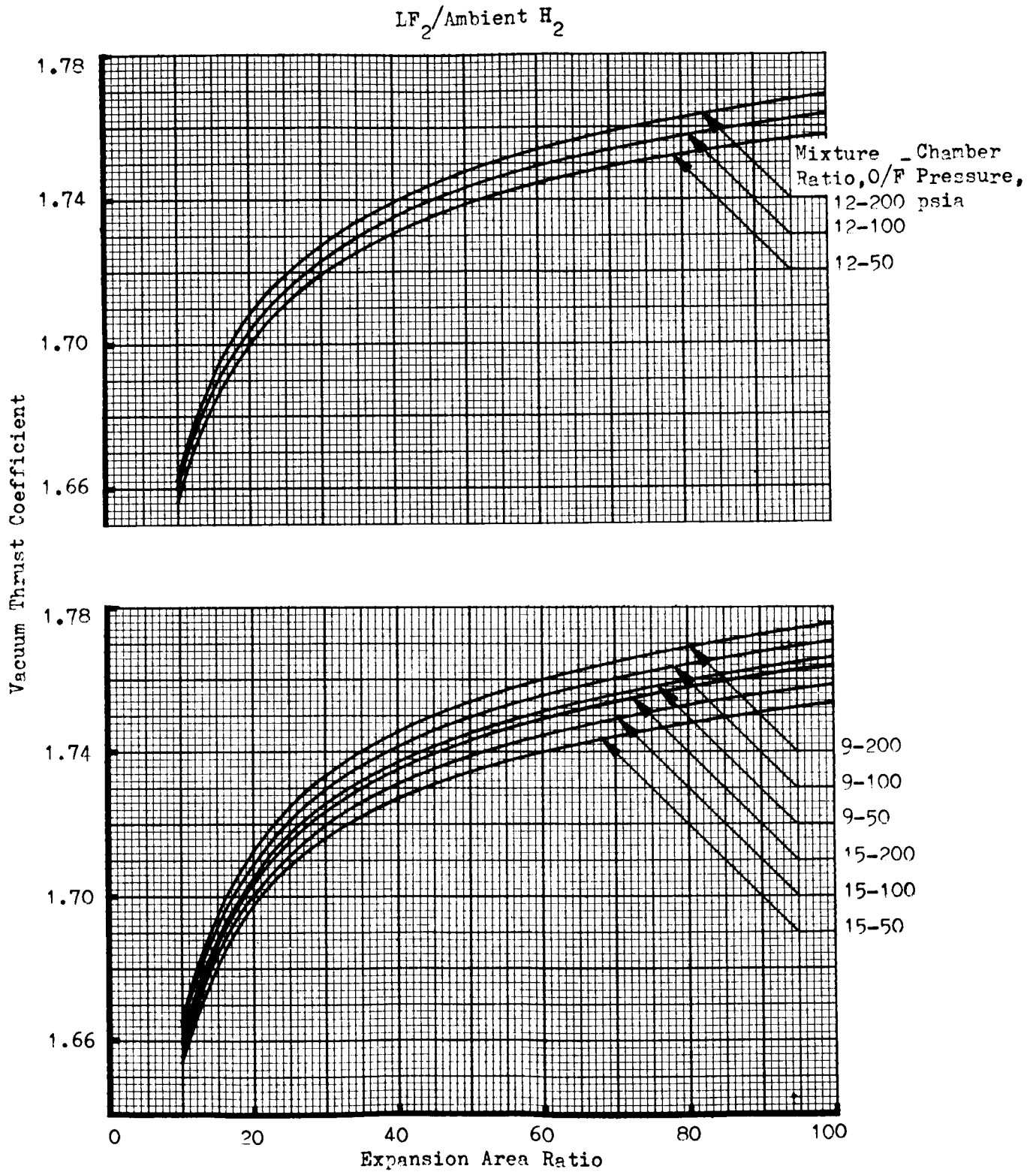


Figure 148. Vacuum Thrust Coefficient vs Expansion Area Ratio - Frozen Composition

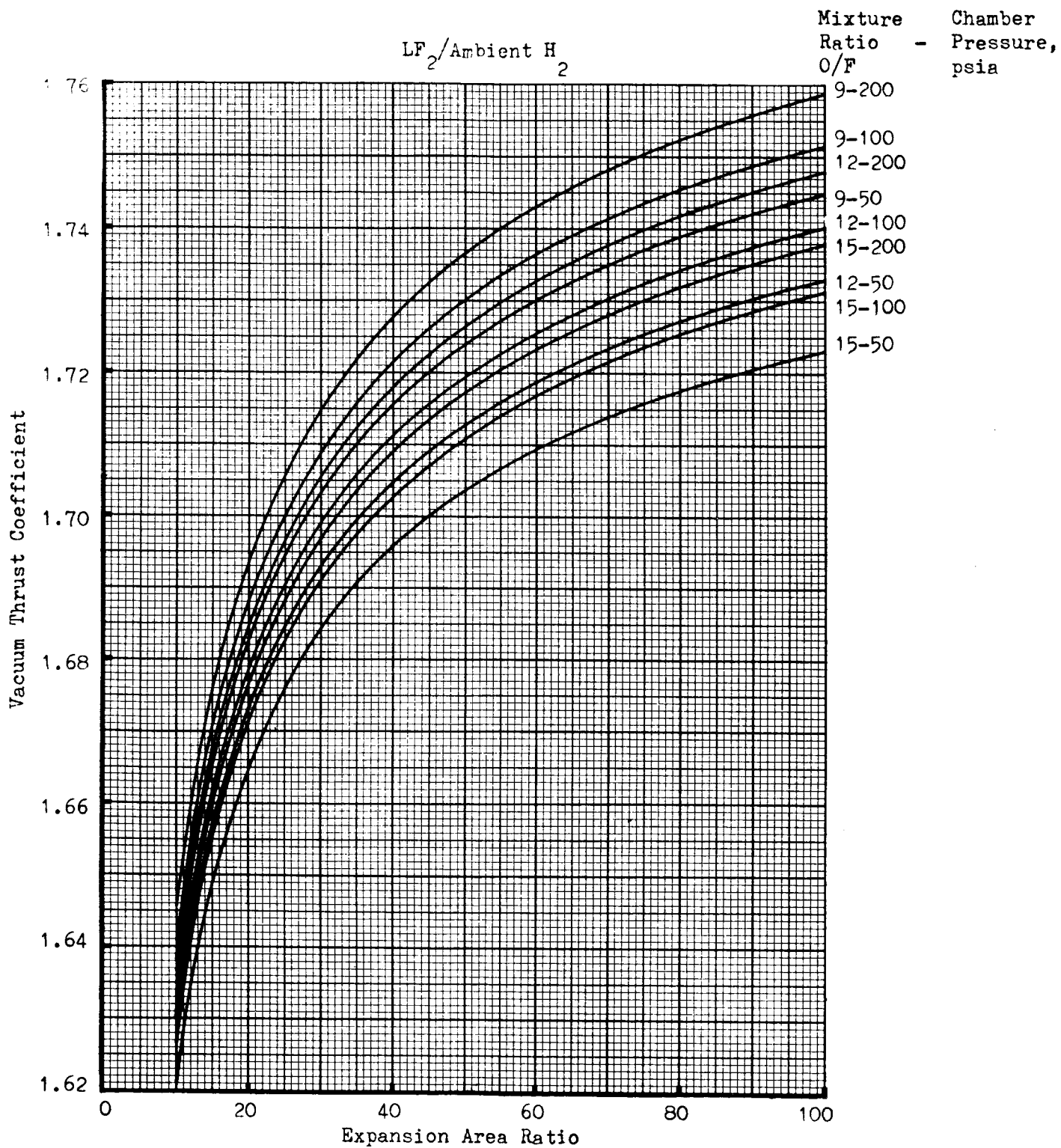


Figure 149. Vacuum Thrust Coefficient vs Expansion Area Ratio - Frozen at the Throat



NOMENCLATURE

NOZZLE PERFORMANCE PARAMETERS

A^*	=	aerodynamic throat area, sq in.
C_d	=	discharge coefficient
$C_{F_{ideal}}$	=	ideal thrust coefficient
$C_{F_{vac}}$	=	actual vacuum thrust coefficient
c^*_{corr}	=	characteristic velocity corrected for aerodynamic throat area, heat loss, and impurities effects, ft/sec
c^*_{theor}	=	theoretical characteristic velocity, ft/sec
c^*_{unc}	=	uncorrected characteristic velocity, ft/sec

$$c^*_{unc} = \frac{P_c A_t g_c}{\dot{w}_{total_{corr}}}$$

K_c	=	critical flow function
$I_{vac_{test}}$	=	test delivered vacuum specific impulse, $\frac{lb_f\text{-sec}}{lb_m}$
$I_{vac_{theor}}$	=	theoretical vacuum specific impulse, $\frac{lb_f\text{-sec}}{lb_m}$
o/f	=	mixture ratio
P_c	=	chamber pressure, psia
PR	=	pressure ratio (P_c/P_a)



T_c	= combustion temperature, R
\dot{w}_a	= actual weight flowrate, lbm/sec
\dot{w}_i	= ideal weight flowrate, lbm/sec
ΔHL_{c*}	= characteristic velocity heat loss ($\xi_{HL_{c*}} - 1$)
ΔI_{c*}	= impurities correction factor ($\xi_{I_{c*}} - 1$)
ϵ^*	= ratio of exit area to aerodynamic throat area (A_e/A^*)
γ	= specific heat ratio
$\eta_{c*_{corr}}$	= corrected combustion efficiency
η_D	= drag efficiency
η_G	= nozzle geometric efficiency
η_k	= kinetic efficiency
$\eta_{I_{vac_{test}}}$	= test vacuum specific impulse efficiency
$\eta_{TC_{exp}}$	= experimental thrust chamber efficiency
$\eta_{TC_{theor}}$	= theoretical thrust chamber efficiency
$\xi_{HL_{c*}}$	= heat loss correction to characteristic velocity
$\xi_{HL_{I_s}}$	= heat loss correction to specific impulse
$\xi_{I_{c*}}$	= impurities correction to characteristic velocity
$\xi_{I_{I_s}}$	= impurities correction to specific impulse



NOZZLE GEOMETRY PARAMETERS

A_e	=	nozzle exit area, sq in.
A_t	=	nozzle geometric throat area, sq in.
L^*	=	characteristic length of combustion chamber, inches
M_D^*	=	design Mach number referenced to sonic conditions
R_t	=	throat radius, inches
X/R_t	=	normalized axial distance (along nozzle axis of symmetry)
Y/R_t	=	normalized radial distance (normal to nozzle axis of symmetry)
$(X/R_t)_B$	=	normalized breakpoint (end of conical section)
α	=	cone half angle, degrees
ϵ	=	area ratio
ρ_i/R_t	=	radius of curvature upstream of nozzle throat
$(\rho/R_t)_1$	=	radius of curvature immediately downstream of the nozzle throat
$(\rho/R_t)_3$	=	radius of curvature following the conical nozzle section
θ_{\max}	=	nozzle wall angle at which the aerodynamic contour attaches to the throat circle for a circular throat bell nozzle, degrees
θ_{\min}	=	nozzle wall angle at nozzle exit, degrees



INSTRUMENTATION PARAMETERS

CPG	= cycles per gallon corrected for water viscosity from calibration curve
CPS	= test run reading of cycles per second determined from oscillograph
D _A	= system zero, when transducer is vented to atmospheric pressure
D _B	= system zero at each engine test
D _R	= R-Cal deflection, recorder deflection for a specified electrical unbalance
D _X	= test deflection
D ₁	= chart zero at low R-Cal
D ₂	= chart zero to high R-Cal
F _M	= measured thrust, lbf
F _{vac}	= vacuum thrust, lbf
g _c	= mass conversion constant (32.174) lbfm/slug
K	= conversion constant for gal/sec to lbfm/sec
KN	= key number, psig, physical input to a transducer corresponding to a specified electrical unbalance
MR _{cor}	= mixture ratio corrected for impurities
P _a	= ambient pressure at time of test, psia
P _m	= measured pressure, psig
P ₃	= intercept of the transducer which is the pressure equivalent to the low R-Cal electrical unbalance as established during calibration, psia



$(\text{Sp G})_{\text{LF}_2}$	=	fluorine specific gravity at test conditions
\dot{w}_f	=	fuel flowrate, lbm/sec
\dot{w}_o	=	oxidizer flowrate, lbm/sec
$\dot{w}_{\text{oxid cor}}$	=	oxidizer flowrate corrected for impurities, lbm/sec
$(\dot{w}_{\text{oxid}})_{\text{avg}}$	=	average apparent flowrate for pure oxidizer, lbm/sec
$\dot{w}_{\text{total cor}}$	=	total flowrate corrected for impurities, lbm/sec
$\rho_{\text{corr oxid}}$	=	density correction caused by impurities

CHEMICAL REACTION KINETIC PARAMETERS

Ar	=	Argon
B	=	ratio of required to available reaction rate at the freezing point
F	=	atomic fluorine
F ₂	=	diatomic fluorine
H	=	atomic hydrogen
H ₂	=	diatomic hydrogen
HF	=	hydrogen fluoride
H ₂ O	=	water
M	=	some third body
N ₂	=	diatomic nitrogen
O ₂	=	diatomic oxygen



OH = hydroxyl

r_{eq} = net equilibrium rate of recombination $cc^2/mole-sec$

r_{kin} = kinetically possible rate of recombination $cc^2/mole-sec$

T = temperature, K

HEAT TRANSFER PARAMETERS

A = coefficient of heat transfer coefficient variation with temperature

B = coefficient of specific heat variation with temperature

Bi = Biot number

b = isolation segment thickness, in.

C = specific heat of segment material, Btu/lbm-R

C_o = specific heat of isolation material extrapolated to zero degree R, Btu/lbm-R

h = heat transfer coefficient, Btu/sq in.-sec-R

h_o = heat transfer coefficient extrapolated to zero, Btu/sq.in.-sec-R

M = Mach number

Pr = Prandtl number

q/A = heat flux to segment, Btu/sq in.-sec

R_T = recovery factor

T_{c_a} = actual combustion temperature, R

Ti = initial wall temperature at $\theta = zero$, R



T_r = recovery temperature, R

T_s = inside wall temperature, R

ρ = isolation segment density, lbm/cu in.

T_w = wall temperature, R

β = time constant, sec^{-1} $\left(\frac{h}{\rho C_b} \right)$

γ = ratio of specific heats

θ = time, seconds



REFERENCE

1. C-910096-11: Investigation of Nonequilibrium Flow Effects in High Expansion Ratio Nozzles, Computer Program Manual, United Aircraft Corporation, East Hartford, Connecticut, 15 September 1964.
2. Bray, K. N. C.: "Simplified Sudden-Freezing Analysis for Non-equilibrium Nozzle Flows", ARS Journal, June 1961, 831-834.
3. Bray, K. N. C.: "Atomic Recombination in a Hypersonic Wind-Tunnel Nozzle", J. Fluid Mech., Vol. 6, July 1959, 1-32.
4. Wegener, P. P.: "A Review of Investigations of Stationary Supersonic Nozzle Flow with a Reacting Gas Mixture", Paper read at 4th AGARD Combustion and Propulsion Colloquium, Milan, April 1960, 261-285.
5. Kalvinskis, J. J.: "Analysis of Chemical Recombination in Rocket Nozzle Flow for Conventional and Annular Nozzles", Presented at AIAA Propulsion Specialists Conference, Air Force Academy, Colorado Springs, Colorado, 14 January 1965, CONFIDENTIAL.
6. Franciscus, Leo C., and Lezberg, Erwin A.: "Effects of Exhaust Nozzle Recombination on Hypersonic Ramjet Performance: Analytical Investigation", AIAA Journal, Vol. 1, September 1963, 2077-2083.
7. Lezberg, Erwin A., and Franciscus, Leo C.: "Effects of Exhaust Nozzle Recombination on Hypersonic Ramjet Performance: Experimental Measurements", AIAA Journal, Vol. 1, September 1963, 2071-2077.
8. Aukerman, Carl A., and Church, Bruce E.: "Experimental Hydrogen-Fluorine Rocket Performance at Low Pressures and High Area Ratios", NASA Technical Memorandum X-724, Lewis Research Center, Cleveland, Ohio, 12 April 1963, CONFIDENTIAL.



9. B-910056-12: Investigation of Nonequilibrium Flow Effects in High Expansion Ratio Nozzles, United Aircraft Corporation, East Hartford Connecticut, 20 September 1963.
10. Wilde, Kenneth A.: "Numerical Study of Hydrogen-Fluorine Kinetics in Nozzles", AIAA Journal, Vol. 2, February 1964, 374-376.
11. Amdur, I.: "Relative Recombination Rates of Atomic Hydrogen and Atomic Deuterium", J. Amer. Chem. Soc., Vol. 57, 1935, 856-858.
12. Amdur, I., and Robinson, A. L.: "Recombination of Hydrogen Atoms", J. Amer. Chem. Soc., Vol. 55, 1933, 1395-1406.
13. Bulewicz, E. M., and Sugden, T. M.: "The Recombination of Hydrogen Atoms and Hydroxyl Radicals in Hydrogen Flame Gases", Trans. Faraday Soc., Vol. 53, May 1958, 1855-1860.
14. Rink, John P., Knight, H. T., and Duff, R. E.: "Shock Tube Determination of Dissociation Rates of Oxygen," Jour. Chem. Phys., Vol. 34, June 1961, 1942-1947.
15. Sutton, Emmett A.: "Measurement of the Dissociation Rates of Hydrogen and Deuterium," Jour. Chem. Phys., Vol. 36, June 1962, 2923-2931.
16. Rink, John P.: "Shock-Tube Determination of Dissociation Rates of Hydrogen", J. Chem. Phys., Vol. 36, January 1962, 262-265.
17. Patch, Richard W.: "Shock-Tube Measurement of Dissociation Rates of Hydrogen", Jour. Chem. Phys., Vol. 36, April 1962, 1919-1924.
18. Gardiner Jr., W. C., and Kistiakowsky, G. B.: "Thermal Dissociation Rate of Hydrogen", Jour. Chem. Phys., Vol. 35, November 1961, 1765-1770.



19. Larkin, F. S., and Thrush, B. A.: "The Kinetics of Hydrogen Atom Recombination", Tenth Symposium (International) on Combustion, The Combustion Institute, Pittsburgh, Pennsylvania, 1965, 397-402.
20. Dixon-Lewis, G., Sutton, M. M., and William, A.: "Some Reactions of Hydrogen Atoms and Simple Radicals at High Temperatures," Tenth Symposium (International) on Combustion, The Combustion Institute, Pittsburgh, Pennsylvania, 1965, 495-502.
21. Rosenfeld, J. L. J., and Sugden, T. M.: "Burning Velocity and Free Radical Recombination Rates in Low Temperature Hydrogen Flames," Combustion and Flame, Vol. 8, March 1964, 44-50.
22. AIAA Paper No. 66-637, Jacobs, T. A., Giedt, R. R. and Cohen, N.: Gas Dynamics, AIAA Second Propulsion Joint Specialist Conference, Colorado Springs, Colorado, June 1966.
23. Johnson, Charles D. and Britton, Doyle: "Shock Waves Chemical Kinetics: The Rate of Dissociation of Fluorine," Jour. Phys. Chem., Vol. 68, October 1964, 3032-3039.
24. Elliot, D. G., Bartz, D. R. and Silver, S.: Calculation of Turbulent Boundary Layer Growth and Heat Transfer in Axi-Symmetric Nozzles, Jet Propulsion Laboratory, Pasadena, California, 15 February 1963.
25. "Flow Meters, Their Theory and Application"; Report of ASME Research Committee on Fluid Meters, 5th Edition, 1959.
26. Orbit, H. A. and Clapp, S. D.: Fluorine-Hydrogen Performance Evaluation. Part I: Analysis, Design and Demonstration of High-Performance Injectors Gaseous Hydrogen Propellant Combination, RR 66-10, Rocketdyne, a Division of North American Aviation, Inc., Canoga Park, California
27. Bartz, D. R.: "A Simple Equation for Rapid Estimation of Rocket Nozzle Convective Heat Transfer Coefficients", Jet Propulsion, Vol. 27(1), January 1957, 49-51.

APPENDIX AEFFECT OF THROAT RADIUS OF CURVATURE ON
BELL NOZZLE CHARACTERISTICS

NOZZLE CONTOUR PARAMETER VARIATION

This appendix presents some of the parameters associated with the nozzles investigated in the circular throat contour study. In each case, the parameter is related to the Rao optimum contour for the specified throat radius of curvature. All calculations represented in Fig. A-1 through A-4 were based upon gas properties at a chamber pressure of 100 psia and a mixture ratio of 12:1.

Two nozzle parameters which characterize the optimum contour are θ_{\max} (the nozzle wall angle at which the aerodynamic section attaches to the throat circle) and θ_{\min} (the wall angle at the nozzle exit).

For a given throat geometry (circular, in this case), there is an optimum aerodynamic contour. As the throat circle radius $(\rho/R_t)_D$ increases, the length available for the optimum aerodynamic contour decreases resulting in a more divergent flow at the nozzle exit, a larger value of θ_{\min} , as shown in Fig. A-1.

For a $(\rho/R_t)_D$ very close to zero, a sharp throat, some value of θ_{\max} exists. As $(\rho/R_t)_D$ increases, θ_{\max} tends to increase to achieve the optimum expansion; however, for a given $(\rho/R_t)_D$ and a fixed nozzle length, an increase of θ_{\max} shortens the available aerodynamic contour length which decreases the nozzle geometric efficiency. For small values of $(\rho/R_t)_D$, the optimum θ_{\max} may be achieved at a small expense in available nozzle length, as shown in Fig. A-3. However, as $(\rho/R_t)_D$ increases,



the length penalty increases. Therefore, a tradeoff exists between obtaining a large value of θ_{\max} to obtain the optimum expansion and the shortening of the available aerodynamic contour length. This tradeoff qualitatively explains the variation of θ_{\max} with $(\rho/R_t)_D$ shown in Fig. A-2.

In the bell contour optimization procedure, the parameters θ_{\max} and the Mach number M^*_D are used at a point on the characteristic line having flow angle at the wall of θ_{\max} . The variation of M^*_D with throat radius of curvature is shown in Fig. A-4.

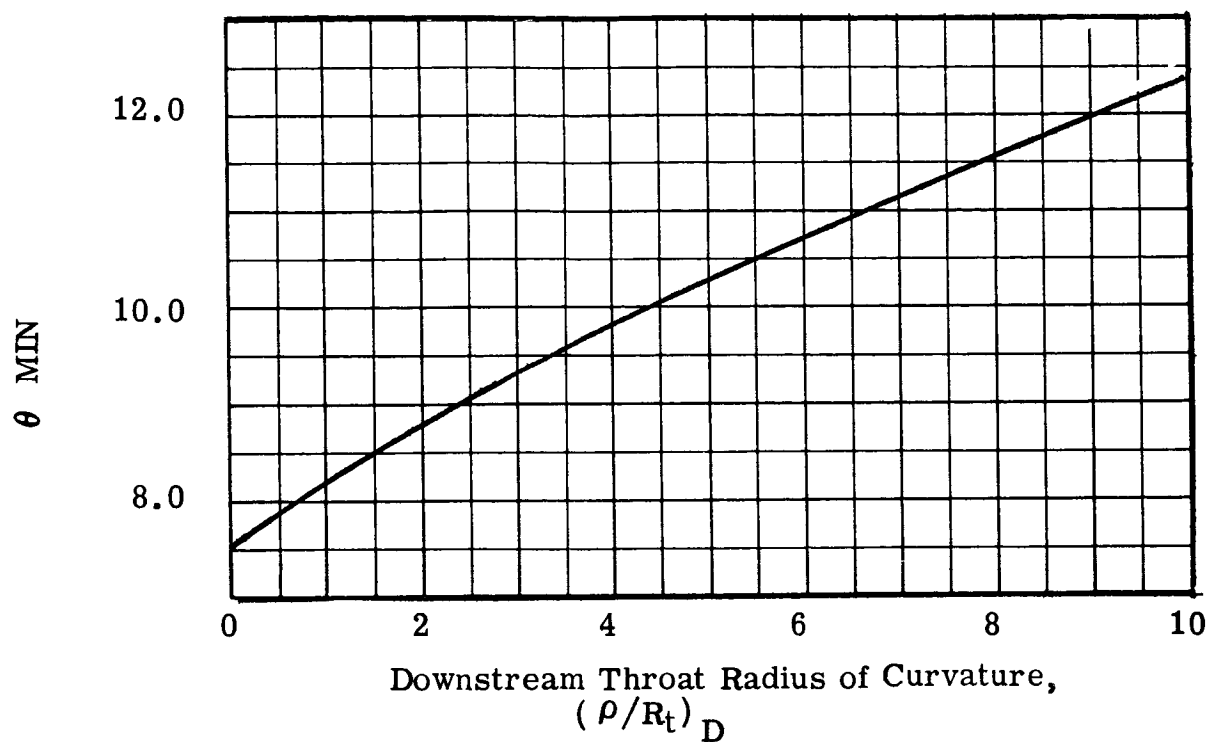


Figure.A-1 Bell Nozzle Contour Parameter Variation - θ_{Min}

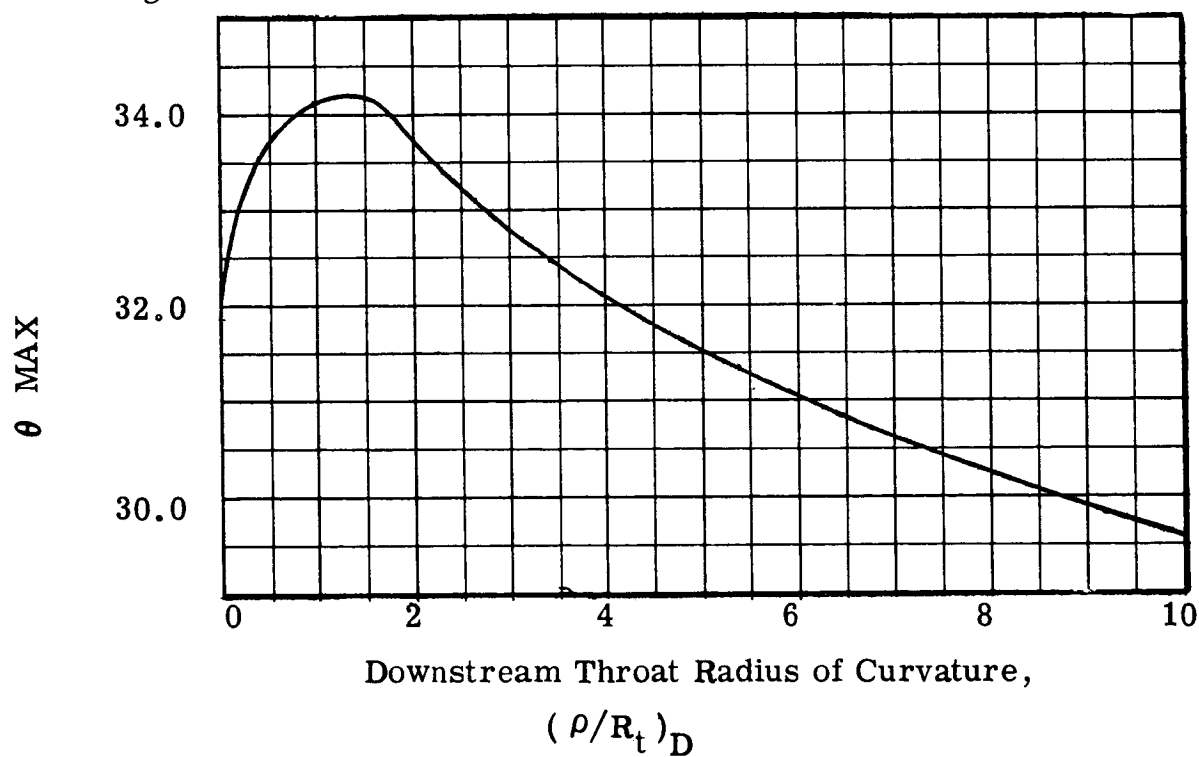


Figure.A-2 Bell Nozzle Contour Parameter Variation -- θ_{Max} .

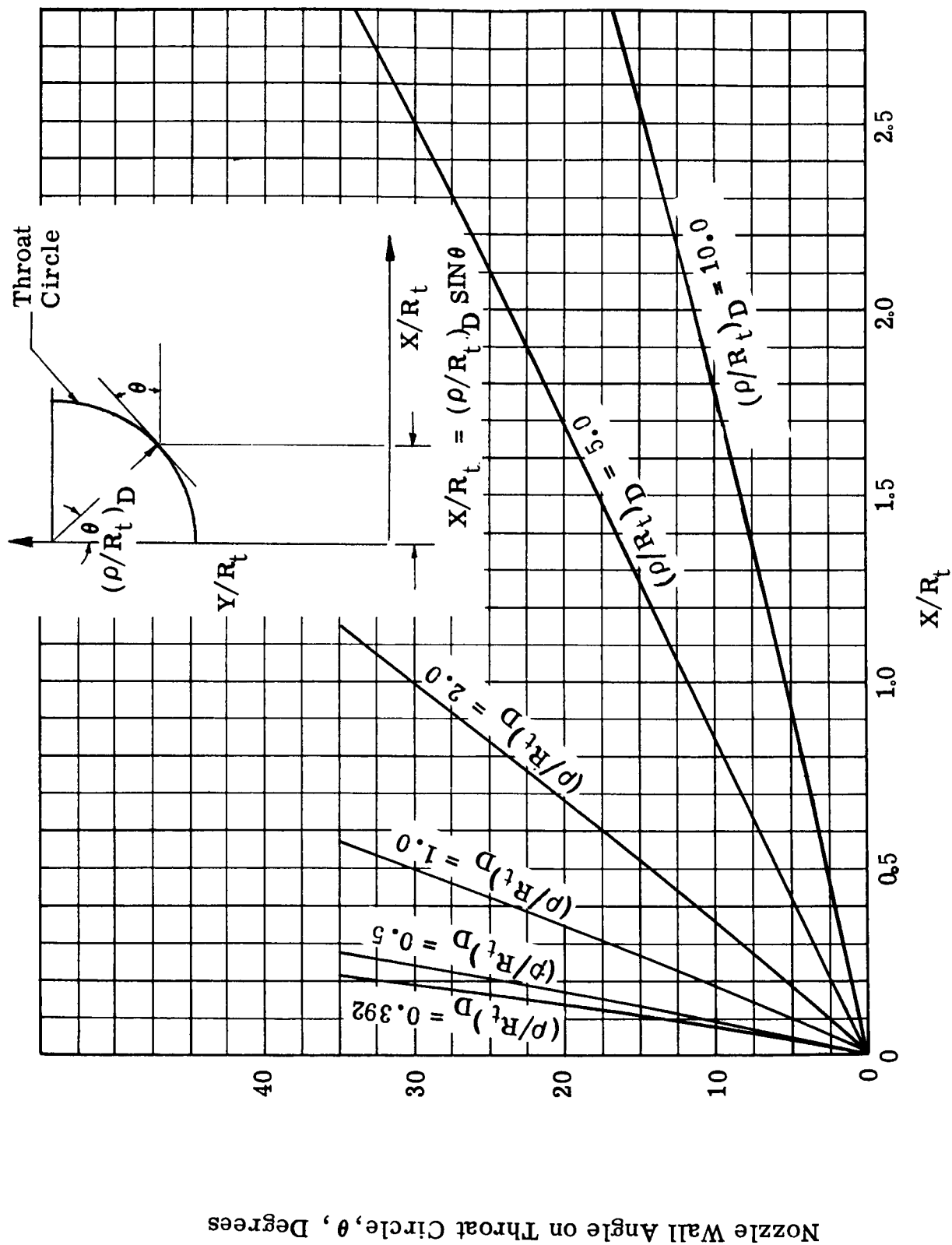


Figure A-3. Throat Circle Length Variation with Throat Circle Radius

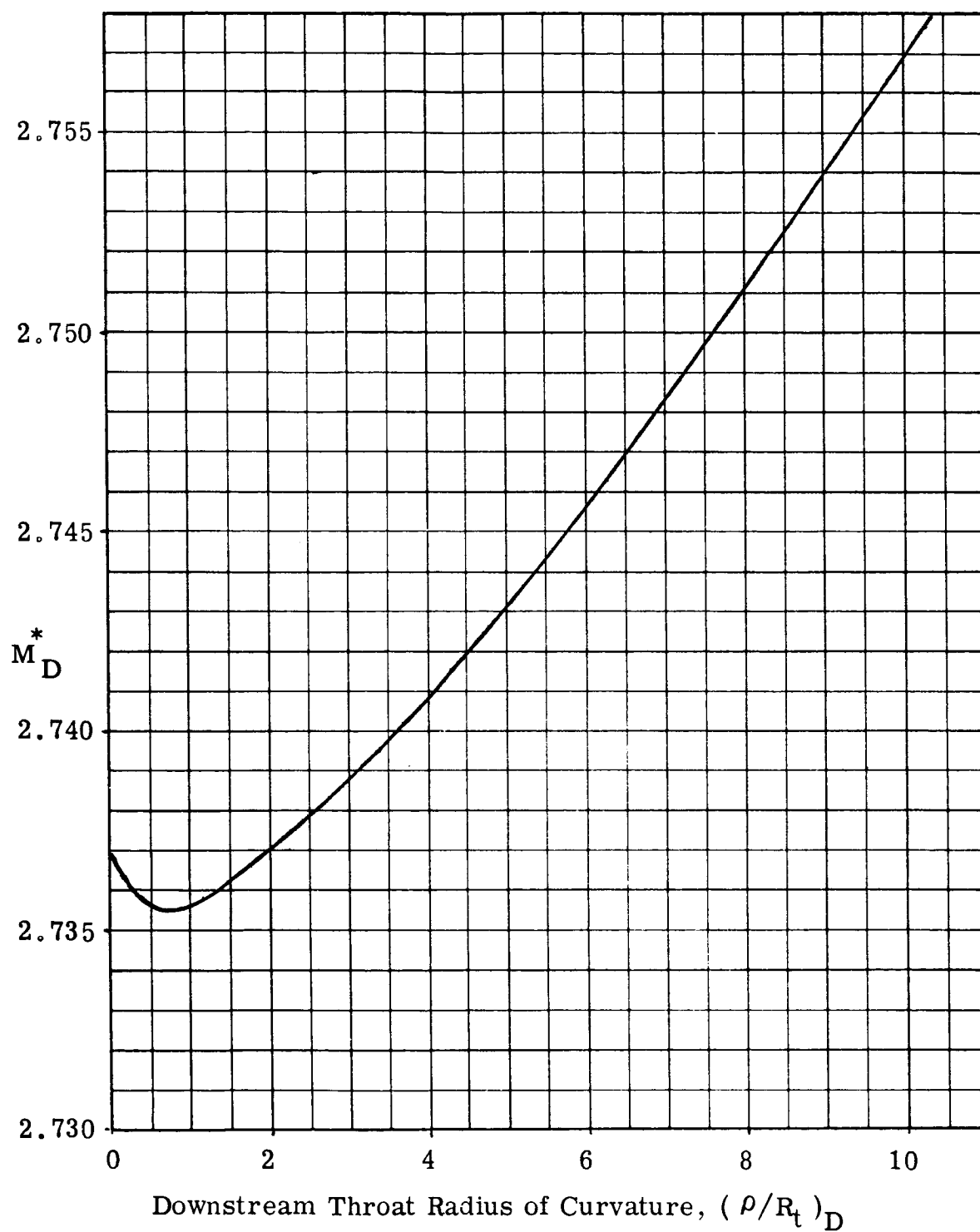


Figure A-4. Bell Nozzle Contour Parameter Variation - M_D^*



APPENDIX B

TEST RESULTS

This appendix summarizes the Task III and IV test programs in terms of test objectives and results.

TASK II

Tests 002 through 014 (1965)

These tests were stand checkout tests. The data are all questionable because of an incorrect (low) pressure ratio across the gaseous hydrogen sonic metering venturi. This was rectified by replumbing of the downstream hydrogen system. Apparently, choking was occurring at or near the injector inlet and not in the venturi meter.

Tests 001 and 002 (1966)

The test conditions were:

Chamber pressure = 100 psia

Mixture ratios = 4, 4

The main oxidizer valve opening was delayed, and then the valve failed to open fully, with the result that no stable data were obtained. No reason could be found for this failure because the valve operated satisfactorily before and after the test. No further difficulty was encountered.



Tests 003 through 005

The test conditions were:

Chamber pressure = 100 psia

Mixture ratios = 9, 9, and 12

The liquid fluorine temperature was high, resulting in low chamber pressures and mixture ratios. The data were somewhat transient: no reduction of the test 004 data was attempted. A slight hydrogen servo-system oscillation at approximately 5 cps was observed. Test 005 exceeded the maximum buzz limit.

Tests 006 through 008

The test conditions were:

Chamber pressure = 100 psia

Mixture ratios = 4, 4, and 15

The liquid fluorine system pressure drop was high because the upstream burst diaphragm relieved after the first test, resulting in low oxidizer flow and chamber pressure. Tests 006 and 007 exceeded the maximum buzz limit.



Tests 009 through 011

The test conditions were:

Chamber pressure = 100 psia

Mixture ratios = 9, 12, and 15

These were satisfactory tests, and mixture ratios and chamber pressure were slightly high but acceptable.

Tests 012 through 014

The test conditions were:

Chamber pressure = 100 psia

Mixture ratios = 4, 12 and 15

These were satisfactory tests.

Tests 015 through 019

The test conditions were:

Chamber pressure - 50 psia

Mixture ratios - 4, 9, 12, 15 and 15



The allowable buzz limit was exceeded on all tests. The measured performance was low.

Tests 020 through 025

The test conditions were:

Chamber pressure = 50 psia

Mixture ratios - 4, 4, 9, 12, 15 and 15

The allowable buzz limit was exceeded on three of the four lower mixture ratio tests. The system was modified by the addition of an orifice upstream of the main oxidizer valve. This seemed to have little effect at the low mixture ratios but significant improvement was noted at mixture ratios of 12 and 15.

Tests 026 through 028

The test conditions were:

Chamber pressure = 100 psia

Mixture ratios - 8, 12 and 15

A pretest modification to the fuel servosystem resulted in a high-amplitude, 1-cps oscillation in upstream pressure with corresponding chamber pressure and mixture ratio shifts.

Tests 029 through 031

The test conditions were:

Chamber pressure = 100 psia

Mixture ratios = 9, 12 and 15

Tests 030 and 031 were satisfactory. The buzz limit was slightly exceeded during test 029 with a high amplitude 25-cps "chug" also evident.

Tests 032 through 034

The test conditions were:

Chamber pressure = 100 psia

Mixture ratios - 8, 12 and 16

Tests 033 and 034 were satisfactory. Apparently, a poor pretest chill caused a transient liquid fluorine temperature on the first test, and poor data resulted.

Tests 035 through 039

The test conditions were:

Chamber pressure = 50 psia

Mixture ratios = 4, 4, 9, 12 and 16



The allowable buzz limit was exceeded on the first four test points. An orifice was located at the liquid fluorine injector inlet with no noticeable improvement in the chamber pressure stability.

Test 040

The test conditions were:

Chamber pressure = 50 psia

Mixture Ratio = 9

There was a failure to reach the intended altitude because of an open door on the altitude capsule. No data reduction was made.

Test 041 through 045

The test conditions were:

Chamber pressure = 50 psia

Mixture Ratio = 12, 12, 15, 15, and 15

This was a satisfactory test. Dual orifices were used in oxidizer system. There was some oscillation in fuel servo control system.



Test 046

The test conditions were:

Chamber pressure = 50 psia

Mixture ratio = 12

Major engine and facility damage occurred from a fire in the altitude capsule. Approximately 2 seconds after start the oxidizer dome inlet failed, apparently because of leakage. Subsequently, the main oxidizer valve failed to close and considerable fire and heat damage to instrumentation and control systems occurred.

Test 047 through 050

The test conditions were:

Chamber pressure = 50 psia

Mixture ratio = 9, 12, 12, and 15

The test appeared satisfactory, however, subsequent evaluation of the data indicated that the altitude capsule pressure reading was high, probably due to transducer leakage.

Test 051 through 054

The test conditions were:

Chamber pressure = 100 psia

Mixture ratio = 9, 12, 15, and 15



The test appeared satisfactory; however, subsequent evaluation of the data indicated that the altitude capsule pressure reading was high, probably due to transducer leakage.

Test 055 through 057

The test conditions were:

Chamber pressure = 100 psia

Mixture ratio = 4, 4, and 6

The allowable buzz level was exceeded on all tests.

Test 058 through 060

The test conditions were:

Chamber pressure = 200 psia

Mixture ratio = 6, 9, and 12

All tests were satisfactory, except that the maximum chamber pressure obtained was 177 psia. This appears to be the stand limit, because tank pressure and hydrogen trailer pressure were near maximum.

Test 061 through 063

The test conditions were:

Chamber pressure = 200 psia

Mixture ratio = 12, 15, and 15

All tests were satisfactory. The maximum chamber pressure was 180 psia.



Test 064

The test conditions were:

Chamber pressure = 175 psia

Mixture ratio = 9

The test was satisfactory. Additional tests were scheduled for this series; however, the facility was cut off when the television observer indicated a possible fire in the capsule. No damage was found.

Test 065 through 067

The test conditions were:

Chamber pressure = 175 psia

Mixture ratio = 9, 12, and 15

All tests were satisfactory.

Test 068 through 070

The test conditions were:

Chamber pressure - 175 psia

Mixture ratio = 9, 12, and 15

All tests were satisfactory.



Test 071 through 073

The test conditions were:

Chamber pressure = 50 psia

Mixture ratio = 12, 12, and 1

No data were obtained because the gaseous hydrogen regulator did not regulate properly, and venturi upstream pressure pegged off scale.

Test 074 through 077

The test conditions were:

Chamber pressure = 50 psia

Mixture ratio = 12, 12, 15, and 15

Test operation was satisfactory; however, a 10 division zero shift in thrust occurred during the last two tests. This was traced to an interference between the thrust chamber and a diffuser pressure tap elbow which was occurring under thermal expansion. No data were reduced.

Test 078 through 081

The test conditions were:

Chamber pressure = 50 psia

Mixture ratio = 12, 12, 15, and 15

All tests were satisfactory. The thrust shift problem was solved by changing the diffuser pressure tap elbow before the test.



Test 082 through 085

The test conditions were:

Chamber pressure = 50 psia

Mixture ratio = 4, 4, 9, and 9

Test 083 exceeded the allowable buzz limit; other tests were satisfactory.

Test 086 through 088

The test conditions were:

Chamber pressure = 100 psia

Mixture ratio = 9, 12, and 15

This was a satisfactory test.

Test 089 through 091

The test conditions were:

Chamber pressure = 100 psia

Mixture ratio = 4, 4, and 6

Some buzzing occurred on all tests, but only test 089 exceeded the allowable buzz limit.



Test 092 through 095

The test conditions were:

Chamber pressure = 50 psia

Mixture ratio = 12, 12, 15, and 15

All tests were satisfactory. A drop in chamber pressure and oxidizer flowmeter pressure occurred near the end of test 092; however, stable operation was obtained prior to this. Operation was normal at cutoff. No reason could be found.

Test 096 through 099

The test conditions were:

Chamber pressure - 50 psia

Mixture ratio = 12, 12, 15, and 15

All tests were satisfactory.

Test 100 through 103

The test conditions were:

Chamber pressure = 50 psia

Mixture ratio = 4, 4, 9, and 9



These were satisfactory tests. Some buzzing occurred on all tests, but all were within allowable limits. Thrust No. 1 was unacceptable on posttest calibration, and was not used for data reduction.

Test 104 through 106

The test conditions were:

Chamber pressure = 100 psia

Mixture ratio = 9, 12, and 15

All tests were satisfactory.

Test 110 through 112

The test conditions were:

Chamber pressure = 175 psia

Mixture ratio = 9, 12, and 15

All tests were satisfactory. The oscillograph record for test 110 was lost because of a latch failure at test start; therefore, flowrates were reduced from the DIGR charts.

Test 113 through 116

The test conditions were:

Chamber pressure = 175 psia

Mixture ratio = 15, 12, 9, and 6



Test 114, 115, and 116 were satisfactory. Test 113 was lost because of an apparent poor oxidizer chill. Indications are that a larger vapor pocket occurred just upstream of the main valve, resulting in transient data throughout the test.

Test 117 through 119

The test conditions were:

Chamber pressure = 50 psia

Mixture ratio = 12, 12, and 15

All tests were satisfactory. A fourth test had been scheduled, but one chamber pressure No. 2 transducer failed during test 119.

Test 120 through 122

The test conditions were:

Chamber pressure = 50 psia

Mixture ratio = 15, 12, and 15

All tests were satisfactory. Test 122 was allowed to go to thrust chamber skin temperature red line value. The duration was approximately 6 seconds. No hardware damage was noted.



Test 123 through 126

The test conditions were:

Chamber pressure = 50 psia

Mixture ratio = 4, 4, 9, and 9

Test 123 and 124 exceeded the maximum allowable buzz limit. Other tests were satisfactory.

Test 127 through 130

The test conditions were:

Chamber pressure = 50 psia

Mixture ratio = 15, 15, 12, and 12

All tests were satisfactory.

TASK IV

The following tests were conducted during Task IV and all had a nominal chamber pressure of 50 psia.

Test 146 through 148 (1966)

The test conditions were:

Mixture ratio = 9, 12, 15



These were the initial tests for Task IV and altitude simulation was deleted. The test purpose was to recalibrate the system after several changes that were made in the feed systems. The LF_2 temperature was colder than anticipated and actual mixture ratio was 11, 14, and 18. Test 149 exceeds the allowable buzz limit.

Test 149 through 151

The test conditions were:

Mixture ratio 9, 15, 9

Calibration tests with no altitude simulation. Test 149 exceeds the allowable buzz limit.

Test 152

The test conditions were:

Mixture ratio = 15

A fire occurred in the fluorine main valve at test start. Damage was limited to the valve and some instrumentation wiring.

Test 153 through 155

Mixture ratio 9.5, 9, 8.5

Calibration test with no altitude simulation. New LF_2 main valve installed pretest.



Test 123 through 126

The test conditions were:

Chamber pressure = 50 psia

Mixture ratio = 4, 4, 9, and 9

Test 123 and 124 exceeded the maximum allowable buzz limit. Other tests were satisfactory.

Test 127 through 130

The test conditions were:

Chamber pressure = 50 psia

Mixture ratio = 15, 15, 12, and 12

All tests were satisfactory.

TASK IV

The following tests were conducted during Task IV and all had a nominal chamber pressure of 50 psia.

Test 146 through 148 (1966)

The test conditions were:

Mixture ratio = 9, 12, 15



These were the initial tests for Task IV and altitude simulation was deleted. The test purpose was to recalibrate the system after several changes that were made in the feed systems. The LF_2 temperature was colder than anticipated and actual mixture ratio was 11, 14, and 18. Test 149 exceeds the allowable buzz limit.

Test 149 through 151

The test conditions were:

Mixture ratio 9, 15, 9

Calibration tests with no altitude simulation. Test 149 exceeds the allowable buzz limit.

Test 152

The test conditions were:

Mixture ratio = 15

A fire occurred in the fluorine main valve at test start. Damage was limited to the valve and some instrumentation wiring.

Test 153 through 155

Mixture ratio 9.5, 9, 8.5

Calibration test with no altitude simulation. New LF_2 main valve installed pretest.



Test 156 through 158

Mixture ratio 9.5, 9.0, 8.5

Repeat of previous test.

Test 159 and 160

Mixture ratio 9, 9

Satisfactory test.

Test 161 through 163

Mixture ratio 9, 9, 9

Allowable buzz level exceeded on all tests.

Test 164 through 167

Mixture ratio 15, 12, 15, 12

Allowable buzz level exceeded on first two tests. Malfunction of hydrogen servo system resulted in excessively low mixture ratio on the second test.



Test 168 through 171

Mixture ratio 15, 12, 15, 12

Required altitude was not attained because of altitude capsule door failing to shut completely.

Test 172 through 175

Mixture ratio 15, 12, 15, 12

Satisfactory test.

Test 001 through 004 (1967)

Mixture ratio 12, 15, 12, 15

Satisfactory test except chamber pressure and mixture ratio low because of excessive oxidizer system pressure drop. No apparent reason.

Test 005 through 007

Mixture ratio 12, 15, 15

Ambient test for system checkout and calibration. Satisfactory test.

Test 008 and 009

Mixture ratio 12, 15

Chamber pressure excessively high.



Test 010 through 012

Mixture ratio 12, 15, 12

Satisfactory test.

Test 013 through 016

Mixture ratio 12, 15, 12, 15

Satisfactory test.

Test 017 through 020

Mixture ratio 12, 15, 12, 15

Data questionable because of excessive thrust system hysteresis in the posttest calibration. The thrust system was realigned after the test.

Test 021 through 024

Mixture ratio 9, 11, 9, 11

The allowable buzz level was exceeded on the first three tests.

Test 025 through 028

Mixture ratio 9, 11, 9, 11

Satisfactory test.



APPENDIX C

MEASUREMENT SYSTEM ANALYSES

As a part of the overall analyses of the test data, an estimate of precision of the vacuum thrust coefficient value was made. This was accomplished by statistically combining the precisions of the parameters which define the thrust coefficient. The term "precision" used here represents an overall measurement uncertainty and includes traceability to the National Bureau of Standards. The mathematical model used to calculate these precisions is consistent with Rocketdyne's formal measurement systems analysis program used in acceptance testing of rocket engines and components. In this method, all precisions are quoted on a 95-percent confidence basis. The results are presented in subsequent paragraphs and summarized in Table C-1.

THRUST

Vacuum thrust is computed from three independent measurements; measured or ambient thrust, environmental (altitude chamber) pressure, and thrust chamber nozzle exit area as follows:

$$F_{vac} = F_{meas} + P_a A_e$$

Each of these measurements is discussed below.

Measured Thrust

Precision for this measurement was computed on the basis of the repeatability of the key number computed from the end-to-end system calibrations conducted before and after each hyperflow operation. The key number is the scaling factor determined for the particular measurement as discussed in the Data Reduction section of this report.



TABLE C-1

MEASUREMENT PRECISION

Parameter	Precision, percent
Measured Thrust	± 0.2015
Environmental Pressure	± 0.175
Exit Area	± 1.79
Vacuum Thrust	± 0.202
Chamber Pressure	± 0.097
Throat Area	± 0.32



APPENDIX C

MEASUREMENT SYSTEM ANALYSES

As a part of the overall analyses of the test data, an estimate of precision of the vacuum thrust coefficient value was made. This was accomplished by statistically combining the precisions of the parameters which define the thrust coefficient. The term "precision" used here represents an overall measurement uncertainty and includes traceability to the National Bureau of Standards. The mathematical model used to calculate these precisions is consistent with Rocketdyne's formal measurement systems analysis program used in acceptance testing of rocket engines and components. In this method, all precisions are quoted on a 95-percent confidence basis. The results are presented in subsequent paragraphs and summarized in Table C-1.

THRUST

Vacuum thrust is computed from three independent measurements; measured or ambient thrust, environmental (altitude chamber) pressure, and thrust chamber nozzle exit area as follows:

$$F_{vac} = F_{meas} + P_a A_e$$

Each of these measurements is discussed below.

Measured Thrust

Precision for this measurement was computed on the basis of the repeatability of the key number computed from the end-to-end system calibrations conducted before and after each hyperflow operation. The key number is the scaling factor determined for the particular measurement as discussed in the Data Reduction section of this report.



TABLE C-1

MEASUREMENT PRECISION

Parameter	Precision, percent
Measured Thrust	± 0.2015
Environmental Pressure	± 0.175
Exit Area	± 1.79
Vacuum Thrust	± 0.202
Chamber Pressure	± 0.097
Throat Area	± 0.32



Precision is calculated from the following equation:

$$\text{Precision} = \left\{ \left[\left(\frac{SP_s}{SP_r} \right)^2 \left(\frac{100t}{Y_{\max}} \right)^2 \right] \left[\sum_{i=1}^N \frac{w_i (\hat{Y} - Y_i)^2}{\bar{W}^2 N(N-K)} \right] + \left[\left(\frac{SP_t}{SP_r} \right) C_t \right]^2 \right\}^{1/2}$$

where

- t = Student's distribution for 95-percent confidence level
- Y_{\max} = Maximum deflection equivalent to 100-percent full scale
- Y = Observed deflection
- SP_s = Recording system span
- SP_r = Required system span
- SP_t = Span at which traceability constant percentage is based
- C_t = Traceability constant
- K = Number of parameters estimated in order to define Y
- N = Number of samples
- w_i = Weighting factor for an individual sample
- \bar{W}^2 = The average of the sum of the squares of the individual weighting factors

$$\bar{W}^2 = \sum_{i=1}^N \frac{w_i^2}{W^2}$$

- \hat{Y} = Weighted mean

$$\hat{Y} = \sum_{i=1}^N \frac{w_i^2 Y_i}{W^2}$$

where

- W^2 = The sum of the squares of the individual weighting factors



Each of the samples is independent and each has equal weight consequently, the equation can be reduced to the form

$$\text{Precision} = \left\{ \left[\left(\frac{SP_s}{SP_r} \right)^2 \left(\frac{100t}{Y_{\max}} \right)^2 \right] \left[\sum_{i=1}^N \frac{(\bar{Y} - Y_i)^2}{N(N-K)} \right] + \left[\left(\frac{SP_t}{SP_r} \right) C_t \right]^2 \right\}^{1/2}$$

Table C-2 shows the calibration key numbers for the four thrust systems used during the latter portion of the test program. The remainder of the terms are:

SP_s	=	1400 pounds
SP_r	=	1200 pounds
Y_{\max}	=	1400 pounds
SP_t	=	4000 pounds
C_t	=	0.025 percent
N	=	7
K	=	1
$\frac{t_{0.05}}{2}$	=	2.45

Substituting in the equation yields the following:

Precision F1-1 (13A)	=	0.3494
Precision F1-2 (13B)	=	0.6363
Precision F2-1 (14A)	=	0.2402
Precision F2-2 (14B)	=	0.2548



TABLE C-2

THRUST CALIBRATION KEY NUMBERS

Test No.	Recorder and Key Number			
	13A	13B	14A	14B
1-4	1160.01	1159.23	1161.94	1161.80
8-9	1154.24	1151.53	1161.15	1161.99
10-12	1149.98	1167.49	1159.63	1160.19
13-16	1150.53	1170.63	1168.33	1166.76
17-20*	1153.92	1170.48	1163.80	1168.00
24	1149.46	1174.81	1163.78	1166.62
25-28	1146.47	1166.66	1160.51	1161.85

*Pretest only



Statistically combining these, a pooled precision is obtained:

$$\text{Precision } F_{\text{meas}}_{\text{pool}} = \left(\frac{\sum \text{Prec}_i^2}{N} \right)^{1/2} = 0.403$$

This can be considered as the best estimate of the precision of each of the measurements. Combining this then, the precision of the averaged value of the four measurements is:

$$\text{Precision } F_{\text{meas}} = \frac{\text{Precision } F_{\text{meas}}_{\text{pool}}}{\sqrt{M}}$$

where M is the number of measurements.

$$\text{Precision } F_{\text{meas}} = 0.2015$$

Environmental Pressure (Altitude Chamber Pressure)

End-to-end calibrations were not made on pressure measurement systems. Consequently, the precision for this measurement had to be estimated by combining the estimated precision of the recording system with that obtained during the laboratory calibration of pressure transducer. The recording system precision was estimated by evaluating the deviation of the system when subjected to a known input. This was accomplished by obtaining a pooled deviation based on the variation of the pre- and posttest electrical simulation.

$$\sigma_{P_a}_{\text{pool}} = \left[\frac{\sum \frac{1}{2} (X_1 - X_2)^2}{N} \right]^{1/2}$$

where

X_1 = pretest span

X_2 = posttest span



Then

$$\text{Precision } P_a = \left\{ \left[\left(\frac{SP_s}{SP_r} \right)^2 \left(\frac{100t}{Y_{\max}} \right)^2 \right] \left[\sigma_{\text{pool}}^2 \right] + PR_x^2 \right\}^{1/2}$$

where PR_x = transducer calibration precision including NBS traceability.

Substituting, using the Task IV set of test data as representative

$$\begin{aligned} \text{Precision } P_a &= \left\{ \left[\left(\frac{0.2}{0.2} \right)^2 \left(\frac{100(2.36)}{0.2} \right)^2 \right] \left[15.44 \times 10^{-8} \right] + \right. \\ &\quad \left. (0.169)^2 \right\}^{1/2} = 0.175 \end{aligned}$$

Exit Area

Four diameter measurements were made each time the exit area was measured. The possible error in this measurement was analyzed in terms of the deviation within each set. These deviations were then combined as above to determine a pooled deviation for the data.

The resultant is then multiplied by the corresponding "t" factor for the 95-percent confidence band

$$\sigma D_{e_{\text{pool}}} (t) = 0.292 \text{ inch}$$

which is equivalent to 0.898 percent. For the area, this then is equivalent to 1.79 percent.



Thrust Vacuum

Because vacuum thrust is a function of the various measurements as indicated previously, the various precisions of these measurements must be combined to obtain the overall precision of the measurement. It is obvious that these measurements do not contribute equally to the final value of thrust; therefore, influence coefficients for each of the parameters must be included in the analysis.

This is accomplished as follows:

$$F_{vac} = F_{meas} + P_a A_e$$

$$\sigma_{F_v}^2 = \left(\frac{\partial F_v}{\partial F_m} \right)^2 \sigma_{F_m}^2 + \left(\frac{\partial F_v}{\partial P_a} \right)^2 \sigma_{P_a}^2 + \left(\frac{\partial F_v}{\partial A_e} \right)^2 \sigma_{A_e}^2$$

Evaluating this at nominal values:

$$\sigma_{F_v}^2 = (1)^2 \sigma_{F_m}^2 + (\bar{A}_e)^2 \sigma_{P_a}^2 + (\bar{P}_a)^2 \sigma_{A_e}^2$$

defining:

$$Prec_{F_{meas}} = \frac{\sigma_{F_m}}{\bar{F}_m}; \quad Prec_{P_a} = \frac{\sigma_{P_a}}{\bar{P}_a}; \quad Prec_{A_e} = \frac{\sigma_{A_e}}{\bar{A}_e};$$

and

$$Prec_{F_{vac}} = \frac{\sigma_{F_{vac}}}{\bar{F}_{vac}}$$

and substituting, then:

$$(\bar{F}_v)^2 Prec_{F_v}^2 = [Prec_{F_m} (\bar{F}_m)]^2 + (\bar{A}_e)^2 (\bar{P}_a Prec_{P_a})^2 + \bar{P}_a^2 (\bar{A}_e Prec_{A_e})^2$$



$$\text{Prec}_{F_v}^2 = \frac{1}{\overline{F_v}} [(\overline{F_m} \text{Prec}_{F_m})^2 + (\overline{A_e} \overline{P_a} \text{Prec}_{P_a})^2 + (\overline{P_a} \overline{A_e} \text{Prec}_{A_e})^2]$$

assuming nominal values

$$\overline{F_v} = 1233 \text{ pounds}$$

$$\overline{F_m} = 1200 \text{ pounds}$$

$$\overline{A_e} = 830 \text{ in.}^2$$

$$\overline{P_a} = 0.04 \text{ psia}$$

then

$$\text{Precision}_{F_{vac}} = 0.202$$

CHAMBER PRESSURE

Precision for the chamber pressure measurement was calculated in a manner similar to that discussed previously for the environmental pressure. A pooled deviation was computed based on the variation of the pre- and post-test electrical simulation, then combining this with transducer precision the following values were obtained.

$$\text{Prec } P_{c-1} = 0.2000$$

$$P_{c2-2} = 0.1288$$

$$P_{c2-3} = 0.1988$$



Early in the program, it was decided that averaging for computing the chamber pressure from the three measurements would be done on a weighed basis utilizing the precision of the transducer to compute the weighing factor. This follows from the assumption that on the average precision one recording system is essentially the same as another. This was subsequently verified when the posttest analysis of the recording system variances was conducted. The averaging method used results in the following:

Assuming A, B, and C represent the precision of the three transducers then

$$P_{c2 \text{ avg}} = \frac{\frac{1}{A} P_{c2A} + \frac{1}{B} P_{c2B} + \frac{1}{C} P_{c2C}}{\frac{1}{A} + \frac{1}{B} + \frac{1}{C}}$$

this reduces to:

$$P_{c2 \text{ avg}} = \frac{(BC) P_{c2A} + (AC) P_{c2B} + (AB) P_{c2C}}{BC + AC + AB}$$

Statistically summing this to obtain the precision of the averaged chamber pressure is accomplished as follows:

$$\begin{aligned} \text{Prec}_{P_{c2 \text{ avg}}} &= \left[\frac{(BC)^2 A^2 + (AC)^2 B^2 + (AB)^2 C^2}{(BC + AC + AB)^2} \right]^{1/2} \\ &= \left[\frac{3 (ABC)^2}{(BC + AC + AB)^2} \right]^{1/2} = \frac{\sqrt{3} ABC}{BC + AC + AB} \end{aligned}$$

Then, substituting the above

$$\text{Prec}_{P_{c2 \text{ avg}}} = 0.097$$



THROAT AREA

Evaluating throat area in the same manner as discussed previously for the exit area:

$$\begin{aligned}\sigma_{D_{t_{\text{pool}}}}(t) &= 0.007 \text{ inch} \\ &= 0.16 \text{ percent}\end{aligned}$$

which would be equal to 0.32 percent for the throat area.

THRUST COEFFICIENT

The precision of the final vacuum thrust coefficient was computed from the basic equation,

$$F_{\text{vac}} = P_{C_{ns}} A_t C_F$$

as shown below

$$C_F = \frac{F_{\text{vac}}}{P_{C_{ns}} A_t}$$

$$\begin{aligned}\sigma_{C_F}^2 &= \left(\frac{\partial C_F}{\partial F} \right)^2 \sigma_F^2 + \left(-\frac{\bar{F}}{\bar{A}_t \bar{P}_c^2} \right)^2 \sigma_{P_c}^2 + \left(-\frac{\bar{F}}{\bar{A}_t^2 \bar{P}_c} \right)^2 \sigma_{A_t}^2 \\ &= \left(\frac{1}{\bar{P}_c \bar{A}_t} \right)^2 \sigma_F^2 + \left(-\frac{\bar{F}}{\bar{A}_t \bar{P}_c^2} \right)^2 \sigma_{P_c}^2 + \left(-\frac{\bar{F}}{\bar{A}_t^2 \bar{P}_c} \right)^2 \sigma_{A_t}^2\end{aligned}$$



$$\frac{\sigma_{C_F}^2}{\bar{C}_F^2} = \frac{\sigma_F^2}{\bar{F}^2} + \frac{\sigma_{P_c}^2}{\bar{P}_c^2} + \frac{\sigma_{A_t}^2}{\bar{A}_t^2}$$

$$\begin{aligned} \text{Prec}_{C_F} &= [\text{Prec}_{F_{\text{vac}}}^2 + \text{Prec}_{P_c}^2 + \text{Prec}_{A_t}^2]^{1/2} \\ &= [0.0408 + 0.0094 + 0.1024]^{1/2} = [0.1626]^{1/2} \\ &= 0.403 \end{aligned}$$

Unclassified

Security Classification

DOCUMENT CONTROL DATA - R&D		
(Security classification of title, body of abstract and indexing annotation must be entered when the overall report is classified)		
1. ORIGINATING ACTIVITY (Corporate author) Rocketdyne, a Division of North American Aviation, Inc., 6633 Canoga Avenue, Canoga Park, California		2a. REPORT SECURITY CLASSIFICATION Unclassified
		2b. GROUP
3. REPORT TITLE FINAL REPORT FLUORINE-HYDROGEN PERFORMANCE EVALUATION PHASE I, PART II: NOZZLE PERFORMANCE ANALYSIS AND DEMONSTRATION		
4. DESCRIPTIVE NOTES (Type of report and inclusive dates) Final Report, April 1967		
5. AUTHOR(S) (Last name, first name, initial) Waldman, B. J. Shuster, E. B.		
6. REPORT DATE 31 July 1967	7a. TOTAL NO. OF PAGES 338 & xxii	7b. NO. OF REFS 27
8a. CONTRACT OR GRANT NO. NASW-1229	9a. ORIGINATOR'S REPORT NUMBER(S) R-6636-2	
b. PROJECT NO.		
c.	9b. OTHER REPORT NO(S) (Any other numbers that may be assigned this report)	
d.	NASA CR-72038	
10. AVAILABILITY/LIMITATION NOTICES		
11. SUPPLEMENTARY NOTES	12. SPONSORING MILITARY ACTIVITY NASA	
13. ABSTRACT <p>This volume, Part II of the Fluorine/Hydrogen Performance Evaluation Program Report presents the results of a research program conducted under NASA Contract NASW-1229. Analytical and experimental studies were performed to establish the deliverable thrust chamber performance of the fluorine/hydrogen propellant combination. Six high area ratio nozzle contours were tested in an altitude simulation facility, and the results were compared to analytical predictions. A new type of nozzle contour, intended to improve delivered performance by encouraging chemical recombination, was designed and experimentally evaluated.</p>		

DD FORM 1473
1 JAN 64

Unclassified

Security Classification

14. KEY WORDS	LINK A		LINK B		LINK C	
	ROLE	WT	ROLE	WT	ROLE	WT
Fluorine Hydrogen Chemical Reaction Kinetics Nozzles Performance Heat Flux						

INSTRUCTIONS

1. **ORIGINATING ACTIVITY:** Enter the name and address of the contractor, subcontractor, grantee, Department of Defense activity or other organization (*corporate author*) issuing the report.

2a. **REPORT SECURITY CLASSIFICATION:** Enter the overall security classification of the report. Indicate whether "Restricted Data" is included. Marking is to be in accordance with appropriate security regulations.

2b. **GROUP:** Automatic downgrading is specified in DoD Directive 5200.10 and Armed Forces Industrial Manual. Enter the group number. Also, when applicable, show that optional markings have been used for Group 3 and Group 4 as authorized.

3. **REPORT TITLE:** Enter the complete report title in all capital letters. Titles in all cases should be unclassified. If a meaningful title cannot be selected without classification, show title classification in all capitals in parenthesis immediately following the title.

4. **DESCRIPTIVE NOTES:** If appropriate, enter the type of report, e.g., interim, progress, summary, annual, or final. Give the inclusive dates when a specific reporting period is covered.

5. **AUTHOR(S):** Enter the name(s) of author(s) as shown on or in the report. Enter last name, first name, middle initial. If military, show rank and branch of service. The name of the principal author is an absolute minimum requirement.

6. **REPORT DATE:** Enter the date of the report as day, month, year, or month, year. If more than one date appears on the report, use date of publication.

7a. **TOTAL NUMBER OF PAGES:** The total page count should follow normal pagination procedures, i.e., enter the number of pages containing information.

7b. **NUMBER OF REFERENCES:** Enter the total number of references cited in the report.

8a. **CONTRACT OR GRANT NUMBER:** If appropriate, enter the applicable number of the contract or grant under which the report was written.

8b, 8c, & 8d. **PROJECT NUMBER:** Enter the appropriate military department identification, such as project number, subproject number, system numbers, task number, etc.

9a. **ORIGINATOR'S REPORT NUMBER(S):** Enter the official report number by which the document will be identified and controlled by the originating activity. This number must be unique to this report.

9b. **OTHER REPORT NUMBER(S):** If the report has been assigned any other report numbers (*either by the originator or by the sponsor*), also enter this number(s).

10. **AVAILABILITY/LIMITATION NOTICES:** Enter any limitations on further dissemination of the report, other than those

imposed by security classification, using standard statements such as:

- (1) "Qualified requesters may obtain copies of this report from DDC."
- (2) "Foreign announcement and dissemination of this report by DDC is not authorized."
- (3) "U. S. Government agencies may obtain copies of this report directly from DDC. Other qualified DDC users shall request through _____."
- (4) "U. S. military agencies may obtain copies of this report directly from DDC. Other qualified users shall request through _____."
- (5) "All distribution of this report is controlled. Qualified DDC users shall request through _____."

If the report has been furnished to the Office of Technical Services, Department of Commerce, for sale to the public, indicate this fact and enter the price, if known.

11. **SUPPLEMENTARY NOTES:** Use for additional explanatory notes.

12. **SPONSORING MILITARY ACTIVITY:** Enter the name of the departmental project office or laboratory sponsoring (*paying for*) the research and development. Include address.

13. **ABSTRACT:** Enter an abstract giving a brief and factual summary of the document indicative of the report, even though it may also appear elsewhere in the body of the technical report. If additional space is required, a continuation sheet shall be attached.

It is highly desirable that the abstract of classified reports be unclassified. Each paragraph of the abstract shall end with an indication of the military security classification of the information in the paragraph, represented as (TS), (S), (C), or (U).

There is no limitation on the length of the abstract. However, the suggested length is from 150 to 225 words.

14. **KEY WORDS:** Key words are technically meaningful terms or short phrases that characterize a report and may be used as index entries for cataloging the report. Key words must be selected so that no security classification is required. Identifiers, such as equipment model designation, trade name, military project code name, geographic location, may be used as key words but will be followed by an indication of technical content. The assignment of links, rules, and weights is optional.